Transactions of the ASME

Technical Editor, **L. B. FREUND**

Division of Engineering
Brown University
Providence, R.I. 02912

APPLIED MECHANICS DIVISION

Chairman, **J. D. ACHENBACH**
Secretary, **M. M. CARROLL**
Associate Editors,
T. BELYTSCHKO
D. B. BOGY
R. M. CHRISTENSEN
R. J. CLIFTON
MAURICE HOLT
W. D. IWAN
W. G. KNAUSS
F. A. LECKIE
L. E. MALVERN
FRANCIS C. MOON
R. P. NORDGREN
R. H. PLAUT
J. R. RICE
R. T. SHIELD
C. T. SUN
J. S. WALKER
G. A. WEMPNER
S. E. WIDNALL

BOARD ON COMMUNICATIONS
Chairman and Vice-President
K. N. REID, JR.

Members-at-Large
W. BEGELL
J. T. COKONIS
W. G. GOTTENBERG
H. C. REEDER
D. KOENIG
M. KUTZ
F. LANDIS
R. E. NICKELL
J. E. ORTLOFF
C. PHILLIPS

President, **G. KOTNICK**
Exec. Dir.
PAUL ALLMENDINGER
Treasurer, **ROBERT A. BENNETT**

PUBLISHING STAFF
Mng. Dir., Pub., **J. J. FREY**
Dep. Mng. Dir., Pub.
JOS. SANSONE
Managing Editor,
CORNELIA MONAHAN
Production Editor, **SUZANNE MAGIDA**
Prod. Asst., **MARISOL ANDINO**

The Journal of Applied Mechanics (ISSN 0021-8936) is published quarterly for $72 per year by The American Society of Mechanical Engineers, 345 East 47th Street, New York, NY 10017. Second class postage paid at New York, NY and additional mailing offices. POSTMASTER: Send address changes to The Journal of Applied Mechanics, c/o THE AMERICAN SOCIETY OF MECHANICAL ENGINEERS, P.O. Box 3199, Grand Central Station, New York, NY 10163. **CHANGES OF ADDRESS** must be received at Society headquarters seven weeks before they are to be effective. Please send old label and new address.

PRICES: To members, $36.00, annually; to nonmembers, $90.00. Add $6.00 for postage to countries outside the United States and Canada.

STATEMENT from By-Laws. The Society shall not be responsible for statements or opinions advanced in papers or . . . printed in its publications (B7.1, Par. 3).

COPYRIGHT © 1984 by the American Society of Mechanical Engineers. Reprints from this publication may be made on condition that full credit be given the TRANSACTIONS OF THE ASME, JOURNAL OF APPLIED MECHANICS, and the author, and date of publication be stated.

INDEXED by the Engineering Index, Inc.

Journal of Applied Mechanics

Published Quarterly by The American Society of Mechanical Engineers

VOLUME 51 • NUMBER 3 • SEPTEMBER 1984

455 Reviewers

TECHNICAL PAPERS

457 **The Study of Gravitational Nozzle Flows by Hodograph Transformations** (84-WA/APM-8)
P. C. Chan and W. L. Chow

465 **The Incremental Strain Growth of an Elastic-Plastic Body Loaded in Excess of the Shakedown Limit** (84-WA/APM-10)
A. R. S. Ponter and A. C. F. Cocks

470 **The Incremental Strain Growth of Elastic-Plastic Bodies Subjected to High Levels of Cyclic Thermal Loading** (84-WA/APM-11)
A. R. S. Ponter and A. C. F. Cocks

475 **Notch-Tip Stresses in a Creeping Solid**
J. L. Bassani

481 **An Investigation of Localization in a Porous Elastic Material Using Homogenization Theory**
R. Abeyaratne and N. Triantafyllidis

487 **Calculations for Uniaxial Stress and Strain Cycling in Plasticity**
P. M. Naghdi and D. J. Nikkel, Jr.

494 **The Estimation of Large Deflections of a Portal Frame Under Asymmetric Pulse Loading** (84-WA/APM-1)
J. L. Raphanel and P.S. Symonds

501 **Impact and Bending of a Rigid-Plastic Fan Blade** (84-WA/APM-14)
W. J. Stronge and T. Shioya

505 **Simplified Large Deflection Mode Solutions for Impulsively Loaded, Viscoplastic, Circular Membranes** (84-APM-41)
N. Perrone and P. Bhadra

510 **Dynamic Characteristics of Large Repetitive Framelike Structures** (84-APM-35)
A. H. Nayfeh and M. S. Hartle

519 **Large Deflections of a Simply Supported Beam Subjected to Moment of One End**
P. Seide

526 **Optimal Forms of Shallow Shells With Circular Boundary Part 1: Maximum Fundamental Frequency** (84-APM-38)
R. H. Plaut, L. W. Johnson, and R. Parbery

531 **Optimal Forms of Shallow Shells With Circular Boundary Part 2: Maximum Buckling Load** (84-APM-39)
R. H. Plaut, and L. W. Johnson

536 **Optimal Forms of Shallow Shells With Circular Boundary Part 3: Maximum Enclosed Volume** (84-APM-40)
R. H. Plaut and L. W. Johnson

540 **Bounds for Elastic Moduli of Multiphase Short-Fiber Composites** (84-APM-36)
S. Nomura and T. -W. Chou

546 **An Elastic Potential for the Nonlinear Response of Unidirectional Graphite Composites** (84-WA/APM-5)
M.-J. Pindera and C. T. Herakovich

551 **A Laminated Beam Theory With Interlayer Slip**
H. Murakami

560 **Asymptotic Behavior of Heavy Column and Riser Stability Boundaries** (84-WA/APM-7)
M. M. Bernitsas and T. Kokkinis

566 **Effects of Mode Interaction on Collapse of Short, Imperfect, Thin-Walled Columns** (84-WA/APM-16)
D. Hui

574 **Analysis of Clamped Plates on Elastic Foundation by the Boundary Integral Equation Method** (84-WA/APM-6)
J. T. Katsikadelis and A. E. Armenakas

581 **Vibrations of Thick Free Circular Plates, Exact Versus Approximate Solutions** (84-WA/APM-19)
J. R. Hutchinson

586 **Simple Waves and Shock Waves Generated by an Incident Shock Wave in Two-Dimensional Hyperelastic Materials** (84-WA/APM-12)
Y. Li and T. C. T. Ting

595 **Torsional Shock Waves in a Viscoelastic Rod**
N. Sugimoto, Y. Yamane, and T. Kakutani

602 **Gas-Gun Experiments Determine Forces on Penatrators Into Geological Targets** (84-WA/APM-3)
M. J. Forrestal, L. M. Lee, B. D. Jenrette, and R. E. Setchell

608 **On the Nonlocal Theory of Wave Propagation in Elastic Plates**
J. L. Nowinski

(Contents continued on Inside Back Cover)

Downloaded 04 May 2010 to 171.66.16.49. Redistribution subject to ASME license or copyright; see http://www.asme.org/terms/Terms_Use.cfm

614 **Finite Element Eigenfunction Method (FEEM) for Elastic Wave Scattering by Arbitrary Three-Dimensional Axisymmetric Scattering** (84-APM-37)
J. H. Su, V. V. Varadan, and V. K. Varadan

622 **An Elastic Punch Moving Across the Surface of a Semi-Infinite Solid** (84-WA/APM-2)
G. G. Adams and I. Zeid

630 **Axisymmetric Solutions in Elastostatics and Elastic Wave Propagation by Ascent Methods** (84-WA/APM-4)
F. R. Norwood

638 **Thermoelastic Displacements and Stresses Due to a Heat Source Moving Over the Surface of a Half Plane** (84-WA/APM-17)
J. R. Barber

641 **Propagation and Scattering of SH-Waves in Semi-Infinite Domains Using a Time-Dependent Boundary Element Method** (84-WA/APM-9)
J. M. Rice and M. H. Sadd

646 **Scattering of Elastic Waves by a Plane Crack of Finite Width** (84-WA/APM-13)
J. H. M. T. van der Hijden and F. L. Neerhoff

652 **On Wave Modes Zero Group Velocity in an Elastic Layer** (84-WA/APM-18)
J. L. Tassoulas, T. R. Akylas

657 **The Improved Frequency Repsonse Function and its Effect on Modal Circle Fits**
K. B. Elliott and L. D. Mitchell

664 **Observation and Evolution of Chaos for an Autonomous System** (84-WA/APM-15)
E. H. Dowell

674 **An Integral Equation Method for the First-Passage Problem in Random Vibration**
P. H. Madsen and S. Krenk

680 **Wheelset Mechanics During Wheelclimb Derailment**
A. Karmel and L. M. Sweet

BRIEF NOTES

Determination of Near-Surface Plastic Deformation in Sliding Contacts 687
F. E. Kennedy, Jr. and L. P. Grotelueschen

On the Buckling of Ring-Stiffened Circular Plates 689
J. N. Rossettos and W. H. Miller

On Laminar Thin-Film Flow Along a Vertical Wall 691
T. R. Roy

Optimum Openings in Circular Cylindrical Shells Under Uniaxial Tension and Torsion by Conformal Transformation 693
K. Rajaiah and R. R. Kumar

694 Disaster of the I-95 Mianus River Bridge. Where Could Lateral Vibration Come From?
A. M. Gorlov

696 A Note on the Flow of a Viscous Liquid Over an Inclined Permeable Bed Under a Surface Traction
H. Guha and T. K. Chaudhury

700 An Elastic-Plastic Solution Around a Tensile Crack in Strain-Hardening Materials
C. Hatleberg

DISCUSSIONS

703-704 Discussion on previously published papers by **C. Y. Wang and D. Chen** and **S. Cheng**

BOOK REVIEWS

705 ***Finite Elements for Structural Analysis*** by **William Weaver Jr.** and **Paul R. Johnson** . . . Reviewed by **A. S. Douglas**

Numerical and Physical Aspects of Aerodynamic Flows II edited by **Tuncer Cebeci** . . . Reviewed by **S. Widnall**

706 ***Nonlinear Deformation Waves*** edited by **U. Nigul and J. Englebrecht** . . . Reviewed by **T. W. Wright**

Finite Elasticity edited by **D. E. Carlson** and **R. T. Shield** . . . Reviewed by **M. M. Carroll**

707 ***Handbook of Applied Mathematics: Selected Results and Methods, Second Edition*** edited by **Carl E. Pearson** . . . Reviewed by **L. B. Freund**

Statistical Mechanics of Elasticity by **J. H. Weiner** . . . Reviewed by **F. Milstein**

708 ***Stress Analysis for Creep*** by **J. T. Boyle** and **J. Spence** . . . Reviewed by **Z. P. Bazant**

Fundamental Concepts in Numerical Solution of Differential Equations by **Joseph Botha** and George Pinder . . . Reviewed by **A. T. Patera**

709 ***Books received by the office of the Technical Editor***

ERRATA

711 Erratum on "An Extended Weight Function Method for Mixed-Mode Elastic Crack analysis," by Y. Bortman and L. Banks-Sills and published in the December 1983 issue.

486, 493, 509	Worldwide Mechanics Meeting List
500, 525, 530, 550, 565, 573	Applied Mechanics Symposium Proceedings
580, 585, 601, 629, 663, 686	Applied Mechanics Symposium Proceedings
464	Change of Address Form
712	Reference Citation Format

Downloaded 04 May 2010 to 171.66.16.49. Redistribution subject to ASME license or copyright; see http://www.asme.org/terms/Terms_Use.cfm

P. C. Chan
Research Scientist,
JAYCOR,
P.O. Box 85154,
San Diego, Calif. 92138
Assoc. Mem. ASME

W. L. Chow
Professor,
Department of Mechanical and Industrial Engineering,
University of Illinois at Urbana-Champaign,
Urbana, Ill. 61801
Mem. ASME

The Study of Gravitational Nozzle Flows by Hodograph Transformations

The effect of gravity on two-dimensional imcompressible potential nozzle flows has been studied using the method of hodograph transformation coupled with numerical computation. It has been demonstrated that although hodograph transformation is an inverse technique, it has the ability to allow curved walls to be prescribed a priori. Calculations have been performed for flows discharging from symmetric nozzles with horizontal lips. The variation of total head versus discharge rate can only be obtained from detailed consideration of the gravitational effect. Some general features of nozzle flows, including the possibility of early flow separation from the top nozzle wall, have been observed.

Introduction

The assessment of the effect of gravity on nozzle flows has been limited by the lack of an effective method that can handle the free surface profiles as well as complex nozzle geometries. For the seemingly simple problem of discharge of an incompressible fluid from the bottom of a two-dimensional tank through a horizontal nozzle, the analysis mentioned in any introductory fluid mechanics textbook is still based on the assumption of a uniform atmospheric pressure across the nozzle exit. Despite the variation of elevation throughout the exit plane, the velocity v across the exit is approximated by $v = (2g\,\Delta h)^{1/2}$ where Δh is the change in elevation from the fluid free surface inside the tank to the nozzle centerline, and g is the gravitational constant (Torricelli's theorem). The validity of such an approximate analysis can only be examined when the detail flow information inside the nozzle becomes available.

However, the determination of the free surface has been the major attention in the past, and nozzles involving only simple straight boundaries were usually investigated. Early approaches included the method of conformal mapping based on Helmholtz's free streamline theory pursued by Marchi [1], Melkonon [2], Gurevich and Pykhteev [3], and Benjamin [4]. Larock [5, 6] attempted to develop a combined conformal mapping and Riemann-Hilbert solution to treat the curved channel boundaries, but the actual curved geometry could not be prescribed a priori. Solutions obtained by the method of matched asymptotic expansion [7–10] have been restricted to a small gravitational effect. Southwell and Vaisey [11] pioneered the application of direct relaxative numerical calculation to free surface flows, and the method was also later pursued by McNown, Hsu, and Yih [12]. However, irregular channel boundaries with sharp curves can cause instability and yield inaccurate results for direct numerical computation in the physical plane. More flexibility has been gained by using the method of finite elements [13–17]. Jeppson [18, 19] employed the inverse method of solving the problem numerically on the potential-stream function ϕ-ψ plane, but curved solid walls could not be prescribed a priori.

It has been demonstrated that hodograph transformation coupled with relaxative numerical calculation is an effective method in analyzing potential channel flows dominated by gravity. Such flow problems as the free-overfall and the sharp-crested weir have been successfully analyzed by Chow, Han, and Wu [20–23], and results compared well with experimental data. Later Chow and Chan [24–25] also demonstrated that the method can handle flow problems when curved channel walls are given. The present effort is an extension of these considerations to incompressible flows discharging from curved symmetric nozzles with horizontal lips into the atmosphere.

Theoretical Consideration

In the method of hodograph transformation, the flow problem is analyzed in the hodograph plane where the independent variables are the velocity magnitude V and the streamline angle θ. After the solution is established in terms of hodograph variables, the results are then transformed back to the physical plane. For a two-dimensional incompressible potential flow problem, such as the one shown in Fig. 1, the governing equation for the stream function ψ [26] can be expressed in terms of V and θ as

$$V^2\psi_{VV} + V\psi_V + \frac{\psi_{\theta\theta}}{\sigma^2} = 0 \qquad (1)$$

Contributed by the Applied Mechanics Division for presentation at the Winter Annual Meeting, New Orleans, La., December 9–14, 1984 of THE AMERICAN SOCIETY OF MECHANICAL ENGINEERS.

Discussion on this paper should be addressed to the Editorial Department, ASME, United Engineering Center, 345 East 47th Street, New York, N.Y. 10017, and will be accepted until two months after final publication of the paper itself in the JOURNAL OF APPLIED MECHANICS. Manuscript received by ASME Applied Mechanics Division, May, 1983; final revision, December, 1983. Paper No. 84-WA/APM-8.

Copies will be available until August, 1985.

Copyright © 1984 by ASME
Downloaded 02 May 2010 to 171.66.16.25. Redistribution subject to ASME license or copyright; see http://www.asme.org/terms/Terms_Use.cfm

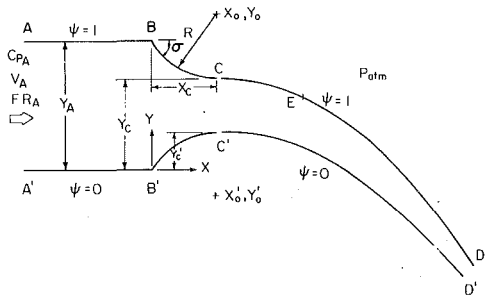


Fig. 1(*a*) Cartesian plane

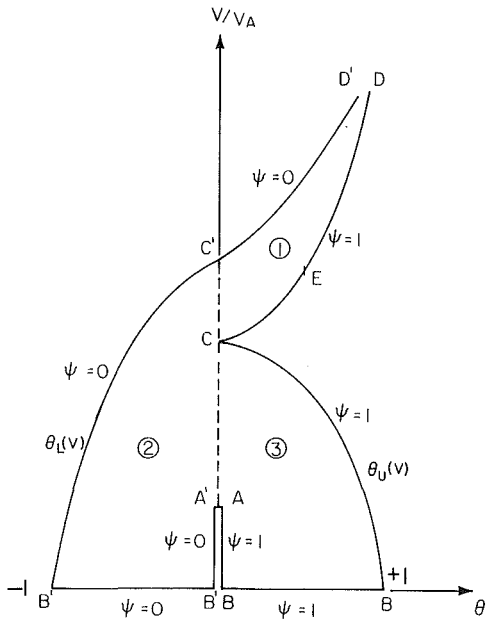


Fig. 1(*b*) Hodograph plane

Fig. 1 Free falling jet from a symmetric nozzle

where σ is a reference flow angle (positive anticlockwise) selected to normalize θ. The coupling with the cartesian X-Y plane is governed by two equations expressed as

$$dX = -\left[\frac{\cos\sigma\theta}{\sigma V^2}\psi_\theta + \frac{\sin\sigma\theta}{V}\psi_V\, dV\right] - \left[\frac{\sin\sigma\theta}{V}\psi_\theta - \sigma\cos\sigma\theta\,\psi_V\right]d\theta \tag{2a}$$

$$dY = -\left[\frac{\sin\sigma\theta}{\sigma V^2}\psi_\theta - \frac{\cos\sigma\theta}{V}\psi_V\right]dV + \left[\frac{\cos\sigma\theta}{V}\psi_\theta + \sigma\sin\sigma\theta\,\psi_V\right]d\theta \tag{2b}$$

One also has the normalized Bernoulli's Equation

$$H_0 = C_{p_A} + 1 + \frac{2}{FR_A^2} = C_p + V^2 + \frac{2}{FR_A{}^2}Y = Z\frac{2}{FR_A{}^2} \tag{3}$$

with

$$FR_A = \frac{V_A}{\sqrt{gY_A}}$$

$$C_p = \frac{P - P_{\text{atm}}}{\frac{1}{2}\rho V_A^2}.$$

FR_A is the Froude number; C_{p_A} is the upstream pressure coefficient; P is the absolute pressure; P_{atm} is the atmospheric pressure; ρ, is the fluid density; V_A is the far upstream uniform velocity; and g is the gravitational constant. H_0 and Z are the modified Bernoulli's constant and the modified total head, respectively, which are constant throughout the entire flow field, including the upstream uniform approaching flow where hydrostatic pressure distribution prevails. All lengths and velocities have been normalized by Y_A and V_A, respectively. A solution to a nozzle flow problem requires the calculation of the stream function ψ governed by equation (1) which in turn should produce the desired flow pattern based on equations (2*a*) and (2*b*) compatible with a given nozzle configuration. For a given Froude number FR_A, the corresponding Bernoulli's constant H_0 (or C_{p_A}) must also be determined as part of the solution.

Calculation and Results of Free Falling Jet From a Symmetric Nozzle With Horizontal Lips

The problem examined was the discharge of an incompressible fluid through a two-dimensional nozzle with horizontal lips into the atmosphere, as shown in Fig. 1(*a*). So far, no detailed theoretical investigation of the effect of gravitation on this problem is available. For the present effort, a family of symmetric nozzles was selected for convenience of study, although nonsymmetrical nozzles can equally be treated with the present scheme. Thus, a symmetric nozzle is selected by specifying the nozzle contraction radius, R, and the lip locations (X_C, Y_C) and $(X_{C'}, Y_{C'})$, which then also defines the corresponding upper and lower centers of contraction (X_0, Y_0) and (X_0', Y_0'). All streamline angles θ are normalized by the turning angle σ at the upper nozzle corner B.

Upon selecting a Froude number FR_A and an upstream pressure coefficient C_{p_A}, the normalized hodograph can be constructed as shown in Fig. 1(*b*) with the upper and lower lip velocities, V_C and $V_{C'}$, determined from equation (3). The hodograph is quite irregular with a branch cut along AA'-BB'. The hodograph boundaries $\theta_U(V)$ and $\theta_L(V)$ for the nozzle contractions BC and $B'C'$, and $V_U(\theta)$ and $V_L(\theta)$ for the free jet boundaries CD and $C'D'$ are not known and must be established in the process of solution. The hodograph domain can be divided into three parts (1), (2), and (3) along C-C' and AA'-C and can be further transformed separately to facilitate finite difference computations. While the division between Parts (1) and (2) is for the convenience of numerical calculation, the division AA'-C between Parts (2) and (3) is necessary to separate the double-valued stream function boundary conditions along the branch cut AA'-BB'.

Part (1) of the hodograph, which contains mainly the free falling jet, can be transformed successively to a square q-β plane as shown in Figs. 2(*a*) and 2(*b*) according to the equations

$$\omega = \frac{1}{V} \tag{4a}$$

$$\theta = \theta \tag{4b}$$

and

$$q = \frac{\omega - \omega_L(\theta)}{\omega_U(\theta) - \omega_L(\theta)} \tag{5a}$$

$$\beta = \theta. \tag{5b}$$

The governing equations (1) and (2) then become

$$\psi_{qq}\left\{\left[\frac{\omega_L + q(\omega_U - \omega_L)}{\omega_U - \omega_L}\right]^2 + \frac{1}{\sigma^2}\left[\frac{\omega_L' + q(\omega_U' - \omega_L')}{\omega_U - \omega_L}\right]^2\right\}$$

Downloaded 02 May 2010 to 171.66.16.25. Redistribution subject to ASME license or copyright; see http://www.asme.org/terms/Terms_Use.cfm

$$+\psi_q\left\{\frac{\omega_L+q(\omega_U-\omega_L)}{\omega_U-\omega_L}\right.$$

$$+\frac{2}{\sigma^2}\frac{(\omega_U'-\omega_L')[\omega_L'+q(\omega_U'-\omega_L')]}{(\omega_U-\omega_L)^2}$$

$$\left.-\frac{1}{\sigma^2}\frac{\omega_L''+q(\omega_U''-\omega_L'')}{\omega_U-\omega_L}\right\}$$

$$-\psi_{q\beta}\frac{2}{\sigma^2}\frac{\omega_L'+q(\omega_U'-\omega_L')}{\omega_U-\omega_L}+\psi_{\beta\beta}\frac{1}{\sigma^2}=0 \qquad (6)$$

$$dX=(A\psi_q+B\psi_\beta)dq+(C\psi_q+D\psi_\beta)d\beta \qquad (7a)$$

$$dY=(E\psi_q+F\psi_\beta)dq+(G\psi_q+K\psi_\beta)d\beta \qquad (7b)$$

with

$$A = -\frac{\cos\ \sigma\beta[\omega_L'+q(\omega_U'-\omega_L')]}{\sigma}-\sin\ \sigma\beta[\omega_L+q(\omega_U-\omega_L)]$$

$$B = \frac{(\omega_U-\omega_L)\cos\ \sigma\beta}{\sigma}$$

$$C = -\frac{\cos\ \sigma\beta[\omega_L'+q(\omega_U'-\omega_L')]^{\,2}}{\sigma(\omega_U-\omega_L)}$$

$$-\sigma\cos\ \sigma\beta\frac{[\omega_L+q(\omega_U-\omega_L)]^2}{\omega_U-\omega_L}$$

$$D = \frac{\cos\ \sigma\beta[\omega_L'+q(\omega_U'-\omega_L')]}{\sigma}-\sin\ \sigma\beta[\omega_L+q(\omega_U-\omega_L)]$$

$$E = -\frac{\sin\ \sigma\beta[\omega_L'+q(\omega_U'-\omega_L')]}{\sigma}+\cos\ \sigma\beta[\omega_L+q(\omega_U-\omega_L)]$$

$$F = \frac{\sin\ \sigma\beta[\omega_U-\omega_L)}{\sigma}$$

$$G = -\frac{\sin\ \sigma\beta[\omega_L'+q(\omega_U'-\omega_L')]^2}{\sigma(\omega_U-\omega_L)}$$

$$-\sigma\sin\ \sigma\beta\frac{[\omega_L+q(\omega_U-\omega_L)]^2}{\omega_U-\omega_L}$$

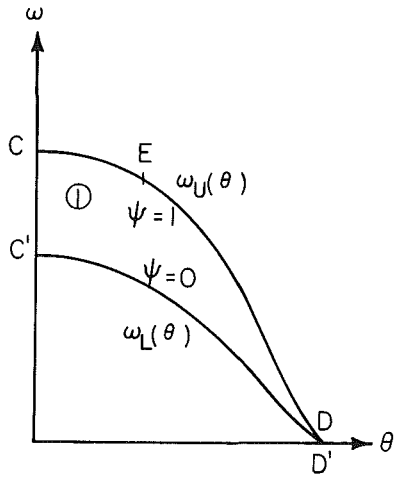


Fig. 2(a) Part 1: ω-θ plane

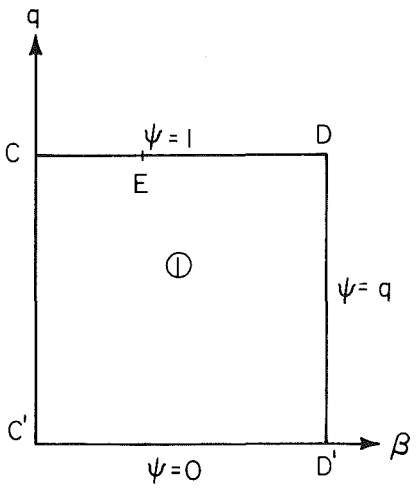


Fig. 2(b) Part 1: q-β plane

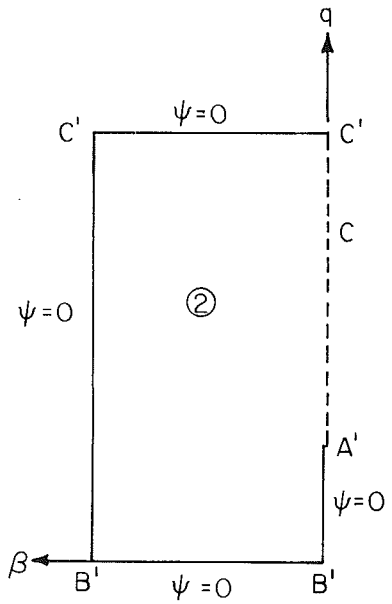


Fig. 2(c) Part 2: q-β plane

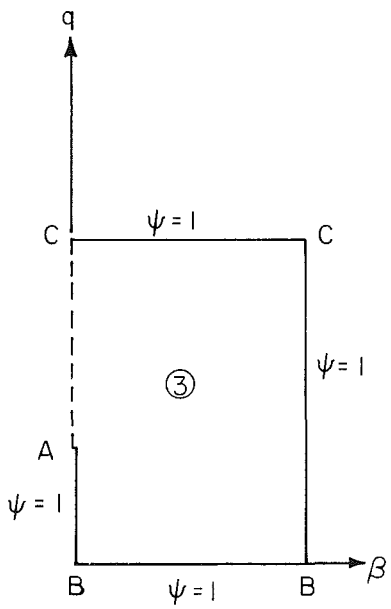


Fig. 2(d) Part 3: q-β plane

Fig. 2 Successive hodograph transformations for free jet from symmetric nozzle

Downloaded 02 May 2010 to 171.66.16.25. Redistribution subject to ASME license or copyright; see http://www.asme.org/terms/Terms_Use.cfm

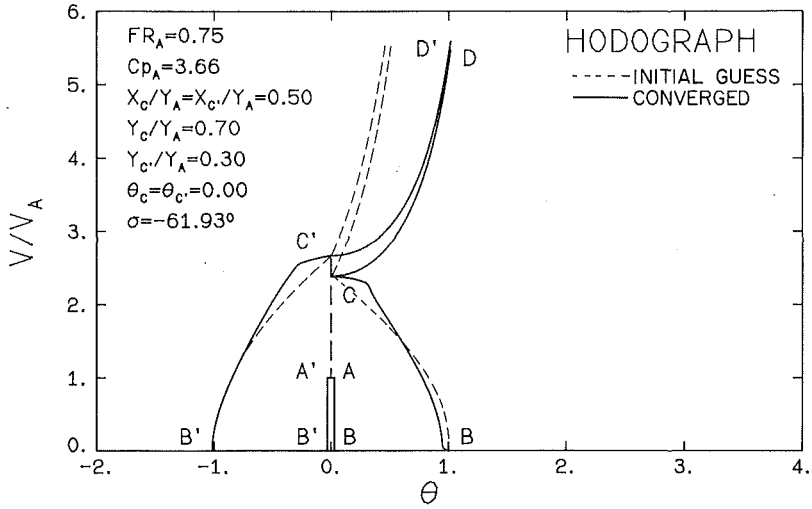


Fig. 3 Iteration of hodograph boundaries for symmetric nozzle

$$K = \frac{\sin \sigma\beta[\omega_L' + q(\omega_U' - \omega_L')]}{\sigma} - \cos \sigma\beta[\omega_L + q(\omega_U - \omega_L)]$$

$\omega_L(\theta)$ and $\omega_U(\theta)$ can be initially approximated as second-degree polynomial functions of θ, and ω_L', ω_L'', ω_U', and ω_U'' are the corresponding first and second derivatives.

Parts (2) and (3) can also be transformed into rectangular q-β planes as shown in Figs. 2(c) and (d) according to the relationships

$$\beta = \frac{\theta}{\theta_i(V)} \tag{8a}$$

and

$$q = V \tag{8b}$$

where $i = L$ and U refer to Parts (2) and (3), respectively. The governing equations (1) and (2) then become

$$\psi_{qq}q^2 + \psi_q q - \psi_{q\beta}q^2 2\beta\frac{\theta_i'}{\theta_i} + \psi_\beta q\beta\left[q\frac{2\theta_i'^2 - \theta_i\theta_i''}{\theta_i^2} - \frac{\theta_i'}{\theta_i}\right]$$

$$+ \psi_{\beta\beta}\left[\left(q\beta\frac{\theta_i'}{\theta_i}\right)^2 + \left(\frac{1}{\sigma\theta_i}\right)^2\right] = 0 \tag{9}$$

$$dX = (A\psi_\beta + B\psi_q)dq + (C\psi_\beta + D\psi_q)d\beta \tag{10a}$$

$$dY = (E\psi_\beta + F\psi_q)dq + (G\psi_\beta + K\psi_q)d\beta \tag{10b}$$

with

$$A = \left(\frac{\cos \sigma\beta\theta_i}{\theta_i}\right)\left(-\frac{1}{\sigma q^2} - \sigma\beta^2\theta_i'^2\right)$$

$$B = -\frac{\sin \sigma\beta\theta_i}{q} + \sigma\beta\theta_i' \cos \sigma\beta\theta_i$$

$$C = -\frac{\sin \sigma\beta\theta_i}{q} - \sigma\beta\theta_i' \cos \sigma\beta\theta_i$$

$$D = \sigma\theta_i \cos \sigma\beta\theta_i$$

$$E = \left(\frac{\sin \sigma\beta\theta_i}{\theta_i}\right)\left(-\frac{1}{\sigma q^2} - \sigma\beta^2\theta_i'^2\right)$$

$$F = \frac{\cos \sigma\beta\theta_i}{q} + \sigma\beta\theta_i' \sin \sigma\beta\theta_i$$

$$G = \frac{\cos \sigma\beta\theta_i}{q} - \sigma\beta\theta_i' \sin \sigma\beta\theta_i$$

$$K = \sigma\theta_i \sin \sigma\beta\theta_i$$

The unknown functions $\theta_i(V)$ can also be initially approximated as second-degree polynomial functions of V, with their first and second derivatives θ_i' and θ_i'' evaluated accordingly.

With the specified boundary values the stream function ψ governed by equations (6) for Part (1) and equation (9) for Parts (2) and (3) were determined by SOR finite difference computation. The meshes chosen were 40 × 40, 40 × 70, and 30 × 40, respectively, for the three parts, and a relaxation factor of 1.8 was also used. Referring to Fig. 1(b) it must be mentioned that the relaxation of the stream function values ψ for the individual Parts (1), (2), and (3) are coupled along the cuts C-C' and AA'-C by the conditions of continuity of stream function and their derivatives $\partial\psi/\partial\theta$ [22, 23, 25]. The stream function values ψ along the cuts were first assumed and were corrected by matching the one-sided derivatives $\partial\psi/\partial\theta$ of each domain along the cuts during each relaxation sweep of the individual computation domain. The ψ-values at A' and A in Parts (2) and (3) are fixed as 0 and 1, respectively, thus requiring no matching. There was also no difficulty in performing the matching near the singularity AA'. The ψ-values were considered established when the difference between successive relaxations at each grid node was within a small value of 10^{-5}.

Once the stream function ψ was stabilized, the assumed functions $\omega_U(\theta)$, $\omega_L(\theta)$, $\theta_U(V)$, and $\theta_L(V)$ could be corrected. To revise the free jet boundaries CD and $C'D'$, starting from the given location C', equations (7a) and (7b) were first integrated along $C'D'$ on the q-β plane in Fig. 2(b) to locate the lower free jet boundary, and were integrated again in the q-direction across the q-β plane to locate the upper free jet boundary CD. Such an integration procedure could also avoid the lower and upper jet boundaries crossing each other during the iteration process. Once the vertical locations of the new jet boundaries were determined, the corresponding new velocity values $V_L(\theta)$ and $V_U(\theta)$ were calculated from the Bernoulli's Equation. The functional values $\omega_L(\theta)$ and $\omega_U(\theta)$ were then revised based on equation (4a). It has been found that the iteration of the free jet boundaries is always convergent.

For Parts (2) and (3), the functions $\theta_L(V)$ and $\theta_U(V)$ are unknown, although their Cartesian coordinates are already given, as shown in Fig. 1(a). The process of iteration must reproduce the functions $\theta_L(V)$ and $\theta_U(V)$ compatible with the given nozzle boundaries. This was accomplished by first integrating equations (10a) and (10b) along $B'C'$ and BC in the q-β planes in Figs. 2(c) and (d), with vanishing ψ_q and $d\beta$

Downloaded 02 May 2010 to 171.66.16.25. Redistribution subject to ASME license or copyright; see http://www.asme.org/terms/Terms_Use.cfm

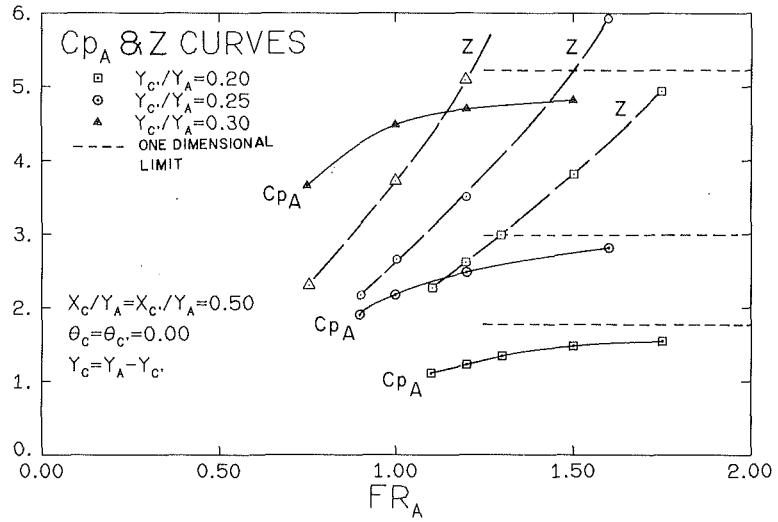


Fig. 4 Variation of C_{P_A} and Z with FR_A for symmetric nozzle

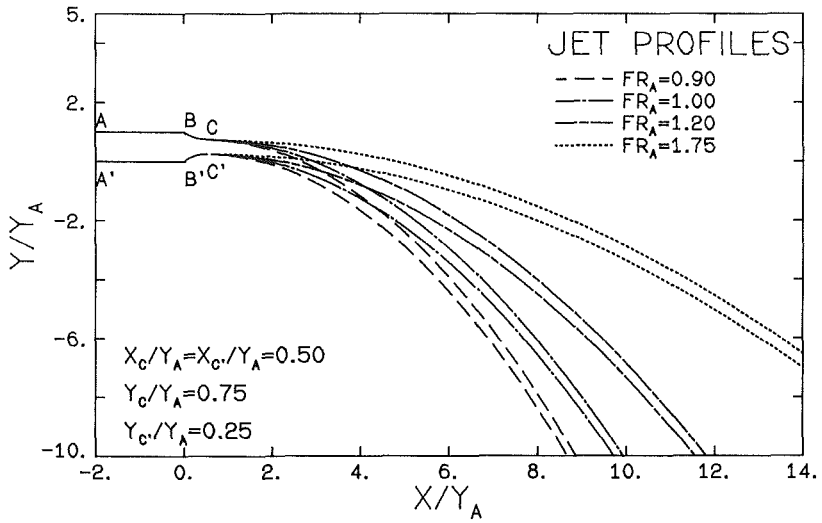


Fig. 5 Effect of Froude number on jet profiles

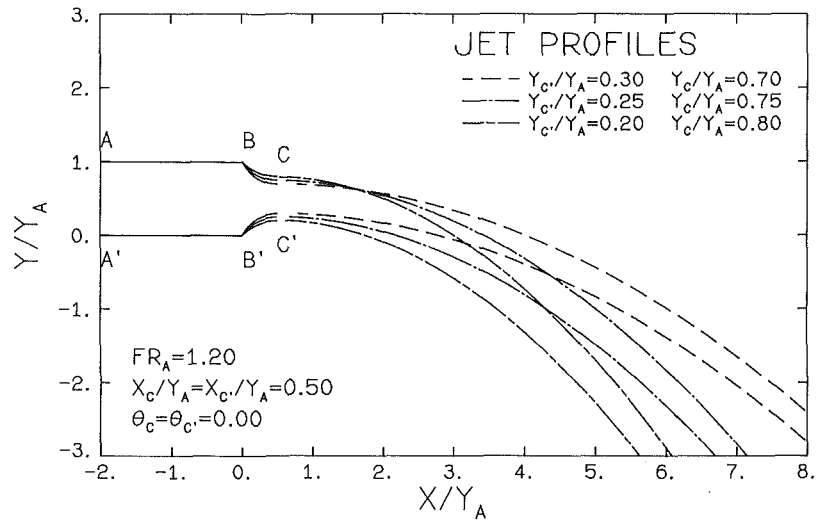


Fig. 6 Effect of nozzle exit width on jet profiles

to obtain the X-Y coordinates of the lower and upper nozzle contractions. The $\theta_L(V)$ and $\theta_U(V)$ values were then revised according to the geometric relationships

$$\frac{dY}{dX} = \tan \sigma\beta\theta_L = -\frac{X - X_0'}{Y - Y_0'} \tag{11a}$$

$$\frac{dY}{dX} = \tan \sigma\beta\theta_U = -\frac{X - X_0}{Y - Y_0} \tag{11b}$$

After the functions $\omega_U(\theta)$, $\omega_L(\theta)$, $\theta_U(V)$ and $\theta_L(V)$ are revised, their first and second derivatives can be evaluated numerically. The stream function ψ governed by equations (6)

Downloaded 02 May 2010 to 171.66.16.25. Redistribution subject to ASME license or copyright; see http://www.asme.org/terms/Terms_Use.cfm

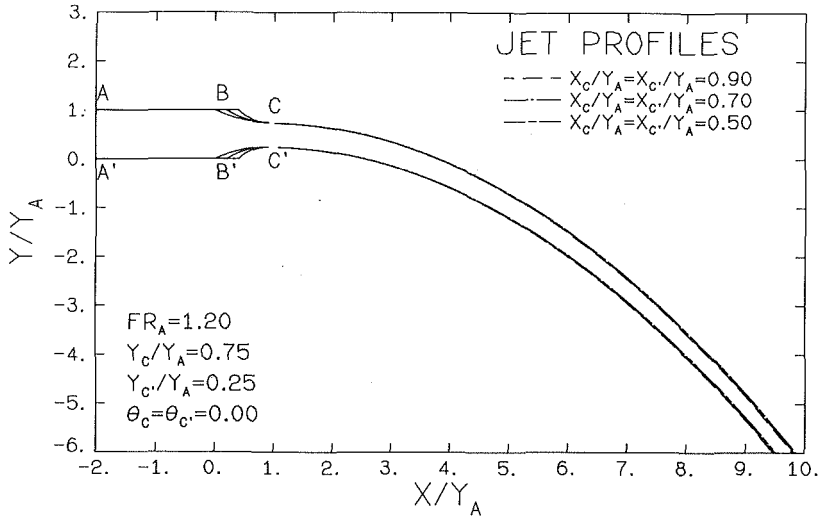


Fig. 7 Effect of nozzle length on jet profiles

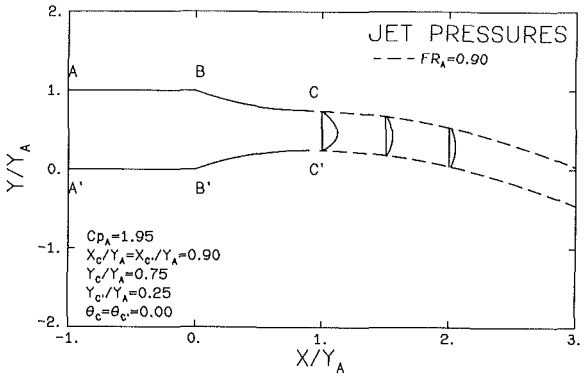


Fig. 8(*a*) $FR_A = 0.9$

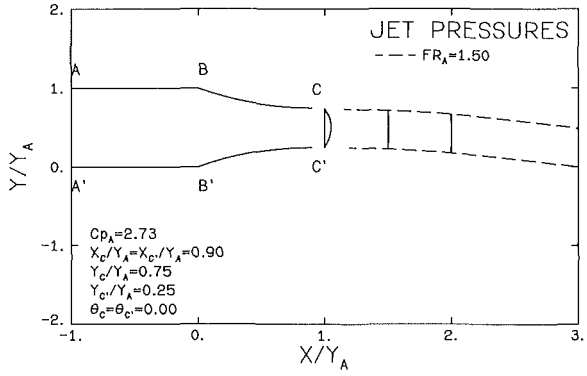


Fig. 8(*b*) $FR_A = 1.5$

Fig. 8 Pressure relaxation along free jets from symmetric nozzles

and (9) for Parts (1), (2), and (3) must also be modified until the functions $\omega_U(\theta)$, $\omega_L(\theta)$, $\theta_U(V)$, and $\theta_L(V)$ are also correctly reproduced. Figure 3 shows typical converged hodograph together with the intitally assumed configuration. Usually, 15–30 iterations were required to establish a complete hodograph boundary.

It is to be noted that so far the upper free jet boundary CD, is only hinged with respect to the lower jet boundary $C'D'$. Specifically, the location of the point C reproduced from the profile integration may not agree with the given physical location of the upper lip. To eliminate this discrepancy, the value of C_{P_A} must be adjusted. Comparison of the prescribed Y_C with the reproduced Y_{C^*} suggests that a simple linear correction of the Bernoulli's constant, through

$$H_o = H_{\text{old}} \frac{Y_{C^*}}{Y_C}$$

would produce the correct H_0, H_{old} being the H_0 value employed to produce Y_{C^*}. It is understood that for each new C_{P_A} value, computation of hodograph boundaries and stream function must be repeated. A satisfactory solution is established when Y_{C^*} is different from Y_C within a small margin (0.003). Usually four to seven corrections are required. Thus, by following the foregoing scheme a selected FR_A value yields a unique set of solution and parameters, including C_{P_A} and Z.

Figure 4 shows the variation of the upstream pressure coefficient C_{P_A} with the Froude number FR_A for three symmetric nozzles of identical lengths X_C/Y_A of 0.5, but with different exit widths $(Y_C - Y_{C'})/Y_A$ of 0.4, 0.5, and 0.6. The corresponding variation of total head Z is also presented. For incompressible channel flows with identical upstream heights under the same gravitational field, the volumetric rate of discharge is identical for identical Froude numbers. Thus, it is expected that a higher total head is needed to overcome a larger obstruction for a narrower nozzle to deliver the same discharge rate. Figure 4 also shows that it is completely inaccurate if a simplified one-dimensional approach is adopted for the problems. Under a one-dimensional flow assumption, the upstream pressure coefficient $C_{P_{A_{1-D}}}$ can be expressed as

$$C_{P_{A_{1-D}}} = \left(\frac{Y_A}{Y_C - Y_{C'}}\right)^2 - 1$$

The values of $C_{P_{A_{1-D}}}$ are independent of Froude numbers as shown by the dotted lines in Fig. 4 for the three nozzles investigated. They can only be considered as asymptotic values being reached when the Froude number increases toward infinity, and they differ significantly from the calculated C_{P_A} values. Such an observation could not have been made if gravity effect was not considered.

The profiles of the free falling jet under different conditions are shown from Figs. 5–7. The effect of Froude number on the free jet profile is evident in Fig. 5. Keeping the Froude number constant, one also expects that a narrower nozzle discharges farther as shown in Fig. 6. Moreover, Fig. 7

Downloaded 02 May 2010 to 171.66.16.25. Redistribution subject to ASME license or copyright; see http://www.asme.org/terms/Terms_Use.cfm

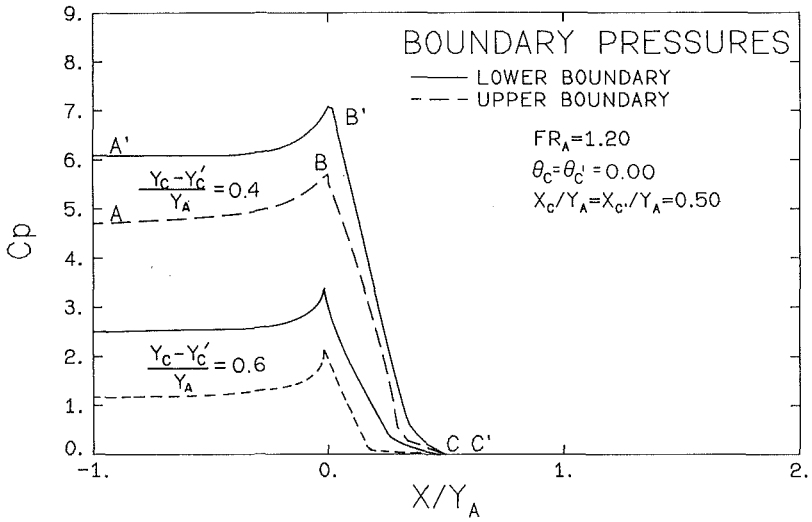


Fig. 9 Pressure variation along symmetric nozzle boundaries

shows that when the three nozzles of same exit width of 0.5 but of lengths 0.5, 0.7, and 0.9 are lined up with the same exit location, their free jet profiles are practically indistinguishable from each other. In addition, the change of nozzle length practically does not alter the resulting pressure coefficient C_{p_A} (or Z). Thus, Fig. 4 can be applied to the nozzles of lengths 0.7 and also to 0.9.

Figure 8 also shows the typical variation of pressure coefficient across the jet under two different Froude numbers. It is evident that the influence of gravity on the jet decreases as the Froude number increases. For a Froude number of 1.2 and above, the pressure across the jet diminishes rapidly toward atmospheric value beyond two exit widths downstream. However, the variation of pressure across the jet near the exit cannot be simply neglected as in Torricelli's theorem. It should be mentioned that if there is no gravity, the free jet boundaries are straight and horizontal. Other then a small pressure variation across the jet due to the curvature effect of the upstream nozzle profile, the pressure inside the jet relaxes rapidly toward atmospheric value. Under the influence of gravity, the jet boundaries are curved, and the difference in curvatures between the upper and the lower jet boundaries is balanced by the pressure force across the jet.

It is important to note that hodograph transformation, unlike the other inverse techniques, has the ability to allow the curved walls to be prescribed. The present calculation has shown that the unknown hodograph boundaries for the curved nozzle contraction can be determined in the process of the entire solution. The converged functions $\theta_L(V)$ and $\theta_U(V)$ on the hodograph plane (Fig. 1) can be verified against the prescribed curved nozzle walls $B'C'$ and BC by integrating equations (10*a*) and (10*b*) on the q-β plane (Figs. 2(*c*) and (*d*)). For all the cases calculated, the error at each grid node along the curved contractions is always less than 2×10^{-3}.

The typical pattern of pressure variation along the lower and upper nozzle boundaries is shown in Fig. 9. The difference in pressure along the lower and upper boundaries of a symmetric nozzle is entirely due to the effect of gravity. Since the pressures at the lips C and C' must be atmospheric, there is always a rapid pressure reduction along the nozzle boundaries BC and $B'C'$, and the process slows down drastically as the lips are approached, especially for the upper contraction. In particular, Fig. 9 shows that as the nozzle exit becomes wider, from 0.4 to 0.6, the pressure along the upper contraction reduces drastically becoming almost atmospheric before the lip C is reached.

For every nozzle discharge problem under the influence of gravity, there must be a minimum level of total mechanical energy of the approaching flow such that the flow would follow fully the top nozzle boundary. Therefore, as the Froude number is reduced, there is a tendency for the fluid along the top boundary to separate from the wall before reaching the lip C. Such a condition exists when the pressure of the flow along the upper nozzle contraction becomes atmospheric before reaching the exit C. Indeed Fig. 9 shows that the pressure gradient along the upper contraction BC diminishes abruptly as it approaches the lip C, especially for the wider nozzle exit 0.6. This suggests that wider nozzles can be more susceptible to early flow separation at higher Froude numbers. The present investigation does not intend to predict this occurrence theoretically, and the flow is always assumed to follow fully the upper nozzle boundary. However, it has been experienced that as the Froude number becomes smaller, the iteration of the upstream pressure coefficient tends to be less stable. Calculation was stopped when such a difficulty occurred. The lowest Froude numbers that have yielded results for the present investigation are 0.75, 0.9, and 1.1 for the nozzle exit widths of 0.4, 0.5, and 0.6, respectively, as shown in Fig. 4.

The application of hodograph transformation to the present problem should yield unique solution. The stream function governing equations (equations (6) and (9)) remain linear even after successive transformations. The hodograph domain is singly connected, even though there exists a branch cut (Fig. 1). After dividing the hodograph plane into three parts, the double ψ-values along the branch cut AA'-BB' become single-valued boundary conditions, including points A and A', for Parts 2 and 3. Furthermore, the stream function values at the stagnation points B and B', lips C and C', and for downstream location DD' are well defined as boundary conditions, even though their successive mappings are not one to one. Inside the computation domains, the successive transformations (equations (4), (5) and (8)) have nonzero Jacobians. Therefore, the computed hodograph is unique and invertible.

Conclusions

The present investigation has adopted the technique of hodograph transformation coupled with numerical computation to study the effect of gravity on nozzle flows. While a problem is sovled on the hodograph domain, the coordinate transformation between the hodograph domain and the

Downloaded 02 May 2010 to 171.66.16.25. Redistribution subject to ASME license or copyright; see http://www.asme.org/terms/Terms_Use.cfm

physical plane are employed for the benefit of determining the unknown hodograph boundaries along free surfaces and curved solid boundaries through successive iterations. The nozzle geometry including curved walls can always be prescribed a priori. This is a significant development of the method of hodograph transformation making it an effective inverse technique. Extensions to compressible flow applications should also be possible.

Detailed calculated results for nozzle flows strongly influenced by gravity have been presented. The important characteristic curve of total head (or upstream pressure coefficient) versus Froude number can only be obtained when gravitational effect is fully considered. For a given nozzle family, the Z-FR_A relationship is governed mainly by the nozzle exit width. The possibility of early flow separation from the top nozzle wall is also identified. The present study also provides guidance for future experimental investigation which can further improve the understanding of incompressible potential channel flow strongly influenced by gravity.

References

1 Marchi, E., "Sue Fenomenidi Efflusso Piano da Luci a Bottente," *Ann. Mat. Pura ed Appl.*, Vol. 35, 1953, pp. 321–341.

2 Melkonan, G. I., *Izv. Akad. Nauk Armenian SSR, Ser. Phys.—Mat. Nauk*, Vol. 10, No. 3, 1957.

3 Gurevich, M. I., and Pykhteev, G. N., "Approximate Solution of the Problem of Flow of a Heavy Ideal Incompressible Fluid From Under a Sluice Gate," *PMTF* (Akad. Nauk), Vol. 2, 1960, pp. 3–14.

4 Benjamin, T. B., "On the Flow in Channels When Rigid Obstacles are Placed in the Stream," *J. Fluid Mech.*, Vol. 1, 1956, pp. 227–248.

5 Larock, B. E., "Jets from Two-Dimensional Symmetric Nozzles of Arbitrary Shape," *J. Fluid Mech.*, Vol. 37, Part 3, 1969, pp. 479–489.

6 Larock, B. E., "A Theory for Free Outflow Beneath Radial Gates," *J. Fluid Mech.*, Vol. 41, Part 4, 1970, pp. 851–864.

7 Keller, J. B., and Weitz, M. L., "Thin Unsteady Heavy Jets," *Inst. Math. Mech.*, New York University Rep. IMM-NYU 186, 1952.

8 Keller, J. B., and Weitz, M. L., "A Theory of Thin Jets," *Proc. 9th Int. Cong. Appl. Mech.*, Brussels, Vol. 1, 1957, pp. 316–323.

9 Clarke, N. S., "On Two-Dimensional Inviscid Flow in a Waterfall," *J. Fluid Mech.*, Vol. 22, Part 2, 1965, pp. 359–369.

10 Keller, J. B., and Geer, J., "Flows of Thin Streams With Free Boundaries," *J. Fluid Mech.*, Vol. 59, Part 3, 1973, pp. 417–432.

11 Southwell, R. V., and Vaisey, G., "Relaxation Methods Applied to Engineering Problems: XII, Fluid Motion Characterized by Free Streamlines," *Philos. Trans. Roy. Soc., London*, Series A, Vol. 240, 1946, pp. 117–161.

12 McNown, J. S., Hsu, E. Y., and Yih, C. S., "Applications of the Relaxation Technique in Fluid Mechanics," *Trans. ASCE*, Vol. 120, 1955.

13 Mogel, T. R., and Street, R. L., "A Numerical Method for Steady State Cavity Flows," *J. Ship Res.*, Vol. 18, No. 1, 1974, pp. 22–31.

14 Ikegawa, M., and Washizu, K., "Finite Element Method Applied to Analysis of Flow Over a Spillway Crest," *Int. J. Num. Method in Eng.*, Vol. 6, 1973, pp. 179–189.

15 Varoglu, E., and Finn, W. D. L., "Variable Domain Finite Element Analysis of Free Surface Gravity Flow," *Computers and Fluids*, Vol. 6, 1977, pp. 103–114.

16 Chan, T. K., Larock, B. E., and Herrmann, L. R., "Free-Surface Ideal Fluid Flows by Finite Elements," *J. Hydraul. Div., ASCE*, Vol. 99, No. HY1, 1973, pp. 959–974.

17 Chan, T. K., and Larock, B. E., "Fluid Flows From Axisymmetric Orifices and Valves," *J. Hydraul. Div., ASCE*, Vol. 99, No. HY1, 1973, pp. 81–96.

18 Jeppson, R. W., "Numerical Solution to Free Surface Axisymmetric Flows," *J. Eng. Mech. Div., ASCE*, Vol. 95, 1969, pp. 1–20.

19 Jeppson, R. W., "Inverse Formulation and Finite Differences Solutions for Flow From a Circular Orifice," *J. Fluid Mech.*, Vol. 40, Part 1, 1970, pp. 215–223.

20 Chow, W. L., Han, T., and Wu, C., "Hydrodynamics Solution for Incompressible Flow as Influenced by Gravitation," *AIAA J.*, Vol. 16, No. 10, 1978, pp. 1097–1098.

21 Chow, W. L., and Han, T., "Inviscid Solution for the Problem of Free Surface Overfall," ASME JOURNAL OF APPLIED MECHANICS, Vol. 46, No. 1, 1979, pp. 1–5.

22 Han, T., "Applications of Hodograph Transformation to Hydrodynamic Problems Influenced by Gravitation," Ph.D. Thesis, Department of Mechanical and Industrial Engineering, University of Illinois at Urbana-Champaign, 1979.

23 Han, T. Y., and Chow, W. L., "The Study of Sluice Gate and Sharp-Crested Weir Through Hodograph Transformation," ASME JOURNAL OF APPLIED MECHANICS, Vol. 48, 1981, pp. 229–238.

24 Chow, W. L., and Chan, P. C., "The Effect of Gravity on Certain Curved Channel Potential Flows," ASME *Journal of Fluids Engineering*, Dec. 1981. Presented in the ASME/ASCE Joint Conference, June 22–24, 1981, Boulder, Colo. ASME Paper 81-FE-10.

25 Chan, P. C., "The Study of the Effect of Gravity on Nozzle Flows by Hodograph Transformation," Ph.D. Thesis, Department of Mechanical and Industrial Engineering, University of Illinois at Urbana-Champaign, 1981.

26 Shapiro A. H., *The Dynamics and Thermodynamics of Compressible Fluid Flow*, Vol. 1, The Ronald Press, New York, 1953, pp. 338–341.

Downloaded 02 May 2010 to 171.66.16.25. Redistribution subject to ASME license or copyright; see http://www.asme.org/terms/Terms_Use.cfm

The Incremental Strain Growth of an Elastic-Plastic Body Loaded in Excess of the Shakedown Limit

A. R. S. Ponter
Professor of Engineering.

A. C. F. Cocks
Research Associate.

Department of Engineering,
Leicester University,
Leicester, LE1 7RH, England

This paper considers the problem of a body composed of an elastic/perfectly plastic solid that is subjected to constant applied load P and a time-varying cyclic temperature distribution, characterized by a maximum thermoelastic stress σ_t. For sufficiently large P and σ_t in excess of the shakedown limit, the body will begin to suffer incremental growth. A linearized theory is used to obtain a relationship between the increase in displacement Δu per cycle and the increase in ΔP and $\Delta\sigma_t$ above the shakedown limit. From the result, a simple lower bound is derived for Bree-type problems, which for kinematically determinate structures shows that for moderate thermal loading the displacement increment per cycle is four times the elastic displacement of the body if it were subjected only to the increase ΔP. From a practical point of view the analysis indicates that ratchet rates are always high, in the sense that only a small increase of load above shakedown will produce substantial ratcheting within relatively few cycles.

1 Introduction

Consider a body composed of an elastic-perfectly plastic material and subjected to constant applied surface traction and a temperature history $\theta(\mathbf{x},t)$ which varies with respect to spacial variables $\mathbf{x}$ and time t in a cyclic manner with cycle time Δt. The magnitude of the loading may be characterized by the load paramter P and a maximum thermoelastic stress σ_t. For sufficiently small P and σ_t either purely elastic behavior occurs or a residual stress field $\bar{\rho}_{ij}$ is developed during the first few cycles, as a result of plastic strains, so that subsequent cycling remains in a state of shakedown with a stress history of the form [1, 2]

$$\sigma^*_{ij} = \hat{\sigma}^p_{ij} + \hat{\sigma}^\theta_{ij} + \bar{\rho}_{ij}$$

where $\hat{\sigma}^p_{ij}$ and $\hat{\sigma}^\theta_{ij}$ are the linear elastic stress histories corresponding to P and σ_t. In this shakedown state σ^*_{ij} lies everywhere within yield. If P and σ_t are increased a shakedown limit is reached where further increase in either P or σ_t may cause the body to deform cyclically producing an increment of compatible plastic strain in each cycle and the body is said to ratchet.

This problem has become of some interest in recent years due to the particular structural design problems of the liquid sodium-cooled fast reactor [3] where many components are subjected to moderate dead weight loading but large thermal fluctuations. Analytic solutions exist for the classic Bree problem and two bar structures [4, 5] and some numerical solutions have been generated [6, 7] that indicate that the rate of ratchet increases rapidly for loads in excess of shakedown, so that the shakedown boundary forms an effective design limit for materials that exhibit limited strain hardening.

As an aid to an understanding of the ratcheting phenomena we pose the following problem: suppose the load parameters P and σ_t are such that the shakedown limit has just been reached and we know, a priori, both the shakedown limit and the displacement and strain increments associated with the shakedown solution. If the load parameters are increased by a small amount ΔP and $\Delta\sigma_t$, at what rate does the body now deform in the subsequent cyclic steady state of strain and displacement growth? The analysis presumes that the increments ΔP and $\Delta\sigma_t$ are sufficiently small to leave the mechanism of plastic strain growth unchanged. It is found that this linearized rate of ratchet may be computed from the elastic strain energy associated with a stress-free elastic body which is given the cycle of incompatible plastic strain of the ratcheting mechanism. The rate of ratchet depends only on the elastic properties through the stored elastic strain energy. Hence the dependence on the yield condition and, for example, the variation of yield stress with temperature, appears only through the way the ratchet mechanism is affected by the plastic properties.

For proportional quasi-static thermal loading a lower bound on the ratchet rate is derived for Bree-type problems with moderate thermal loading, which yields a particularly simple result for kinematically determinate problems. If the applied load is increased by an amount ΔP above shakedown then the increase in displacement Δu of the load cycle is

Contributed by the Applied Mechanics Division for presentation at the Winter Annual Meeting, New Orleans, La., December 9-14, 1984 of THE AMERICAN SOCIETY OF MECHANICAL ENGINEERS.

Discussion on this paper should be addressed to the Editorial Department, ASME, United Engineering Center, 345 East 47th Street, New York, N.Y. 10017, and will be accepted until two months after final publication of the paper itself in the JOURNAL OF APPLIED MECHANICS. Manuscript received by ASME Applied Mechanic Division, September, 1983; final revision, December, 1983. Paper No. 84-WA/APM-10.

Copies will be available until August, 1985.

Copyright © 1984 by ASME
Downloaded 02 May 2010 to 171.66.16.25. Redistribution subject to ASME license or copyright; see http://www.asme.org/terms/Terms_Use.cfm

greater than $4\Delta u^e$, where Δu^e is the elastic displacement due to a static load ΔP. The result, which is exact for the classic Bree problem, indicates that high ratchet rates are a general phenomena for this type of thermal loading. Although the result is strictly correct only for kinematically determinate structures it is well known that many shell problems exhibit relatively little variation in the mode of deformation for differing inelastic material properties and the result may be expected to be a good approximation.

2 The Linearized Ratchet Rate of a Body Subjected to Loads in Excess of the Shakedown Limit

Consider a body of volume V and surface S composed of an elastic/perfectly plastic material with a temperature-dependent yield surface given by

$$f(\sigma,\theta)=0, \tag{1}$$

where θ denotes the instantaneous temperature. The region of elastic behavior is defined by $f\leq 0$. An increment of plastic strain occurring at some stress σ_{ij} which satisfies the yield condition, is given by the associated flow rule

$$d\epsilon = d\mu \frac{\partial f}{\partial \sigma}, \tag{2}$$

where $d\mu$ is a scalar plastic multiplier. The total strain at any instant is given by

$$\epsilon = \mathbf{e} + \epsilon' + \alpha\delta(\theta-\theta_0) \tag{3}$$

and

$$\epsilon = C\sigma \tag{4}$$

where α and δ denote the coefficient of linear expansion and the unit tensor, respectively, and $\mathbf{C}$ denotes the elastic compliance tensor C_{ijkl} which possesses the usual symmetry properties,

$$C_{ijkl}=C_{jikl}=C_{ijlk}=C_{klij} \tag{5}$$

We assume that $\mathbf{C}$ is independent of temperature as shakedown theory, as it exists at the present time, requires this assumption. The coefficient of linear thermal expansion α in equation (3) is similarly assumed to be temperature-independent, and θ_0 denotes a fixed reference temperature.

Part of the surface S is subjected to constant surface tractions

$$\mathbf{P}=P\mathbf{q}(\mathbf{x}) \quad \text{on} \quad S_T, \tag{6}$$

where P is a scalar loading parameter and $\mathbf{q}$ a distribution function. Within V a distribution of temperature $\theta(\mathbf{x},t)$ varies cyclically with cycle time Δt. As the plasticity problem is time-independent, time appears in the problem as a parameter that defines sequence, although there may be rate effects associated with $\theta(x,t)$.

Corresponding to the surface tractions $\mathbf{P}$ there exists a linear elastic solution $P\hat{\sigma}$ where $\hat{\sigma}$ is the elastic solution for unit load. The instantaneous distribution of temperature $\theta(\mathbf{x},t)$ and the corresponding thermoelastic stresses may be expressed in the form,

$$\left.\begin{aligned} &\theta(\mathbf{x},t)=\Delta\theta\ g(\mathbf{x},t)\\ &\hat{\sigma}^{\theta}(\mathbf{x},t)=\sigma_t\mathbf{h}(\mathbf{x},t), \quad \sigma_t=AE\alpha\Delta\theta \end{aligned}\right\} \tag{7}$$

where $\Delta\theta$ denotes a maximum temperature difference and σ_t a maximum thermoelastic stress. From dimensional arguments the quantity A depends only on the nondimensional temperature history function $g(\mathbf{x},t)$.

For combinations of P and σ_t that lie at the shakedown limit, the following conditions are satisfied:

(*a*) There exists a unique constant residual stress field $\bar{\rho}$ so that the stress history

$$\sigma^* = P\hat{\sigma} + \sigma_t\mathbf{h} + \bar{\rho} \tag{8}$$

satisfies the yield condition $f(\sigma^*)\leq 0$.

(*b*) There exists a cyclic history of plastic strains $\dot{\epsilon}(\mathbf{x},t)$ which gives rise to an accumulation over the cycle

$$\Delta\epsilon' = \int_0^{\Delta t} \dot{\epsilon}'\ dt \tag{9}$$

which is compatible and derivable from a displacement field Δu.

(*c*) At time t at each point $\mathbf{x}$, either $\dot{\epsilon}'=0$ or $\dot{\epsilon}'$ is associated through the flow rule, equation (2), with σ^*. Hence we may write

$$\sigma'\dot{\epsilon}' = (P\hat{\sigma} + \sigma_t\mathbf{h}(t) + \bar{\rho})\dot{\epsilon}' \tag{10}$$

where σ' is the stress on the yield surface associated with $\dot{\epsilon}'$.

A relationship between P and σ_t at shakedown may now be derived from (10) by integrating over the volume V and cycle Δt and applying the principle of virtual work. The following result is obtained:

$$\int_V\int_0^{\Delta t}\sigma'\dot{\epsilon}'\,dtdV = P\Delta u + \sigma_t\int_V\int_0^{\Delta t}\mathbf{h}(t)\,\dot{\epsilon}'\,dtdV \tag{11}$$

where $\Delta u=\int_{S_T}\mathbf{q}\Delta\mathbf{u}ds$. The term involving $\bar{\rho}$ is zero as $\Delta\epsilon'$ is compatible.

For some problems, the plastic strain rate cycle remains unchanged for a range of values of P and σ_t, resulting in a linear relationship between P and σ_t. This circumstance is observed in many problems [4–7] when P is close to the static limit load.

If the load parameters P and σ_t are increased by small amounts ΔP and $\Delta\sigma_t$, to first order, the plastic strain rate cycle remains unchanged provided $\dot{\epsilon}'$ lies at a point on the yield surface where the normal vector varies continuously. There now exists a cyclic history of stress of the form

$$\sigma^* + d\sigma^* = (P+\Delta P)\hat{\sigma} + (\sigma_t+\Delta\sigma_t)\mathbf{h} + \bar{\rho} + d\bar{\rho} + \rho(t) \tag{12}$$

with a corresponding history of strain

$$\epsilon^* = (P+\Delta P)\hat{\epsilon}^p + \hat{\epsilon}^{\theta} + d\hat{\epsilon}^{\theta} + \bar{\epsilon}' + \epsilon'(t) \tag{13}$$

Here $\bar{\epsilon}'$ denotes plastic strains that exist at the beginning of the cycle which in a stress free elastic body, would induce residual stress $\bar{\rho}+d\bar{\rho}$. The cyclic history of plastic strain $\epsilon'(t)$ similarly induces elastically the residual stress cycle $\rho(t)$ and satisfies the condition

$$\epsilon'(0)=0, \quad \epsilon'(\Delta t)=\Delta\epsilon', \tag{14}$$

and hence

$$\rho(0)=\rho(\Delta t)=0 \tag{15}$$

The result that relates the increase in load to the rate of increase in strain may best be derived for the class of problems where

$$\Delta\epsilon' = \Delta\epsilon_1 + \Delta\epsilon_2 + \ \ldots\ + \Delta\epsilon_n, \tag{16}$$

where each of the constituent components $\Delta\epsilon_i$ occurs at distinct instants in the cycle t_1, t_2 etc., at fixed points on the yield surface. Hence, to first order, at t_i

$$\begin{aligned}(\sigma_i'\Delta\epsilon_i) = (P+\Delta P)\hat{\sigma}\Delta\epsilon_i + (\sigma_t+\Delta\sigma_t)\mathbf{h}_i\Delta\epsilon_i\\ + (\bar{\rho}+d\bar{\rho})\Delta\epsilon_i + \rho(t_i)\Delta\epsilon_i\end{aligned} \tag{17}$$

and

$$(\sigma_i'\Delta\epsilon_i) = P\hat{\sigma}\Delta\epsilon_i + \sigma_t\mathbf{h}_i\Delta\epsilon_i + \bar{\rho}\Delta\epsilon_i \tag{18}$$

Hence, subtracting (18) from (17) and summing over i, we obtain,

$$\Delta P\hat{\sigma}\Delta\epsilon' + \Delta\sigma_t\sum_i\mathbf{h}_i\Delta\epsilon_i = -\sum_i(\rho(t_i)\Delta\epsilon_i + d\bar{\rho}\Delta\epsilon_i) \tag{19}$$

Integrating over the volume V and applying the principle of virtual work, we obtain

Downloaded 02 May 2010 to 171.66.16.25. Redistribution subject to ASME license or copyright; see http://www.asme.org/terms/Terms_Use.cfm

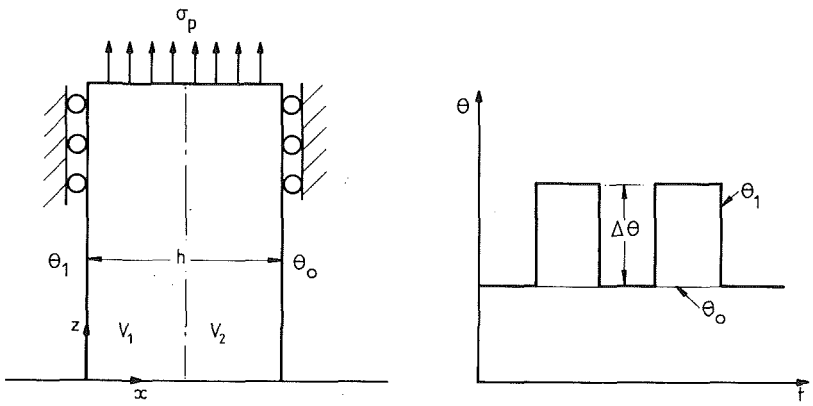


Fig. 1 The Bree problem

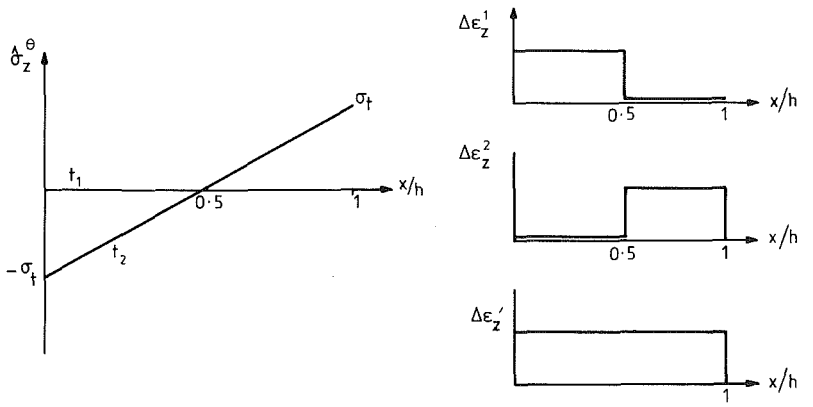


Fig. 2 Thermoelastic stress history and ratchet strain history at shakedown for Bree problem

$$\Delta P\,\Delta u+\Delta\sigma_t\int_V\sum_i \mathbf{h}_i\Delta\epsilon_i dV=-\int_V\sum_i \boldsymbol{\rho}(t_i)\,\Delta\epsilon_i dV \qquad (20)$$

The left-hand side of equation (20) is identical to the right-hand side of equation (11) with P and σ_t replaced by ΔP and $\Delta\sigma_t$. Equation (20) yields the rate of strain and displacement growth per cycle as the left-hand side is linear in the magnitude of the plastic strain while the right-hand side is quadratic.

For quasi-static thermal loading where the surface temperature changes remain proportional, the histories of thermoelastic stress $\hat{\boldsymbol{\sigma}}^\theta(t)$ describes a straight line in stress space between $\hat{\boldsymbol{\sigma}}^\theta(t_1)$ and $\hat{\boldsymbol{\sigma}}^\theta(t_2)$. As plastic strains can only occur at t_1 and t_2, assume $t_1<t_2$, then

$$\Delta\epsilon'=\Delta\epsilon_1+\Delta\epsilon_2, \qquad (21)$$

and

$$\boldsymbol{\rho}(t_1)=\Delta\boldsymbol{\rho},\ \ \boldsymbol{\rho}(t_2)=\boldsymbol{\rho}(\Delta t)=0. \qquad (22)$$

The equation (20) may now be expressed in terms of a single residual field $\Delta\boldsymbol{\rho}$ derived from $\Delta\epsilon_1$:

$$\Delta P\Delta u+\Delta\sigma_t\int_V\{\mathbf{h}(t_1)\Delta\epsilon_1+\mathbf{h}(t_2)\Delta\epsilon_2\}dV$$

$$=-\int_V\Delta\boldsymbol{\rho}\Delta\epsilon_1 dV=\chi \qquad (23)$$

Hence the ratchet rate may be calculated from the solution of a single elastic initial strain problem. For the remainder of this paper attention will be confined to this class of problems. Thermal transient problems [6] will not be discussed here but will be considered in a forthcoming publication.

Bounds on the Linearized Ratchet Rate. A better understanding of equation (23) may be obtained by relating the volume integral to the elastic strain energy density associated with the residual stress field $\Delta\boldsymbol{\rho}$. The incompatible strain field $\Delta\epsilon_1$ is related to $\Delta\boldsymbol{\rho}$ by,

$$\boldsymbol{\epsilon}=\mathbf{C}\,\Delta\,\boldsymbol{\rho}+\Delta\,\boldsymbol{\epsilon}_i \qquad (24)$$

where $\boldsymbol{\epsilon}$ is a compatible strain field. Hence

$$\chi=-\int_V\Delta\boldsymbol{\rho}\Delta\epsilon_1 dV=\int_V\mathbf{C}\Delta\boldsymbol{\rho}\Delta\boldsymbol{\rho}dV=2\bar{U}(\Delta\boldsymbol{\rho}) \qquad (25)$$

where $\bar{U}(\Delta\boldsymbol{\rho})$ is the total complementary elastic strain energy associated with $\Delta\boldsymbol{\rho}$.

The bounds on χ may be constructed in terms of $\tilde{\rho}$ an arbitrary residual stress field and $\Delta\epsilon^c$, an arbitrary compatible strain field,

$$-2\int_V\tilde{\rho}\Delta\epsilon_1 dV-2\bar{U}(\tilde{\rho})\le\chi\le 2U(\Delta\epsilon^c-\Delta\epsilon_1) \qquad (26)$$

where $U(\epsilon)=1/2\ \int_V\mathbf{D}\epsilon\epsilon dV$ denotes the total elastic strain energy of the body and $\mathbf{D}$ denotes the inverse of $\mathbf{C}$. The upper bound on χ which yields a lower bound on the ratchet rate may be given a very simple interpretation for particular types of problems, which will be described after a discussion of the classic Bree problem [4].

3 The Bree Problem

For a structure subjected to a load P close to the limit load the constituent strains $\Delta\epsilon_1$ and $\Delta\epsilon_2$ occur in two nonoverlapping volumes V_1 and V_2 of the total volume V. A solution to such a problem has been given by Bree [4] for a

Downloaded 02 May 2010 to 171.66.16.25. Redistribution subject to ASME license or copyright; see http://www.asme.org/terms/Terms_Use.cfm

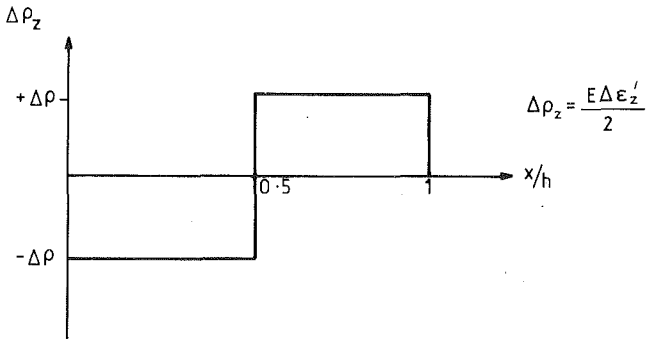


Fig. 3 Residual stress fields $\Delta\rho_z$ due to $\Delta\epsilon_z'$. The elastic strain energy associated with this stress distribution gives the linearized ratchet rate above shakedown.

plate subjected to a varying through thickness temperature difference $\Delta\theta$ and constant uniaxial stress σ_p. The plate is assumed to suffer uniform axial strain through the thickness, as an approximation to an element of a thin-walled tube under internal pressure. The idealized situation is shown in Fig. 1. The thermoelastic solution varies linearly with extreme values of $\pm\sigma_t$ given by

$$\sigma_t = \frac{E\alpha\Delta\theta}{2(1-\nu)} \tag{27}$$

where ν denotes Poissons ratio. As the thermoelastic field is biaxial there appears to be an element of approximation in Bree's solution by treating it as a uniaxial problem. The important approximation is that there is no plastic strain in the equivalent of the axial direction, i.e., the y direction perpendicular to the paper in Fig. 1. This approximation is, in fact, correct if $\sigma_y = \sigma_p/2$ and hence Bree's solution is correct for the thin cylinder problem.

The thermoelastic stress history $\hat{\sigma}_z^\theta$ and the components of the ratchet mechanism

$$\Delta\epsilon_z' = \Delta\epsilon_z^1 + \Delta\epsilon_z^2, \tag{28}$$

corresponding to the two halves of the cycle are shown in Fig. 2. Using this mechanism the shakedown limit may easily be computed from (11), using σ_p instead of the load parameter P

$$\sigma_p + \frac{\sigma_t}{4} = \sigma_y. \tag{29}$$

The residual stress field $\Delta\rho_z$ induced by $\Delta\epsilon_z^1$ is shown in Fig. 3. Hence the ratchet rate given by equation (23) becomes,

$$\left(\Delta\sigma_p + \frac{\Delta\sigma_t}{4}\right)\Delta\epsilon_z' = E\left(\frac{\Delta\epsilon_z'}{2}\right)^2 \tag{30}$$

i.e.,

$$\Delta\epsilon_z' = \frac{4\Delta(\sigma_p + \sigma_t/4)}{E} \tag{31}$$

The exact solution is given by [4],

$$\Delta\epsilon_z' = 2\frac{\sigma_t + \Delta\sigma_t}{E}\left[1 - \left(1 - 4\left(\frac{\Delta\sigma_p + \Delta\sigma_t/4}{(\sigma_t + \Delta\sigma_t)}\right)\right)^{1/2}\right] \tag{32}$$

which for small values of $\Delta\sigma_p$ and $\Delta\sigma_t$ reduces to equation (31). A comparison between these equations in the form of contours of constant $\delta = E\Delta\epsilon_z'/\sigma_y$ is shown in Fig. 4. It is worth noting that as $\sigma_y/E \simeq 0.1$ percent for most metals a value of $E\Delta\epsilon_z'/\sigma_y = 0.2$ corresponds to a ratchet rate of 1 percent strain in 50 cycles, which, from a design point of view, is a high rate of ratcheting. For higher rates of ratchet the linearized form underestimates the exact solution.

For this type of problem as the components $\Delta\epsilon_1$ and $\Delta\epsilon_2$ of the ratchet mechanism occurs in distinct regions V_1 and V_2 of the total volume V, a very simple lower bound on the ratchet

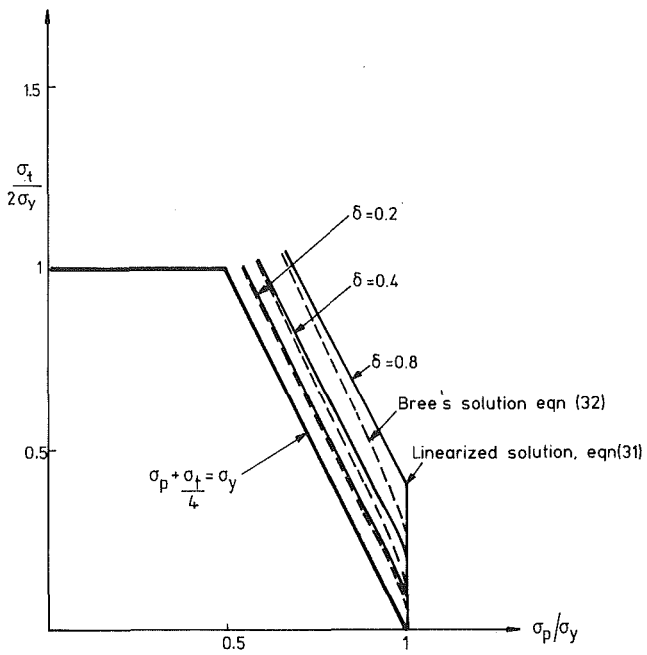


Fig. 4 Comparison between contours of constant $\delta = E\Delta\epsilon_z'/\sigma_y$ for the analytic solution of Bree [4] and the linearized approximation

rate exists which may be derived from the upper bound on χ. In this case,

$$\Delta\epsilon_1 = \begin{cases} \Delta\epsilon' & \text{in } V_1 \\ 0 & \text{in } V_2, \end{cases}$$
$$\Delta\epsilon_2 = \begin{cases} 0 & \text{in } V_1 \\ \Delta\epsilon' & \text{in } V_2. \end{cases} \tag{33}$$

If we choose $\Delta\epsilon^c = \mu\Delta\epsilon'$ and optimize the upper bound (26) with respect to the parameter μ we obtain,

$$\chi \le 2\frac{U_1 U_2}{U} \le \frac{U}{2} \tag{34}$$

where U_1, U_2, and U refer to the elastic strain energy associated with $\epsilon = \Delta\epsilon'$ in V_1, V_2, and V respectively. If we assume for simplicity, that $\Delta\sigma_t = 0$ but $\Delta P \ge 0$ then we obtain the bound

$$\Delta P\Delta u \le \frac{1}{2}U(\Delta\epsilon') \tag{35}$$

i.e.,

$$\Delta u \ge \frac{2\Delta P}{U\left(\frac{\Delta\epsilon'}{\Delta u}\right)} \tag{36}$$

For kinematically determinate structures this bound may be further simplified by noting that Δu and $\Delta\epsilon'$ are proportional to the elastic strains and displacements, hence

$$\Delta\epsilon^e = \frac{\Delta\epsilon'}{\Delta u}\Delta u^e \tag{37}$$

where $\Delta\epsilon^e$ and Δu^e are elastic values. If the body is loaded elastically by load ΔP then

$$\Delta P\Delta u_e = 2U(\Delta\epsilon^e) = 2U\left(\frac{\Delta\epsilon'}{\Delta u}\right)(\Delta u^e)^2, \tag{38}$$

and the bound (36) becomes

$$\Delta u \ge 4\Delta u^e \tag{39}$$

Hence the rate of ratchet per cycle is greater than 4 times the

Downloaded 02 May 2010 to 171.66.16.25. Redistribution subject to ASME license or copyright; see http://www.asme.org/terms/Terms_Use.cfm

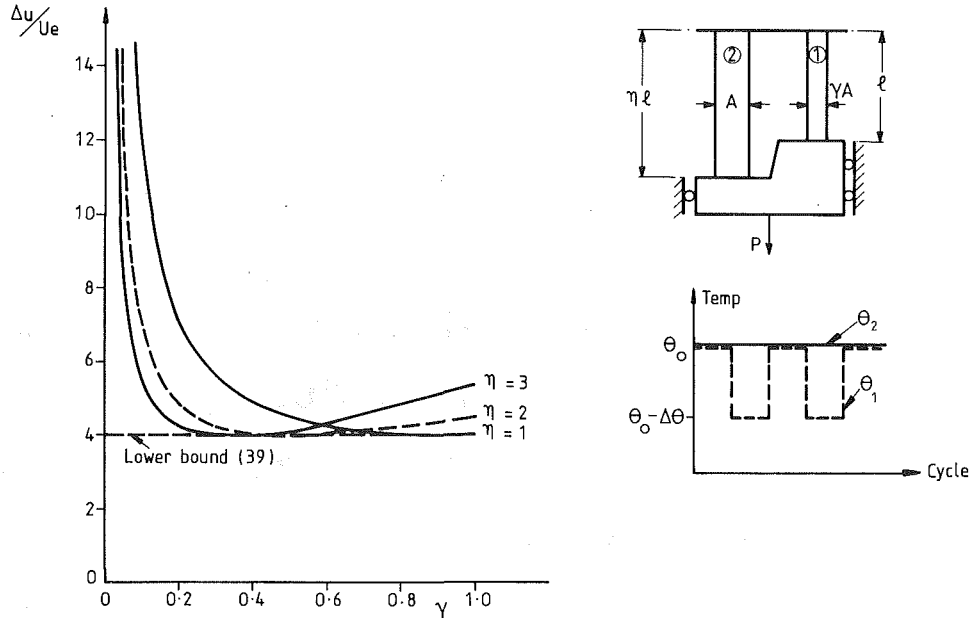


Fig. 5 Ratchet-rate for two-bar structure in terms of geometric parameters η and γ. Δu denotes the ratchet displacement per cycle and U_e the elastic deflection due to ΔP, the increase in P above the shakedown limit

elastic displacement induced in the body by the load ΔP. As this implies 100 u_e for 25 cycles it is clear that P must always be kept very small to prevent unacceptably large accumulations of strain. It can be seen from equation (31) that the bound (39) is exact for the Bree problem.

An alternative interpretation of this result is that if the shakedown load is to be exceeded by 1 percent then the structure would accumulate a ratchet displacement equal to the elastic displacement at the shakedown load in 25 cycles.

Kinematically determinate structures are an important class that includes the Bree problem, and other axially symmetric problems. For problems where the bound (39) does not hold, the result (36) still applies and may be expected to yield results of a similar order of magnitude. An indication of the ranges of values that can occur is given in Fig. 5 where the ratchet rates for two bar structures is compared with the lower bound, for a range of values of the bar length ratio η and bar area ratio γ. The exact solutions have been given by Megahed [5] and are always seen to exceed the lower bound. The highest rates occur for smaller values of γ and large values of η, i.e., when the ratio of volumes V_1/V_2 is small.

4 Conclusions

A linearized theory is used to obtain a relationship between the increment of displacement Δu per cycle and the increase in ΔP and $\Delta\sigma_t$ above the shakedown limit. The key result is equation (20) which requires a priori knowledge of the mechanism of incremental deformation associated with the shakedown boundary. In the paper attention is focused on quasi-static thermal loading, which results in a thermoelastic stress history that describes a straight line in stress space at a material point. Plastic strains then only occur at the extremes of the thermoelastic stress history. For loading cycles where plastic strains are only experienced by a material element at one extreme of the cycle a simple lower bound is obtained, which for kinematically determinate structures, shows that the displacement increment per cycle is at least four times the elastic displacement of the body if it were only subjected to the increase ΔP.

Acknowledgment

The authors are grateful for discussion and assistance in the preparation of Fig. 5 with Dr. M. M. Megahed of the University of Cairo. The work was carried out with the assistance of a grant from the Science and Engineering Research Council of Great Britain.

References

1 Koiter, W. T., "General Theorems for Elastic-plastic Solids," *Progress in Solid Mechanics*, Hill, R., and Sneddon, I., eds., North Holland Press, 1960, p. 167.

2 Prager, W., "Shakedown in Elastic-plastic Media Subjected to Cycles of Load and Temperature," *Symposium su la Plasticita' Nella Scienza Delle Construzioni*, Bologna, 1957, pp. 239–244.

3 Holmes, J. A. G., "High Temperature Problems Associated With Design of the Commercial Fast Reactor," *Creep in Structures*, 3rd IUTAM Symposium Leicester 1980, Ponter, A. R. S., and Hayhurst, D. R., eds., Springer Verlag, 1981, pp. 279–286.

4 Bree, J., "Elastic-Plastic Behaviour of Thin Tubes Subjected to Internal Pressure and Intermittent High Heat Fluxes With Application to Fast Nuclear-Reactor Fuel Elements," *J. Strain Analysis*, Vol. 2, No. 3, 1967, pp. 226–238.

5 Megahed, M. M., "Influences of Hardening Rule on the Elasto-Plastic Behaviour of a Simple Structure Under Cyclic Loading," *Int. J. Mech. Sci.*, Vol. 23, 1981, pp. 169–182.

6 Goodman, A. M., "The Influence of Rapid Thermal Transients on Elastic-Plastic Ratchetting," CEGB, Berkeley Nuclear Laboratories, Report No. RD/B/N4492, Feb. 1979.

7 Arnaudeau, F., Zarka, J., and Geriji, J., "Thin Circular Cylinder Under Axisymmetrical Thermal and Mechanical Loading," Paper L6/5, 4th SMIRT Conference, San Francisco 1977, North Holland, 1977.

Downloaded 02 May 2010 to 171.66.16.25. Redistribution subject to ASME license or copyright; see http://www.asme.org/terms/Terms_Use.cfm

The Incremental Strain Growth of Elastic-Plastic Bodies Subjected to High Levels of Cyclic Thermal Loading

A. R. S. Ponter
Professor of Engineering.

A. C. F. Cocks
Research Associate.

Department of Engineering,
Leicester University,
Leicester, LE1 7 RH, England

A linearized method of analysis proposed in an accompanying paper [1] is used to obtain the ratchet rate for two types of thermal loading problems where parts of the structure experience reversed plastic straining. For structures that can shakedown plasticially it is found that for a given increment of load beyond the plastic shakedown boundary, the rate of ratchet increases with increasing level of thermal loading. When a structure is unable to shakedown plastically it ratchets at low mechanical loading as the result of a localized mechanism that involves some reversed plasticity. It is shown that the ratchet rate in such situations can be substantial but its value is very dependent on the local curvature of the yield and not the accuracy of the yield surface itself.

1 Introduction

In an accompanying paper [1] a linearized theory is used to obtain a relationship between the increment of displacement per cycle and the increase of load above the shakedown limit for a body subjected to a constant load P and a time-varying cyclic temperature distribution, characterized by the maximum thermoelastic stress σ_t. It is assumed that both the shakedown limit and strain increments associated with the shakedown solution are known a priori. When the thermal loading is quasi-static, and the surface temperature changes remain proportional, the thermoelastic stress history at a material point describes a straight line in stress space between $\hat{\sigma}_1^\theta = \sigma_t \mathbf{h}_1$ and $\hat{\sigma}_2^\theta = \sigma_t \mathbf{h}_2$. Plastic strains can occur at these two extremes and the resulting total plastic strain, $\Delta\epsilon'$, accumulated at a point over a cycle is

$$\Delta\epsilon' = \Delta\epsilon_1 + \Delta\epsilon_2 \tag{1}$$

where $\Delta\epsilon_1$ and $\Delta\epsilon_2$ represent the increments of plastic strain at instants 1 and 2 in the cycle. If Δu is the increment of displacement that results from the compatible strain field $\Delta\epsilon'$, then at the shakedown limit [1]

$$\sigma_y \int_V \Delta\epsilon_e' dV = P\Delta u + \sigma_t \int_V (\mathbf{h}_1 \Delta\epsilon_1 + \mathbf{h}_2 \Delta\epsilon_2) dV \tag{2}$$

where σ_y is the yield stress and $\Delta\epsilon_e'$ is the effective increment of plastic strain during a cycle. For an increase of load, ΔP or $\Delta\sigma_t$, above the shakedown boundary, the increment of displacement over a cycle is given by [1]

$$\Delta P\, \Delta u + \Delta\sigma_t \int_V (\mathbf{h}_1 \Delta\epsilon_1 + \mathbf{h}_2 \Delta\epsilon_2) dV = -\int_V \Delta\rho\, \Delta\epsilon_1\, dV = \chi \tag{3}$$

where $\Delta\rho$ is the residual stress field resulting from the incompatible strain distribution $\Delta\epsilon_1$. The left-hand side of equation (3) is identical to the right-hand side of equation (2) with P and σ_t replaced by ΔP and $\Delta\sigma_t$.

In [1] equations (2) and (3) are used to analyze problems where the plastic strain increment at a material point occurs only at one instant in the cycle. In the present paper we extend the analysis to include situations where plastic straining can occur at each extreme of the thermal loading cycle in a material element. The method of [1] is applied to two problems that represent distinct types of thermal loading situations where the region of severe thermal stress does or does not contain a mechanism, and whose ability to withstand large thermal stress is markedly different. The ratchet rates given by the simple linearized theory are compared with analytic [2] and numerical solutions [3]. A comparison of the solutions for Tresca and Mises yield conditions demonstrates that small changes in the curvature of the yield surface may have little effect on the shakedown loads but can have a substantial effect on the rate of ratchet beyond shakedown when a reverse-plasticity mechanism is involved.

2 The Ratchet Rate Beyond the Reversed Plasticity Boundary

When a structure is subjected to high levels of cyclic thermal loading its response depends on its ability to

Contributed by the Applied Mechanics Division for presentation at the Winter Annual Meeting, New Orleans, La., December 9-14, 1984 of THE AMERICAN SOCIETY OF MECHANICAL ENGINEERS.

Discussion on this paper should be addressed to the Editorial Department, ASME, United Engineering Center, 345 East 47th Street, New York, N.Y. 10017, and will be accepted until two months after final publication of the paper itself in the JOURNAL OF APPLIED MECHANICS. Manuscript received by ASME Applied Mechanics Division, December, 1983. Paper No. 84-WA/APM-11.

Copies will be available until August, 1985.

Copyright © 1984 by ASME
Downloaded 02 May 2010 to 171.66.16.25. Redistribution subject to ASME license or copyright; see http://www.asme.org/terms/Terms_Use.cfm

redistribute the mechanical load. In the present section we consider structural problems where, for low levels of mechanical load, regions of the structure that suffer large cyclic thermoelastic strains can shed their load to other parts of the structure. As a result these regions suffer reverse plastic straining with no net increase of plastic strain over a cycle. The structure is then said to have shaken down plastically. In these situations it is not the deformation of the structure that limits the level of thermal loading in design, but the fatigue characteristics of the material. This is a separate problem and will not be discussed further here.

If the mechancial load is gradually increased then the structure will eventually begin to ratchet. The method of analysis described in [1] can be extended to calculate the ratchet rate for small excursions into the ratcheting region from the plastic shakedown boundary. On the boundary, part of the structure suffers reversed plastic straining, the volume V_F in Fig. 1, while the remainder shakes down, suffering only elastic cyclic strains once a stable cyclic state is attained. For a small increase of primary load beyond this boundary, the linearized method assumes that: (*a*) the same volume of material experiences reversed plasticity, although a net increase of plastic strain can occur in this volume during each cycle. (*b*) The direction of the plastic strain-rate vectors remain the same when the increment of load is added for each element of material at every point in the cycle in both V_F and V_s. As a result the residual stress field in V_F is unaffected by the increase of load that must be entirely supported by the volume V_s. Equation (3) then becomes

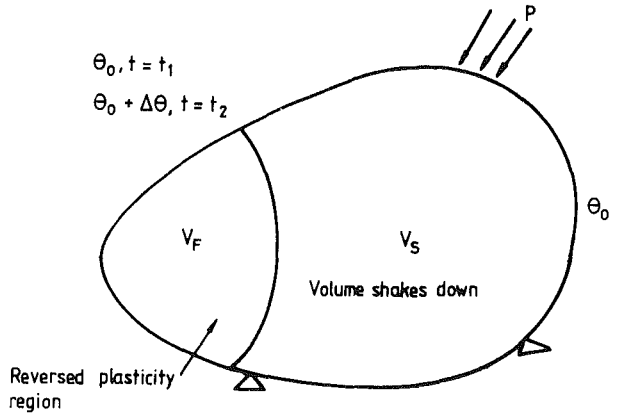


Fig. 1 Structure subjected to a constant primary load and cyclic thermal loading. Part of the structure suffers reversed plastic straining while the remainder shakes down.

$$\Delta P \Delta u = -\int_{V_s} \Delta\rho \Delta\epsilon_1 \, dV = \chi \tag{4}$$

where $\Delta\rho$ is the residual stress field resulting from the incompatible strain field $\Delta\epsilon_1$ in V_s when the volume V_F is removed from the structure.

A typical example of this class of problems is the classic Bree plate problem [2]. The two volumes are shown in Fig. 2 for a loading point on the reversed plasticity/ratcheting boundary of Fig. 3, which is given by [2]

$$\sigma_p \sigma_t = \sigma_y^2 \tag{5}$$

when the yield stress is assumed to be invariant with temperature. The volume V_s is of width 2α, where

$$\alpha = \frac{\sigma_y}{\sigma_t} h \tag{6}$$

The ratchet mechanism and residual stress field in this inner volume are the same as those in the shakedown regime (see Figs. 2 and 3 of [1]). If the temperature is uniform through the structure at time t_1, and is nonuniform at time t_2, then

$$\Delta\epsilon_z^1 = \begin{cases} \Delta\epsilon_z' & \text{in } V_s^1 \\ 0 & \text{in } V_s^2 \end{cases}$$

$$\Delta\epsilon_z^2 = \begin{cases} 0 & \text{in } V_s^1 \\ \Delta\epsilon_z' & \text{in } V_s^2 \end{cases} \tag{7}$$

and the resulting residual stress field at t_1 is

$$\Delta\rho_z = \begin{cases} E\Delta\epsilon_z^1/2 & \text{in } V_s^1 \\ -E\Delta\epsilon_z^1/2 & \text{in } V_s^2 \end{cases} \tag{8}$$

Substituting equations (7) and (8) into equation (4) gives the rate of ratchet beyond the plastic shakedown boundary:

$$\Delta\sigma_p \Delta\epsilon_z' = E\left[\frac{\Delta\epsilon_z'}{2}\right]^2 \frac{2\sigma_y}{\sigma_t} \tag{9}$$

i.e.,

$$\Delta\epsilon_z' = 2\frac{\sigma_t}{\sigma_y}\frac{\Delta\sigma_p}{E}$$

which is the same as the exact result given by Bree [2]. Contours of constant $\delta = E\Delta\epsilon_z'/\sigma_y$ are shown in Fig. 3. As observed in [1], a high rate of ratchet, for a design point of view, is obtained for small excursions into the ratchet region.

For problems where assumptions (*a*) and (*b*) are satisfied, which may be decided by consideration of the particular case, the lower bound to the rate of ratchet given in [1] increases as

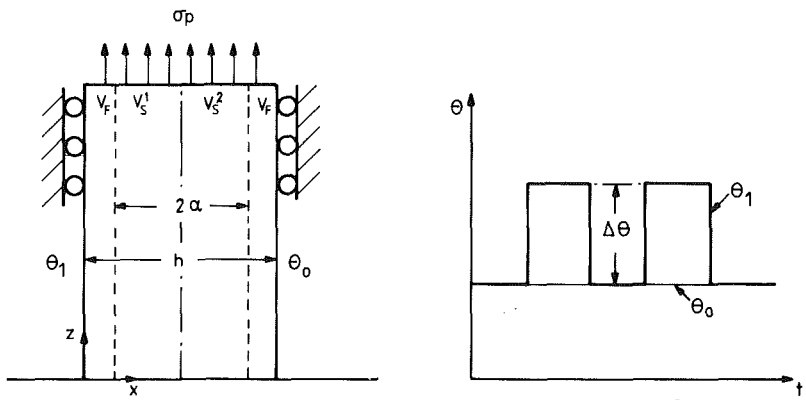


Fig. 2 The Bree problem analyzed in Section 2. The volumes V_s^1 and V_s^2 shakedown while V_F suffers reversed plastic straining.

Downloaded 02 May 2010 to 171.66.16.25. Redistribution subject to ASME license or copyright; see http://www.asme.org/terms/Terms_Use.cfm

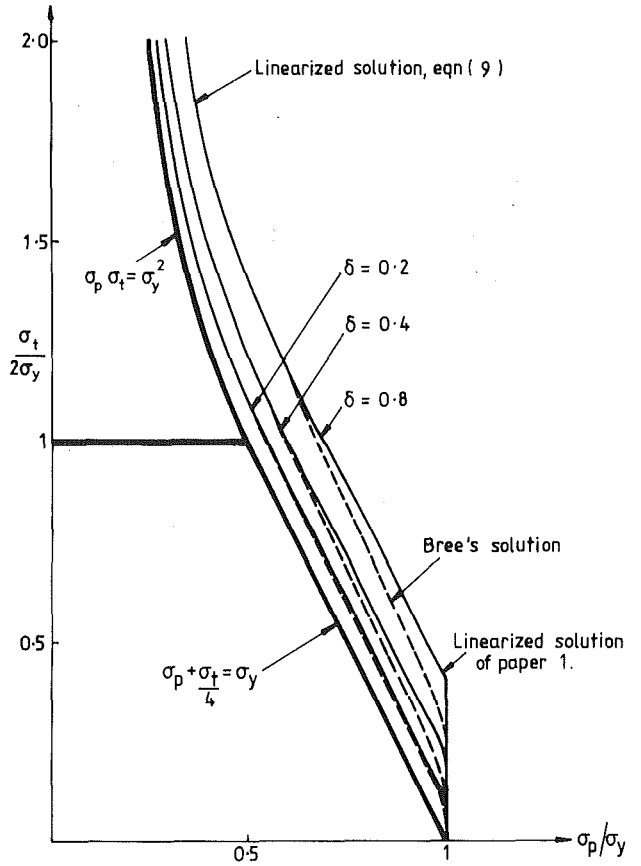


Fig. 3 Comparison between contours of constant $\delta = E\Delta\epsilon_z'/\sigma_y$ for the analytical solution of Bree [2] and the linearized approximations of Section 2 and reference [1].

σ_t increases. This can be clearly seen in the Bree problem where the bound, which in fact equals the exact solution equation (9), states that the ratchet rate equals 4 times the elastic deflection of the plate reduced in thickness from h to 2α. This result implies that, for problems of a similar nature to the Bree problem, the rate of ratchet is greater in the reverse plasticity regime than the shakedown regime.

3 Ratcheting Due to Reversed Plastic Cycling

A separate class of ratcheting problem occurs for large thermal loading when the volume of material where the maximum effective thermoelastic stress exceeds twice the uniaxial yield stress contains a mechanism of deformation that may be activated by the applied load P. Unlike the Bree problem where some applied load may always be carried by the lowly stressed central part of the plate, in these problems ratcheting can occur at very small applied loads by a very localized ratchet mechanism. Although the resulting overall distortion of the body may be small the local strains may grow rapidly.

The simplest example of this situation is shown in Fig. 4 where a tube of radius R and thickness $t << R$ is subjected to a constant axial stress σ_p and a temperature discontinuity that oscillates over a short length of tube a. Each element of material in this length of tube experiences a hoop component of stress whose range of oscillation is $2\sigma_t$, where $\sigma_t = E\alpha\Delta\theta/2$. Beyond the shakedown boundary, the mechanism of ratcheting is one of local thinning over the length a. The shakedown boundaries and the linearized ratchet rates for this mechanism are derived in the Appendix for both Mises and Tresca yield conditions and the results are shown in Fig. 5. The shakedown boundaries differ by a maximum of about $0.15\ \sigma_t/\sigma_y$ at $\sigma_p/\sigma_y = 0.5$ with a much smaller difference near

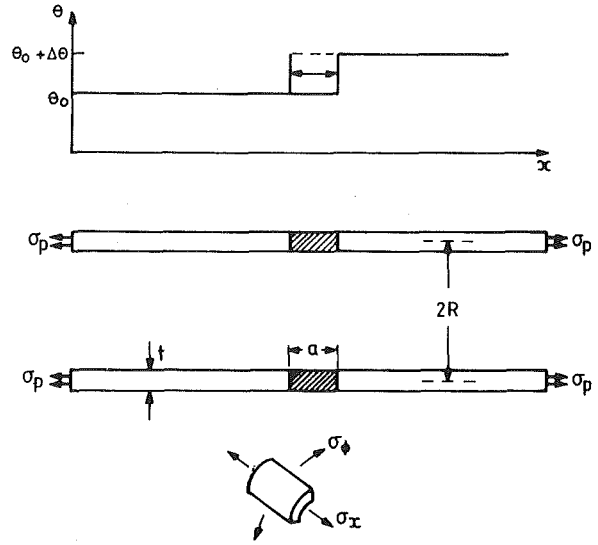


Fig. 4 A tube subjected to a constant axial stress σ_p and a temperature discontinuity that oscillates over a short length of tube a. The ratchet mechanims consists of a uniform axial strain in a.

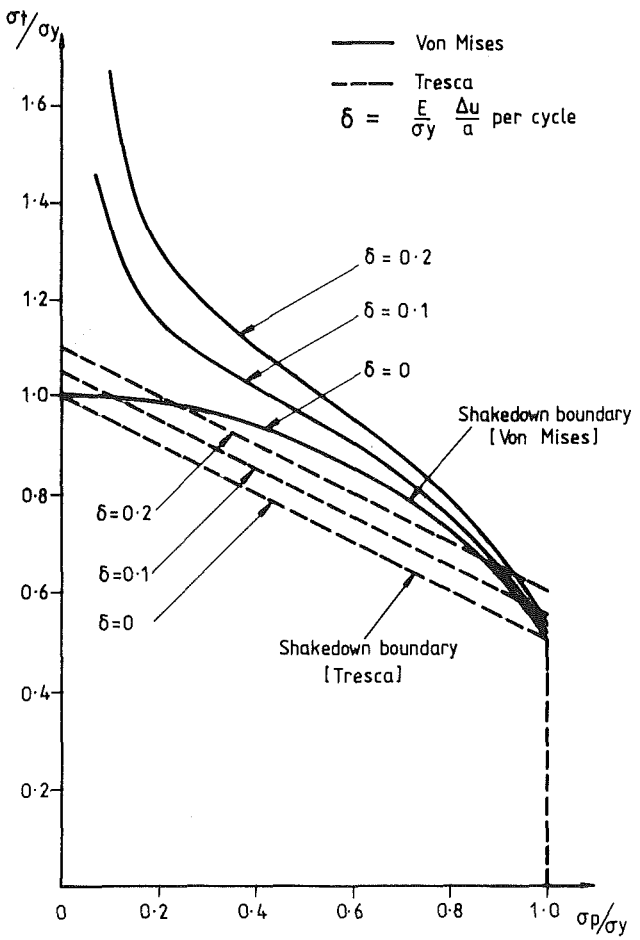


Fig. 5 Shakedown boundaries and contours of constant ratchet rate for the problem shown in Fig. 4

$\sigma_p = 0$. The contours of constant ratchet rate, however, show considerable deviations near $\sigma_p = 0$, with a much lower rate for the von Mises yield condition. This difference is due to the difference in the curvature of the yield surfaces, shown in Figs. $A1$ and $A2$, near $\sigma_x = 0$. This calculation indicates that a very accurate description of the yield surfaces is required to obtain an accurate assessment of the ratchet rate.

Downloaded 02 May 2010 to 171.66.16.25. Redistribution subject to ASME license or copyright; see http://www.asme.org/terms/Terms_Use.cfm

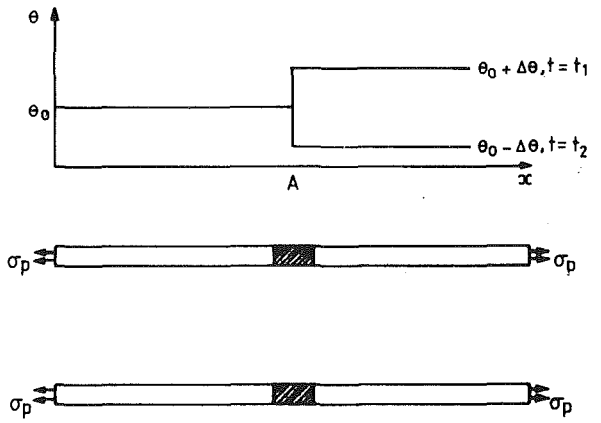


Fig. 6 Tube subjected to a constant stress σ_P and a changing temperature discontinuity at A. The ratchet mechanism consists of a nonuniform axial strain within a small volume of tube on either side of the discontinuity.

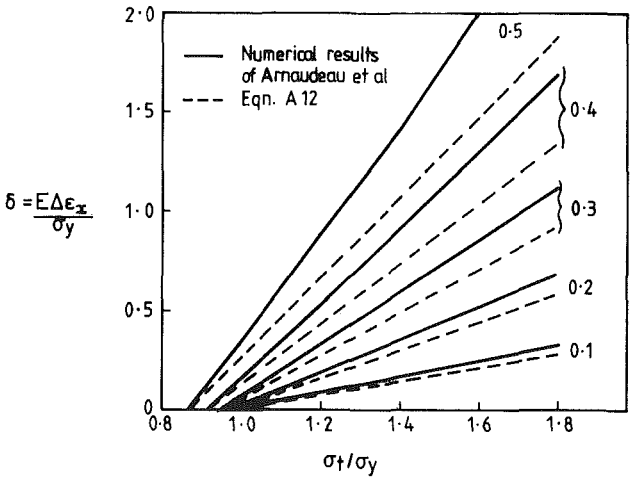


Fig. 7 Maximum axial strain per cycle for a range of values of $x = \sqrt{3}\,\sigma_P/2\sigma_y$ for problem of Fig. 5 for a von Mises material

The ratchet rates for both yield conditions are nevertheless quite substantial and comparable in magnitude to the Bree problem, except for very small values of σ_p in the von Mises solution.

Arnaudeau et al. [3] have obtained numerical results for the thermal loading problem of Fig. 6 for a von Mises material, where to the left of A the temperature remains constant at $\theta = \theta_0$ but to the right it oscillates between $\theta_0 + \Delta\theta$ and $\theta_0 - \Delta\theta$. An analysis similar to that performed in the Appendix results in a shakedown boundary and a maximum axial strain rate per cycle, which occurs at the point A, which are the same as those for the short travel problem of Fig. 4. A comparison between the maximum axial strain rate per cycle given by Arnaudeau et al. [3][1] and equation ($A12$), the linearized ratchet rate for a von Mises material, is given in Fig. 7. Agreement is good, with the linearized method underestimating the numerical results by no more than 25 percent.

Acknowledgment

The work was carried out with the assistance of a grant from the Science and Engineering Research Council of Great Britain.

[1] Extrapolation of Arnaudeau et al.'s [3] results to zero ratchet rate results in a shakedown boundary given by $x^2 + y^2 = 1$, where they define x as σ_p/σ_y and y as σ_t/σ_y. The shakedown boundary is in fact given by $3/4(\sigma_p/\sigma_y)^2 + (\sigma_t/\sigma_y)^2 = 1$. In the comparison of the present results with theirs we have therefore assumed that x should have been defined as $x = \sqrt{3}/2\ \sigma_p/\sigma_y$.

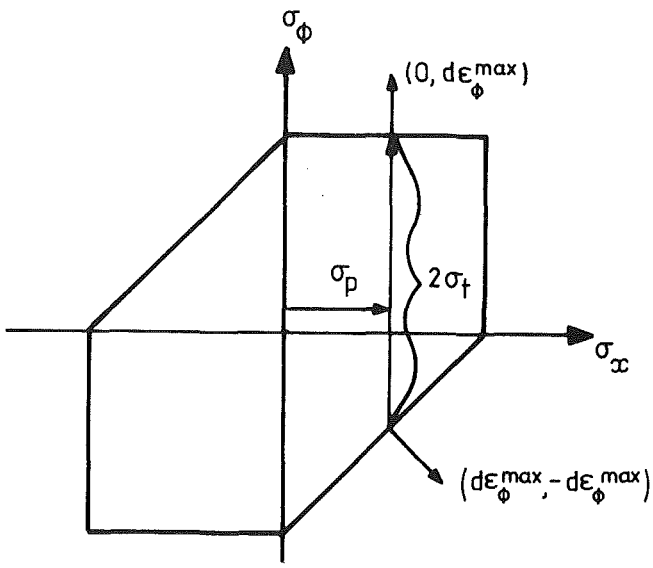


Fig. $A1$ Plastic strains associated with the Tresca yield condition in the ratcheting volume

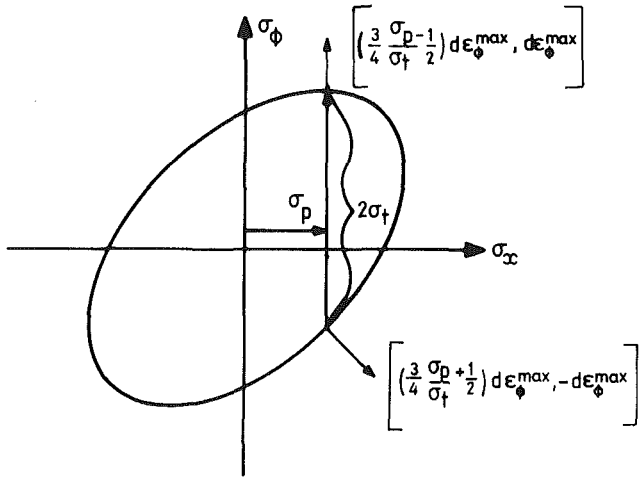


Fig. $A2$ Plastic strains associated with the Mises yield condition in the ratcheting volume

References

1 Ponter, A. R. S., and Cocks, A. C. F., "The Incremental Strain Growth of an Elastic-Plastic Body Loaded in Excess of the Shakedown Limit," ASME Journal of Applied Mechanics, Vol. 51, 1984, pp. 00-00.

2 Bree, J., "Elastic-Plastic Behavior of Thin Tubes Subjected to Internal Pressure and Intermittent High Heat Fluxes With Application to Fast Nuclear-Reactor Fuel Elements," *J. Strain Analysis*, Vol. 2, No. 3, 1967, pp. 226-238.

3 Arnaudeau, F., Zarka, J., and Gerij, J., "Thin Circular Cylinder Under Axisymmetrical Thermal and Mechanical Loading," Paper L6/5, 4th SMIRT Conference, San Francisco, 1977, North Holland, 1977.

APPENDIX

Shakedown and Ratchet Rates for the Tube Problem

When a temperature front oscillates over a short length of tube, Fig. 4, the mechanism of deformation just outside the shakedown boundary is one of local thinning. At each point of the tube over which the temperature front moves the variation of stress for a loading point on the shakedown boundary is shown in Figs. $A1$ and $A2$ for materials that yield according to the Tresca and von Mises conditions, respectively. If the load is increased by a small amount, then as the temperature front moves along the tube there is a buildup of

Downloaded 02 May 2010 to 171.66.16.25. Redistribution subject to ASME license or copyright; see http://www.asme.org/terms/Terms_Use.cfm

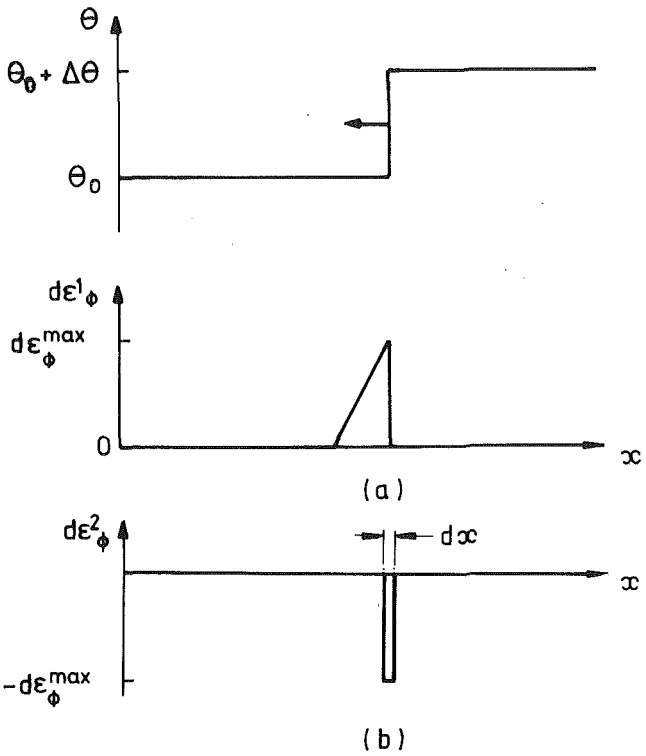


Fig. A3 (a) Distribution of plastic hoop strain ahead of moving temperature front. (b) The change of plastic hoop strain when the front moves a small amount dx.

plastic strain ahead of the front, and as the front passes a material element there is a sudden increment of plastic strain in the reversed direction, Fig. A3.

The analysis of [1] assumes that the direction of the plastic strain rate does not change for an increase of load beyond the shakedown boundary. Because the axial stress cannot redistribute, this condition can only be fulfilled for a von Mises material if $\Delta\sigma_p$ is set to zero and only an increment of thermal loading is considered. The shakedown boundary and rate of ratchet beyond the boundary can be found by calculating the amount of plastic strain accumulated in an element of tube as the front passes.

When the front is directly above an element of material $d\epsilon_\phi^1 = d\epsilon_\phi^{\max}$, see Fig. A3, and we can write

$$\sigma_y d\epsilon_e^1 = \sigma_p d\epsilon_x^1 + (\sigma_t + \Delta\sigma_t) d\epsilon_\phi^1 + \rho_\phi^1 d\epsilon_\phi^1 \tag{A1}$$

where $d\epsilon_e^1$ is the effective strain increment associated with $d\epsilon_\phi^1$ and depends on the choice of flow rule, and $\Delta\sigma_t$ is the increment above the shakedown boundary for which the ratchet rate is required. When the front moves a small distance, the material element experiences a further increment of hoop strain $d\epsilon_\phi^2 = -d\epsilon_\phi^{\max}$, as $\hat{o}_\phi^\theta$ changes from $\sigma_t + \Delta\sigma_t$ to $-(\sigma_t + \Delta\sigma_t)$ while, to first order, there is no further increase of plastic strain in the rest of the tube, then

$$\sigma_y d\epsilon_e^2 = \sigma_p d\epsilon_x^2 - (\sigma_t + \Delta\sigma_t) d\epsilon_\phi^2 + \rho_\phi^2 d\epsilon_\phi^2 \tag{A2}$$

Combining equations (A1) and (A2) gives

$$\sigma_y (d\epsilon_e^1 + d\epsilon_e^2) = \sigma_p (d\epsilon_x^1 + d\epsilon_x^2) + 2(\sigma_t + \Delta\sigma_t) d\epsilon_\phi^{\max} + \Delta\rho_\phi d\epsilon_\phi^{\max} \tag{A3}$$

where $\Delta\rho_\phi = \rho_\phi^1 - \rho_\phi^2$ and is the change in the residual stress field as the front passes.

On the shakedown boundary $\Delta\sigma_t$ and $\Delta\rho_\phi$ equal zero and

$$\sigma_y (d\epsilon_e^1 + d\epsilon_e^2) = \sigma_p (d\epsilon_x^1 + d\epsilon_x^2) + 2\sigma_t d\epsilon_\phi^{\max} \tag{A4}$$

which we could have found directly from equation (2). This equation is used later to obtain shakedown boundaries for the different flow rules.

Combining equations (A3) and (A4) we find

$$2\Delta\sigma_t d\epsilon_\phi^{\max} = -\Delta\rho_\phi d\epsilon_\phi^{\max} \tag{A5}$$

which, again, could have been obtained from equation (3). The residual stress $\Delta\rho_\phi$ can be found by noting that as the front passes a material element, the change in plastic hoop strain at that point is $d\epsilon_\phi^{\max}$. Elsewhere there is no change of plastic strain, so $\Delta\rho_\phi$ results from the elastic analysis of a tube subjected to a plastic prestrain $d\epsilon_\phi^{\max}$ over an infinitesimally small length, and we need not know the distribution of plastic strain ahead of the front. Because the length of tube over which the prestrain exists is so small, the remainder of the tube constrains the deformation so that the total strain is zero. The residual stress in the element is then

$$\Delta\rho_\phi = -E d\epsilon_\phi^{\max} \tag{A6}$$

Substituting this into equation (A5) gives

$$d\epsilon_\phi^{\max} = \frac{2\Delta\sigma_t}{E} \tag{A7}$$

The increment of axial strain for a passage of the temperature front is related to $d\epsilon_\phi^{\max}$ through the choice of flow rule. For a Tresca flow rule, Fig. A1,

$$d\epsilon_x = d\epsilon_x^1 + d\epsilon_x^2 = d\epsilon_\phi^{\max}$$

and the increment of plastic strain as the front passes is

$$d\epsilon_x = \frac{2\Delta\sigma_t}{E} \tag{A8}$$

The shakedown boundary is given by equation (A4), where

$$d\epsilon_e^1 + d\epsilon_e^2 = 2d\epsilon_\phi^{\max}$$

and equation (A4) becomes

$$\sigma_y = \frac{\sigma_p}{2} + \sigma_t \tag{A9}$$

For a von Mises material, Fig. A2,

$$d\epsilon_x = d\epsilon_x^1 + d\epsilon_x^2 = \frac{3}{2}\frac{\sigma_p}{\sigma_t} d\epsilon_\phi^{\max} \tag{A10}$$

and

$$d\epsilon_e^1 + d\epsilon_e^2 = 2\frac{\sigma_y}{\sigma_t} d\epsilon_\phi^{\max} \tag{A11}$$

The resulting ratchet rate is

$$d\epsilon_x = \frac{3\Delta\sigma_t}{E}\frac{\sigma_p}{\sigma_t} \tag{A12}$$

above the shakedown boundary

$$\sigma_y^2 = \frac{3}{4}\sigma_p^2 + \sigma_t^2 \tag{A13}$$

Equations (A8) and (A12) represent the increment of axial plastic strain for each pass of the front. The increment of strain per cycle is twice that given by these equations.

Downloaded 02 May 2010 to 171.66.16.25. Redistribution subject to ASME license or copyright; see http://www.asme.org/terms/Terms_Use.cfm

Notch-Tip Stresses in a Creeping Solid

J. L. Bassani
Department of Mechanical Engineering and Applied Mechanics, University of Pennsylvania, Philadelphia, Pa. 19104
Mem. ASME

At high stress levels the creep strain rate for many materials varies as the exponential of stress while at low stresses it varies as stress to some power. An analysis is presented for a sharp notch under antiplane shear loading in a material that deforms by hyperbolic-sine-law creep, $\dot{\epsilon}^c = \dot{\epsilon}_0[\sinh(\sigma/\sigma_0)]^n$. The asymptotic notch-tip stress intensification is weaker and the strain-rate intensification is stronger than for a power-law creeping material.

Introduction

At elevated temperatures many materials, including polycrystalline and amorphous metals, exhibit a uniaxial secondary creep behavior that can be described by the hyperbolic-sine creep relation

$$\dot{\epsilon} = \dot{\epsilon}_0[\sinh(\sigma/\sigma_0)]^n \tag{1}$$

where $\dot{\epsilon}$ is the creep strain rate associated with the uniaxial stress σ, and $\dot{\epsilon}_0$, σ_0, and n are material constants [1, 2]. At low stress levels, $\sigma \ll \sigma_0$, equation (1) reduces to the well-known power law

$$\dot{\epsilon} = \dot{\epsilon}_0(\sigma/\sigma_0)^n, \quad \text{for } \sigma \ll \sigma_0 \tag{2}$$

while at high stress levels, $\sigma \ll \sigma_0$, equation (1) reduces to the exponential law

$$\dot{\epsilon} = 2^{-n}\dot{\epsilon}_0 \exp(n\sigma/\sigma_0), \quad \text{for } \sigma \gg \sigma_0 \tag{3}$$

These limiting forms of the hyperbolic-sine relation suggest that the reference stress σ_0 can be interpreted as the so-called power-law breakdown stress level. Note that the power-law form involves two material constants: n and $\dot{\epsilon}_0/\sigma_0{}^n$, while the hyperbolic-sine form involves three: n, $\dot{\epsilon}_0$, and σ_0.

Even when nominal stress levels are well below the power-law breakdown stress, σ_0, stress concentrators such as sharp notches and cracks can elevate stresses in the notch-tip region well above σ_0 [1]. In this paper the stress and strain-rate fields around a sharp notch loaded in antiplane shear (Mode *III*) are analyzed for a material that deforms by hyperbolic-sine secondary creep. Here, as in most power-law creep analyses, the isotropic, multiaxial generalization of the uniaxial law (1) is obtained in terms of the Mises effective stress

$$\bar{\sigma} = \left(\frac{3}{2}\sigma'_{ij}\sigma'_{ij}\right)^{1/2} \tag{4}$$

where σ'_{ij} denotes the deviatoric components of the stress tensor. The creep strain rates are taken to be parallel to σ'_{ij} [1]:

$$\dot{\epsilon}_{ij} = \frac{3}{2}\dot{\epsilon}_0[\sinh(\bar{\sigma}/\sigma_0)]^n \sigma'_{ij}/\bar{\sigma} \tag{5}$$

The analysis of the notch-tip fields is based on a hodograph transformation, whereby the spatial coordinates x_1 and x_2 are regarded as functions of the nonzero stress components σ_{31} and σ_{32}. As Neuber [3] and Rice [4] have noted, this hodograph transformation can be adapted for any uniaxial creep relation with the Mises multiaxial generalization. The governing equations are derived in the next section for a general creep function and then specialized for hyperbolic-sine and exponential-law creep. At the notch tip the fields become singular and, therefore, the asymptotic behavior is governed by the high stress limit of the hyperbolic-sine law, i.e., the exponential law (2). The notch-tip stress singularity is found to be weaker than in the power-law case, while the strain-rate singularity is stronger.

Hodograph Transformation for General Creep Law

In this section the hodograph transformation is used to derive a second-order, linear, partial differential equation for a scalar potential function $\psi(\tau)$, which is used subsequently to find the asymptotic notch-tip fields. Boundary conditions for ψ associated with traction-free notch surfaces lead to separable solutions in terms of polar stress variables τ and ϕ defined in the following. The antiplane shear problem corresponds to zero in-plane displacement-rates, $\dot{u}_1 = \dot{u}_2 = 0$, and nonzero $\dot{u}_3(x_1, x_2)$. The normalized and non-dimensional nonzero strain-rates are $\gamma_1 = 2\dot{\epsilon}_{31}/\dot{\gamma}_0 = \dot{u}_{3,1}/\dot{\gamma}_0$ and $\gamma_2 = 2\dot{\epsilon}_{32}/\dot{\gamma}_0 = \dot{u}_{3,2}/\dot{\gamma}_0$ (where a comma denotes a partial derivative) and the corresponding stresses are $\tau_1 = \sigma_{31}/\tau_0$ and $\tau_2 = \sigma_{32}/\tau_0$. Here $\dot{\gamma}_0$ and τ_0 are material parameters that replace $\dot{\epsilon}_0$ and σ_0 in equations (1)–(3).

Governing Equations. The rate form of the compatibilty condition is

$$\gamma_{1,2} - \gamma_{2,1} = 0 \tag{6a}$$

or in vector notation in terms of the vector cross product

$$\nabla_x \times \boldsymbol{\gamma} = \mathbf{0} \tag{6b}$$

where $\boldsymbol{\gamma}$ is a two-dimensional vector with cartesian components γ_1 and γ_2, and ∇_x is the gradient operator with

Contributed by the Applied Mechanics Division for publication in the JOURNAL OF APPLIED MECHANICS.
Discussion on this paper should be addressed to the Editorial Department, ASME, United Engineering Center, 345 East 47th Street, New York, N.Y. 10017, and will be accepted until two months after final publication of the paper itself in the JOURNAL OF APPLIED MECHANICS. Manuscript received by ASME Applied Mechanics Division, June, 1983; final revision, December, 1983.

Copyright © 1984 by ASME
Downloaded 02 May 2010 to 171.66.16.25. Redistribution subject to ASME license or copyright; see http://www.asme.org/terms/Terms_Use.cfm

respect to the physical coordinates x_1 and x_2. The equilibrium condition is

$$\tau_{1,1} + \tau_{2,2} = 0 \tag{7a}$$

or in terms of the scalar product

$$\nabla_x \cdot \tau = 0 \tag{7b}$$

where τ has cartesian components τ_1 and τ_2.

A general form for the creep law in terms of the creep function $f(\tau)$ that is useful for the present analysis is

$$\gamma_\alpha = f(\tau)\frac{\tau_\alpha}{\tau} \tag{8}$$

where the subscript α takes on the values 1 and 2. Here the nondimensional effective stress and strain rates are, respectively,

$$\tau = (\tau_1^2 + \tau_2^2)^{1/2} \tag{9}$$

$$\gamma = (\gamma_1^2 + \gamma_2^2)^{1/2} \tag{10}$$

so that $\gamma = f(\tau)$.

For other than a linear, homogeneous creep function, $f(\tau)$, equations (6)–(8) form a quasilinear system. They are simplified using a hodograph transformation [1, 3, 4], whereby the coordinates x_α are regarded as functions of the stresses τ_α or strain rates γ_α. The presentation given in the following closely follows the one given by Rice [4], although Rice chose γ for the primary independent variables whereas τ is chosen for the present analysis.

Let $\mathbf{x}$ be considered a function of γ. Then the compatibility equation (6) can be rewritten as [1, 3, 4].

$$\nabla_\gamma \times \mathbf{x} = \mathbf{0} \tag{11}$$

when the Jacobian $\partial(x_1, x_2)/\partial(\gamma_1, \gamma_2) \neq 0$. Here, ∇_γ is the two-dimensional gradient vector with respect to the strain-rate vector $\boldsymbol{\gamma}$. Similarly, let $\mathbf{x}$ be considered a function of τ. Then the equilibrium equation (7) can be rewritten as

$$\nabla_\tau \cdot \mathbf{x} = 0 \tag{12}$$

when the Jacobian $\partial(x_1, x_2)/\partial(\tau_1, \tau_2) \neq 0$. Here, ∇_τ is the gradient vector in the stress variables.

With the general Mises constitutive relation equation (8), it is easy to verify that (summation over repeated subscript $\alpha = 1, 2$ is implied and $f' = df/d\tau$)

$$\frac{\partial}{\partial \gamma_\beta} = \frac{\partial \tau_\alpha}{\partial \gamma_\beta}\frac{\partial}{\partial \tau_\alpha}$$

$$= \left[\frac{\tau}{f}\delta_{\beta\alpha} + \left(\frac{1}{f'} - \frac{\tau}{f}\right)\frac{1}{\tau^2}\tau_\beta\tau_\alpha\right]\frac{\partial}{\partial \tau_\alpha} \tag{13}$$

and therefore,

$$\nabla_\gamma = \left[\frac{\tau}{f}\mathbf{I} + \left(\frac{1}{f'} - \frac{\tau}{f}\right)\frac{1}{\tau^2}\tau\,\tau\right]\cdot\nabla_\tau \tag{14}$$

where $\mathbf{I}$ is the two-dimensional, second-order identity tensor with Cartesian components given in terms of the Kronecker delta $\delta_{\beta\alpha}$.

The compatibility condition equation (11) implies the existence of a scalar potential ψ such that

$$\mathbf{x} = \nabla_\gamma \psi \tag{15}$$

which identically satisfies equation (11). With equations (14) and (15), the equilibrium condition equation (11) takes the form

$$\nabla_\tau \cdot \left[\frac{\tau}{f}\mathbf{I} + \left(\frac{1}{f'} - \frac{\tau}{f}\right)\frac{1}{\tau^2}\tau\,\tau\right]\cdot\nabla_\tau\psi = 0 \tag{16}$$

This is the governing linear, second-order, partial differential equation for ψ that, as Neuber [3] and Rice [4] observe, is valid for any constitutive relation of the form of equation (8).

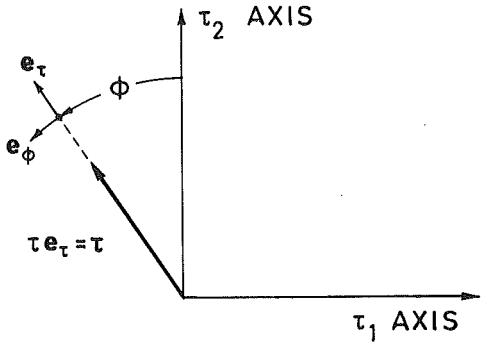


Fig. 1 Polar variables τ and ϕ in stress space

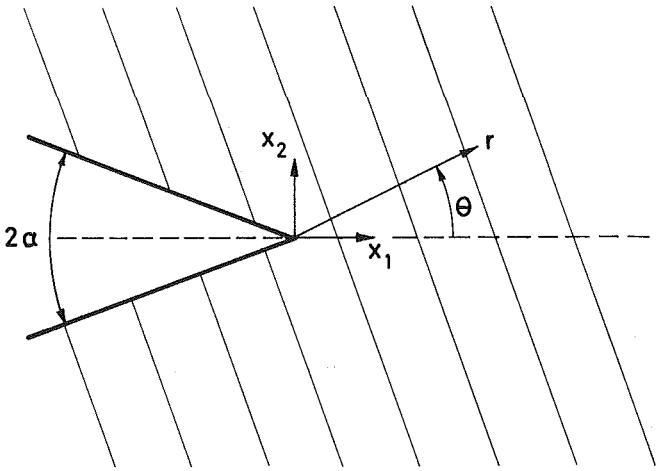


Fig. 2 Sharp notch-tip with total opening angle 2α

Rice [4] first used this approach to study the notch-tip fields in a power-law material of the form of equation (2).

Equation (16) takes a particularly simple form if polar coordinates (τ, ϕ) are used in the stress plane, with

$$\tau = \tau\,\mathbf{e}_\tau \tag{17a}$$

$$\phi = \tan^{-1}(-\tau_1/\tau_2) = \tan^{-1}(-\gamma_1/\gamma_2) \tag{17b}$$

$$\nabla_\tau = \mathbf{e}_\tau\frac{\partial}{\partial \tau} + \mathbf{e}_\phi\frac{1}{\tau}\frac{\partial}{\partial \phi} \tag{17c}$$

where $\mathbf{e}_\tau$ and $\mathbf{e}_\phi$ are the orthonormal polar base vectors. As shown in Fig. 1, positive ϕ is measured counterclockwise from the τ_2 axis. This convention is convenient for mapping the notch problem since for the symmetric notch $\theta \geq 0$ corresponds to $\phi \geq 0$. Noting that $\mathbf{e}_{\tau,\tau} = 0$, $\mathbf{e}_{\phi,\tau} = 0$, $\mathbf{e}_{\tau,\phi} = \mathbf{e}_\phi$, and $\mathbf{e}_{\phi,\phi} = -\mathbf{e}_\tau$ we can show that with equations (17) the equilibrium condition equation (16) reduces to

$$\frac{1}{f'}\psi_{,\tau\tau} + \left[\frac{1}{\tau f'} - \frac{f''}{(f')^2}\right]\psi_{,\tau} + \frac{1}{\tau f}\psi_{,\phi\phi} = 0 \tag{18}$$

Notch-Tip Boundary Conditions and Separable Solutions. Consider a two-dimensional sharp notch with the notch tip lying along the line $x_1 = x_2 = 0$ $(r = 0)$ and total opening angle $2\alpha < \pi$ as shown in Fig. 2. The notch-tip polar coordinates in the $x_1 - x_2$ plane are r and θ.

The boundary conditions for $\psi(\tau, \phi)$ associated with traction-free notch surfaces are derived from the equations for the spatial coordinates expressed in terms of ψ, τ, and ϕ. First, note that

$$\frac{\partial}{\partial \gamma_\alpha} = \frac{\partial \tau}{\partial \gamma_\alpha}\frac{\partial}{\partial \tau} + \frac{\partial \phi}{\partial \gamma_\alpha}\frac{\partial}{\partial \phi} \tag{19}$$

Downloaded 02 May 2010 to 171.66.16.25. Redistribution subject to ASME license or copyright; see http://www.asme.org/terms/Terms_Use.cfm

Then, from equation (15) with equations (8), (17), and (19) the coordinates are given as

$$x_1 = \frac{\partial \psi}{\partial \gamma_1} = -(\sin\phi/f')\,\psi_{,\tau} - (\cos\phi/f)\,\psi_{,\phi} \tag{20a}$$

$$x_2 = \frac{\partial \psi}{\partial \gamma_2} = (\cos\phi/f')\,\psi_{,\tau} - (\sin\phi/f)\,\psi_{,\phi} \tag{20b}$$

$$r = (x_1^2 + x_2^2)^{1/2} = [(\psi_{,\tau}/f')^2 + (\psi_{,\phi}/f)^2]^{1/2} \tag{20c}$$

Zero traction along $\theta = \pi - \alpha$ requires that $\tan\alpha = -\tau_2/\tau_1$, so that with equation (17*b*),

$$\phi = \phi_\alpha = \tan^{-1}(\cot\alpha) = \frac{\pi}{2} - \alpha \quad \text{along } \theta = \pi - \alpha.$$

Along this notch face,

$$-x_2/x_1 = \tan\alpha = \cot\left(\frac{\pi}{2} - \alpha\right) = \cot\phi_\alpha$$

and from equations (20*a*, *b*)

$$-x_2/x_1 = \frac{(\cos\phi/f')\,\psi_{,\tau} - (\sin\phi/f)\,\psi_{,\phi}}{(\sin\phi/f')\,\psi_{,\tau} + (\cos\phi/f)\,\psi_{,\phi}} \tag{21}$$

Therefore, $-x_2/x_1 = \cot\phi$ along this notch face if

$$\psi_{,\phi} = 0, \quad \text{on } \phi = \pi/2 - \alpha \tag{22a}$$

Similarly, zero traction along $\theta = -\pi + \alpha$ leads to the second boundary condition

$$\psi_{,\phi} = 0, \quad \text{on } \phi = -\pi/2 + \alpha \tag{22b}$$

The differential equation (18) with the boundary conditions (22*a*,*b*) form a homogeneous system that admits separable solutions of the form

$$\psi(\tau,\phi) = S(\tau)\,P(\phi) \tag{23}$$

where $P(\phi)$ is a linear combination of $\sin(\lambda\phi)$ and $\cos(\lambda\phi)$, with λ = constant. The eigenvalues associated with $P'(\phi) = 0$ along $\phi = \pi/2 - \alpha$ and $-\pi/2 + \alpha$ are

$$\lambda_k = \frac{(2k-1)\pi}{\pi - 2\alpha}; \; k = 1,2, \ldots \tag{24}$$

and the corresponding eigenfunctions are

$$P_k = \sin(\lambda_k\phi) \tag{25}$$

With equation (25) the separable solution (23) is rewritten as

$$\psi(\tau,\phi) = -\sum_{k=1}^{\infty} A_k S_k(\tau)\sin(\lambda_k\phi) \tag{26}$$

where the A_k's are the Fourier coefficients. When the far field conditions are time varying and, in particular, where the effects of elasticity are included in the far field, the A_k's are time dependent.

The governing ordinary differential equation for $S_k(\tau)$ is obtained by substituting equation (26) into equation (18):

$$\frac{\tau f}{f'} S_k'' + \frac{f}{f'}\left(1 - \frac{\tau f''}{f'}\right) S_k' - \lambda_k^2 S_k$$

$$= f\left(\frac{\tau}{f'} S_k'\right)' - \lambda_k^2 S_k = 0 \tag{27}$$

If the creep relation (8) for a particular material implies unbounded stresses when the strain rates become unbounded, then the (small-strain) asymptotic behavior for the sharp notch-tip problem is associated with the solution to equation (27) as $\tau \to \infty$. The solution to equation (27) in this limit is presented in the next section for the hyperbolic-sine creep law.

In closing this section the following observation, which is incorporated in the next section, is made. An integral solution to equation (27) exists for any creep function $f(\tau)$ when $\lambda_k = 1$, which corresponds to a sharp crack with $\alpha = 0$ and $k = 1$, i.e., the leading term in equation (26); this integral is [3, 4]

$$S_1(\tau) = f(\tau)\int^{\tau} \frac{f'(\xi)}{\xi f^2(\xi)}\,d\xi \tag{28}$$

Notch-Tip Solutions for Hyperbolic-Sine Creep

The asymptotic behavior of $S_k(\tau)$ in the region around the notch tip is found from the solution to equation (27) in the limit as $\tau \to \infty$. We anticipate the notch-tip solution for the hyperbolic-sine law of equation (1) corresponds to the high stress limit of this creep function, which is the exponential form of equation (3). A proof of this correspondence for a crack is given in the Appendix.

For brevity we choose

$$f(\tau) = e^{\tau} \tag{29}$$

which follows from equation (3) with $\dot\gamma_0 = \sqrt{3}\,2^{-n}\,\dot\epsilon_0$ and $\tau_0 = \sigma_0/(n\sqrt{3})$. With this exponential-creep law, equation (18) reduces to

$$\tau\psi_{,\tau\tau} + (1-\tau)\psi_{,\tau} + \psi_{,\phi\phi} = 0 \tag{30}$$

and equation (27), which governs the τ dependence in the separable solution for $\psi(\tau, \phi)$, reduces to the confluent hypergeometric or Kummer differential equation

$$\tau S_k'' + (1-\tau)S_k' - \lambda_k^2 S_k = 0 \tag{31}$$

The eigenvalues λ_k are given in equation (24).

The linearly independent solutions to equation (31) can be expressed in terms of the confluent hypergeometric or Kummer functions $M(\lambda_k^2, 1, \tau)$ and $U(\lambda_k^2, 1, \tau)$ [5, 6]. As $\tau \to \infty$ [5, 6]

$$M(a,b,\tau) = \frac{\Gamma(b)}{\Gamma(a)} e^{\tau}\tau^{a-b} \tag{32}$$

$$U(a,b,\tau) = \tau^{-a} \tag{33}$$

where Γ denotes the gamma function. Formulas for derivatives are [5, 6]

$$\frac{dM(a,b,\tau)}{d\tau} = \frac{a}{b} M(a+1,b+1,\tau) \tag{34}$$

$$\frac{dU(a,b,\tau)}{d\tau} = -aU(a+1,b+1,\tau) \tag{35}$$

We will now demonstrate that if $\tau \to \infty$ only at $r = 0$ then $S_k(\tau) = U(\lambda_k^2, 1, \tau)$ is the only admissible solution. From equation (20*c*) with equation (29)

$$r = e^{-\tau}(\psi_{,\tau}^2 + \psi_{,\phi}^2)^{1/2} \tag{36}$$

If $S_k(\tau) = M(\lambda_k^2, 1, \tau)$ is substituted into eqution (26) for ψ and the result substituted into equation (36), then in the limit as $\tau \to \infty$, with equations (32) and (34),

$$r = \tau^{\lambda_k^2} \times \text{function of } \phi \tag{37}$$

For any α with $2\alpha < \pi$, from equation (24) it follows that $\lambda_k \geq 1$ for $k \geq 1$. Therefore, from equation (37), if $\tau \to \infty$ only at $r = 0$ then $S_k(\tau) = M(\lambda_k^2, 1, \tau)$ is inadmissible. On the other hand, if $S_k(\tau) = U(\lambda_k^2, 1, \tau)$, then from equation (36) with equations (33) and (35), as $\tau \to \infty$

$$r = e^{-\tau}\tau^{-\lambda_k^2} \times \text{function of } \phi \tag{38}$$

so that $\tau \to \infty$ only at $r = 0$. Note that this dominant term comes from the $\psi_{,\phi}$ contribution to r in equation (36).

The complete notch-tip solution is given in equation (26) with $S_k(\tau) = U(\lambda_k^2, 1, \tau)$. Noting that the $\tau \to \infty$ limit of $dU/d\tau$ given in equation (35) is obtained directly from derivatives of the $\tau \to \infty$ limit of U given in equation (33), we can write the general asymptotic solution for the wedge as

Downloaded 02 May 2010 to 171.66.16.25. Redistribution subject to ASME license or copyright; see http://www.asme.org/terms/Terms_Use.cfm

$$\psi(\tau,\phi) = -\sum_{k=1}^{\infty} A_k \tau^{-\lambda_k^2} \sin(\lambda_k \phi) \tag{39}$$

with λ_k given in equation (24). The coefficients A_k are matched, typically, to far-field conditions (e.g., $\tau \ll 1$; see [4]). If elastic deformation is included then these coefficients can be time dependent. For example, when creep strains are larger than the elastic strains only in the notch-tip region then, under constant far-field load, the notch-tip stresses relax with time [1].

Leading Term for Physical Coordinates. The leading term for $\mathbf{x}(\tau)$ that will be inverted to give $\tau(\mathbf{x})$ around the notch tip is found from the $k = 1$ term in equations (38) and (39). To demonstrate this we first note from equation (24) that $\lambda_1 \geq 1$ and $\lambda_k = (2k - 1)\lambda_1$. Therefore, for instance, $\lambda_2 > \lambda_1 + 1$. From equation (20) with equations (29) and (39) or, more obviously, from equation (38), it follows that as $\tau \to \infty$ with $r \to 0$ the dominant term comes from the $k = 1$ contribution to ψ:

$$\psi_1 = -A_1 \tau^{-\gamma_1^2} \sin(\lambda_1 \phi) \tag{40}$$

As noted in the foregoing, for the exponential law material the $\psi_{,\phi}$ contribution to r in equation (36) dominates the $\psi_{,\tau}$ contribution as $\tau \to \infty$ as long as the function of ϕ that multiplies the function of τ in the $\psi_{,\phi}$ contribution is nonzero. Therefore, from equations (36) and (40), as $\tau \to \infty$

$$r = \lambda_1 A_1 e^{-\tau} \tau^{-\lambda_1^2} \cos(\lambda_1 \phi) \tag{41}$$

From equation (21), with $f = e^{\tau}$

$$\tan\theta = x_2/x_1 = \frac{\sin\phi\ \psi_{,\phi} - \cos\phi\ \psi_{,\tau}}{\cos\phi\ \psi_{,\phi} + \sin\phi\ \psi_{,\tau}} \tag{42}$$

Once again, as $\tau \to \infty$ the $\psi_{,\phi}$ terms in equation (42) dominate the $\psi_{,\tau}$ terms as $\tau \to \infty$ and the leading term behavior ($\psi = \psi_1$) gives

$$\tan\theta = \tan\phi \tag{43}$$

Therefore, $\theta = \phi$ in the range $-\pi/2 + \alpha \leq \theta \leq \pi/2 - \alpha$ and in this range r is given by equation (41); see the hatched regions in Fig. 3.

The full range of θ is $-\pi + \alpha \leq \theta \leq \pi - \alpha$. The leading term given in equation (40) maps $\phi = -\pi/2 + \alpha$ and $\phi = \pi/2 - \alpha$ onto the notch faces $\theta = -\pi + \alpha$ and $\pi - \alpha$, respectively, as well as onto $\theta = -\pi/2 + \alpha$ and $\pi/2 - \alpha$. In the sectors with angular extent of $\pi/2$ adjacent to the two notch surfaces the dominant behavior is found from the $\psi_{,\tau}$ terms but still corresponding to $k = 1$ (recall that $\lambda_2 > \lambda_1 + 1$) since for $\phi = -\pi/2 + \alpha$ or $\phi = \pi/2 - \alpha$, $\psi_{,\phi} = 0$. In these sectors, as $\tau \to \infty$

$$r \propto e^{-\tau} \tau^{-\lambda_1^2 - 1} \tag{44}$$

which tends to zero faster than equation (41). Finally, we note that when the $\psi_{,\phi}$ terms in equation (42) are negligible compared to the $\psi_{,\tau}$ terms that

$$\tan\theta = -\cot\phi \tag{45}$$

or $\theta = \phi \pm \pi/2$. In this limit $\phi = -\pi/2 + \alpha$ and $\phi = \pi/2 - \alpha$ map onto the notch surfaces $\theta = -\pi + \alpha$ and $\theta = \pi - \alpha$, respectively.

The remainder of this paper focuses on inverting the asymptotic solution previously summarized to determine $\tau(\mathbf{x})$ in the notch-tip region where $\theta = \phi$, that is, $-\pi/2 + \alpha \leq \theta \leq \pi/2 - \alpha$. In this region, which is in front of the notch, the stresses have the strongest singularity as $r \to 0$.

Inverting the Leading Term. In the region ahead of the notch where $\theta = \phi$ and $-\pi/2 + \alpha \leq \theta \leq \pi/2 - \alpha$ (see hatched regions in Fig. 3), from equation (17*b*)

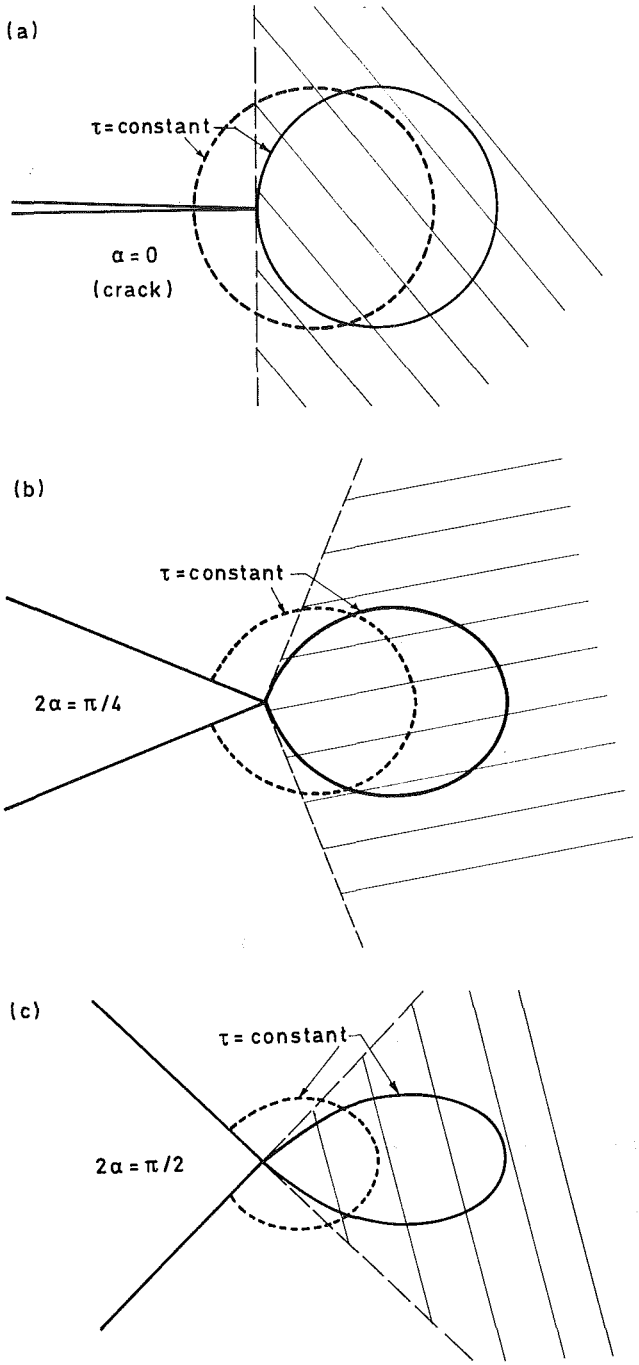


Fig. 3 Loci of constant effective stress τ (or effective strain-rate γ) for: (*a*) $\alpha = 0$ (crack), (*b*) $2\alpha = \pi/4$, and (*c*) $2\alpha = \pi/2$. Solid loci are for hyperbolic-sine-law creep and hatched regions are where the leading term in the asymptotic solution is valid; $-\pi/2 + \alpha \leq \theta \leq \pi/2 - \alpha$. Dashed loci are for power-law creep with $n = 3$.

$$\tau_1 = -\tau \sin\theta \tag{46}$$

$$\tau_2 = \tau \cos\theta$$

and, from equation (41) with equations (43),

$$\tau^{\lambda_1^2} e^{\tau} = R(r,\theta) \tag{47}$$

where

$$R(r,\theta) = \frac{\lambda_1 A_1}{r} \cos(\lambda_1 \theta) \tag{48}$$

Note, for a crack, where $\alpha = 0$ and $\lambda_1 = 1$, that equation (47) implies that $\tau\gamma \propto r^{-1}$ as $r \to 0$; this is consistent with the path

Downloaded 02 May 2010 to 171.66.16.25. Redistribution subject to ASME license or copyright; see http://www.asme.org/terms/Terms_Use.cfm

independence of the C^* integral [1]. In fact $\sigma\dot{\epsilon} \propto r^{-1}$ as $r \to 0$ for all planar crack-tip fields including those with Mode *I*, *II*, or general loadings.

Equation (47) cannot be solved explicitly for $\tau(r, \theta)$ although an approximation can be found to any desired accuracy for small r. Taking logarithms of equation (47) we obtain

$$\tau = ln\ R - \lambda_1^2 ln\ \tau \tag{49}$$

Now successive substitution of $ln\ R - \lambda_1^2\ ln\ \tau$ for τ on the right side of equation (49) gives

$$\begin{aligned}\tau &= ln\ R - \lambda_1^2 ln[ln\ R - \lambda_1^2 ln(\ldots)] \\ &= ln\ \{R/\lambda_1^2 ln[R/\lambda_1^2 ln(\ldots)]\}\end{aligned} \tag{50}$$

The leading term in this equation gives the effective stress as $r \to 0$ (or $R \to \infty$) as $\tau = ln\, R$;

$$\tau = ln \frac{\lambda_1 A_1 \cos(\lambda_1 \theta)}{r} \tag{51}$$

Given $\tau(r, \theta)$, $\tau_1(r, \theta)$, and $\tau_2(r, \theta)$ follow from equations (46).

The leading term for the effective strain rate $\gamma = e^{\tau}$ (at high stress) is found in a similar manner from equation (47):

$$\begin{aligned}\gamma &= \frac{R}{(ln\ R)^{\lambda_1^2}} \\ &= \frac{\lambda_1 A_1\ \cos(\lambda_1 \theta)}{r\ \{ln\ [\lambda_1 A_1\ \cos(\lambda_1 \theta)/r]\}^{\lambda_1^2}}\end{aligned} \tag{52}$$

In the region ahead of the notch where $\theta = \phi$ and $-\pi/2 + \alpha \le \theta \le \pi/2 - \alpha$, from equation (17*b*)

$$\begin{aligned}\gamma_1 &= -\gamma \sin\theta \\ \gamma_2 &= \gamma \cos\theta\end{aligned} \tag{53}$$

The reader is cautioned that although this asymptotic result for γ along with $\tau = ln\, R$ is consistent with equation (47) it is not obtained directly from $\tau = ln\ R$ and the constitutive relation $\gamma = e^{\tau}$.

Loci of constant effective stress or strain rate within the asymptotic fields are found from equation (47) and correspond to $R(r, \theta) =$ constant. From equation (48) it is seen that these loci are symmetric with respect to $\theta = 0$. For a crack, $\alpha = 0$, these loci are circles centered ahead of the crack tip along $x_2 = 0$ at a distance equal to their radius. For $\alpha > 0$ these loci are oblate and they become flatter as α increases. Some examples are given in Fig. 3. The hatched regions in Fig. 3 correspond to the regions where the asymptotic solution of equations (40), (51), and (52) are valid.

Discussion

Although the hyperbolic-sine-creep law reduces to a power law at low stresses, it is the high-stress exponential-law behavior that governs the stress and strain-rate fields around the tip of a sharp notch. The power-law results are outlined in the following for comparison. The power-law fields are shown to exhibit notch-tip stresses ($\tau \propto r^{-\omega}$ as $r \to 0$, with $\omega > 0$) that are more singular or intense than those for the hyperbolic-sine materials ($\tau \propto ln\ (1/r)$ as $r \to 0$). The opposite is true for strain rates.

Summary of Power-Law Notch-Tip-Fields. The analysis in the preceding section is carried out in a straightforward and simpler manner for the case of power-law creep. Various aspects of the power-law analysis, particularly for a crack, are discussed by Rice [4]. With the power-law creep function

$$f(\tau) = \tau^n \tag{54}$$

where n is a material constant, it is easy to show that equation (27) has solutions of the form

$$S_k(\tau) = \tau^{\beta_k} \tag{55}$$

where

$$\beta_k = \frac{n-1}{2} - \left[\left(\frac{n-1}{2}\right)^2 + \lambda_k^2 n\right]^{1/2} \tag{56}$$

and the λ_k's are given in equation (24). Since $n \ge 1$, $\lambda_1 \ge 1$, and $\lambda_{k+1} > \lambda_k$, it follows that $\beta_{k+1} < \beta_k$. The leading behavior as $r \to 0$ once again comes from the $k = 1$ term in equation (26).

From equation (20*c*) with equations (26) and (55), as $r \to 0$ with $\beta \equiv \beta_1\ (\alpha, n)$

$$r = A_1 \tau^{\beta - n}\{\ (\beta/n)^2 + [\lambda_1^2 - (\beta/n)^2]\cos^2(\lambda_1 \phi)\ \} \tag{57}$$

The relationship between the physical polar angle θ and the polar angle in the stress plane ϕ is found from equation (21) with equations (26) and (55); as $r \to 0$

$$\tan\theta = \frac{\lambda_1 n\ \sin\phi\ \cos(\lambda_1 \phi) - \beta \cos\phi\ \sin(\lambda_1 \phi)}{\lambda_1 n\ \cos\phi\ \cos(\lambda_1 \phi) + \beta \sin\phi\ \sin(\lambda_1 \phi)} \tag{58}$$

Finally, the singular nature of the notch-tip stresses in the power-law case follows from equations (57) and (58); as $r \to 0$ the effective stress has the form

$$\tau = (A_1/r)^{1/(n-\beta)} g(\theta; \alpha, n) \tag{59}$$

where $g(\theta; \alpha, n)$ is known, at least implicity, from equations (57) and (58). The effective strain rate $\gamma = \tau^n$ follows directly from equation (59). For the case of a crack, $\alpha = 0$ and $\beta = -1$, and equation (59) reduces to the well-known result $\tau \propto r^{-1/(n+1)}$ as $r \to 0$ [4].

Comparison of Power-Law and Hyperbolic-Sine-Law Notch-Tip Fields. Loci of constant effective stress or strain-rate within the asymptotic, power-law notch-tip fields follow from equations (57) and (58). With $\tau =$ constant equation (57) gives $r(\phi)$ and equation (58) gives $\theta(\phi)$; alternatively, for a given θ, equation (58) can be solved numerically for $\phi(\theta)$ and then equation (57) determines $r(\theta)$ at constant τ. These loci are shown in Fig. 3 as dashed contours for the case where the power-law-creep exponent $n = 3$. The scale is chosen so that the maximum height of each power-law locus is the same as the maximum height of the corresponding hyperbolic-sine-law locus. The hyperbolic-sine-law loci are seen to extend further ahead of the notch than the power-law loci whereas the latter extend behind the notch tip and along the notch flanks while the former do not. It is interesting to note that in the case of a crack that the hyperbolic-sine-law locus corresponds to the $n \to \infty$ limit (perfect plasticity) of the power-law locus (this may also be true for $\alpha > 0$ but this has not been checked).

The notch-tip stresses for the hyperbolic-sine-law case exhibit a logarithmic singularity in r, equation (51), while the power-law case exhibits a more intense power singularity as seen in equation (59). As seen from equations (52) and (59) raised to the nth power, the opposite is true for strain rates. This has certain implications concerning fracture that depend on the mechanisms of material damage. For instance, for either diffusion-controlled grain-boundary cavitation or oxidation, the local damage is most directly influenced by the notch-tip stress while for creep-controlled cavitation the notch-tip strains are more important. Expected differences in fracture behavior for power-law and hyperbolic-sine-law materials are obvious in these cases.

The present analysis only concerns the notch-tip fields without regard to the far-field geometry and loading conditions. That is, the coefficients A_k in equation (39) or, more importantly A_1 in equation (51) have not been determined. In general, the determination of these quantities requires numerical analysis. Finite element calculations have been carried out for the case of a crack [1, 7] in materials that deform both elastically and by hyperbolic-sine creep. These

Downloaded 02 May 2010 to 171.66.16.25. Redistribution subject to ASME license or copyright; see http://www.asme.org/terms/Terms_Use.cfm

calculations have demonstrated the existence of the crack-tip fields summarized in the foregoing.

One analytical result is obtained quite easily in the case of a crack under steady-state creep or extensive creep conditions. In terms of the path-independent integral C^*, which is an important fracture parameter for extensive creep conditions, for the hyperbolic-sine-law crack-tip fields, it can be shown that [1]

$$A_1 = \frac{2}{\pi} \frac{C^*}{\tau_0 \gamma_0} \tag{60}$$

This result is obtained through substitution of the asymptotic results equations (46), (51), (52), and (53) into the integral expression for C^*.

Acknowledgments

The support of the Department of Energy under Grant DE-AC02-83ER13037 is gratefully acknowledged.

References

1 Bassani, J. L., "Cracks in Materials With Hyperbolic-Sine Law Creep Behavior," to appear in *Elastic-Plastic Fracture: Vol. I-Inelastic Crack Analysis, ASTM STP 803*, Shih, C. F., and Gudas, J. P., eds., American Society for Testing and Materials, Philadelphia, 1983.

2 Steif, P. S., Spaepen, F., and Hutchinson, J. W., "Strain Localization in Amorphous Metals," *Acta Metall.*, Vol. 30, 1982, pp. 447–455.

3 Neuber, H., "Theory of Stress Concentration for Shear-Strained Prismatical Bodies With Arbitrary Nonlinear Stress-Strain Law," ASME JOURNAL OF APPLIED MECHANICS, Vol. 28, 1961, pp. 544–550.

4 Rice, J. R., "Stresses Due to a Sharp Notch in a Work-Hardening Elastic-Plastic Material Loaded by Longitudinal Shear," ASME JOURNAL OF APPLIED MECHANICS, Vol. 34, 1967, pp. 287–298.

5 Abramowitz, M., and Stegun, I. A., eds., *Handbook of Mathematical Functions*, Dover, New York, 1970, Chapter 13.

6 Erdélyi, A., *Higher Transcendental Functions*, Vol. 1, McGraw-Hill, New York, 1953, Chapter 6.

7 Bassani, J. L., and Do, G., "Crack-Tip Stress Relaxation in a Hyperbolic-Sine Creeping Solid," in preparation, 1983.

APPENDIX

For a sharp crack ($\alpha = 0$) and any creep function $f(\tau)$ the leading term for $\psi(\tau, \phi)$ has a τ dependence, which is given in closed form by equation (28):

$$S_1(\tau) = f(\tau) \int^{\tau} \frac{f'(\xi)}{\xi f^2(\xi)} d\xi \tag{A1}$$

Using this integral solution we will show for both the exponential law $\gamma = f = e^{\tau}$ and the hyperbolic-sine law $\gamma = f = \sinh^n \tau$ that as $\tau \to \infty$, $S_1(\tau) = -1/\tau$.

For the exponential law the solution (A1) takes the form

$$S_1(\tau) = e^{\tau} \int^{\tau} \frac{d\xi}{\xi e^{\xi}} \tag{A2}$$

Integration of equation (A2) by parts yields

$$S_1(\tau) = -\frac{1}{\tau} - e^{\tau} \int^{\tau} \frac{d\xi}{\xi^2 e^{\xi}} \tag{A3}$$

so that a comparison of the integrands in equations (A2) and (A3) reveals that as $\tau \to \infty$, $S_1 = -1/\tau$.

For the hyperbolic-sine law the solution (A1) takes the form

$$S_1(\tau) = \sinh^n \tau \int^{\tau} \frac{n \cosh \xi}{\xi \sinh^{n+1} \xi} d\xi \tag{A4}$$

Integration of equation (A4) by parts yields

$$S_1(\tau) = -\frac{1}{\tau} - \sinh^n \tau \int^{\tau} \frac{d\xi}{\xi^2 \sinh^n \xi} \tag{A5}$$

so that a comparison of the integrands in equations (A4) and (A5) reveals that as $\tau \to \infty$, $S_1 = -1/\tau$.

Therefore, the solution to equation (27) in the case of a crack, $\lambda_1 = 1$, has an asymptotic behavior as $\tau \to \infty$ that is the same for both the exponential law and hyperbolic-sine law material behaviors.

Downloaded 02 May 2010 to 171.66.16.25. Redistribution subject to ASME license or copyright; see http://www.asme.org/terms/Terms_Use.cfm

R. Abeyaratne
College of Engineering,
Michigan State University,
East Lansing, MI 48824
Associate Mem. ASME

N. Triantafyllidis
Aerospace Engineering Department,
University of Michigan,
Ann Arbor, MI 48109
Associate Mem. ASME

An Investigation of Localization in a Porous Elastic Material Using Homogenization Theory

In this work we use a consistent homogenization theory approach to study the overall behavior of a highly porous elastic material at finite levels of strain. Although the matrix material in the problem considered here remains elliptic at all deformations, the resulting "homogenized" material is found to admit a loss of ellipticity at sufficiently high strains, i.e., can fail in a localized shear mode.

1 Introduction

To study the elastic behavior of a compressible material at finite strain, Blatz and Ko [1] carried out a series of experiments on a foamed polyurethane rubber. The material tested was obtained by chemically treating an (incompressible) vulcanized rubber, thereby generating a fine distribution of pores in it (with porosity $\simeq 50$ percent). The resulting inhomogeneous material is assumed, in an overall sense, to behave in a homogeneous and compressible manner. Based on their experiments, these investigators proposed a particular isotropic strain-energy density function characterizing the overall mechanical behavior of the foam rubber. This idealized model is commonly referred to as the "Blatz-Ko material."

A striking feature of the Blatz-Ko material is that the displacement equations of equilibrium associated with it lose ellipticity at sufficiently severe levels of strain (Knowles and Sternberg [2]) which implies the possibility of failure by shear localization (shear band formation). This is somewhat unexpected since existing constitutive models for vulcanized rubber (e.g. Mooney-Rivlin material) do not admit such a possibility. It should however be noted that this phenomenon is predicted to occur in a Blatz-Ko material at strain levels that are more severe than those tested and thus could possibly be a result of improper extrapolation. In addition, certain deficiencies in the fit of the aforementioned model with Blatz and Ko's own experiments have also been noted [2]. On the other hand, it is conceivable that the porous vulcanized rubber does indeed exhibit shear localization in its "macroscopic" behavior, which could, for example, be an averaged manifestation of a loss of stability at the "microstructural" level (e.g. void buckling).

In the present study the plane strain problem for a rectangular block of a Mooney-Rivlin-like material having a very fine periodic distribution of identical cylindrical voids is considered. We determine the overall constitutive behavior of this porous material theoretically, and then examine the possibility of a loss of ellipticity in the "averaged" material. Despite the obvious differences between the orthotropic two-dimensional model analyzed here and the isotropic three-dimensional material tested by Blatz and Ko certain interesting qualitative similarities have been found.

A number of different techniques for determining the effective constitutive relations for inhomogeneous linearly elastic materials have been developed. (The interested reader is referred to the review articles by Watt et al. [3], Willis [4], and Walpole [5]). Both bounds on the overall material properties as well as direct estimates of them have been obtained. The so-called self-consistent estimates, based in part on Eshelby's strain transformation problem, appear to be the most widely used and are not restricted to problems in which the inhomogeneity is distributed periodically. It has been observed however that these estimates are inappropriate in the limiting case in which one of the constituents consists of voids and its concentration is large (Budiansky [6]) – precisely the case of interest in the present study.

A second method, applicable only in the particular case when the composite has a periodic structure, is the "homogenization theory" which was initiated by Sanchez-Palencia [7] and is described in detail in a monograph by Bensoussan, Lions, and Papanicolaou [8]. The method utilizes a singular perturbation analysis based on the multiple scales involved in the problem, viz. that of the entire body and that of the microstructure, and calculates the limiting material properties as the "size" of the microstructure tends to zero.

The method of homogenization is only applicable to situations governed by linear boundary-value problems. While the phenomenon of interest here is one that occurs at finite strain, it should be kept in mind that to examine the question of overall ellipticity, it is only the averaged incremental moduli of the body that one needs to know. These moduli in turn are associated with the equations of in-

Contributed by the Applied Mechanics Division for publication in the JOURNAL OF APPLIED MECHANICS.

Discussion on this paper should be addressed to the Editorial Department, ASME, United Engineering Center, 345 East 47th Street, New York, N.Y. 10017, and will be accepted until two months after final publication of the paper itself in the JOURNAL OF APPLIED MECHANICS. Manuscript received by ASME Applied Mechanics Division, June, 1983; final revision, December, 1983.

Copyright © 1984 by ASME
Downloaded 02 May 2010 to 171.66.16.25. Redistribution subject to ASME license or copyright; see http://www.asme.org/terms/Terms_Use.cfm

cremental equilibrium, which are in fact linear in the incremental displacements.

Many investigators, mainly in the areas of metal plasticity and geomechanics, have examined the role of voids in shear localization, e.g., [9–15]. It has been observed that the strain level at which most classical plastically incompressible elastic-plastic solids with a smooth yield surface admit shear bands is unrealistically high. Physically motivated modifications to the aforementioned constitutive descriptions have been proposed (e.g., Rudnicki and Rice [9], Gurson [10]) which allow for plastic dilatancy, arising for example as a macroscopic consequence of microvoids. These phenomenological constitutive relations lead to signficantly lower values for the strain at localization and have been utilized to study the development of shear bands, e.g., Yamamoto [11], Iwakuma and Nemat-Nasser [12], Saje, Pan, and Needleman [13], Tvergaard [14], and Ohno and Hutchinson [15].

It is important to emphasize the difference between the present study and the work on elastic-plastic solids referred to in the foregoing. As mentioned previously, a homogeneous block of a classical elastic-plastic solid loses ellipticity at an unrealistically high load level. If one were to consider a block of such material with a void in it, ellipticity would clearly be lost at smaller values of the applied load – the stress concentration effect of the void would generate the necessary conditions locally, near the cavity. Consequently, one can argue that it is merely the stress concentration at the voids that leads to the smaller critical load level in these studies of porous elastic-plastic solids. If one wishes to determine, conclusively, whether the voids play a role that is more fundamental than this, it is essential to consider a porous material whose matrix material itself does *not* lose ellipticity, no matter how large the loads. This is the case considered in the present paper.

In Section 2.1 we outline the principal steps involved in formally deriving the formulas for the homogenized moduli of a periodic solid. The elastostatic problem governing the equilibrium of a Mooney-Rivlin-like material with voids is then formulated in Section 2.2. In Section 3 we discuss the finite element solution of the unit cell problem and also describe the numerical implementation of the homogenization formulas. The results are presented in Section 4.

2 Formulation

The first subsection here deals with the homogenization procedure for an incrementally linear solid with periodic structure while in the second, the elastostatic problem for the porous material is formulated.

2.1 Homogenization Theory for Periodic Structures. The mathematical theory of homogenization for linearly elastic periodic structures has been presented in the applied mathematics literature (and the interested reader is referred to the comprehensive monograph by Bensoussan, Lions, and Papanicolaou [8] and the references cited therein). For reasons of completeness however, a brief review of its principal results is outlined here.

Suppose that the equations of incremental equilibrium for a solid under plane strain conditions, occupying a region $\Omega \subset R^2$ in its undeformed configuration, are given by

$$\frac{\partial}{\partial x_\beta}\left[L^\epsilon{}_{\alpha\beta\gamma\delta}(\mathbf{x})\frac{\partial v^\epsilon_\gamma}{\partial x_\delta}(\mathbf{x})\right]+f_\alpha(\mathbf{x})=0,\quad \mathbf{x}=(x_1,x_2)\in\Omega. \tag{2.1}$$

[1] Greek subscripts range over the integers (1,2) and summation over repeated subscripts is taken for granted.

Here $\mathbf{v}^\epsilon$ is the incremental displacement vector, $\mathbf{f}$ the body force vector, and $\mathbf{L}^\epsilon$ the (uniformly bounded) incremental modulus tensor of the material which is endowed with the symmetry $L^\epsilon{}_{\alpha\beta\gamma\delta}=L^\epsilon{}_{\gamma\delta\alpha\beta}$. The incremental moduli are assumed to be doubly periodic with periods $2\epsilon a_1$ and $2\epsilon a_2$ with respect to the x_1 and x_2 directions, i.e.,

$$\mathbf{L}^\epsilon(x_1,x_2)=\mathbf{L}^\epsilon(x_1+2\epsilon a_1,x_2)=\mathbf{L}^\epsilon(x_1,x_2+2\epsilon a_2),\quad \mathbf{x}\in\Omega. \tag{2.2}$$

The differential equation (2.1), together with certain prescribed boundary conditions on $\partial\Omega$ (which do not concern us here), constitute the governing boundary-value problem for $\mathbf{v}^\epsilon$. Here interest is focused on the behavior of the incremental displacement $\mathbf{v}^\epsilon$ as the periodic structure of the material becomes very fine, i.e., as $\epsilon\to 0$. *The basic result of homogenization theory* asserts that one can construct a set of *constants* $\mathcal{L}_{\alpha\beta\gamma\delta}$ such that $\mathbf{v}^\epsilon\to\mathbf{v}$ (in an appropriate sense) as $\epsilon\to 0$ where $\mathbf{v}$ is the solution of

$$\frac{\partial}{\partial x_\beta}\left[\mathcal{L}_{\alpha\beta\gamma\delta}\frac{\partial v_\gamma}{\partial x_\delta}(\mathbf{x})\right]+f_\alpha(\mathbf{x})=0,\mathbf{x}\in\Omega, \tag{2.3}$$

subject to certain boundary conditions. The coefficients $\mathcal{L}_{\alpha\beta\gamma\delta}$ are termed the "homogenized moduli" of the material and are related to $\mathbf{L}^\epsilon$ (by (2.7) below).

To establish this result and obtain a constructive formula for $\mathcal{L}$ one supposes the $\mathbf{v}^\epsilon(\mathbf{x})$ admits the following asymptotic expansion:

$$\mathbf{v}^\epsilon(\mathbf{x})=\hat{\mathbf{v}}(\mathbf{x},\mathbf{y})+\epsilon\overset{1}{\mathbf{v}}(\mathbf{x},\mathbf{y})+\epsilon^2\overset{2}{\mathbf{v}}(\mathbf{x},\mathbf{y})+\ldots,\ \mathbf{y}=\mathbf{x}/\epsilon, \tag{2.4}$$

where $\hat{\mathbf{v}}$, $\overset{1}{\mathbf{v}}$, $\overset{2}{\mathbf{v}}$, . . . are Y periodic[2] functions in $\mathbf{y}$ for each $\mathbf{x}$ in Ω with $Y=[-a_1,a_1]\times[-a_2,a_2]$ being the unit cell of the structure. Assuming that $\mathbf{L}^\epsilon(\mathbf{x})$ depends on ϵ only through $\mathbf{x}/\epsilon$, we may set $\mathbf{L}^\epsilon(\mathbf{x})=\mathbf{L}(\mathbf{x}/\epsilon)$ where according to (2.2), $\mathbf{L}(\mathbf{y})$ is Y periodic. Substituting (2.4) into (2.1) and grouping the terms of like order in ϵ allows one to deduce (from the terms of order ϵ^{-2}, ϵ^{-1} and ϵ^0, respectively,) that

(*a*) $\hat{\mathbf{v}}$ is independent of $\mathbf{y}$, i.e., $\hat{\mathbf{v}}(\mathbf{x},\mathbf{y})\equiv\hat{\mathbf{v}}(\mathbf{x})$,

(*b*) one can represent the function $\overset{1}{\mathbf{v}}$ in the form

$$\overset{1}{\mathbf{v}}(\mathbf{x},\mathbf{y})=\chi^{\gamma\delta}(\mathbf{y})\frac{\partial\hat{v}_\gamma}{\partial x_\delta}(\mathbf{x})+\mathbf{c}(\mathbf{x}), \tag{2.5}$$

where the Y periodic functions $\chi^{\gamma\delta}(\mathbf{y})$ are the unique (up to an additive constant) solutions of

$$\frac{\partial}{\partial y_\beta}\left[L_{\alpha\beta\zeta\eta}(\mathbf{y})\frac{\partial\chi_\zeta{}^{\gamma\delta}}{\partial y_\eta}(\mathbf{y})\right]=-\frac{\partial}{\partial y_\beta}[L_{\alpha\beta\gamma\delta}(\mathbf{y})],\ \mathbf{y}\in Y, \tag{2.6}$$

(*c*) a function $\overset{2}{\mathbf{v}}$, consistent with (2.1), (2.4) exists only if (2.3) holds with $\mathbf{v}$ replaced by $\hat{\mathbf{v}}$ and with the constants $\mathcal{L}_{\alpha\beta\gamma\delta}$ given by

$$\mathcal{L}_{\alpha\beta\gamma\delta}=\frac{1}{4a_1a_2}Y4\int\left[L_{\lambda\mu\zeta\eta}(\mathbf{y})\frac{\partial}{\partial y_\mu}(\chi_\lambda^{\alpha\beta}(\mathbf{y})+y_\beta\delta_{\alpha\lambda})\frac{\partial}{\partial y_\eta}(\chi_\zeta^{\gamma\delta}(\mathbf{y})+y_\delta\delta_{\gamma\zeta})\right]d\mathbf{y}. \tag{2.7}$$

Therefore in the limit $\epsilon\to 0$ when the structure of the medium becomes very fine, the leading order term of the displacement increment, $\hat{\mathbf{v}}(\mathbf{x})$, obeys the linear differential equation (2.3) with constant coefficients $\mathcal{L}_{\alpha\beta\gamma\delta}$. These coefficients, termed the "homogenized moduli" of the

[2] A function $\mathbf{g}(\mathbf{y})$ is termed Y periodic if it assumes identical values on opposite faces of the boundary of the rectangle Y.

Downloaded 02 May 2010 to 171.66.16.25. Redistribution subject to ASME license or copyright; see http://www.asme.org/terms/Terms_Use.cfm

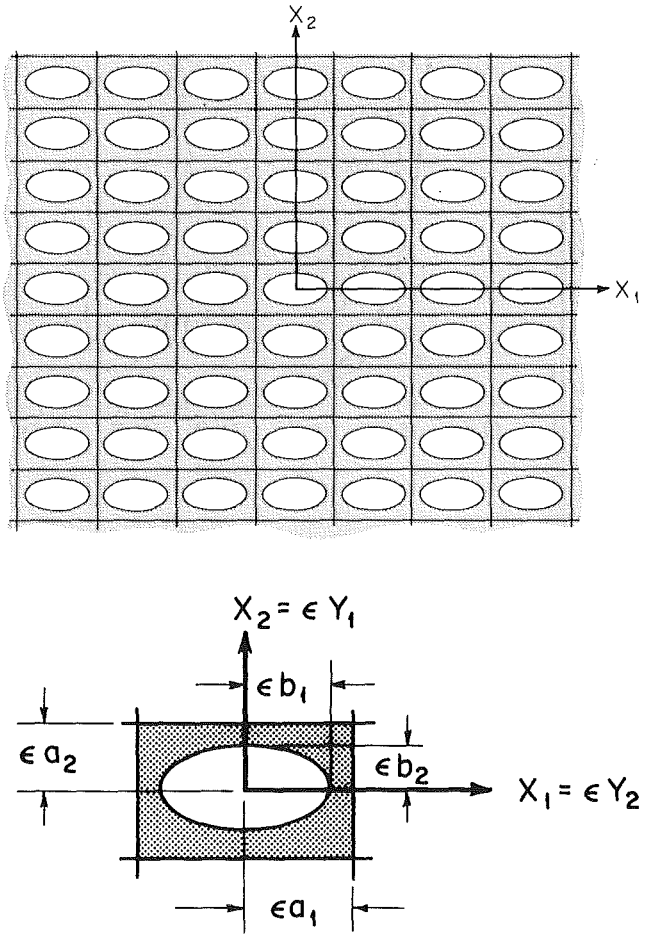


Fig. 1 Cross section of the body and the unit cell

material, are given by (2.7) with $\chi^{\alpha\beta}(\mathbf{y})$ being the Y periodic functions satisfying (2.6), or equivalently

$$\int_Y L_{\alpha\beta\gamma\delta}\frac{\partial}{\partial y_\beta}(\chi_\alpha{}^{\xi\eta}+y_\eta\delta_{\xi\alpha})\frac{\partial\phi_\gamma}{\partial y_\delta}\,d\mathbf{y}=0 \quad \text{for every } Y \text{ periodic function } \boldsymbol{\phi}(\mathbf{y}). \tag{2.8}$$

It should be noted at this point that the preceding results can be rigorously justified (see [8]) under certain restrictive conditions on $\mathbf{L}(\mathbf{y})$. Moreover, it has been shown that when these conditions hold, the homogenized moduli $\mathcal{L}$ are elliptic (see [8], [16]), i.e.,

$$\det[\mathcal{L}_{\alpha\beta\gamma\delta}n_\beta n_\delta]\neq 0 \quad \text{for all unit vectors } \mathbf{n}. \tag{2.9}$$

It is interesting to observe that the boundary conditions of the original problem (i.e. those for $\mathbf{v}^\epsilon$ on $\partial\Omega$) do not affect the calculation of the homogenized moduli.

Finally we turn to the case in which the material contains a periodic array of identical holes so that for some $D\subset Y$ one has $\mathbf{L}(\mathbf{y})=\mathbf{0}$ for $\mathbf{y}\epsilon D$ and $\mathbf{L}(\mathbf{y})\neq\mathbf{0}$ on $Y-D$. A formal derivation again leads to (2.7), (2.8) with the integrals now being evaluated over $Y-D$ instead of Y. These modified formulas will be utilized in what follows, though, to the best of our knowledge, a rigorous justification of this result does not (as yet) exist. The strong conditions (previously mentioned) used in [8] for this justification do not hold in the presence of voids. Further, one cannot ensure a priori that the homogenized moduli $\mathcal{L}$ are elliptic. Indeed, the numerical results obtained here indicate that they are not always so.

2.2 Formulation of Problem. Incremental Moduli. Consider a cylindrical block of material whose cross section in its undeformed state is rectangular with dimensions

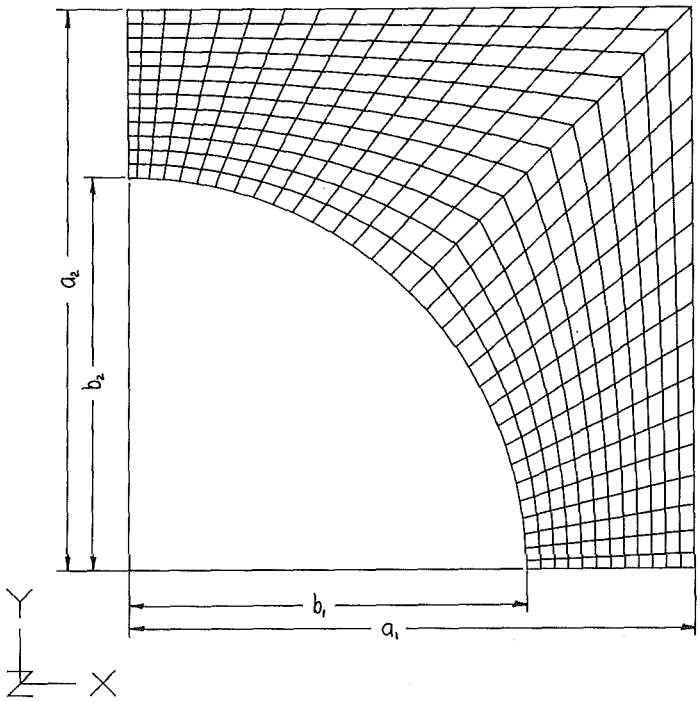


Fig. 2 The finite element grid

$2A_1\times 2A_2$. The block contains a periodic array of identical cylindrical cavities of elliptical cross section as shown in Fig. 1. The centers of the ellipses are spaced $2\epsilon a_1$ (and $2\epsilon a_2$) apart in the x_1 (and x_2) directions, and the semimajor and semiminor axes of each ellipse are ϵb_1 and ϵb_2, respectively. In what follows, a Lagrangian formulation of the problem in Cartesian coordinates is adopted.

The lateral boundaries of this block are free of shear tractions and are subjected to prescribed stretches λ_1, $\lambda_2(>0)$. Thus if $\mathbf{x}$ denotes the position vector of a particle in the undeformed body, the displacement field[3] $\mathbf{u}^\epsilon(\mathbf{x})$ and the first Piola-Kirchhoff stress field $\boldsymbol{\sigma}^\epsilon(\mathbf{x})$ obey

$$\begin{aligned} &u_1{}^\epsilon(\mathbf{x})=(\lambda_1-1)x_1, \quad \sigma_{21}\epsilon(\mathbf{x})=0 \quad \text{on} \quad x_1=\pm A_1,\\ &u_2{}^\epsilon(\mathbf{x})=(\lambda_2-1)x_2, \quad \sigma_{12}\epsilon(\mathbf{x})=0 \quad \text{on} \quad x_2=\pm A_2. \end{aligned} \tag{2.10}$$

If $W(\mathbf{F})$ denotes the strain energy density of the material, we have $\sigma^\epsilon{}_{\alpha\beta}(\mathbf{x})=\partial W(\mathbf{F}^\epsilon(\mathbf{x}))/F_{\alpha\beta}$ and the equilibrium equations in the absence of body forces can be written in the form

$$\frac{\partial}{\partial x_\beta}\left[\frac{\partial W}{\partial F_{\alpha\beta}}(\mathbf{F}^\epsilon(\mathbf{x}))\right]=0 \quad \text{with} \quad F^\epsilon{}_{\alpha\beta}(\mathbf{x}) = \delta_{\alpha\beta}+\frac{\partial u^\epsilon{}_\alpha}{\partial x_\beta}(\mathbf{x}), \tag{2.11}$$

Lastly, since the cavities are free of traction we must have

$$\frac{\partial W}{\partial F_{\alpha\beta}}(\mathbf{F}^\epsilon(\mathbf{x}))\quad N_\beta=0 \tag{2.12}$$

at every point on the boundaries of the cavities.

On taking increments in (2.11) (i.e., by linearizing (2.11) about $\mathbf{u}^\epsilon(\mathbf{x})$) one obtains

$$\frac{\partial}{\partial x_\beta}\left[L^\epsilon_{\alpha\beta\gamma\delta}(\mathbf{x})\frac{\partial v^\epsilon_\gamma}{\partial x_\delta}(\mathbf{x})\right]=0. \tag{2.13}$$

Similarly (2.12) yeilds $L^\epsilon{}_{\alpha\beta\gamma\delta}\partial v_\gamma{}^\epsilon/\partial x_\delta N_\beta=0$ on the boundary of the cavities. Here we have denoted the increment of $\mathbf{u}^\epsilon$ by $\mathbf{v}^\epsilon$ and the incremental moduli $\mathbf{L}^\epsilon(\mathbf{x})$ are given by

[3] The problem is presumed to be one of plane strain.

Downloaded 02 May 2010 to 171.66.16.25. Redistribution subject to ASME license or copyright; see http://www.asme.org/terms/Terms_Use.cfm

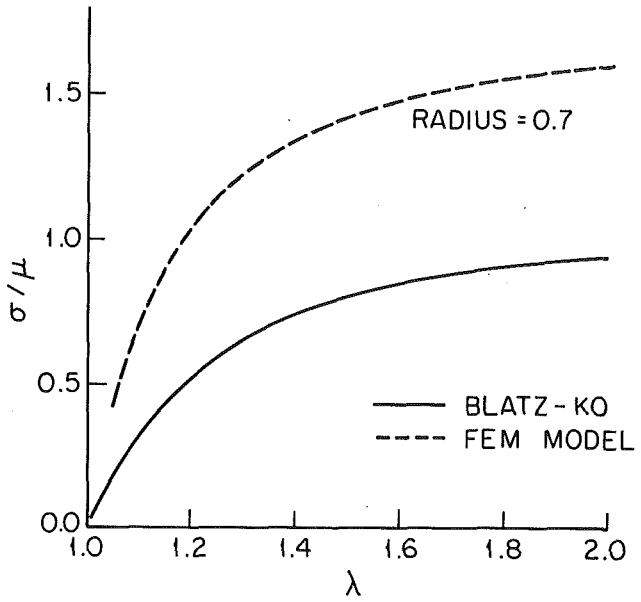


Fig. 3 Stress-stretch response in plane-strain equibiaxial stretching (homogenized and Blatz-Ko materials)

$$L^{\epsilon}{}_{\alpha\beta\gamma\delta}(\mathbf{x}) = \frac{\partial^2 W}{\partial F_{\alpha\beta}\partial F_{\gamma\delta}}(\mathbf{F}^{\epsilon}(\mathbf{x})). \tag{2.14}$$

In view of the nature of the geometry and loading in the present problem, it is evident that the deformation gradient $\mathbf{F}^{\epsilon}(\mathbf{x})$ depends on ϵ through $\mathbf{x}/\epsilon$ alone, i.e., $\mathbf{F}^{\epsilon}(\mathbf{x}) = \mathbf{F}(\mathbf{x}/\epsilon)$, so that we also have $\mathbf{L}^{\epsilon}(\mathbf{x}) = \mathbf{L}(\mathbf{x}/\epsilon)$. Moreover $\mathbf{L}^{\epsilon}(\mathbf{x})$ clearly satisfies the periodicity condition (2.2). Consequently the mathematical problem governing the displacement increment $\mathbf{v}^{\epsilon}(\mathbf{x})$ here is identical to that stated in Section 2.1.

The overall incremental moduli $\mathcal{L}(\lambda_1, \lambda_2)$ of the body may now be calculated from (2.7) after first solving the boundary value problem (2.10)–(2.12) for $\mathbf{u}^{\epsilon}(\mathbf{x})$, then determining $\mathbf{F}^{\epsilon}(\mathbf{x})$ and $\mathbf{L}^{\epsilon}(\mathbf{x})$ from $(2.11)_2$ and (2.14), and finally solving[4] (2.8) for the periodic functions $\chi^{\alpha\beta}$. In what follows, we carry out these calculations in the case when the (matrix) material is isotropic and is characterized by the plane-strain elastic potential

$$W(I,J) = \frac{\mu}{2}\left[(I-2) - 2(J-1) + \frac{1}{1-2\nu}(J-1)^2\right], \tag{2.15}$$

where $I = \text{trace}(\mathbf{F}\mathbf{F}^T)$, $J = \det \mathbf{F}$. This particular choice for W was made for three reasons. First, in the small strain limit the preceding material reduces to an isotropic linearly elastic one with shear modulus μ and Poisson's ratio ν. Second, for values of ν approaching 0.5 the preceding material presumably approaches[5] a Mooney-Rivlin material which is a suitable model for a class of rubbers under finite strain. Finally, and most importantly, for all values of $\mu > 0$ and $0 < \nu < 0.5$ the material characterized by (2.15) is strongly elliptic in all plane deformations as may be readily verified from (2.15) and equations (2.41) and (2.42) of Knowles and Sternberg [18]. The Blatz-Ko material, with which we will compare the homogenized model, is characterized by the plane strain elastic potential

$$W(I,J) = \frac{\mu}{2}\left(\frac{I+1}{J^2} + 2J - 5\right). \tag{2.16}$$

[4] As mentioned previously, the integrals in (2.7) and (2.8) are taken over $Y-D$. Moreover, note that the boundary conditions for $\chi^{\alpha\beta}$ on ∂D are natural boundary conditions in (2.8).

[5] A rigorous proof of such a claim can be given under certain conditions (not satisfied by (2.15)), e.g., [17]. It is considerably more convenient for numerical reasons, to consider a nearly imcompressible material rather than an incompressible one.

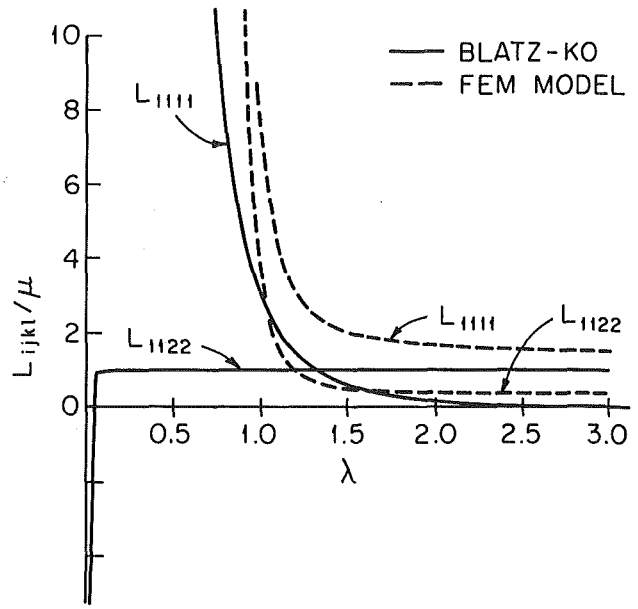


Fig. 4(a) Variation of the normal incremental moduli in plane-strain equibiaxial stretching (homogenized and Blatz-Ko materials)

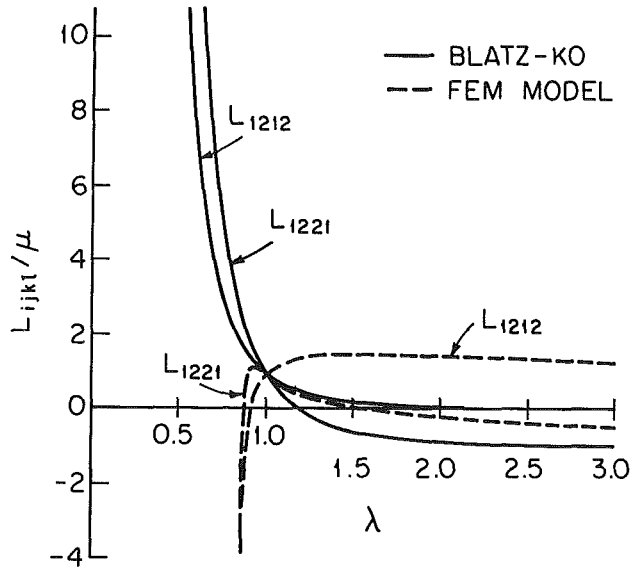


Fig. 4(b) Variation of the shear incremental moduli in plane-strain equibiaxial stretching (homogenized and Blatz-Ko materials)

Fig. 4

3 Numerical Method

As seen from the preceding analysis, the computation of the homogenized incremental moduli $\mathcal{L}$ at a given state of deformation requires the fundamental solution of the nonlinear boundary value problem (2.10)–(2.12) for the unit cell Y. One can then calculate the corresponding incremental moduli $\mathbf{L}(\mathbf{y})$ based on this solution and subsequently use this information to solve the linear problem (2.8) for $\chi_{\gamma}^{\alpha\beta} + y_{\beta}\delta_{\alpha\gamma}$. These solutions can be obtained most efficiently, in the present problem, by using the finite element method.

The unit cell Y, a rectangle of (undeformed) dimensions $2a_1 \times 2a_2$, has a concentric elliptical hole of major and minor semiaxes b_1 and b_2, respectively. In view of the geometric and loading symmetries involved in this problem, only one quarter of Y need be analyzed. The finite element grid (see Fig. 2)

Downloaded 02 May 2010 to 171.66.16.25. Redistribution subject to ASME license or copyright; see http://www.asme.org/terms/Terms_Use.cfm

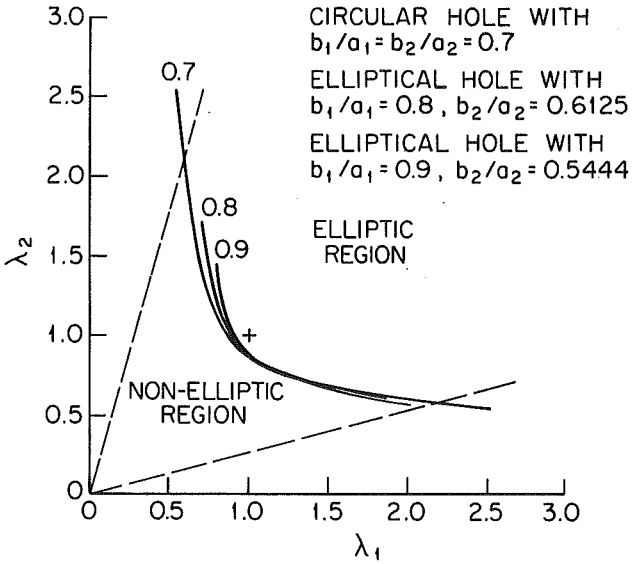


Fig. 5 Domain of ellipticity on the $(\lambda_1 \lambda_2)$-plane. The solid lines denote the boundary of the elliptic region for the homogenized material; the dashed lines correspond to the Blatz-Ko material.

consists of isoparametric bilinear quadrilaterals. Numerical integration over each element was based on a 2×2 Gauss–Legendre scheme. Most of the calculations here were based on a 10 (in the radial direction) by 20 (in the circumferential direction) grid. The mesh was properly refined at the end sections $y_1 = 0$ and $y_2 = 0$ in view of the large strain concentrations occurring at these locations. The adequacy of the mesh was decided on the basis that any further refinement (meshes of up to 18×36 elements have been investigated) should yield displacements no more different than 0.1 percent and homogenized incremental moduli different by less than 1 percent. Finally, the matrix material was taken to be approximately incompressible by using the value $\nu = 0.49$ for the Poisson ratio in (2.15).

An incremental Newton-Raphson method (see [19] for further details) was employed to determine the fundamental solution for the unit cell Y. The calculations were carried out along different "radial" paths through the undeformed state on the (λ_1, λ_2)-plane, i.e., along lines $(\lambda_2 - 1)/(\lambda_1 - 1) =$ constant. Once convergence has been achieved at a given load level, the corresponding discretized incremental stiffness matrix, say $[K]$, could be used to immediately yield the nodal values of $\chi_\gamma^{\alpha\beta}(\mathbf{y}) + y_\beta \delta_{\alpha\gamma}$, say $[d^{\alpha\beta}]$ (see (2.8)). Note from (2.7) that the corresponding values of the homogenized incremental moduli $\mathcal{L}$ are simply calculated by the following scalar product:

$$\mathcal{L}_{\alpha\beta\gamma\delta} = [d^{\alpha\beta}]^T [K] [d^{\gamma\delta}]. \tag{3.1}$$

The ellipticity of $\mathcal{L}$ (given by (3.1)) was examined by a direct numerical check of condition (2.9) at every $\pi/720$ radian increment of ϕ where $n_1 = \cos\phi$, $n_2 = \sin\phi$.

4 Results

The selection of the hole size in our calculations was dictated by the requirement of a 50 percent porosity – the same as that observed in the specimens used by Blatz and Ko [1]. Three different void shapes are considered here; a circular one with $b_1/a_1 = b_2/a_2 = 0.7$, an elliptical one with $b_1/a_1 = 0.8$, $b_2/a_2 = 0.6125$, and a second elliptical one with $b_1/a_1 = 0.9$, $b_2/a_2 = 0.5444$. The unit cell was taken to be a square, $a_1 = a_2$.

As mentioned previously, the model used in this work has an overall response that is orthotropic and is thus a somewhat poor approximation to the (isotropic) Blatz-Ko material (2.16). To minimize the influence of this difference, we first carried out a series of calculations for a body with circular cavities under conditions of equibiaxial stretch $\lambda_1 = \lambda_2$. The effective principal true stresses $(\sigma_1 = \sigma_2 = \sigma)$ as well as the homogenized incremental moduli $\mathcal{L}_{\alpha\beta\gamma\delta}$ were computed and compared with the corresponding quantities for the Blatz-Ko material.

In Fig. 3 we compare the principal Cauchy stress $\sigma_1 = \sigma_2 = \sigma$ of the Blatz-Ko material with the corresponding average principal stress (defined as the average of the normal Cauchy stress over the side $y_1 = a_1$ or $y_2 = a_2$ of the unit cell) both being evaluated at the same stretch ratio $\lambda_1 = \lambda_2 = \lambda$. The infinitesimal shear modulus of the Blatz-Ko material was chosen to be the same as that of the homogenized material and the results shown are normalized with respect to this common shear modulus μ. It may be observed that the two curves show the same trends, and roughly appear to be scaled versions of each other.

A similar comparison of the homogenized and Blatz-Ko incremental moduli in equibiaxial stretching is made in Figs. 4(*a*) and 4(*b*). These calculations were carried out for circular voids with radius $b_1/a_1 = 0.7$. The qualitative agreement is reasonably good in the case of extension. On the other hand, in the case of contraction, we observe large differences, even to the point of predicting negative incremental shear moduli for the homogenized model. This may be attributed to the fact that the constitutive model for the matrix material (2.15) utilized here is unrealistic at high compressive strains; note for instance that the strain energy density W (see (2.15)) remains bounded as $J \to 0$ for fixed values of the Poisson's ratio ν.

Finally attention is turned to the results pertaining to a loss of ellipticity for the homogenized material and Fig. 5 displays the corresponding elliptic and nonelliptic domains on the (λ_1, λ_2)-plane. The points associated with the onset of a failure of ellipticity lie on a curve which looks roughly like a hyperbola. The corresponding curves (straight lines, in this case) for a Blatz-Ko material are also shown on this figure. One can observe that the homogenized material loses ellipticity after the Blatz-Ko material in extensional deformations while the converse is true in compression. This is not entirely unexpected since, as can be readily verified from (2.15) and (2.16), the response of the matrix material is much stiffer (and softer) than that of the Blatz-Ko material in tension (and compression, respectively).

To estimate the sensitivity of the aforementioned results to the void shape, the preceding calculations were repeated for the case when the voids had an elliptical cross-section while keeping the void ratio constant at 50 percent as in the previous case. The results, for two different elliptical cross-sections, are also shown in Fig. 5. The influence of the void shape appears to be small, and as one might expect (in view of the stress concentration effects) the homogenized material based on elliptical cavities with $b_1 > b_2$, is stiffer than that corresponding to circular cavities in the case when $\lambda_2 < \lambda_1$. The opposite is true when $\lambda_2 > \lambda_1$.

5 Concluding Remarks

This work is not aimed at providing a micromechanical justification for a particular constitutive model but rather is concerned with certain aspects of the influence of voids on the stability properties of an elastic material. The most significant feature of the results of this investigation is that although the matrix material used is stable in the sense that it remains elliptic at all deformations, the resulting homogenized medium (obtained through a formal adaptation of the method of homogenization) exhibits a loss of ellipticity at adequately high strain levels. One possible mechanism that explains this macroscopic instability is that it is a global manifestation of void buckling in a banded pattern at the microstructural level.

Downloaded 02 May 2010 to 171.66.16.25. Redistribution subject to ASME license or copyright; see http://www.asme.org/terms/Terms_Use.cfm

Acknowledgments

The authors are indebted to Mr. Peter Washabauch for his enthusiastic help with the computational part of this work. This work was supported by the U.S. National Science Foundation under Grant CME 81-06581 (R.A.) and Grant MEA-8116449 (N.T.).

References

1 Blatz, P. J., and Ko, W. L., "Application of Finite Elastic Theory to the Deformation of Rubbery Materials," *Trans. Soc. Rheology*, Vol. 6, 1962, pp. 223-251.

2 Knowles, J. K., and Sternberg, E., "On the Ellipticity of the Equations of Nonlinear Elastostatics for a Special Material," *J. Elasticity*, Vol. 5, 1975, pp. 341-361.

3 Watt, J. P., Davis, G. F., and O'Connell, R. J., "The Elastic Properties of Composite Materials," *Rev. Geophys. Space Phys.*, Vol. 14, 1976, pp. 541-563.

4 Willis, J. R., "Variational and Related Methods for the Overall Properties of Composites," in *Advances in Applied Mechanics*, Yih, C-S., ed., Academic Press, New York, Vol. 21, 1981, pp. 1-78.

5 Walpole, L. J., "Elastic Behavior of Composite Materials: Theoretical Foundations," in *Advances in Applied Mechanics*, Yih, C-S., ed., Academic Press, New York, Vol. 21, 1981, pp. 169-242.

6 Budiansky, B., "On the Elastic Moduli of Some Heterogeneous Materials," *J. Mech. Phys. Solids*, Vol. 13, 1965, pp. 223-227.

7 Sanchez-Palencia, E., "Comportements Local et Macroscopique d'un Type de Milieux Physiques Heterogenes," *Int. J. Engineering Science*, Vol. 12, 1974, pp. 331-351.

8 Bensoussan, A., Lions, J. L., and Papanicolaou, G., *Asymptotic Analysis for Periodic Structures*, North Holland, Amsterdam, 1978.

9 Rudnicki, J. W., and Rice, J. R., "Conditions for the Localization of Deformation in Pressure Sensitive Dilatant Materials," *J. Mech. Phys. Solids*, Vol. 23, 1975, pp. 371-394.

10 Gurson, A. L., "Continuum Theory of Ductile Rupture by Void Nucleation and Growth: Part 1—Yield Criteria and Flow Rules for Porous Ductile Media," ASME *Journal of Materials and Technology*, Vol. 99, 1977, pp. 2-15.

11 Yamamoto, H., "Conditions for Shear Localization in the Ductile Fracture of Void-Containing Materials," *Int. J. Fracture*, Vol. 14, 1978, pp. 347-365.

12 Iwakuma, T., and Nemat-Nasser, S., "An Analytical Estimate of Shear Band Initiation in a Necked Bar," *Int. J. Solids Structures*, Vol. 18, 1982, pp. 69-83.

13 Saje, M., Pan, J., and Needleman, A., "Void Nucleation Effects on Shear Localization in Porous Plastic Solids," *Int. J. Fracture*, Vol. 19, 1982, pp. 163-182.

14 Tvergaard, V., "Influence of Voids on Shear Band Instabilities Under Plane Strain Conditions," *Int. J. Fracture*, Vol. 17, 1981, pp. 389-407.

15 Ohno, N., and Hutchinson, J. W., "Plastic Flow Localization Due to Nonuniform Void Distribution," Harvard University Technical Report No. MECH-42, April 1983.

16 Fichera, G., "Existence Theorems in Elasticity," in *Handbuch der Physik*, Flugge, S., ed., Volume VI a/2, Springer-Verlag, Berlin, 1972.

17 Rostamian, R., "Internal Constraints in Boundary Value Problems of Continuum Mechanics," *Indiana Univ. Math. J.*, Vol. 27, 1978, pp. 637-657.

18 Knowles, J. K., and Sternberg, E., "On the Failure of Ellipticity of the Equations for Finite Elastostatic Plane Strain," *Arch. Rat. Mech. Anal.*, Vol. 63, 1977, pp. 321-336.

19 Abeyaratne, R., and Triantafyllidis, N., "The Emergence of Shear Bands in Plane Strain," *Int. J. Solids Structures*, Vol. 17, 1981, pp. 1113-1134.

Downloaded 02 May 2010 to 171.66.16.25. Redistribution subject to ASME license or copyright; see http://www.asme.org/terms/Terms_Use.cfm

P. M. Naghdi
Honorary Mem. ASME

D. J. Nikkel, Jr.
Student Mem. ASME

Department of Mechanical Engineering,
University of California,
Berkeley, Calif. 94720

Calculations for Uniaxial Stress and Strain Cycling in Plasticity

Within the framework of an existing purely mechanical, rate-type theory of plasticity, detailed calculations are presented for certain types of material response during stress and strain cycling in a uniaxial homogeneous deformation. These features pertain specifically to material response in stress cycling between fixed values of stress in tension and compression (not necessarily equal in magnitude) resulting in ratcheting of strain, and a type of saturation hardening caused by strain cycling between any two fixed values of strain when the mean value of stress (in tension and compression) tends to zero.

1 Introduction

Starting from a general theory of plasticity developed in stress space by Green and Naghdi [1, 2] and its formulation relative to strain space by Naghdi and Trapp [3], Caulk and Naghdi [4] have discussed hardening response and in particular have compared the predictions of the theory with two sets of experimental results. In [4], with the limitation to small deformation, systematic specialization of the constitutive equations of the general theory were specifically applied to saturation hardening and other types of stress or strain cycling were not considered. Additional developments of saturation hardening in the context of strain-space formulation were discussed by Casey and Naghdi [5]; and, for the class of materials for which detailed comparisons with experiments were made in [4], the results for saturation hardening in [4] and [5] are equivalent.

More recently, the stress and strain cycling has also been discussed by Drucker and Palgen [6], who employed an approach to plasticity different from that of strain-space formulation utilized in [4, 5]. In the course of their development, Drucker and Palgen [6] have also discussed the material response appropriate for unsymmetric plastic cycles of stress or of strain. While it may not be obvious at first sight, one would expect that a suitable specialization of the general theory should be capable of accommodating the type of unsymmetric cycles mentioned and discussed by Drucker and Palgen [6]. The purpose of this paper is to show that this is the case. In particular, in what follows we demonstrate the predictive capability of the theory in [1-3] for two types of uniaxial material response, namely:

1) ratcheting of strain caused by stress cycling between fixed values of stress in tension and compression (not necessarily equal in magnitude) similar to that shown in Fig. 1, and

2) progressive relaxation to zero of the mean stress caused by strain cycling between any two fixed values of strain similar to that shown in Fig. 2.

These two types of responses in the light of experimental results were described and discussed by Drucker and Palgen [6, p. 480]. By way of background and for definiteness, some features of these two types of responses are recalled here with reference to a uniaxial homogeneous deformation in a tension-compression test. In the context of small deformation, let e and s stand, respectively, for the component e_{11} of the strain tensor and the component s_{11} of the stress tensor.[1] Then, a stress cycle such as $A_1B_1C_1D_1E_1F_1A_2$ in Fig. 1 consists of loading in one direction from some chosen value of stress, say at A_1, to a limiting value of stress at C_1 followed by reversing the direction of loading until another limiting value of stress (not necessarily equal to that at C_1) is reached at F_1 and the direction of loading is again reversed until the stress reaches a value at A_2 equal to that of the initial choice at A_1. More generally, again with reference to Fig. 1, during the nth cycle ($n = 1,2,3, \ldots$) the response that begins at any point such as $A_n, B_n, \ldots,$ or F_n and ends at a corresponding value of stress at $A_{n+1}, B_{n+1}, \ldots,$ or F_{n+1} constitutes a stress cycle. Consider now a specimen cyclically loaded into the plastic range between stress limits whose average is nonzero[2] i.e., stress limits that are unsymmetric about the strain axis in the s-e plane. During a typical stress cycle of this kind (e.g., $A_2B_2C_2D_2E_2F_2A_3$ in Fig. 1) the strain at the beginning and end of the cycle (and hence also the minimum and maximum values of strain attained during the cycle) vary from one cycle to the next. Evidently, experimental observations (see, for example Dolan [7, Fig. 14]) indicate that if the average of the stress limits[3] is positive, both the minimum and maximum strains attained in a given cycle can

Contributed by the Applied Mechanics Division for publication in the JOURNAL OF APPLIED MECHANICS.

Discussion on this paper should be addressed to the Editorial Department, ASME, United Engineering Center, 345 East 47th Street, New York, N.Y. 10017, and will be accepted until two months after final publication of the paper itself in the JOURNAL OF APPLIED MECHANICS. Manuscipt received by ASME Applied Mechanics Division, October, 1983.

[1] A distinction between the Cauchy stress tensor or either of the Piola-Kirchhoff stresses is unnecessary when only a small deformation is being considered.

[2] This feature is referred to in [6] as "unsymmetric cycles of stress in the plastic range."

[3] The terminology of the average of the stress level is referred to in [6] as the "mean stress" and "mean stress in the cycle."

Copyright © 1984 by ASME
Downloaded 02 May 2010 to 171.66.16.25. Redistribution subject to ASME license or copyright; see http://www.asme.org/terms/Terms_Use.cfm

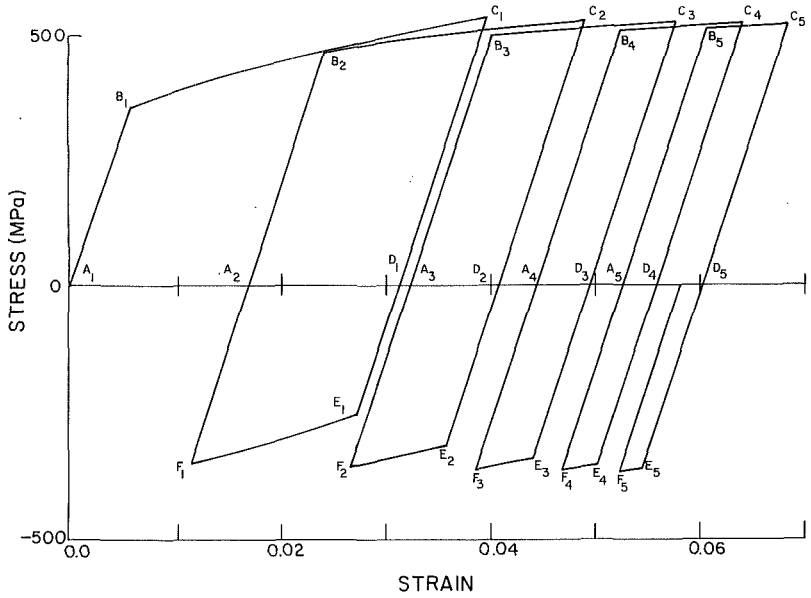


Fig. 1 Calculated uniaxial stress-strain response in *s-e* plane to cyclic loading between fixed values of stress in tension and compression (not necessarily equal in magnitude) resulting in ratcheting of strain. The material constants used in the calculation are given by equation (50).

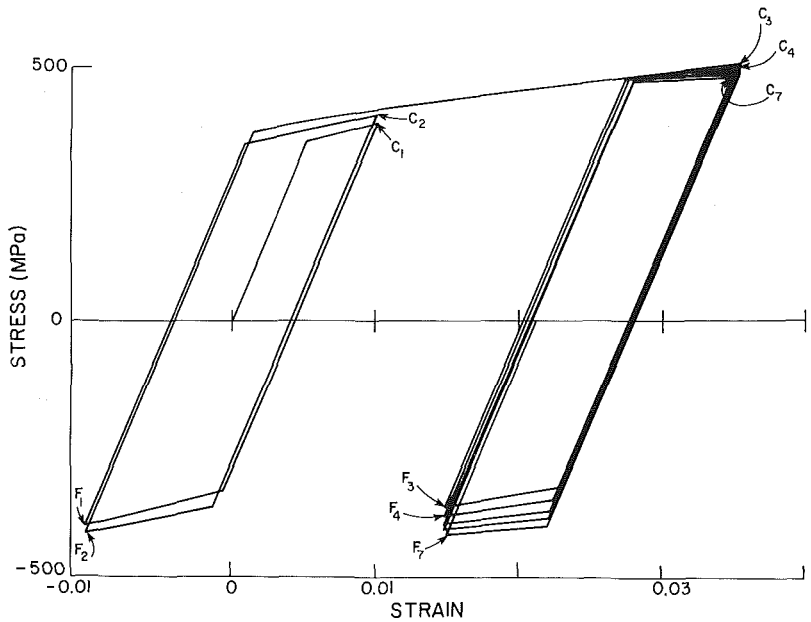


Fig. 2 Calculated uniaxial stress-strain response in s-e plane showing progressive relaxation to zero of the mean stress caused by strain cycling between any two fixed values of strain. The material constants used in the calculation are given by equation (50).

progressively increase from one cycle to the next. Similarly, it may be inferred from the discussion in Sandor's book [8, pp. 97–100] that if the average of the stress limits is negative, then both the minimum and maximum values of strain attained in a given cycle can progressively decrease from one cycle to the next. Thus, while the stress limits remain fixed for repeated cyclic loading, the strain limits of the cycles can be progressively displaced along the strain axis from one cycle to the next[4]. A well-known phenomenon of this type, called ratcheting of strain, refers to progressive increase in plastic strain during cycling between any two fixed values of stress levels. Evidently such a progressive increase in plastic strain may take place irrespective of the starting point in the cycle. Indeed, as is clear from Fig. 1, the strains at $A_{n+1}, B_{n+1}, \ldots, F_{n+1}$ all have been increased along the *e*-axis from the values of strain at $A_n, B_n, \ldots, F_n$.

For cycling in the plastic range between fixed strain limits, on the other hand, for most metals the extent of the elastic range during each successive strain cycle increases (or decreases) until a limiting periodic response is reached in which the stress-strain curve of each succeeding cycle is the same (see Fig. 3). This phenomenon, which was previously discussed in [4], is sometimes called saturation hardening and a material is said to saturate when it reaches this limiting behavior. Moreover, if the specimen is cycled between fixed strain limits whose average is nonzero, it has been observed by

[4] The strain limits of the cycles will be displaced in the positive strain direction if the average of the stress limits is positive (as depicted in Fig. 1) and in the negative strain direction if the average of the stress limits is negative (see [8, Fig. 98]).

Downloaded 02 May 2010 to 171.66.16.25. Redistribution subject to ASME license or copyright; see http://www.asme.org/terms/Terms_Use.cfm

Morrow and Sinclair [9] and by Dolan [7, Fig. 15][5] that for a certain class of materials the average of the limiting stresses in the cycle will progressively relax and tend to zero. For example, with reference to Fig. 2, the average value of the stresses at C_n and F_n ($n \geqslant 3$) tends to zero for repeated cyclic loading between fixed strain limits. For completeness, we also briefly indicate in Fig. 3 the prediction of the theory (by means of the procedure of the present paper) for the case of saturation hardening, and examine its comparison with that in [4].

2 Basic Equations

Using a strain-space formulation of plasticity, we summarize here the basic equations of a purely mechanical theory contained in the papers of Green and Naghdi [1, 2], Naghdi and Trapp [3], and Casey and Naghdi [5]. In addition to the strain tensor e_{KL}, we assume the existence of a symmetric second-order plastic strain e^p_{KL} and a scalar κ representing a measure of work hardening. It is assumed that the stress tensor s_{KL} is given by a constitutive equation of the form

$$s_{KL} = \hat{s}_{KL}(\mathfrak{U}), \quad \mathfrak{U} = (e_{MN}, e^p_{MN}, \kappa) \tag{1}$$

and that, for fixed values of e^p_{MN} and κ, $(1)_1$ can be inverted in the form

$$e_{KL} = \hat{e}_{KL}(\mathfrak{V}), \quad \mathfrak{V} = (s_{MN}, e^p_{MN}, \kappa). \tag{2}$$

The response functions $\hat{s}_{KL}$ and $\hat{e}_{KL}$ in (1) and (2) are taken to be smooth. We must admit the existence of a smooth yield (or loading) function $g(\mathfrak{U})$ in strain space such that for fixed values of (e^p_{KL}, κ) the equation $g(\mathfrak{U}) = 0$ represents a closed orientable hypersurface of dimension five enclosing a region of strain space. With the use of $(2)_1$, we obtain a corresponding function $f(\mathfrak{V})$ through the formula

$$g(\mathfrak{U}) = g(\hat{e}_{MN}(\mathfrak{V}), e^p_{MN}, \kappa) = f(\mathfrak{V}). \tag{3}$$

Because of the assumed smoothness of $(2)_1$, for fixed values of (e^p_{KL}, κ) the equation $f(\mathfrak{V}) = 0$ represents a hypersurface in stress space having the same geometrical properties as the hypersurface in strain space.

The loading criteria of strain-space formulation will be regarded as primary. Also, for our present purpose, it is sufficient to consider only a special case of the stress response in which $\hat{s}_{KL}$ in $(1)_1$ is independent of κ and its dependence on the variables (e_{MN}, e^p_{MN}) occurs only through the difference $e_{MN} - e^p_{MN}$. Then, the constitutive equations for the rate of plastic strain $\dot{e}^p_{KL}$ and rate of work-hardening parameter $\dot{\kappa}$ during loading (i.e., when $g = 0$ and $\hat{g} > 0$)[6] may be expressed as (see the development among equations (36)–(42) in [5]):

$$\dot{e}^p_{KL} = \frac{\hat{g}}{\Gamma + \Lambda} \frac{\partial f}{\partial s_{KL}}, \quad \dot{\kappa} = \mathfrak{C}_{KL} \dot{e}^p_{KL}, \tag{4}$$

where

$$\hat{g} = \frac{\partial g}{\partial e_{KL}} \dot{e}_{KL}, \tag{5}$$

$$\Lambda = \frac{\partial f}{\partial s_{KL}} \frac{\partial g}{\partial e_{KL}},$$

$$\Gamma = -\frac{\partial f}{\partial s_{KL}} \left(\frac{\partial f}{\partial e^p_{KL}} + \frac{\partial f}{\partial \kappa} \mathfrak{C}_{KL} \right), \quad \Gamma + \Lambda > 0 \tag{6}$$

and where the response coefficients $\mathfrak{C}_{KL}$ are functions of the variables $(1)_2$. It should be noted that in obtaining the expression $(4)_1$ a condition resulting from a work inequality proposed in [10] has been also imposed on the constitutive equations for plastic strain rate.

[5] See also [6, Fig. 2].

[6] The scalar $\hat{g}$ is defined by equation (5).

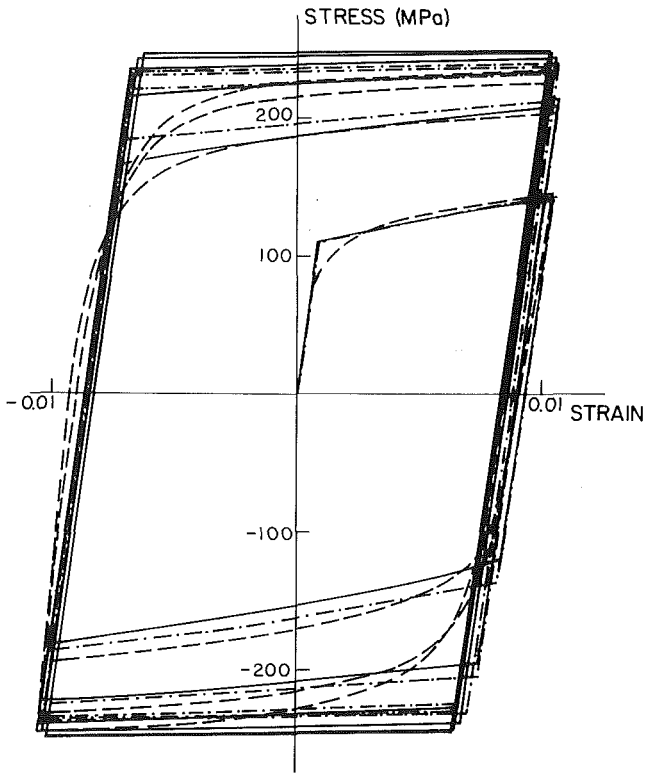


Fig. 3 Comparison of theoretical cyclic stress-strain behavior for 304 stainless steel with the experimental data of reference [13]. The theoretical stress-strain curves (—) are calculated using the material constants in (51); the theoretical curves (-•••-) are those calculated previously in [4]; and comparison with the experimental data (- - -) is shown for the first three strain cycles only, since curves for additional cycles would crowd the figure

The characterization of strain-hardening behavior by means of the rate-independent quotient $\hat{f}/\hat{g}$, with $\hat{f} \equiv (\partial f/\partial s_{KL})\dot{s}_{KL}$, is discussed in [5]. More recently, a scalar quantity Φ is defined in [11] in such a way that does not presuppose a condition of loading and is such that during loading it has the same value as $\hat{f}/\hat{g}$. For our present purpose, the scalar function Φ can be defined as [12, equation (4.13)]

$$\Phi = \frac{\Gamma}{\Gamma + \Lambda}, \tag{7}$$

and a particle of an elastic-plastic material is then said to exhibit [11, 12]

$$\begin{cases} \text{hardening behavior if and only if } \Phi > 0, & (a) \\ \text{softening behavior if and only if } \Phi < 0, & (b) \\ \text{perfectly plastic behavior if and only if } \Phi = 0. & (c) \end{cases} \tag{8}$$

Moreover, the strain-hardening response of a material is said to saturate to one of the values $\{K_h, K_s, 0\}$ and exhibits either (a) saturation hardening, (b) saturation softening, and (c) saturation to perfectly plastic behavior, in that order, if

$$\lim_{t \to \infty} \Phi = \begin{cases} K_h > 0, & (a) \\ K_s < 0, & (b) \\ 0. & (c) \end{cases} \tag{9}$$

3 Special Constitutive Response Functions

It is convenient to prescribe the various constitutive response functions in terms of the components of deviatoric stress τ_{KL} and deviatoric strain γ_{KL}, namely

Downloaded 02 May 2010 to 171.66.16.25. Redistribution subject to ASME license or copyright; see http://www.asme.org/terms/Terms_Use.cfm

$$\tau_{KL}=s_{KL}-\bar{s}\delta_{KL}, \quad \tau_{KK}=0,$$
$$\gamma_{KL}=e_{KL}-\bar{e}\delta_{KL}, \quad \gamma_{KK}=0, \tag{10}$$

with similar definition for the components of deviatoric plastic strain γ^p_{KL}, where $\bar{s}$ and $\bar{e}$ are the mean normal stress and mean normal strain, respectively. In the context of small deformation and for materials that are isotropic in the reference state, we specify the stress response by generalized Hooke's law and this can be written in the form

$$\tau_{KL}=2\mu(\gamma_{KL}-\gamma^p_{KL}), \quad \bar{s}=3k(\bar{e}-\bar{e}^p), \tag{11}$$

where μ is the shear modulus of elasticity and k is the bulk modulus.

In regard to the characterization of material response to stress and strain cycling of the types referred to 1) and 2) in Section 1, we first observe that it is the translation of the yield surface (whose interior represents the elastic domain), and not its size, which is particularly significant here. For the response described under 1) in Section 1, while the plastic strain progressively increases from one cycle to the next, the overall translation of the yield surface in stress space is not significantly different between the later and earlier cycles. For the response described under 2) in Section 1, on the other hand, the amount of translation of the yield surface in stress space becomes progressively smaller as the material is cycled between fixed strain limits. In the yield function utilized previously by Caulk and Naghdi [4, equation (40)], the quantity representing translation of the yield surface in stress space can be regarded as a constant represented by ½ α times the plastic strain. Hence, at a given value of plastic strain the translation of the yield surface is determined independently of the loading history. By contrast, in our present discussion it is important to account for the effect of loading history pertinent to the translation of the yield surface. A simple way to achieve this is to generalize the restricted equations of Caulk and Naghdi [4, equations (40), (56), and $(70)_1$] by replacing the constant coefficient α with a scalar function $\hat{\alpha}$ of the work-hardening parameter κ which is 0(1). In particular we take $\hat{\alpha}$ to be linear in κ, with an initial value α_0 when $\kappa=\kappa_0$ and a value α_s at saturation when $\kappa=\kappa_s$. Thus, we specify the loading function in the form

$$f=\left(\tau_{KL}-\frac{\hat{\alpha}(\kappa)}{2}\gamma^p_{KL}\right)\left(\tau_{KL}-\frac{\hat{\alpha}(\kappa)}{2}\gamma^p_{KL}\right)-\kappa$$
$$=4\mu^2\left[\gamma_{KL}-\left(1+\frac{\hat{\alpha}(\kappa)}{4\mu}\right)\gamma^p_{KL}\right]\left[\gamma_{KL}-\left(1+\frac{\hat{\alpha}(\kappa)}{4\mu}\right)\gamma^p_{KL}\right]-\kappa=g, \tag{12}$$

with $\hat{\alpha}(\kappa)$ given by

$$\hat{\alpha}(\kappa)=\frac{(\alpha_0-\alpha_s)\kappa+(\alpha_s\kappa_0-\alpha_0\kappa_s)}{\kappa_0-\kappa_s}. \tag{13}$$

It should be noted that for the special case in which $\alpha_0=\alpha_s=\alpha$, $\hat{\alpha}(\kappa)$ becomes simply α and the loading functions (12) reduce to those used by Caulk and Naghdi [4, equations $(40)_1$, (56), $(70)_1$]. In (12), ½$\hat{\alpha}(\kappa)\gamma^p_{KL}$ may be interpreted as the center of the yield surface in the deviatoric stress space. Similarly, the quantity $(1+(1/4\mu)\hat{\alpha}(\kappa))\gamma^p_{KL}$ may be interpreted as the center of the yield surface in deviatoric strain space. The size of the loading surfaces (which represents the extent of the elastic region) depends on the work-hardening parameter κ.

Supplementary to (12) and (13), we also need to specify the work-hardening coefficients $\mathcal{C}_{KL}$ in (4). As noted earlier, a significant feature of the material response described under 1) and 2) in Section 1 is the translation of the yield surface, and not its size. However, with reference to the phenomenon of saturation hardening examined in [4], it is the size of the yield surface which is of particular interest. To account also for saturation hardening, it is sufficient to specify $\mathcal{C}_{KL}$ in the same form as that in [4, equation $(56)_2$], by[7]

$$\mathcal{C}_{KL}=\left(\frac{\kappa-\kappa_s}{\kappa_0-\kappa_s}\right)(\beta_1\gamma_{KL}+\beta_2\gamma^p_{KL})$$
$$=\left(\frac{\kappa-\kappa_s}{\kappa_0-\kappa_s}\right)(\beta\tau_{KL}+\eta\gamma^p_{KL}), \tag{14}$$

where β_1,β_2,κ_0, and κ_s are constants and where with the use of (11) β and η are given by $\beta_1=2\mu\beta$ and $\beta_2=\eta-2\mu\beta$.

With the constitutive equations (11)–(14), it follows from (6) that on the yield surface the scalar functions Λ and Γ assume the values

$$\Lambda=8\mu\kappa>0 \quad (f=g=0), \tag{15}$$
$$\Gamma=2\hat{\alpha}\kappa+2\left[1+\left(\frac{\alpha_0-\alpha_s}{\kappa_0-\kappa_s}\right)(\tau_{KL}-\frac{\hat{\alpha}}{2}\gamma^p_{KL})\gamma^p_{KL}\right](\hat{\beta}\tau_{MN}$$
$$+\hat{\eta}\gamma^p_{MN})\left(\tau_{MN}-\frac{\hat{\alpha}}{2}\gamma^p_{MN}\right) \quad (f=g=0), \tag{16}$$

where the quantities $\hat{\beta}$ and $\hat{\eta}$ are given by

$$\hat{\beta}=\hat{\beta}(\kappa)=\left(\frac{\kappa-\kappa_s}{\kappa_0-\kappa_s}\right)\beta, \quad \hat{\eta}=\hat{\eta}(\kappa)=\left(\frac{\kappa-\kappa_s}{\kappa_0-\kappa_s}\right)\eta \tag{17}$$

subject to the restrictions

$$\hat{\beta}(\kappa_s)=\hat{\eta}(\kappa_s)=0. \tag{18}$$

In view of (7), (15), and $(6)_3$, it is easily seen that the strain-hardening is characterized by

$$\Phi=1-\frac{\Lambda}{\Gamma+\Lambda}=1-\frac{8\mu\kappa}{\Gamma+\Lambda}<1. \tag{19}$$

4 Uniaxial Cyclic Loading

Consider now a homogeneous extensional deformation sustained by a uniaxial stress $s_{11}=s(t)$ say. Adopting the notations $e_{11}=e$, $e^p_{11}=e^p$, as in [4, 5] in matrix notation we write

$$\|\tau_{KL}\|=\frac{1}{3}s\|b_{KL}\|, \quad \|\gamma^p_{KL}\|=\frac{1}{2}e^p\|b_{KL}\|, \tag{20}$$

where the constant matrix $\|b_{KL}\|$ defined by

$$\|b_{KL}\|=\begin{Vmatrix}2 & 0 & 0\\ 0 & -1 & 0\\ 0 & 0 & -1\end{Vmatrix}$$

is introduced for convenience. For the uniaxial homogeneous deformation under discussion, each of the two variables e and s is represented as a line in the $s-e$ plane (corresponding to the six-dimensional strain space and stress space). The yield surfaces are now points on these lines and the elastic range (corresponding to the interior regions of the yield surfaces) is a line segment between these points. The midpoint of the line segment corresponds to the center of the yield surface and the length of this line segment corresponds to the size of the yield surface whose interior represents the extent of the elastic region.

The loading function (12) now assumes the simplified form

$$f=\frac{2}{3}\left(s-\frac{3}{4}\hat{\alpha}(\kappa)e^p\right)^2-\kappa \tag{22}$$

and the constitutive equations (11) and $(4)_{1,2}$ with (14)[8] reduce to

[7] The hardening response coefficient in [4] is denoted by $\mathfrak{M}_{KL}$ instead of $\mathcal{C}_{KL}$ of the present paper.

[8] We have used the form $(14)_2$ rather than $(14)_1$ simply to make the form of the resulting equations more compact.

Downloaded 02 May 2010 to 171.66.16.25. Redistribution subject to ASME license or copyright; see http://www.asme.org/terms/Terms_Use.cfm

$$s=E(e-e^p) \tag{23}$$

and

$$\dot{e}^p=\frac{\frac{4}{3}E\left(s-\frac{3}{4}\hat{\alpha}e^p\right)\dot{e}}{\left(\frac{4}{3}E+\hat{\alpha}\right)\left(s-\frac{3}{4}\hat{\alpha}e^p\right)+\left[1+\left(\frac{\alpha_0-\alpha_s}{\kappa_0-\kappa_s}\right)\left(s-\frac{3}{4}\hat{\alpha}e^p\right)e^p\right]\left(\hat{\beta}s+\frac{3}{2}\hat{\eta}e^p\right)} \tag{24}$$

$$\dot{\kappa}=\left(\hat{\beta}(\kappa)s+\frac{3}{2}\hat{\eta}(\kappa)e^p\right)\dot{e}^p, \tag{25}$$

where E is Young's modulus. In the uniaxial case under discussion, Λ is still given by (15) but on the yield surface Γ and Φ assume the values

$$\Gamma_1=2\hat{\alpha}\kappa+\frac{4}{3}\left[1+\left(\frac{\alpha_0-\alpha_s}{\kappa_0-\kappa_s}\right)\left(s-\frac{3}{4}\hat{\alpha}e^p\right)e^p\right]\left(\hat{\beta}s+\frac{3}{2}\hat{\eta}e^p\right)\left(s-\frac{3}{4}\hat{\alpha}e^p\right) \tag{26}$$

and

$$\Phi=\frac{\Gamma_1}{\Gamma_1+\Lambda}. \tag{27}$$

Then, from (23)–(25), we have

$$\frac{d\kappa}{ds}=\frac{\frac{8}{3}\left(\hat{\beta}s+\frac{3}{2}\hat{\eta}e^p\right)}{\Gamma_1}. \tag{28}$$

For the special case in which the coefficients $\alpha_0,\alpha_s,\hat{\eta},\hat{\beta}$ satisfy the conditions

$$\alpha_0=\alpha_s=\alpha(\text{say}),\quad 2\hat{\eta}+\hat{\alpha}\hat{\beta}=0, \tag{29}$$

after adopting $(29)_{1,2}$ and making use of the condition $f=0$ with f given by (22), Γ_1 given by (26) reduces to

$$\Gamma_{10}=2(\alpha+\hat{\beta})\kappa \tag{30}$$

and (28) becomes

$$\frac{d\kappa}{ds}=\frac{\pm 2\hat{\beta}(\kappa)\sqrt{\frac{2}{3}\kappa}}{\alpha+\hat{\beta}(\kappa)}, \tag{31}$$

where in writing the right-hand side of (31) again use has been made of the condition $f=0$ with f given by (22) and the plus and minus signs correspond to tensile and compressive values of the stress.

In view of $(6)_3$ and (7), in the present discussion Γ can also be used to characterize the strain-hardening behavior. Keeping this in mind and the fact that $\kappa>0$, it follows from (30) and definitions in (8) that

$$\alpha+\hat{\beta}(\kappa)\begin{cases}>0 \text{ for hardening}, & (a)\\ <0 \text{ for softening}, & (b)\\ =0 \text{ for perfectly plastic}. & (c)\end{cases} \tag{32}$$

The results (32) hold only for the special case in which the various coefficients satisfy $(29)_{1,2}$. They are the same as those noted previously in [12] but are obtained here in a slightly different manner.

Consider now a typical uniaxial cyclic loading which, for the nth cycle in the $s-e$ plane, passes through the two points—such as A_{n+1} and D_n in Fig. 1—whose (e,s) coordinates are $({}^ne_1^p,0)$ and $({}^ne_2^p,0)$ and such that

$${}^ne_2^p>{}^ne_1^p. \tag{33}$$

Let the maximum value of compressive and tensile stresses attained during the nth cycle – at points such as F_n and C_n in Figs. 1 and 2 – be denoted, respectively, by ${}^ns_1$ and ${}^ns_2$, and similarly during the nth cycle designate the corresponding values of the strain, respectively, by ${}^ne_1$ and ${}^ne_2$. Then, by (23) the values of the plastic strain in (33) are given by

$${}^ne_2^p={}^ne_2-\frac{1}{E}{}^ns_2,\quad {}^ne_1^p={}^ne_1-\frac{1}{E}{}^ns_1. \tag{34}$$

From the condition $f=0$ with f specified by (22), the uniaxial stress s on the yield surface is found to be

$$s=\frac{3}{4}\hat{\alpha}(\kappa)e^p\pm\sqrt{\frac{3}{2}\kappa}, \tag{35}$$

where the plus and minus correspond to tensile and compressive values of s, respectively.

Next, as in [4], we suppose that there is a limiting value κ_s of the work-hardening parameter κ as $t\to\infty$, i.e.,

$$\lim_{t\to\infty}\kappa=\kappa_s, \tag{36}$$

so that with the help of (18) and (25)

$$\lim_{t\to\infty}\dot{\kappa}=0. \tag{37}$$

Then, from (35), (13), and (34) the limiting value of the mean stress in a cycle may be represented as[9]

$$\lim_{t\to\infty}s_{\text{mean}}=\lim_{n\to\infty}\frac{1}{2}({}^ns_1+{}^ns_2)=\frac{3}{8}\alpha_s\lim_{n\to\infty}\left[({}^ne_1+{}^ne_2)-\frac{1}{E}({}^ns_1+{}^ns_2)\right], \tag{38}$$

or after a slight rearrangement as

$$\lim_{t\to\infty}s_{\text{mean}}=\left(\frac{3E\alpha_s}{8E+6\alpha_s}\right)\lim_{n\to\infty}({}^ne_1+{}^ne_2)=\left(\frac{3E\alpha_s}{4E+3\alpha_s}\right)e_{\text{mean}} \tag{39}$$

where for cycling between fixed strain limits (for which the superscript n may be suppressed) we have defined

$$e_{\text{mean}}=\frac{1}{2}\lim_{n\to\infty}({}^ne_1+{}^ne_2) \tag{40}$$

to be the mean value of the strain limits. Moreover, in view of (18) and (36), from (26), (27), (15), and (13) we obtain

$$\lim_{t\to\infty}\Phi=\frac{\alpha_s}{\alpha_s+4\mu}<1. \tag{41}$$

Hence, if $\alpha_s>0$, then by (9) and (41) the material saturates to the value K_h given by the right-hand side of (41). Correspondingly, with $\alpha_s=0$, the right-hand side of (41) vanishes and by $(9)_3$ the material saturates to perfectly plastic behavior. Since $\dot{e}^p/\dot{s}=de^p/ds$, with the help of (23) and (24) we obtain

[9] It should be noted that for repeated cyclic loading the number of cycles is a monotonically increasing function of time so that in the present development the limits at $t\to\infty$ and as $n\to\infty$ can be interpreted to be equivalent.

Downloaded 02 May 2010 to 171.66.16.25. Redistribution subject to ASME license or copyright; see http://www.asme.org/terms/Terms_Use.cfm

$$\frac{de^p}{ds} = \frac{\frac{4}{3}\left(s - \frac{3}{4}\hat{\alpha}e^p\right)}{\hat{\alpha}\left(s - \frac{3}{4}\hat{\alpha}e^p\right) + \left[1 + \left(\frac{\alpha_0 - \alpha_s}{\kappa_0 - \kappa_s}\right)\left(s - \frac{3}{4}\hat{\alpha}e^p\right)e^p\right]\left(\hat{\beta}s + \frac{3}{2}\hat{\eta}e^p\right)}, \tag{42}$$

and the slope of the stress-strain curve during loading is given by

$$\frac{ds}{de} = \left(\frac{de}{ds}\right)^{-1} = \left(\frac{1}{E} + \frac{de^p}{ds}\right)^{-1}. \tag{43}$$

At initial yield this has the value

$$\left(\frac{ds}{de}\right)_{e^p=0,\kappa=\kappa_0} = \left[\frac{1}{E} + \frac{4/3}{\alpha_0 + \beta}\right]^{-1}. \tag{44}$$

In the limit as $t \to \infty$, it follows from (43) and (42) that[10]

$$\lim_{t\to\infty} \frac{ds}{de} = 0 \quad \text{if } \alpha_s = 0, \tag{45a}$$

$$\lim_{t\to\infty} \frac{ds}{de} = \frac{3E\alpha_s}{4E + 3\alpha_s} = \frac{9\mu k K_h}{3k + \mu K_h} \quad \text{if } \alpha_s > 0, \tag{45b}$$

where in writing the second of (45*b*) use has been made of (41) and (9*a*) and the elastic constants μ and k were introduced earlier in (11).

To demonstrate the predictive capability of the basic theory for the type of response described under 1) and 2) of Section 1, we now consider a uniaxial elastic-plastic state specified by

$$s = s^*_{(1)},\ e^p = e^{p*} \neq 0,\ \kappa = \kappa^* \tag{46}$$

and suppose that the material is unloaded from this state and the load is reversed until it again yields in the reverse direction at $s = s^*_{(2)}$. For fixed values of e^p and κ, $s^*_{(1)}$, and $s^*_{(2)}$ correspond to the two roots of (22) given by (35). It follows from the sum and difference of these roots that

$$\kappa^* = \frac{1}{6}(s^*_{(1)} - s^*_{(2)})^2, \quad \hat{\alpha}(\kappa^*) = \frac{2}{3}\frac{s^*_{(1)} + s^*_{(2)}}{e^{p*}}. \tag{47}$$

A value of κ_0 follows from $f = 0$ at initiation of yield and κ_s is calculated from $(47)_1$ and the experimental data from stress reversals at saturation. It follows form (39) and $(45b)_1$ that

$$\lim_{t\to\infty} \frac{ds}{de} = \frac{\lim_{t\to\infty} s_{\text{mean}}}{e_{\text{mean}}} \tag{48}$$

so that a value for the quantity α_s may be determined either from $(45b)_1$ and the measured slope of the stress-strain curve at saturation, or from (39) and the limiting value of the mean stress in strain cycling between fixed strain limits. An elastic-plastic state between the initial yield and saturation is specified by (46). After evaluating (13) at $\kappa = \kappa^*$ and equating the result to $(47)_2$, there results

$$\alpha_0 = \frac{2}{3}\left(\frac{s^*_{(1)} + s^*_{(2)}}{e^{p*}}\right)\left(\frac{\kappa_0 - \kappa_s}{\kappa^* - \kappa_s}\right) + \alpha_s\left(\frac{\kappa^* - \kappa_0}{\kappa^* - \kappa_s}\right), \tag{49}$$

where κ^* is calculated from $(47)_1$. Next, we introduce (49) into (44) to determine β from the expression for the slope of the stress-strain curve at initial yield. Since η does not occur in the yield function and does not appear in either of the limiting slopes (44) or (45*a*,*b*), its value must be determined by using the general expression resulting from (42) and (43). Hence, we need to measure the slope of the stress-strain curve at several points during loading between the initial yield and saturation. The value of κ at such a loading point may be determined from (22) and (13), or from $(47)_1$ if it is at the point of a stress reversal. This value is then used in (42) and (43) to estimate an appropriate value for η.

[10] The condition (45*a*) also follows from the first of (45*b*) with $\alpha_s = 0$.

The preceding procedure is suggested as one way of determining the material constants, and is by no means unique.

For purposes of illustration, we now specify the material constants for a material similar to the 2024-T351 aluminum alloy considered in [4]. In particular, we assume the same values for E, κ_0, and κ_s as those given in [4, equations (92) and (93)]. In addition, we specify α_s to be zero so that the mean stress will progressively relax and tend to zero during strain cycling. Now instead of using the procedure outlined in the preceding paragraph, the coefficients α_0, β, and η were adjusted until the predicted stress-strain curve exhibits ratcheting behavior under a loading program of stress cycling between unsymmetric stress limits.[11] In this way, one is able to choose the material constants as

$$\frac{\alpha_0}{E} = 0.14, \quad \alpha_s = 0, \quad \frac{\beta}{E} = 0.03, \quad \frac{\eta}{E^2} = -2.1\times10^{-3},$$

$$\frac{\kappa_0}{E^2} = 1.8\times10^{-5}, \quad \frac{\kappa_s}{E^2} = 3.0\times10^{-5}, \tag{50}$$

$$E = 69 \text{ GPa}.$$

Stress-strain response curves were calculated by explicit numerical integration of (24) using the values (50) for the material coefficients. The calculated uniaxial material response to stress cycling beween fixed unsymmetric stress limits is shown in Fig. 1, and the calculated response to strain cycling between two sets of fixed strain limits is shown in Fig. 2. From (15), (26), (35), (27) and the values in (50),[12] the value of Φ is calculated to be 0.10 at initial yield and it tends to zero at saturation.

Finally, a brief comparison is made of the prediction of the theory with experimental results for 304 stailess steel reported by Pugh et al. [13]. Employing the procedure described earlier [see the paragraph following (45)], the material constants were determined to be

$$\frac{\alpha_0}{E} = 1.4\times10^{-2}, \quad \frac{\alpha_s}{E} = 1.7\times10^{-3}, \quad \frac{\beta}{E} = 3.2\times10^{-2},$$

$$\frac{\eta}{E^2} = -1.2\times10^{-3}, \quad \frac{\kappa_0}{E^2} = 5.4\times10^{-7}, \quad \frac{\kappa_s}{E^2} = 2.7\times10^{-6},$$

$$E = 123 \text{ GPa}. \tag{51}$$

The calculated response is shown in Fig. 3 along with the experimental curves for the first three cycles from [13], as well as the results calculated previously by Caulk and Naghdi [4]. The only noteworthy difference between the present calculations and those in [4] is that the stress level at saturation matches the experimental data even more closely in the present calculations. From (15), (26), (35), (27), (9), (41), and the values in[13] (51) the value of Φ is calculated to be 0.029 at initial yield, and it tends to the value $K_h = 0.0011$ at saturation.

[11] This manner of determining the coefficients α_0, β, and η is analogous to the procedure used in [4] for obtaining different coefficients.

[12] Also assuming a value $\nu = 0.3$ for Poisson's ratio, with $(50)_7$ the shear modulus μ is calculated to be 26.5 GPa.

[13] As in [5] assuming a value $\nu = 0.3$ for Poisson's ratio, μ is calculated to be 47.3 GPa.

Downloaded 02 May 2010 to 171.66.16.25. Redistribution subject to ASME license or copyright; see http://www.asme.org/terms/Terms_Use.cfm

Acknowledgment

The results reported here were obtained in the course of research supported by the U.S. Office of Naval Research under Contract N00014-75-C-0148, Project NR 064-436 with the University of California, Berkeley (U.C.B.). Also, the work of one of us was partially supported by a grant-in-aid from General Motors Research Laboratories to the Department of Mechanical Engineering at U.C.B.

References

1 Green, A. E., and Naghdi, P. M., "A General Theory of an Elastic-Plastic Continuum," *Archive for Rational Mechanics and Analysis*, Vol. 18, 1965, pp. 251–281.

2 Green, A. E., and Naghdi, P. M., "A Thermodynamic Development of Elastic-Plastic Continua," *Proceedings of the IUTAM Symposium on Irreversible Aspects of Continuum Mechanics and Transfer of Physical Characteristics in Moving Fluids*, Parkus, H., and Sedov, L. I., eds., Springer-Verlag, New York, 1966, pp. 117–131.

3 Naghdi, P. M., and Trapp, J. A., "The Significance of Formulating Plasticity Theory With Reference to Loading Surfaces in Strain Space," *International Journal of Engineering Science*, Vol. 13, 1975, pp. 785–797.

4 Caulk, D. A., and Naghdi, P. M., "On the Hardening Response in Small Deformation of Metals," ASME JOURNAL OF APPLIED MECHANICS, Vol. 45, 1978, pp. 755–764.

5 Casey, J., and Naghdi, P. M., "On the Characterization of Strain-Hardening in Plasticity," ASME JOURNAL OF APPLIED MECHANICS, Vol. 48, 1981, pp. 285–296.

6 Drucker, D. C., and Palgen, L., "On Stress-Strain Relations Suitable for Cyclic and Other Loading," ASME JOURNAL OF APPLIED MECHANICS, Vol. 48, 1981, pp. 479–485.

7 Dolan, T. J., "Nonlinear Response Under Cyclic Loading Conditions," *Proceedings of the Ninth Midwestern Mechanics Conference*, Madison, Wis., 1965, pp. 3–21.

8 Sandor, B. I., *Fundamentals of Cyclic Stress and Strain*, University of Wisconsin Press, Madison, Wis., 1972.

9 Morrow, J., and Sinclair, G. M., "Cycle-Dependent Stress Relaxation," *Symposium on Mechanics of Fatigue*, ASTM STP 237, American Society for Testing and Materials, 1958, pp. 83–109.

10 Naghdi, P. M., and Trapp, J. A., "Restrictions on Constitutive Equations of Finitely Deformed Elastic-Plastic Materials," *Quarterly Journal of Mechanics and Applied Mathematics*, Vol. 28, 1975, pp. 25–46.

11 Casey, J., and Naghdi, P. M., "A Remark on the Definition of Hardening, Softening and Perfectly Plastic Behavior," *Acta Mechanica*, Vol. 48, 1983, pp. 91–94.

12 Casey, J., and Naghdi, P. M., "Strain-Hardening Response of Elastic-Plastic Materials," in *Constitutive Laws for Engineering Materials: Theory and Application*, Wiley, New York, in press.

13 Pugh, C. E., et al., "Current Recommended Constitutive Equations for Inelastic Design Analysis of FFTF Components," ORNL-TM-3602, 1972.

Downloaded 02 May 2010 to 171.66.16.25. Redistribution subject to ASME license or copyright; see http://www.asme.org/terms/Terms_Use.cfm

The Estimation of Large Deflections of a Portal Frame Under Asymmetric Pulse Loading[1]

J. L. Raphanel[2]
Research Assistant.

P. S. Symonds
Professor of Engineering.
Fellow ASME

Division of Engineering,
Brown University,
Providence, R.I. 02912

Modifications of a simple elastic-plastic technique [1–4] are shown which allow estimation of local deformation in the loaded column of a portal frame as well as the side-sway deflections of the frame. A wholly elastic response stage provides input to a simplified rigid-plastic solution, in which velocity patterns first of local and then of modal (side-sway) type occur, and which furnishes estimates of final plastic deflections. Maximum (elastic plus plastic) deflections are estimated by adding displacements corresponding to the elastic strain field defined by the stresses of the closing rigid-plastic mode. The method is described for perfectly plastic and for strain-rate sensitive material, and comparisons are shown here with values computed[3] for both types of material by a finite element program. Emphasis in this paper is put on the inclusion of elastic and vicoplastic effects.

1 Introduction

This paper is concerned with approximation techniques capable of estimating maximum and permanent deflections of structures subjected to pulse loading. Much of the difficulty of these problems comes from the mixing of elastic and plastic behavior; plastic straining occurs in isolated regions whose boundaries change and which may disappear and reappear. Under certain conditions of strong loading, it becomes permissible to drop elastic strain increments (take Young's modulus infinite). This so-called rigid-plastic analysis results in considerable simplification compared to elastic-plastic treatments; some simple problems even allow closed-form solutions, while elastic-plastic solutions are obtainable only by computer programs and may need extensive calculations. However rigid-plastic solutions are unsatisfactory at low load levels, and some criterion is needed for the load conditions for which one is valid. No general criterion for pulse loading is available, although for very short pulses where the loading is defined by initial velocities an energy ratio is often invoked: the rigid-plastic treatment is expected to be valid if the ratio R of initial kinetic energy to the elastic strain energy capacity greatly exceeds unity. The required lower limit is uncertain, however, and it fails for pulses of arbitrary duration [4].

A *simplified elastic-plastic* (SEP) method has been described [1–4] which is meant to be more realistic than a rigid-plastic treatment but to have comparable simplicity. It is also meant to mirror the essential structure of the response, and hence help in understanding the basic processes of elastic-plastic dynamic response.

The problem treated in this paper is that of a fixed base portal frame or bent subjected to a uniform pressure pulse on one column. As illustrated by the computed deflection profiles shown in Fig. 1(*b*) (obtained by a finite element program that will be described later), the analysis must deal both with a "local" dishing deformation of the column and with a "general" side-sway motion. The two types of deformation reinforce each other at the foot of the loaded column, but cause the upper corner of this column to deform plastically first in closing and then in opening the corner.

We will assume the simplest model of plastic behavior for beam/frame structures; as sketched in Fig. 2, the moment-curvature relations is linear to the fully plastic moment M_0, at which unlimited deformation at constant moment can occur. We are concerned with strain-rate-sensitive plastic behavior, and will assume a simple dynamic overstress type of relation between moment and plastic curvature rate applied by Bodner and Symonds [5] among others.

The SEP approach involves a separation of elastic and plastic responses. Plastic deformations are assumed to occur in a rigid-plastic response stage. This is preceded by a wholly elastic stage, and is followed by elastic vibrations that continue until damped out by the usual damping mechanisms. The initial elastic stage is terminated by a somewhat artificial "global yield condition," and then provides input momentum

[1] This research was supported by grant CEE-7926147 from the U.S. National Science Foundation.

[2] Presently at Institut National Polytechnique de Grenoble, France.

[3] The computations reported on here were made on the Brown University, Division of Engineering, VAX-11/780 computer, the acquisition of which was made possible by grants from the U.S. National Science Foundation (grant ENG78-19378), the General Electric Foundation, and the Digital Equipment Corporation.

Contributed by the Applied Mechanics Division for presentation at the Winter Annual Meeting New Orleans, La., December 9–14, 1984 of THE AMERICAN SOCIETY OF MECHANICAL ENGINEERS.

Discussion on this paper should be addressed to the Editorial Department, ASME United Engineering Center, 345 East 47th Street, New York, N.Y. 10017 and will be accepted until two months after final publication of the paper itself in the JOURNAL OF APPLIED MECHANICS. Manuscript received by ASME Applied Mechanics Division, May, 1983. Paper No. 84-WA/APM-1.

Copies will be available until August 1985.

Copyright © 1984 by ASME
Downloaded 02 May 2010 to 171.66.16.25. Redistribution subject to ASME license or copyright; see http://www.asme.org/terms/Terms_Use.cfm

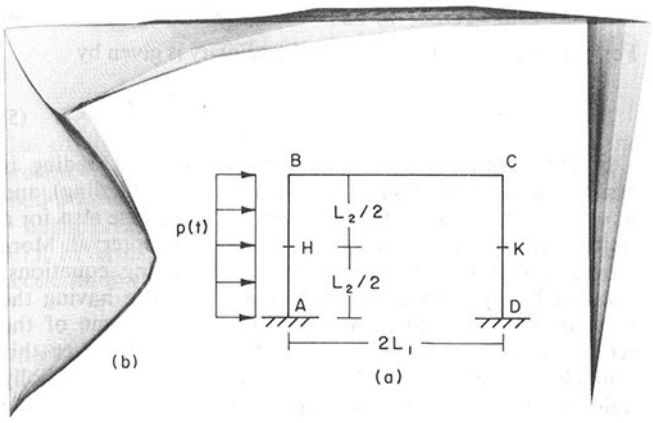


Fig. 1 (*a*) Frame under side loading, and (*b*) deflection profiles at successive times by finite element "complete solution"

to the rigid-plastic stage. In the following section a rigid-plastic model adequate for our purposes is reviewed briefly; further discussions of the rigid-plastic treatment of this structure will be found in [6]. In Section 3 the elastic model is outlined. Section 4 presents the condition adopted for terminating the elastic stage, and the technique for transmitting momentum from the elastic stage. In Section 5 is outlined a scheme for estimating maximum (plastic plus elastic) deflections. Finally in Section 6 the comparisons of the estimated maximum and permanent deflection magnitudes with those obtained by a finite element numerical program are briefly discussed.

2 Rigid-Plastic Model

Here we briefly sketch the features of the rigid plastic response required in the present method. The idealization of perfectly plastic behavior is central to the method. We will consider the material as perfectly plastic even though it is strongly rate sensitive. The yield stress depends on the plastic strain rate and strain rate history, but as an approximation we neglect the latter and assume that a constant dynamic yield stress may be used for the whole response. A considerable body of research (exemplified by references [5, 11, 12] among many others) shows that this is a good approximation for structural response of rate-sensitive structural metals such as steel and titanium, when the dynamic yield stress is computed from a measure of average strain rates in the response. The characteristic slow dependence of yield stress on strain rate suggests that we may even use initial strain rates as a first approximation to the average values, with acceptable error. The use of a dynamic yield stress in any rigid-plastic treatment requires a means of estimating strain rates; these cannot be obtained solely from a rigid-plastic solution when the structural action involves only flexure, since the response is then obtained in terms of rotations at plastic hinges with indeterminate strains and strain rates. The present approach [1–4] obtains the dynamic yield-stress factor from strain rates in the elastic solution which immediately precedes the rigid-plastic one. This is a reasonable method, but does involve some arbitrary decisions, as will be seen.

The treatment of strain-rate sensitivity in this way implies additional uncertainties beyond those in a treatment for a perfectly plastic (rate-insensitive) material. To obtain evidence about these, comparisons will be shown for both types of material, between displacement estimates by the present approach and those obtained by a complete solution using a numerical (finite element) program.

In view of the foregoing discussion, the following summary of rigid-plastic response is presented for a perfectly plastic material with fully plastic moment M_0. For the strain-rate-

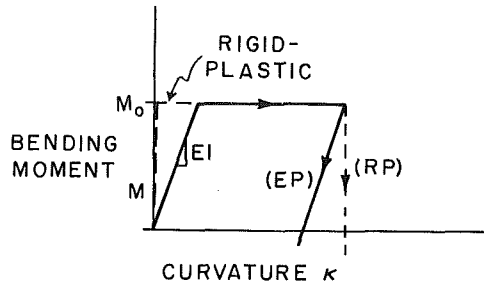


Fig. 2 Idealized beam behavior: elastic-plastic and rigid-plastic

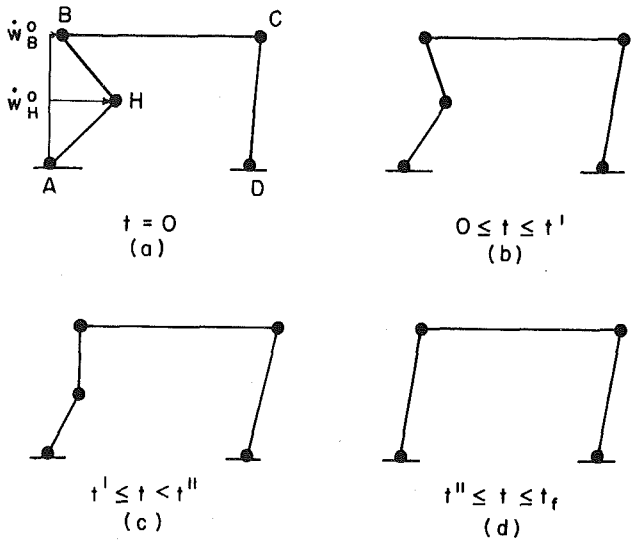


Fig. 3 Velocity patterns of simple rigid-plastic analysis (assumed applicable for rate-dependent as well as independent behavior). Plastic hinges are considered only at sections *A, H, B, C, D*.

sensitive material, M_0 is replaced by $M_0' = \mu M_0$, where the dynamic factor μ is obtained by the method to be described in Section 4.

The complete rigid-plastic solution for the frame subjected to a pressure pulse on one column is discussed in [6]. The plastic deformation of the loaded column occurs first with two traveling plastic hinges, which coalesce into a single hinge. The hinge at the top corner disappears, and when the traveling hinge reaches the corner the succeeding motion takes place in the simple side-sway pattern with plastic hinges at top and bottom of each column; the velocity pattern is indicated in Fig. 3(*d*). This illustrates a property of all rigid-plastic solutions for constant external loads; namely that, as the pattern of velocities changes with time, it tends toward a mode-form solution. Following pulse loading, it remains in this pattern until the velocities are reduced to zero. The "mode approximation" technique proposed for rigid-plastic analysis in [7] took the entire response to be in such a modal form. It was shown that if the initial velocity of this one-degree-of-freedom solution is determined from the specified initial velocity field in such a way as to minimize a difference functional $\Delta(t)$, satisfactory estimates are obtained of the final displacement magnitudes of the mode form response. This functional will be defined and used later in this paper. Previous applications [1–4] of the SEP technique also took the rigid-plastic stage to be a mode form solution. In the present problem this would be unsatisfactory since it omits the local deformation in the column.

We adopt a simplified rigid-plastic model whose velocity patterns are sketched in Fig. 3. Plastic hinges are allowed to

Downloaded 02 May 2010 to 171.66.16.25. Redistribution subject to ASME license or copyright; see http://www.asme.org/terms/Terms_Use.cfm

Table 1

i	=	1	2	3
$\sqrt{\frac{\bar{\rho}L_2^4}{EI}}\omega_i$	=	2.6830	19.200	22.073
$\phi^{(i)}$	=	$\begin{bmatrix} 0.41772 \\ 1 \\ 0.41772 \end{bmatrix}$	$\begin{bmatrix} 1 \\ 0 \\ -1 \end{bmatrix}$	$\begin{bmatrix} 1 \\ -0.23393 \\ 1 \end{bmatrix}$
ν_i(Hz)[a]	=	38.4	275	316
T_i(sec)[a]	=	26.1×10^{-3}	3.64×10^{-3}	3.17×10^{-3}

[a] values computed for steel frames with $2L_1 = 305$ mm (12.0 in.), $L_2 = 203$ mm (8.0 in.); all members have width $b = 18.8$ mm (0.74 in.), depth $H = 3.1$ mm (0.122 in.), mass density $\rho = 7.80 \times 10^3$ kg/m^3 (0.73 lb sec^2/in.^{4}), Young's modulus $E = 207 \times 10^3$ MN/m^2 (30×10^3 ksi), yield stress $\sigma_0 = 228$ MN/m^2 (33.1 ksi), viscoplastic constants $\dot{\epsilon}_0 = 40\ \text{sec}^{-1}$, $n = 5$.

occur only at discrete sections, and the simplest such model has hinges at the corners A, B, C, D, and at the midpoint H of the loaded column. The velocity field thus is defined by the velocities at the two points H and B, $\dot{w}_H$ and $\dot{w}_B$. Assuming $\dot{w}_H > \dot{w}_B$, the equations for the accelerations $\ddot{w}_H$, $\ddot{w}_B$ due to an applied uniform pressure p can be found from the free body diagrams (or Tamuzh's principle [6]) to be

$$\frac{\bar{\rho}L_2}{12}\begin{bmatrix} 4 & 1 \\ 1 & 6+24\beta \end{bmatrix}\begin{bmatrix} \ddot{w}_H \\ \ddot{w}_B \end{bmatrix} = \begin{bmatrix} 2 \\ 1 \end{bmatrix}\frac{pL_2}{4} + \begin{bmatrix} -8 \\ 2 \end{bmatrix}\frac{M_0}{L_2} \quad (1)$$

Here $\bar{\rho}$ is the mass paper unit length of each column and $\beta = \bar{\rho}_1 L_1/\bar{\rho}L_2$, where $\bar{\rho}_1$ is the mass per unit length of the transverse member; the frame has span $2L_1$, and height L_2, Fig. 1. In our present example we consider a frame with $\beta = 0.75$, corresponding to $\bar{\rho}_1 = \bar{\rho}$, $L_1/L_2 = 0.75$. For this case, solving for $\ddot{w}_H$ and $\ddot{w}_B$ we obtain

$$\begin{bmatrix} \ddot{w}_H \\ \ddot{w}_B \end{bmatrix} = \frac{3}{95}\begin{bmatrix} 47 \\ 2 \end{bmatrix}\frac{p}{\bar{\rho}} + \frac{12}{95}\begin{bmatrix} -194 \\ 16 \end{bmatrix}\frac{M_0}{\bar{\rho}L_2^2} \quad (2)$$

Integrating, we obtain velocities

$$\begin{bmatrix} \dot{w}_H \\ \dot{w}_B \end{bmatrix} = \begin{bmatrix} \dot{w}_H^0 \\ \dot{w}_B^0 \end{bmatrix} + \frac{3}{95}\begin{bmatrix} 47 \\ 2 \end{bmatrix}\frac{1}{\bar{\rho}}\int_{t_1}^{t} p\,dt + \frac{12}{95}\begin{bmatrix} -194 \\ 16 \end{bmatrix}\frac{M_0(t-t_1)}{\bar{\rho}L_2^2} \quad (3)$$

Here t_1 is the time when the rigid-plastic motion begins, and $\dot{w}_H^0$, $\dot{w}_B^0$ are the velocities at this time.

The preceding equations hold for $\dot{w}_H > \dot{w}_B$. For $\dot{w}_H \le \dot{w}_B$, $t \ge t'$, new equations are required with $\dot{w}_H \le \dot{w}_B$, depending on the bending moment at corner B, and valid for $\dot{w}_B/2 < \dot{w}_H < \dot{w}_B$. At the instant $t = t''$ when $\dot{w}_H = \dot{w}_B/2$ the plastic hinge at H disappears, and the simple side-sway mode-form solution applies. The interval $t' \le t \le t''$ is easily dealt with [6], but we omit details here. For the mode-form motion of Fig. 3(d) the equation of dynamics is

$$\bar{\rho}L_2^2(4+12\beta)\ddot{w}_B = 3pL_2^2 - 24M_0. \quad (4)$$

For our example with $\beta = 0.75$, the velocity is given by

$$\dot{w}_B^* = \dot{w}_B(t'') + \frac{3}{13\bar{\rho}}\int_{t''}^{t} p\,dt - \frac{24}{13}\frac{M_0(t-t'')}{\bar{\rho}L_2^2} \quad (5)$$

In the example frame to be considered, the loading is assumed a vanishingly short pulse ("impulsive" loading), and $p = 0$ in equations (1)–(5). This would be the case also for a finite pulse of duration less than t_1, the elastic interval. More general pulses can be treated by the foregoing equations. Youngdahl [8] showed that a rectangular pulse having the same impulse and duration twice the centroid time of the actual pulse provides a simpler equivalent. However this equivalence was shown only for treatments assuming wholly rigid-plastic behavior; its applicability to elastic-plastic responses has not been demonstrated.

3 Elastic Analysis

The load first excites a wholly elastic response, which provides input to the rigid-plastic stage outlined in the foregoing, i.e., provides $\dot{w}_H^0$, $\dot{w}_B^0$ in equation (3). To compute the elastic motion any available computer program may be used. In many cases deflections in the elastic stage of the SEP method remain small enough so that a linear program is adequate. The fully fixed beam problems treated in [2, 3] illustrate cases where geometric nonlinear capability is necessary. Here we assume linear elastic behavior and treat the elastic stage by a three-degree-of-freedom model. A microcomputer was used to make the final calculations, but they are feasible for a programmable hand calculator.

Finite elements in our model had four free nodes at H, B, C, and K (Fig. 1(a)). Standard element flexural stiffness matrices were used first to derive a 7×7 structure stiffness matrix in terms of displacements w_H w_B w_K and rotations at H, B, C, and K; length changes of the three members were disregarded. Since no moment loads are applied at the free nodes the usual static condensation was applied to obtain the 3×3 structure stiffness matrix $\underset{\sim}{\mathbf{K}}$. The displacement column vector $\mathbf{w}$ is defined as $\{w_1\ w_2\ w_3\} = \{w_H\ w_B\ w_K\}$.

$$\underset{\sim}{\mathbf{K}} = \frac{24EI}{L_2^3}\begin{bmatrix} \frac{224+176\alpha+24\alpha^2}{(7+\alpha)(7+3\alpha)} & -\frac{10+12\alpha}{7+3\alpha} & \frac{24\alpha}{(7+\alpha)(7+3\alpha)} \\ -\frac{10+12\alpha}{7+3\alpha} & \frac{8+15\alpha}{7+3\alpha} & -\frac{10+12\alpha}{7+3\alpha} \\ \frac{24\alpha}{(7+\alpha)(7+3\alpha)} & -\frac{10+12\alpha}{7+3\alpha} & \frac{224+176\alpha+24\alpha^2}{(7+\alpha)(7+3\alpha)} \end{bmatrix} \quad (6)$$

where $\alpha = E_1I_1L_2/EIL_1$, EI being the flexural rigidity of the columns and E_1I_1 that of the transverse member; note the lengths are L_2 and $2L_1$, respectively.

We derive the mass matrix for the structure from element mass matrices based on linear variation of acceleration between nodes. This is preferable to the usual lumped mass matrix because it leads to the same structure mass matrix as obtained by rigid-plastic analysis of the discretized structure. To be explicit, for an element between nodes i and j where accelerations are $\ddot{w}_i$, $\ddot{w}_j$, the following matrix furnishes the conjugate nodal forces:

$$\underset{\sim}{\mathbf{G}}_i = \frac{1}{6}(\bar{\rho}l)_i\begin{bmatrix} 2 & 1 \\ 1 & 2 \end{bmatrix} \quad (7)$$

where l_i is the length and $(\bar{\rho}l)_i$ is the mass of the element. For the frame with nodes at A, H, B, C, K, D the mass matrix is derived as

Downloaded 02 May 2010 to 171.66.16.25. Redistribution subject to ASME license or copyright; see http://www.asme.org/terms/Terms_Use.cfm

$$\underset{\sim}{\mathbf{G}} = \frac{1}{12}\bar{\rho}L_2 \begin{bmatrix} 4 & 1 & 0 \\ 1 & 4+24\beta & 1 \\ 0 & 1 & 4 \end{bmatrix} \tag{8}$$

Use of this instead of a lumped mass matrix enables the present elastic-plastic method to closely approach results of a rigid-plastic analysis in the appropriate circumstances.

In the present example with $\bar{\rho}_1 = \bar{\rho}$, $EI_1 = EI$, $\beta = 1/\alpha = 0.75$, in terms of displacement vector $\mathbf{w} = \{w_H\ w_B\ w_K\}$ and acceleration vector $\ddot{\mathbf{w}} = \{\ddot{w}_H\ \ddot{w}_B\ \ddot{w}_K\}$ the equations are

$$\underset{\sim}{\mathbf{K}}\mathbf{w} + \underset{\sim}{\mathbf{G}}\ddot{\mathbf{w}} = \mathbf{p} \tag{9}$$

where

$$\underset{\sim}{\mathbf{K}} = \frac{24EI}{L_2^3}\begin{bmatrix} 5.4691 & -2.3636 & 0.34909 \\ -2.3636 & 2.5454 & -2.3636 \\ 0.34909 & -2.3636 & 5.4691 \end{bmatrix} \tag{10a}$$

$$\underset{\sim}{\mathbf{G}} = \frac{\bar{\rho}L_2}{12}\begin{bmatrix} 4 & 1 & 0 \\ 1 & 22 & 1 \\ 0 & 1 & 4 \end{bmatrix};\quad \mathbf{p} = \frac{pL_2}{4}\begin{bmatrix} 2 \\ 1 \\ 0 \end{bmatrix} \tag{10b,c}$$

Coefficients for the natural (radian) frequencies ω_i and mode shape functions $\phi(i)$ are shown in Table 1, which includes also frequencies ν_i and periods T_i in physical units for the particular frame used as example.

In our example problem we consider only impulsive loading specified by initial velocity V_0 of column AB, while members BC, CD are at rest. By standard methods the response displacement vector is found to be

$$\mathbf{w} = V_0\sqrt{\frac{\bar{\rho}L_2^4}{EI}}\,10^{-2} \begin{bmatrix} 3.4199 & 3.9060 & 2.9030 \\ 8.1873 & 0 & -0.6791 \\ 3.4199 & -3.9060 & 2.9060 \end{bmatrix}\begin{bmatrix} \sin\omega_1 t \\ \sin\omega_2 t \\ \sin\omega_3 t \end{bmatrix} \tag{11}$$

4 Simplified Elastic-Plastic (SEP) Method

The concept of three separated stages (elastic, rigid-plastic, and elastic) requires that the elastic solution be terminated at a time t_1. Its velocity field at time t_1 furnishes input to the rigid-plastic stage. The SEP method obviously depends critically on the condition used to determine the time t_1. This is arbitrary, and unless the final deformations are insensitive to its details, the SEP method will be unsatisfactory.

The basis for choice of a terminating condition is that the bending moments of the elastic solution should match in some sense the moments of the rigid-plastic stage which it introduces. In the present case this is the five-hinge velocity pattern sketched in Fig. 3. As a highly tentative choice we take the following condition for a rate-insensitive material:

$$M_e = M_e[M_\alpha(t_1)] = \left[(1/5)\sum_\alpha M_\alpha^2(t_1)\right]^{1/2} = M_0 \tag{12}$$

where $\alpha = A, H, B, C, D$ in turn. For a plastic strain-rate-sensitive material the right-hand side is replaced by M_0', an estimate of dynamic fully plastic moment corresponding to the strain rates at time t_1. A possible form is

$$M_0'[\dot{\kappa}_\alpha(t_1)] = M_0\left[1 + \left(\frac{\dot{\kappa}_e}{\dot{\kappa}_0}\right)^{1/n}\right];\quad \dot{\kappa}_e = \left[(1/5)\sum_\alpha \dot{\kappa}_\alpha^2(t_1)\right]^{1/2} \tag{13a,b}$$

where $\dot{\kappa}_\alpha$ are the curvature rate magnitudes at the five hinge sections and $\dot{\kappa}_0$, n are constants for the material and beam section, given in the following. This follows the overstress power law for a beam and for uniaxial stress, respectively, [5]:

$$M_0' = M_0[1 + (\dot{\kappa}/\dot{\kappa}_0)^{1/n}];\quad \sigma_0' = \sigma_0[1 + (\dot{\epsilon}/\dot{\epsilon}_0)^{1/n}] \tag{14a,b}$$

where $\dot{\epsilon}$ is the plastic strain rate and σ_0', σ_0 are the dynamic and static yield stress, respectively; $\dot{\epsilon}_0$, n, and σ_0 are material constants.[4] Equation (14b) provides a good fit to experimental data for strongly rate sensitive materials such as mild steel and titanium [9, 10]. For many mild steels $\dot{\epsilon}_0 = 40$ sec^{-1} and $n = 5$ have been found to hold, with appropriate σ_0. For the rectangular beam of depth H, $\dot{\kappa}_0 = 2(1+1/2n)^n\,\dot{\epsilon}_0/H$ [5].

The forms of the functions in equations (12) and (13) are provisional, and further study is required. The conditions (12) and (13) state that the root mean square magnitude of the moments (computed from the elastic response) at the five sections where hinges form in the subsequent rigid-plastic stage, agrees with a appropriate moment magnitude for fully plastic flow, static or dynamic.

Having found t_1 and the velocity field $\dot{w}^e(s,t_1) = \dot{w}^{e1}(s)$, this must be used to determine the initial velocity field of the rigid-plastic stage. This field is defined by the values $\dot{w}_H^0$, $\dot{w}_B^0$ of Fig. 3(a) and equation (3). The "minimum Δ_0" technique is a suitable means of determining $\dot{w}_H^0$ and $\dot{w}_B^0$. And pointed out in [7] and illustrated in [6] minimization of Δ_0 corresponds to a form of conservation of momentum, as well as minimizing the mean square "error" in connecting the two velocity fields. If we denote the initial velocity field of the rigid-plastic stage as $\dot{w}^{p0}(s)$, this is expressed in terms of coordinate s on each column axis, with origin at the base, by

$$\begin{aligned} &\text{In } AH: && \dot{w}^{p0} = \dot{w}_H^0(2s/L_2) \\ &\text{In } HB: && \dot{w}^{p0} = \dot{w}_H^0(2-2s/L_2) + \dot{w}_B^0(2s/L_2 - 1) \\ &\text{In } BC: && \dot{w}^{p0} = \dot{w}_B^0 \\ &\text{In } CD: && \dot{w}^{p0} = \dot{w}_B^0(s/L_2) \end{aligned} \tag{15}$$

where $0 \le s \le L_2$. Given the elastic velocity field $\dot{w}^{e1}(s)$,

$$\Delta_0(\dot{w}_H^0\ \dot{w}_B^0) = 1/2\int \bar{\rho}[\dot{w}^{e1}(s) - \dot{w}^{p0}(s)]^2 ds \tag{16}$$

minimizing with respect to $\dot{w}_H^0$ and $\dot{w}_B^0$ by differentiating and solving the two simultaneous equations furnishes the desired values of $\dot{w}_H^0$, $\dot{w}_B^0$.

Having these values, the final plastic deformations are obtained by means of equations (1)–(5). In the present example of impulsive loading, we have $p = 0$ in these equations; the load is applied only in the elastic stage. The final displacements w_H^f and w_B^f are plotted in Fig. 5 for a rate-insensitive material. In this figure they are shown as functions of $\sqrt{R}$, R being the energy ratio defined as

$$R = (1/2)\bar{\rho}L_2V_0^2/\frac{M_0^2L_2}{EI}(1 + L_1/L_2) \tag{17}$$

This is the ratio of initial kinetic energy to the elastic energy capacity of the structure, for which each element is assumed to contain strain energy $M_0^2/2EI$ per unit length.[5]

For R less than some value R_e the condition equation (12) cannot be satisfied. According to the present model this implies wholly elastic behavior. Clearly this represents the actual response only to a limited degree. The condition ex-

[4] Our calculation actually uses an elastic rather than a plastic average strain rate at time t_1; the former is more easily calculated and should be an adequate approximation for present purposes.

[5] In [6] the ratio $R_1 = 3.5R$ was also used; R_1 is based on the elastic energy capacity of the loaded column, rather than the whole structure. The scale for $\sqrt{R_1}$ is used also in Figs. 5 and 7.

Downloaded 02 May 2010 to 171.66.16.25. Redistribution subject to ASME license or copyright; see http://www.asme.org/terms/Terms_Use.cfm

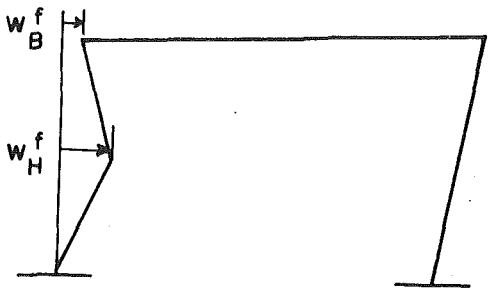


Fig. 4 Typcial pattern of final displacements by rigid-plastic treatment

pressed by equation (12) is artificial, and other idealizations have been made (such as the bilinear elastic-perfectly plastic moment curvature relation of Fig. 2). Plastic deformations will undoubtedly occur for $R < R_e$ in the real structure. These are assumed to be small and of a local character. The plastic deformations computed according to the present model, when $R \geq R_e$, correspond rougly to the concept of *uncontained* plastic deformations; we note that in our model the rigid-plastic response always leads to side-sway deflections as well as to local dishing deformation of the column. When $R < R_e$, the actual deformations may be regarded as *contained* plastic deformation, and are outside the scope of the present method.

When the material is rate sensitive, the procedure for finding the final plastic displacements is essentially the same as the used for the rate-independent material, since we are using the artifice of treating the rate sensitive material as a perfectly plastic one with raised yield stress. The resulting curves of w_H^f and w_B^f are shown in Fig. 7(*a, b*). The difference from the rate-independent case is in the use of $M_0' = \mu M_0$ instead of M_0 in the calculation of final displacements, where μ is determined from the elastic solution at time t_1 using equations (12) and (13). However, the deflections are plotted against the same load parameter as used for the rate-independent material (R is computed from equation (17) using M_0, not M_0'.

5 Estimation of Maximum Displacements

In Figs. 5 and 7 are shown curves for maximum values $w_H^{\max}$, $w_B{}^{\max}$ of the displacement at H and B. These are obtained by adding an elastic displacement to the final plastic displacements w_H^f, w_B^f given by the rigid-plastic stage. The elastic strains and displacements vary greatly during the response, and there is no way to obtain them accurately by any simple method. However they can be estimated in the late part of the plastic response, when the rigid-plastic motion is taking place in the simple side-sway mode. For a perfectly plastic material this is a response in which the stress field remains constant, with shape indicated in Fig. 6. If we denote the moment field of the rigid-plastic mode by $M^{rp}(s)$, we can associate with it elastic curvatures $\kappa^{rp} = M^{rp}/EI$. Time independent displacements computed from these curvatures may be added to the final displacements of the rigid-plastic solution to obtian the maximum displacements of the structure. These can be visualized as the displacements corresponding to a given moment field that result when the flexural rigidity EI is relaxed from infinity to its actual value. Continuity across plastic hinges is not required. To compute the elastic displacements in the columns corresponding to the moment diagrams sketched in Fig. 6 we use for simplicity the straight line curves shown dashed, which neglect the small contribution due to the accelerations. We obtain

$$w_B^{ep} = 2w_H^{ep} = M_0 L_2^2/6EI \tag{18}$$

In the example frame (Table 1) the value of w_B^{ep} is about 7.4 mm (0.29 in.). This magnitude is added to the curve for w_B^f in

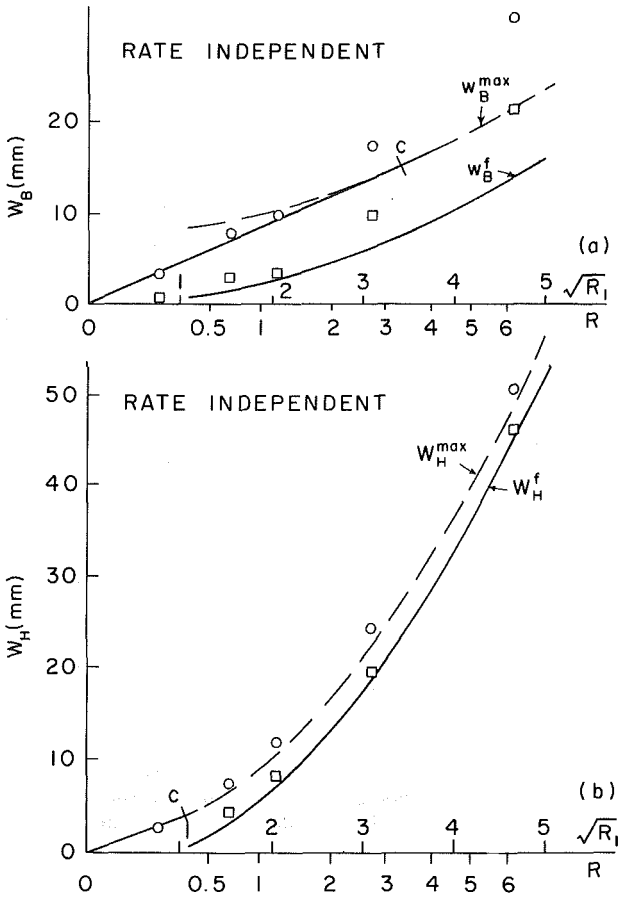


Fig. 5 Final (plastic) and maximum (plastic plus elastic) deflections at corner point *B* (*a*) and at midpoint *H* of loaded column (*b*), for frame of rate independent perfectly plastic material. The horizontal scale is proportional to $\sqrt{R}_1$ and shows values of energy ratio $R = R_1/3.5$, equation (17).

Fig. 5(*a*), and 3.7 mm (0.15 in.) to w_H^f in Fig. 5(*b*), to give the curves shown dashed.

The dashed curves would be expected to give reasonable estimates for $w_B^{\max}$, $w_H^{\max}$ only for sufficiently large load impulses. Although the SEP method assumes that a rigid-plastic stage occurs that always lead to a final four-hinge mode-form response, in the actual elastic-plastic frame this would not occur at small impulses for which plastic deflections are local and small compared to elastic ones, so that the four-hinge mode is not reached even approximately.

To obtain a crude estimate for small R values, we note that if the response is wholly elastic the maximum deflections vary linearly with $\sqrt{R}$ (proportional to initial velocity), and that as plastic flow occurs the slope of the curve increases; deflections increase with load at a faster rate. The simplest scheme is to draw a straight line from the origin that touches the dashed curve tangentially at a point C, and to take the straight line up to C as providing estimates of maximum deflections for $\sqrt{R}$ values to the left of C and the dashed curve for larger $\sqrt{R}$ values.

This procedure for obtaining maximum deflections, by adding to the final plastic deflections an elastic component derived from the stress field of the closing mode-form response pattern of the rigid-plastic stage, has a theoretical basis in the fact that these constitute an exact solution for the elastic-plastic structure model. (The stress field of the rigid-plastic mode response is constant, and the corresponding elastic displacements can be added to those of the rigid-plastic response to form a complete solution). Moreover, the convergence theorem for elastic-plastic structures [13] shows that

Downloaded 02 May 2010 to 171.66.16.25. Redistribution subject to ASME license or copyright; see http://www.asme.org/terms/Terms_Use.cfm

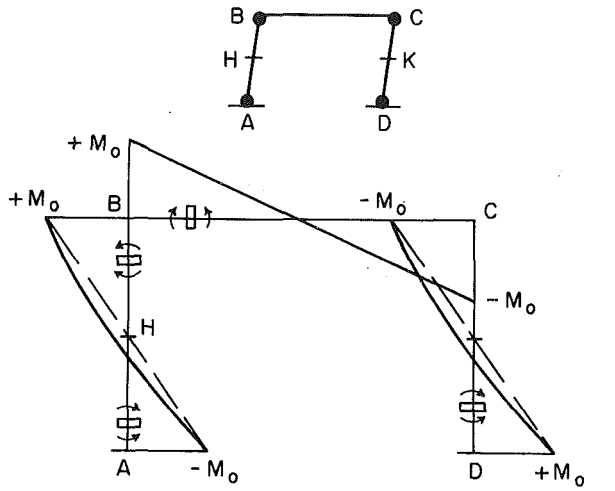


Fig. 6 Stress field of the rigid-plastic mode form solution in which the response terminates

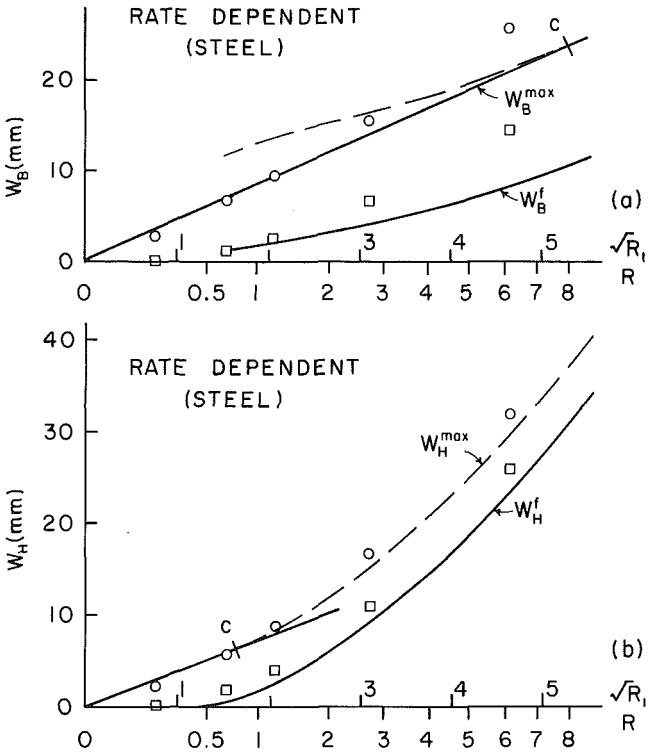


Fig. 7 Final (plastic) and maximum (plastic plus elastic) deflections at corner point *B*(*a*) and at midpoint *H* of loaded column (*b*) for rate-dependent material. The horizontal scale is the same as that used in Fig. 5.

the actual motion tends toward this solution as the response proceeds. The velocity field of the elastic-plastic response becomes notably smoother.

When the material is rate sensitive, the procedure for estimating the maximum elastic component can be followed, by means of the artifice of treating the material as perfectly plastic with a raised yield stress. The theoretical basis mentioned in the foregoing for a perfectly plastic material is not applicable to a rate-sensitive one, of course; the estimate is empirical and tentative.

5 Comparisons and Discussion

It is obviously necessary to check predictions of the present method against tests and/or complete numerical solutions. In the previous applications [1-3] of the simplified elastic-plastic approach comparisons were made with tests; in general fairly good agreement was observed between estimated final and maximum displacements and those obtained in tests. (In one case [3] remarkable agreements were shown, in contrast to a wholly rigid-plastic treatment.) In the present frame problems the response history is more complex than in the previous applications, and comparisons with both tests and complete solutions will be essential. Although a program of experiments is under way, tests with impulsive loading suitable for comparison with the present results have not yet been made. For the present, comparisons are restricted to ones with complete solutions obtained by computations using a finite element code.

For this purpose the program ABAQUS[6] was used. This is a general purpose program providing for material and geometric nonlinearity at small strains. The element used in our calculations was a beam element based on linear strain variation over the cross-section, integrating stress over nine points across the thickness. Elastic shear deformation could be considered in the sense of a rotation of the cross-section plane with respect to the axis. Material behavior either of perfectly plastic or strain rate dependent type (without strain hardening) was elected for each element. ABAQUS treats rate dependence by the same "dynamic over stress" constitutive law adopted in our work (equation (14)). For most of our calculations a 44-node model was used with 16 equal elements in the loaded column. Lumped mass matrices obtained by linear interpolation of mass over the element, including rotation, were used. The time integration was done with implicit nonlinear equations solved by Newton's method, using the Hilber-Hughes operator for controllable numerical damping. The most distinctive feature of ABAQUS is its provision for automatic change of the time step in accordance with an "error" (force residual) computed at the midpoint of each computed time step. This feature is highly advantageous for efficient solution of our dynamic elastic-plastic problems, where the time step initially must be very short (e.g., 10^{-7} sec) but which can soon be lengthened to 10^{-5} sec or longer without loss of accuracy.

Deflections computed at the midpoint H and corner B of the loaded column are shown as points in Figs. 5 and 7. The impulsive loading (initial velocity) was modeled as a high intensity pressure applied over the column for 3 μsec. The final permanent deflection magnitudes are not computed directly, since physical damping is not included. These had to be estimated from the plots of displacement with time after completion of the plastic deformation. There is some uncertainty about these values, since the continuing elastic vibrations are not sinusoidal, although much smoother than the early elastic and elastic-plastic response patterns. Thus unfortunately the quantities (w_H^f, w_B^f) which are furnished with least uncertainty by the approximation technique are given somewhat roughly by the complete solution; conversely the maximum values w_H^{max} and w_B^{max} are estimated by a crude empirical process, but furnished "exactly" by the numerical program. These difficulties should be kept in mind in the comparisons.

The agreement between the present estimations and the values computed numerically is generally fair in the range of low loading, where the response is substantially elastic. This is the range where a rigid-plastic analysis is inapplicable and a new approach was needed. To this extent the comparisons seem to indicate that the simplified elastic-plastic approach has some promise of applicability to structural response

[6] ABAQUS was kindly made available for our use by its owners Hibbitt, Karlsson and Sorensen, Inc., 35 South Angell Street, Providence, R.I. 02906.

Downloaded 02 May 2010 to 171.66.16.25. Redistribution subject to ASME license or copyright; see http://www.asme.org/terms/Terms_Use.cfm

problems of the type considered here. The agreement is markedly worse at the largest value for which ABAQUS calculations were made ($R \cong 6$). This is surprising, since the simple method gives estimates approaching those of a wholly rigid-plastic analysis as the load parameter R increases, and the latter analysis has been found to approach agreement with elastic-plastic solutions (with errors in final deflection on the high side). Disagreements of this type were not found in the previous comparisons with experiments [1-3]. Further study of this question, is required, which could relate to the simple rigid-plastic model used. Difficulties in the "exact" numerical solution are not ruled out. The fact that the discrepancies are similar in both the rate-independent and rate-dependent cases does suggest that our grossly simplified treatment of rate sensitivity is not seriously at fault.

References

1 Symonds, P. S., and Raphanel, J. L. "Large Deflections of Impulsively Loaded Plane Frames—Extensions of the Mode Approximation Technique," *Proc. Conf. on Mechanical Properties of Materials at High Rates of Strain*, Institute of Physics Conf., Series No. 47 Harding, J., ed., London and Bristol, 1979, pp. 277-287.

2 Symonds, P. S., "Elastic, Finite Deflection and Strain Rate Effects in a Mode Approximation Technique for Plastic Deformation of Pulse Loaded Structures," *J. Mechanical Engineering Science*, Vol. 22, No. 4, 1980, pp. 189-197.

3 Symonds, P. S., "Finite Elastic and Plastic Deformations of Pulse Loaded Structures by an Extended Mode Technique," *Int. J. Mech. Sci.*, Vol. 22, 1980, pp. 597-605.

4 Symonds, P. S., "Elastic-Plastic Deflections due to Pulse Loading," in Proceedings of the Second Specialty Conference on "*Dynamic Response of Structures: Experimentation, Observation, Prediction, and Control*," Hart, G., ed., ASCE New York, 1980, pp. 887-901.

5 Bodner, S. R., and Symonds, P. S., "Experimental and Theoretical Investigation of the Plastic Deformation of Cantilever Beams Subjected to Impulsive Loading," ASME JOURNAL OF APPLIED MECHANICS, Vol. 29, 1962, pp. 719-727.

6 Symonds, P. S., and Raphanel, J. L., "Rigid-Plastic and Simplified Elastic-Plastic Solutions for Dynamically Side-Loaded Frames," in *Mechanics of Material Behavior — The Daniel C. Drucker Anniversary Volume*, Dvorak, G. T., and Shield, R. T., eds., Elsevier, Amsterdam, 1983, in press.

7 Martin, J. B., and Symonds, P. S., "Mode Approximations for Impulsively Loaded Rigid-Plastic Structures," *J. Eng. Mech. Div.*, Proc. ASCE, Vol. 92, No. EM5, 1966, pp. 43-66.

8 Youngdahl, C. K., "Correlation Parameters for Eliminating the Effect of Pulse Shape on Dynamic Plastic Deformation," ASME JOURNAL OF APPLIED MECHANICS, Vol. 37, 1970, pp. 744-752.

9 Bodner, S. R., and Symonds, P. S., "Experiments on Dynamic Plastic Loading of Frames," *Int. Journal Solids Structures*, Vol. 15, 1979, pp. 1-13.

10 Bodner, S. R., and Symonds, P. S., "Experiments on Viscoplastic Response of Circular Plates to Impulsive Loading," *J. Mech. Phys. Solids*, Vol. 27, 1979, pp. 91-113.

11 Perrone, N., "On a Simplified Method for Solving Impulsively Loaded Structures of Rate-Sensitive Materials," ASME JOURNAL OF APPLIED MECHANICS, Vol. 32, 1965, pp. 489-492.

12 Symonds, P. S., and Wierzbicki, T., "Membrane Modes for Impulsively Loaded Circular Plates," ASME JOURNAL OF APPLIED MECHANICS, Vol. 46, 1979, pp. 58-63.

13 Martin, J. B., and Lee, L. S. S., "Approximate Solutions for Impulsively Loaded Elastic-Plastic Beams," ASME JOURNAL OF APPLIED MECHANCIS, Vol. 35, 1968, pp. 803-809.

Downloaded 02 May 2010 to 171.66.16.25. Redistribution subject to ASME license or copyright; see http://www.asme.org/terms/Terms_Use.cfm

Impact and Bending of a Rigid-Plastic Fan Blade

W. J. Stronge

T. Shioya[1]

Department of Engineering,
University of Cambridge,
Cambrige CB2 1PZ, England

A rigid-plastic fan blade is subjected to a transverse impact force at the tip in addition to radial centrifugal forces caused by fan rotation. Large and small deflection formulations for inplane bending of the cantilevered blade are calculated and compared. If the effects of centrifugal force are completely considered, the difference between these calculations is shown to be small within the beam. Most of the deflection originates from plastic deformation far from the tip so the large deflection effects near the tip have little influence. The largest curvature is inversely proportional to the centrifugal force, directly proportional to the third power of impact force, and always occurs near the point of impact.

Introduction

When subjected to transverse impact at the tip, a rigid-plastic cantilever will bend at a discrete plastic hinge that moves away from the impact site toward the root. If the impact is away from the tip, two additional hinges may be formed, one at the impact site and the other within the segment between this point and the tip. All permanent deformation of the beam develops at these plastic hinges [1-3].

A fan blade is a cantilever that is subjected to a continuous acceleration in the radial direction due to fan rotation. When also subjected to transverse impact, blade bending again occurs at discrete hinges if the blade is rigid-plastic. The centripetal acceleration in a fan strongly affects both the hinge position and the final curvature. These effects are significant at both large and small deflection.

This paper compares plastic deformations determined from small and large deflection formulations for a uniform rigid-plastic cantilever of semi-infinite length subjected to both a constant acceleration along the initial axis and transverse impact by a fluid jet. In contrast to the rigid body impact which Parkes considered, this fluid jet imparts a time-dependent force with finite magnitude [4].

Large Deflection Formulation

Consider a uniform, semi-infinite beam with mass per unit length m, which is subjected to a transverse force $f(t)$ acting at tip. The beam is also subject to a constant body force of magnitude gm per unit length that acts in the initial axial direction and is positive toward the tip. This body force represents the effect of fan blade rotation about the hub. At any instant of time the moment distribution in a rigid-plastic beam causes the plastically deforming region to be concentrated in a hinge where the bending moment equals the yield moment M_0 and the shear force is zero. At time t this hinge is a distance λ from the initial tip position as shown in Fig. 1(*a*). When the force is monotonically decreasing, the hinge *always* moves away from the tip and there is a one-to-one correspondence between λ and t. Consequently, λ can replace t as an independent variable.

Let s be an intrinsic coordinate, measured along the neutral axis from the tip. Further, let u and w be coordinates of the point s of the deformed beam measured from the hinge in the x and z directions, respectively.

$$u(s,\lambda) = \int_s^\lambda \cos\theta(\xi,\lambda)\, d\xi \tag{1a}$$

$$w(s,\lambda) = \int_s^\lambda \sin\theta(\xi,\lambda)\, d\xi \tag{1b}$$

where the inclination of the beam at s when the hinge is at λ is

$$\theta(s,\lambda) = \int_s^\lambda \kappa(\xi)\, d\xi \tag{2}$$

and $\kappa(s)$ is the curvature of the neutral axis. The velocity of any point on the neutral axis will be

$$\dot{u}(s,\lambda) = -\dot{\theta}(\lambda,\lambda)w(s,\lambda) \tag{3a}$$

$$\dot{w}(s,\lambda) = \dot{\theta}(\lambda,\lambda)u(s,\lambda) \tag{3b}$$

where the rate of rotation at the hinge is

$$\dot{\theta}(\lambda,\lambda) = \dot{w}(0,\lambda)/u(0,\lambda) = \dot{u}(0,\lambda)/w(0,\lambda) \tag{4a}$$

and $\dot{u}$ denotes the derivative of u with respect to time t. When the hinge is moving, $\dot{\lambda} > 0$ and we can define the rate of rotation throughout the tip-to-hinge segment of the beam as

$$\dot{\psi} \triangleq \dot{\theta}(\lambda,\lambda) = \dot{\lambda}\kappa(\lambda) \tag{4b}$$

The second moment of the deformed part of the beam

[1] On Leave from the Department of Aeronautics, University of Tokyo, Japan.

Contributed by the Applied Mechanics Division for presentation at the Winter Annual Meeting, New Orleans, La., December 9-14, 1984 of THE AMERICAN SOCIETY OF MECHANICAL ENGINEERS.

Discussion on this paper should be addressed to the Editorial Department, ASME United Engineering Center, 345 East 47th Street, New York, N.Y. 10017, and will be accepted until two months after final publication of the paper itself in the JOURNAL OF APPLIED MECHANICS. Manuscript received by ASME Applied Mechanics Division, November, 1983. final revision, January, 1984. Paper No. 84-WA/APM-14.

Copies will be available until August, 1985.

Copyright © 1984 by ASME

Downloaded 02 May 2010 to 171.66.16.25. Redistribution subject to ASME license or copyright; see http://www.asme.org/terms/Terms_Use.cfm

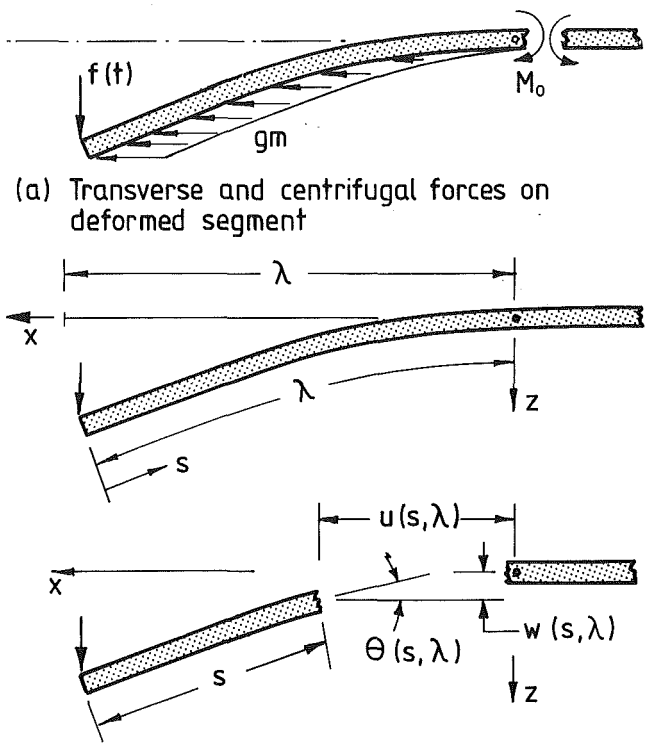


Fig. 1 Transverse impact force on tip of cantilever

about the plastic hinge and first moments about the z,x axes are, respectively

$$i_0(\lambda) = \int_0^\lambda [u^2(s,\lambda) + w^2(s,\lambda)]ds \tag{5a}$$

$$i_1(\lambda) = \int_0^\lambda u(s,\lambda)\, ds \tag{5b}$$

$$i_2(\lambda) = \int_0^\lambda w(s,\lambda)\, ds \tag{5c}$$

These definitions are similar to those of Ting [3]. When the hinge is moving ($d\lambda/dt > 0$), these definitions provide

$$di_0/d\lambda = 2i_1(\lambda) \tag{6a}$$

$$di_1/d\lambda = \lambda - i_2(\lambda)\,\kappa(\lambda) \tag{6b}$$

$$di_2/d\lambda = i_1(\lambda)\,\kappa(\lambda) \tag{6c}$$

and

$$du/d\lambda = \cos\theta(\lambda,\lambda) - w(s,\lambda)\,\kappa(\lambda) \tag{7a}$$

$$dw/d\lambda = \sin\theta(\lambda,\lambda) + u(s,\lambda)\,\kappa(\lambda) \tag{7b}$$

Two equations of motion will be derived, one associated with forces and momentum transverse to the initial beam position and a second associated with moments and the moment of momentum about the current hinge position. Axial elongation is neglected.

(*i*) Since the transverse shear force is zero at a moving hinge and the beam was initially at rest, the transverse momentum at any time is equal to the impulse that has been applied by $f(t)$,

$$\int_0^t f(t)\, dt = m\int_0^\lambda \dot{w}(s,\lambda)\, ds = m\dot{\psi} i_1(\lambda) \tag{8}$$

Consequently, at any time

$$f = m\ddot{\psi} i_1(\lambda) + m\dot{\psi}\dot{\lambda}[\lambda - i_2(\lambda)\,\kappa(\lambda)] \tag{9}$$

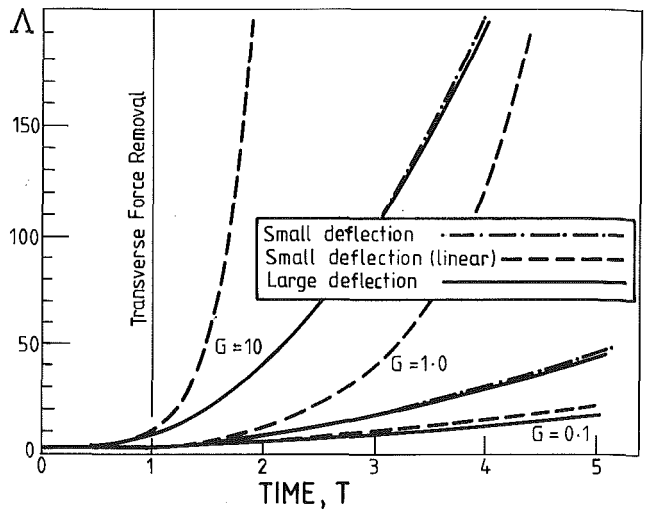


Fig. 2 Hinge position for force duration $\Upsilon = 1$

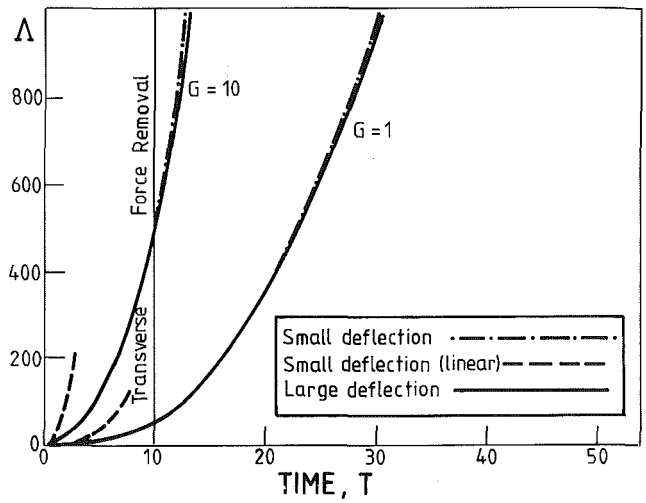


Fig. 3 Hinge position for force duration $\Upsilon = 10$

(*ii*) In a deformed beam, both the impact and the body force have moments about the current hinge position. The difference between the rate of work done by these external forces and the rate of energy dissipation at the plastic hinge is equal to the rate of change in kinetic enegy

$$f(t)\, u(0,\lambda) - gmi_2(\lambda) - M_0 = m[\ddot{\psi} i_0(\lambda) + \dot{\psi}\dot{\lambda} i_1(\lambda)] \tag{10}$$

When the impact force is a constant F during the impact duration τ and zero thereafter, a set of nondimensional variables can be defined for this analysis; for example,

$$S = sF/M_0,\ \Lambda = \lambda F/M_0,\ K = \kappa M_0/F,\ T = tF^{3/2}/M_0 m^{1/2},$$
$$\dot{\Psi} = \dot{\psi} M_0 m^{1/2}/F^{3/2},\quad G = gmM_0/F^2 \tag{11}$$

where $\dot{\psi} = d\psi/dt$ and $\dot{\Psi} = d\Psi/dT$. Hence, the nondimensional equations of motion during $T < \Upsilon$ are

$$1 = \ddot{\Psi} I_1 + \dot{\Psi}\dot{\Lambda}[\Lambda - I_2 K],\quad T < \Upsilon \tag{12a}$$

$$U(0,\Lambda) - GI_2 - 1 = \ddot{\Psi} I_0 + \dot{\Psi}\dot{\Lambda} I_1,\quad T < \Upsilon \tag{12b}$$

and, after the impact force is removed

$$0 = \ddot{\Psi} I_1 + \dot{\Psi}\dot{\Lambda}[\Lambda - I_2 K],\quad T > \Upsilon \tag{13a}$$

$$-GI_2 - 1 = \ddot{\Psi} I_0 + \dot{\Psi}\dot{\Lambda} I_1,\quad T > \Upsilon \tag{13b}$$

Small Deflection Approximation

If $\theta(S,\Lambda)$ is small, it is convenient to define deflections relative to the tip deflection $W_0 \triangleq W(0,\Lambda)$, so

Downloaded 02 May 2010 to 171.66.16.25. Redistribution subject to ASME license or copyright; see http://www.asme.org/terms/Terms_Use.cfm

$$\dot{W}_0 = \Lambda\dot{\Psi}, \quad \ddot{W}_0 = \Lambda\ddot{\Psi} + \dot{\Lambda}\dot{\Psi} \tag{14}$$

and

$$I_0 \simeq \Lambda^3/3,\ I_1 \simeq \Lambda^2/2,\ I_2 = \int_0^{\Lambda} W(\xi,\Lambda)\, d\xi \tag{15}$$

Since $\Lambda = \Lambda(T)$ and $W(S,T) = \int_0^T (1 - S/\Lambda)\dot{W}_0 dT$, the first moment about the x axis can also be expressed as

$$I_2 = \frac{1}{2}\int_0^T \Lambda\dot{W}_0(T)\ dT \tag{16}$$

An upper bound on I_2 is provided by an approximation that assumes Λ is the current hinge position rather than a function of time

$$I_2 \simeq \Lambda W_0/2 \tag{17}$$

This approximation is the same as neglecting curvature developed previously between the current hinge position and the tip.

The equations of motion for the case of small inclination (small deflection during $T < \Upsilon$) will be

$$2 = \Lambda\ddot{W}_0 + \dot{\Lambda}\dot{W}_0 \tag{18a}$$

$$6(\Lambda - GI_2 - 1) = 2\Lambda^2\ddot{W}_0 + \Lambda\dot{\Lambda}\dot{W}_0 \tag{18b}$$

and for $T > \Upsilon$

$$0 = \Lambda\ddot{W}_0 + \dot{\Lambda}\dot{W}_0 \tag{19a}$$

$$-6(GI_2 + 1) = 2\Lambda^2\ddot{W}_0 + \Lambda\dot{\Lambda}\dot{W}_0 \tag{19b}$$

Before calculating a solution for these sets of equations it will be useful to rearrange them; so, while the transverse force is acting

$$\dot{\Lambda}\dot{W}_0 = (6 + 6GI_2 - 2\Lambda)/\Lambda, \quad T < \Upsilon \tag{20a}$$

$$\ddot{W}_0 = (-6 - 6GI_2 + 4\Lambda)/\Lambda^2, \quad T < \Upsilon \tag{20b}$$

while after the impact force is removed,

$$\dot{\Lambda}\dot{W}_0 = (6 + 6GI_2)/\Lambda, \quad T > \Upsilon \tag{21a}$$

$$\ddot{W}_0 = -(6 + 6GI_2)/\Lambda^2, \quad T > \Upsilon \tag{21b}$$

Numerical Solutions

Initial Values. The initial conditions are the cantilever is straight and at rest. The initial values for dependent variables are determined by examining forward difference forms of the differential equations in the limit as $T \to 0$. At $T = 0$ irrespective of G, equation (20a) implies that the hinge is located at

$$\Lambda(0) = 3 \tag{22}$$

which results in an initial tip acceleration

$$\ddot{W}_0(0) = 2/3 \tag{23}$$

This acceleration causes an initial increment in the first moment $I_2 = (\Delta T)^2/2$. Assuming that the initial hinge acceleration is a constant, equations (20a) and (20b) imply that the hinge speed after ΔT will be

$$\dot{\Lambda}(\Delta T) = G\Delta T \tag{24}$$

Curvature developed at a moving hinge is $K = \dot{W}_0/\Lambda\dot{\Lambda}$ so the plastic deformation nearest the tip results in a curvature

$$K(3) = 2/9G \tag{25}$$

If $G = 0$, the hinge is stationary during $T < \Upsilon$ and the radius of curvature at $\Lambda = 3$ is zero.

Transient Response. Finite difference forms of the equations of motion have been calculated with these initial values using Newton's method of approximation. The independent variable is Λ. This hinge position has been calculated at intervals of $\Delta T = 0.005$. For each step, either spatial integration of the deformed configuration is required to calculate equation (5) or temporal integration of the history of deformation is required to calculate equation (16).

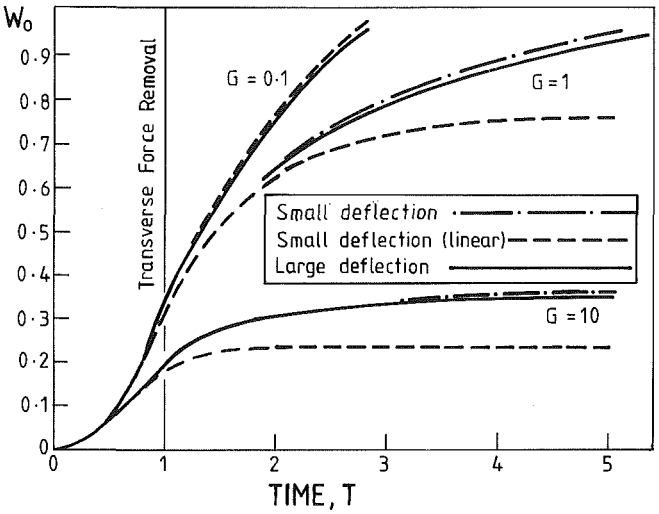


Fig. 4 Tip deflection for force duration $\Upsilon = 1$

Discussion

At impact, a plastic hinge is formed at a distance $\Lambda = 3$ from the tip. When $G = 0$ and the impact force is constant, the hinge does not move along the beam until the force is removed. A "kink" develops at $\Lambda = 3$ where the discontinuity in inclination is proportional to the product of the impact force and the applied impulse squared,

$$\theta(3) = F^3T^2/9mM_0^2 \quad \text{for} \quad g = 0 \tag{26}$$

When $G > 0$ the hinge begins to move away from $\Lambda = 3$ during the time of action for the force. After the force is removed, momentum acquired by the end segment makes plastic deformation continue at a hinge that moves monotonically away from the tip. Curvature, following passage of this moving hinge, decreases as the speed of the hinge increases. Hinge position as a function of time is shown in Fig. 2 for three values of the axial body force G. The effect of G is to increase the hinge speed away from the tip. In Fig. 3, the hinge position is shown for an impact force duration $\Upsilon = 10$ rather than for $\Upsilon = 1$ (i.e., for a larger applied impulse). The force duration $\Upsilon = 10$ has larger deflection so G has more effect.[2]

Two different small deflection approximations have been compared with the large deflection theory in Fig. 2. The difference between these approximations is in the moment due to the axial body force G, acting on the previously deformed beam; equation (16) uses the complete expression for the first moment I_2, while equation (17) uses a linear displacement approximation. The latter is shown to be a poor approximation whenever $G > 0.1$; it grossly overestimates the moment due to the axial force so it becomes less accurate as deformation increases. When the complete expression for the first moment is used, large and small deflection results are indistinguishable for $G < 10$ when the impact duration is $\Upsilon = 1$. The deflections remain small in these cases.

The final tip deflection shown in Figs. 4 and 5 is a measure of the effect of axial body forces. These forces have a moment about any point on the neutral axis that is counter to the moment caused by the impact force. Hence, the plastic hinge

[2] Typical impact force and duration parameters for a big bird ingested by a large transport turbofan engine will be $G = 3$ and $\Upsilon = 0.3$. These numbers correspond to a 0.5 kg bird impact on a flat titanium blade with one meter tip radius, 10 mm × 100 mm cross section, and 300 m/s tip speed.

Downloaded 02 May 2010 to 171.66.16.25. Redistribution subject to ASME license or copyright; see http://www.asme.org/terms/Terms_Use.cfm

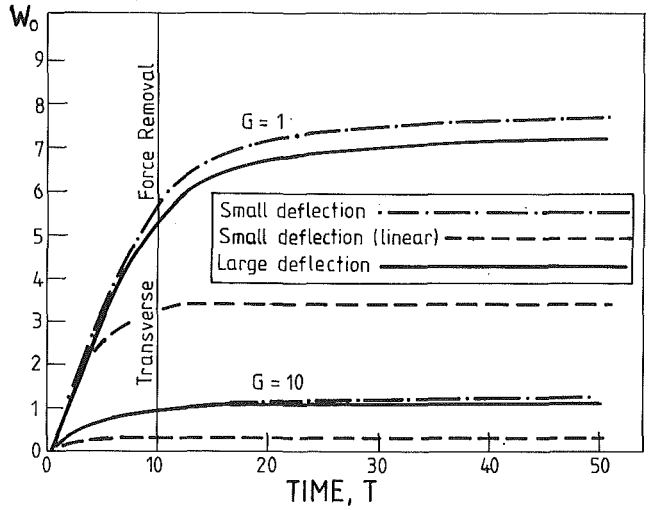


Fig. 5 Tip deflection for force duration $\Upsilon = 10$

moves away from its initial position more rapidly and the curvature after passage of the hinge is smaller. Since the moment of the body force increases with tip deflection, G has more effect when the impulse applied to the tip is larger; i.e., for $\Upsilon = 10$ rather than for $\Upsilon = 1$. Consequently, most deflection occurs while the force is acting if the applied impulse is large.

The deforming configuration is shown at four different times in Fig. 6. Generally, the axial body force decreases the deflection. Because the hinge continuously accelerates away from the initial position, the largest curvature is at $\Lambda = 3$ and is formed at $T = 0$. This largest curvature is

$$\kappa = 2F^3/9gmM_0^2 \tag{27}$$

As the body force approaches zero the initial curvature increases without bound.

The comparisons in Figs. 4–6 have been calculated for a yield moment that is independent of the axial force. In cross sections where the yield moment is reduced by the axial force, sensitivity of the tip deflection w_0 and maximum curvature to the impact parameter g is smaller than indicated by these Figures.

Significance of this analysis for fluid impact on rotating fan blades can be illustrated by considering a fluid mass flux $\dot{m}_f$ impacting a blade with tip speed v. When the body force is caused by centripetal acceleration of the tip at radius r, $g = v^2/r$. The impulse imparted to the blade will be proportional to $\dot{m}_f v$; consequently, the largest curvature within the blade κ_{max} is

$$\kappa_{max} : \dot{m}_f^3 rv/mM_0^2$$

and this occurs at the deformed section of the beam that is nearest to the tip.

Conclusion

The time-dependent deflection and curvature in a semi-infinite, rigid-plastic beam impacted by a transverse force has been calculated when the beam is subjected to an axial body force. These calculations have examined applied pulses that are either short or long in comparison with the structural response time. When the applied impulse is of long duration, there is the most difference between large and small deflection formulations. The small deflection formulation slightly exaggerates the deformation.

If the body force is nonzero, the largest beam curvature is directly proportional to impulse to the third power, inversely proportional to the body force, and is close to the impact end.

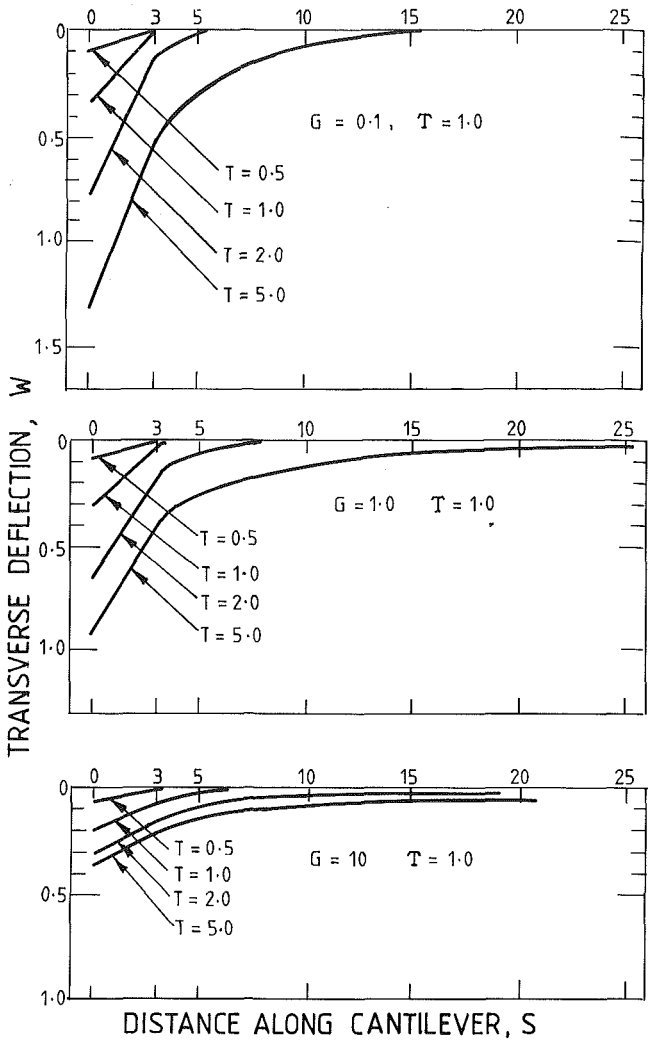


Fig. 6 History of deformation

This largest curvature occurs at impact so it is located at $\lambda = 3M_0/F$. Thereafter, the plastic hinge moves away from this section and the curvature remaining behind diminishes. When the force arises from fluid impact on a fan blade, the largest curvature is proportional to the tip speed.

Although the axial body force in a fan blade is not constant but decreases with distance from the tip, this analysis will be useful for cantilevered blades when the impact force is large in comparison with the static plastic limit force for the cantilever. Then, the largest deformation will be concentrated near the impact point so the variation in axial force with radius has only a small effect on the results. A comparatively large force is also a requirement for applicability of the rigid-plastic material approximation. Consequently, this analysis of bending represents fan blade deformation near the impact point when the impact force is large.

References

1 Parkes, E. W., "The Permanent Deformation Due to Impact of a Cantilever Struck Transversely at its Tip," *Proceedings Royal Society, London*, Series *A*, Vol. 228, 1955, pp. 462.

2 Bodner, S. R., and Symonds, P. S., "Experimental and Theoretical Investigation of the Plastic Deformation of Cantilever Beams Subjected to Impulsive Loading," ASME JOURNAL OF APPLIED MECHANICS, Vol. 29, 1962, pp. 719–728.

3 Ting, T. C. T., "Large Deformation of a Rigid, Ideally Plastic Cantilever Beam," ASME JOURNAL OF APPLIED MECHANICS, Vol. 32, 1965, pp. 295–302.

4 Johnson, W., *Impact Strength of Materials*, Edward Arnold, London, 1972.

Downloaded 02 May 2010 to 171.66.16.25. Redistribution subject to ASME license or copyright; see http://www.asme.org/terms/Terms_Use.cfm

Simplified Large Deflection Mode Solutions for Impulsively Loaded, Viscoplastic, Circular Membranes

N. Perrone[1]
Adjunct Professor,
Catholic University
Fellow ASME

P. Bhadra
Carroll Associates

The title problem is solved by estimating the maximum strain rate field in a circular membrane associated with a modal velocity condition when one-half the kinetic energy in the system has been dissipated. The radial stress may only vary in the radial direction, but is taken as a constant with time at any given location. Internal plastic energy absorbed during the large deformation is found by integrating while accounting for rate sensitivity effects; this absorbed energy is equated to the initial kinetic energy in the system to obtain the final deformed configuration. Correlation of analytically determined results with a series of experiments reported elsewhere is very good. The procedure described here is potentially extendable to any planform membrane shape as well as to axisymmetric shells. The method is applicable to plate problems when membrane effects dominate over bending, that is for deformations of the order of two thicknesses or more. A simple general formula for final plate deformation is devised and also agrees well with experimental results.

Introduction

Determination of the dynamic plastic response of structures is complicated by a number of potential problems. Among these difficulties are included severe nonlinearities due to rate sensitive variation of yield stress, strain hardening, and large deformation membrane-related effects. The solution of resulting response equations, be they differential equations of motion or a numerically evolved set of algebraic equations, will still contain annoying and complex nonlinearities which will significantly impede the solution process.

Contributions and problem areas concerned with the dynamic plastic response of structures have been reviewed in a number of survey papers; two are cited for references [1, 2]. While no attempt is made to provide a detailed discussion of the literature, some papers will be highlighted. A number of experimental studies have been conducted on various structural elements using a variety of techniques [3–6]. An analytical approach which has been shown to be most promising is based on a modal approximation technique. This method which is widely used and being improved dates back some years [7–9]. Other simplified approaches to determine the dynamic plastic response of structures have also been utilized with some success [10–13]. In addition, more rigorous finite element procedures have been employed occasionally and shown to be quite accurate although requiring, in general, much more effort [14, 15]. Among the application areas where determination of improved dynamic plastic response procedures are useful include automobile crashworthiness [16, 17], explosive metal forming, and containment vessels for accidental explosion events.

Building on a previous result, which essentially applies to one-dimensional string type problem [11], the present paper utilizes a simplified modal approach to determine the plastic rate sensitive response of impulsively loaded circular membranes (or plates) in the large deflection range. In [9] a similar problem was addressed and solved by setting up the field equations rigorously and obtaining a solution by first neglecting and later iteratively including rate sensitivity effects. In the present case, a procedure is described that is potentially applicable to the circular as well as any other planform plate or membrane or indeed an axisymmetric shell.

In [11] an impulsively loaded central mass is supported by a rate sensitive string; a simplified solution to the response is determined by making an effective estimate of the strain rate and noting from an accurate numerical solution to the problem that the string stress is substantially constant during the response time. The maximum strain rate in the string is associated with a condition when half the kinetic energy in the system has been dissipated. Knowing the initial impulsive velocity (V_0), one can readily determine the velocity field associated with the half kinetic energy dissipation condition (i.e., $V_0/\sqrt{2}$). By effecting an energy balance between the initial kinetic energy and work done by plastic stretching of the string, the final deformation is obtained.

In the next section the essence of the modal approximation approach is described including the selection of shape func-

[1] Also, Consulting Engineer.

Contributed by the Applied Mechanics Division and presented at the 1984 PVP Conference and Exhibition, Joint with Applied Mechanics Division and Materials Division, San Antonio, Texas, June 17–21, 1984 of THE AMERICAN SOCIETY OF MECHANICAL ENGINEERS.

Discussion on this paper should be addressed to the Editorial Department, ASME, United Engineering Center, 345 East 47th Street, New York, N.Y. 10017, and will be accepted until two months after final publication of the paper itself in the JOURNAL OF APPLIED MECHANICS. Manuscript received by ASME Applied Mechanics Division, December, 1982; final revision, October, 1983. Paper No. 84-APM-41.

Copies will be available until February, 1985.

Copyright © 1984 by ASME
Downloaded 02 May 2010 to 171.66.16.25. Redistribution subject to ASME license or copyright; see http://www.asme.org/terms/Terms_Use.cfm

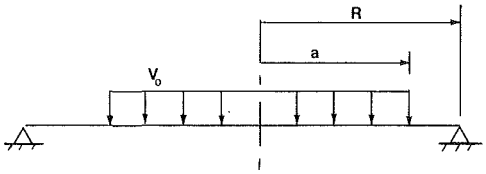


Fig. 1 Circular plate with uniform axisymmetric impulsive velocity

tions and the energy balance procedure. Correlations of analytically determined results with a series of simple generalized analyses are described and the resulting formula correlated with the same experimental series of results. Extensions of the approach described in this paper to generalized structural elements consisting of plates with any planform or axisymmetric shell response are discussed in the concluding section.

Membrane Modal Approximations Via Shape Function and Energy Balance

We wish to determine the final deformation field of a circular plate which is subjected to a uniform axisymmetric impulsive velocity, Fig 1. The outer edge of the plate is fixed and the impulsive velocity covers a region of radius a which could extend over the entire plate region. The plate is made of a perfectly plastic rate sensitive material whose yield stress behaves in accordance with the exponential law in equation (1).

$$\sigma/\sigma_0 = 1 + (\dot{\epsilon}/\dot{\epsilon}_0)^{1/n} \tag{1}$$

where $\dot{\epsilon}_0$ and n are material properties and σ_0 is the static yield stress. Membrane effects are presumed to dominate over bending, or in other terms bending effects are ignored. The method of analysis is an extension of a previously developed procedure discussed in [11].

Determining Modal Velocity and Shape Function. The response of the plate is in general a function of time and space. Considerable mathematical simplification is achieved by assuming that this response is describable in a modal form, that is, the product of a function of time by a function of the space variable, equation (2).

$$w(r,t) = w_*(t)\,\phi(r) \tag{2}$$

The notation being employed is similar to that in [9]. The first steps in the solution process are the determination of the initial modal velocity of the plate and the selection of a shape function $\phi(r)$. The modal velocity, of course, differs from the initial uniformly imposed velocity described in Fig. 1. Determination of the initial modal velocity is based on the Martin and Symonds criterion suggested in [7], equation (3).

$$\dot{w}^0_* = \frac{\int_0^R \bar{\rho}\,\dot{w}^0\,\phi\,r\,dr}{\int_0^R \bar{\rho}\,\phi^2\,r\,dr} \tag{3}$$

where $\bar{\rho}$ is the mass/unit area and zero superscripts refer to initial conditions. Selection of the ϕ or shape function is necessary before equation (3) can be evaluated.

It is presumed here that this function will be a parabolic one, that is, having a quadratic form that is kinematically consistent with the boundaries (at $r=R$, deflection $=0$). A parabolic shape function is selected because this is an accurate representation for a statically uniformly loaded infinite strip membrane [18] as well as a good approximation based on examination of various experimental results [3, 4]. The prescribed impulsive velocity field is taken as constant in the central region of radius a, Fig. 1. Substitution of the parabolic

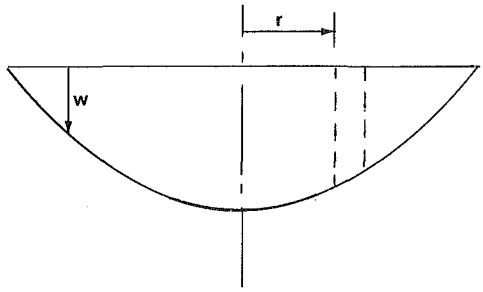


Fig. 2 Kinematics of strain field for generic element during dynamic deformation

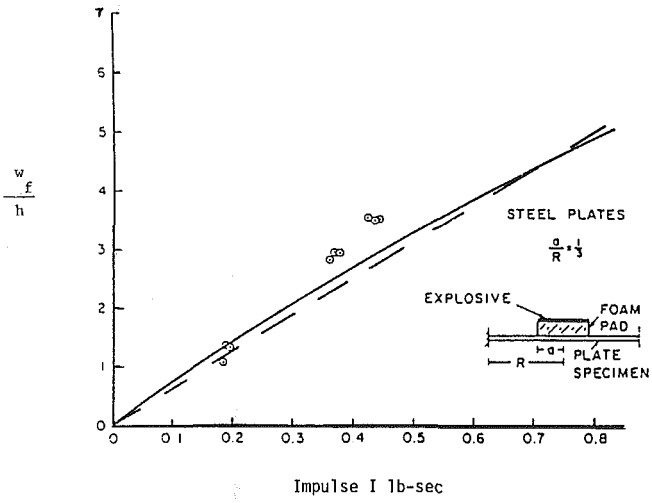


Fig. 3 Comparison of experimental results of [5] (circled dots) with present analytic results of equation (11) (solid line) and simplified equation (12) (broken line). Steel, $a/R = 1/3$.

shape function into equation (3) results in equation (4) as the initial modal velocity of the plate.

$$\dot{w}^0 = (3\,V_0/2)\underbrace{[2(a/R)^2 - (a/R)^4]}_{f(a)}\underbrace{[1-(r/R)^2]}_{\phi(r)} \tag{4}$$

Strain and Strain Rate Determination. It is assumed that the only motion of the plate is associated with a transverse or w deflection field. Motions due to deflections within the plane (u,v) are ignored. This assumption is tantamount to demanding that equilibrium is required in the transverse direction but not in the secondary horizontal direction. A similar assumption is essentially made in other modal approaches [9]. The kinematics of the associated strain field is described in Fig. 2. The circumferential strain component is negligible whereas the radial component has the value given in equation (5),

$$\epsilon_r = \frac{1}{2}(w_{,r})^2 \tag{5}$$

where the comma denotes differentiation. Substitution of equation (2), the modal approximation into the strain displacement equation, equation (5), results in the following general equations (6) and (7) for the strain and strain rate, respectively.

$$\epsilon_r = (1/2)w^2_*(t)\,\phi^2_{,r} \tag{6}$$

$$\dot{\epsilon}_r = w_*(t)\,\dot{w}_*(t)\,\phi^2_{,r} \tag{7}$$

It becomes an important part of the solution process to estimate the maximum strain rate field. This field will be found for the particular modal problem prescribed by

Downloaded 02 May 2010 to 171.66.16.25. Redistribution subject to ASME license or copyright; see http://www.asme.org/terms/Terms_Use.cfm

equation (4). Based on the solution described earlier [11], the maximum strain rate condition occurs when the deflection field is approximately two-thirds the final value (namely, 2/3 w_f), and the velocity field is $1/\sqrt{2}$ multiplied by the initial modal velocity field, equation (8). (In other terms, maximum strain rates occur when half the initial kinetic energy has been dissipated.)

$$\dot{\epsilon}_r \max = \left(\frac{2}{3} w_f\right)\left(\frac{1}{\sqrt{2}}\right)\left(\frac{3}{2} V_0 f(a)\, \phi,_r^2\right)$$

$$\dot{\epsilon}_r \max = w_f V_0 [2(a/R)^2 - (a/R)^4]\, \phi,_r^2/\sqrt{2} \tag{8}$$

Finding w_f From Energy Balance. Because the initial velocity field is provided by equation (4) we can readily determine the initial kinetic energy in the plate as a function of the input field variables. The plastic energy absorbed by an elemental area of the membrane undergoing membrane stretch is as indicated in equation (9*a*). If integration is effected circumferentially as well as radially, the total plastic energy is given by (9*b*).

$$\text{Elemental Energy Absorbed} = (rd\theta\sigma_r h)\,\epsilon_r dr \tag{9a}$$

Total Energy Absorbed

$$= 2\pi \int_0^R \sigma_0 [1 + (\dot{\epsilon}_r/\dot{\epsilon}_0)^{1/n}](w_f^2\, \phi,_r^2/2) r dr \tag{9b}$$

In the determination of the plastic energy absorbed in equation (9*b*) which accounts for rate sensitivity we use an average maximum strain rate value (that is, one-half the quantity given in equation (8)) as discussed in reference [11]. In view of the very slow variation of yield stress with strain rate, this estimate of the strain rate will suffice to account for large deflection and rate sensitivity effects. By equating (9*b*) to the initial modal kinetic energy obtained by using equation (4) we determine equation (10) which enables us to find the amplitude of the final deformation parameter, w_f.

$$w_f^2 = \frac{9\bar{\rho}\, V_0^2 f^2}{4\sigma_0 h} \frac{\int_0^R [1 - 2(r/R)^2 + (r/R)^4] r\, dr}{\int_0^R [1 + (w_f V_0 \phi,_r^2 f/(2\sqrt{2}\dot{\epsilon}_0))^{1/n}] \phi,_r^2\, dr} \tag{10}$$

After substitution of ϕ and f (see equation (4)), integration with respect to r and considerable simplification, this equation reduces to equation (11)

$$w_f/h = [I[2 - (a/R)^2]/(h^2 R\pi)]\sqrt{3/(8\,\rho\,\sigma_0)} \cdot \{1 + [2n/(2n+1)][f w_f h V_0 \sqrt{2}/(h\dot{\epsilon}_0 R^2)]^{1/n}\}^{-1/2} \tag{11}$$

where the applied impulse $I = \pi a^2 \bar{\rho}\, V_0 = \pi a^2 h\, \rho\, V_0$.

Equation (11) provides us with an expression to solve for the final deflection of the plate. It is solved in a trivial iterative manner by first assuming the w_f term in the right-hand side of the equation is zero and subsequently solving once or twice to determine its actual final value. It is important to note when determining w_f that its final value is insensitive to the actual maximum strain value discussed earlier. Rate sensitivity effects are encompassed in the right-hand term in curly brackets. When n approaches infinity (see equation (1)) rate sensitivity effects vanish and the aforementioned term approaches unity.

Summary of Solution Procedure. For the current circular membrane problem, uniform impusively loaded conditions encompassing either the complete membrane area or a central portion are considered. Following Martin and Symonds [7] a velocity field associated with a modal deformation pattern is obtained. A solution of elastic membrane problem [18], when extended into the plastic range suggests that a parabolic deformation pattern would be most useful and that is the shape selected for the current circular membrane problem. Unlike the previously mentioned string problem, the circular membrane will have strain rates that vary in the radial direction, and so also will the rate sensitive yield stress. A modal velocity pattern associated with the maximum strain rate condition is determined as a function of the radius, and the average strain rate during the entire response time trivially found. The yield stress at any position is taken as constant with time and is determined from the average strain rate from a modal viewpoint. Again an energy balance is set up wherein the plastic work associated with membrane stretching is determined from a simple integration and equated to the original kinetic energy in the system. The resulting equation is used to determine the final deformation amplitude of the membrane; the deflection is found after a single iteration to account for the nonlinear rate sensitivity term.

Correlation of Present Analysis With Experimental Results

In [5] a series of careful experiments were conducted by Bodner and Symonds on impulsively loaded circular plates made of steel and titanium. The values of the material constants described by equation (1) as measured by Bodner and Symonds are given in Table 1.

The sheet explosives applied to the circular plates were placed in a radially symmetric manner to achieve uniform velocity in a circular central region. The plates were rigidly clamped at the outer region but some very small amount of slipping did occur at times. Figures 3–8 give a display of the experimental results from the series of tests by circled dots as each test result. On these figures are superposed the analytical predictions (as solid lines) from the current approach based on an energy and shape function approach. In general, current results are slightly less than those found by Symonds and Wierzbicki in [9]. However, correlations with experimental results are quite good, being comparable to those obtained in [9].

A Simple General Response Formula

The second term on the right-hand side of equation (11) represents the factor attributed to rate sensitivity effects. It is clear based on a series of solutions obtained that this factor does not vary greatly. As a result, a very simple formula can be presented selecting as the rate sensitivity factor for both steel and titanium materials a value of 0.6 (= 1/1.67). It may be of interest to note that the same rate sensitivity factor was recommended in designs using structural steel for highway

Table 1 Material/geometric parameters in Bodner/Symonds tests [5]

Parameter		Steel	Titanium
Rate sensitivity	σ_0	223 MPa (32.4 ksi)	251 MPa (36.4 ksi)
	n	5	9
	$\dot{\epsilon}_0$	40/sec	120/sec
Mass density	ρ	7800 kg/m (0.73 × 10 lb sec/in.)	4500 kg/m 0.42 × 10 lb. sec/in.)
Plate radius	R	31.8mm (1.25 in.)	31.8mm (1.25 in.)
Plate thickness	h	1.9mm (0.076 in.)	2.3mm (0.92 in.)

Downloaded 02 May 2010 to 171.66.16.25. Redistribution subject to ASME license or copyright; see http://www.asme.org/terms/Terms_Use.cfm

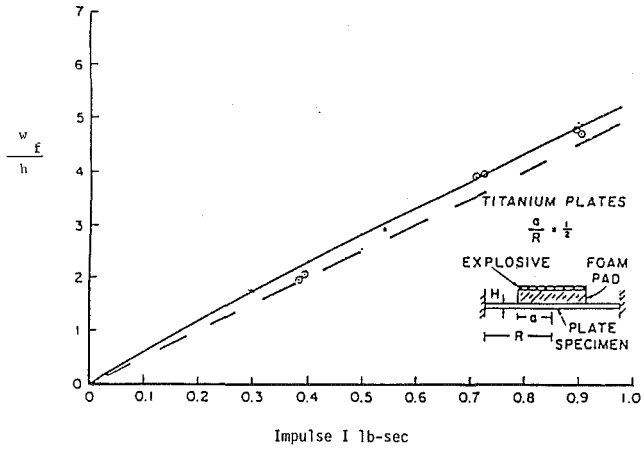


Fig. 4 Comparison of experimental results of [5] (circled dots) with present analytic results of equation (11) (solid line) and simplified equation (12) (broken line). Steel, $a/R = 1/2$.

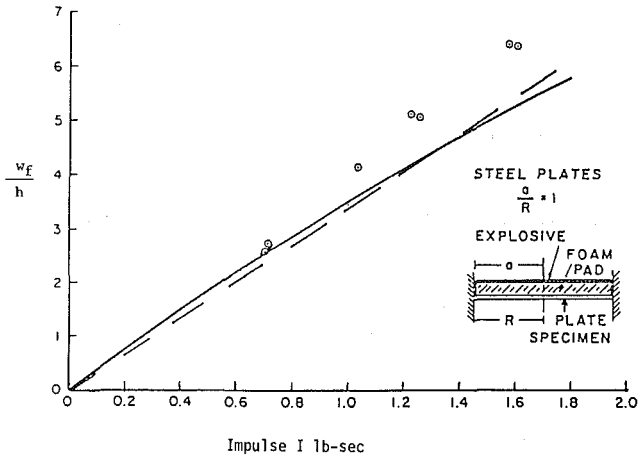


Fig. 5 Comparison of experimental results of [5] (circled dots) with present analytic results of equation (11) (solid line) and simplified equation (12) (broken line). Steel, $a/R = 1$.

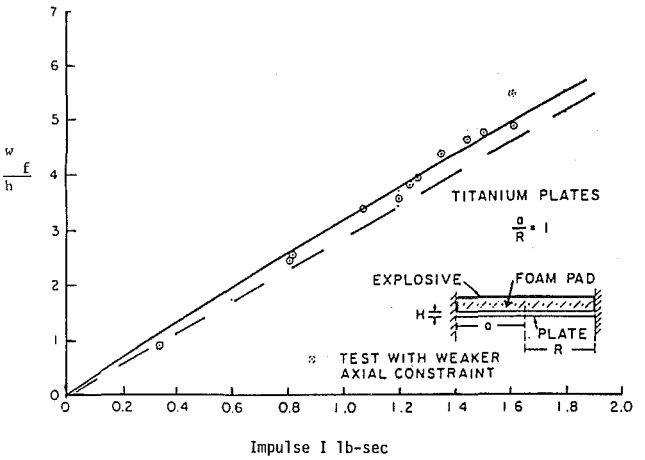


Fig. 6 Comparison of experimental results of [5] (circled dots) with present analytic results of equation (11) (solid line) and simplified equation (12) (broken line). Titanium, $a/R = 1$.

crashworthiness applications [19] and successfully implemented [20, 21]. The rate sensitivity factor has been combined with all other constants into a collective result in equation (12).

$$w_f/h = 0.117I[2-(a/R)^2]/[h^2R]\sqrt{\rho\sigma_0} \qquad (12)$$

Obviously, the final deformation, in this very simple form,

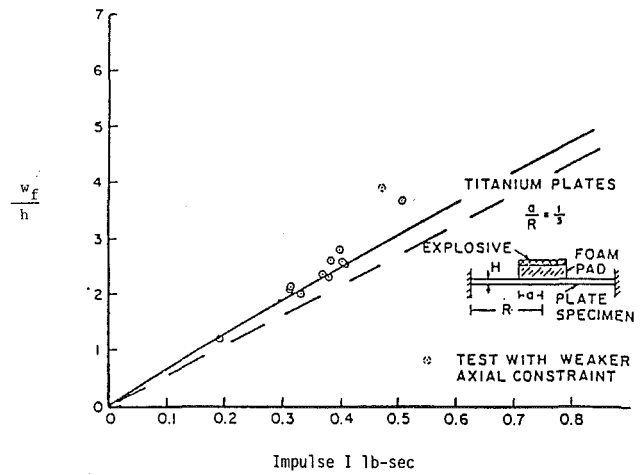


Fig. 7 Comparison of experimental results of [5] (circled dots) with present analytic results of equation (11) (solid line) and simplified equation (12) (broken line). Titanium, $a/R = 1/3$.

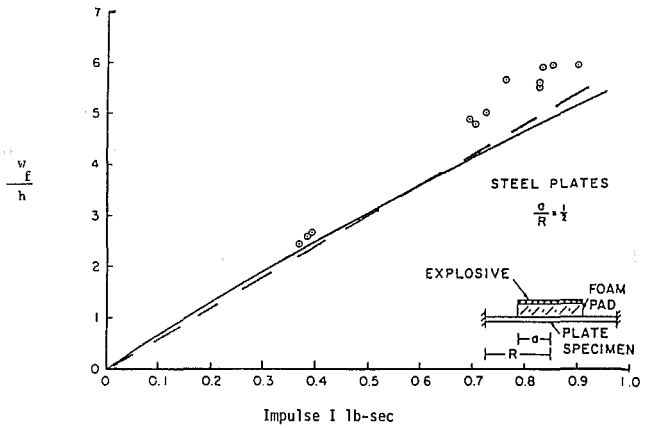


Fig. 8 Comparison of experimental results of [5] (circled dots) with present analytic results of equation (11) (solid line) and simplified equation (12) (broken line). Titanium, $a/R = 1/2$.

varies precisely linearly with applied impulse, I. All previous analyses as well as the experimental results also demonstrate an approximately linear behavior.

Equation (12) is still a very comprehensive description of the response as indicated by the correlations (broken lines) in Figs. 3–8. Clearly, the correlations are quite adequate from an engineering viewpoint. However, it should be noted that the rate sensitivity factors selected as 0.6 for both materials based on the more accurate approach described in the previous sections may not be appropriate for other materials which may be more or less rate sensitive than the ones described here. In general, steel demonstrated a slightly greater rate sensitivity effect than titanium.

Conclusions and Discussion

Based on a procedure described in [11], a method is presented and illustrated whereby the response of impulsively loaded, perfectly plastic rate sensitive circular membranes. The results are also pertinent for circular plates if final deflections of two or more thicknesses occur since membrane action dwarfs any bending effects. Correlations of predicted deflections with a series of experimental results [5] are good and comparable to those obtained by Symonds and Wierzbicki [9] using a different simplifying procedure. A useful simple formula is derived with an overall rate sensitivity factor that should apply to steel and titanium plates (equation (12)). This formula also demonstrated good correlation with experimental results (See dashed lines in Figs. 3–8.)

Downloaded 02 May 2010 to 171.66.16.25. Redistribution subject to ASME license or copyright; see http://www.asme.org/terms/Terms_Use.cfm

The key to the solution of the impulsively loaded membrane problem which is solved using a modal approximation technique is the very trivial estimation of the maximum strain rate field. This field is associated with a modal velocity magnitude of $1/\sqrt{2}$ of its original value (i.e. when half the kinetic energy of the system has been dissipated). The final deflection field is determined by equating the initial kinetic energy to the plastic work of deformation. A constant local yield stress is assumed associated with the average strain rate at each point.

Essentially the same procedure should be applicable for any other planform; for example, for an impulsively loaded rectangular membrane oriented with sides parallel to the x and y axes the modal shape pattern could be the product of parabolic functions of x and y with an open amplitude parameter. Alternatively, the shape function may be the product of sinusoidal functions in each of the coordinate directions multiplied by the amplitude parameter. The solution procedure would be completely analogous to what has been described in the paper for the circular problem. Moreover, the same methodology could be employed in shell problems. The key to all the simple approximations is the trivial estimation of the maximum strain rate field.

References

1 Jones, N., "Recent Progress in the Dynamic Plastic Behavior of Structures—Part II," *The Shock and Vibration Digest*, Vol. 13, No. 10, Oct. 1981, pp. 3-16.

2 Jones, N., "Response of Structures to Dynamic Loading," *Institute of Physics*, Conference Series No. 47, Chapter 3, 1979, pp. 254-276.

3 Symonds, P. S., and Jones, N., "Impulsive Load of Fully Clamped Beams With Finite Plastic Deflections and Strain-rate Sensitivity," *International Journal of Mechanical Sciences*, Vol. 14, 1972, pp. 49-69.

4 Jones, N., Uran, T. O., and Tekin, S. A., "The Dynamic Plastic Behavior of Fully Clamped Rectangular Plates," *International Journal of Solids and Structures*, Vol. 6, 1970, pp. 1499-1512.

5 Bodner, S. R., and Symonds, P. S., "Experiments on Viscoplastic Response of Circular Plates to Impulsive Loading," *Journal of Mechanics and Physics of Solids*, Vol. 27, 1979, pp. 91-113.

6 Bednarski, T., "The Dynamic Deformation of a Circular Membrane," *International Journal of Mechanical Sciences*, Vol. 11, Dec. 1969, pp. 949-959.

7 Martin, J. B., and Symonds, P. S., "Mode Approximations for Impulsively Loaded Rigid Plastic Structures," *Journal of Engineering Mechanics Division*, Proceedings of the American Society of Civil Engineers, Vol. 92, 1966, pp. 43-66.

8 Chon, C. T., and Symonds, P. S., "Large Dynamic Plastic Deflection of Plates by Mode Method," *Journal of the Engineering Mechanics Division*, Proceedings of the American Society of Civil Engineers, Vol. 103, Feb. 1977, pp. 169-187.

9 Symonds, P. S., and Wierzbicki, T., "Membrane Mode Solutions for Impulsively Loaded Circular Plates," ASME JOURNAL OF APPLIED MECHANICS, Vol. 46, No. 1, 1979, pp. 58-64.

10 Perrone, N., "On a Simplified Method for Solving Impulsively Loaded Structures of Sensitive Materials," ASME JOURNAL OF APPLIED MECHANICS, Vol. 32, 1965, pp. 489-492.

11 Perrone, N., and Bhadra, P., "A Simplified Method to Account for Plastic Rate Sensitivity With Large Deformations," ASME JOURNAL OF APPLIED MECHANICS, Vol. 46, 1979, pp. 811-816.

12 Wojno, W., and Wierzbicki, T., "On Perturbations Solutions for Impulsively Loaded Viscoplastic Structures," *Journal of Applied Mathematics and Physics (ZAMP)*, Vol. 30, 1979, pp. 41-55.

13 Perrone, N., "Response of Rate Sensitive Frames to Impulsive Load," *Journal of the Engineering Mechanics Division*, Proceedings of the American Society of Civil Engineers, Vol. 97, 1971, pp. 49-62.

14 Wu, R. W. H., "The Dynamic Plastic Large Deflections of Clamped Rectangular Plate," ASME JOURNAL OF APPLIED MECHANICS, Vol. 41, No. 2, 1974, pp. 531-533.

15 Tuomala, N. T. E., and Mikkola, M. J., "Transient Dynamic Large Deflection Analysis of Elastic Viscoplastic Plates by the Finite Element Method," *International Journal of Mechanical Sciences*, Vol. 22, 1980, pp. 151-166.

16 Wierzbicki, T., and Akerstrom, T., "Dynamic Crushing of Strain Rate Sensitive Box Columns," *Proceedings of Second International Conference on Vehicle Structural Mechanics*, Society of Automotive Engineers, Paper No. 770592, 1977, pp. 19-31.

17 Perrone, N., "Dynamic Plastic Energy Absorption in Vehicle Impact," Proceedings of Euromech 121 meeting, Warsaw, Poland, 1980.

18 Shaw, F. S., and Perrone, N., "A Numerical Solution for the Nonlinear Deflection of Membranes," ASME JOURNAL OF APPLIED MECHANICS, Vol. 21, 1954, pp. 117-208.

19 Perrone, N., "Thick Walled Rings For Energy Absorbing Bridge Rail Systems," Federal Highway Administration Report RD73-49, Dec. 1972.

20 Michie, J. D., "Development of a New Energy Absorbing Bridge Railing," Quarterly Report No. 2, Department of Transportation project FH-11-7985, July 1973.

21 Carney III, J. F., and Sazinski, R. J., "Portable Energy Absorbing System for Highway Service Vehicles," *Transportation Engineering Journal*, Proceedings of American Society of Civil Engineers, Vol. 104, July 1978, pp. 407-421.

Downloaded 02 May 2010 to 171.66.16.25. Redistribution subject to ASME license or copyright; see http://www.asme.org/terms/Terms_Use.cfm

Adnan H. Nayfeh
Mem. ASME

Michael S. Hartle

College of Engineering,
Yarmouk University,
Irbid, Jordan

Dynamic Characteristics of Large Repetitive Framelike Structures

Using a building block approach and starting with a single element, expressions for the energy of various two-dimensional frametype gridwork configurations are derived. These are then used to develop energy equivalent continua for the gridworks. Equations of motion and associated boundary conditions are obtained for the continua. Some dynamic characteristics of these continua are investigated and compared with corresponding results obtained from finite element codes and also with some available theoretical predictions.

1 Introduction

The coming years will see an increasing utilization of space through the use of very large, lightweight structures constructed in orbit for such purposes as antennas, energy collection platforms, and work stations [1–5]. It will be most desirable that these structures be made of repeating subassemblies in order to aid in the ease of construction, minimize fabrication costs, and reduce complications in analysis. These subassemblies will be composed of individual discrete members having identical geometric and material properties.

To assess the utility of such discrete structures, complete understanding of their mechanical (both static and dynamic) and thermal behavior is needed. A quick review of the existing literature reveals three major possible techniques for analyzing lattice structures. These consist of the direct methods, also known by the matrix structural analysis method [6–8], the discrete field methods [9–17], and the continuum methods [18–33].

The direct methods are characterized by writing the system of equations of equilibrium and compatibility at each node and solving the resulting system to obtain nodal displacements and member forces. This of course applies to either repetitive or nonrepetitive structures. The discrete field methods, on the other hand, are attractive for repetitive structures where a representative unit cell of the structure is isolated and its equations of motion are written in terms of differential (in time) finite difference (in space) format. The utility of this approach is somewhat limited. It is mostly applicable to very simple discrete structures; specifically for the (0, 90 deg) (orthogonal) layups. Closed-form solutions of the difference equations pertaining to the free vibrations of the (0, 90 deg) layups have been reported by Ellington and McCallion [14], Wah [15], and Smith and Dean [16] (see also [17] for other references).

The continuum methods provide practical alternatives to the preceding methods especially if one is interested in describing the overall behavior of repetitive structures. In its broadest sense the continuum approach is not unique. In fact, it borrows most of its fundamental ideas from the other two methods. For instance, in the case of repetitive structures, a representative repeating cell can be isolated and studied by the direct method. If one then relates its force or deformation characteristic (or both) to that of similar element of the continuum, one can obtain the effective continuum properties. A second approach to the continuum modeling involves the expansion in Taylor series of the finite difference equations obtained using the discrete field methods [12].

In three recent papers [18–20] we introduced a straightforward construction procedure to derive continuum equivalence of discrete pin-jointed and rigid-jointed repetitive structures. For pin-jointed structures we outline the method as follows: once the actual structure is specified, symmetry consideration are used to identify its independent property constants. The actual values of these constants are constructed in accordance with a building block approach consisting of the following three consecutive steps: (*a*) all sets of parallel members are identified; (*b*) unidirectional "effective continuum" properties are derived for each of these sets; and (*c*) orthogonal transformations are finally used to determine the contribution of each set to the overall effective continuum properties of the structure. Here the term properties is general and includes mechanical (stiffnesses), thermal (coefficients of thermal expansions), and material densities. The method is then applied to a variety of structures.

In [20] we extended the analysis of [18, 19] to derive the effective properties of rigid-jointed (framelike) repetitive structures. This differed substantially from the corresponding analysis of trusslike structures because the influence of in-plane bending rigidities to the structure had to be included. The fact that the individual rod in a rigid-jointed array can resist in-plane bending dictated that the smallest subcell of the structure, which could be used for the building block approach, was no longer unidirectional and thus had to be a two-dimensional substructure. The simplest basic two-

Contributed by the Applied Mechanics Division and presented at the 1984 PVP Conference and Exhibition, Joint with Applied Mechanics Division and Materials Division, San Antonio, Texas, June 17–21, 1984 of THE AMERICAN SOCIETY OF MECHANICAL ENGINEERS.

Discussion on this paper should be addressed to the Editorial Department, ASME, United Engineering Center, 345 East 47th Street, New York, N.Y. 10017, and will be accepted until two months after final publication of the paper itself in the JOURNAL OF APPLIED MECHANICS. Manuscript received by ASME Applied Mechanics Division, December, 1982; final revision, June, 1983. Paper No. 84-APM-35.

Copies will be available until February, 1985.

Copyright © 1984 by ASME
Downloaded 02 May 2010 to 171.66.16.25. Redistribution subject to ASME license or copyright; see http://www.asme.org/terms/Terms_Use.cfm

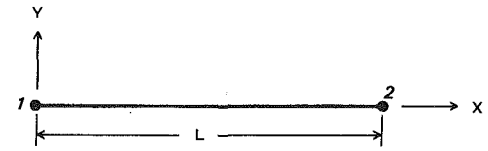


Fig. 1 Single beam element

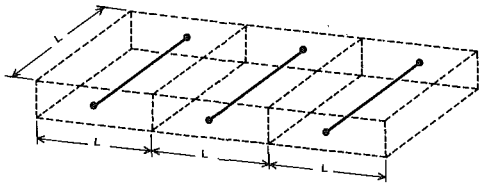


Fig. 2 Single element configuration

dimensional frame structures are the (0 deg, 90 deg) and (0 deg, ±60 deg) layups. Effective properties for these simple structures were constructed using the direct analysis method. The derived effective properties were then used in a building block format to derive the effective properties of more complicated two and three-dimensional structures. This last step was done by employing the orthogonal transformation.

Another approach which has recently been widely utilized in developing substitute continuums to discrete systems is the use of the energy equivalence. Essentially, this amounts to equating the kinetic and strain energies of the repeating discrete cell to those of the similar continuum element. Previous studies that utilized the energy equivalence approach include the works of Askar and Cakmak [26], Bazant and Christensen [27, 28], Sun and Yang [29], Noor et al. [30–32], and Nemeth [33]. Askar and Cakmak derived equations of motion with a microstructure for a (0, 90 deg, ±45 deg) layup model. Bazant and Christensen derived an equivalent micropolar continuum for large grid frameworks to solve the extensional buckling of a multistory, multibay, rectangular frames. Sun and Yang established a two-dimensional, in-plane continuum model with couple-stresses for a (0 deg, 90 deg) layup. Noor et al. constructed the equivalent continuum of a double layer grid assuming all joints to be pinned. In [32], Noor and Nemeth developed micropolar models for large repetitive beamlike planar lattices with rigid joints. Nemeth [33] derived the strain energy of the single layer grids with rigid joints in terms of its beam members strains and curvatures. These are then expressed in terms of the strains and curvatures of the continuum.

The present study utilizes a combination of the linear transformation and the energy approach and presents a simple method to model the dynamic behavior of large rigid-jointed lattices as continuous media with microstructure. This is done by first forming discrete expressions for the strain and kinetic energies of a single unrotated element in terms of its nodal displacements, rotations, and their respective time derivatives. While keeping the nodal displacements and rotations to be independent of each other, the discrete energy expressions are changed to continuous forms by expanding these nodal displacement and rotations in Taylor series about a suitable origin. This establishes the equivalent continuum energy for the single bar. Following [18–20] equivalent continuum energies for other gridwork configurations can be formed from this single-element energy by making use of the building block approach, which can be summarized as follows: (*i*) The repeating unit cell of the structure is identified. (*ii*) Continuum energies for each individual element in the unit cell are obtained by using orthogonal transformations on the single unrotated element's continuum energy. (*iii*) Superposing the individual element energies and dividing by the area occupied by the unit cell, the continuum energy densities of the structure is obtained.

These energy densities can then be employed to find equations of motion for the continuum through the use of Hamilton's principle. Related boundary conditions will result at the same time. The equivalent continuum contains the same amount of energy as does the original gridwork; therefore, the dispersion relations and frequencies obtained from the equations of motion should be comparable to those of the gridwork itself. In other words, beginning with the mass and stiffness matrices of a single element only, certain characteristics of the dynamic behavior of almost any regular gridwork configuration can be obtained.

Finally, the results of our dynamic analysis are compared with the results obtained by Ellington and McCallion [14] and Wah and Calcote [17] for the vibration frequencies of the orthogonal structure (0, 90 deg) who used the finite difference calculus approach. Agreements are found to be very good. Our general results are also compared to the results of finite element analysis. As will be seen, agreements are found to be good, especially when the wave lengths are large in comparison to the size of the unit cell.

2 Single Element

It is desired to obtain expressions for the strain kinetic energies of a single unrotated beam column element (shown in Fig. 1) using the continuous displacement and velocity functions. These continuous energy functions can then be used as building blocks in constructing other continuous energy functions for the unit cell of a configuration of interest. The equations of motion for the single element can also be obtained from these energy equations so that even the unrealistic vibration characteristics of individual sets of parallel members when modeled as a continuum can be examined.

2.1 Discrete Forms. The first step in obtaining the continuous forms of strain and kinetic energy for the single unrotated element is to use the stiffness matrix and consistent mass matrix of the element to find the discrete forms of these energies. The strain energy is calculated using the equation [7]

$$U = \frac{1}{2}\{d\}^T[K]\{d\} \tag{1}$$

where $\{d\}$ is a column vector of nodal displacements and rotations, $\{d\}^T$ denotes the transpose of this vector, and $[K]$ is the stiffness matrix of the element.

The kinetic energy is calculated using the equation [34]

$$T = \frac{1}{2}\{\dot{d}\}^T[M]\{\dot{d}\} \tag{2}$$

where $\{\dot{d}\}$ is a column vector of nodal velocities and $[M]$ is the consistent mass matrix of the element. It should be noted that all torsion terms in the mass matrix are neglected.

2.2 Continuous Forms. To change these discrete equations to continuous ones, the nodal displacements, rotations, and velocities are expanded in a Taylor series about node 1 [20, 29]. For future interest in investigating out-of-plane vibrations, and since the transverse vibration of a continuum is a higher order phenomena than the in-plane vibration of the continuum, the transverse displacement variable, w, is expanded as a second-order Taylor series while all other displacements are expanded as first-order Taylor series. In addition, after substituting the Taylor series expansions in the energy equations, each term is examined individually and only the lowest order parts of the in-plane vibration terms are retained while all parts of the transverse vibration terms are kept.

Downloaded 02 May 2010 to 171.66.16.25. Redistribution subject to ASME license or copyright; see http://www.asme.org/terms/Terms_Use.cfm

The Taylor series expansions used for the displacement and rotation variables are

$$u_2 - u_1 = Lu_{,x}, \qquad \theta_2^x - \theta_1^x = L\theta^x{}_{,x}$$
$$v_2 - v_1 = Lv_{,x}, \qquad \theta_2^y - \theta_1^y = L\theta^y{}_{,x}$$
$$w_2 - w_1 = Lw_{,x} + \frac{L^2}{2} w_{,xx}, \qquad \theta_2^z - \theta_1^z = L\theta^z{}_{,x} \tag{3}$$

where L is the length of the beam. Similar expansions are used for the velocities. Making these substitutions in the expanded forms of (1) and (2) and dividing by the effective area occupied by one element, L^2, in the array of elements as shown in Fig. 2, the resulting continuous form of the single-element continuum strain and kinetic energy densities are given by

$$\begin{aligned} U = \frac{1}{2}\Big\{ & \frac{AE}{L}(u_{,x})^2 + \frac{12EI_z}{L^3}(v_{,x})^2 + \frac{12EI_y}{L^3}(w_{,x})^2 \\ & + \frac{12EI_y}{L^2} w_{,x} w_{,xx} + \frac{3EI_y}{L}(w_{,xx})^2 \\ & + \frac{4EI_z}{L}(\theta^z{}_{,x})^2 + \frac{12EI_z}{L^3}\theta^{z2} + \frac{4EI_y}{L}(\theta^y{}_{,x})^2 \\ & + \frac{12EI_y}{L^2}\theta^{y2} - \frac{24EI_z}{L^3}\theta^z v_{,x} + \frac{24EI_y}{L^3}\theta^y w_{,x} \\ & + \frac{GJ}{L}(\theta^x{}_{,x})^2 + \frac{12EI_y}{L^2}\theta^y\theta^y{}_{,x} + \frac{12EI_y}{L^2} w_{,x}\theta^y{}_{,x} \\ & + \frac{12EI_y}{L^2}\theta^y w_{,xx} + \frac{6EI_y}{L}\theta^y{}_{,x} w_{,xx}\Big\} \end{aligned} \tag{4}$$

$$\begin{aligned} T = \frac{\rho AL}{2}\Big\{ & \frac{1}{3}(\dot{u}_{,x})^2 + \frac{13}{35}(\dot{v}_{,x})^2 + \frac{13}{35}(\dot{w}_{,x})^2 \\ & + \frac{13L}{35}\dot{w}_{,x}\dot{w}_{,xx} + \frac{13L^2}{140}(\dot{w}_{,xx})^2 + \frac{1}{L^2}(\dot{u}^2 + \dot{v}^2 + \dot{w}^2) \\ & + \frac{L^2}{105}(\dot{\theta}^z{}_{,x})^2 + \frac{1}{210}\dot{\theta}^{z2} + \frac{L^2}{105}(\dot{\theta}^y{}_{,x})^2 + \frac{1}{210}\dot{\theta}^{y2} \\ & - \frac{1}{6}\dot{v}\,\dot{\theta}^z{}_{,x} - \frac{3}{70}\dot{\theta}^z\dot{v}_{,x} + \frac{1}{6}\dot{w}\,\dot{\theta}^y{}_{,x} + \frac{3}{70}\dot{\theta}^y\dot{w}_{,x} \\ & + \frac{1}{L}\dot{w}\,w_{,x} + \frac{1}{2}\dot{w}\,w_{,xx} + \frac{L}{210}\dot{\theta}^y\dot{\theta}^y{}_{,x} + \frac{11L}{105}\dot{w}_{,x}\dot{\theta}^y{}_{,x} \\ & + \frac{11L^2}{210}\dot{w}_{,xx}\dot{\theta}^y{}_{,x}\frac{\partial\dot{\theta}^y}{\partial x} + \frac{3L}{140}\dot{\theta}^y\dot{w}_{,xx} \end{aligned} \tag{5}$$

2.3 Equations of Motion. Having obtained the energy densities for the single element they can now be used to find the displacement equations of motion for this element. This is done by making use of Hamilton's principle, which can be stated as

$$\int_{t_i}^{t} dt \int_R \int (\delta T - \delta U)\, dxdy + \int_{t_i}^{t} dt\, \delta W_e = 0 \tag{6}$$

The first term of this equation contains the variations of the kinetic and strain energy densities just found and the second term contains the work done by the external forces and moments acting on the region, R and its boundary, C. This variation of work is expressed as

$$\begin{aligned} \delta W_e = & \int_R \int (F_x\delta u + F_y\delta v + F_z\delta w + M_z\delta\theta^z)\, dS \\ & + \oint_C (f_x\delta u + f_y\delta v + f_z\delta w + m_z\delta\theta^z)\, dC \end{aligned} \tag{7}$$

Using integration by parts to obtain variations of the displacements and rotations and then setting the coefficients of these variations to zero results in three in-plane and one out-of-plane equation of motion. Since we are interested in obtaining results for plane harmonic motions and for the sake of brevity we will only list the equations of motions. The associate boundary conditions can be easily obtained and for space saving, will not be listed here. The in-plane equations of motion for the single element are then

$$\frac{EA}{L}u_{,xx} - \frac{\rho A}{L}\ddot{u} + \frac{\rho AL}{3}u_{,xx} + F_x = 0 \tag{8}$$

$$\begin{aligned} & \frac{12EI_z}{L^3}(v_{,xx} - \theta^z{}_{,x}) + \frac{13\rho AL}{35}\left(\ddot{v}_{,xx} + \frac{1}{6}\ddot{\theta}^z{}_{,x}\right) \\ & \quad - \frac{\rho A}{L}\ddot{v} + F_y = 0 \end{aligned} \tag{9}$$

$$\begin{aligned} & \frac{4EI_z}{L}\theta^z{}_{,xx} + \frac{12EI_z}{L^3}(v_{,x} - \theta^z) \\ & \quad + \frac{\rho AL}{105}\left(L^2\ddot{\theta}^z{}_{,x} - \frac{1}{2}\ddot{\theta}^z - \frac{13}{2}\ddot{v}_{,x}\right) + M_z = 0 \end{aligned} \tag{10}$$

and the out-of-plane equations of motions

$$\begin{aligned} & \frac{12EI_y}{L^3}(w_{,xx} + \theta^y{}_{,x}) - \frac{3EI_y}{L}(w_{,xxxx} + \theta^y{}_{,xxx}) \\ & - \frac{\rho AL}{210}(27\ddot{w}_{,xx} + 13\ddot{\theta}^y{}_{,x}) - \frac{\rho AL^3}{420}(39\ddot{w}_{,xxxx} \\ & + 11\ddot{\theta}^y{}_{,xxx}) + \frac{\rho AL^3}{24}\ddot{\theta}^y{}_{,xx} - \frac{\rho A}{L}\ddot{w} + F_z = 0 \end{aligned} \tag{11}$$

$$\frac{GJ}{L}\theta^x{}_{,xx} + C\rho AL^3\ddot{\theta}^x{}_{,xx} - B\rho AL\ddot{\theta}^x + M_x = 0 \tag{12}$$

$$\begin{aligned} & \frac{EI_y}{L}(3w_{,xxx} + 4\theta^y{}_{,xx}) - \frac{12EI_y}{L^3}(w_{,x} + \theta^y) \\ & + \frac{\rho AL}{105}\left(L^2\ddot{\theta}^y{}_{,xx} - \frac{1}{2}\ddot{\theta}^y + \frac{13}{2}\ddot{w}_{,x}\right) \\ & + \frac{\rho AL^2}{24}\ddot{w}_{,xx} + \frac{11\rho AL^3}{420}\ddot{w}_{,xxx} + M_y = 0 \end{aligned} \tag{13}$$

3 0, 90 deg Configuration

Beginning from the single element strain and kinetic energy expressions, the strain and kinetic energy densities and the equations of motion of various regular gridwork configurations can be formed. The one that will be examined now is the 0, 90 deg configuration (Fig. 3) which consists of two perpendicular sets of parallel members.

The unit cell of the 0, 90 deg gridwork is shown in Fig. 4. Using orthogonal transformations, superposing, and multiplying by the ratio of the effective area occupied by the single element to that occupied by the 0, 90 deg unit cell gives the strain and kinetic energy densities for the 0, 90 deg gridwork. The generalized orthogonal transformations can be conveniently expressed as

$$u_i' = u_j\beta_{ij} \qquad i,j = 1,2,3,4 \tag{14a}$$
$$u_{i,j}' = u_{k,l}\beta_{ik}\beta_{jl} \qquad i,k = 1,2,3,4;\ i,l = 1,2 \tag{14b}$$
$$u_{i,jk}' = u_{l,mn}\beta_{il}\beta_{jm}\beta_{kn} \qquad i,l = 1,2,3,4;\ j,k,m,n = 1,2 \tag{14c}$$

where the usual summation convention holds; u_1–u_4 are the four variables u, v, w, and θ^z, respectively; the prime denotes

Downloaded 02 May 2010 to 171.66.16.25. Redistribution subject to ASME license or copyright; see http://www.asme.org/terms/Terms_Use.cfm

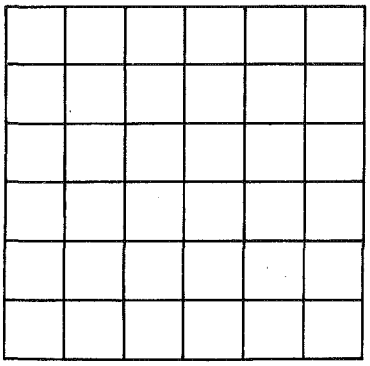


Fig. 3 0, 90 deg configuration

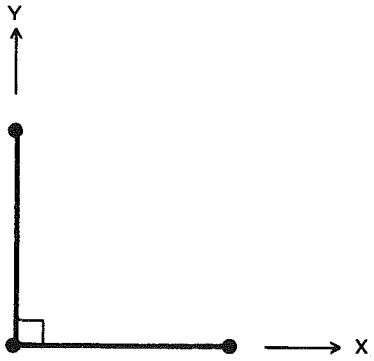


Fig. 4 0, 90 deg unit cell (all elements length L)

the variables being transformed; and β_{ij} represents the cosine of the angle between the i axis and the j axis. Similar transformations hold for the velocity variables.

For the element at 90 deg the direction cosines are

$$\beta_{ij} = \begin{bmatrix} 0 & 1 & 0 & 0 \\ -1 & 0 & 0 & 0 \\ 0 & 0 & 1 & 0 \\ 0 & 0 & 0 & 1 \end{bmatrix} \quad i,j = 1,2,3,4 \tag{15}$$

Forming the variations of the strain energy and kinetic energy densities as was done for the single element, and using these variations in the equation of Hamilton's principle (7) gives the equations of motion and boundary conditions for the 0, 90 deg configuration. The in-plane equations of motion are

$$\frac{EA}{L}u_{,xx} + \frac{12EI_z}{L^3}(u_{,yy} + \theta^z{}_{,y}) - \frac{2\rho A}{L}\ddot{u} + \frac{13\rho AL}{35}\left(\ddot{u}_{,yy} - \frac{1}{6}\ddot{\theta}^z{}_{,y}\right) + \frac{\rho AL}{3}\ddot{u}_{,xx} + F_x = 0 \tag{16}$$

$$\frac{EA}{L}v_{,yy} + \frac{12EI_z}{L^3}(v_{,xx} - \theta^z{}_{,x}) - \frac{2\rho A}{L}\ddot{v} + \frac{13\rho AL}{35}\left(\ddot{v}_{,xx} + \frac{1}{6}\ddot{\theta}^z{}_{,x}\right) + \frac{\rho AL}{3}\ddot{v}_{,yy} + F_y = 0 \tag{17}$$

$$\frac{4EI_z}{L}(\theta^z{}_{,xx} + \theta^z{}_{,yy}) - \frac{12EI_z}{L^3}(2\theta^z + u_{,y} - v_{,x}) + \frac{\rho AL^3}{105}(\ddot{\theta}^2{}_{,xx} + \ddot{\theta}^z{}_{,yy}) + \frac{\rho AL}{105}[13(\ddot{u}_{,y} - \ddot{v}_{,x}) - 2\ddot{\theta}^z] + M_z = 0 \tag{18}$$

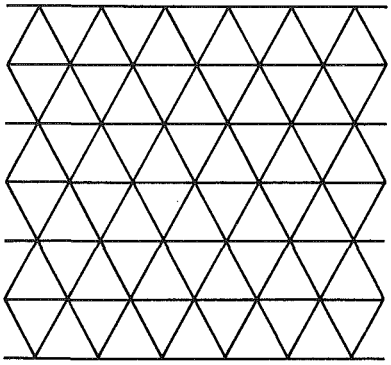


Fig. 5 0, ±60 deg configuration

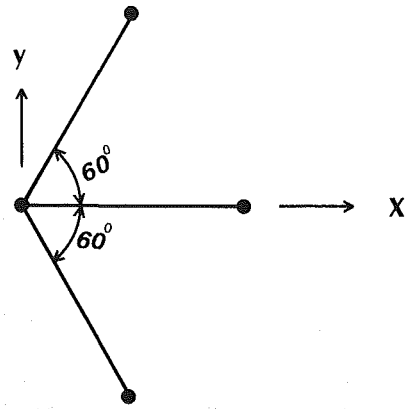


Fig. 6 0±60 deg unit cell (all elements length L)

and the out-of-plane equations

$$\frac{12EI_y}{L^3}(w_{,xx} + w_{,yy} + \theta^y{}_{,x} - \theta^x{}_{,y}) - \frac{3EI_y}{L}(w_{,xxxx} + w_{,yyyy} - \theta^y{}_{,xxx} + \theta^x{}_{,yyy}) - \frac{\rho AL}{210}(27\ddot{w}_{,xx} + 27\ddot{w}_{,yy} + 13\ddot{\theta}^y{}_{,x} - 13\ddot{\theta}^x{}_{,y}) - \frac{\rho AL^3}{420}(39\ddot{w}_{,xxxx} + 39\ddot{w}_{,yyyy} + 11\ddot{\theta}^y{}_{,xxx} - \ddot{\theta}^x{}_{,yyy}) - \frac{2\rho Aw}{L} - \frac{\rho AL^2}{2v}(\ddot{\theta}^x{}_{,yy} - \ddot{\theta}^y{}_{,xx}) + F_z = 0 \tag{19}$$

$$\frac{EI_y}{L}(4\theta^x{}_{,yy} - 3w_{,yyy}) + \frac{12EI_y}{L^3}(w_{,y} - \theta^x) + \frac{GJ}{L}\theta^x{}_{,xx} - \frac{\rho AL^2}{24}\ddot{w}_{,yy} - \frac{11\rho AL^3}{420}\ddot{w}_{,yyy} - \frac{13\rho AL}{210}\ddot{w}_{,y} + \frac{\rho AL^4}{105}\ddot{\theta}^x{}_{,yy} - \left(\frac{\rho AL}{210} + B\rho AL\right)\ddot{\theta}^x + C\rho AL^3\ddot{\theta}^x{}_{,xx} + M_x = 0. \tag{20}$$

$$\frac{EI_y}{L}(4\theta^y{}_{,xx} + 3w_{,xxx}) - \frac{12EI_y}{L^3}(w_{,x} + \theta^y) + \frac{GJ}{L}\theta^y{}_{,yy} - \frac{13\rho AL}{210}\ddot{w}_{,x} + \frac{\rho AL^2}{24}\ddot{w}_{,x} + \frac{11\rho AL^3}{420}\ddot{w}_{,xxx} + \frac{\rho AL^y}{105}\ddot{\theta}^y{}_{,xx} - \left(\frac{\rho AL}{210} + B\rho AL\right)\ddot{\theta}^y + C\rho AL^3\ddot{\theta}^y{}_{,yy} + M_y = 0 \tag{21}$$

Downloaded 02 May 2010 to 171.66.16.25. Redistribution subject to ASME license or copyright; see http://www.asme.org/terms/Terms_Use.cfm

Here we indicate that the in-plane equations of motion (16)-(18) and boundary conditions are identical to those found by Sun and Yang [29].

4 0 ± 60 deg Configuration

Another configuration examined is the $0, \pm 60$ deg configuration shown in Fig. 5. This is particularly interesting gridwork due to its isotropic properties [20]. The unit cell for this gridwork configuration consists of three individual members, two requiring transformations. The same orthogonal transformations (14) apply as before. The direction cosines for the $+60$ deg transformation are

$$\beta_{ij} = \begin{bmatrix} \frac{1}{2} & \frac{\sqrt{3}}{2} & 0 & 0 \\ -\frac{\sqrt{3}}{2} & \frac{1}{2} & 0 & 0 \\ 0 & 0 & 1 & 0 \\ 0 & 0 & 0 & 1 \end{bmatrix} \tag{22}$$

The direction cosines for the -60 deg can be obtained by changing the signs of β_{12} and β_{21} in (22). Multiplying the result by $2/\sqrt{3}$, which is the ratio between effective areas occupied by the single element and the $0, \pm 60$ deg unit cell, gives the strain energy density and kinetic energy density for the $0, \pm 60$ deg configuration.

Again, the equations of motion and boundary conditions for the $0, \pm 60$ deg configuration are obtained, as with the previous cases, by making use of Hamilton's principle (7). The resulting in-plane equations of motion are

$$\left(\frac{9AE}{\sqrt{43}L} + \frac{9EI_z}{\sqrt{3}L^3}\right)u_{,xx} + \left(\frac{3AE}{4\sqrt{3}L} + \frac{27EI_z}{\sqrt{3}L^3}\right)u_{,yy}$$
$$+ \left(\frac{3AE}{2\sqrt{3}L} - \frac{18EI_z}{\sqrt{3}L^3}\right)v_{,xy} + \frac{36EI_z}{\sqrt{3}L^3}\theta^z{}_{,y}$$
$$+ \frac{36\rho AL}{35\sqrt{3}}\ddot{u}_{,xx} + \frac{38\rho AL}{35\sqrt{3}}\ddot{u}_{,yy} - \frac{2\rho AL}{35\sqrt{3}}\ddot{v}_{,xy}$$
$$- \frac{6\rho A}{\sqrt{3}L}\ddot{u} - \frac{13AL}{70\sqrt{3}}\ddot{\theta}^z{}_{,y} + F_x = 0 \tag{23}$$

$$\left(\frac{3AE}{4\sqrt{3}L} + \frac{27EI_z}{\sqrt{3}L^3}\right)v_{,xx} + \left(\frac{9AE}{4\sqrt{3}L} + \frac{9EI_z}{\sqrt{3}L^3}\right)v_{,yy}$$
$$+ \left(\frac{3AE}{2\sqrt{3}L} - \frac{18EI_z}{\sqrt{3}L^3}\right)u_{,xy} - \frac{36EI_z}{\sqrt{3}L^3}\theta^z{}_{,x}$$
$$+ \frac{38\rho AL}{35\sqrt{3}}\ddot{v}_{,xx} + \frac{36\rho AL}{35\sqrt{3}}\ddot{v}_{,yy} - \frac{2\rho AL}{35\sqrt{3}}\ddot{u}_{,xy}$$
$$- \frac{6\rho A}{\sqrt{3}L}\ddot{v} + \frac{13\rho AL}{70\sqrt{3}}\ddot{\theta}^z{}_{,x} + F_y = 0 \tag{24}$$

$$\frac{12EI_z}{\sqrt{3}L} - \frac{72EI_z}{\sqrt{3}L^3}\theta^z - \frac{36EI_z}{\sqrt{3}L^3}(u_{,v} - v_{,x})$$
$$+ \frac{\rho AL^3}{35\sqrt{3}}\ddot{\theta}^z + \frac{13\rho AL}{70\sqrt{3}}(\ddot{u}_{,y} - \ddot{v}_{,x}) + M_z = 0 \tag{25}$$

and the out-of-plane equations

$$\frac{36EI_y}{\sqrt{3}L^3}(w_{,xx} + w_{,yy} - \theta^x{}_{,y} + \theta^y{}_{,x})$$
$$- \frac{27EI_y}{4\sqrt{3}L}(w_{,xxxx} + 2w_{,xxyy} + w_{,yyyy} - \theta^x{}_{,xxy}$$
$$+ \theta^y{}_{,xyy} + \theta^y{}_{,xxx} - \theta^x{}_{,yyy}) + \frac{13\rho AL}{70\sqrt{3}}(6\ddot{w}_{,xx}$$
$$+ 6\ddot{w}_{,yy} - \ddot{\theta}^y{}_{,x} + \ddot{\theta}^x{}_{,y}) - \frac{117\rho AL^3}{560\sqrt{3}}(\ddot{w}_{,xxxx}$$
$$+ 2\ddot{w}_{,xxyy} + \ddot{w}_{,yyyy}) + \frac{33\rho AL^3}{560\sqrt{3}}(\ddot{\theta}^x{}_{,xxy}$$
$$- \ddot{\theta}^y{}_{,xxx} - \ddot{\theta}^y{}_{,xyy} + \ddot{\theta}^x{}_{,yyy}) - \frac{6\rho A}{\sqrt{3}L^2}\ddot{w}$$
$$- \frac{3\rho AL}{2\sqrt{3}}(\ddot{w}_{,xx} + \ddot{w}_{,yy}) - \frac{\rho AL^2}{8\sqrt{3}}\ddot{\theta}^x{}_{,xy}$$
$$+ \frac{35\rho AL^2}{336\sqrt{3}}\ddot{\theta}^y{}_{,xx} + \frac{\rho AL^2}{16\sqrt{3}}\ddot{\theta}^y{}_{,yy} + F_z = 0. \tag{26}$$

$$\frac{\sqrt{3}EI_y}{L}\left(\theta^x{}_{,xx} + 3\theta^x{}_{,yy} - 2\theta^y{}_{,xy} - \frac{12\theta^x}{L^2}\right)$$
$$+ \frac{\sqrt{3}}{4}\frac{GJ}{L}(3\theta^x{}_{,xx} + \theta^x{}_{,yy} + 2\theta^y{}_{,xy}) - \frac{27EI_y}{4\sqrt{3}L}(w_{,xxy}$$
$$+ w_{,yyy}) + \frac{36EI_y}{\sqrt{3}L^2}w_{,y} + \frac{\rho AL^3}{140\sqrt{3}}(\ddot{\theta}^x{}_{,xx} + 3\ddot{\theta}^x{}_{,yy}$$
$$- 2\ddot{\theta}^y{}_{,xy}) + \frac{3C\rho AL^3}{4\sqrt{3}}(\ddot{\theta}^x{}_{,yy} + 3\ddot{\theta}^x{}_{,xx} - 2\ddot{\theta}^y{}_{,xy})$$
$$- \left(\frac{\rho AL}{70\sqrt{3}} + \frac{3B\rho AL}{\sqrt{3}}\right)\ddot{\theta}^x - \frac{13\rho AL}{70\sqrt{3}}\ddot{w}_{,y} - \frac{\rho AL^2}{8\sqrt{3}}\ddot{w}_{,xy}$$
$$- \frac{33\rho AL^3}{560\sqrt{3}}(\ddot{w}_{,xxy} + \ddot{w}_{,yyy}) + M_x = 0 \tag{27}$$

$$\frac{3EI_y}{L}(\theta^y{}_{,yy} + 3\theta^y{}_{,xx} - 2\theta^x{}_{,xy})$$

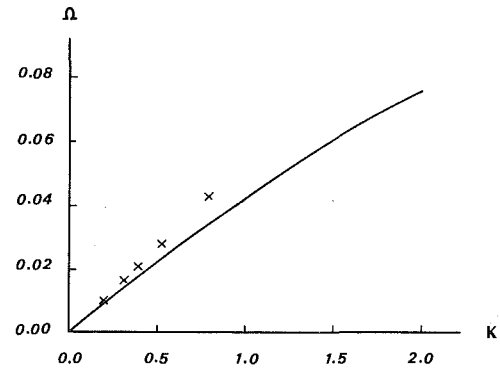


Fig. 7 Ω Versus K for 0, 90 deg configuration, in-plane transverse vibrations

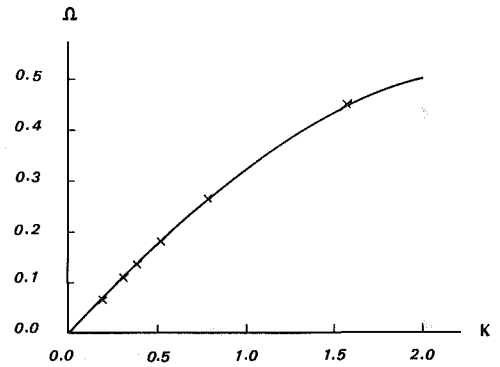


Fig. 8 Ω Versus K for $0, \pm 60$ deg configuration, in-plane transverse vibrations

Downloaded 02 May 2010 to 171.66.16.25. Redistribution subject to ASME license or copyright; see http://www.asme.org/terms/Terms_Use.cfm

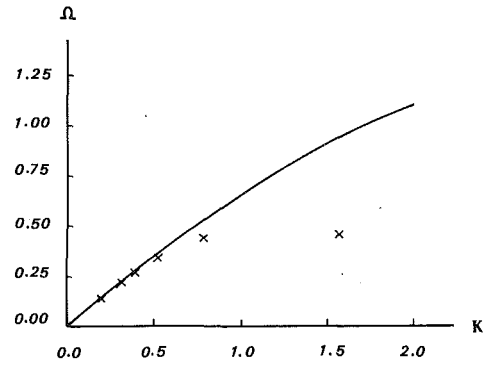


Fig. 9 Ω Versus K for 0, 90 deg configuration, longitudinal vibrations

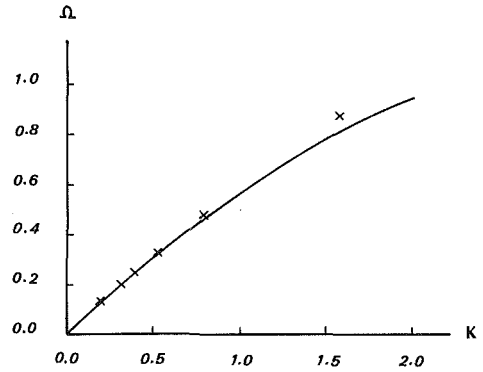


Fig. 10 Ω Versus K for 0, ±60 deg configuration, longitudinal vibrations

$$-\frac{36EI_y}{\sqrt{3}L^3}(w_{,x}+\theta^y)+\frac{\sqrt{3}}{4}\frac{GJ}{L}(\theta^y{}_{,xx}+3\theta^y{}_{,yy}$$

$$+2\theta^x{}_{,xy})+\frac{27EI_y}{\sqrt{3}L}(w_{,xyy}+w_{,xxx})$$

$$+\frac{\rho AL^3}{140\sqrt{3}}(\ddot{\theta}^y{}_{,yy}+3\ddot{\theta}^y{}_{,xx}-2\ddot{\theta}^x{}_{,xy})$$

$$+\frac{\sqrt{3}}{4}C\rho AL^3(\ddot{\theta}^y{}_{,xx}+3\ddot{\theta}^y{}_{,yy}+2\ddot{\theta}^x{}_{,xy})$$

$$-\left(\frac{\rho AL}{70\sqrt{3}}+\frac{3B\rho AL}{\sqrt{3}}\right)\ddot{\theta}^y+\frac{13\rho AL}{70\sqrt{3}}\ddot{w}_{,x}+\frac{\rho AL^2}{48\sqrt{3}}(5\ddot{w}_{,xx}$$

$$+3\ddot{w}_{,yy})+\frac{33\rho AL^2}{560\sqrt{3}}(\ddot{w}_{,xxx}+\ddot{w}_{,xyy})+M_y=0 \qquad (28)$$

5 Application of Equations

The equations of motion derived in the foregoing represent those for a continuum having energy equivalence with the discrete gridwork of interest. Therefore, the energy in the continuum due to vibratory motion is exactly what is in the gridwork, undergoing a similar vibratory motion. Because of this, relationships between frequency and wave number, and phase velocity and wave number obtained using the continuous equations are the same as for the discrete gridwork.

5.1 In-Plane Transverse Vibrations. For the case in which the gridwork is the infinite extent, a transverse vibration occurring within the plane of the gridwork can be described as

$$v=LV\sin kx\, e^{i\omega t}$$
$$\theta^z=\Theta\cos kx\, e^{i\omega t} \qquad (29)$$

where V and Θ are amplitude constants, L is the member length, k is the wave number, and ω is the angular frequency.

5.1.1 0, 90 deg Configuration. Substitution of (29) into the equations of motion (17) and (18) for the 0, 90 deg configuration, setting the external forces and moments to zero, and solving the determinant of coefficients results in the characteristic equation

$$\frac{A^2}{L^4}\left(\frac{13}{3675}K^4+\frac{827}{44100}K^2+\frac{2}{105}\right)\Omega^4-\frac{AI_z}{L^6}\left(\frac{56}{35}K^4\right.$$

$$\left.+\frac{648}{35}K^2+48\right)\Omega^2+\frac{I_z^2}{L^8}(48K^4+144K^2)=0 \qquad (30)$$

where the dimensionless frequency and wave number

$$\Omega=\frac{\omega L}{(E/\rho)^{1/2}},\quad K=kL \qquad (31)$$

are used.

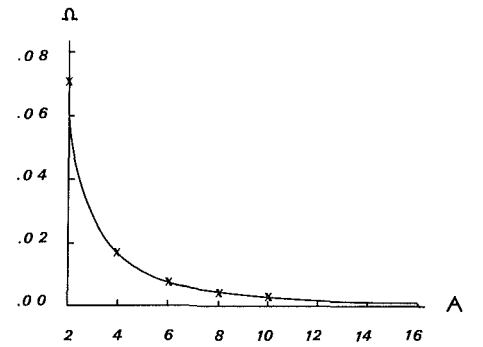


Fig. 11 Ω Versus horizontal side length for 0, 90 deg configuration, out-of-plane vibrations

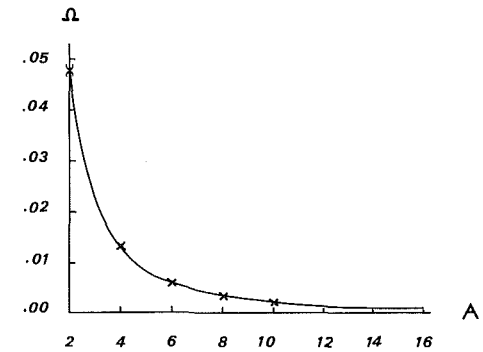


Fig. 12 Ω Versus horizontal side length for 0, ±60 deg configuration, out-of-plane vibrations

Applying the quadratic formula to obtain the roots of this equation gives the desired relationship between the nondimensional frequency and the nondimensional wave number for the 0, 90 deg configuration. Assuming a nondimensionalized area and moment of inertia of each member to be

$$A=0.5\times10^{-2}L^2,\quad I_z=0.3125\times10^{-5}L^4 \qquad (32)$$

the resulting dispersion relationship is shown in Fig. 7.

5.1.2 0, + 60 deg Configuration. Substituting (29) into the equations of motion (23) and (24) for the 0, ± 60 deg configuration and proceeding as previously, results in

$$\left(\frac{38A^2}{1225L^4}K^4+\frac{823A^2}{4900L^4}K^2+\frac{6A^2}{35L^4}\right)\Omega^4-\left[\left(\frac{3A^2}{140L^4}\right.\right.$$

$$\left.+\frac{483AI_z}{35L^6}\right)K^4+\left(\frac{3A^2}{140L^4}+\frac{5751AI_z}{35L^6}\right)K^2$$

Downloaded 02 May 2010 to 171.66.16.25. Redistribution subject to ASME license or copyright; see http://www.asme.org/terms/Terms_Use.cfm

Table 1 Comparisons With Available Theories

			Ellington and McCallion	Wah and Calcote	Present	
					General	Reduced
	n	m	u	u	u	u
	1	1	0.7853	0.7854	0.7769	0.7854
$p=q=4$	1	2	1.336	1.339	1.303	1.34
	1	3	1.924	1.963	1.902	1.987
	2	2	1.565	1.571	1.524	1.570
	2	3	2.016	2.057	1.987	2.07
	3	3	2.281	2.356	2.254	2.356
	1	1	0.7195	0.7196	0.7125	0.7196
	1	2	1.094	1.095	1.072	1.094
$p=4$	1	3	1.582	1.591	1.54	1.596
$q=5$	1	4	2.021	2.08	2.023	2.118
	2	1	1.324	1.327	1.29	1.329
	2	2	1.435	1.439	1.4	1.44
	2	3	1.736	1.748	1.69	1.748
	2	4	2.101	2.161	2.095	2.189
	3	1	1.920	1.96	1.898	1.983
	3	2	1.960	1.999	1.936	2.02
	3	3	2.104	2.15	2.07	2.159
	3	4	2.341	2.436	2.33	2.438

$$+\frac{432AI_z}{L^6}\Big]\Omega^2+\Big[\Big(\frac{324I_z^2}{L^8}+\frac{9AI_z}{L^6}\Big)K^4$$

$$+\Big(\frac{54AI_z}{L^6}+\frac{648I_z^2}{L^8}\Big)K^2\Big]=0 \tag{33}$$

The relationship between the dimensionless frequency and dimensionless wave number, using the same geometric properties as before in (31) and (32), is shown in Fig. 8.

5.2 Longitudinal Vibrations. A second type of in-plane vibration is one that is characterized by a displacement in the same direction in which the wave is moving. This motion can be described using a single displacement variable since it is assumed to be independent of the y coordinate. This displacement is described as

$$u=U\sin kx\, e^{i\omega t} \tag{34}$$

where U is an amplitude constant, k is the wave number, and ω is the angular frequency.

5.2.1 0, 90 deg Configuration. Using (34) in the equations of motion (16) for the 0, 90 deg configuration results in one equation that after nondimensionalizing and solving for the frequency yields the following relationship

$$\Omega^2=\frac{K^2}{\frac{K^2}{3}+2} \tag{35}$$

Using the properties (31) and (32) this relationship is shown in Fig. 9.

5.2.2 0, + 60 deg Configuration. Substitution of (34) into the 0, ± 60 deg in-plane equations of motion (23) gives an equation, which after nondimensionalizing, is used to obtain the relationship

$$\Omega^2=\frac{\Big(\frac{9}{4}+\frac{9I_z}{AL^2}\Big)K^2}{\frac{36}{35}K^2+6} \tag{36}$$

Using element properties (31) and (32) as before, the relationship shown in Fig. 10 is obtained.

5.3 Out-of-Plane Vibrations. Vibrations causing displacements out of the plane of the gridwork are examined now. This type of vibration must be transverse in nature due to the two dimensionality of the gridwork. A rectangular section of the gridwork, which is assumed pinned at the edges, is examined. We will limit our investigations to the case in which the terms containing time derivatives are ignored except for the leading term, which is related to $\ddot{w}$. This is done for two reasons. First, except for this leading term, all time derivate terms are of higher order and can be neglected, and second, to compare our results with similarly restricted results of Wah and Calcote [17] and Ellington and McCallion [14].

For harmonic motion solutions of equations (19)–(21), when neglecting higher order time derivatives, can be assumed as

$$w=\sum_{-\infty}^{\infty}\sum_{-\infty}^{\infty}w_0\sin\frac{n\pi x}{a}\sin\frac{m\pi y}{b}e^{i\omega t} \tag{37a}$$

$$\theta^x=\sum_{-\infty}^{\infty}\sum_{-\infty}^{\infty}\theta_0^x\sin\frac{n\pi x}{a}\cos\frac{m\pi y}{b}e^{i\omega t} \tag{37b}$$

$$\theta^y=\sum_{-\infty}^{\infty}\sum_{-\infty}^{\infty}\theta_0^y\cos\frac{n\pi x}{a}\sin\frac{m\pi y}{b}e^{i\omega t} \tag{37c}$$

where ω is circular frequency, a and b are the side lengths of the plate, and w_0, θ_0^x, θ_0^y are certain constant amplitudes. Substituting these expressions into equations (19)–(21) and setting the external forces to zero yields the characteristic equation (displayed for comparisons in the format of reference [17])

$$u^4=\frac{K_1K_2}{K_3}+\frac{T_1T_2}{T_3} \tag{38}$$

where

$$u^4=(2\rho A\omega^2L^4/EI) \tag{39a}$$

$$K_1=\Big(\frac{n\pi}{p}\Big)^3+\frac{\nu m^2n\pi^3}{pq^2},\quad K_2=\frac{12n\pi}{p}+3\Big(\frac{n\pi}{p}\Big)^3 \tag{39b}$$

$$K_3=2\Big\{4\Big(\frac{n\pi}{p}\Big)^2+12+\nu\Big(\frac{m\pi}{q}\Big)^2\Big\} \tag{39c}$$

$$T_1=\Big(\frac{m}{q}\Big)^3+\frac{\nu n^2m\pi^3}{p^2q},\quad T_2=12\frac{m\pi}{q}+3\Big(\frac{m\pi}{q}\Big)^3 \tag{39d}$$

$$T_3=2\Big\{4\Big(\frac{m\pi}{q}\Big)^2+12+\nu\Big(\frac{n\pi}{p}\Big)^2\Big\} \tag{39e}$$

and

$$\nu=\frac{GJ}{EI},\quad a=pL,\quad b=qL \tag{40}$$

Downloaded 02 May 2010 to 171.66.16.25. Redistribution subject to ASME license or copyright; see http://www.asme.org/terms/Terms_Use.cfm

Figure 11 shows the variation of the fundamental frequency with the side length of a square configuration. In the calculations we choose the properties $E = 10^7$ psi, $G = 3.84 \times 10^6$ psi, $\mu = 0.3$, $\rho = 0.3$ lb/in.^{3}, $J = 01563$ in.^{4}, $I_y = 0.03125$ in.^{4}, $A = 0.5$ in.^{2}, and $L = 10$ in. as the modulus of elasticity, shear modulus, Poisson's ratio, mass density, torsional moment, y-moment of inertia, cross-sectional area, and element length, respectively.

By setting $\nu = 0$ our results can also be compared with the finite difference results of Wah and Calcote [17] and Ellington and McCallion [14]. Results of such comparison are listed in Table 1. Also, we included results for the reduced model in which the three coupled equations (19)–(21) were combined into the single equation

$$\frac{EI_y}{L}\left(\frac{\partial^4\omega}{\partial x^4}+\frac{\partial^4\omega}{\partial y^4}\right)+\frac{2GJ}{L}\frac{\partial^4\omega}{\partial x^2\partial y^2}+\frac{\rho AL^3}{20}\left(\frac{\partial^4\ddot{\omega}}{\partial x^2}+\frac{\partial^4\ddot{\omega}}{\partial y^2}\right)+\frac{2\rho A\ddot{\omega}}{L}=0 \tag{41}$$

by introducing the rotation-displacement constraints

$$\theta^x=\frac{\partial\omega}{\partial y},\quad \theta^y=-\frac{\partial\omega}{\partial x} \tag{42}$$

These constraints are a result of the classified plate assumption $\epsilon_{13} = \epsilon_{23} = 0$. Following the same restrictions introduced in the foregoing, namely $\nu = 0$ and neglecting higher order time derivatives, the characteristic equation of equation (41) yields

$$u^4=\frac{1}{2}\left[\left(\frac{n\pi}{p}\right)+\left(\frac{m\pi}{q}\right)^4\right] \tag{43}$$

From the numerical comparisons it is obvious that our reduced results are almost identical with those predicted by the finite difference analysis. This is perhaps due to the fact that in the finite difference solutions of references [14, 17] the constraints (42) are implicitly satisfied by the specific choice of the single operators that relates the space variation of displacements and rotations.

Numerical results for the out-of-plane vibrations of the 0, ± 60 deg configuration can be similarly obtained by introducing the formal solutions (37) into equations (26)–(28) and writing down their characteristic equation. These results will not be reported here, however.

6 Finite Element Analysis

Solutions for the vibrations of the 0, 90 deg gridwork and the 0 ± 60 gridwork are obtained using finite element techniques in order to compare these with the continuum theory results. The structural analysis program (SAP) is used to analyze the gridwork.

The gridwork is assembled using three-dimensional beam elements with constraints applied in order to obtain the type of motion under investigation. The program transforms the individual element stiffness and mass matrices as necessary to coincide with the element orientation and superposes these to form a global stiffness and mass matrix for the structure. A lumped mass matrix is used, which assumes that the mass of the element is concentrated at the nodal points.

For all the cases involving displacements in the plane of the gridwork, four finite elements per structural member are used. This gives a solution for the frequency of vibration which is sufficiently converged. For cases involving displacements out of the gridwork plane, the use of four finite elements per beam creates storage problems in the models with larger areas due to the number of nodal points involved. The number of finite elements per member is reduced as needed to satisfy this constraint.

6.1 In-Plane Transverse Vibrations. For in-plane transverse vibrations only translations in the y direction and rotations about the z axis are allowed. Wave number values of

$$k=\pi/l \tag{44}$$

are used, where l is the gridwork width and is an integer multiple of the member length. Values used for l are $2L$, $4L$, $6L$, $8L$, $10L$, and $16L$. For wave number values as given in (44), it can be seen from (29) that the displacement at the boundaries $x = 0$ and $x = l$ is zero and that the moment at these same boundaries is zero. Therefore, the gridwork is constrained by pinning the nodes at $x = 0$ and at $x = l$. The frequency and wave number are nondimensionalized as before in (31). The material and section properties used are listed in Section 5.3.

The gridwork examined in the continuum analysis was assumed to be of infinite extent. For the finite element analysis, the x dimension is fixed by the value of the wave number. The y dimension is picked so as to get a more converged solution. For the 0, 90 deg configuration, a gridwork having five rows vertically was found to be sufficiently converged. For the $0, \pm 60$ deg configuration, four rows vertically yields good results. However, for some of the lower wave number cases ($l = 16L$, $10L$) the number of rows of the gridwork must be reduced in order not to exceed available storage.

The finite element results relating the nondimensional frequency and wave number are shown in Fig. 7 for the 0, 90 deg configuration and in Fig. 8 for the $0, \pm 60$ deg configuration.

6.2 In-Plane Longitudinal Vibrations. For this type of vibration only translation in the x direction and rotation about the z axis is allowed. The same values for the wave number k are used as for the in-plane transverse case, along with the same gridwork widths of 2, 4, 6, 8, 10, and 16 times the member length. The boundary conditions are the same as for the in-plane transverse case as well. By using five rows in the y direction a solution that is well converged is obtained. The frequency and wave number are nondimensionalized in accordance with (31), and the material and section properties are again those used in Section 5.3.

The finite element solutions for the 0, 90 deg gridwork are shown in Fig. 9 and for the $0, \pm 60$ deg in Fig. 10.

6.3 Out-of-Plane Vibrations. To investigate out-of-plane vibrations, a rectangular gridwork with pinned edges is used. Rotation about the z axis is allowed for all nodes. For both the 0, 90 deg configuration and the $0, \pm 60$ deg configuration the number of rows in the y direction is equal to the number of bays in the x direction. This means that the gridwork is square for the 0, 90 deg configuration, but for the 0 ± 60 deg configuration the sides are of different length being related by

$$b=\sqrt{3}\,a \tag{45}$$

Solutions are obtained for gridworks with the side of length a being $2L$, $4L$, $6L$, $8L$, and $10L$ where L is the member length. The frequency and wave number are nondimensionalized as in (31), and the material and section properties are as listed in Section 5.3.

The finite element results for out-of-plane vibrations are shown in Fig. 11 for the 0, 90 deg configuration and in Fig. 12 for the $0, \pm 60$ deg configuration. In both cases the finite element results are compared with those obtained from the reduced models.

7 Summary and Conclusions

Equations of motion for gridworks have been found by transforming the discrete strain and kinetic energy of the

Downloaded 02 May 2010 to 171.66.16.25. Redistribution subject to ASME license or copyright; see http://www.asme.org/terms/Terms_Use.cfm

beam element used to assemble the gridwork to a continuous form through the use of a Taylor's series expansion, employing the building block approach to obtain the continuous strain and kinetic energy of the gridwork unit cell, and finally generating the equations of motion for the gridwork from these energy expressions using Hamilton's principle. These equations of motion were then used to produce dispersion relations for the gridworks undergoing certain types of vibratory motion.

It was found that the use of the building block approach directly on the equations of motion for the single element produced the same results in a much quicker and easier fashion than the derivation of the equations of motion from the energy densities for each individual gridwork. Therefore, it is possible to construct the equations of motion for a large variety of gridworks composed of repeating unit cells by application of the building block approach to the single element equations of motion (8)–(13). All that is required are the appropriate direction cosines.

The dispersion relations obtained in the manner previously described were compared with finite element solutions of the same gridwork for various individual wave numbers. Comparing the finite element results for in-plane vibrations with those from the continuum theory approach it is seen that agreement between the two is excellent for the 0 ± 60 deg configuration, but not nearly as good for the 0, 90 deg configuration. It is also seen that the two methods agree much better when the wave number is smaller or in other words, when the wavelength is larger compared to member length. These two characteristics can be attributed to the same factor, which is that the continuum theory is more effective when the gridwork under investigation more closely approximates a continuum in relation to the wave traveling through it. In other words, the more gridwork material contained in the wave, the better the continuum theory results will be.

The 0 ± 60 deg gridwork configuration approximates a continuum more closely than the 0, 90 deg gridwork configuration since each element of the 0 ± 60 deg gridwork occupies an area which is $1/\sqrt{3}$ times less than that occupied by an element of the 0, 90 deg gridwork. Also, when the wavelength becomes larger in comparison to the length L, the wave covers more unit cells, i.e., contains more material, and so the continuum theory is better able to predict the response of the gridwork to that wave.

Comparing the two methods for out-of-plane vibrations, the same type of behavior can be seen; agreement is better in general for the 0 ± 60 deg configuration and agreement is also better when the wave includes many unit cells.

It must be concluded, therefore, that the use of a continuum theory type of approach to obtain equations of motion and dispersion relationships gives good results provided that the wavelength is fairly large in relation to the unit cell of the gridwork. The continuum approach is also very effective for gridworks having a large number of elements per unit area. In fact, this is quite advantageous since in these cases when the continuum theory is most effective, it becomes increasingly costly in terms of computer time and memory to model the gridwork using the finite element method. Therefore, the continuum theory approach has definite value as a tool for analysis of gridworks and warrants further development.

Acknowledgment

This research was supported by NASA Langley Research Center, Grant NSG-11850.

References

1 Card, M. F., Kruszewski, E. T., and Gusastaferro, A., "Technology Assessment and Outlook," *Astronautics and Aeronautics*, Vol. 16, Oct. 1978, pp. 48–54.

2 Hedgepeth, J. M., Mikulas, M. M., Jr., and Macneal, R. H., "Practical Design of Low-Cost Large Space Structures," *Astronautics and Aeronautics*, Vol. 16, Oct. 1978, pp. 30–34.

3 Daros, C. J., Freitag, R., and Kline, R., "Toward Large Space Systems," *Astronautics and Aeronautics*, Vol. 15, May 1977, pp. 22–30.

4 Woodcock, G. R., "Solar Satellites Space Key to Our Power Future," *Astronautics and Aeronautics*, Vol. 15, July/Aug. 1977, pp. 30–43.

5 Priest, C. C., "Space Platforms/Stations," *AIAA Student Journal*, Vol. 19, No. 3, Fall 1981, pp. 16–23.

6 Martin, H. C., *Introduction to Matrix Methods of Structural Analysis*, McGraw-Hill, New York, 1966.

7 Vanderbilt, M. D., *Matrix Structural Analysis*, Quantum Publishers.

8 Kollar, L., "Analysis of Double-Layer Space Truss With Diagonally Square Mesh by the Continuum Methods," *Acta Technica Academiae Scientiarum Hungaricae*, Tomus 76, 1974, pp. 273–292.

9 Dean, D. L., and Evert, R. R., *State of the Art of Discrete Field Analysis of Space Structures*, Supple, W. J., ed., University of Surrey, Guildford, England, Sept. 1975, pp. 7–16.

10 Renton, J. D., "On the Gridwork Analogy for Plates," *Journal of Mech. Phys. Solids*, Vol. 13, 1965, pp. 413–420.

11 Renton, J. D., "General Properties of Space Grids," *Int. J. Mech. Sci.*, Vol. 12, 1970, pp. 801–810.

12 Renton, J. D., "The Related Behavior of Plane Grids and Plates," *Space Structures*, Blackwell, Oxford, 1967, pp. 19–32.

13 Renton, J. D., "On the Analysis of Triangular Mesh Grillages," *Int. J. Solids Structures*, Vol. 2, 1966, pp. 307–318.

14 Ellington, J. P., and McCallion, H., "The Free Vibration of Grillages," ASME JOURNAL OF APPLIED MECHANICS, Vol. 26, 1959, p. 603.

15 Wah, T., "Analysis of Laterally Loaded Gridworks," *Journal of Eng. Mechanics Division, ASCE*, Vol. 90, No. EM2, Apr. 1964, pp. 83–106.

16 Smith, J. C., and Dean, D. L., "Field Analysis of Torsionless Bridge Grids," *Journal of Structural Division, ASCE*, Vol. 99, ST9, 1973.

17 Wah, T., and Calcote, L. R., *Structural Analysis by Finite Difference Calculus*, Van Nostrand Reinhold, New York, 1970.

18 Nayfeh, A. H., and Hefzy, M. S., "Continuum Modeling of Three-Dimensional Truss-Like Space Structures," *AIAA Journal*, Vol. 16, No. 8, Aug. 1978, pp. 779–787.

19 Nayfeh, A. H., and Hefzy, M. S., "Continuum Modeling of the Mechanical and Thermal Behavior of Discrete Large Structures," *AIAA Journal*, Vol. 19, No. 6, June 1981, pp. 766–773.

20 Nayfeh, A. H., and Hefzy, M. S., "Effective Constitutive Relations for Large Repetitive Frame-Like Structures," *Int. Journal of Solids and Structures*, Vol. 18, No. 11, 1982, pp. 975–987.

21 Heki, K., "One the Effective Rigidities of Lattice Plates," *Recent Researches of Structural Mechanics*, Tokyo, 1968, pp. 31–46.

22 Heki, K., and Saka, T., "Stress Analysis of Lattice Plates as Anisotropic Continuum Plates," *Proc. 1971 IASS Pacific Symposium, Part II on Tension Structures and Space Frames*, Tokyo and Kyoto, Paper No. 7-7, 1972, pp. 663–674.

23 Wright, D. T., "Membrane Forces and Buckling in Reticulated Shells," *Journal of the Structural Division, ASCE*, Vol. 91, No. ST1, Feb. 1965, pp. 173–201.

24 Flower, W. R., and Schmidt, L. C., "Analysis of Space Truss as Equivalent Plate," *Journal of the Structural Division, ASCE*, Vol. 97, No. ST12, Dec. 1971, pp. 2777–2789.

25 Benard, E. F., "A Study of the Relationship Between Lattice and Continuous Structure," Ph.D. thesis, University of Ilinois, at Urbana, Ill., 1965.

26 Askar, A., and Cakmak, A. S., "A Structural Model of a Micropolar Continuum," *Int. J. Eng. Sci.*, Vol. 6, 1968, pp. 583–589.

27 Bazant, Z. P., and Christensen, M., "Analogy Between Micropolar Continuum and Grid Frameworks Under Initial Stress," *Int. J. of Solids and Structures*, Vol. 8, 1972, pp. 327–346.

28 Bazant, Z. P., and Christensen, M., "Continuum Solutions for Long-Wave Extensional Buckling of Rectangular Frames," *Int. J. of Engineering Sciences*, Vol. 11, pp. 1255–1263.

29 Sun, C. T., and Yang, T. Y., "A Continuum Approach Toward Dynamic of Gridworks," ASME JOURNAL OF APPLIED MECHANICS, Vol. 40, 1973, pp. 186–192.

30 Noor, A. K., Greene, W. H., and Anderson, M. S., "Continuum Models for Static and Dynamic Analysis of Repetitive Lattices," presented at the AIAA/ASME/SAE 18th Structures, Structural Dynamics and Materials Conference, San Diego, Calif., Mar. 21–23, 1977.

31 Noor, A. K., Anderson, M. S., and Greene, W. H., "Continuum Models for Beam-Like and Plate-Like Lattice Structures," *AIAA Journal*, Vol. 16, No. 12, Dec. 1978, pp. 1219–1228.

32 Noor, A. K., and Nemeth, M. P., "Micropolar Beam Models for Lattice Grids With Rigid Joints," to appear in *Computer Methods in Applied Mechanics and Engineering*.

33 Nemeth, M. P., "Continuum Models for Repetitive Lattice Structures With Rigid Joints," M.S. thesis, George Washington University, Washington, D.C., 1979.

34 Archer, J. S., "Consistent Mass Matrix for Distributed Mass Systems," *Journal of Structural Division Proceedings of the ASCE*, Vol. 89, 1963, pp. 161–177.

Downloaded 02 May 2010 to 171.66.16.25. Redistribution subject to ASME license or copyright; see http://www.asme.org/terms/Terms_Use.cfm

Large Deflections of a Simply Supported Beam Subjected to Moment at One End

P. Seide
Department of Civil Engineering,
University of Southern California,
Los Angeles, Calif. 90007
Fellow ASME

The large deflections of a simply supported beam, one end of which is free to move horizontally while the other is subjected to a moment, are investigated by means of inextensional elastica theory. The linear theory is found to be valid for relatively large angles of rotation of the loaded end. The beam becomes transitionally unstable, however, at a critical value of the bending moment parameter M_1L/EI equal to 5.284. If the angle of rotation is controlled, the beam is found to become unstable when the rotation is 222.65 deg.

Theory

Consider a beam of length L which is simply supported at both ends. One support is free to move horizontally, however, while the other is restricted (Fig. 1(*a*)). When the immovable end is subjected to a moment M_1, let the resulting distance between the supports be denoted by l. Then the statically determinate equal and opposite support reactions are given by M_1/l (Fig. 1l(*b*)), which is the constant vertical force acting on each cross section of the beam. An element of the deformed bean is acted on by the forces shown in Fig. 2 for which the equilibrium equation is:

$$\frac{dM}{ds} - \frac{M_1}{l}\frac{dx}{ds} = 0 \tag{1}$$

But

$$\frac{dx}{ds} = \cos\theta \tag{2}$$

and the constitutive relation for the beam is

$$M = EI\frac{d\theta}{ds} \tag{3}$$

Thus the equation for the determination of the beam deformations is given by

$$EI\frac{d^2\theta}{ds^2} - \frac{M_1}{l}\cos\theta = 0 \tag{4}$$

A first integral of equation (4) is

$$\frac{EI}{2}\left(\frac{d\theta}{ds}\right)^2 - \frac{M_1}{l}\sin\theta = C_1 \tag{5}$$

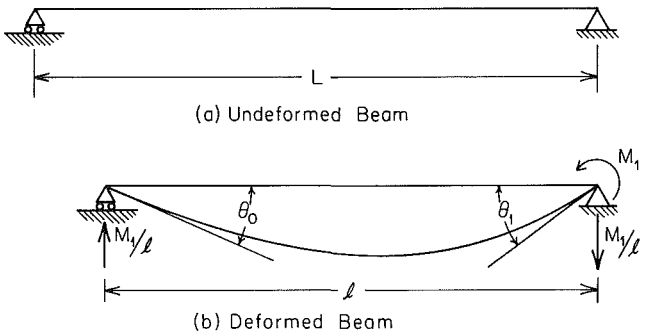


Fig. 1 Simply-supported beam subjected to moment at one end

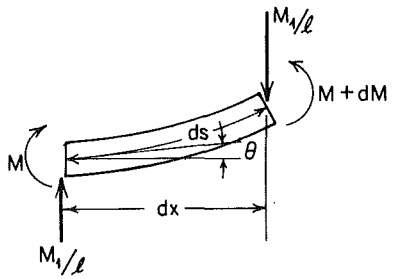


Fig. 2 Element of beam

The constant of integration is determined from the condition that the moment vanishes at the left end at which

$$\theta = -\theta_0 \tag{6}$$

Thus, equation (5) may be written as

$$\frac{d\theta}{ds} = 2\sqrt{\frac{M_1}{EIl}\left[\sin^2\left(\frac{\frac{\pi}{2}+\theta_0}{2}\right) - \sin^2\left(\frac{\frac{\pi}{2}-\theta}{2}\right)\right]} \tag{7}$$

Contributed by the Applied Mechanics Division for publication in the JOURNAL OF APPLIED MECHANICS.
Discussion on this paper should be addressed to the Editorial Department, ASME, United Engineering Center, 345 East 47th Street, New York, N.Y. 10017, and will be accepted until two months after final publication of the paper itself in the JOURNAL OF APPLIED MECHANICS. Manuscript receivd by ASME Applied Mechanics Division, February 1983; final revision, September, 1983.

Copyright © 1984 by ASME
Downloaded 02 May 2010 to 171.66.16.25. Redistribution subject to ASME license or copyright; see http://www.asme.org/terms/Terms_Use.cfm

The positive sign is chosen by consideration of the curvature implied by Fig. 1(*b*) which is valid so long as no portion of the beam is to the left of the moveable support. The change of variable given by

$$\sin\phi = \frac{\sin\left(\frac{\frac{\pi}{2}-\theta}{2}\right)}{\sin\left(\frac{\frac{\pi}{2}+\theta_0}{2}\right)} \tag{8a}$$

then yields

$$d\theta = \frac{-2\sin\left(\frac{\frac{\pi}{2}+\theta_0}{2}\right)\cos\phi}{\sqrt{1-\sin^2\left(\frac{\frac{\pi}{2}+\theta_0}{2}\right)\sin^2\phi}} \tag{8b}$$

so that equation (7) may be written as

$$ds = \frac{-d\phi}{\sqrt{\frac{M_1}{EIl}\left[1-\sin^2\left(\frac{\frac{\pi}{2}+\theta_0}{2}\right)\sin^2\phi\right]}} \tag{9}$$

If the beam is assumed to be inextensional, the integral of ds over the length of the beam is equal to the original length. Thus,

$$L = \frac{1}{\sqrt{\frac{M_1}{EIl}}}\int_{\phi_1}^{\frac{\pi}{2}} \frac{d\phi}{\sqrt{1-\sin^2\left(\frac{\frac{\pi}{2}+\theta_0}{2}\right)\sin^2\phi}}$$

$$= \frac{1}{\sqrt{\frac{M_1}{EIl}}}\left[K\left(\frac{\frac{\pi}{2}+\theta_0}{2}\right) - F\left(\frac{\frac{\pi}{2}+\theta_0}{2},\phi_1\right)\right] \tag{10a}$$

where K and F are the standard complete and incomplete elliptic integrals of the first kind

$$\phi_1 = \sin^{-1}\frac{\sin\left(\frac{\frac{\pi}{2}+\theta_1}{2}\right)}{\sin\left(\frac{\frac{\pi}{2}+\theta_0}{2}\right)} \tag{10b}$$

and θ_1 is the positive slope at the end at which the moment M_1 is applied.

Equation (10*a*) is not sufficient to determine the beam deformations, however, since the variation of θ_0, θ_1, and l with applied moment M_1 is unknown as yet. Two additional equations for this purpose may be obtained from the relations

$$\frac{dx}{ds} = \cos\theta \tag{11a}$$

$$\frac{dy}{ds} = \sin\theta \tag{11b}$$

The use of equations (8) and (9) yields

$$dx = -\frac{2}{\sqrt{\frac{M_1}{EIl}}}\sin\left(\frac{\frac{\pi}{2}+\theta_0}{2}\right)\sin\phi\, d\phi \tag{12a}$$

$$dy = -\frac{1}{\sqrt{\frac{M_1}{EIl}}}\left[\sqrt{1-\sin^2\left(\frac{\frac{\pi}{2}+\theta_0}{2}\right)\sin^2\phi} - \frac{1}{\sqrt{1-\sin^2\left(\frac{\frac{\pi}{2}+\theta_0}{2}\right)\sin^2\phi}}\right]$$

from which (12*b*)

$$\int_{\theta=-\theta}^{\theta=\theta_1} dx = l = \sqrt{\frac{2\sin\theta_1+\sin\theta_0}{\frac{M_1}{EIl}}} \tag{13a}$$

and

$$\int_{\theta=-\theta_1}^{\theta=\theta_1} dy = 0 = 2\left[E\left(\frac{\frac{\pi}{2}+\theta_0}{2}\right) - E\left(\frac{\frac{\pi}{2}+\theta_0}{2},\phi_1\right)\right]$$

$$-\left[K\left(\frac{\frac{\pi}{2}+\theta_0}{2}\right) - F\left(\frac{\frac{\pi}{2}+\theta_0}{2},\phi_1\right)\right] \tag{13b}$$

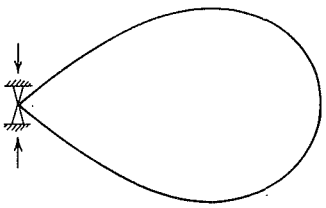
The equations that determine the parameters of the beam deflection pattern are now equation (13*b*), which relates θ_0 and θ_1, and from equations (10*a*) and (13*a*),

$$\frac{M_1 L}{EI} = \sqrt{2(\sin\theta_1+\sin\theta_0)}\left[K\left(\frac{\frac{\pi}{2}+\theta_0}{2}\right) - F\left(\frac{\frac{\pi}{2}+\theta_0}{2},\phi_1\right)\right] \tag{14}$$

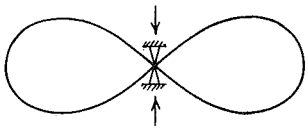
which relates θ_1 and the parameter M_1L/EI.

The distance between supports is given by

Downloaded 02 May 2010 to 171.66.16.25. Redistribution subject to ASME license or copyright; see http://www.asme.org/terms/Terms_Use.cfm



(a) Beam with ends touching



(b) "Pretzel" shape for beam with ends touching

Fig. 3 Limiting shapes for beams with ends touching

$$\frac{l}{L}=\frac{\sqrt{2(\sin\theta_1+\sin\theta_0)}}{K\left(\frac{\frac{\pi}{2}+\theta_0}{2}\right)-F\left(\frac{\frac{\pi}{2}+\theta_0}{2},\phi_1\right)} \tag{15}$$

The coordinates of points on the deflection curve are given by the parametric equations:

$$\frac{x}{L}=\frac{1}{L}\int_{\theta_1}^{\theta}dx=\frac{\sqrt{2(\sin\theta+\sin\theta_0)}-\sqrt{2(\sin\theta_1+\sin\theta_0)}}{K\left(\frac{\frac{\pi}{2}+\theta_0}{2}\right)-F\left(\frac{\frac{\pi}{2}+\theta_0}{2},\phi_1\right)} \tag{16a}$$

$$\frac{y}{L}=\frac{1}{L}\int_{\theta_1}^{\theta}dy=\frac{2E\left(\frac{\frac{\pi}{2}+\theta_0}{2}\right)-K\left(\frac{\frac{\pi}{2}+\theta_0}{2}\right)-\left[2E\left(\frac{\frac{\pi}{2}+\theta_0}{2}\right)-F\left(\frac{\frac{\pi}{2}+\theta_0}{2},\phi\right)\right]}{K\left(\frac{\frac{\pi}{2}+\theta_0}{2}\right)-F\left(\frac{\frac{\pi}{2}+\theta_0}{2},\phi_1\right)} \tag{16b}$$

where equation (13*b*) has been used.

It will be noted from equation (15*a*) that if θ_1 is equal to $\pi + \theta_0$, the distance between supports vanishes. Equation (14) indicates that the applied moment vanishes as well. Thus, the solution in this case corresponds to the elastica solution for the simply supported buckeled beam which has been deformed so that its end touch (Fig. 3*a*). The value of θ_0 calculated from equation (13*b*) that satisfies this condition is:

$$\theta_0 = 40.71 \text{ deg}$$

yielding

$$\theta_1 = 220.71 \text{ deg}$$

If the movable support moves to the right of the support point as in Fig. 4, the solution must be modified. Inflection points must exist at the moveable support and at any point of the beam directly above the moveable support since the bending moment at these joints is equal to zero. The curvature of any part of the beam to the right of the moveable support is then positive while the curvature of those parts of the beam to the left of the moveable support is negative. If the beam is as shown in Fig. 4, the revised equations for the determination of the parameter of the beam deflectin pattern are:

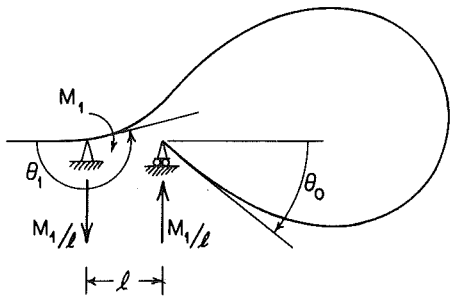


Fig. 4 Beam with moveable support to right of fixed support

$$3\left[2E\left(\frac{\frac{\pi}{2}+\theta_0}{2}\right)-K\left(\frac{\frac{\pi}{2}+\theta_0}{2}\right)\right]+\left[2E\left(\frac{\frac{\pi}{2}+\theta_0}{2},\phi_1\right)-F\left(\frac{\frac{\pi}{2}+\theta_0}{2},\phi_1\right)\right]=0 \tag{17a}$$

and

$$\frac{M_1L}{EI}=-\sqrt{2(\sin\theta_1+\sin\theta_0)}\left[3K\left(\frac{\frac{\pi}{2}+\theta_0}{2}\right)+F\left(\frac{\frac{\pi}{2}+\theta_0}{2},\phi_1\right)\right] \tag{17b}$$

where it is understood that elliptic integrals of negative arguments are negative. The distance between supports is now given by:

Downloaded 02 May 2010 to 171.66.16.25. Redistribution subject to ASME license or copyright; see http://www.asme.org/terms/Terms_Use.cfm

$$\frac{l}{L} = \frac{-\sqrt{2(\sin\theta_1 + \sin\theta_0)}}{3K\left(\frac{\frac{\pi}{2}+\theta_0}{2}\right) + F\left(\frac{\frac{\pi}{2}+\theta_0}{2}, \phi_1\right)} \tag{18}$$

and the coordinates of points on the deflection curve are given by:

$$\frac{x}{L} = \frac{\sqrt{2(\sin\theta_1 + \sin\theta_0} - \sqrt{2(\sin\theta + \sin\theta_0)}}{3K\left(\frac{\frac{\pi}{2}+\theta_0}{2}\right) + F\left(\frac{\frac{\pi}{2}+\theta_0}{2}, \phi_1\right)} \quad \theta_1 < \theta < \pi + \theta_0$$

$$= \frac{\sqrt{2(\sin\theta_1 + \sin\theta_0)} + \sqrt{2(\sin\theta + \sin\theta_0)}}{3K\left(\frac{\frac{\pi}{2}+\theta_0}{2}\right) + F\left(\frac{\frac{\pi}{2}+\theta_0}{2}, \phi_1\right)} \quad -\theta_0 < \theta < \pi + \theta_0 \tag{19a}$$

$$\frac{y}{L} = \frac{2E\left(\frac{\frac{\pi}{2}+\theta_0}{2}, \phi\right) - F\left(\frac{\frac{\pi}{2}+\theta_0}{2}, \phi\right) - \left[2E\left(\frac{\frac{\pi}{2}+\theta_0}{2}, \phi_1\right) - F\left(\frac{\frac{\pi}{2}+\theta_0}{2}, \phi_1\right)\right] \quad \theta_1 < \theta < \pi + \theta_0}{3K\left(\frac{\frac{\pi}{2}+\theta_0}{2}\right) + F\left(\frac{\frac{\pi}{2}+\theta_0}{2}, \phi_1\right)}$$

$$= -\frac{\left\{2E\left(\frac{\frac{\pi}{2}+\theta_0}{2}, \phi_1\right) - F\left(\frac{\frac{\pi}{2}+\theta_0}{2}, \phi_1\right) + 2E\left(\frac{\frac{\pi}{2}+\theta_0}{2}, \phi\right) - F\left(\frac{\frac{\pi}{2}+\theta_0}{2}, \phi\right) + 2\left[2E\left(\frac{\frac{\pi}{2}+\theta_0}{2}\right) - K\left(\frac{\frac{\pi}{2}+\theta_0}{2}\right)\right]\right\}}{3K\left(\frac{\frac{\pi}{2}+\theta_0}{2}\right) + F\left(\frac{\frac{\pi}{2}+\theta_0}{2}, \phi_1\right)}$$

$$-\theta_0 < \theta < \pi + \theta_0 \tag{19b}$$

The distance between supports vanishes when θ_1 is equal to $\pi + \theta_0$, as before, but also when θ_1 is equal to $-\theta_0$. In both cases the value of θ_0 given by equation (17*a*) is 40.71 deg. The interpretation of this second limiting case so that the beam has twisted into a "pretzel" shape that corresponds to a simply supported beam which has buckled into two lobes whose ends touch (Fig. 3*b*).

In the two cases considered in the foregoing, the beam progresses from a shape having only positive curvature to a shape having one region that is positive and one region that is negative. Subsequent equilibrium shapes will have regions of positive curvature separated by regions of negative curvature. These shapes will not be considered further since they are extremely unstable.

Results and Discussions

Equations (13*b*) and (17*a*) were solved numerically with the use of IBM System/360 Scientific Subroutine Package (SSP) computer codes DCEL2 and DELI2, which, respectively, yield values of the complete and incomplete generalized elliptic integrals of the second kind, and computer code DRTMI that determines a root of a general nonlinear equation of one variable in a given range by means of Mueller's iteration scheme of successive bisection and inverse parabolic iteration (reference [1]). Values of θ_0 were generally calculated for given values of θ_1. In some regions, however, it was necessary to vary θ_0 and to calculate θ_1. The results of the computations are shown in Fig. 5.

As θ_1 increases from 0 deg, the value of θ_0 computed from equation (13*b*), the solid portion of the curve of Fig. 5, is at first very close to the value of $1/2\theta_1$, given by linear theory. For example, when θ_1 is equal to 90 deg, the error of the linear solution is only about 10 percent. For larger values of θ_1, the calculated value of θ_0 reaches a maximum, however, and then decreases. The results indicate that θ_1 can increase to a value of 222.65 deg and then must decrease to a value of 220.71 deg with decreasing θ_0. Thus for values of θ_1 between the two preceding values, there are two equilibrium positions on the branch of the equilibrium path being investigated.

The rotation angle θ_1 continues to decrease if the moveable support is permitted to move to the right of the fixed report. The corresponding values of θ_0 and θ_1 obtained from equation (17*a*) are shown by the dashed portion of the curve of Fig. 5. The angle θ_0 at first decreases with decreasing θ_1, reaches a minimum value, then increases to a maximum and finally decreases to a value of 40.71 deg at which point the ends of the beam touch again. Subsequent portions of the curve relating θ_0 and θ_1 will pass through the three points marked by a cross in Fig. 5. The point to the right corresponds to a twisted shape with an odd number of simply supported beam lobes with ends touching, the point to the left at θ_1 equal to -40.71 deg corresponds to a twisted shape with an even number of lobes, while the central point at θ_1 equal to 90 deg corresponds to a twisted shape with an integral number of complete lobes and an additional half lobe (similar to the beam in Fig. 3(*b*), but with the fixed support moved to the point having a vertical tangent at the right). In each case the angle θ_0 is equal to 40.71 deg.

The variation of end rotation angle θ_1 and the moment parameter M_1L/EI was obtained from equations (14) and (17*b*) using the corresponding values of θ_0 and θ_1 together with the SSP subroutines DCEL1 and DELI1 for the calculation of complete and incomplete elliptic integrals of the first kind. The results are shown in Fig. 6. Here again the linear solution of

Downloaded 02 May 2010 to 171.66.16.25. Redistribution subject to ASME license or copyright; see http://www.asme.org/terms/Terms_Use.cfm

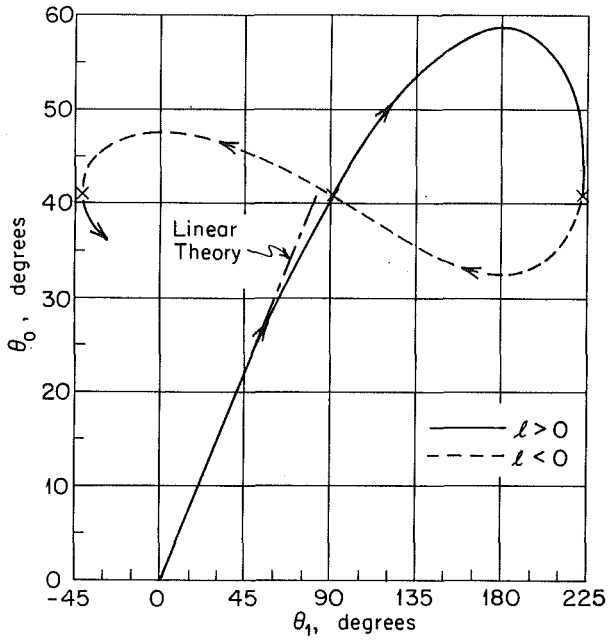


Fig. 5 Variation of θ_0 with rotation angle

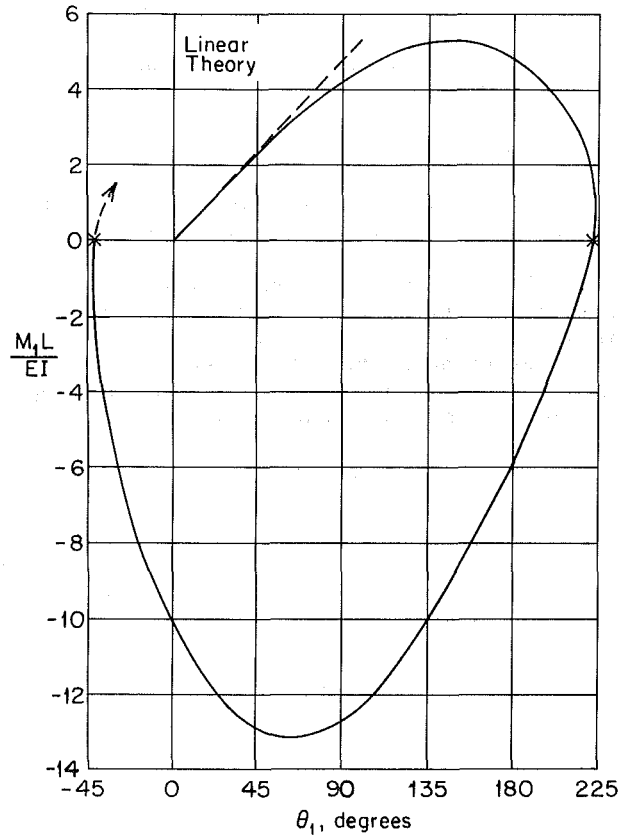


Fig. 6 Variation of applied moment with rotation angle

$$\frac{M_1 L}{EI} = 3\theta_1 \quad (\theta_1 \text{ in radians})$$

is found to be valid for relatively large values of θ_1. At θ_1 of 90 deg, the error in the linear value of the moment parameter is about 12 percent. As the angle θ_1 increases, the moment parameter reaches a maximum of 5.284 when θ_1 is near 145 deg and then decreases. Thus, if the rotation is produced by

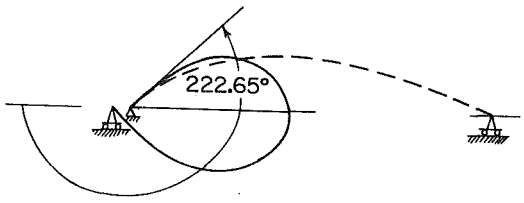


Fig. 7 Alternate equilibrium shapes

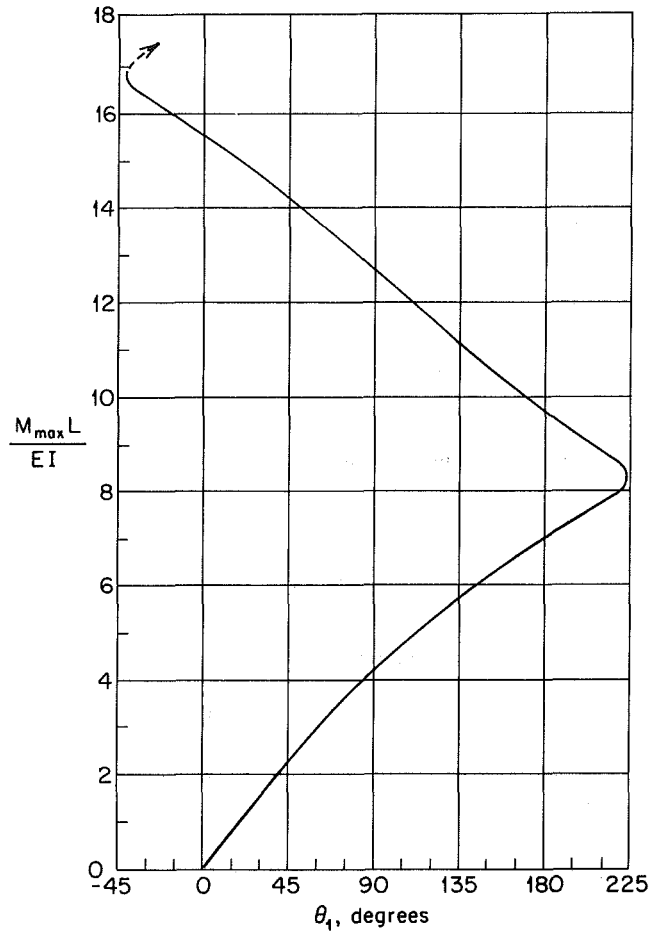


Fig. 8 Variation of maximum moment with rotation angle

applied moment, the beam becomes unstable when the moment parameter reaches the critical value of 5.284.

The moment for subsequent unstable equilibrium positions behaves in a spiral fashion as the shape of the beam becomes more twisted. The moment always vanishes at the angular positions indicated by a cross which correspond to buckled simply supported beam shapes with ends touching. The moments when θ_1 is equal to 90 deg can also be obtained by noting that each deflected shape for this angle of rotation contains $2n-1$ ($n=1,2,\ldots$) simply supported half-buckled beam shapes of length $L/(2n-1)$. Thus, the moment parameter $M_1 L/_{EI}$ is $2n-1$ times the value of the parameter for n equal to unity; i.e.,

$$\frac{M_1 L}{EI} = 4.219\,(2n-1) \tag{21}$$

If the rotation angle θ_1 is controlled, it is obvious that the angle of rotation cannot exceed 220.65 deg on the branch of the equilibrium path under investigation. Lower energy equilibrium positions for angles of rotation equal to or greater

Downloaded 02 May 2010 to 171.66.16.25. Redistribution subject to ASME license or copyright; see http://www.asme.org/terms/Terms_Use.cfm

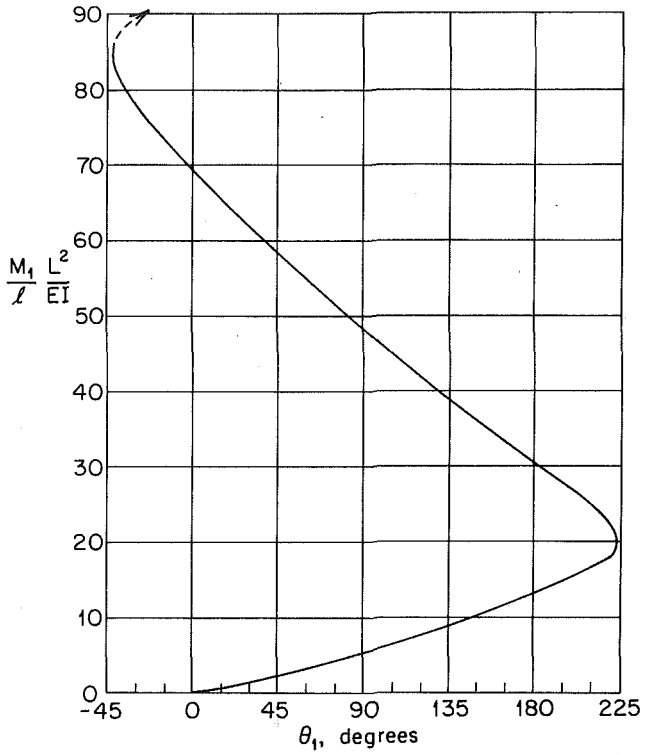


Fig. 9 Variation of beam reactions with rotation angle

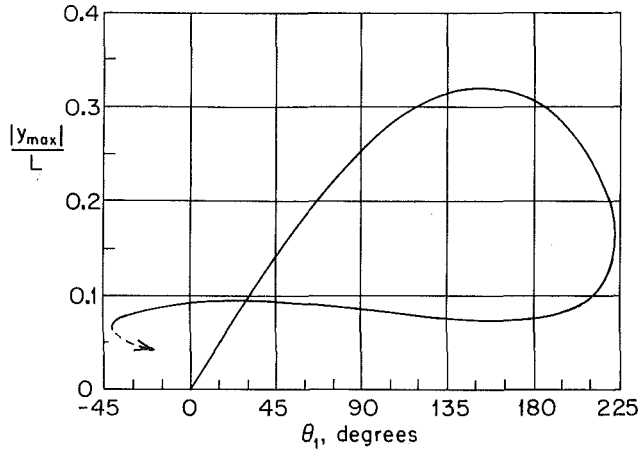


Fig. 11 Variation of maximum displacement with rotation angle

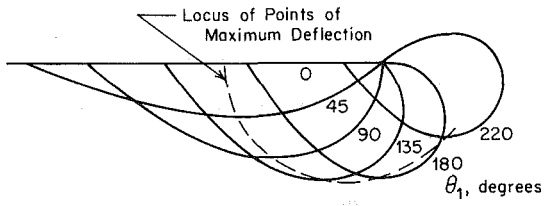


Fig. 12 Variation of deflected shape with rotation angle

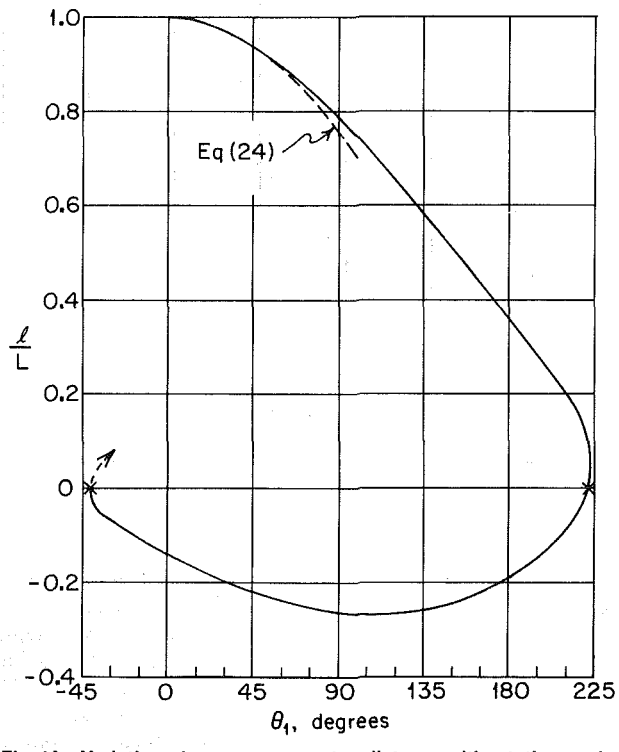


Fig. 10 Variation of support separation distance with rotation angle

than 220.65 deg are those that proceed from an unstressed straight beam shape in which the moveable support is to the right of the fixed support (Fig. 7). The angle θ_1 for the straight beam is then 180 deg rather than 0 deg. The beam shapes and moments for values of θ_1 greater than 180 deg are those for beams having angles of rotation of $\theta_1 - 180$. There is no static equilibrium path that permits the attainment of these positions from the assumed starting position. The beam moves rapidly from the one position to the other while uncoiling provided the roller support can move to the right of the fixed support.

Although the applied moment for the beam reaches a maximum and decreases, the maximum moment in the beam continues to increase rapidly with increasing complexity of the deformed shape. The maximum moment in the beam is equal to the applied moment when θ_1 is initially less than 90 deg. When the maximum slope of the beam is greater than 90 deg the location of the maximum bending moment shifts to the point of verticle slope at the largest distance from the moveable support. The maximum bending moment is then given by

$$M_{max} = \sqrt{\frac{1+\sin\phi}{\sin\theta_1 + \sin\theta_0}}\,|M_1| \tag{22}$$

The results calculated for the equilibrium positions discussed in the foregoing are shown in Fig. 8. Here again the values at the points $\theta_1 = -40.71$, 90, and 220.71 deg can be obtained once the first value for 90 deg is known since the deflected shapes are multiples of the simply supported half-buckled beam shapes. Thus the respective values of the bending moment parameter are:

$$\begin{aligned} \frac{M_{max}L}{EI} &= 4.219\,(2n-1) \quad \theta_1 = 90 \text{ deg} \\ &= 8.438\,(2n-1) \quad \theta_1 = 220.71 \text{ deg} \\ &= 16.88 \qquad\quad \theta_1 = -40.71 \text{ deg} \\ & n = 1,2,3, \ldots \end{aligned} \tag{23}$$

The support reaction also continues to increase rapidly with increasing complexity of the beam shape. The shear force parameter $M_1/L^2/EII$ is shown as a function of rotation angle in Fig. 9. The values at the three points discussed in the foregoing are given by:

$$\frac{M_1}{l}\frac{L^2}{EI} = 5.387\,(2n-1)^2 \qquad \theta_1 = 90 \text{ deg}$$

Downloaded 02 May 2010 to 171.66.16.25. Redistribution subject to ASME license or copyright; see http://www.asme.org/terms/Terms_Use.cfm

$$= 21.55\,(2n-1)^2 \qquad \theta_1 = 220.71 \text{ deg}$$
$$= 86.20\,n^2 \qquad \theta_1 = 40.71 \text{ deg}$$
$$n = 1,2,3, \ldots \tag{24}$$

As indicated in the previous discussion, the support separation ration l/L calculated from equations (15) and (18) decreases from unity j and alternates from positive to negative as the beam shape becomes increasingly complex. The results are shown in Fig. 10 and indicate that the displacement ratio of the left end varies as the square of the end rotation angle for small angles. A good approximation to the end movement ratio is:

$$\frac{u}{L} = 1 - \frac{l}{L} \cong \frac{1}{10}\theta_1^2 \quad (\theta_1 \text{ in radians}) \tag{24}$$

which is in error by about 14 percent for θ_1 of 90 deg.

The support separation ratio curve passes through the two fixed points indicated by crosses. For θ_1 equal to 90 deg, the separation distance can be found to be given by:

$$l/L = \frac{0.783}{2n-1} \quad n = 1,2, \ldots \tag{25}$$

The maximum deflection can be obtained from equations (16*b*) and (19*b*) as the greater of the values obtained when the angle θ is equal to 0 or 180 deg. The calculated values are shown in Fig. 11 and are very well approximated by the relationship given by linear theory as:

$$\frac{y_{\max}}{L} = -\frac{\sqrt{3}}{9}\theta_1 \quad (\theta_1 \text{ in radians}) \tag{26}$$

for θ_1 less than about 60 deg, at which the error is about 7.5 percent. The linear relationship between maximum deflection ratio and moment parameter, which is given by

$$\frac{y_{\max}}{L} = -\frac{\sqrt{3}}{27}\frac{M_1 L}{EI} \tag{27}$$

is initially accurate up to the maximum permitted value of the parameter of about 5.28, however. The error is then only about 6.3 percent although the value of θ_1 is about 145 deg. As the beam becomes more twisted, however, the relationship becomes invalid.

Finally, the variation of the shapes of the deflected beam with end rotation angle is shown in Fig. 12. The larger angles of rotation would be attainable in the elastic range only for relatively flexible beams.

Acknowledgment

The author wishes to thank the reviewers for pointing out some faulty reasoning in the original version of this paper.

References

1 Anon.; Programmer's Manual, "IBM Systems/360 Scientific Subroutine Package," Version III, Program No. 360A-CM-03x.

Downloaded 02 May 2010 to 171.66.16.25. Redistribution subject to ASME license or copyright; see http://www.asme.org/terms/Terms_Use.cfm

R. H. Plaut
Professor,
Department of Civil Engineering.
Mem. ASME

L. W. Johnson
Professor,
Department of Mathematics.

Virginia Polytechnic Institute
and State University,
Blacksburg, Va. 24061

R. Parbery
Senior Lecturer,
Department of Mechanical Engineering,
The University of Newcastle,
New South Wales 2308, Australia

Optimal Forms of Shallow Shells With Circular Boundary

Part 1: Maximum Fundamental Frequency

Thin, shallow, elastic shells with given circular boundary are considered. We seek the axisymmetric shell form which maximizes the fundamental frequency of vibration. The boundary conditions, material, surface area, and uniform thickness of the shell are specified. We employ a bimodal formulation and use an iterative procedure based on the optimality condition to obtain optimal forms. Results are presented for clamped and simply supported boundary conditions. For the clamped case, the optimal forms have zero slope at the boundary. The maximum fundamental frequency is significantly higher than that for the corresponding spherical shell if the boundary is clamped, but only slightly higher if it is simply supported.

Introduction

One basic problem in structural optimization is that of maximizing the fundamental frequency of vibration. This may be desirable to avoid resonance if the structure is subjected to dynamic forces or excitation of its supports. Many frequency optimization results have been obtained for bars, beams, and plates, in which the material is distributed in an optimal manner (e.g., see [1-3]).

Recently, shallow arches were optimized with respect to vibrations. In [4], the form of the arch was varied for given cross section, length, and span, while both the form and material distribution were varied in [5]. For the case of clamped ends, the optimal arch forms have zero slope at the ends and have a significantly higher fundamental vibration frequency than the corresponding circular arch. If the ends are simply supported, however, the circular form is almost optimal.

In this study, we consider thin, shallow, elastic shells with a given circular boundary. The shells are either clamped or simply supported at the boundary. The material, surface area, and uniform thickness of the shell are specified. Hence, the total volume and mass of the shell are given. Our objective in Part 1 is the determination of the axisymmetric form of the shell that has maximum fundamental vibration frequency. (In Parts 2 and 3, we will optimize buckling load and enclosed volume, respectively [6, 7].)

Marguerre's equations [8], including a transverse inertia term, are linearized to yield the governing equations for small vibrations. The optimality condition is derived by the calculus of variations. We allow for the possibility that the fundamental frequency is a double eigenvalue (i.e., the solution is bimodal). An iterative procedure is utilized, based on the optimality condition, and a shooting method is used to obtain numerical results. Optimal forms are determined for several cases, and the maximum fundamental frequencies are compared to those for the corresponding spherical shells.

Shell Equations

Consider a thin, shallow, elastic shell with a circular boundary of radius a. The shell has constant thickness h, density ρ, Young's modulus E, and Poisson's ratio ν. We define polar coordinates r and θ in the base plane, and denote time by T. The middle surface of the shell is assumed to be axisymmetric and is denoted $Z(r)$, with $Z(a)=0$. The slope $Z'(a)$ at the edge is not specified.

The area S of the middle surface is given by

$$S=2\pi\int_0^a [(Z')^2+1]^{1/2} r\, dr. \tag{1}$$

For shallow shells, we can write (1) approximately as

$$S=\pi a^2+\pi\int_0^a (Z')^2 r\, dr. \tag{2}$$

We define the nondimensional surface area parameter λ by

$$\lambda^4=4(S-\pi a^2)/(\pi\, c^2) \tag{3}$$

where

$$c=h/\sqrt{12(1-\nu^2)}. \tag{4}$$

Contributed by the Applied Mechanics Division and presented at the 1984 PVP Conference and Exhibition, Joint with Applied Mechanics Division and Materials Division, San Antonio, Texas, June 17-21, 1984 of THE AMERICAN SOCIETY OF MECHANICAL ENGINEERS.

Discussion on this paper should be addressed to the Editorial Department, ASME, United Engineering Center, 345 East 47th Street, New York, N.Y. 10017, and will be accepted until two months after final publication of the paper itself in the JOURNAL OF APPLIED MECHANICS. Manuscript received by ASME Applied Mechanics Division, June, 1983; final revision, October, 1983. Paper No. 84-APM-38.

Copies will be available until February, 1985.

Copyright © 1984 by ASME
Downloaded 02 May 2010 to 171.66.16.25. Redistribution subject to ASME license or copyright; see http://www.asme.org/terms/Terms_Use.cfm

For shallow spherical shells with central height H, we have $Z(r)=(a^2-r^2)H/a^2$ [9], and (3) yields $\lambda^4=4(H/c)^2$, which is the usual definition of the geometric parameter λ for such shells.

We let $W(r,\theta,T)$ be the downward deflection of the shell and $F(r,\theta,T)$ be a stress function [9]. In the equations of motion, we include a downward axisymmetric distributed load $q(r)$ for reference in Parts 2 and 3, and we neglect inplane inertia. Marguerre's theory leads to the following equations [8, 9]:

$$D\nabla^2\nabla^2 W=\frac{1}{r}\left(F_r+\frac{1}{r}F_{\theta\theta}\right)(W_{rr}-Z'')+\frac{1}{r^2}F_{rr}W_{\theta\theta}+\frac{1}{r}(W_r-Z')F_{rr}-\frac{2}{r^2}\left(F_{r\theta}-\frac{1}{r}F_\theta\right)\left(W_{r\theta}-\frac{1}{r}W_\theta\right)-\rho h\,W_{TT}+q, \tag{5}$$

$$\frac{1}{Eh}\nabla^2\nabla^2 F=\frac{1}{r}\left(W_r+\frac{1}{r}W_{\theta\theta}\right)(Z''-W_{rr})+\frac{1}{r}Z'W_{rr}+\frac{1}{r^2}\left(W_{r\theta}-\frac{1}{r}W_\theta\right)^2, \tag{6}$$

where

$$D=\frac{Eh^3}{12(1-\nu^2)},\quad \nabla^2(\ )=\left(\frac{\partial^2}{\partial r^2}+\frac{1}{r}\frac{\partial}{\partial r}+\frac{1}{r^2}\frac{\partial^2}{\partial\theta^2}\right)(\ ), \tag{7}$$

and subscripts r,θ, and T denote partial derivatives.

We introduce the nondimensional quantities

$$x=r/a,\ z=Z/c,\ w=W/c,\ f=F/D,\quad t=T\sqrt{D/(\rho h a^4)},\ p=qa^4/(4\lambda^4 Dc) \tag{8}$$

and also define

$$g(x)=z'(x). \tag{9}$$

In the optimization procedure, $g(x)$ will be the design function. For a spherical shell, $g(x)=-\lambda^2 x$. In nondimensional terms, equation (2) becomes

$$\int_0^1 g^2\,x\,dx=\lambda^4/4, \tag{10}$$

while (5) and (6) become

$$\nabla^2\nabla^2 w=\frac{1}{x}\left(f_x+\frac{1}{x}f_{\theta\theta}\right)(w_{xx}-g')+\frac{1}{x^2}f_{xx}w_{\theta\theta}+\frac{1}{x}(w_x-g)f_{xx}-\frac{2}{x^2}\left(f_{x\theta}-\frac{1}{x}f_\theta\right)\left(w_{x\theta}-\frac{1}{x}w_\theta\right)-w_{tt}+4\lambda^4 p, \tag{11}$$

$$\nabla^2\nabla^2 f=\frac{1}{x}\left(w_x+\frac{1}{x}w_{\theta\theta}\right)(g'-w_{xx})+\frac{1}{x}g\,w_{xx}+\frac{1}{x^2}\left(w_{x\theta}-\frac{1}{x}w_\theta\right)^2, \tag{12}$$

where

$$\nabla^2(\ )=\left(\frac{\partial^2}{\partial x^2}+\frac{1}{x}\frac{\partial}{\partial x}+\frac{1}{x^2}\frac{\partial^2}{\partial\theta^2}\right)(\ ) \tag{13}$$

and subscripts x,θ, and t denote partial derivatives.

To examine small, natural vibrations of the shell, we set $p=0$ and linearize (11) and (12) in w and f. We then write

$$w(x,\theta,t)=\sum_{n=0}^{\infty}\beta_n(x)\cos n\theta\cos\omega_n t, \tag{14}$$

$$f(x,\theta,t)=\sum_{n=0}^{\infty}\psi_n(x)\cos n\theta\cos\omega_n t, \tag{15}$$

where the ω_n are nondimensional vibration frequencies. This leads to the equations

$$L_nL_n\beta_n=-\frac{1}{x}\left(\psi_n'-\frac{n^2}{x}\psi_n\right)g'-\frac{1}{x}g\psi_n''+\omega_n^2\beta_n, \tag{16}$$

$$L_nL_n\psi_n=\frac{1}{x}\left(\beta_n'-\frac{n^2}{x}\beta_n\right)g'+\frac{1}{x}g\,\beta_n'', \tag{17}$$

where $n=0,1,2,\ldots$, and

$$L_n(\ )=\left(\frac{d^2}{dx^2}+\frac{1}{x}\frac{d}{dx}-\frac{n^2}{x^2}\right)(\ ). \tag{18}$$

For a given value of n, equations (16) and (17), along with appropriate boundary conditions, lead to an infinite number of eigenvalues ω_n. We will let ω_n denote the lowest of these eigenvalues for that n. As an example, ω_0 will denote the lowest frequency associated with axisymmetric vibrations, and $\beta_0(x)$ and $\psi_0(x)$ will be the corresponding vibration mode and stress function, respectively.

If the edge of the shell is simply supported (with no radial and tangential displacements), the boundary conditions at $x=1$ are [10]

$$\beta_n=0, \tag{19}$$

$$\beta_n''+\nu\beta_n'=0, \tag{20}$$

$$\psi_n''-\nu\psi_n'+\nu n^2\psi_n=0, \tag{21}$$

$$\psi_n'''-[1-\nu+(2+\nu)n^2]\psi_n'+3n^2\psi_n-g\beta_n'=0. \tag{22}$$

If the edge is clamped (with no radial and tangential displacements), the boundary conditions are (19), (21), (22), and

$$\beta_n'=0. \tag{23}$$

At $x=0$, finiteness requirements and symmetry properties lead to the following conditions (see Appendix of [7]):

$$\beta_0'=\beta_0'''=\psi_0'=\psi_0'''=0, \tag{24}$$

$$\beta_1=\beta_1''=\psi_1=\psi_1''=0, \tag{25}$$

$$\beta_2=\beta_2'=\beta_2'''=\psi_2=\psi_2'=\psi_2'''=0, \tag{26}$$

$$\beta_n=\beta_n'=\ldots=\beta_n^{(n-1)}=\psi_n=\psi_n'=\ldots=\psi_n^{(n-1)}=0\quad\text{for}\quad n\geq 3. \tag{27}$$

Optimization Equations

Based on (16)-(27), we can write ω_n^2 as the following Rayleigh quotient:

$$\omega_n^2=\Gamma_n/\int_0^1\beta_n^2 x\,dx \tag{28}$$

where

$$\Gamma_n=\int_0^1\left\{(L_n\beta_n)^2-(L_n\psi_n)^2-\frac{2}{x}\left(\psi_n'-\frac{n^2}{x}\psi_n\right)g\beta_n'+\frac{2n^2}{x}\left(\frac{1}{x}\psi_n\right)'g\,\beta_n\right\}x\,dx+(1+\nu)\left[(\psi_n')^2-n^2\left(\frac{1}{x}\psi_n^2\right)'\right]_{x=1}+(\nu-1)\left[\left(\beta_n'\right)^2\right]_{x=1} \tag{29}$$

(see [9]). It is convenient to normalize the vibration mode $\beta_n(x)$ by

$$\int_0^1\beta_n^2 x\,dx=1. \tag{30}$$

Our objective is to determine the design function $g(x)$ which maximizes the fundamental vibration frequency for a given value of the surface area parameter λ. In some cases the optimal design is associated with a double frequency, say

Downloaded 02 May 2010 to 171.66.16.25. Redistribution subject to ASME license or copyright; see http://www.asme.org/terms/Terms_Use.cfm

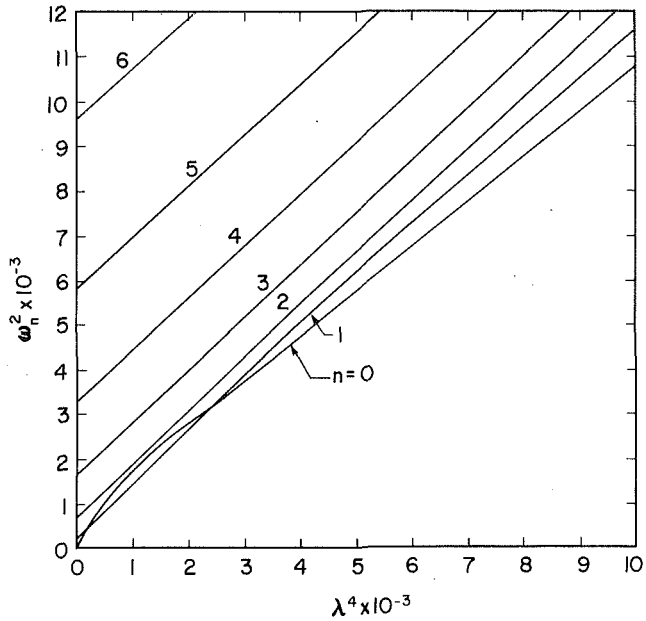


Fig. 1 Vibration frequencies for simply supported spherical shells

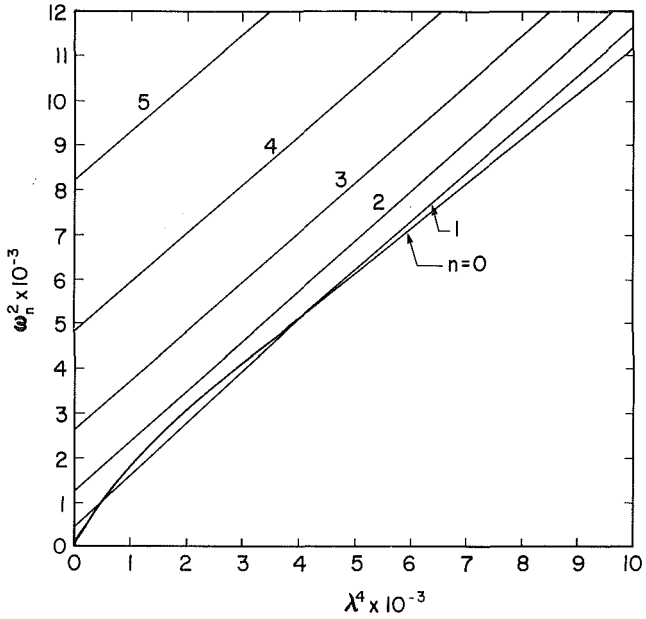


Fig. 2 Vibration frequencies for clamped spherical shells

$\omega_n = \omega_m$, and involves two independent modes, $\beta_n(x)$ and $\beta_m(x)$. Hence we allow for this possibility and consider a bimodal formulation [5].

The objective function is given by (28) and the constraints by $\omega_n = \omega_m$, equation (10), and (30) for $\beta_n(x)$ and $\beta_m(x)$. With the use of Lagrange multipliers ϵ, γ, μ_n, and μ_m, we construct the following augmented functional:

$$\Gamma_n^* = \Gamma_n - \epsilon(\Gamma_n - \Gamma_m) - \gamma\left[\int_0^1 g^2\, x\, dx - (\lambda^4/4)\right]$$

$$- \mu_n\left(\int_0^1 \beta_n^2\, x\, dx - 1\right) - \mu_m\left(\int_0^1 \beta_m^2 x\, dx - 1\right). \tag{31}$$

If the fundamental frequency ω_n^2 is unimodal, then $\epsilon = 0$ and $\mu_m = 0$.

Stationarity of Γ_n^* with respect to $\beta_n(x)$ and $\psi_n(x)$ leads to (16) and (17), respectively, with the appropriate boundary conditions, and to $\mu_n = 0$. A similar result occurs for $\beta_m(x)$ and $\psi_m(x)$. Stationarity of Γ_n^* with respect to the design function $g(x)$ leads to the optimality condition

$$\gamma g(x) = (1-\epsilon)s_n(x) + \epsilon s_m(x) \tag{32}$$

where

$$s_n(x) = \frac{n^2}{x}\left(\frac{\psi_n}{x}\right)'\beta_n - \frac{1}{x}\left(\psi_n' - \frac{n^2}{x}\psi_n\right)\beta_n' \tag{33}$$

and $s_m(x)$ is defined similarly. If the edge of the shell is clamped, we note that (19), (23), and (32) imply that $g(1) = 0$, i.e., the optimal form has zero slope at the clamped edge.

Solution Procedure

The solution procedure involves successive iterations. A spherical shell is usually taken as the initial form, and modifications are based on the optimality condition (32), which provides a formula for the design function $g(x)$. The procedure is concluded when the increase in fundamental frequency for successive designs becomes insignificant.

We specify Poisson's ratio ν, the surface area parameter λ, and the boundary conditions. For the design function $g_i(x)$ at the ith iteration, we solve (16) and (17) with various values of n to determine the fundamental frequency ω_n and the corresponding functions $\beta_n(x)$ and $\psi_n(x)$. The numerical technique used here is described in the Appendix of Part 3 [7]. The next step depends on whether ω_n is distinct or a double eigenvalue.

For the unimodal case (distinct ω_n), $\epsilon = 0$ in (32). If we write $\hat{g}(x) = s_n(x)/\gamma$, then γ^2 is determined by substituting $\hat{g}(x)$ into (10), the sign of γ is chosen so that the shell form corresponding to $\hat{g}(x)$ lies above the base plane, and the design function to be used in the next iteration is given by the recurrence relation

$$g_{i+1}(x) = b[g_i(x) + k\hat{g}(x)]. \tag{34}$$

In (34), k is a parameter which we choose to facilitate convergence of the procedure (e.g., $k = 0.1$), and b is chosen such that $g_{i+1}(x)$ satisfies (10).

For the bimodal case, with $\omega_n = \omega_m$, we denote $g(x) = \hat{g}(x)$ in (32). Substitution of $\hat{g}(x)$ into (10) yields one equation in γ and ϵ. A second equation is obtained by substituting $\hat{g}(x)$ into the bimodal condition $\Gamma_n = \Gamma_m$, along with the functions $\beta_n(x)$, $\psi_n(x)$, $\beta_m(x)$, and $\psi_m(x)$ associated with $g_i(x)$; this is based on the need to increase the two equal frequencies simultaneously. The two equations can be solved for γ and ϵ, with $0 < \epsilon < 1$. We then use those values in $\hat{g}(x)$ and apply (34) to determine the design function for the next iteration.

Results

In all the numerical results, we use $\nu = 1/3$. For comparison purposes, the frequencies of a spherical shell were determined first, i.e., we solved (16) and (17) with $g(x) = -\lambda^2 x$. The resulting values of ω_n^2 for small n are plotted versus λ^4 in Figs. 1 and 2 for simply supported and clamped edge conditions, respectively. (We recall that ω_n denotes the lowest frequency for that value of n.) The frequency ω_0, associated with axisymmetric vibration, is the fundamental one for sufficiently small and sufficiently large values of λ, while ω_1, associated with a mode having a single nodal diameter, is the fundamental frequency in an intermediate range. For $n \geq 1$, the relation between ω_n^2 and λ^4 is almost linear, and is approximately given by

$$\omega_n^2 = \omega_{np}^2 + 1.1\lambda^4, \quad n \geq 1, \tag{35}$$

where ω_{np} is the frequency for the corresponding plate[1]. We

[1] Using another shell theory, Soedel [11] obtained a formula similar to (35) but with the coefficient 1.1 replaced by unity, independent of the value of ν.

Downloaded 02 May 2010 to 171.66.16.25. Redistribution subject to ASME license or copyright; see http://www.asme.org/terms/Terms_Use.cfm

Table 1 Optimal forms $\tilde{z}(x)$

x	Spherical	$S;\lambda=\sqrt{10}$	$S;\lambda=7$	$C;\lambda=4$	$C;\lambda=10$
0.0	1.00	1.09	1.02	1.13	1.03
0.1	0.99	1.08	1.01	1.11	1.02
0.2	0.96	1.04	0.99	1.07	0.97
0.3	0.91	0.97	0.94	0.99	0.89
0.4	0.84	0.88	0.86	0.88	0.77
0.5	0.75	0.76	0.77	0.74	0.59
0.6	0.64	0.63	0.65	0.58	0.42
0.7	0.51	0.48	0.50	0.39	0.42
0.8	0.36	0.32	0.34	0.21	0.34
0.9	0.19	0.16	0.17	0.07	0.14
1.0	0.00	0.00	0.00	0.00	0.00
Frequency ratio		1.03	1.03	1.21	1.42



Fig. 3 Optimal form for maximum fundamental frequency: simply supported edge, $\lambda=\sqrt{10}$



Fig. 4 Optimal form for maximum fundamental frequency: simply supported edge, $\lambda=7$



Fig. 5 Optimal form for maximum fundamental frequency: clamped edge, $\lambda=4$



Fig. 6 Optimal form for maximum fundamental frequency: clamped edge, $\lambda=10$

note that the dimensional frequency, say Ω_n, is related to the nondimensional frequency ω_n by $\Omega_n=\omega_n\sqrt{D/(\rho ha^4)}$.

Optimal forms were determined for simply supported shells with $\lambda=\sqrt{10}$ and $\lambda=7$, and for clamped shells with $\lambda=4$ and $\lambda=7$. They are listed in Table 1 (where S denotes simply supported and C denotes clamped) and depicted in Figs. 3–6, using the nondimensional function

$$\tilde{z}(x)=2z(x)/(\lambda^2). \tag{36}$$

The spherical form, $\tilde{z}(x)=1-x^2$, is also listed in Table 1, as well as the ratio between the fundamental frequency for the optimal form and that for the spherical cap.

For the simply supported shell with $\lambda=\sqrt{10}$, the spherical shell has $\omega_0=16.2$ and $\omega_1=17.9$, while the optimal form has $\omega_0=16.7$ and $\omega_1=18.0$. A bimodal solution did not occur in this case. For $\lambda=7$, we have $\omega_0=55.9$ and $\omega_1=56.5$ for the spherical shell. After a number of iterations, ω_0 and ω_1 coalesced and then were raised further using the bimodal formulation, finally reaching the value $\omega_0=\omega_1=57.8$. Relative to the spherical cap, the increase in fundamental frequency for these two cases is only 3 percent. The optimal forms, shown in Figs. 3 and 4, are convex functions near the edge.

For both cases with a clamped edge, the optimal solutions are bimodal. When $\lambda=4$, the spherical shell has $\omega_0=24.8$ and $\omega_1=27.5$, while the optimal form has $\omega_0=\omega_1=30.1$. When $\lambda=10$, the spherical shell has $\omega_0=106$ and $\omega_1=108$, while the optimal form has $\omega_0=\omega_1=150$. Here the improvement in fundamental frequency is significant. Both optimal forms, shown in Figs. 5 and 6, have zero slope at the edge, as mentioned earlier. Also, the optimal form for the case $\lambda=10$ has a plateau around $x=0.65$. Perspectives of these optimal shells are depicted in Figs. 7 and 8.

Concluding Remarks

We have formulated the problem of maximizing the fundamental vibration frequency of a shallow shell when its form is variable. The shell has a given circular boundary and a given value of the surface area parameter λ. Numerical solutions have been obtained for two cases with a simply supported boundary and two cases with a clamped boundary. For a spherical cap, the fundamental vibration mode (i.e., the mode associated with the lowest frequency) is either axisymmetric ($n=0$) or has one nodal diameter ($n=1$). In the four examples analyzed here, the optimal form either has an

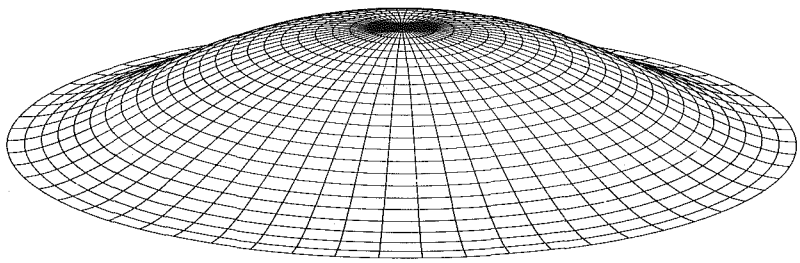


Fig. 7 Geometry of optimal shell for clamped edge, $\lambda=4$

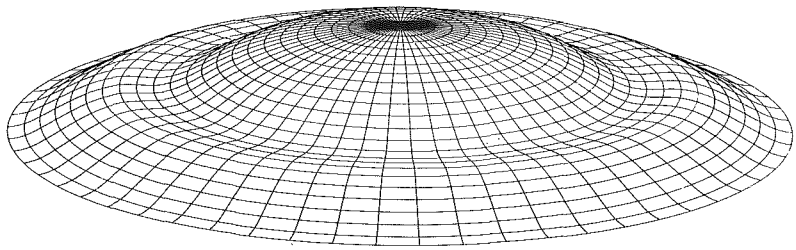


Fig. 8 Geometry of optimal shell for clamped edge, $\lambda=10$

Downloaded 02 May 2010 to 171.66.16.25. Redistribution subject to ASME license or copyright; see http://www.asme.org/terms/Terms_Use.cfm

axisymmetric fundamental vibration mode or a bimodal solution involving the $n = 0$ and $n = 1$ modes (i.e., $\omega_0 = \omega_1$).

The slope of the shell at the boundary is not specified, even when the boundary is clamped. If it were, the optimal form would have a discontinuous slope at the edge. All the optimal forms obtained in this part are convex in regions adjacent to the edge (see Figs. 3–6). For a clamped edge, the slope at the edge is zero, and the fundamental frequency is significantly higher than that for the corresponding spherical cap.

It is interesting to compare the optimal shell forms obtained here with the optimal arch forms determined in [4]. For maximum fundamental frequency, the optimal form of a simply supported arch is sinusoidal, which is almost identical to the form in Fig. 3, while the optimal clamped arch is somewhat similar in form to Fig. 5. For the arch, the optimal fundamental frequency corresponds to a symmetric mode for sufficiently small values of the length parameter, and an antisymmetric mode for sufficiently large values; a bimodal solution only occurs at the transition value. Here, for shallow shells, it appears that a bimodal solution will govern for most values of the geometric parameter λ.

The iterative solution procedure was effective in modifying a design to improve the objective function. The direction of the modification was based on the optimality condition (32). Typically, 10–15 iterations were sufficient to obtain satisfactory convergence of the fundamental frequency. At some steps, the parameter k in (34) has to be altered to avoid overshooting the maximum point. Since the governing set of equations is nonlinear, we cannot guarantee that the solution procedure leads to the global optimum. In a few cases, however, we chose different initial designs and arrived at the same final design.

Acknowledgments

The first author was supported by the National Science Foundation under Grant CEE-8210222, a NATO Senior Fellowship, and Grant No. 16-3077 from the Danish Council for Scientific and Industrial Research. The authors would like to acknowledge Dr. N. Olhoff of the Technical University of Denmark for helpful discussions, and Dr. J. Jensen of the same university for making the computer drawings, Figs. 7 and 8.

References

1 Olhoff, N., "Optimal Design With Respect to Structural Eigenvalues," *Theoretical and Applied Mechanics*, Proceedings of the 15th International Congress of Theoretical and Applied Mechanics, Rimrott, F. P. J., and Tabarrok, B., eds., North-Holland, Amsterdam, 1980, pp. 133–149.

2 Haug, E. J., "A Review of Distributed Parameter Structural Optimization Literature," *Optimization of Distributed Parameter Structures*, Haug, E. J., and Cea, J., eds., Sijthoff & Noordhoff, Alphen aan den Rijn, The Netherlands, 1981, pp. 3–74.

3 Lev, O. E., ed., *Structural Optimization: Recent Developments and Applications*, American Society of Civil Engineers, New York, 1981.

4 Plaut, R. H., and Olhoff, N., "Optimal Forms of Shallow Arches With Respect to Vibration and Stability," *Journal of Structural Mechanics*, Vol. 11, 1983, pp. 81–100.

5 Olhoff, N., and Plaut, R. H., "Bimodal Optimization of Vibrating Shallow Arches," *International Journal of Solids and Structures*, Vol. 19, 1983, pp. 553–570.

6 Plaut, R. H., and Johnson, L. W., "Optimal Forms of Shallow Shells With Circular Boundary. Part 2: Maximum Buckling Load," ASME JOURNAL OF APPLIED MECHANICS, Vol. 51, 1984, pp. – .

7 Plaut, R. H., and Johnson, L. W., "Optimal Forms of Shallow Shells With Circular Boundary. Part 3: Maximum Enclosed Volume," ASME JOURNAL OF APPLIED MECHANICS, Vol. 51, 1984, pp. – .

8 Marguerre, K., "Zur Theorie der gekrümmten Platte grosser Formänderung," *Proceedings of the 5th International Congress of Applied Mechanics*, den Hartog, J. P., and Peters, H., eds., Wiley, New York, 1939, pp. 93–101.

9 Huang, N. C., "Unsymmetrical Buckling of Thin Shallow Spherical Shells," ASME JOURNAL OF APPLIED MECHANICS, Vol. 31, 1964, pp. 447–457.

10 Weinitschke, H. J., "On Asymmetric Buckling of Shallow Spherical Shells," *Journal of Mathematics and Physics*, Vol. 44, 1965, pp. 141–163.

11 Soedel, W., "A Natural Frequency Analogy Between Spherically Curved Panels and Flat Plates," *Journal of Sound and Vibration*, Vol. 29, 1973, pp. 457–461.

Downloaded 02 May 2010 to 171.66.16.25. Redistribution subject to ASME license or copyright; see http://www.asme.org/terms/Terms_Use.cfm

Optimal Forms of Shallow Shells With Circular Boundary

Part 2: Maximum Buckling Load

R. H. Plaut
Professor,
Department of Civil Engineering.

L. W. Johnson
Professor,
Department of Mathematics.

Virginia Polytechnic Institute
and State University,
Blacksburg, Va. 24061

In Part 1, optimal forms were determined for maximizing the fundamental vibration frequency of a thin, shallow, axisymmetric, elastic shell with given circular boundary. Our objective in this part is to maximize the critical load for buckling under a uniformly distributed load or a concentrated load at the center. Again, the shell form is varied and the material, surface area, and uniform thickness of the shell are specified. Both clamped and simply supported boundary conditions are considered for the case of uniform loading, while one example is presented involving a concentrated load acting on a clamped shell. The optimality condition leads to forms that have zero slope at the boundary if it is clamped. The maximum critical load is sometimes associated with a limit point and sometimes with a bifurcation point. It is often substantially higher than the critical load for the corresponding spherical shell.

Introduction

As in Part 1 of this study [1], we optimize the forms of thin, shallow, elastic shells with a given circular boundary. In this part, however, the shell is loaded quasi-statically and we maximize the critical load. Optimization of structures with respect to buckling has received much attention (e.g., see [2, 3]). Also, buckling of shallow spherical shells has been studied extensively (e.g., see [4]). However, the problem considered here has not been treated previously.

A similar type of investigation was carried out for shallow arches in [5]. As here, the boundary conditions were either clamped or simply supported, and the load was applied uniformly over the structure or was concentrated at the center. For simply supported ends, the optimal arches were almost circular. For clamped ends, the optimal forms had zero end slopes and had significantly higher critical loads than the corresponding circular arches.

The initial formulation in this part is similar to that in Part 1. The shell has specified material, surface area, and uniform thickness, but an arbitrary axisymmetric form. Marguerre's theory [6] is used to describe the shell behavior. In this case, we have a set of nonlinear differential equations to be solved for the primary equilibrium state of the shell under the applied load. Then we examine small vibrations about this state, and find the critical load when a vibration frequency decreases to zero [7]. The optimality condition, derived by the calculus of variations, is used to improve the shell form by successive iterations. The solution procedure is the same as that described in Part 1. After obtaining optimal forms, we compare the corresponding critical loads to those for spherical shells.

Shell Equations

The shell parameters are the same as those defined in [1]. In nondimensional terms, x and θ are polar coordinates, t is the time, $z(x)$ is the shell form, $g(x)$ is defined by $g(x) = z'(x)$, λ is the surface area parameter, $p(x)$ is the downward axisymmetric load, $w(x, \theta, t)$ is the downward deflection, and $f(x, \theta, t)$ is the corresponding stress function. The shell lies above the base plane (i.e., $z(x) \geq 0$), and at the boundary we have $z(1) = 0$. Equations (1)–(13) of [1] are also valid in this part.

First we determine the governing equations for the primary equilibrium state. This state will be axisymmetric, so that w and f will only be functions of x. We delete the inertia term in (11) of [1], introduce the functions

$$\alpha(x) = -w'(x), \quad \phi(x) = f'(x), \tag{1}$$

and then integrate (11) and (12) of [1] with respect to x. This yields

$$A \equiv (x\,\alpha')' - \frac{1}{x}\,\alpha - (g+\alpha)\,\phi + 4\,\lambda^4 \int_0^x p(\zeta)\,\zeta\,d\zeta = 0, \tag{2}$$

$$B \equiv (x\,\phi')' - \frac{1}{x}\,\phi + g\alpha + \frac{1}{2}\,\alpha^2 = 0, \tag{3}$$

Contributed by the Applied Mechanics Division and presented at the 1984 PVP Conference and Exhibition, Joint with Applied Mechanics Division and Materials Division, June 17–21, 1984 of THE AMERICAN SOCIETY OF MECHANICAL ENGINEERS.

Discussion on this paper should be addressed to the Editorial Department, ASME, United Engineering Center, 345 East 47th Street, New York, N.Y. 10017, and will be accepted until two months after final publication of the paper itself in the JOURNAL OF APPLIED MECHANICS. Manuscript received by ASME Applied Mechanics Division, June, 1983; final revision October, 1983. Paper No. 84-APM-39.

Copies will be available until February, 1985.

Copyright © 1984 by ASME
Downloaded 02 May 2010 to 171.66.16.25. Redistribution subject to ASME license or copyright; see http://www.asme.org/terms/Terms_Use.cfm

where we denote the left sides of (2) and (3) by A and B, respectively. Similar equations are used in [8–11] for spherical caps. If the edge of the shell is simply supported [9],

$$\alpha' + \nu\alpha = 0, \quad \phi' - \nu\phi = 0 \quad \text{at } x = 1. \tag{4}$$

If the edge is clamped [8],

$$\alpha = 0, \quad \phi' - \nu\phi = 0 \quad \text{at } x = 1. \tag{5}$$

Symmetry and finiteness conditions imply that [9]

$$\alpha = 0, \quad \phi = 0 \quad \text{at } x = 0. \tag{6}$$

Now we consider small vibrations about the primary equilibrium state. In (11) and (12) of [1], we replace $w(x, \theta, t)$ and $f(x, \theta, t)$ by $w(x) + \beta(x, \theta, t)$ and $f(x) + \psi(x, \theta, t)$, respectively. Then we delete nonlinear terms in β and ψ from the resulting equations. This leads to

$$\nabla^2\nabla^2\beta = \frac{1}{x}\phi\beta_{xx} + \frac{1}{x}\phi'\beta_x + \frac{1}{x^2}\phi'\beta_{\theta\theta} - \frac{1}{x}(g+\alpha)\psi_{xx} - \frac{1}{x}(g'+\alpha')\left(\psi_x + \frac{1}{x}\psi_{\theta\theta}\right) - \beta_{tt}, \tag{7}$$

$$\nabla^2\nabla^2\psi = -\frac{1}{x}(g+\alpha)\beta_{xx} - \frac{1}{x}(g'+\alpha')\left(\beta_x + \frac{1}{x}\beta_{\theta\theta}\right), \tag{8}$$

where $\alpha(x)$ and $\phi(x)$ are defined in (1), ∇^2 is defined in (13) of [1], and subscripts x, θ, and t denote partial derivatives.

If the edge of the shell is simply supported (with no radial and tangential displacements), the boundary conditions at $x = 1$ are [9]

$$\beta = 0, \tag{9}$$

$$\beta_{xx} + \nu\beta_x = 0, \tag{10}$$

$$\psi_{xx} - \nu\psi_x - \nu\psi_{\theta\theta} = 0, \tag{11}$$

$$\psi_{xxx} + (\nu-1)\psi_x + (2+\nu)\psi_{x\theta\theta} - 3\psi_{\theta\theta} - (g+\alpha)\beta_x = 0. \tag{12}$$

If the edge is clamped (with no radial and tangential displacements), the boundary conditions at $x = 1$ are (9), (11), (12), and [8]

$$\beta_x = 0. \tag{13}$$

We now write

$$\beta(x,\theta,t) = \sum_{n=0}^{\infty} \beta_n(x) \cos n\theta \cos \omega_n t, \tag{14}$$

$$\psi(x,\theta,t) = \sum_{n=0}^{\infty} \psi_n(x) \cos n\theta \cos \omega_n t, \tag{15}$$

where the ω_n are nondimensional vibration frequencies. This leads to the equations

$$L_nL_n\beta_n = \frac{1}{x}(\phi\beta_n')' - \frac{n^2}{x^2}\phi'\beta_n - \frac{1}{x}[(g+\alpha)\psi_n']' + \frac{n^2}{x^2}(g'+\alpha')\psi_n + \omega_n^2\beta_n, \tag{16}$$

$$L_nL_n\psi_n = \frac{1}{x}[(g+\alpha)\beta_n']' - \frac{n^2}{x^2}(g'+\alpha')\beta_n, \tag{17}$$

where $n = 0,1,2, \ldots$, and L_n is defined in (18) of [1]. The boundary conditions on $\beta_n(x)$ and $\psi_n(x)$ are given by (19)–(27) of [1], except that g in (22) is replaced by $g + \alpha$.

To determine the critical load, we increase the load magnitude until one of the frequencies ω_n decreases to zero [7]. The corresponding vibration mode $\beta_n(x)$ is then the buckling mode. If $n = 0$ governs, so that $\omega_0 = 0$ at the critical load, the primary equilibrium state is at a limit point on the equilibrium path and axisymmetric buckling occurs; an increase in load leads to a jump in deflection. If $\omega_n = 0$, $n \geq 1$, at the critical load, we are at a bifurcation point on the equilibrium path, and whether the deflection is continuous or not depends on the properties of the branching path (i.e., the postbuckling behavior). If the branching path initially "falls" while the primary path continues to "rise," and the equilibrium states on both these paths are unstable, then the deflection exhibits a jump (asymmetric buckling) when the critical load is reached. If the branching path "rises," however, and its equilibrium states are stable while those on the primary path are not, the deflection becomes asymmetric as the bifurcation point is passed, but does not exhibit a jump [11].

Optimization Equations

We define

$$\Lambda_n = \Gamma_n + \int_0^1 \left[\frac{1}{x}\phi(\beta_n')^2 + \frac{n^2}{x^2}\phi'\beta_n^2 - \frac{2}{x}\left(\psi_n' - \frac{n^2}{x}\psi_n\right)\alpha\beta_n' + \frac{2n^2}{x}\left(\frac{\psi_n}{x}\right)'\alpha\beta_n\right]x\,dx \tag{18}$$

where Γ_n is given in (29) of [1]. If $\omega_n = 0$, the functional Λ_n is stationary when (16) and (17) are satisfied. We present a unimodal formulation, which assumes that only one frequency ω_n is zero at the critical load.

A uniformly distributed load and a concentrated load will be treated in the examples. These can both be included if we write

$$p(x) = \begin{cases} p & \text{if } 0 \leq x < \bar{x} \\ 0 & \text{if } \bar{x} \leq x \leq 1 \end{cases} \tag{19}$$

where $\bar{x} = 1$ for the first case and $\bar{x} \to 0$ for the second. (In the computations involving a concentrated load, we put $\bar{x} = 0.01$.) The critical value of p will be maximized.

We have the following constraints: (2) and (3), the equations governing the equilibrium state; (16) and (17) with $\omega_n = 0$, the buckling equations, which are included through the functional Λ_n; (10) of [1], the given surface area of the shell; and (30) of [1], the normalization condition on the buckling mode $\beta_n(x)$. These constraints are appended to the load p with the use of Lagrange multipliers $\xi(x)$, $\eta(x)$, κ, γ, and μ. We then obtain the augmented functional

$$p^* = p - \int_0^1 \xi A\,dx - \int_0^1 \eta B\,dx - \kappa\Lambda_n - \gamma\left[\int_0^1 g^2 x\,dx - (\lambda^4/4)\right] - \mu\left[\int_0^1 \beta_n^2 x\,dx - 1\right] \tag{20}$$

where A, B, and Λ_n are defined in (2), (3), and (18), respectively.

Stationarity of p^* with respect to $\beta_n(x)$ and $\psi_n(x)$ leads to (16) and (17), respectively, with the appropriate boundary conditions, and to $\mu = 0$ (since $\omega_n = 0$). Stationarity of p^* with respect to $\alpha(x)$ and $\phi(x)$ leads to the following equations governing $\xi(x)$ and $\eta(x)$:

$$(x\xi')' - \frac{1}{x}\xi - \phi\xi + (g+\alpha)\eta = 2\kappa\left[\left(\psi_n' - \frac{n^2}{x}\psi_n\right)\beta_n' - n^2\left(\frac{1}{x}\psi_n\right)'\beta_n\right], \tag{21}$$

$$(x\eta')' - \frac{1}{x}\eta - (g+\alpha)\xi = \kappa\left[n^2\left(\frac{1}{x}\beta_n^2\right)' - (\beta_n')^2\right]. \tag{22}$$

The boundary conditions on $\xi(x)$ and $\eta(x)$ are the same as

Downloaded 02 May 2010 to 171.66.16.25. Redistribution subject to ASME license or copyright; see http://www.asme.org/terms/Terms_Use.cfm

Table 1 Optimal forms $\bar{z}(x)$

		Uniform load				Concentrated load
x	Spherical	$S;\lambda=\sqrt{10}$	$S;\lambda=7$	$C;\lambda=4$	$C;\lambda=8$	$C;\lambda=8.5$
0	1.00	1.03	0.97	1.07	0.97	0.86
0.1	0.99	1.02	0.96	1.06	0.99	0.86
0.2	0.96	1.00	0.94	1.03	1.01	0.84
0.3	0.91	0.95	0.89	0.98	0.96	0.82
0.4	0.84	0.87	0.82	0.88	0.85	0.78
0.5	0.75	0.77	0.74	0.75	0.75	0.75
0.6	0.64	0.64	0.64	0.57	0.62	0.61
0.7	0.51	0.49	0.52	0.37	0.45	0.36
0.8	0.36	0.33	0.37	0.18	0.25	0.16
0.9	0.19	0.16	0.20	0.05	0.08	0.04
1.0	0.00	0.00	0.00	0.00	0.00	0.00
Load ratio		1.06	1.24	2.10	1.22	3.43

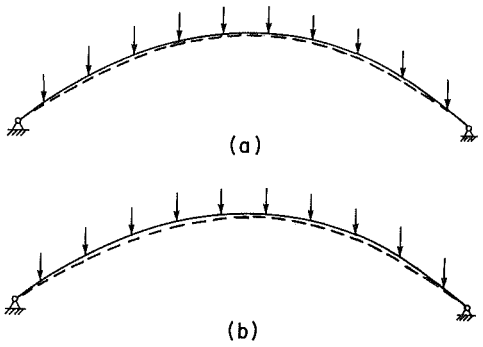


Fig. 1 Shell form and deflected shape at critical uniform load for simply supported edge, $\lambda = \sqrt{10}$: (a) spherical form; (b) optimal form

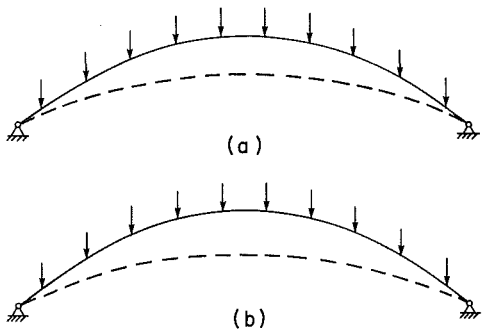


Fig. 2 Shell form and deflected shape at critical uniform load for simply supported edge, $\lambda = 7$: (a) spherical form; (b) optimal form

those on $\alpha(x)$ and $\phi(x)$, respectively, which are given in (4)–(6).

Stationarity of p^* with respect to p yields the following normalization condition on $\xi(x)$:

$$\int_0^{\bar{x}} \xi(x)x^2\,dx+\bar{x}^2\int_{\bar{x}}^1 \xi(x)\,dx=1/(2\lambda^4). \tag{23}$$

Finally, stationarity of p^* with respect to the design function $g(x)$ furnishes the optimality condition

$$\gamma g(x)=\frac{1}{2x}[\phi(x)\xi(x)-\alpha(x)\eta(x)]-\kappa s_n(x) \tag{24}$$

where $s_n(x)$ is defined in (33) of [1]. As in [1], if the edge of the shell is clamped, the optimal form has zero slope there, i.e., $g(1) = 0$.

Solution Procedure

We employ successive iterations based on the optimality condition to improve the design of the shell. We choose an initial form, often spherical, and then, for given values of ν, λ, and $\bar{x}$, carry out the following algorithm:

I. Assign a small value to p.

II. Solve (2) and (3) for $\alpha(x)$ and $\phi(x)$.

III. For various n, solve (16) and (17) for vibration frequencies ω_n and corresponding eigenfunctions $\beta_n(x)$ and $\psi_n(x)$, normalized using (30) of [1].

IV. Increase p and return to *II*, unless one of the frequencies ω_n has decreased to zero, in which case continue to *V*.

V. Solve (21) and (22) for $\xi(x)$ and $\eta(x)$, with κ determined from (23).

VI. Obtain $g(x) = \hat{g}(x)$ from the optimality condition (24), with γ determined from (10) of [1].

VII. Choose the next design according to (34) of [1]. Then return to *I*.

The algorithm is concluded when the critical load (i.e., the value p at which $\omega_n = 0$) does not increase significantly for successive designs.

The inner loop, involving increments of the load p, is desirable to make certain we find the first limit point ($n=0$) or bifurcation point ($n\geq 1$) on the primary equilibrium path. The number of values of n which have to be investigated depends on the value of λ (e.g., see Table 2 in [8] with respect to limit and bifurcation loads for spherical caps). At different iterations, the governing value of n may be different. Using the optimality condition (24) tends to increase the critical value relative to the nth mode, but may decrease the critical values for some other modes.

The numerical technique used to solve the pairs of equations (2) and (3), (16) and (17), and (21) and (22), which are involved in the solution algorithm, is described in the Appendix of Part 3 of this study [12].

Results

We use $\nu = 1/3$ in all the numerical examples. For a load distributed uniformly over the shell, $\bar{x}=1$ in (19). For a concentrated load P applied at the center of the shell, results are presented in terms of the nondimensional load

$$Q=P\,a^2/(2\pi\lambda^2 Dc) \tag{25}$$

where λ, c, and D are defined in (3), (4), and (7) of [1], respectively. In the special case of a spherical shell, the critical value of Q reduces to the parameters p_c in [10] and Q_c in [11].

The results are listed in Table 1, where $\bar{z}(x)$ is defined in

Downloaded 02 May 2010 to 171.66.16.25. Redistribution subject to ASME license or copyright; see http://www.asme.org/terms/Terms_Use.cfm

(36) of [1], S denotes a simply supported edge, C denotes a clamped edge, and the last row gives the ratio of the optimal critical load to the critical load of the corresponding spherical cap. In Figs. 1–4 and 7, the spherical and optimal forms are plotted with solid curves in (*a*) and (*b*), respectively, and the deflected shapes at the critical point are shown as dashed curves. The critical loads computed for the spherical cap are in close agreement with earlier values given in [8–10].

In Figs. 1 and 2, the shell is simply supported and subjected to a uniform load. For $\lambda = \sqrt{10}$ (Fig. 1), both the spherical and optimal shells exhibit axisymmetric buckling ($n=0$), with $p_0 = 0.490$ for the spherical shell and $p_0 = 0.517$ for the optimal one. Here we denote the critical load by p_n, where n refers to the governing buckling mode. The optimal shell in Fig. 1(*b*) is slightly convex near the edge. For $\lambda = 7$ (Fig. 2), the spherical shell has $p_4 = 0.656$ and the optimal one has $p_3 = 0.816$, so that the governing modes are different for the two shells.

Results for clamped, uniformly loaded shells are depicted in Figs. 3 and 4. We note again that the slopes of the optimal forms at the clamped edge are zero. For $\lambda = 4$ (Fig. 3), we have $p_0 = 0.573$ for the spherical shell and $p_1 = 1.204$ for the optimal shell, i.e., an increase of 110 percent in the critical load. For $\lambda = 8$ (Fig. 4), the spherical shell has $p_4 = 0.766$ and the optimal shell has $p_1 = 0.934$, an increase of 22 percent. The optimal form in Fig. 4(*b*) possesses a crater at the center, for unexplained reasons, and develops much larger deflections than the spherical shell at the onset of buckling. Perspectives of the optimal forms in Figs. 3(*b*) and 4(*b*) are shown in Figs. 5 and 6, respectively.

Finally, one case involving a central concentrated load was analyzed: a clamped shell with $\lambda = 8.5$. At this value of λ, a spherical cap exhibits limit point instability at $Q = 15.6$, and axisymmetric snap-through occurs at this load. As seen in Fig. 7(*a*), the corresponding deflection is very large. Following the optimization algorithm, we arrived at the form shown in Fig. 7(*b*), with a critical load $Q = 53.4$. As in the previous two examples involving a clamped shell, the buckling mode associated with the form in Fig. 7(*b*) has one nodal diameter (i.e., $n=1$).

It is interesting that buckling of a clamped spherical shell, subjected to a uniform load or a concentrated load at the apex, is never governed by the $n=1$ mode [8, 10], yet the three optimal forms obtained here with clamped boundary conditions are governed by that mode.

Concluding Remarks

The form of a shell can have a large effect on the critical value of an applied load. We have considered shallow shells with a given circular boundary and a given value of the surface area parameter λ. Five examples have been treated, involving clamped or simply supported boundaries and uniform or concentrated loads. As in Part 1 [1], where the

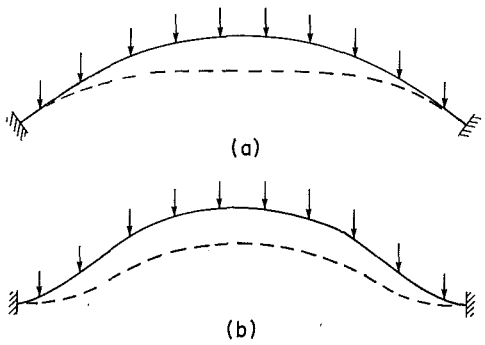


Fig. 3 Shell form and deflected shape at critical uniform load for clamped edge, $\lambda = 4$: (*a*) spherical form; (*b*) optimal form

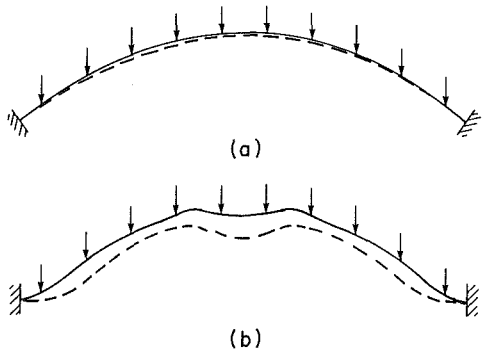


Fig. 4 Shell form and deflected shape at critical uniform load for clamped edge, $\lambda = 8$: (*a*) spherical form; (*b*) optimal form

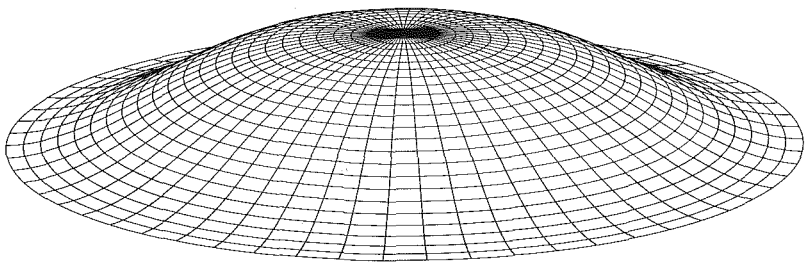


Fig. 5 Geometry of optimal shell for uniform load, clamped edge, $\lambda = 4$

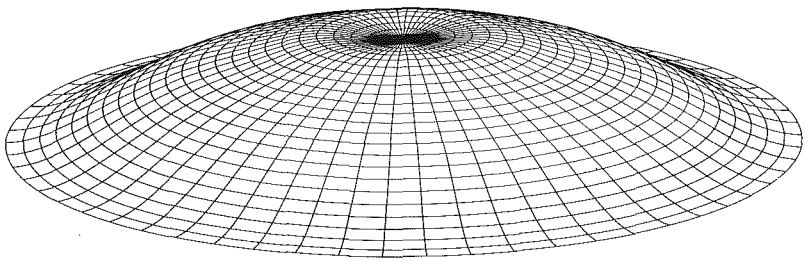


Fig. 6 Geometry of optimal shell for uniform load, clamped edge, $\lambda = 8$

Downloaded 02 May 2010 to 171.66.16.25. Redistribution subject to ASME license or copyright; see http://www.asme.org/terms/Terms_Use.cfm

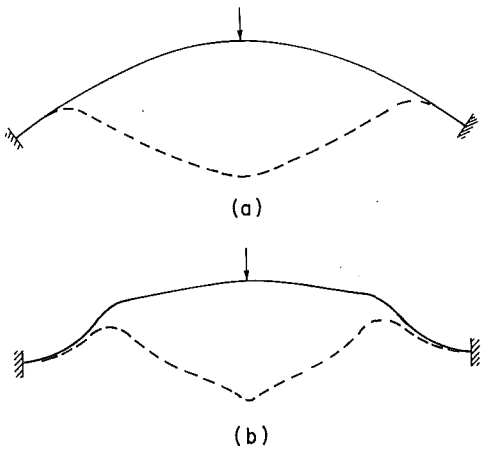


Fig. 7 Shell form and deflected shape at critical concentrated load for clamped edge, $\lambda = 8.5$: (a) spherical form; (b) optimal form

fundamental vibration frequency was maximized, the optimal forms for clamped shells have zero slope at the boundary.

Between 5 and 13 iterations were carried out in the examples. The numerical computations were much more lengthy and difficult in this part than in Part 1. This was partly due to the inner loop in the solution algorithm, in which the critical point was obtained for the current design function. At certain stages during the incremental increase of the load, determination of the primary equilibrium path was hampered by the existence of other nearby equilibrium states. This was especially true for the example involving a concentrated load.

At all stages of the iteration procedure, we found that the critical load was very sensitive to changes in design, as might be expected (at least in the uniform load case) from the imperfection-sensitivity properties of shallow spherical shells [11]. Due to the computational difficulties and this sensitivity, our convergence criterion in this part was not as stringent as in Parts 1 and 3 [1, 12]. The forms presented in Figs. 1(*b*)–4(*b*) and 7(*b*) are certainly more efficient than the spherical form with respect to stability, but they may not be the exact, globally optimal designs.

We expected that the iteration procedure would lead to the coalescence of two or more eigenvalues, at least for the higher values of λ where a number of bifurcation points are close together on the primary equilibrium path of the spherical cap [8]. However, this did not occur before we ended the procedure. For this reason, only a unimodal formulation has been described in this part. Perhaps with many small iterative steps (i.e., very small values of k in (34) of [1]) one could reach a bimodal solution, and then with substantial computational effort one might be able to raise the double eigenvalue slightly. However, the resulting forms would probably not differ much from those presented here, and they would probably be more imperfection-sensitive due to the multiple eigenvalue (e.g., see [13], Ch. 13).

The significance of the critical value of the load depends on the postbuckling behavior of the shell. The critical load for the optimal form in Fig. 1(*b*) is associated with a limit point, so that a jump in deflection will occur, but the size of this jump may be small or large. For the other optimal forms, having one or three circumferential waves in their buckling modes, the sensitivity of the critical load to small imperfections depends on the properties of the branching path at the critical bifurcation point. As described earlier, there may be a discontinuity in deflection, or just a transition to an asymmetric equilibrium state.

The critical load may not be the relevant quantity for optimization. For example, if λ is small or if the load is localized, the deflections may become unacceptable before the load reaches its critical value (e.g., see Fig. 7). Therefore it may be desirable to optimize the shell form with respect to deflection. A problem of this type will be treated in Part 3 [12].

Acknowledgment

The first author was supported by the National Science Foundation under Grant CEE-8210222. The authors would like to thank Dr. J. Jensen of the Technical University of Denmark for making the computer drawings, Figs. 5 and 6.

References

1 Plaut, R. H., Johnson, L. W., and Parbery, R., "Optimal Forms of Shallow Shells With Circular Boundary. Part 1: Maximum Fundamental Frequency," ASME JOURNAL OF APPLIED MECHANICS, Vol. 51, 1984, pp.

2 Olhoff, N., "Optimal Design With Respect to Structural Eigenvalues," *Theoretical and Applied Mechanics*, Proceedings of the 15th International Congress of Theoretical and Applied Mechanics, Rimrott, F. P. J., and Tabarrok, B., eds., North-Holland, Amsterdam, 1980, pp. 133–149.

3 Haug, E. J., "A Review of Distributed Parameter Structural Optimization Literature," *Optimization of Distributed Parameter Structures*, Haug, E. J., and Cea, J., eds., Sijthoff & Noordhoff, Alphen aan den Rijn, The Netherlands, 1981, pp. 3–74.

4 Kaplan, A., "Buckling of Spherical Shells," *Thin-Shell Structures: Theory, Experiment, and Design*, Fung, Y. C., and Sechler, E. E., eds., Prentice-Hall, Englewood Cliffs, N.J., 1974, pp. 247–288.

5 Plaut, R. H., and Olhoff, N., "Optimal Forms of Shallow Arches with Respect to Vibration and Stability," *Journal of Structural Mechanics*, Vol. 11, 1983, pp. 81–100.

6 Marguerre, K., "Zur Theorie der gekrümmten Platte grosser Formänderung," *Proceedings of the 5th International Congress of Applied Mechanics*, den Hartog, J. P., and Peters, H., eds., Wiley, New York, 1939, pp. 93–101.

7 Archer, R. R., and Famili, J., "On the Vibration and Stability of Finitely Deformed Shallow Spherical Shells," ASME JOURNAL OF APPLIED MECHANICS, Vol. 32, 1965, pp. 116–120.

8 Huang, N. C., "Unsymmetrical Buckling of Thin Shallow Spherical Shells," ASME JOURNAL OF APPLIED MECHANICS, Vol. 31, 1964, pp. 447–457.

9 Weinitschke, H. J., "On Asymmetric Buckling of Shallow Spherical Shells," *Journal of Mathematics and Physics*, Vol. 44, 1965, pp. 141–163.

10 Fitch, J. R., "The Buckling and Post-Buckling Behavior of Spherical Caps Under Concentrated Load," *International Journal of Solids and Structures*, Vol. 4, 1968, pp. 421–446.

11 Fitch, J. R., and Budiansky, B., "Buckling and Postbuckling Behavior of Spherical Caps Under Axisymmetric Load," *AIAA Journal*, Vol. 8, 1970, pp. 686–693.

12 Plaut, R. H., and Johnson, L. W., "Optimal Forms of Shallow Shells with Circular Boundary. Part 3: Maximum Enclosed Volume," ASME JOURNAL OF APPLIED MECHANICS, Vol. 51, 1984, pp.

13 Thompson, J. M. T., and Hunt, G. W., *A General Theory of Elastic Stability*, Wiley, New York, 1973.

Downloaded 02 May 2010 to 171.66.16.25. Redistribution subject to ASME license or copyright; see http://www.asme.org/terms/Terms_Use.cfm

Optimal Forms of Shallow Shells With Circular Boundary

Part 3: Maximum Enclosed Volume

R. H. Plaut
Professor,
Department of Civil Engineering.

L. W. Johnson
Professor,
Department of Mathematics.

Virginia Polytechnic Institute
and State University,
Blacksburg, Va. 24061

In Parts 1 and 2, we determined optimal forms of shallow shells with respect to vibration and stability, respectively. In this final part, we consider a given load and find the shell form for which the volume between the base plane and the deflected shell is a maximum. As before, the shell is assumed to be thin, elastic, and axisymmetric, with a given circular boundary that is either clamped or simply supported. The material, surface area, and uniform thickness of the shell are specified. Both uniformly distributed loads and concentrated central loads are treated. In the numerical results, the maximum enclosed volume is on the order of 10 percent higher than that for the corresponding spherical shell.

Introduction

Our objective in Part 1 of this study was maximization of the fundamental vibration frequency of a shallow shell [1]. In Part 2, a quasi-static load was applied and its critical value was maximized [2]. In some cases, particularly if the load is localized, the shell may exhibit prebuckling deflections which are larger than desired (e.g., see Fig. 7 in [2]). Therefore we now consider an objective function that is related to the deflection of the shell under a given load.

Optimal structural design with respect to deflection has been investigated for various structural elements, including beams, plates, and arches [3, 4]. In [4], the form of a shallow arch was chosen to minimize the central deflection. When the ends of the arch were simply supported and the load was distributed uniformly, the optimal form turned out to be sinusoidal.

Here, we do not use a direct measure of deflection as the objective function. Since the form of the shell is variable in our formulation, the deflection relative to this form may not be a meaningful criterion. For example, a shell with a deep crater in the middle may not deflect much under a concentrated central load, yet the deflected shape may be very low in the center and hence undesirable. As an appropriate objective which involves the deflection, we will maximize the volume enclosed between the base plane and the deflected configuration of the shell.

The formulation is similar to that in Part 2. The shells are thin, elastic, and axisymmetric, with given material, surface area, and uniform thickness. Both clamped and simply supported boundary conditions are treated, and the load is either distributed uniformly or concentrated at the center of the shell. The appropriate optimality condition is derived and then utilized in an iterative procedure to obtain optimal forms.

In the special case of no load, the maximum enclosed volume (for given surface area) is obtained for a spherical form, as is well known. Otherwise, the optimal form depends on the load distribution and magnitude, the value of the surface area parameter, and the boundary conditions. Unlike the results of Parts 1 and 2, in this case the optimal forms with a clamped edge do not have zero slope at the edge.

Formulation

Equations (1)–(13) of [1] and (1)–(6) of [2] are also valid in this part. In dimensional terms, the enclosed volume is given by

$$V = 2\pi \int_0^a (Z - W) r \, dr \tag{1}$$

where Z is the shell form and W is the downward deflection. In nondimensional terms, the use of (8) of [1] gives

$$v = 2 \int_0^1 (z - w) \, x \, dx \tag{2}$$

where $v = V/(\pi a^2 c)$. Then, using integration by parts, we can write

$$v = - \int_0^1 (g + \alpha) x^2 \, dx \tag{3}$$

where $g(x) = z'(x)$ and $\alpha(x) = - w'(x)$. The right side of (3) is to be maximized.

The constraints are given by (2) and (3) of [2], which govern

Contributed by the Applied Mechanics Division and presented at the 1984 PVP Conference and Exhibition, Joint with Applied Mechanics Division and Materials Division, June 17–21, 1984 of THE AMERICAN SOCIETY OF MECHANICAL ENGINEERS.

Discussion on this paper should be addressed to the Editorial Department, ASME, United Engineering Center, 345 East 47th Street, New York, N.Y. 10017, and will be accepted until two months after final publication of the paper itself in the JOURNAL OF APPLIED MECHANICS. Manuscript received by ASME Applied Mechanics Division, June, 1983; final revision, October, 1983. Paper No. 84-APM-40.

Copies will be available until February, 1985.

Copyright © 1984 by ASME
Downloaded 02 May 2010 to 171.66.16.25. Redistribution subject to ASME license or copyright; see http://www.asme.org/terms/Terms_Use.cfm

Table 1 Optimal forms $\bar{z}(x)$

x	Spherical	Uniform load S;λ=2	Uniform load C;λ=2.5	Concentrated load S;λ=√10	Concentrated load C;λ=8.5
0.0	1.00	1.10	1.17	1.20	0.97
0.1	0.99	1.09	1.15	1.17	0.97
0.2	0.96	1.04	1.10	1.10	0.96
0.3	0.91	0.97	1.01	0.99	0.93
0.4	0.84	0.88	0.89	0.87	0.86
0.5	0.75	0.76	0.75	0.73	0.76
0.6	0.64	0.63	0.60	0.60	0.63
0.7	0.51	0.48	0.45	0.45	0.50
0.8	0.36	0.32	0.29	0.31	0.35
0.9	0.19	0.16	0.14	0.16	0.19
1.0	0.00	0.00	0.00	0.00	0.00
Volume ratio		1.08	1.10	1.14	1.09

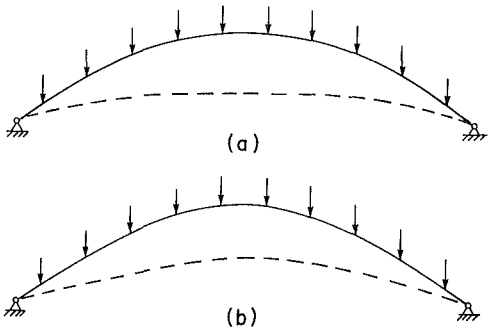


Fig. 1 Shell form and deflected shape at uniform load p = 0.469 for simply supported edge, λ = 2: (*a*) spherical form; (*b*) optimal form for maximum enclosed volume

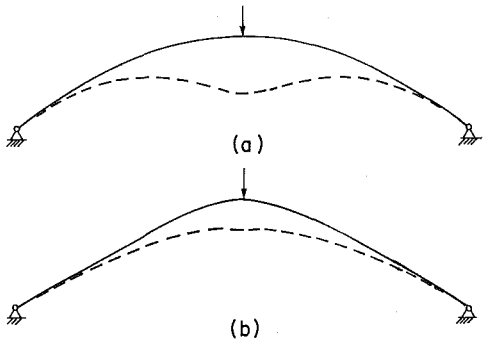


Fig. 3 Shell form and deflected shape at concentrated load Q = 3 for simply supported edge, λ = √10: (*a*) spherical form; (*b*) optimal form for maximum enclosed volume

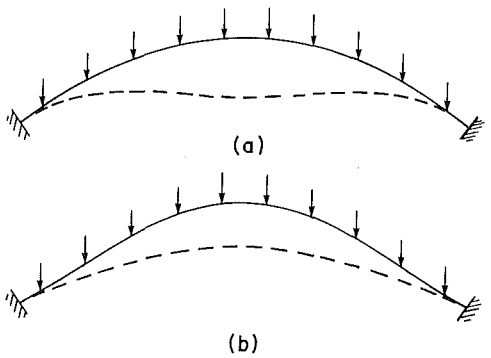


Fig. 2 Shell form and deflected shape at uniform load p = 0.96 for clamped edge, λ = 2.5: (*a*) spherical form; (*b*) optimal form for maximum enclosed volume

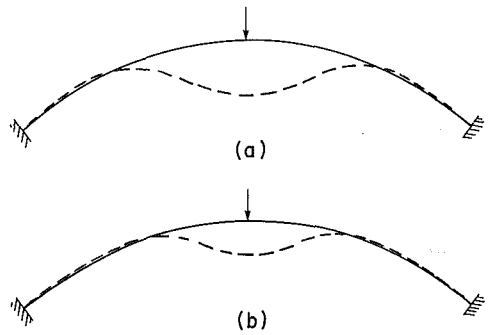


Fig. 4 Shell form and deflected shape at concentrated load Q = 6.92 for clamped edge, λ = 8.5: (*a*) spherical form; (*b*) optimal form for maximum enclosed volume

the equilibrium state under the given load $p(x)$, and (10) of [1], which specifies the surface area parameter λ. Thus, we construct the augmented functional

$$v^* = -\int_0^1 (g+\alpha)x^2\,dx - \int_0^1 \xi A\,dx - \int_0^1 \eta\,B\,dx$$

$$-\gamma\left[\int_0^1 g^2 x\,dx - (\lambda^4/4)\right] \tag{4}$$

where A and B are defined in (2) and (3) of [2], respectively, and $\xi(x)$, $\eta(x)$, and γ are Lagrange multipliers.

Stationarity of v^* with respect to $\alpha(x)$ and $\phi(x)$ leads to the following equations governing $\xi(x)$ and $\eta(x)$:

$$(x\xi')' - \frac{1}{x}\,\xi - \phi\xi + (g+\alpha)\eta = -x^2, \tag{5}$$

$$(x\eta')' - \frac{1}{x}\,\eta - (g+\alpha)\xi = 0. \tag{6}$$

The boundary conditions on $\xi(x)$ and $\eta(x)$ are the same as (4)–(6) of [2] on $\alpha(x)$ and $\phi(x)$, respectively. Stationarity of v^* with respect to $g(x)$ yields the optimality condition

$$\gamma g(x) = \frac{1}{2x}\left[\phi(x)\xi(x) - \alpha(x)\eta(x)\right] - \frac{x}{2}. \tag{7}$$

If $p(x) = 0$, then we get $\alpha(x) = \phi(x) = 0$ from (2) and (3) of [2], and (7), along with (10) of [1], gives $g(x) = -\lambda^2 x$, i.e., the optimal form is spherical if the shell is not loaded.

In the solution procedure, we specify the boundary conditions, Poisson's ratio ν, the surface area parameter λ, and the load distribution and magnitude (e.g., p and $\bar{x}$ in (19) of [2]). Then we choose an initial design function $g(x)$, usually corresponding to a spherical form, and solve (2) and (3) of [2] for the functions $\alpha(x)$ and $\phi(x)$ describing the deflected configuration of the shell. Next, (5) and (6) are solved for the Lagrange multipliers $\xi(x)$ and $\eta(x)$. Following this, equation (7) yields $g(x) = \hat{g}(x)$, where we determine γ using (10) of [1]. The design function for the subsequent iteration is chosen according to (34) of [1], and the successive iterations are concluded when the enclosed volume v, defined by (2), converges to a maximum value. The numerical technique used

Downloaded 02 May 2010 to 171.66.16.25. Redistribution subject to ASME license or copyright; see http://www.asme.org/terms/Terms_Use.cfm

to solve (2) and (3) of [2], and then (5) and (6), is described in the Appendix.

Results

The numerical results are presented in Table 1 and Figs. 1-4. In all cases, $\nu = 1/3$. The function $\bar{z}(x)$ is defined in (36) of [1], S denotes simply supported boundary conditions, C denotes a clamped edge, and the last row in Table 1 lists the ratio of the optimal enclosed volume to that for the corresponding spherical cap. The spherical and optimal forms are plotted in Figs. 1-4, and the deflected shapes under the given load are shown as dashed curves. Naturally, the value chosen for the load in each case is less than the critical load.

For the first example, depicted in Fig. 1, $\lambda = 2$ and the load is distributed uniformly with nondimensional magnitude $p = 15/(2\lambda^4) = 0.469$. Relative to the spherical shell, the optimal form has an 8 percent increase in enclosed volume and a 51 percent increase in central height (after loading). In Fig. 2, a uniform load is considered again, but the edge is clamped. Here $\lambda = 2.5$ and $p = 75/(2\lambda^4) = 0.96$. The increase in enclosed volume over a spherical shell is 10 percent and the increase in central height is 108 percent. Both the optimal form in Fig. 1(*b*) and the one in Fig. 2(*b*) are slightly convex adjacent to the edge.

A concentrated central load is considered in Figs. 3 and 4. In the first of these, the edge is simply supported, $\lambda = \sqrt{10}$, and the nondimensional load magnitude is $Q = 30/(\lambda^2) = 3$, where Q is defined by (25) of [2]. The enclosed volume for the deflected equilibrium state of the optimal shell is 14 percent higher than that for the spherical cap, and the central height turns out to be 122 percent higher. In Fig. 4, the edge is clamped, $\lambda = 8.5$, and $Q = 500/(\lambda^2) = 6.92$. The volume ratio is 1.09 and the central height ratio is 1.65 between the deflected shapes in Fig. 4(*b*) and Fig. 4(*a*).

Concluding Remarks

In this final part, we have considered a given applied load and have determined shell forms that lead to maximum enclosed volume between the base plane and the deflected configuration of the shell. As before, the shell has been assumed to be shallow, with given boundary conditions (clamped or simply supported) and a given value of the surface area parameter λ. Uniform and concentrated loads have been analyzed (however, as in Part 2, other axisymmetric loading distributions also could have been treated by the same method).

The iteration procedure is simpler in this part than in the previous ones. Asymmetric modes do not have to be considered, since the specified load is smaller than the critical load. Therefore we do not have the parameter n to consider, and the governing equations are only of second order. There is no eigenvalue, and no question of a multimodal formulation.

Between 6 and 11 iterations were required in the examples treated. The resulting optimal forms lead to enclosed volumes which are 8-14 percent higher than those for the corresponding spherical shell. The central heights of the deflected optimal shells turn out to be 51-122 percent higher than those for the spherical shells, which is a desirable feature. (We had previously tried to formulate the problem of maximizing the central height, but it was not well-posed; the optimal form would have a singularity at the center.)

We also previously considered maximizing the area under the function $z(x)$ which defines the shell form along a diameter. The quantity x^2 in the integrand of (3) would be replaced by x, the right side of (5) would become $-x$, and the last term in (7) would be replaced by $-1/2$. From (7), $g(0)$ would not be zero, so that the optimal form $z(x)$ would have a discontinuity in slope at $x = 0$. For the special case of no loading, equation (7) would imply that $g(x)$ is constant, i.e., a conical form would be optimal. We carried out one example, in which the area under $z(x)$ was maximized for the same load Q, parameter λ, and boundary conditions as those used in Fig. 4. The resulting optimal form was almost identical to that in Fig. 4(*b*) for maximum enclosed volume, and only had a slight discontinuity in slope at the center.

Acknowledgment

The first author was supported by the National Science Foundation under Grant CEE-8210222.

References

1 Plaut, R. H., Johnson, L. W., and Parbery, R., "Optimal Forms of Shallow Shells With Circular Boundary. Part 1: Maximum Fundamental Frequency," ASME JOURNAL OF APPLIED MECHANICS, Vol. 51, 1984, pp. - .

2 Plaut, R. H., and Johnson, L. W., "Optimal Forms of Shallow Shells With Circular Boundary. Part 2: Maximum Buckling Load," ASME JOURNAL OF APPLIED MECHANICS, Vol. 51, 1984, pp. - .

3 Haug, E. J., "A Review of Distributed Parameter Structural Optimization Literature," *Optimization of Distributed Parameter Structures*, Haug, E. J., and Cea, J., eds., Sijthoff & Noordhoff, Alphen aan den Rijn, The Netherlands, 1981, pp. 3-74.

4 Stadler, W., "Uniform Shallow Arches of Minimum Weight and Minimum Maximum Deflection," *Journal of Optimization Theory and Applications*, Vol. 23, 1977, pp. 137-165.

5 Johnson, L. W., and Riess, R. D., *Numerical Analysis*, 2nd ed., Addison-Wesley, Reading, Mass., 1982.

6 Huang, N. C., "Unsymmetrical Buckling of Thin Shallow Spherical Shells," ASME JOURNAL OF APPLIED MECHANICS, Vol. 31, 1964, pp. 447-457.

APPENDIX

In each of the problems treated here and in [1] and [2], the basic technique used to generate approximations to an optimal form is an iteration

$$g_{i+1}(x) = b[g_i(x) + k\hat{g}(x)] \tag{8}$$

(see (34) of [1]). In (8), $g_i(x)$ denotes the current design function and $\hat{g}(x)$ is determined by an optimality condition such as (32) in [1] or (24) in [2]. Finding $\hat{g}(x)$ requires the solution of a set of coupled boundary-value problems and eigenvalue problems, and in this appendix we outline the numerical procedures used to determine $\hat{g}(x)$.

There are several ways to solve eigenvalue problems such as (16) and (17) in [1] or boundary-value problems such as (2) and (3) in [2]. The usual course is to use a finite-difference method. However, (2) and (3) in [2] are a pair of nonlinear differential equations and a finite-difference approach would lead to a large system of nonlinear equations $F(x) = 0$ that would have to be solved by an iterative procedure such as Newton's method. For this reason, and because high quality codes for solving ordinary differential equations (such as DVERK and DGEAR in the IMSL library) have become widely available in the last few years, we decided to use a shooting method for the boundary-value problems and the eigenvalue problems. We used a variable-step Runge-Kutta method (a Runge-Kutta-Fehlberg method; see [5]) as our differential equation solver.

We also needed a scheme to represent the current design function $g_i(x)$ and the various solutions such as $\alpha(x)$ and $\phi(x)$ of (2) and (3) in [2] or $\beta_n(x)$ and $\psi_n(x)$ of (16) and (17) in [1]. For $0 \le x \le 1$, we elected to represent $g(x)$ and the various solutions as piecewise cubic Hermite interpolators at the knots $x_j = j\Delta x$; $j = 0,1, \ldots, 10$; $\Delta x = 1/10$. That is, suppose $g(x)$ denotes the current estimate to the optimal form. We save the values $g(x_j)$, $g'(x_j)$ for $j = 0,1, \ldots, 10$, and then for $x_k \le x \le x_{k+1}$, $0 \le k \le 9$, we represent $g(x)$ as $p_k(x)$ where

Downloaded 02 May 2010 to 171.66.16.25. Redistribution subject to ASME license or copyright; see http://www.asme.org/terms/Terms_Use.cfm

$p_k(x)$ is the cubic polynomial interpolating the values $g(x_k), g'(x_k), g(x_{k+1}), g'(x_{k+1})$. We could have used a cubic spline to represent $g(x)$, but the piecewise cubic Hermite interpolator generally has a smaller error. Of course, a Hermite interpolator cannot be used unless derivative data are available, but the differential equation solver gives us this information.

To illustrate the technique, we describe how shooting was employed on (16) and (17) of [1]. As before, let $g(x)$ denote the current design function appearing in (16) and (17). Now, since $g(x)$ is a known function (a piecewise cubic polynomial), we can use the Runge-Kutta-Fehlberg code to solve (16) and (17) once we provide a guess for ω_n and guesses for the missing initial conditions. Having solved (16) and (17), we update our estimates to ω_n and the initial conditions, iterating until we find a nontrivial solution that satisfies the appropriate boundary conditions (19)–(23) at $x = 1$. Having the correct eigenvalue and initial conditions for (16) and (17), we tabulate $\beta_n(x)$, $\psi_n(x)$, and their derivatives at the knots x_j. We use these values in (33) to obtain $s_n(x)$ and $s_n'(x)$ at the knots and then use (32) and (34) to generate the next estimate to the optimal form.

In the numerical solution of (16) and (17), it is convenient to make the variable changes $\beta_n(x) = x^n\tilde{\beta}_n(x)$ and $\psi_n(x) = x^n\tilde{\psi}_n(x)$, since $\beta_n(x) \sim x^n$ and $\psi_n(x) \sim x^n$ near $x=0$ [6]. Equations (14) and (15) of [1] imply that $\beta_n(x)$ and $\psi_n(x)$ are even functions if n is even, and odd functions if n is odd. Hence, $\tilde{\beta}_n(x)$ and $\tilde{\psi}_n(x)$ are even functions, and their odd derivatives are zero at $x=0$. In our shooting procedure, we set $\tilde{\beta}_n(0) = 1$, $\tilde{\beta}_n'(0) = 0$, $\tilde{\beta}_n''(0) = J$, $\tilde{\beta}_n'''(0) = 0$, $\tilde{\psi}_n(0) = K$, $\tilde{\psi}_n'(0) = 0$, $\tilde{\psi}_n''(0) = L$, and $\tilde{\psi}_n'''(0) = 0$. The boundary conditions (19)–(23) at $x = 1$ become $\tilde{\beta}_n = 0$; $\tilde{\beta}_n'' + 2n\tilde{\beta}_n' + n(n-1)\tilde{\beta}_n + \nu[\tilde{\beta}_n' + n\tilde{\beta}_n] = 0$; etc. Given a guess ω for the eigenvalue ω_n and guesses J, K, and L for the initial conditions, let $\tilde{\beta}_n(x,J,K,L,\omega)$ and $\tilde{\psi}_n(x,J,K,L,\omega)$ denote the solution of (16) and (17), after these equations have been transformed by the change of variables.

For a given J, K, L, and ω, we evaluate $\tilde{\beta}_n(x,J,K,L,\omega)$ and $\tilde{\psi}_n(x,J,K,L,\omega)$ at $x = 1$ using the differential equation solver. In a shooting method our aim is to solve the system of equations

$$\begin{aligned} F_1(J,K,L,\omega) &= 0 \\ F_2(J,K,L,\omega) &= 0 \\ F_3(J,K,L,\omega) &= 0 \\ F_4(J,K,L,\omega) &= 0 \end{aligned} \tag{9}$$

where the $F_i(J,K,L,\omega)$ denote the appropriate four transformed boundary conditions in (19)–(23), which depend on whether the edge of the shell is clamped or simply supported. We solve this system of equations by Newton's method, using the variational equations of F_i to obtain the required Jacobian matrix.

Finally, we note that the various systems of differential equations that must be solved (such as (16) and (17) in [1], (2) and (3) in [2], etc.) have general solutions which contain components that are singular at $x=0$. For example, $\beta(x) = x^{-n}$ is a solution of $L_nL_n\beta = 0$ where the operator L_n is defined in (18) of [1]. This singular behavior causes problems for the error estimator in the differential equation solver when we try to start the solution at $x=0$; starting at $x=0$, the integration step is repeatedly reduced but the error tolerance is never met. To overcome this problem, we started the solution at $x=d$, where $d=0.01$. To get the proper initial conditions at $x=d$, we expanded the solutions and their derivatives in a Taylor's series about $x=0$.

For example, consider (2) and (3) of [2] with the boundary condition (6) at $x=0$. The standard implementation of shooting is to guess the missing initial conditions M and N, then solve (2) and (3) with initial conditions $\alpha(0)=0$, $\alpha'(0)=M$, $\phi(0)=0$, $\phi'(0)=N$, and then update M and N until the appropriate boundary condition at $x=1$ is satisfied. Instead of starting the solution at $x=0$, we start at $x=d$ using initial conditions

$$\alpha(d) = \alpha(0) + \alpha'(0)d + \alpha''(0)\frac{d^2}{2!} + \ldots \tag{10}$$

and similar series for $\alpha'(d)$, $\phi(d)$, and $\phi'(d)$, truncated after terms of order d^3, giving the initial values needed by the differential equation solver. The required values for $\alpha''(0)$, $\alpha'''(0)$, etc., can be obtained directly from (2) and (3), and we note that $\alpha''(0)$, $\alpha'''(0)$, etc., are functions of M and N.

Downloaded 02 May 2010 to 171.66.16.25. Redistribution subject to ASME license or copyright; see http://www.asme.org/terms/Terms_Use.cfm

Bounds for Elastic Moduli of Multiphase Short-Fiber Composites[1]

S. Nomura
Assistant Professor,
Department of Mechanical Engineering,
University of Texas at Arlington,
Arlington, Texas 76019

T.-W. Chou
Professor,
Mechanical and Aerospace
Engineering Department,
University of Delaware,
Newark, Del. 19711

This paper examines upper and lower bounds of the effective elastic modulus of unidirectional short-fiber composites. The short-fibers are modeled by aligned ellipsoidal inclusions of the same aspect ratio but not necessarily the same size. We adopt a perturbation expansion of the composite local strain field by using the Green function tensor. Explicit expressions of the effective elastic modulus are derived up to the third-order term by use of the information on the correlation functions. The variational method is then employed to optimize the bounds of the effective modulus in a closed form. Numerical examples of the bounds as functions of the fiber aspect ratio and the fiber volume fraction are given for a glass/epoxy system. The present approach predicts narrower bounds than those of Hashin and coworkers for the limiting cases of spherical particles and continuous fibers since their bounds corresponds to a model that take the correlation functions up to the second order into account.

1 Introduction

The development of short-fiber composites is gaining increasing technological importance. However, as was pointed out by Chou and Kelly [1], the physical and mechanical properties of those composites are not well understood. The interactions between the fiber-ends and the matrix as well as the variations in the fiber length and orientation are the key factors contributing to the complexity of the problem (see Vinson and Chou [2], and Chou and Kelly [3]). This paper addresses a basic problem in short-fiber composites: their effective moduli.

The subject of effective elastic moduli of unidirectional short-fiber composites was treated by Chou, Nomura, and Taya [4] using the self-consistent approach of Hill [5–7]. The effective composite modulus was expressed implicitly as a function of the elastic stiffness of the constituent phases, the inclusion aspect ratio, and the inclusion volume fraction. The limitation of this approach is at high-filler volume fractions where the inclusion-inclusion interaction becomes more pronounced.

In this paper, we present a method of evaluating upper and lower bounds of the effective modulus of short-fiber composites. We adopt a perturbation expansion of the local strain field by using the Green function tensor. The correlations of elastic constants are evaluated based on the characteristics of the phase geometry. The bounds are then determined from the variational treatment. To provide a background of the present work, it is appropriate to briefly review the approaches of Dederichs and Zeller [8], Zeller and Dederichs [9], and Kröner [10–12]. Dederichs and Zeller [8] and Zeller and Dederichs [9] treated a polycrystalline aggregate without texture in which the crystallographic orientations of different grains are not correlated and the orientations are independent of the shape of the grains. As a result of these assumptions, the polycrystal is regarded as isotropic. They have shown that the basic equation for a disordered material has a form of the Lippmann-Schwinger equation in statistical scattering theory and made use of its technique such as the T-matrix expansion to sum up the infinite series. Kröner [10] treated materials about which the complete statistical information in form of the correlation function is known. It was shown that a compact form of the macroscopic modulus can be derived for the class of the material known as "perfectly disordered." Bolotin and Moskalenko [13] also treated isotropic polycrystalline aggregates by using the Green function.

This paper deals with a composite system composed of different kinds of materials. Each component has the ellipsoidal shape sumulating the short-fiber and is aligned unidirectionally. The unidirectionally aligned fibers in the present model render transverse isotropy to the composite. By requiring "ellipsoidal symmetry" and a "cell structure" to the composite, the series expression of the effective moduli was evaluated up to the third order.

Upper and lower bounds of the effective modulus obtained by the variational method give narrower values than those of

[1] This work was supported by the U.S. Army Research Office.

[2] Presently at Department of Mechanical Engineering, University of Texas at Arlington, Arlington, Texas 76019.

Contributed by the Applied Mechanics Division and presented at the 1984 PVP Conference and Exhibition Joint with Applied Mechanics Division and Materials Division, San Antonio, Texas, June 17–21, 1984 of THE AMERICAN SOCIETY OF MECHANICAL ENGINEERS.

Discussion on this paper should be addressed to the Editorial Department, ASME, United Engineering Center, 345 East 47th Street, New York, N.Y. 10017, and will be accepted until two months after final publication of the paper itself in the JOURNAL OF APPLIED MECHANICS. Manuscript received by ASME Applied Mechanics Division, January, 1982; final revision, September, 1982. Paper No. 84-APM-36.

Copies will be available until February, 1985.

Copyright © 1984 by ASME
Downloaded 02 May 2010 to 171.66.16.25. Redistribution subject to ASME license or copyright; see http://www.asme.org/terms/Terms_Use.cfm

Hashin and Shtrikman [14] and Hashin [15] since their bounds are based on the information up to the second-order correlation function.

The basic equations are developed in Section 2. The evaluation of the second and the third-order terms of the effective modulus is given in Section 3. The variational method is adopted in Section 4 to determine the upper and lower bounds. Comparison of the results with experiments is presented in Section 5.

2 Definitions and Basic Equations

In this section, we derive a formal expression of the effective moduli $\mathbf{C}^*$ for general heterogeneous materials in an infinite series form by a statistical approach. We consider an unbounded material with its elastic moduli varying spatially. Assume that at each point, the stress and the strain are related by the linear constitutive relation

$$\boldsymbol{\sigma}=\mathbf{C}\,\boldsymbol{\epsilon} \tag{1}$$

where $\mathbf{C}$ denotes the elastic stiffness and is assumed to be isotropic. For shortness, we denote tensor quantities by bold letters and omit indices where possible. Summation convention is adopted where applicable. The effective elastic modulus of the composite is defined by the relation

$$<\boldsymbol{\sigma}>=\mathbf{C}^*<\boldsymbol{\epsilon}> \tag{2}$$

Here, the bracket $<.>$ means the spatial average over the total volume V defined by

$$<.>=\lim_{V\to\infty}\frac{1}{V}\int_V (.)\,d\mathbf{r} \tag{3}$$

The quantities $\mathbf{C}$, $\boldsymbol{\sigma}$, and $\boldsymbol{\epsilon}$ can be uniquely decomposed into the spatial average and the fluctuating part as

$$\begin{aligned}\mathbf{C}&=<\mathbf{C}>+\mathbf{C}'\\ \boldsymbol{\sigma}&=<\boldsymbol{\sigma}>+\boldsymbol{\sigma}'\\ \boldsymbol{\epsilon}&=<\boldsymbol{\epsilon}>+\boldsymbol{\epsilon}'\end{aligned} \tag{4}$$

where the prime means fluctuation from the spatial average. Substitution of (3) into (1) yields

$$<\boldsymbol{\sigma}>+\boldsymbol{\sigma}'=<\mathbf{C}><\boldsymbol{\epsilon}>+\mathbf{C}'<\boldsymbol{\epsilon}>+<\mathbf{C}>\boldsymbol{\epsilon}'+\mathbf{C}'\boldsymbol{\epsilon}' \tag{5}$$

After averaging both sides of (5), we have

$$<\sigma>=<C><\epsilon>+<C'\epsilon'>=C^*<\epsilon> \tag{6}$$

Equation (6) shows that it is necessary to know $<C'\epsilon'>$ in order to calculate C^*.

We next derive the expression that related ϵ' to $<\epsilon>$. First, the equilibrium equation without body force is

$$\partial_i(C_{ijkl}\epsilon_{kl})'=0 \tag{7}$$

where ∂_i is the derivative with respect to the r_i coordinate. Substitution of (4) into (7) gives

$$<C_{ijkl}>\partial_i\partial_k u_l'+\partial_i(C'_{ijkl}<\epsilon_{kl}>+(C'_{ijkl}\epsilon'_{kl}))=0 \tag{8}$$

where we used the relation $\epsilon'_{ij}=1/2(\partial_i u'_j+\partial_j u'_i)$.

To solve (8) with respect to u'_i, we introduce the elastic Green function $g_{km}(\mathbf{r})$ for an infinite mean medium defined by

$$<C_{ijkl}>\partial_i\partial_k g_{lm}(\mathbf{r})+\delta_{jm}\delta(\mathbf{r})=0 \tag{9}$$

where $\delta(\mathbf{r})$ is the Dirac delta function and δ_{im} is the Kronecker delta. Since $<\mathbf{C}>$ is isotropic, the explicitly expression of $g_{ij}(\mathbf{r})$ is given by

$$g_{ij}(\mathbf{r})=\frac{1}{8\pi<2\mu+\lambda><\mu>}\left(\frac{<3\mu+\lambda>\delta_{ij}}{r}+\frac{<\mu+\lambda>r_i r_j}{r^3}\right) \tag{10}$$

where μ and λ are the Lamé constants and r is the absolute value of $\mathbf{r}$. The solution of the displacement u'_i in (8) is obtained by regarding the second term of the left-hand side of (8) as an imaginary body force and is given formally by a system of integrodifferential equation as

$$\epsilon'_{ij}(\mathbf{r})=\int_V G_{ijkl}(\mathbf{r}-\mathbf{r}')\{C'_{klmn}(\mathbf{r}')<\epsilon_{mn}>+(C'_{klmn}(\mathbf{r}')\epsilon'_{mn}(\mathbf{r}'))'\}d\mathbf{r}' \tag{11}$$

where the integral is taken over the whole volume V. Integrating (11) by parts and taking the partial derivative of (11), we obtain

$$\epsilon_{ij}'(\mathbf{r})=\int_V G_{ijkl}(\mathbf{r}-\mathbf{r}')\{C'_{klmn}(\mathbf{r}')<\epsilon_{mn}>+(C'_{klmn}(\mathbf{r}')\epsilon'_{mn}(\mathbf{r}'))'\}d\mathbf{r}' \tag{12}$$

where

$$G_{ijkl}(\mathbf{r})=\partial_j\partial_l g_{ki}(\mathbf{r})_{(ij)(kl)} \tag{13}$$

and (ij) denotes the symmetrization with respect to i and j. In deriving (12), the surface integral vanishes for the infinite surface since we can replace the stress distribution at the boundary by a uniformly distributed stress according to the Saint-Venant principle. Rewriting (12) in a symbolic form, we have

$$\boldsymbol{\epsilon}'=\boldsymbol{\Gamma}\mathbf{C}'<\boldsymbol{\epsilon}>+\boldsymbol{\Gamma}(\mathbf{C}'\boldsymbol{\epsilon}')' \tag{14}$$

Here, $\boldsymbol{\Gamma}$ is an integral operator of the fourth-rank tensor defined as

$$\Gamma_{ijkl}f_{klmn}(\mathbf{r})=\int_V G_{ijkl}(\mathbf{r}-\mathbf{r}')f_{klmn}(\mathbf{r}')\,d\mathbf{r}' \tag{15}$$

where $f_{klmn}(\mathbf{r})$ is an arbitrary fourth-rank tensor.

Equation (14) is of the Fredholm integral equation of the second kind. To solve (14) with respect to $\boldsymbol{\epsilon}'$ we will impose successive substitutions of (14) into itself. Thus, we obtain formally

$$\boldsymbol{\epsilon}'=\boldsymbol{\Gamma}\mathbf{C}'<\boldsymbol{\epsilon}>+\boldsymbol{\Gamma}(\mathbf{C}'\boldsymbol{\Gamma}\mathbf{C}'<\boldsymbol{\epsilon}>)'+\boldsymbol{\Gamma}(\mathbf{C}'\boldsymbol{\Gamma}(\mathbf{C}'\boldsymbol{\Gamma}\mathbf{C}'<\boldsymbol{\epsilon}>)')'+\cdots\cdots\cdots\cdots \tag{16}$$

The series (16) is convergent when an appropriately chosen norm of $\boldsymbol{\Gamma}\mathbf{C}'$ is less than unity. Substitution of (16) into (6) yields

$$\begin{aligned}\mathbf{C}^*<\boldsymbol{\epsilon}>=&<\mathbf{C}><\boldsymbol{\epsilon}>+<\mathbf{C}'\boldsymbol{\Gamma}\mathbf{C}'><\boldsymbol{\epsilon}>+\\ &<\mathbf{C}'><\mathbf{C}'\boldsymbol{\Gamma}\mathbf{C}'>'<\boldsymbol{\epsilon}>\\ &+<\mathbf{C}'\boldsymbol{\Gamma}(\mathbf{C}'\boldsymbol{\Gamma}(\mathbf{C}'\boldsymbol{\Gamma}\mathbf{C}')')'><\boldsymbol{\epsilon}>+\cdots\cdots\cdots\end{aligned} \tag{17}$$

Therefore, we finally have

$$\begin{aligned}\mathbf{C}^*=&<\mathbf{C}>+<\mathbf{C}'\boldsymbol{\Gamma}\mathbf{C}'>+<\mathbf{C}'\boldsymbol{\Gamma}\mathbf{C}'\boldsymbol{\Gamma}\mathbf{C}'>\\ &+(<\mathbf{C}'\boldsymbol{\Gamma}\mathbf{C}'\boldsymbol{\Gamma}\mathbf{C}'\boldsymbol{\Gamma}\mathbf{C}'>-<\mathbf{C}'\boldsymbol{\Gamma}\mathbf{C}'>\boldsymbol{\Gamma}<\mathbf{C}'\boldsymbol{\Gamma}\mathbf{C}'>)\\ &+(<\mathbf{C}'\boldsymbol{\Gamma}\mathbf{C}'\boldsymbol{\Gamma}\mathbf{C}'\boldsymbol{\Gamma}\mathbf{C}'\boldsymbol{\Gamma}\mathbf{C}'>-<\mathbf{C}'\boldsymbol{\Gamma}\mathbf{C}'\boldsymbol{\Gamma}\mathbf{C}'>\boldsymbol{\Gamma}<\mathbf{C}'\boldsymbol{\Gamma}\mathbf{C}'>\\ &-<\mathbf{C}'\boldsymbol{\Gamma}\mathbf{C}'>\boldsymbol{\Gamma}<\mathbf{C}'\boldsymbol{\Gamma}\mathbf{C}'\boldsymbol{\Gamma}\mathbf{C}'>)+\cdots\cdots\end{aligned} \tag{18}$$

Equation (18) is rather formal because it contains multiple integrations in high order terms.

The convergence of the series (18) is guaranteed when the norm of $\boldsymbol{\Gamma}\mathbf{C}'$ is less than unity. However, as will be shown in Section 4, we will use the truncated strain expression of (16) as a trial function of the variational method and are not concerned with the convergence of (16) and (18).

An expression similar to (18) can be obtained for the effective elastic compliances $\mathbf{S}^*$. The result is

$$\begin{aligned}\mathbf{S}^*=&<\mathbf{S}>+<\mathbf{S}'\boldsymbol{\Delta}\mathbf{S}'>+<\mathbf{S}'\boldsymbol{\Delta}\mathbf{S}'\boldsymbol{\Delta}\mathbf{S}'>\\ &+(<\mathbf{S}'\boldsymbol{\Delta}\mathbf{S}'\boldsymbol{\Delta}\mathbf{S}'\boldsymbol{\Delta}\mathbf{S}'>-<\mathbf{S}'\boldsymbol{\Delta}\mathbf{S}'>\boldsymbol{\Delta}<\mathbf{S}'\boldsymbol{\Delta}\mathbf{S}'>)+\cdots\cdots\end{aligned} \tag{19}$$

Downloaded 02 May 2010 to 171.66.16.25. Redistribution subject to ASME license or copyright; see http://www.asme.org/terms/Terms_Use.cfm

where

$$\Delta = -(<\mathbf{S}>^{-1} + <\mathbf{S}>^{-1}\Gamma_s <\mathbf{S}>^{-1}) \tag{20}$$

and Γ_s is constructed by changing $<\mathbf{C}>$ in (9) to $<\mathbf{S}>^{-1}$.

3 Evaluation of Series

In this section, we show that the evaluation of (18) invovles the correlation functions of constitutive phases. The second term of the right-hand side of (18) can be evaluated exactly with the information that the composite possesses ellipsoidal symmetry explained later. The evaluation of the third term of (18) can be done if the composite has an ellipsoidal cell structure proposed by Miller [16].

We assume that each component of the composite is homogeneous and isotropic but the whole composite is transversely isotropic. We further adopt the ergodic assumption that the spatial average defined by (3) can be replaced by the ensemble average $\overline{(\,.\,)}$ defined by

$$\overline{(\,.\,)} = \int_\Omega (\,.\,) P(d\omega) \tag{21}$$

where Ω is a sample space whose element ω is a realizable composite material and $P(d\omega)$ is a probability measure over Ω. The ergodic assumption implies that the material is statistically homogeneous.

We first evaluate the second term of the right-hand side of (18). Since the elastic properties of the composite are piecewise constant, we can set

$$\mathbf{C}'(\mathbf{r}) = \sum_\alpha \mathbf{C}'_\alpha \psi_\alpha(\mathbf{r}) \tag{22}$$

where the subscript α denotes the αth phase and $\psi_\alpha(r)$ is the characteristic function of the αth phase defined as

$$\psi_\alpha(r) = \begin{cases} 1 & \mathbf{r} \in \Omega_\alpha \\ 0 & \mathbf{r} \notin \Omega_\alpha \end{cases} \tag{23}$$

where Ω_α is the domain of the αth phase. By use of this characteristic function, the second term of the series (18) can be rewritten as

$$\begin{aligned} <\mathbf{C}'\Gamma\mathbf{C}'> &= \sum_{\alpha,\beta} \mathbf{C}'_\alpha \mathbf{C}'_\beta <\psi_\alpha(\mathbf{r}) \int_V \mathbf{G}(\mathbf{r}-\mathbf{r}')\psi_\beta(\mathbf{r}')d\mathbf{r}'>_{\mathbf{r}} \\ &= \sum_{\alpha,\beta} \mathbf{C}'_\alpha \mathbf{C}'_\beta \int_V d\mathbf{r}\mathbf{G}(\mathbf{r}) \frac{1}{V} \int_V d\mathbf{r}' \psi_\alpha(\mathbf{r}')\psi_\beta(\mathbf{r}'+\mathbf{r}) \\ &= \sum_{\alpha,\beta} \mathbf{C}'_\alpha \mathbf{C}'_\beta \int_V \mathbf{G}(\mathbf{r}) <\psi_\alpha(\mathbf{r}')\psi_\beta(\mathbf{r}'+\mathbf{r})>_{\mathbf{r}'} d\mathbf{r} \end{aligned} \tag{24}$$

where $<\ >_{\mathbf{r}'}$ is the spatial average with respect $\mathbf{r}'$. Note that we changed the order of integrations in the calculation of (24).

We now replace the spatial average $<\ >$ in the last formula of (24) by the ensemble average defined in (21) according to the ergodic assumption as

$$<\psi_\alpha(\mathbf{r}')\psi_\beta(\mathbf{r}'+\mathbf{r})>_{\mathbf{r}'} = R_{\alpha\beta}(\mathbf{0},\mathbf{r}) \tag{25}$$

where

$$R_{\alpha\beta}(\mathbf{0},\mathbf{r}) = \overline{\psi_\alpha(\mathbf{r}')\psi_\beta(\mathbf{r}'+\mathbf{r})} \tag{26}$$

The quantity $R_{\alpha\beta}(\mathbf{0}, \mathbf{r})$ is called the two-point correlation function and denotes the probability that a point $\mathbf{0}$ is found in the αth phase and $\mathbf{r}$ in the βth phase.

We further require, in addition to the ergodic assumption, that $R_{\alpha\beta}(\mathbf{0}, \mathbf{r})$ possesses ellipsoidal symmetry as

$$R_{\alpha\beta}(\mathbf{0},\mathbf{r}) = R_{\alpha\beta}(\rho) \tag{27}$$

where

$$\rho^2 = \left(\frac{r_1}{t}\right)^2 + r_2^2 + r_3^2 \tag{28}$$

Here, the symmetrical axis is chosen as the r_1-axis and t is called the inclusion aspect ratio. Equation (28) reduces to complete isotropy when t is 1. Using the aforementioned assumption for $R_{\alpha\beta}(\mathbf{0}, \mathbf{r})$, equation (24) can be written as

$$<\mathbf{C}'\Gamma\mathbf{C}'> = \sum_{\alpha,\beta} \mathbf{C}'_\alpha \mathbf{C}'_\beta \int_V R_{\alpha\beta}(\rho)\mathbf{G}(\mathbf{r})d\mathbf{r} \tag{29}$$

We now use the fact that the function $\mathbf{G}(\mathbf{r})$ in (29) behaves like the Dirac delta function (Wu and McCullough [17]) as

$$\int_V \mathbf{G}(r)\mathbf{f}(\rho)dr = \hat{\mathbf{\Gamma}}\mathbf{f}(0) \tag{30}$$

where $\mathbf{f}(\rho)$ is an arbitrary function of ρ only and $\hat{\mathbf{\Gamma}}$ is a constant tensor depending on the material constants and the inclusion aspect ratio. The proof of (30) is here carried out only for the case $t=1$, but the extension to a general t is straightforward. First, from the Parseval relation of the Fourier integral, we have

$$\begin{aligned} \int_V \mathbf{G}(\mathbf{r})\mathbf{f}(\rho)d\mathbf{r} &= \left(\frac{1}{2\pi}\right)^3 \int_{V_k} \hat{\mathbf{G}}(\mathbf{k})\hat{\mathbf{f}}(k)d\mathbf{k} \\ &= \left(\frac{1}{2\pi}\right)^3 \int_0^\infty dk\, k^2 \hat{\mathbf{f}}(k) \int_0^{2\pi} d\psi \int_0^\pi d\beta \sin\beta\, \hat{\mathbf{G}}(\mathbf{k}) \end{aligned} \tag{31}$$

where $\hat{\mathbf{G}}(\mathbf{k})$ and $\hat{\mathbf{f}}(\mathrm{k})$ are the Fourier transforms of $\mathbf{G}(\mathbf{r})$ and $\mathbf{f}(\rho)$, respectively. Explicit expressions of $\hat{\mathbf{G}}(\mathbf{k})$ is obtained from (10) as

$$\hat{G}_{ijkl}(\mathbf{k}) = \frac{<\mu+\lambda>}{<2\mu+\lambda><\mu>} \frac{k_i k_j k_k k_l}{k^4} - \frac{1}{4<\mu>} \frac{\delta_{(ij}\delta_{k)l)}}{k^2} \tag{32}$$

Note that $\hat{\mathbf{G}}(\mathbf{k})$ is not a function of k. Substituting (32) into (31) and by use of the following relations

$$\begin{aligned} \int_0^{2\pi} d\psi \int_0^\pi d\beta \sin\beta \frac{k_i k_j k_k k_l}{k^4} &= \frac{4}{15} \delta_{(ij}\delta_{k)l)} \\ \int_0^{2\pi} d\psi \int_0^\pi d\beta \sin\beta \frac{k_i k_j}{k_2} &= \frac{4}{3} \delta_{ij} \end{aligned} \tag{33}$$

we obtain

$$\begin{aligned} \int_V \mathbf{G}(\mathbf{r})\mathbf{f}(\rho)d\mathbf{r} &= \left(\frac{1}{2\pi}\right)^3 \int_{V_k} \hat{\mathbf{f}}(\mathbf{k})d\mathbf{k} \\ &= \hat{\mathbf{\Gamma}}\mathbf{f}(0) \end{aligned} \tag{34}$$

where

$$\hat{\Gamma}_{ijkl} = \frac{<\mu+\lambda>}{<2\mu+\lambda><\mu>} \delta_{ij}\delta_{kl} - \frac{<8\mu+3\lambda>}{15<\mu><2\mu+\lambda>} I_{ijkl} \tag{35}$$

For the case in which t is other than 1, the calculation can be carried out in a similar manner. Five independent components of $\hat{\mathbf{\Gamma}}$ are given by (see [17])

$$\begin{aligned} \hat{\Gamma}_{1111} &= \frac{<\mu+\lambda>}{<2\mu+\lambda><\mu>} h_5(t) - \frac{1}{<\mu>} h_2(t) \\ \hat{\Gamma}_{1122} &= \frac{<\lambda+\mu>}{<2\mu+\lambda><\mu>} \frac{h_4(t)}{2} \\ \hat{\Gamma}_{1212} &= \frac{<\lambda+\mu>}{<2\mu+\lambda><\mu>} \frac{h_4(t)}{2} - \frac{1}{4<\mu>}\left(\frac{h_1(t)}{2} + h_2(t)\right) \\ \hat{\Gamma}_{2222} &= \frac{3<\mu+\lambda>}{8<\mu><2\mu+\lambda>} h_3(t) - \frac{h_1(t)}{2<\mu>} \\ \hat{\Gamma}_{2233} &= \frac{<\mu+\lambda>}{8<\mu><2\mu+\lambda>} h_3(t) \end{aligned} \tag{36}$$

Downloaded 02 May 2010 to 171.66.16.25. Redistribution subject to ASME license or copyright; see http://www.asme.org/terms/Terms_Use.cfm

where $h_i(t)$'s are given by

$$h_1(t)=\frac{t^2}{t^2-1}\left\{1-\frac{1}{2}\left[\left(\frac{t^2}{t^2-1}\right)^{1/2}-\left(\frac{t^2-1}{t^2}\right)^{1/2}\right]ln\left(\frac{t+(t^2-1)^{1/2}}{t-(t^2-1)^{1/2}}\right)\right\}$$

$$h_2(t)=\frac{1}{t^2-1}\left\{-1+\frac{1}{2}\left(\frac{t^2}{t^2-1}\right)^{1/2}ln\left(\frac{t+(t^2-1)^{1/2}}{t-(t^2-1)^{1/2}}\right)\right\}$$

$$h_3(t)=\left(\frac{t^2}{t^2-1}\right)^2\left\{1+\frac{1}{2t^2}+\left[\frac{1}{4}\left(\frac{t^2-1}{t^2}\right)^{2/3}+\frac{1}{2}\left(\frac{t^2-1}{t^2}\right)^{1/2}-\frac{3}{4}\left(\frac{t^2}{t^2-1}\right)^{1/2}\right]ln\left(\frac{t+(t^2-1)^{1/2}}{t-(t^2-1)^{1/2}}\right)\right\}$$

$$h_4(t)=\frac{t^2}{(t^2-1)^2}\left\{\frac{3}{2}+\left[\frac{1}{4}\left(\frac{t^2-1}{t^2}\right)^{1/2}+\frac{3}{4}\left(\frac{t^2}{t^2-1}\right)^{1/2}\right]ln\left(\frac{t+(t^2-1)^{1/2}}{t-(t^2-1)^{1/2}}\right)\right\}$$

$$h_5(t)=\frac{1}{(t^2-1)}\left\{1+\frac{t^2}{2}-\frac{3}{4}\left(\frac{t^2}{t^2-1}\right)^{1/2}ln\left(\frac{t+(t^2-1)^{1/2}}{t-(t^2-1)^{1/2}}\right)\right\} \tag{37}$$

Note that $\hat{\mathbf{\Gamma}}$ in (36) is transversely isotropic.

By substituting these relations into (29), we have

$$\begin{aligned}<\mathbf{C}'\mathbf{\Gamma}\mathbf{C}'> &= \sum_{\alpha,\beta}\mathbf{C}'_\alpha\mathbf{C}'_\beta\hat{\mathbf{\Gamma}}R_{\alpha\beta}(0)\\ &= \sum_{\alpha,\beta}\mathbf{C}'_\alpha\mathbf{C}'_\beta\,\overline{\psi_\alpha(\mathbf{r})\psi_\beta(\mathbf{r})}\,\hat{\mathbf{\Gamma}}\\ &= \sum_{\alpha,\beta}\mathbf{C}'_\alpha\mathbf{C}'_\beta\hat{\mathbf{\Gamma}}V_\alpha\delta_{\alpha\beta}\\ &= \sum_{\alpha}V_\alpha\mathbf{C}'_\alpha\hat{\mathbf{\Gamma}}\mathbf{C}'_\alpha\end{aligned} \tag{38}$$

where V_α is the volume fraction of the αth phase. We can set

$$\mathbf{E}=\hat{\mathbf{\Gamma}}\mathbf{C}' \tag{39}$$

The fourth-rank tensor $\mathbf{E}$ is related with the so-called Eshelby's tensor in his inclusion problem [18]. Note that $\mathbf{E}$ is not self-adjoint.

Equation (38) can be therefore finally written as

$$<\mathbf{C}'\mathbf{\Gamma}\mathbf{C}'>=<\mathbf{C}'\mathbf{E}> \tag{40}$$

where the bracket of the right-hand side of (40) is now understood as the spatial average.

The evaluation of the third term of (18) needs further information about the three-point correlation function. First, we have

$$\begin{aligned}<\mathbf{C}'\mathbf{\Gamma}\mathbf{C}'\mathbf{\Gamma}\mathbf{C}'> &= \sum_{\alpha,\beta,\gamma}\mathbf{C}'_\alpha\mathbf{C}'_\beta\mathbf{C}'_\gamma<\psi_\alpha(\mathbf{r})\int_V\mathbf{G}(\mathbf{r}+\mathbf{r}')\psi_\beta(\mathbf{r}')d\mathbf{r}'\\ &\quad\int_V\mathbf{G}(\mathbf{r}'+\mathbf{r}'')\psi_\beta(\mathbf{r}'')>_{\mathbf{r}}\\ &= \sum_{\alpha,\beta,\gamma}\mathbf{C}'_\alpha\mathbf{C}'_\beta\mathbf{C}'_\gamma\int_V d\mathbf{r}'\mathbf{G}(\mathbf{r}')\int_V d\mathbf{r}\,\mathbf{G}(\mathbf{r})R\alpha\beta\gamma(\mathbf{0},\mathbf{r},\mathbf{r}')\end{aligned} \tag{41}$$

where

$$R_{\alpha\beta\gamma}(\mathbf{0},\mathbf{r},\mathbf{r}')=\overline{\psi_\alpha(\xi)\psi_\beta(\xi+\mathbf{r})\psi_\gamma(\xi+\mathbf{r}+\mathbf{r}')} \tag{42}$$

Note that we used the ergodic assumption to replace the spatial average by the ensemble average and changed the order of the integrations in (41). The quantity $R_{\alpha\beta\gamma}(\mathbf{0},\mathbf{r},\mathbf{r}')$ is called the three-point correlation function and denotes the probability that a point $\mathbf{0}$ is found in the αth phase, $\mathbf{r}$ in the βth phase, and $\mathbf{r}'$ in the γth phase.

To proceed the evaluation of (41), we have further to specify the properties of the three-point correlation function in addition to ellipsoidal symmetry.

We show that the relation similar to (40) holds for the material that has the ellipsoidal cell structure (Miller [16]). The cell structure material is composed of cells each of which has statistically identical properties and is independent of the one another. In our case, each cell is assumed to have the ellipsoidal shape expressed by (28). For this model, we obtain, as the third-order correlation function,

$$<\mathbf{C}'(\mathbf{0})\mathbf{C}'(\mathbf{r})\mathbf{C}'(\mathbf{r}')>=<\mathbf{C}'^3>P(\mathbf{0},\mathbf{r},\mathbf{r}') \tag{43}$$

where $P(\mathbf{0},\mathbf{r},\mathbf{r}')$ is the probability that three points $\mathbf{0},\mathbf{r},\mathbf{r}'$ are all found in the same ellipsoidal cell. We can express $P(\mathbf{0},\mathbf{r},\mathbf{r}')$ as

$$P(\mathbf{0},\mathbf{r},\mathbf{r}')=\frac{1}{\Omega}\int_\Omega d\mathbf{r}''\psi(\mathbf{r}-\mathbf{r}')\psi(\mathbf{r}'-\mathbf{r}'') \tag{44}$$

where

$$\psi(\mathbf{r})=\begin{cases}1 & \mathbf{r}\text{ is inside the cell}\\ 0 & \text{otherwise.}\end{cases} \tag{45}$$

and Ω is the domain of ellipsoidal cell. Substituting (44) into (41), we have

$$\begin{aligned}<\mathbf{C}'\mathbf{\Gamma}\mathbf{C}'\mathbf{\Gamma}\mathbf{C}'> &= \frac{1}{\Omega}\sum_\alpha V_\alpha\mathbf{C}'_\alpha\mathbf{C}'_\alpha\mathbf{C}'_\alpha\int_V d\mathbf{r}'\mathbf{G}(\mathbf{r}')\int_V d\mathbf{r}\mathbf{G}(\mathbf{r})\\ &\quad\int_\Omega d\mathbf{r}''\psi(\mathbf{r}''-\mathbf{r}')\psi(\mathbf{r}''-\mathbf{r})\\ &= \frac{1}{\Omega}\sum_\alpha V_\alpha\mathbf{C}'_\alpha\mathbf{C}'_\alpha\mathbf{C}'_\alpha\int_\Omega d\mathbf{r}''\int_\Omega d\mathbf{r}'\int_\Omega d\mathbf{r}\;\mathbf{G}(\mathbf{r}''-\mathbf{r})\mathbf{G}(\mathbf{r}''-\mathbf{r})\\ &=<\mathbf{C}'\mathbf{E}\mathbf{E}>\end{aligned} \tag{46}$$

where we used the fact that the integration of $\mathbf{G}(\mathbf{r}-\mathbf{r}')$ with respect to both $\mathbf{r}$ and $\mathbf{r}'$ is constant when the domain is ellipsoidal (Eshelby [18]).

Finally, by combining the results of (40) and (46), we obtain the expression of composite effective moduli

$$\mathbf{C}^*=<\mathbf{C}>+<\mathbf{C}'\mathbf{E}>+<\mathbf{C}'\mathbf{E}\mathbf{E}>+\cdots\cdots \tag{47}$$

The first term of the right-hand side of (47) is isotropic as mentioned in Section 2. Transverse isotropy is due to the terms beyond the first term of the right-hand side of (47).

4 Upper and Lower Bounds

In this section, we adopt the variational method to derive an upper bound expression of the effective stiffness. We here use the definition of $\mathbf{C}^*$ based on the strain energy as

$$\mathbf{C}^*<\epsilon><\epsilon>=<\mathbf{C}\epsilon\epsilon> \tag{48}$$

The equivalence of the two definitions of $\mathbf{C}^*$ in (48) and (2) is discussed by Hill [5].

We begin the treatment with the statement of the principle of minimum potential energy

$$\begin{aligned}<\mathbf{C}\epsilon\epsilon>&=\mathbf{C}^*<\epsilon><\epsilon>\\ &\leqq<\mathbf{C}\epsilon^0\epsilon^0>\end{aligned} \tag{49}$$

where ϵ is the true strain and ϵ^0 is an arbitrary strain that

Downloaded 02 May 2010 to 171.66.16.25. Redistribution subject to ASME license or copyright; see http://www.asme.org/terms/Terms_Use.cfm

satisfies the requirement that the displacement caused by ϵ^0 on the boundary of the domain is equal to that caused by ϵ. From this condition, we obtain

$$<\epsilon^0> = <\epsilon> \tag{50}$$

We take a trial function ϵ^0 in (49) as the average strain itself, which obviously satisfies (50), as

$$\epsilon^0 = <\epsilon> \tag{51}$$

Then, equation (49) becomes

$$\mathbf{C}^* \leqq <\mathbf{C}> \tag{52}$$

This is the well-known Voigt bound [19] of the "rule of mixtures." Equation (52) is the "best" possible bound with the knowledge of the volume fraction of each phase alone. Here, "best" means that a material that achieves the equality in (52) is realizable. Note that the inequality $\mathbf{A} \leqq \mathbf{B}$ is understood that $\mathbf{B} - \mathbf{A}$ is positive semidefinite.

It has been shown in (16) that ϵ can be expressed in a form of an infinite series as

$$\epsilon = <\epsilon> + \epsilon' = [I + \Gamma\mathbf{C}' + (\Gamma\mathbf{C}'\Gamma\mathbf{C}' - \Gamma <\mathbf{C}'\Gamma\mathbf{C}'> + \ldots\ldots]<\epsilon> \tag{53}$$

Therefore, as a second trial function, we can choose, after truncating the higher order terms in (53) beyond the second term, as

$$\epsilon^0 = (\mathbf{I} + \eta\Gamma\mathbf{C}') \tag{54}$$

where η is a variational parameter. It is obvious that ϵ^0 in (54) satisfies (50). Substitution of (54) into (49) yields

$$<\epsilon>\mathbf{C}^*<\epsilon> \leqq <\epsilon^0\mathbf{C}\epsilon^0> = <(<\epsilon> + \eta\Gamma\mathbf{C}'<\epsilon>)(<\mathbf{C}> + \mathbf{C}')(<\epsilon> + \eta\Gamma\mathbf{C}'<\epsilon>)> \tag{55}$$

Equation (55) can be reduced to a more condensed form as

$$\mathbf{C}^* \leqq <\mathbf{C}> + 2\eta<\mathbf{C}'\Gamma\mathbf{C}'> + \eta^2(<\mathbf{C}'\Gamma\mathbf{C}'\Gamma\mathbf{C}'> - <\mathbf{C}'\Gamma\mathbf{C}'>) \tag{56}$$

For $\eta = 1$, equation (56) recovers the series expression of (18) up to the third order.

Taking the derivative of the right-hand side of (56) with respect to η and equating it with zero, we obtain

$$\eta = -\frac{<\epsilon><\mathbf{C}'\Gamma\mathbf{C}'><\epsilon>}{<\epsilon>(<\mathbf{C}'\Gamma\mathbf{C}'\Gamma\mathbf{C}'> - <\mathbf{C}'\Gamma\mathbf{C}'>)<\epsilon>} \tag{57}$$

Thus, an upper bound of the effective stiffness is given by

$$\mathbf{C}^* \leqq <\mathbf{C}> - <\mathbf{C}'\Gamma\mathbf{C}'>^2(<\mathbf{C}'\Gamma\mathbf{C}'\Gamma\mathbf{C}'> - <\mathbf{C}'\Gamma\mathbf{C}'>)^{-1} \tag{58}$$

This is an upper bound with the information of the correlation function up to the third order.

For the case of short-fiber composites in which the correlation functions possess the properties discussed in the preceding section, we showed

$$<\mathbf{C}'\Gamma\mathbf{C}'> = <\mathbf{C}'\mathbf{E}> \tag{59}$$

$$<\mathbf{C}'\Gamma\mathbf{C}'\Gamma\mathbf{C}'> = <\mathbf{C}'\mathbf{E}\mathbf{E}>$$

Therefore, we obtain

$$\mathbf{C}^* \leqq <\mathbf{C}> - <\mathbf{C}'\mathbf{E}>^2(<\mathbf{C}'\mathbf{E}\mathbf{E}> - <\mathbf{C}'\mathbf{E}>)^{-1} \tag{60}$$

Again, the inequality (60) is in the sense of positive semidefinite.

As an example of the obtained result of (60), we can express the effective axial shear modulus $G_{12}{}^*$ for short-fiber composites as

$$G_{12}{}^* \leqq <\mu> - \frac{4\hat{\Gamma}_{1212}<\mu'^2>^2}{4\hat{\Gamma}_{1212}<\mu'^3> - <\mu'^2>} \tag{61}$$

where $\hat{\Gamma}_{1212}$ is given by (36).

A lower bound of the effective stiffness can be derived from the elastic compliance $\mathbf{S}$ in a manner parallel to the above discussions. The result is

$$\mathbf{S}^* \leqq <\mathbf{S}> - <\mathbf{S}'\Delta\mathbf{S}'>^2(<\mathbf{S}'\Delta\mathbf{S}'\Delta\mathbf{S}'> - <\mathbf{S}'\Delta\mathbf{S}'>)^{-1} \tag{62}$$

where Δ is given by (20).

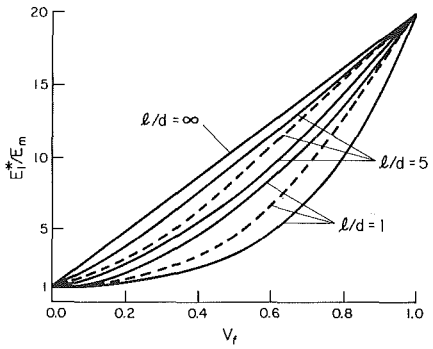


Fig. 1 The variation of $E_{11}{}^*/E_m$ with V_F for $E_f/E_m = 20$, $\nu_m = 0.4$, and $\nu_f = 0.3$ where E and ν are Young's modulus and Poisson's ratio, respectively. The subscripts f and m are for fiber and matrix, respectively. The fiber aspect ratio $l/d = 1$, 5 and ∞. Solid line: present theory; broken line: self-consistent model.

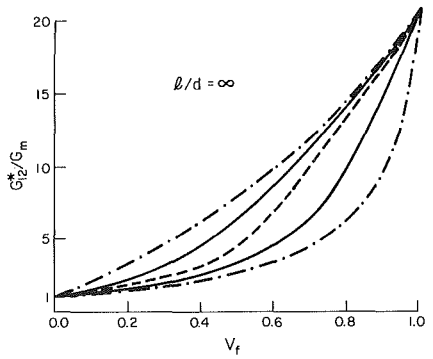


Fig. 2 The variation of $G_{12}{}^*/G_m$ with V_f for $E_f/E_m = 20$, $\nu_m = 0.4$, $\nu_f = 0.3$, and $l/d = \infty$. Solid line: present theory; broken line: self-consistent model; chain-dotted line: Hashin's theory.

5 Discussions

The predictions of (60) and (62) are examined in the following by comparing them with other existing theories as well as experimental results for some limiting cases. Figure 1 illustrates the variation of the axial Young's modulus $E_{11}{}^*$ (normalized by the matrix Young's modulus E_m) with the fiber volume fraction V_f and the fiber aspect ratio traditionally denoted by l/d, calculated from the following relations:

$$E_{11}{}^*(\text{upper bound}) = C^*_{1111} - \frac{2C^*_{1122}{}^2}{(C^*_{1111} + C^*_{2233})} \tag{63}$$

$$E_{11}{}^*(\text{lower bound}) = \frac{1}{S^*_{1111}}$$

The composite material properties used in the calculation are chosen so as to simulate those of a typical glass/epoxy system. The solid lines indicate the upper and lower bound predictions of the present theory. The predictions of the self-consistent model of Chou, Nomura, and Taya [4] are indicated by broken lines. The self-consistent model prediction is close to the lower bound at low fiber volume fractions. The gap between the two bounds at a fixed fiber volume fraction narrows as the fiber aspect ratio increases. For long-

Downloaded 02 May 2010 to 171.66.16.25. Redistribution subject to ASME license or copyright; see http://www.asme.org/terms/Terms_Use.cfm

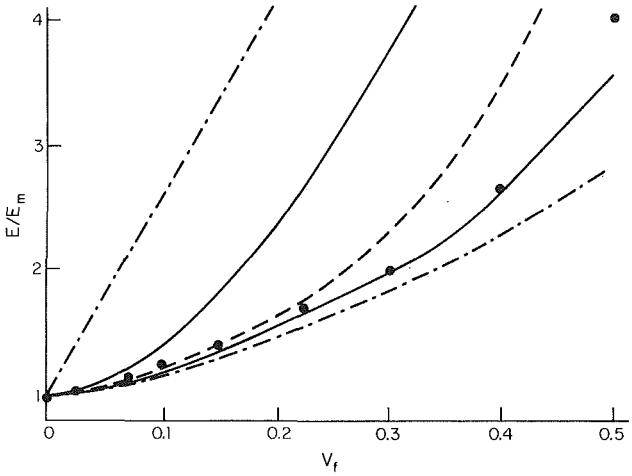


Fig. 3 The variation of E^*/E_m with V_f for $E_f/E_m = 25$, $\nu_m = 0.39$, $\nu_f = 0.23$, and $l/d = 1$. Solid line: present theory; broken line: self-consistent model; chain-dotted lines: bounds of Hashin and Shtrikman; solid circles: experimental data of Smith [22].

continuous fibers, the present model and the self-consistent model both predict the rule of mixture relation.

It was found numerically that as the aspect ratio goes beyond 50, the upper and lower bounds merge and the rule of mixture is valid for the effective axial Young modulus. For other effective engineering moduli such as E_{22}^* (transverse Young's modulus), ν_{12}^* (axial Poisson's ratio), and G_{12}^* (axial shear modulus) it was shown numerically that they are not sensitive to the change of the aspect ratio. This agrees with the result of the authors' self-consistent model [4].

Figure 2 shows the comparison of our theory with Hashin's results [13] for the effective axial shear modulus G_{12}^* (normalized by the matrix shear modulus G_m) of continuous-fiber composites. The present theory predicts tighter bounds than those of Hashin.

There are not many experimental data available on short-fiber composites. References [20, 21] treat the effective Young's modulus for short-fiber composites. Comparisons of those results to theoretical predictions are found in reference [4].

Figure 3 gives the results of the present theory, Hashin and Shtrikman [12], and the self-consistent model [4] for the composite reinforced by spherical particles. The elastic modulus data used for the calculations of Fig. 5 are based on the experimental results of a glass/epoxy system tested by Smith [22]. All the experimental data are indicated by solid circles. The lower bound prediction of the present theory coincides very well with the experimental results.

To narrow bounds, we need more information of the correlation functions beyond the third order on the phase geometry of the composite.

References

1 Chou, T.-W., and Kelly, A., "Fiber Composites," in *Challenges and Opportunities in Material Science and Engineering, Material Science Engineering*, Vol. 25, 1976, pp. 35-40.

2 Vinson, J., and Chou, T.-W., *Composite Materials and Their Use in Structures*, Elsevier-Applied Science, 1975.

3 Chou, T.-W., and Kelly, A., "Mechanical Properties of Composites," *Annual Review of Material Science*, Vol. 10, 1980, pp. 229-259.

4 Chou, T.-W., Nomura, S., and Taya, M., "A Self-Consistent Approach to the Elastic Stiffness of Short-Fiber Composites," *Journal of Composite Materials*, Vol. 14, 1980, pp. 178-188. Also in *Modern Developments in Composite Materials*, Vinson, J. R., ed., ASME, 1979.

5 Hill, R., "The Elastic Behavior of a Crystalline Aggregate," *Proceedings of the Physical Society*, Series B, Vol. 65, 1952, pp. 349-354.

6 Hill, R., "A Self-Consistent Mechanics of Composite Materials," *Journal of Mechanics and Physics of Solids*, Vol. 13, 1965, pp. 213-222.

7 Walpole, L. J., "On the Overall Elastic Moduli of Composite Materials," *Journal of Mechanics and Physics of Solids*, Vol. 17, 1969, pp. 235-251.

8 Dederichs, P. H., and Zeller, R., "Variational Treatment of the Elastic Constants of Disordered Materials," *Zeitschrift für Physik*, Vol. 259, 1973, pp. 103-116.

9 Zeller, R., and Dederichs, P. H., "Elastic Constants of Polycrystals," *Physica Status Solidi, (b)*, Vol. 55, 1973, pp. 831-842.

10 Kröner, E., "Elastic Moduli of Perfectly Disordered Composite Materials," *Journal of Mechanics and Physics of Solids*, Vol. 15, 1967, pp. 319-329.

11 Kröner, E., "Bounds for Effective Elastic Moduli of Disordered Materials," *Journal of Mechanics and Physics of Solids*, Vol. 25, 1977, pp. 137-155.

12 Kröner, E., *Statistical Continuum Mechanics*, Courses and Lectures, No. 92, Udine, Springer-Verlag, Wien, 1972.

13 Bolotin, V. V., and Moskalenko, V. N., "Macroscopic Characteristics of Microinhomogeneous Solids," *Soviet Physics-Doklady*, Vol. 13, 1968, pp. 73-75.

14 Hashin, Z., and Shtrikman, S., "A Variational Approach to the Theory of the Elastic Behavior of Multiphase Materials," *Journal of Mechanics and Physics of Solids*, Vol. 11, 1963, pp. 127-134.

15 Hashin, Z., "On Elastic Behavior of Fiber-Reinforced Materials of Arbitrary Transverse Phase Geometry," *Journal of Mechanics and Physics of Solids*, Vol. 25, 1965, pp. 119-134.

16 Miller, M. N., "Bounds for Effective Electrical, Thermal, and Magnetic Properties of Heterogeneous Materials," *Journal of Mathematical Physics*, Vol. 10, 1969, pp. 1988-2004.

17 Wu, C-T. D., and McCullough, R., "Constitutive Relationships for Heterogeneous Materials," *Developments in Composite Materials*, Vol. 1, Applied Science Publishers, 1977, pp. 119-187.

18 Eshelby, J. D., "The Determination of the Elastic Field of an Ellipsoidal Inclusion and Related Problems," *Proceedings of the Royal Society*, Series A, Vol. 241, 1957, pp. 376-396.

19 Voigt, W., *Lehrbuch der Kristalphysik*, Teubner, 1910.

20 Blumentrit, B. H., Vu, B. T., and Cooper, S. L., "The Mechanical Properties of Oriented Discontinuous Fiber-Reinforced Thermoplastics-I. Unidirectional Fiber Orientation," *Polymer Engineering and Science*, Vol. 14, 1974, pp. 633-640.

21 Lees, J. K., "A Study of the Tensile Modulus of Short Fiber Reinforced Plastics," *Polymer Engineering and Science*, Vol. 8, 1968, pp. 186-194.

22 Smith, J. C., "The Elastic Constants of a Particulate-Filled Glassy Polymer: Comparison of Experimental Values With Theoretical Predictions," *Society of Plastics Engineers*, EPS Div. Meeting, Akron, Ohio, 1975.

Downloaded 02 May 2010 to 171.66.16.25. Redistribution subject to ASME license or copyright; see http://www.asme.org/terms/Terms_Use.cfm

M.-J. Pindera
Senior Research Engineer,
Levecque Technical Center,
Certainteed Corp.,
Blue Bell. Pa. 19422

C. T. Herakovich
Professor of Engineering
Science and Mechanics,
Virginia Polytechnic Institute
and State University,
Blacksburg, Va. 24061
Mem. ASME

An Elastic Potential for the Nonlinear Response of Unidirectional Graphite Composites

An elastic potential is proposed that is capable of modeling the reversible portion of the observed nonlinear response of unidirectional graphite fiber composites. The model includes both the stiffening stress-strain behavior as well as the softening Poisson's response for loading in the fiber direction. The model is compared with experimental results for Celion 6000/PMR-15 graphite-polyimide.

Introduction

It has been known for some time that unidirectional graphite fiber composites exhibit nonlinear stress-strain responses when subjected to tensile loading in the fiber direction [1–8]. The observed response indicates that Young's modulus in the fiber direction increases with increasing applied load. The percent increase of modulus can be significant; a 20 percent increase is not uncommon. Recent tests by the authors on unidirectional Celion 6000/PMR-15 graphite-polyimide indicate that the longitudinal response exhibits nearly bilinear stiffening behavior with average initial and final moduli of 136 GPa (19.8×10^6 psi) and 161 GPa (23.4×10^6 psi), respectively (Fig. 1). The nonlinear response appears to be reversible for almost the entire range of allowable stress. This was verified by the authors using cyclic tests at several unloading levels. It appears that the response is no longer reversible only after significant damage occurs in the specimen. For the material considered in this investigation, significant damage was evident only above 90 percent of the ultimate stress.

The strain-strain or Poisson's response of unidirectional graphite composites also appears to be of a bilinear, reversible character with average initial and final Poisson's ratios of 0.350 and 0.318, respectively. Such behavior will be called softening. Typical strain-strain response of Celion 6000/PMR-15 is shown in Fig. 2.

Similar observations do not hold for the transverse and shear response of unidirectional graphite composites [1]. Both of these responses exhibit considerable nonlinearity of the softening type as well as dissipation characterized by permanent strain accumulation.

Several causes are believed to be responsible for the tendency of graphite fiber composites to stiffen when loaded in the fiber direction. The two most commonly postulated phenomena considered in the literature are the fiber waviness introduced into the lamina during the fabrication process and nonlinear response of the graphite fiber itself.

Curtis, Milne, and Reynolds [2] employed an acoustic wave propagation technique on carbon fibers to measure the longitudinal Young's modulus as a function of load. They identified two distinct regions for the increasing values of the longitudinal Young's modulus with applied load. Initially, the Young's modulus exhibited a power-law type of dependence with decreasing slope—this was attributed to the movement and subsequent pinning of basal dislocations in the crystallite structure of carbon fibers. The second region showed a linear

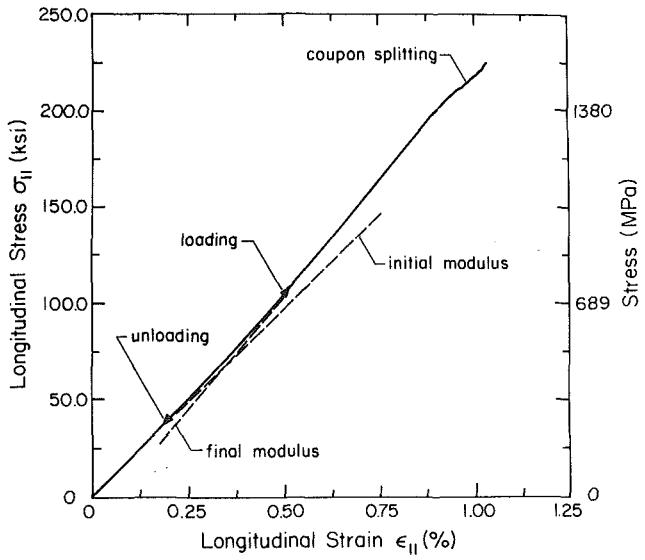


Fig. 1 Typical longitudinal stress-strain response of 0 deg Celion 6000/PMR-15

Contributed by the Applied Mechanics Division for presentation at the Winter Annual Meeting, New Orleans, La., December 9–14, 1984 of THE AMERICAN SOCIETY OF MECHANICAL ENGINEERS.

Discussion on this paper should be addressed to the Editorial Department, ASME, United Engineering Center, 345 East 47th Street, New York, N.Y. 10017, and will be accepted until two months after final publication of the paper itself in the JOURNAL OF APPLIED MECHANICS. Manuscript received by ASME Applied Mechanics Division, April, 1983; final revision, September, 1983. Paper No. 84-WA/APM-5.

Copies will be available until August 1985.

Copyright © 1984 by ASME
Downloaded 02 May 2010 to 171.66.16.25. Redistribution subject to ASME license or copyright; see http://www.asme.org/terms/Terms_Use.cfm

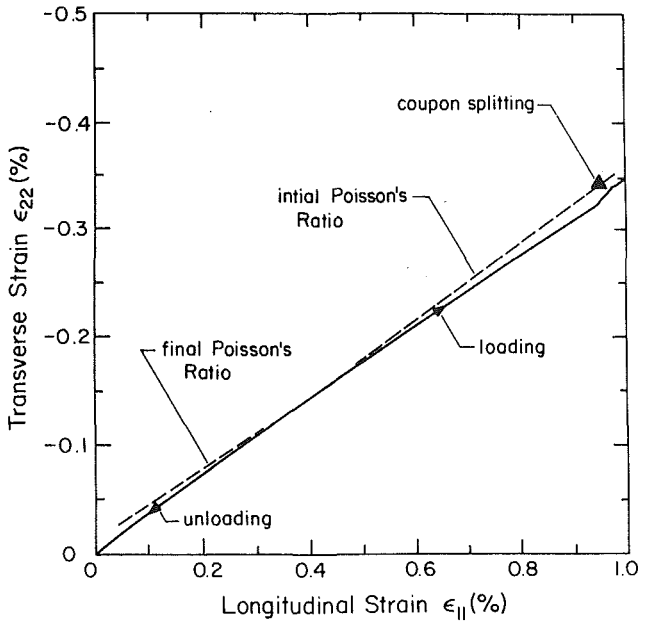


Fig. 2 Typical Poisson's response of 0 deg Celion 6000/PMR-15

dependence on the applied load and was suggested to be due to straightening of the cellular structure of the fiber itself. More recent evidence of such stiffening effects has been reported by Beetz [3].

Mansfield and Purslow [4] studied analytically the influence of fiber waviness on shear and Young's moduli of unidirectional lamina using the material modeling approach. The study was undertaken to explain the higher experimental values for the shear modulus than those predicted theoretically on the basis of various models. Analytical results indicated negligible effect on both moduli if constraints were imposed on allowable fiber and matrix deformation modes such that failure strains in either phase used in the considered composite were not exceeded. This effectively imposed upper limits on the fiber wave amplitude to wavelength ratio which controlled the nonlinear behavior. The study revealed, on the other hand, the possibility of significant influence of the fiber waviness for those systems with ductile matrices and flexible fibers. Other examples of the micromechanical approach employed to study the effect of fiber curvature on the stress-strain response can be found in the works of Bazant [5], Comninou and Yannas [6], and more recently Bert [7] where various commonly employed techniques have been reviewed and extended.

Van Dreumel and Kamp [8] carried out an experimental study aimed at separating the influence of fiber waviness and fiber nonlinear response on the stiffening behavior of 0 deg graphite-epoxy laminae. Laminates with fibers having amplitude-to-wavelength ratios between 0.05/55 and 0.75/55 were tested and a linear relationship was found between longitudinal modulus and applied stress. The relationship was $E = E_0 + 21\sigma$. The authors concluded that no significant influence of fiber waviness was found for the amplitude-to-wavelength ratios tested. (It should be noted that Mansfield and Purslow's analysis indicated that the amplitude-to-wavelength ratios considered by van Dreumel and Kamp would not result in significantly different responses.) The study also showed that Poisson's ratio increased from 0.29 to 0.59 with increased waviness ratios in the range considered by the authors.

The foregoing discussion indicates that the stiffening behavior of certain types of graphite or carbon composites is a well-documented phenomenon, whatever the causes underlying such response. However, there appears to be little evidence presented in the available literature that this behavior has been accounted for in the course of structural analysis of multidirectional laminates. With the exception of Bert's micromechanical approach [7] which requires an iterative method of solution and is based on the assumption of fiber waviness, the authors are not aware of any other three-dimensional constitutive model that accounts for the stiffening behavior of graphite composites in a systematic fashion.

This paper is an attempt to ameliorate this situation with the aid of the phenomenological or empirical approach, in contrast with the approaches mentioned in the foregoing. To this end an elastic potential is proposed that is capable of modeling the reversible portion of the observed nonlinear response of the Gr/Pi system under consideration. The model includes both the stiffening stress-strain behavior along the fiber direction as well as the softening Poisson's response. The empirical model is compared with experimental results.

The reader is referred to reference [9] for an outline of a methodology of incorporating the proposed elastic potential into a more comprehensive model for multidirectional loading of graphite composites.

Theoretical Development

Consider an elastic potential of the following form, expressed in the so-called reduced notation:

$$-G_0 = \frac{1}{2}A_{ij}\sigma_i\sigma_j + \frac{1}{\alpha}\left(e^{-\alpha\sqrt{l_{ij}\sigma_i\sigma_j}} - 1\right) + \sqrt{l_{ij}\sigma_i\sigma_j} \qquad (1)$$

$$(i, j = 1,2, \ldots 6)$$

so that the reversible strains are given by:

$$\epsilon_i = -\frac{\partial G_0}{\partial \sigma_i} = A_{ij}\sigma_j + \frac{l_{ij}\sigma_j}{\sqrt{l_{mn}\sigma_m\sigma_n}}\left[1 - e^{-\alpha\sqrt{l_{mn}\sigma_m\sigma_n}}\right] \qquad (2)$$

In the foregoing the following are assumed at the outset, l_{ij} is positive semidefinite and the parameter α is greater than zero. The physical significance of these parameters will be discussed subsequently. Applying the stability condition $\delta^2(-G_0) > 0$ [10] and examining the limiting behavior of the foregoing, the following thermodynamic constraints are obtained as is illustrated in Appendix A:

$$\lim_{\sigma_i \to 0} \delta^2(-G_0) = (A_{ij} + \alpha l_{ij})\,\delta\sigma_i\delta\sigma_j > 0 \qquad (3)$$

so that $(A_{ij} + \alpha l_{ij})$ must be positive definite;

$$\lim_{\sigma_i \to \infty} \delta^2(-G_0) = A_{ij}\delta\sigma_i\delta\sigma_j > 0 \qquad (4)$$

and therefore A_{ij} by itself must also be positive definite. Furthermore, it can also be shown (see Appendix A) that the preceding constraints in conjunction with the initial two assumptions that l_{ij} is positive semidefinite and α is positive are sufficient for the condition $\delta^2(-G_0) > 0$ to hold for all plane stress loading situations.

The physical significance of the various material parameters can best be illustrated through hypothetical loading experiments along the specified material principal directions. Let us consider the following loading situation to illustrate the general methodology.

Example: $\sigma_1 \neq 0$, All Other Zero. The following stress-strain equations are obtained from equation 2:

$$\epsilon_1 = A_{11}\sigma_1 + \sqrt{l_{11}}\left(1 - e^{-\alpha\sqrt{l_{11}}\sigma_1}\right) \qquad (5)$$

$$\epsilon_2 = A_{12}\sigma_1 + \frac{l_{12}}{\sqrt{l_{11}}}\left(1 - e^{-\alpha\sqrt{l_{11}}\sigma_1}\right)$$

The significance of the various material parameters is brought forth by examining the limiting behavior of the

Downloaded 02 May 2010 to 171.66.16.25. Redistribution subject to ASME license or copyright; see http://www.asme.org/terms/Terms_Use.cfm

Table 1 Potential parameters for loading Celion 6000/PMR-15 Gr/Pi in the fiber direction

A_{11} (1/GPa)	A_{12} (1/GPa)	l_{11} ($\times 10^{-6}$)	l_{12} ($\times 10^{-6}$)	α (1/GPa)
0.00620	−0.00200	0.378	−0.200	2890

$$-G_0 = \frac{1}{2}A_{ij}\sigma_i\sigma_j + \frac{1}{\alpha}(e^{-\alpha\sqrt{l_{ij}\sigma_i\sigma_j}} - 1) + \sqrt{l_{ij}\sigma_i\sigma_j}$$

foregoing system of equations. Differentiating the first of equation (5) with respect to σ_1 we obtain:

$$\frac{\partial \epsilon_1}{\partial \sigma_1} = A_{11} + \alpha l_{11} e^{-\alpha\sqrt{l_{11}}\sigma_1}$$

so that:

$$\left.\frac{\partial \epsilon_1}{\partial \sigma_1}\right|_{\sigma_1 = 0} = A_{11} + \alpha l_{11}; \tag{6}$$

$$\left.\frac{\partial \epsilon_1}{\partial \sigma_1}\right|_{\sigma_i = \infty} = A_{11}$$

And since $\alpha > 0$, $A_{11} > 0$, and $l_{11} \geq 0$, the initial compliance (stiffness) is greater (smaller) than the limiting compliance (stiffness) for the strict inequality A_{11}, $l_{11} > 0$. Therefore, stiffening response in the fiber direction has been generated for A_{11}, $l_{11} > 0$. The initial and final responses along the fiber direction are, respectively:

$$\epsilon_1(\sigma_1 \to 0) = (A_{11} + \alpha l_{11})\sigma_1$$
$$\epsilon_1(\sigma_1 \to \infty) = A_{11}\sigma_1 + \sqrt{l_{11}} \tag{7}$$

Further, $\sqrt{l_{11}}$ is the $\sigma_1 = 0$ intercept of the final limiting response. The geometric interpretation of α can now be obtained upon finding the intersection of the two limiting slopes $\sigma_1 \to 0$ and $\sigma_1 \to \infty$. Setting $\epsilon_1(\sigma_1 \to 0) = \epsilon_1(\sigma_1 \to \infty)$ we obtain:

$$\alpha = \frac{1}{\sqrt{l_{11}}\sigma_1^*} \tag{8}$$

where σ_1^* is the common stress at the intersection of these two curves. We can therefore adjust the initial stiffening response in conjunction with the "knee" of the stress-strain curve by varying the parameter α for a given l_{11}. The features of the model outlined in the foregoing are illustrated in Fig. 3. In summary we note that the three material parameters A_{11}, l_{11}, and α can easily be obtained from a single longitudinal tension test and equations (6) and (7).

Some of the interesting features of the Poisson's or strain-strain behavior in longitudinal tension inherent in the model are best examined by separating the response into constant and stress-dependent components. Solving equation (5) for ϵ_2 as a function of ϵ_1 and then differentiating with respect to the ϵ_1-strain we obtain:

$$-\nu_{12} = \frac{\partial \epsilon_2}{\partial \epsilon_1} = \frac{l_{12}}{l_{11}} + \frac{(A_{12}l_{11} - A_{11}l_{12})}{l_{11}} \frac{\partial \sigma_1}{\partial \epsilon_1} \tag{9}$$

Three types of longitudinal strain-strain response are, therefore, now possible depending on the value of the term $(A_{12}l_{11} - A_{11}l_{12})$:

(*i*) $A_{12}l_{11} - A_{11}l_{12} = 0$;

$$\frac{\partial \epsilon_2}{\partial \epsilon_1} = \text{constant}$$

(*ii*) $A_{12}l_{11} - A_{11}l_{12} < 0$;

$$\frac{\partial \epsilon_2}{\partial \epsilon_1} = \text{constant} - f(\sigma_1), \tag{10}$$

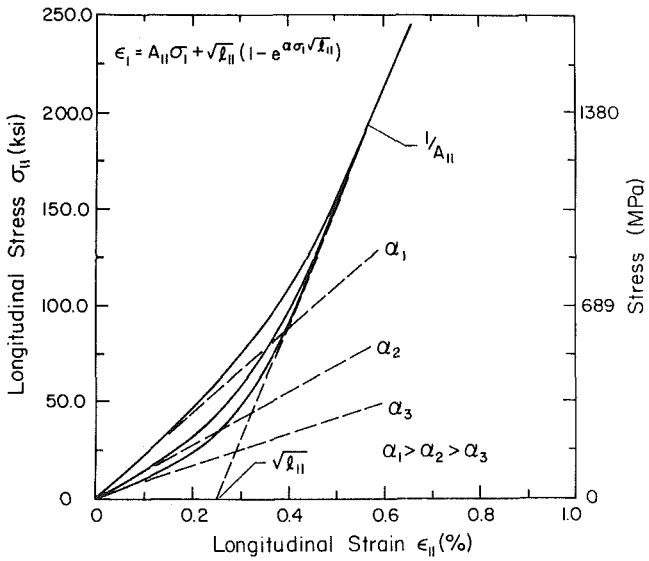


Fig. 3 Features of proposed model for stiffening behavior of unidirectional graphite composites

(*iii*) $A_{12}l_{11} - A_{11}l_{12} > 0$;

$$\frac{\partial \epsilon_2}{\partial \epsilon_1} = \text{constant} + f(\sigma_1),$$

where $\partial f_1/\partial \sigma_1 > 0$ for stiffening longitudinal stress-strain behavior.

Thus either a constant, stiffening, or softening Poisson's response can be generated according to the foregoing scheme. The unknown constants A_{12} and l_{12} are obtained by examining the limiting response as outlined previously. To this end it is more convenient to express the instantaneous Poisson's ratio in a more direct way by differentiating the second of equation (5) with respect to the ϵ_1-strain to obtain:

$$\frac{\partial \epsilon_2}{\partial \epsilon_1} = (A_{12} + \alpha l_{12} e^{-\alpha\sqrt{l_{11}}\sigma_1}) \frac{\partial \sigma_1}{\partial \epsilon_1} \tag{11}$$

so that

$$\left.\frac{\partial \epsilon_2}{\partial \epsilon_1}\right|_{\sigma_1 = 0} = (A_{12} + \alpha l_{12}) \left.\frac{\partial \sigma_1}{\partial \epsilon_1}\right|_{\sigma_1 = 0}, \tag{12}$$

$$\left.\frac{\partial \epsilon_2}{\partial \epsilon_1}\right|_{\sigma_1 = \infty} = A_{12} \left.\frac{\partial \sigma_1}{\partial \epsilon_1}\right|_{\sigma_1 = \infty}$$

and thus the entire treatment in analyzing major Poisson's response follows along the sames lines as that for the longitudinal behavior.

Experimental-Theoretical Correlation

The various material parameters of the proposed elastic potential for plane stress applications have been evaluated on the basis of average limiting responses of test results using the relations developed above. It has been illustrated in reference [1] that these parameters obey the derived thermodynamic

Downloaded 02 May 2010 to 171.66.16.25. Redistribution subject to ASME license or copyright; see http://www.asme.org/terms/Terms_Use.cfm

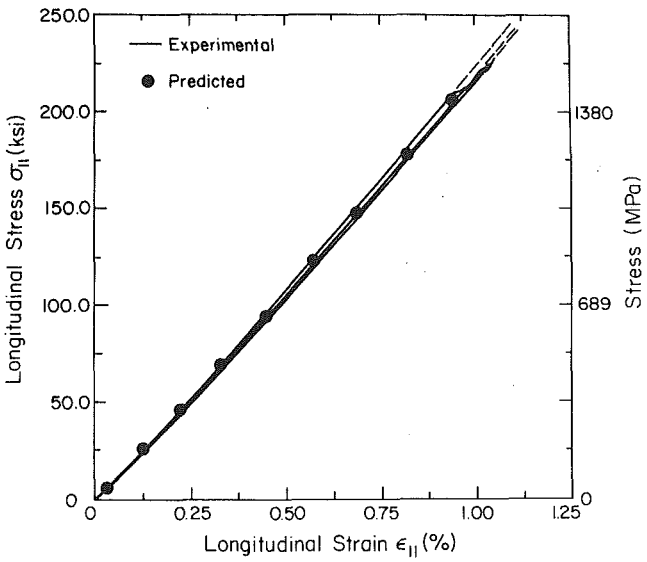


Fig. 4 Theoretical/experimental comparison for longitudinal tension of 0 deg Celion 6000/PMR-15

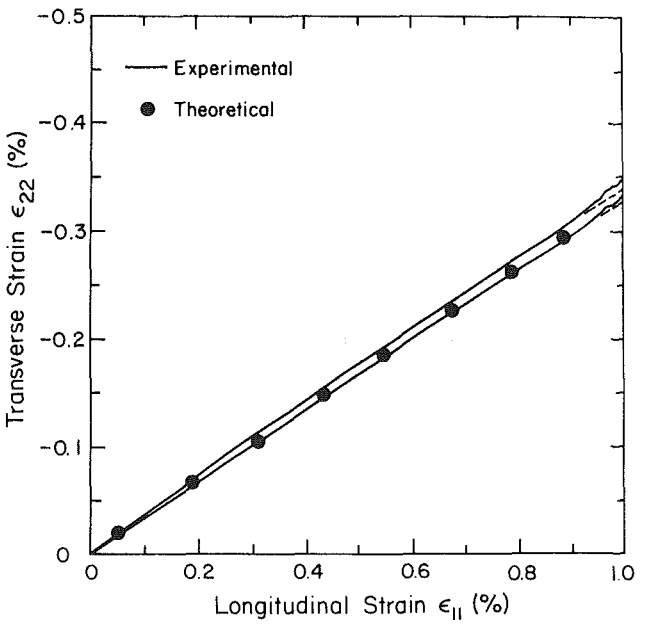


Fig. 5 Theoretical/experimental comparison for Poisson's response for 0 deg Celion 6000/PMR-15

constraints. The parameters for loading along the fiber direction are given in Table 1.

The predicted average response in longitudinal tension is shown in Figs. 4 and 5 with selected experimental data included for comparison. The agreement appears to be good. It must be mentioned that even better agreement can be obtained if specific test coupon results are used to evaluate the necessary parameters and then compared directly with the predicted response on a one-to-one, instead of average, basis.

Summary

The proposed elastic potential discussed in this paper has been shown to successfully model the stiffening longitudinal response as well as softening Poisson's response of 0 deg Gr/Pi laminae subjected to uniaxial loading. It has also been demonstrated that the model is sufficiently versatile to describe three types of Poisson's response, namely: constant, softening or stiffening depending on the sign of certain material parameters. The thermodynamic constraints as well as physical significance of various material parameters in the model have been derived from the stability condition $\delta^2(-G_0) > 0$ and consideration of the limiting response for a hypothetical loading situation. The potential should be useful in analyses of graphite fiber multidirectional composites that exhibit significant stiffening characteristics along the fiber direction.

Acknowledgment

This work was supported by the NASA-Virginia Tech Composites Program, NASA Cooperative Agreement NCC1-15.

References

1 Pindera, M. J., and Herakovich, C. T., "An Endochronic Theory for Transversely Isotropic Fibrous Composites," VPI-E-81-27, Virginia Polytechnic Institute and State University, Oct. 1981.

2 Curtis, G. J., Milne, J. M., and Reynolds, W. N., "Non-Hookean Behaviour of Strong Carbon Fibres," *Nature*, Vol. 220, Dec. 1968, p. 1024.

3 Beetz, C. P., Jr., "Strain-Induced Stiffening of Carbon Fibres," *Fibre Science and Technology*, Vol. 16, 1982.

4 Mansfield, E. H., and Purslow, D., "The Influence of Fiber Waviness on the Moduli of Unidirectional Fiber Reinforced Composites," CP No. 1339, Dec. 1974.

5 Bazant, Z. P., "Effect of Curvature of the Reinforcing Fibers on the Moduli of Elasticity and Strength of Composites," *Polymer Mechanics*, Vol. 4, No. 2, 1968, pp. 251-258.

6 Comninou, M., and Yannas, I. V., "Dependence of Stress-Strain Nonlinearity of Connective Tissues on the Geometry of Collagen Fibers," *Journal of Biomechanics*, Vol. 9, 1976, pp. 427-433.

7 Bert, C. W., "Micromechanics of the Different Elastic Behavior of Filamentary Composites in Tension and Compression," *Mechanics of Bimodulus Materials*, AMD Vol. 33, ASME, N.Y., 1979, pp. 17-28.

8 van Dreumel, W. H. M., and Kamp, J. L. M., "Non-Hookean Behaviour in the Fibre Direction of Carbon-Fibre Composites and the Influence of Fibre Waviness on the Tensile Properties," *J. Composite Materials*, Vol. 11, Oct. 1977, p. 461.

9 Pindera, M. J., and Herakovich, C. T., "An Endochronic Model for the Response of Unidirectional Composites Under Off-Axis Tensile Load," *Mechanics of Composite Materials: Recent Advances*, Hashin, Z., and Herakovich, C. T., eds., Pergamon Press, 1983.

10 Drucker, D. C., "On the Postulate of Stability of Material in the Mechanics of Continua," *Journal de Mécanique*, Vol. 3, No. 2, June 1964.

APPENDIX A

Proposed Elastic Potential G_0 and Associated Thermodynamic Constraints

The proposed elastic potential is reproduced in the following for convenience.

$$-G_0 = \frac{1}{2}A_{ij}\sigma_i\sigma_j + \frac{1}{\alpha}\left(e^{-\alpha\sqrt{l_{ij}\sigma_i\sigma_j}} - 1\right) + \sqrt{l_{ij}\sigma_i\sigma_j} \tag{A.1}$$

Applying the stability condition $\delta^2(-G_0) > 0$ we obtain:

$$\delta^2(-G_0) = A_{ij}\delta\sigma_i\delta\sigma_j + \frac{l_{ij}\delta\sigma_i\delta\sigma_j}{\sqrt{l_{mn}\sigma_m\sigma_n}}\left(1 - e^{-\alpha\sqrt{l_{mn}\sigma_m\sigma_n}}\right) - \frac{(l_{ij}\sigma_j\delta\sigma_i)^2}{(l_{mn}\sigma_m\sigma_n)^{3/2}}\left(1 - e^{-\alpha\sqrt{l_{mn}\sigma_m\sigma_n}}\right) + \frac{(l_{ij}\sigma_j\delta\sigma_j)^2}{(l_{mn}\sigma_m\sigma_n)}e^{-\alpha\sqrt{l_{mn}\sigma_m\sigma_n}} > 0 \tag{A.2}$$

Series expansion of the exponential terms and subsequent simplification of the resulting expression yields:

$$\delta^2(-G_0) = A_{ij}\delta\sigma_i\delta\sigma_j + \alpha l_{ij}\delta\sigma_i\delta\sigma_j\left(1 - \frac{\alpha\sqrt{\ }}{2!} + \frac{\alpha^2\sqrt{\ }^2}{3!} - \ldots\right) + \frac{\alpha(l_{ij}\sigma_j\delta\sigma_j)^2}{(l_{mn}\sigma_m\sigma_n)}\left[\alpha\sqrt{\ }\left(\frac{1}{2!} - 1\right) + \alpha^2\sqrt{\ }^2\left(\frac{1}{2!} - \frac{1}{3!}\right) + \alpha^3\sqrt{\ }^3\left(\frac{1}{4!} - \frac{1}{3!} + \ldots\right)\right] > 0 \tag{A.3}$$

Downloaded 02 May 2010 to 171.66.16.25. Redistribution subject to ASME license or copyright; see http://www.asme.org/terms/Terms_Use.cfm

where $\sqrt{\ } = \sqrt{l_{mn}\sigma_m\sigma_n}$. Thus from equation (*A*.3) it is clear that:

$$\lim_{\sigma_i \to 0} \delta^2(-G_0) = (A_{ij} + \alpha l_{ij})\,\delta\sigma_i\delta\sigma_j > 0 \qquad (A.4)$$

whereas from equation (*A*.2) we readily obtain:

$$\lim_{\sigma_i \to \infty} \delta^2(-G_0) = A_{ij}\,\delta\sigma_i\delta\sigma_j > 0 \qquad (A.5)$$

To show that the foregoing constraints are sufficient for the stability condition to be satisfied for all plane-stress loading situations, equation (*A*.2) is rearranged as follows:

$$\delta^2(-G_0) = A_{ij}\delta\sigma_i\delta\sigma_j + \frac{(1-e^{-\alpha\sqrt{l_{mn}\sigma_m\sigma_n}})}{\sqrt{l_{mn}\sigma_m\sigma_n}}\left[l_{ij}\delta\sigma_i\delta\sigma_j - \frac{(l_{ij}\sigma_j\delta\sigma_i)^2}{(l_{mn}\sigma_m\sigma_n)}\right] + \alpha\frac{(l_{ij}\sigma_j\delta\sigma_i)^2}{(l_{mn}\sigma_m\sigma_n)}e^{-\alpha\sqrt{l_{mn}\sigma_m\sigma_n}} > 0 \qquad (A.6)$$

The foregoing will be certainly satisfied if

$$l_{ij}\delta\sigma_i\delta\sigma_j - \frac{(l_{ij}\sigma_i\delta\sigma_j)^2}{(l_{mn}\sigma_m\sigma_n)} \geq 0$$

For loading situations of the form $\sigma_i = \beta_i\sigma$, i.e., proportional, where σ is a scalar parameter, the left-hand side of the preceding expression becomes zero, which satisfies the stability requirement. For general plane stress loadings on the other hand, expansion of the foregoing yields:

$$[l_{11}\sigma_1^2 + 2l_{12}\sigma_1\sigma_2 + l_{22}\sigma_2^2 + l_{66}\sigma_6^2] \cdot [l_{11}\delta\sigma_1^2 + 2l_{12}\delta\sigma_1\delta\sigma_2 + l_{22}\delta\sigma_2^2 + l_{66}\delta\sigma_6^2] - [l_{11}\sigma_1\delta\sigma_1 + l_{12}(\sigma_1\delta\sigma_2 + \sigma_2\delta\sigma_1) + l_{22}\sigma_2\delta\sigma_2 + l_{66}\sigma_6\delta\sigma_6] \geq 0$$

Omitting superfluous algebra, the foregoing can be shown to reduce to the following form:

$$(\sigma_1\delta\sigma_2 - \sigma_2\delta\sigma_1)^2(l_{11}l_{22} - l_{12}^2) + l_{66}\{l_{11}(\sigma_6\delta\sigma_1 - \sigma_1\delta\sigma_6)^2 + l_{22}(\sigma_6\delta\sigma_2 - \sigma_2\delta\sigma_6)^2 + 2l_{12}(\sigma_6\delta\sigma_1 - \sigma_1\delta\sigma_6)(\sigma_6\delta\sigma_2 - \sigma_2\delta\sigma_6)\} \geq 0$$

The first part is always positive or zero since l_{ij} is positive semidefinite, whereas the second part is a quadratic form with coefficients l_{ij} and thus must also be positive or zero for the same reason.

Downloaded 02 May 2010 to 171.66.16.25. Redistribution subject to ASME license or copyright; see http://www.asme.org/terms/Terms_Use.cfm

A Laminated Beam Theory With Interlayer Slip

H. Murakami
Assistant Professor,
Department of Applied Mechanics
and Engineering Sciences,
University of California, San Diego,
La Jolla, Calif. 92093

A Timoshenko beam theory with built-in interlayer slip is developed to facilitate analytical means of simulating the effect of interlayer slip on the stiffness degradation of laminated beam structures. The proposed theory is unique in the sense that any well-structures interlay slip law can be adopted in the beam model. Based on the principle of virtual work, well-posed boundary value problems of the proposed beam theory are defined. It is shown that the proposed theory reduces to the existing Bernoulli-Euler beam theory with interlayer slip by introducing the kinematic constraint of zero transverse shear strain. As a demonstration of the theory the load-deflection curves of a simply supported sandwich beam subjected to a concentrated load at the center are computed for several characteristic interlayer slip laws. It is found that the proposed model has the capability of simulating the deformation of beams with wide range of interlayer bond qualities, from interface with perfect bond to interface without connectors.

1 Introduction

The degradation of laminated beam structures is typically associated with interlayer slip caused either by the flexibility of the adhesive and subsequent delamination in the case of continuously bonded interlayer surfaces, or by the deformation of mechanical connectors, such as nails. The interlay slip causes stiffness degradation and separation of bonded layers, which is frequently observed as the fracture mode of laminated beam structures.

Due to the importance of laminated beam structures in structural design, the interlayer slip of laminated beams has been studied using: (*i*) the beam theory [1-4], and (*ii*) the theory of elasticity [15, 16] assuming that interlayer slip is proportional to the shear stress. The pioneering work on laminated beam structures with interlayer slip was conducted by Newmark, Siess, and Viest [1] on a composite T-beam, and by Granholm [2] and Pleshkov [3] on composite wooden beams. The theory developed by Newmark et al. [1] was based on the "Bernoulli-Euler beam theory" and became the basis of subsequent investigations of interlayer slip. Goodman and coworkers [4-7] studied the interlayer slip problem extensively, and introduced nonlinear interface shear stress-slip relations. They modified the linear slip law by using either the secant or tangent moduli based on interface shear stress-slip diagrams. Norris, Erickson, and Kommers [8] and Kuenzi and Wilkinson [9] developed a sandwich beam theory with interlayer slip. Closed form solutions of the second-order differential equation relating the interlayer slip and the longitudinal force in each layer, developed in [1], were obtained for two layer systems by Hoyle and McGee [10], Vanderbilt et al. [7], and Itani and Brito [11], and for three layers system by Anderson [12]. Besides the aforementioned closed-form solutions, numerical methods employing finite element and finite difference methods have been used. Thompson, Goodman, and Vanderbilt [13] developed a finite element program to analyze multilayer systems. Itani and Hiremath [14] extended the Newmark's two-layer theory [1] for multiple layers, and developed a finite difference program to solve composite action in diaphrams. The foregoing references dealt with the beam theory without the effect of transverse shear, that is, the Timoshenko beam theory [17] was not used.

The theory of elasticity approach was adopted for sandwich beams by Rao and Ghosh [15], and Fazio and Hussein [16]. Due to the analytical complexity, only special boundary conditions and a linear shear stress and slip relation at the interfaces were considered. Fazio et al. [16] introduced assumptions that are adopted in the Bernoulli-Euler beam theory and neglected the effect of transverse shear.

Existing methods of layered beams face difficulty if more general interlayer slip laws are required in order to reflect nonlinear shear stress-slip relations with different moduli in loading and unloading, deterioration of the slip surface due to cyclic loading, and creep under long term loading. In the beam theory approach, the Timoshenko beam theory or a higher order theory that includes the effect of transverse shear should be utilized in order to admit complex slip laws that require the bookkeeping of the evolution of interlayer shear stress and slip, since the slip is, in general, path-dependent in stress space [18].

This paper presents a Timoshenko beam theory with built-in interlayer slip, in the sense that beam equations are derived without making any reference to specific slip laws. As a result,

Contributed by the Applied Mechanics Division for publication in the JOURNAL OF APPLIED MECHANICS.
Discussion on this paper should be addressed to the Editorial Department, ASME, United Engineering Center, 345 East 47th Street, New York, N.Y. 10017, and will be accepted until two months after final publication of the paper itself in the JOURNAL OF APPLIED MECHANICS. Manuscript received by ASME Applied Mechanics Division, March, 1983; final revision, January, 1984.

Copyright © 1984 by ASME
Downloaded 02 May 2010 to 171.66.16.25. Redistribution subject to ASME license or copyright; see http://www.asme.org/terms/Terms_Use.cfm

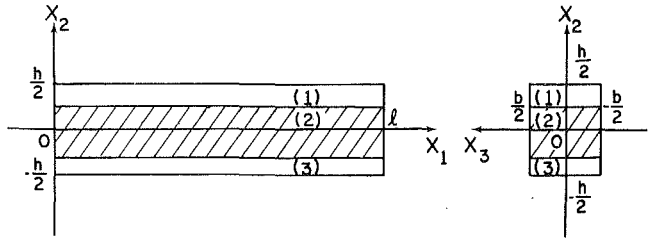


Fig. 1 A sandwich beam and coordinates

any complex slip law can be used to simulate the interlayer slip in the proposed beam equations. For simplicity, the theory is developed for sandwich beams. The Bernoulli-Euler beam theory with interlayer slip proposed by Newmark et al. [1] has been recovered from the proposed theory by introducing the kinematic constraint of zero shear strain. To clarify the effect of the interlayer slip on the stiffness degradation of the beam, characteristic slip laws were examined. As a demonstration of the theory, the load-deflection curves of a simply supported sandwich beam subjected to a concentrated load at the center are computed for several characteristic interlayer slip laws and results compare qualitatively well with the experimental data obtained by Goodman and Popov [4] for nailed wooden layers. It is found that the proposed model has the capability of simulating the deformation of beams with a wide range of interlayer bond qualities, from interface with perfect bond to interface without connectors.

2 Formulation

Consider a sandwich beam of length l, thickness h, and width b as illustrated in Fig. 1. Let rectangular Cartesian coordinates x_1, x_2, x_3 be selected with x_2 normal to the middle plane defined by x_1, x_3. For notational convenience, $(\ )^{(\alpha)}$, $\alpha = 1,2,3$ will denote quantities associated with the upper face, core and lower face layers, respectively, of the sandwich beam. The volume fraction of layer α is denoted by $n^{(\alpha)}$, which satisfies

$$n^{(1)} + n^{(2)} + n^{(3)} = 1 \tag{1}$$

The coordinates of upper and lower interfaces, become

$$x_2 = \left(\frac{1}{2} - n^{(1)}\right)h \text{ and } -\left(\frac{1}{2} - n^{(3)}\right)h$$

respectively. The usual Cartesian indicial notation will be employed where Latin indices range from 1 to 2 and repeated indices imply the summation convention, unless otherwise noted. The notation $(\ )_{,i}$ denotes $\partial(\ )/\partial x_i$.

The governing relations for the displacement vector $u_i^{(\alpha)}$ and the stress tensor $\sigma_{ij}^{(\alpha)}$ in the layer α are

(*a*) Equilibrium equations:

$$\sigma_{ji,j}^{(\alpha)} + f_i^{(\alpha)} = 0, \quad \sigma_{ij}^{(\alpha)} = \sigma_{ij}^{(\alpha)} \tag{2}$$

where $f_i^{(\alpha)}$ is body force;

(*b*) Constitutive relations for orthotropic layers:

$$\begin{bmatrix} \sigma_{11} \\ \sigma_{22} \\ \sigma_{12} \end{bmatrix}^{(\alpha)} = \begin{bmatrix} C_{11} & C_{12} & 0 \\ C_{12} & C_{22} & 0 \\ 0 & 0 & C_{33} \end{bmatrix}^{(\alpha)} \begin{bmatrix} u_{1,1} \\ u_{2,2} \\ u_{1,2} + u_{2,1} \end{bmatrix}^{(\alpha)} \tag{3}$$

where $C_{\beta\gamma}^{(\alpha)}$ ($\beta,\gamma = 1$ to 3) are elastic constants;

(*c*) Interface continuity conditions:

$$\sigma_{2i}^{(1)} = \sigma_{2i}^{(2)} = T_i^{(u)}, \quad u_i^{(1)} - u_i^{(2)} = [u_i]^{(u)} \quad \text{on } x_2 = \left(\frac{1}{2} - n^{(1)}\right)h \tag{4a,b}$$

$$\sigma_{2i}^{(2)} = \sigma_{2i}^{(3)} = T_i^{(l)}, \quad u_i^{(2)} - u_i^{(3)} = [u_i]^{(l)} \quad \text{on } x_2 = -\left(\frac{1}{2} - n^{(3)}\right)h \tag{5a,b}$$

where $[u_1]$ is the pure slip and $[u_2]$ is the interlayer gap; the superscripts (u) and (l) denote quantities associated with the upper and lower interfaces, respectively;

(*d*) Slip laws on the interfaces:

$$\Delta[u_i]^{(u)} = F_{ik}^{(u)}(T_j^{(u)}, [u_j]^{(u)})\Delta T_{jk}^{(u)} \quad \text{on} \quad x_2 = \left(\frac{1}{2} - n^{(1)}\right)h \tag{6a}$$

$$\Delta[u_i]^{(l)} = F_{ik}^{(l)}(T_j^{(l)}, [u_j]^{(l)})\Delta T_{jk}^{(l)} \quad \text{on} \quad x_2 = -\left(\frac{1}{2} - n^{(3)}\right)h \tag{6b}$$

where equations (6) imply that the increment of slip, $\Delta[u_i]$, is a function of the history of the interface stress T_i and the slip $[u_i]$;

(*e*) Upper and lower surface stress conditions:

$$\sigma_{2i}^{(1)} = T_i^+ \quad \text{on } x_2 = \frac{1}{2}h, \tag{7a}$$

$$\sigma_{2i}^{(3)} = T_i^- \quad \text{on } x_2 = -\frac{1}{2}h; \tag{7b}$$

(*f*) Boundary conditions at $x = 0, l$.

In the preceding formulation it is assumed that field variables are independent of x_3.

Newmark et al. [1] assumed a liner shear stress-slip relation:

$$[u_i] = S\,T_i, \quad [u_2] \equiv 0 \tag{8}$$

A more general expression is the one given in (6) which is similar to the flow rule of incremental plasticity theory. Drucker and Prager [18] have applied a plasticity theory to a thin transition layer and shown the possibility of developing a slip theory with critical slip surface and slip law which are analogue of yield surface and flow rule. The objective of the subsequent analysis is to derive a laminated beam theory with built-in interlayer slip in which any well-structured slip law can be admitted. Thus, in the present derivation, it is understood that such a slip law is provided as a constitutive relation of layer interfaces.

The basis of a new beam theory is facilitated by the principle of virtual work applied to each layer. Adding the resulting equations one obtains:

$$\begin{aligned} &\int_o^l \Big\{ \sum_{\alpha=1}^{3} \iint_{\Omega^{(\alpha)}} f_i^{(\alpha)}\,\delta u_i^{(\alpha)}\,dx_2dx_3 \\ &\qquad + b\,(T_i^+\,\delta u_i^{(1)+} - T_i^-\,\delta u_i^{(3)-})\Big\}dx_1 \\ &\qquad + \Big[\sum_{\alpha=1}^{3} \iint_{\Omega^{(\alpha)}} T_i^{(\alpha)}\,\delta u_i^{(\alpha)}\,dx_2dx_3\Big]_{x_1=0}^{x_1=l} \\ &= \int_o^l \Big\{ \sum_{\alpha=1}^{3} \iint_{\Omega^{(\alpha)}} \sigma_{ij}^{(\alpha)}\,\delta e_{ij}^{(\alpha)}\,dx_2dx_3 \\ &\qquad + b\,(T_i^{(u)}\,\delta[u_i]^{(u)} + T_i^{(l)}\,\delta[u_i]^{(l)})\Big\}dx_1 \end{aligned} \tag{9}$$

where

$$e_{ij}^{(\alpha)} = \frac{1}{2}\,(u_{i,j}^{(\alpha)} + u_{i,j}^{(\alpha)}), \tag{10a}$$

$$u_i^{(1)+} = u_i^{(1)}\,|\,x_2 = \frac{h}{2}, \; u_i^{(3)-} = u_i^{(3)}\,|\,x_2 = -\frac{h}{2} \tag{10b}$$

Downloaded 02 May 2010 to 171.66.16.25. Redistribution subject to ASME license or copyright; see http://www.asme.org/terms/Terms_Use.cfm

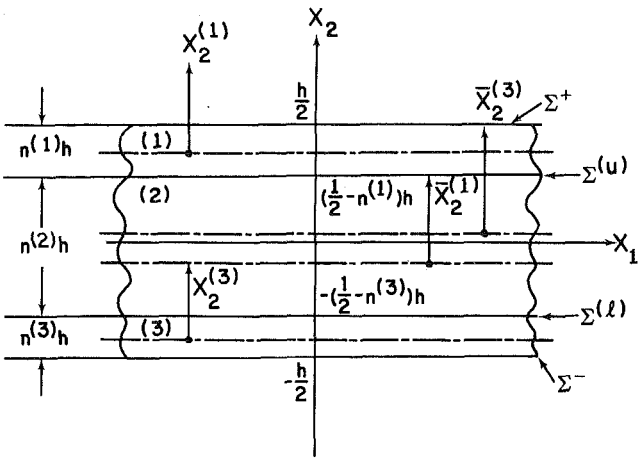


Fig. 2 Local coordinate system

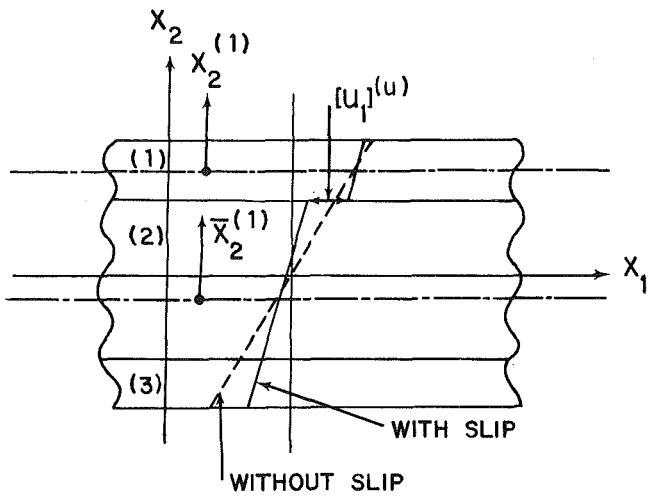


Fig. 3 The profile of u_1 with and without slip at the upper interface

and

$$\Omega^{(1)}=\left\{x_2,x_3 \mid \left(\frac{1}{2}-n^{(1)}\right)h<x_2<\frac{h}{2},-\frac{b}{2}<x_3<\frac{b}{2}\right\}$$

$$\Omega^{(2)}=\left\{x_2,x_3 \mid -\left(\frac{1}{2}-n^{(3)}\right)h<x_2<\left(\frac{1}{2}-n^{(1)}\right)h,\ -\frac{b}{2}<x_3<\frac{b}{2}\right\}$$

$$\Omega^{(3)}=\left\{x_2,x_3 \mid -\frac{1}{2}h<x_2<-\left(\frac{1}{2}-n^{(3)}\right)h,\ -\frac{b}{2}<x_3<\frac{b}{2}\right\} \tag{11}$$

The additional dissipation terms, $T_i^{(\beta)}\delta[u_i]^{(\beta)};\ \beta = u,l$ in (9), due to slip can be computed only if an appropriate slip law is specified on the interfaces. However, these terms do not require integration with respect to x_2. This implies that $[u_i]^{(\beta)}$ can be displacement type variables in the present beam theory with slip. Thus, a specific slip law is handled in the solution process of the beam equations, not in the process of deriving the beam theory.

3 A Beam Theory With Interlayer Slip

A beam theory with built-in interlayer slip can be obtained by substituting an appropriate trial displacement field that satisfies the displacement boundary conditions into the principle of virtual work (9). For the lowest order beam theory with the effect of transverse shear, one may choose the following trial displacement field:

$$u_i^{(1)}=U_i(x_1)+\psi_i(x_1)x_2-\frac{2}{h}[u_i]^{(u)}(x_1)x_2^{(1)} - \frac{2}{h}[u_i]^{(l)}(x_1)\bar{x}_2^{(3)}+\delta_{i2}\zeta_2(x_1)g(x_2) \tag{12a}$$

$$u_i^{(2)}=U_i(x_1)+\psi_i(x_1)x_2-\frac{2}{h}[u_i]^{(u)}(x_1)\bar{x}_2^{(1)} - \frac{2}{h}[u_i]^{(l)}(x_1)\bar{x}_2^{(3)}+\delta_{i2}\zeta_2(x_1)g(x_2) \tag{12b}$$

$$u_i^{(3)}=U_i(x_1)+\psi_i(x_1)x_2-\frac{2}{h}[u_i]^{(u)}(x_1)\bar{x}_2^{(1)} - \frac{2}{h}[u_i]^{(l)}(x_1)\bar{x}_2^{(3)}+\delta_{i2}\zeta_2(x_1)g(x_2) \tag{12c}$$

where

$$x_2^{(1)}=x_2-\frac{1}{2}(1-n^{(1)})h,\ x_2^{(3)}=x_2+\frac{1}{2}(1-n^{(3)})h, \tag{13a,b}$$

$$\bar{x}_2^{(1)}=x_2+\frac{1}{2}n^{(1)}h,\ \bar{x}_2^{(3)}=x_2-\frac{1}{2}n^{(3)}h, \tag{13c,d}$$

$$g(x_2)=x_2^2-\frac{h^2}{4}, \tag{14}$$

and δ_{i2} is the Kroecker delta. These local coordinates are shown in Fig. 2. In (13), $x_2^{(1)}$ and $x_2^{(3)}$ are the thickness coordinates with origin at the center of layer 1 and 3, respectively. The local coordinates $\bar{x}_2^{(1)}$ and $\bar{x}_2^{(3)}$ are thickness coordinates with origins at the middle plane of the two layer systems $2-3$ and $1-2$, respectively, and are conjugate coordinate systems to $x_2^{(1)}$ and $x_2^{(3)}$ with respect to the total thickness of the beam.

A displacement profile of $u_i^{(\alpha)}$ is depicted in Fig. 3 for the case of $[u_1]^{(u)}\neq 0$ and $[u_1]^{(l)}=0$.

If equations (12) are substituted into (9) with the assumption that $\zeta_{2,1}=0$ one obtains

$$\int_o^l\Big\{\delta U_i f_i^{(\alpha)}+\delta\psi_i f_i^1-\frac{2}{h}\delta[u_i]^{(u)}f_i^{(u)}-\frac{2}{h}\delta[u_i]^{(l)}f_i^{(l)} + b\,T_i^+\left(\delta U_i+\frac{h}{2}\delta\psi_i-n^{(1)}\delta[u_i]^{(u)}-(n^{(1)}+n^{(2)})\delta[u_i]^{(l)}\right) - b\,T_i^-\left(\delta U_i-\frac{h}{2}\delta\psi_i+(n^{(2)}+n^{(3)})\right)\delta[u_i]^{(u)} + n^{(3)}\delta[u_i]^{(l)}\Big)\Big\}dx_1$$

$$+\left[\delta U_i\,{}^1T_i^q+\delta\psi_i\,{}^1T_i^\eta-\frac{2}{h}\delta[u_i]^{(u)}\,{}^1T_i^{(u)} - \frac{2}{h}\delta[u_i]^{(l)}T_i^{(l)}\right]_{x_1=0}^{x_1=l}$$

$$=\int_o^l\Big\{\delta U_{1,1}N_{11}+\delta\psi_{1,1}M_{11}-\frac{2}{h}\delta]u_1],_1^{(u)}N_{11}^{(u)} - \frac{2}{h}\delta[u_1],_1^{(l)}N_{11}^{(l)}$$

Downloaded 02 May 2010 to 171.66.16.25. Redistribution subject to ASME license or copyright; see http://www.asme.org/terms/Terms_Use.cfm

$$+(\delta U_{2,1}+\delta\psi_1)N_{12}-\frac{2}{h}(\delta[u_1]^{(u)}+\delta[u_1]^{(l)})N_{12}+\delta\psi_{2,1}M_{12}$$

$$-\frac{2}{h}\delta[u_2],_1^{(u)}N_{12}^{(u)}-\frac{2}{h}\delta[u_2],_1^{(l)}N_{12}^{(l)}$$

$$+2\delta\zeta_2 M_{22}+\delta\psi_2 N_{22}-\frac{2}{h}(\delta[u_2]^{(u)}$$

$$+\delta[u_2]^{(l)})N_{22}+b(T_i^{(u)}\delta[u_i]^{(u)}+T_i^{(l)}\delta[u_i]^{(l)})\Big\}dx_1 \tag{15}$$

where

$$(f_i^a,\overset{1}{f_i^l})=\sum_{\alpha=1}^{3}\iint_{\Omega^{(\alpha)}}(1,x_2)f_i^{(\alpha)}dx_2dx_3, \tag{16}$$

$$(\overset{1}{T_i^a},\overset{1}{T_i^l})=\sum_{\alpha=1}^{3}\iint_{\Omega^{(\alpha)}}(1,x_2)\overset{1}{T_i^{(\alpha)}}dx_2x_3, \tag{17}$$

$$(N_{ij},M_{ij})=\sum_{\alpha=1}^{3}\iint_{\Omega^{(\alpha)}}(1,x_2)\sigma_{ij}^{(\alpha)}dx_2dx_3. \tag{18}$$

$$(f_i^{(u)},\overset{1}{T_i^{(u)}},N_{ij}^{(u)})=\iint_{\Omega^{(1)}}x_2^{(1)}(f_i^{(1)},\overset{1}{T_i^{(1)}}\sigma_{ij}^{(1)})dx_2dx_3$$

$$+\sum_{\alpha=2}^{3}\iint_{\Omega^{(\alpha)}}\bar{x}_2^{(1)}(f_i^{(\alpha)},\overset{1}{T_i^{(\alpha)}},\sigma_{ij}^{(\alpha)})\,dx_2dx_3 \tag{19}$$

$$(f_i^{(l)},\overset{1}{T_i^{(l)}},N_{ij}^{(l)})=\sum_{\alpha=1}^{2}\iint_{\Omega^{(\alpha)}}\bar{x}_2^{(3)}(f_i^{(\alpha)},\overset{1}{T_i^{(\alpha)}},\sigma_{ij}^{(\alpha)})\,dx_2dx_3$$

$$+\iint_{\Omega^{(3)}}x_2^{(3)}(f_i^{(3)},\overset{1}{T_i^{(3)}},\sigma_{ij}^{(3)})dx_2dx_3 \tag{20}$$

In (15) the virtual work terms with $\delta\zeta_2$ associated with f_i is assumed to be negligible. Integrating by parts the Euler-Lagrange equations of (15) become

$$N_{1i,1}+b(T_i^+-T_i^-)+f_i^a=0 \tag{21}$$

$$M_{1i,1}-N_{2i}+\frac{bh}{2}(T_i^++T_i^-)+f_i^l=0 \tag{22}$$

$$\frac{bh}{2}T_i^{(u)}=-N_{1i,1}^{(u)}+N_{2i}-f_i^{(u)}-\frac{bh}{2}\left\{n^{(1)}T_i^++(n^{(2)}+n^{(3)})T_i^-\right\} \tag{23}$$

$$\frac{bh}{2}T_i^{(l)}=-N_{1i,1}^{(l)}+N_{2i}-f_i^{(l)}-\frac{bh}{2}\left\{(n^{(1)}+n^{(2)})T_i^++n^{(3)}T_i^-\right\} \tag{24}$$

The remaining equation $M_{22}=0$ which corresponds to $\delta\zeta_2$ will be used to eliminate ζ_2 from the constitutive relations in order to obtain the lowest order theory.

The boundary conditions at $x_1=0$ and l are

$$\overset{1}{T_i^a}=N_{1i}\quad\text{or}\quad\delta U_i=0 \tag{25}$$

$$\overset{1}{T_i^l}-M_{1i}\quad\text{or}\quad\delta\Psi_i=0 \tag{26}$$

$$\overset{1}{T_i^{(u)}}=N_{1i}^{(u)}\quad\text{or}\quad\delta[u_i]^{(u)}=0 \tag{27}$$

$$\overset{1}{T_i^{(l)}}=N_{1i}^{(l)}\quad\text{or}\quad\delta[u_i]^{(l)}=0 \tag{28}$$

It is interesting to note that equations (23) and (24) give interface stresses whether slip exists or not. Thus, equations (21) and (22) with the interface stresses computed by (23) an (24) can be used with any well-structured interface slip law. Furthermore, these results are obtained without making any specific reference to the constitutive behavior of each layer.

As a result, the beam equations obtained in the foregoing can also be used to simulate nonlinear material behavior of the sandwich beam. If the stress-strain relations are expressed by (3) the beam constitutive relations are obtained by substituting (3) with (12) into (18), (19c), and (20c) and eliminating ζ_2 by $M_{22}=0$. The results are

$$S=[E]e \tag{29a}$$

where

$$S=[N_{11},N_{22},N_{12},M_{11},M_{12},N_{11}^{(u)},N_{11}^{(l)},N_{12}^{(u)},N_{12}^{(l)}]^T \tag{29b}$$

$$e=[U_{1,1}\Psi_2-\frac{2}{h}[u_2]^{(u)}-\frac{2}{h}[u_2]^{(l)},U_{2,1}$$

$$+\Psi_1-\frac{2}{h}[u_1]^{(u)}-\frac{2}{h}[u_1]^{(l)},$$

$$\Psi_{1,1},\Psi_{2,1},-\frac{2}{h}[u_1],_1^{(u)},-\frac{2}{h}[u_1],_1^{(l)},$$

$$-\frac{2}{h}[u_2],_1^{(u)},-\frac{2}{h}[u_2],_1^{(l)}]^T \tag{29c}$$

and $[E]$ is a symmetric 9×9 matrix whose nonzero elements are

$$(E_{11},E_{12},E_{22},E_{33})=bh(C_{11}^a,-6C_{12}^{b2}/C_{22}^c,C_{12}^a$$

$$-6C_{12}^bC_{22}^b/C_{22}^e-C_{22}^a-C_{22}^{b2}/C_{22}^c,C_{33}^a)$$

$$(E_{16},E_{26},E_{38})=\frac{b}{2}n^{(2)}n^{(3)}h^2\Big((C_{11}^{(2)}-C_{11}^{(3)}),$$

$$-C_{12}^bC_{12}^d/C_{22}^c,(C_{12}^{(2)}-C_{12}^{(3)},-C_{22}^bC_{12}^d/C_{22}^c,(C_{33}^{(2)}-C_{33}^{(3)})\Big)$$

$$(E_{17},E_{27},E_{39})=\frac{b}{2}n^{(1)}n^{(2)}h^2\Big((C_{11}^{(1)}-C_{11}^{(2)}),$$

$$-C_2^bC_{12}^e/C_{22}^c,(C_{12}^{(1)}-C_{12}^{(2)}),-C_{22}^bC_{12}^e/C_{22}^e,(C_{33}^{(1)}-C_{33}^{(2)})\Big)$$

$$(E_{14},E_{24},E_{35})=\frac{b}{2}h^2(C_{11}^b,$$

$$-C_{12}^b,C_{12}^bC_{12}^c/C_{22}^c,C_{12}^b-C_{22}^bC_{12}^c/C_{33}^c)$$

$$(E_{44},E_{46},E_{47},E_{58},E_{59},E_{66},E_{67},E_{77},E_{88},E_{89},E_{99})$$

$$=\frac{bh^3}{24}(C_{11}^c,-C_{12}^{c2}/C_{22}^c,C_{11}^d,-C_{12}^cC_{12}^d/C_{22}^c,C_{11}^e,$$

$$-C_{12}^cC_{12}^e/C_{22}^c,C_{33}^c,C_{33}^d,C_{33}^e,C_{11}^f,-C_{12}^{d2}C_{22}^c,$$

$$C_{11}^g,-C_{12}^dC_{12}^e/C_{22}^c,C_{11}^h,-C_{12}^eC_{12}^e/C_{22}^c,C_{33}^f,C_{33}^g,C_{33}^h) \tag{30}$$

and

$$C_{ij}^a=n^{(1)}C_{ij}^{(1)}+n^{(2)}C_{ij}^{(2)}+n^{(3)}C_{ij}^{(3)}$$

$$C_{ij}^b=n^{(1)}(1-n^{(1)})C_{ij}^{(1)}+n^{(2)}(n^{(3)}-n^{(1)})C_{ij}^{(2)}-n^{(3)}(1-n^{(3)})C_{ij}^{(3)}$$

$$C_{ij}^c=\left\{1-(1-2n^{(1)})^3\right\}C_{ij}^{(1)}+\left\{(1-2n^{(1)})^3+(1-2n^{(3)})^3\right\}C_{ij}^{(2)})$$

$$+\left\{1-(1-2n^{(3)})^3\right\}C_{ij}^{(3)}$$

$$C_{ij}^d=2n^{(1)^3}C_{ij}^{(1)}+\Big[\Big\{(1-2n^{(1)})^3+(1-2n^{(3)})^3\Big\}$$

$$+6n^{(1)}n^{(2)}(n^{(3)}-n^{(1)})\Big]C_{ij}^{(2)}$$

$$+\Big[\Big\{1-(1-2n^{(3)})^3\Big\}-6n^{(1)}n^{(3)}(1-n^{(3)})\Big]C_{ij}^{(3)}$$

Downloaded 02 May 2010 to 171.66.16.25. Redistribution subject to ASME license or copyright; see http://www.asme.org/terms/Terms_Use.cfm

$$C_{ij}^{e}=\left[\left\{1-(1-2n^{(1)})^3\right\}-6n^{(1)}n^{(3)}(1-n^{(1)})\right]C_{ij}^{(1)}$$

$$+\left[\left((1-2n^{(1)})^3+(1-2n^{(3)})^3\right)\right.$$

$$\left.-6n^{(2)}n^{(3)}(n^{(3)}-n^{(1)})\right]C_{ij}^{(2)}+2n^{(3)^3}C_{ij}^{(3)}$$

$$C_{ij}^{f}=2n^{(1)^3}C_{ij}^{(1)}+\left\{(n^{(2)}+n^{(3)})^3-(n^3-n^{(2)})^3\right\}C_{ij}^{(2)}$$

$$+\left\{(n^{(3)}-n^{(2)})^3+(n^{(2)}+n^{(3)})^3\right\}C_{ij}^{(3)}$$

$$C_{ij}^{g}=2n^{(1)^3}C_{ij}^{(1)}+\left[\left\{(1-2n^{(1)})^3+(1-2n^{(3)})^3\right\}\right.$$

$$\left.-6n^{(2)}(n^{(1)}-n^{(3)})^2-6n^{(1)}n^{(2)}n^{(3)}\right]C_{ij}^{(2)}$$

$$+2n^{(3)^3}C_{ij}^{(3)}$$

$$C_{ij}^{h}=\left\{(n^{(1)}+n^{(2)})^3-(n^{(2)}-n^{(1)})^3\right\}C_{ij}^{(1)}$$

$$+\left\{(n^{(2)}-n^{(1)})^3+(n^{(1)}+n^{(2)})^3\right\}C_{ij}^{(2)}+2n^{(3)^3}C_{ij}^{(3)} \tag{31}$$

In (29) the slip plays the same role as the plastic strain in plasticity theory. Thus, the numerical implementation of the beam theory with interlayer slip does not require major modification of available nonlinear finite element codes. In addition, it is possible to introduce shear correction factors in (30) to improve the accuracy of the Timoshenko beam theory [19–21]. Furthermore, it is interesting to note that two-layer beam equations with interlayer slip can also be obtained from the preceding results by setting $n^{(3)} = 0$ and $[u_i]^{(l)} = 0$.

In the application of the theory, it is critical to judge the validity of the assumptions adopted. It is expected that the model will be useful to simulate large-scale slip of laminated beams. However, because beam theories, like plate and shell theories, have the nature of an outer solution in the matched asymptotic expansions [22, 23], it might become necessary to include additional edge or inner layer analyses in the domain where the thickness scale has to be magnified, such as domains near free edges [24–27], and delamination fronts [28, 29]. This approach has been adopted, for example, in laminated composite plates [26, 27]. Typically, the edge layer solution requires the solution of three-dimensional boundary value problems. To avoid the complex matching process, higher order plate theories have been proposed to accommodate the important three-dimensional aspects [30–33]. Due to the limited scope of the present paper to include the interlayer slip the foregoing subjects of improving certain three-dimensional aspects are not considered.

4 A Simply Supported Beam

To clarify the relation between the present theory and the Bernoulli-Euler beam theory with interlayer slip, a simply supported sandwich beam made of like material layers of equal thickness is considered. In the sequel, it is shown that the present theory yields the Bernoulli-Euler beam theory with interlayer slip, derived for a sandwich wooden beam by Goodman and Popov [4], if one introduces the kinematic constraint of zero shear strain. Then, the proposed beam equations are solved for some characteristic interface slip relations and the applied load—central beam deflection relations are depicted to clarify the effect of interface bond strength on the stiffness degradation of the beam.

It is obvius that the opening mode delamination $[u_2]$ is also important in the structural design of layered beams. However, due to the lack of experimental data with which to compare the model simulation, the opening-mode delamination will not be demonstrated. It is included in the preceding theory in order to incorporate a slip law with dilatancy [18].

4.1 Description of Problem. The foregoing beam theory can be applied to a sandwich beam made of like material layers of equal thickness for which

$$n^{(1)}=n^{(2)}=n^{(3)}=\frac{1}{3},\quad C_{ij}^{(1)}=C_{ij}^{(2)}=C_{ij}^{(3)}=C_{ij} \tag{32}$$

If the opening-type delamination and the effect of body force are neglected, equations (21)–(31) reduce to

$$N_{12,1}+b(T_2^{+}-T_2^{-})=0 \tag{33}$$

$$M_{11,1}-N_{21}+\frac{bh}{2}(T_1^{+}+T_1^{-})=0 \tag{34}$$

$$\frac{bh}{2}T_1^{(u)}=-N_{11,1}^{(u)}+N_{21}-\frac{bh}{2}\left(\frac{1}{3}T_1^{+}+\frac{2}{3}T_1^{-}\right) \tag{35a}$$

$$\frac{bh}{2}T_1^{(l)}=-N_{11,1}^{(l)}+N_{21}-\frac{bh}{2}\left(\frac{2}{3}T_1^{+}+\frac{1}{3}T_1^{-}\right) \tag{35b}$$

$$N_{12}=N_{21}=\text{b h }C_{33}\left(U_{2,1}+\Psi_1-\frac{2}{h}[u_1]^{(u)}-\frac{2}{h}[u_1]^{(l)}\right) \tag{36}$$

$$M_{11}=I\left\{\Psi_{1,1}-\frac{1}{3}\left(\frac{2}{h}[u_1],_1^{(u)}+\frac{2}{h}[u_1],_1^{(l)}\right)\right\} \tag{37}$$

$$N_{11}^{(u)}=\frac{I}{3}\left(\Psi_{1,1}-\frac{2}{h}[u_1],_1^{(u)}\right) \tag{38a}$$

$$N_{11}^{(l)}=\frac{I}{3}\left(\Psi_{1,1}-\frac{2}{h}[u_1],_1^{(l)}\right) \tag{38b}$$

where

$$I=b\,h^3C_{11}-C_{12}^2/C_{22}/12 \tag{39}$$

For a beam of length l, simply supported at both ends, $x_1 = \pm l/2$, subjected to a concentrated load P at $x = 0$, as shown in Fig. 4, the loading terms become

$$T_i^{+}=T_i^{-}=0\quad \text{at } x\neq 0. \tag{40}$$

The appropriate boundary conditions are obtained from (25)–(28) as

$$U_2=M_{11}=N_{11}^{(u)}=N_{11}^{(l)}=0\quad \text{at } x=\pm\frac{l}{2} \tag{41a}$$

if the slip at the ends is not constrained and

$$U_2=M_{11}=[u_1]^{(u)}=[u_1]^{(l)}=0\quad \text{at } x=\pm\frac{l}{2} \tag{41b}$$

if the slip at the ends is constrained. Due to the symmetry of the problem it is possible to consider only $0 \le x \le l/2$ by introducing the symmetry conditions

$$\Psi_1=[u_1]^{(u)}=[u_1]^{(l)}=N_{12}=0\quad \text{at } x=0 \tag{42}$$

For this special problem, it is easily proven that

$$[u_1]^{(u)}=[u_1]^{(l)}=[u_1] \tag{43a}$$

and

$$T_1^{(u)}=T_1^{(l)}=T_1 \tag{43b}$$

The problem defined by (40)–(43) was solved by Goodman and Popov [4] using the Bernoulli-Euler beam theory and their results were compared with experimental data. In the sequel, Goodman and Popov's beam equations are reduced from (33)–(40) by setting the transverse shear strain to zero.

Downloaded 02 May 2010 to 171.66.16.25. Redistribution subject to ASME license or copyright; see http://www.asme.org/terms/Terms_Use.cfm

4.2 Reduction to the Bernoulli-Euler Beam Theory With Interlayer Slip. The Bernoulli-Euler beam theory with interlayer slip was first developed by Newmark et al. [1] for T-beams and extended to a sandwich beam of equal thickness by Goodman et al. [4]. The Bernoulli-Euler beam theory, which does not include the effect of transverse shear, can be reduced from (33)–(40) by introducing the assumption in (37)

$$\Psi_1 = -U_{2,1} + 2 \cdot \frac{2}{h}[u_1] \tag{44}$$

Substituting (44) and (43a) into (37) one obtains a moment-curvature relation for the Bernoulli-Euler beam theory

$$M_{11} = -I\left(U_{2,11} - \frac{4}{3} \cdot \frac{2}{h}[u_1],_1\right) \tag{45}$$

If one adopts a linear shear stress-slip relation of the form (8) on the interfaces

$$\frac{bh}{2} T_1 = k \cdot \frac{2}{h}[u_1] \tag{46}$$

and eliminates $[u_1]$ from (45) and (46), one obtains

$$U_{2,11} = -\frac{M_{11}}{I} + \frac{4}{3k} \cdot \frac{bh}{2} T_{1,1} \tag{47}$$

which is equivalent to (21) of reference [4] in which the different sign convention for U_2, $[u_1]$, M_{11}, different definitions of h and I, and the following relations are used

$$b\, T_1 = -F,_1 = -\frac{K\, n}{S} \Delta s = k\left(\frac{2}{h}\right)^2 [u_1] \tag{48}$$

where F_1, $K\, n/S$, and Δs are axial force, slip stiffness, and slip, respectively, defined in [4]. Substituting (34), (40), (37), and (44) into (35) one finds

$$\frac{bh}{2} T_1 = \frac{I}{3}\left(U_{2,111} - \frac{2}{h}[u_1],_{11}\right) + M_{11,1} \tag{49}$$

If $U_{2,11}$ and $[u_1]$ are eliminated using (45) and (46), respectively, one obtains

$$b\left(T_{1,11} - \frac{9k}{I} T_1\right) = -\frac{4}{3h} \cdot \frac{9k}{I} M_{11,1} \tag{50}$$

Equation (50) is equal to the derivative of equation (16) of [4] with respect to x_1. A further elimination of T_1 in (47) and (50) yields

$$\frac{I}{9} U_{2,111} - \frac{k}{I}(I\, U_{2,11} + M_{11}) = -M_{11,11} \tag{51}$$

which is equivalent to equation (24) of [4]. As a result, it has been proven that the Bernoulli-Euler beam theory with interlayer slip can be obtained from the proposed beam theory by introducing the kinematic constraint (44). The advantage of the proposed beam theory compared with the classical beam theory with interlayer slip by Newmark et al. [1] is the capability of (*i*) simulating more complex interface slip relations than (46), (*ii*) including the effect of transverse shear, (*iii*) treating more general loading conditions than (40), and (*iv*) having the explicit boundary conditions, (25)–(28), especially for $N_i^{(u)}$ and $N_i^{(l)}$ which are conjugate to $[u_i]^{(u)}$ and $[u_i]^{(l)}$, respectively, with respect to work. In (51), $k \to \infty$ corresponds to a solid beam case with flexural rigidity I, while $k \to 0$ corresponds to the interface without bond or connectors for which the flexural rigidity becomes $3 \times (I/27)$ in which $I/27$ is the flexural rigidity of each constituent layer.

4.3 Solution of the Simply Supported Beam Problem. To demonstrate the efficacy of the proposed model the boundary value problem defined by (33)–(41a)) is solved using an incrementally linear shear stress-slip relation:

$$\frac{bh}{2} \Delta T_1 = k_T \frac{2}{h} \Delta[u_1] \tag{52}$$

where k_T is the tangent stiffness of a shear stress-slip curve. In the sequel, only the domain $0 \le x_1 \le l/2$ is considered. By elementary calculations one obtains

$$\Delta N_{12} = \frac{\Delta P}{2}, \quad \Delta M_{11} = \frac{\Delta P}{2}\left(x_1 - \frac{l}{2}\right) \tag{53a,b}$$

where ΔP is the increment of P. Equations (35), (38), (52), (53), and (43) imply that

$$\frac{bh}{2} \Delta T_1 = -\frac{I}{3}\left(\Delta \Psi_{1,11} - \frac{2}{h} \Delta[u_1],_{11}\right) + \frac{\Delta P}{2} = k_T \frac{2}{h} \Delta[u_1] \tag{54}$$

From (37), (43), and (53b)

$$\Delta M_{11} = I\left(\Delta \Psi_{1,1} - \frac{2}{3} \cdot \frac{2}{h} \Delta[u_1],_1\right) = \frac{\Delta P}{2}\left(x_1 - \frac{l}{2}\right) \tag{55}$$

If equation (55) is used to eliminate $\Delta \Psi_{1,1}$ in (54), one obtains the differential equation for slip

$$\frac{2}{h} \Delta[u_1],_{11} - \frac{9\, k_T}{I} \frac{2}{h} \Delta[u_1] = -\frac{3\, \Delta P}{I} \tag{56}$$

The integration of (56) with (42) and (43a) yields

$$\frac{2}{h} \Delta[u_1] = \Delta A \sinh\sqrt{\frac{9\, k_T}{I}} x_1 + \frac{\Delta P}{3\, k_T}\left(1 - \cosh\sqrt{\frac{9\, k_T}{I}} x_1\right), \tag{57}$$

where ΔA is an integration constant. Using (57) and (55) one obtains

$$\Delta \Psi_{1,1} = \frac{\Delta P}{2I}\left(x_1 - \frac{l}{2}\right) + \frac{2}{3}\sqrt{\frac{9\, k_T}{I}}\left(\Delta A \cosh\sqrt{\frac{9\, k_T}{I}} x_1 - \frac{\Delta P}{3\, k_T} \sinh\sqrt{\frac{9\, k_T}{I}} x_1\right) \tag{58}$$

If one poses the boundary condition $N_{11}^{(u)} = N_{11}^{(l)} = 0$ at $x_1 = l/2$, one obtains

$$\Delta A = \frac{\Delta P}{3\, k_T} \tanh\sqrt{\frac{9\, l^2 k_T}{4I}} \tag{59}$$

Now equation (57) can be rewritten as

$$\frac{2}{h} \Delta[u_1] = \frac{\Delta P}{3\, k_T}\left(\tanh\sqrt{\frac{9\, l^2 k_T}{4I}} \sinh\sqrt{\frac{9\, k_T}{I}} x_1 - \cosh\sqrt{\frac{9\, k_T}{I}} x_1 + 1\right) \tag{60}$$

If equation (58) with (59) is integrated with the symmetry condition (42), one obtains

$$\Delta \Psi_1 = \frac{\Delta P}{4I}(x_1^2 - l\, x_1) + \frac{2\, \Delta P}{9\, k_T}\left(\tan\sqrt{\frac{9\, l^2 k_T}{4I}} \sinh\sqrt{\frac{9\, k_T}{I}} x_1 - \cosh\sqrt{\frac{9\, k_T}{I}} x_1 + 1\right) \tag{61}$$

The transverse displacement U_2 is obtained by integrating the incremental form of (36) with (53a), (43a), (60), (61), and (41a). The result is

$$\Delta U_2 = \frac{\Delta P}{2bh\, C_{22}}\left(x_1 - \frac{l}{2}\right) - \frac{\Delta P}{4I}\left(\frac{x_1^3}{3} - \frac{l\, x_1^2}{2} + \frac{l^3}{12}\right) + \frac{4\, \Delta P}{9\, k_T}\sqrt{\frac{I}{9\, k_T}}\left(\tanh\sqrt{\frac{9\, l^2\, k_T}{4I}} \cosh\sqrt{\frac{9\, k_T}{I}} x_1\right.$$

Downloaded 02 May 2010 to 171.66.16.25. Redistribution subject to ASME license or copyright; see http://www.asme.org/terms/Terms_Use.cfm

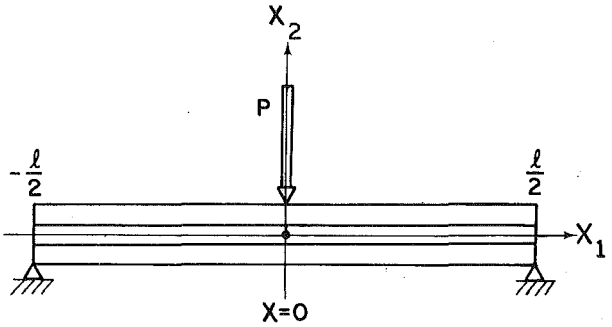


Fig. 4 A simply supported sandwich beam

$$-\sinh\sqrt{\frac{9\,k_T}{I}}x_1\Big) + \frac{4\,\Delta\,P}{9\,k_T}\left(x_1 - \frac{l}{2}\right) \tag{62}$$

$$-\Delta\,U_2(0) = \Delta\,P\Big(\frac{l}{4bh\,C_{33}} + \frac{l^3}{48\,I} + \frac{2l}{9\,k_T}$$

$$-\frac{4}{9\,k_T}\sqrt{\frac{I}{9\,k_T}}\tanh\sqrt{\frac{9\,l^2\,k_T}{4I}}\Big) \tag{63}$$

In equations (62) and (63) the terms due to the effect of transverse shear are the ones with C_{33}. Since the assumption (44) is equivalent to $C_{33} \to \infty$, these correction terms become important if the slenderness l/h decreases. The interface shear force is computed from (54) and (60)

$$\frac{bh}{2}\Delta\,T_1 = \frac{\Delta P}{3}\Big(\tanh\sqrt{\frac{9\,l^2\,k_T}{4I}}\sinh\sqrt{\frac{9\,k_T}{I}}x_1$$

$$-\cosh\sqrt{\frac{9\,k_T}{I}}x_1 + 1\Big) \tag{64}$$

From (64), it is observed that, in general, the numerical technique is necessary to solve the problem since $\Delta\,T_1$ varies with respect to x_1. However, the above results explain the important aspects of the sandwich beam deflection with interlayer slip. For the rigid bond, $k_T \to \infty$, equations (63) and (64) yield

$$\frac{bh}{2}\,T_1 = \frac{P}{3} \tag{65a}$$

$$-U_2(0) = P\Big(\frac{l}{4bh\,C_{33}} + \frac{l^3}{48I}\Big), \tag{65b}$$

and for the lubricated interface, $k_T \to 0$

$$\frac{bh}{2}\,T_1 = 0 \tag{66a}$$

$$-U_2(0) = P\Big(\frac{l}{4bh\,C_{33}} + \frac{9\,l^3}{48I}\Big) \tag{66b}$$

Furthermore, equation (63) can be used if the interface slip relations are those represented in Fig. 5(*a*) by the curves *A*, *B*, *C*, *F*. The curves *B*, *C* correspond to the cases where the slip commences when the interface shear exceeds the critical value T_1^*. The corresponding load-deflection curves obtained by (63) are shown in Fig. 5(*b*). The curves *D* and *E* correspond to $k_T \to 0$ and $k_T \to \infty$, respectively. For the curve *G* in Fig. 5(*a*) a numerical method such as a nonlinear finite element method [34] should be used to obtain the load-deflection curve *G* in Fig. 5(*b*) (See Appendix). However, equation (63) can be used to obtain the bounding load-deflection curves for the curve *G* in Fig. 5(*b*). From these results, it is concluded that the proposed model has the capability of simulating the deformation of laminated beams with wide range of interface bond qualities from interface with perfect bond to interface without

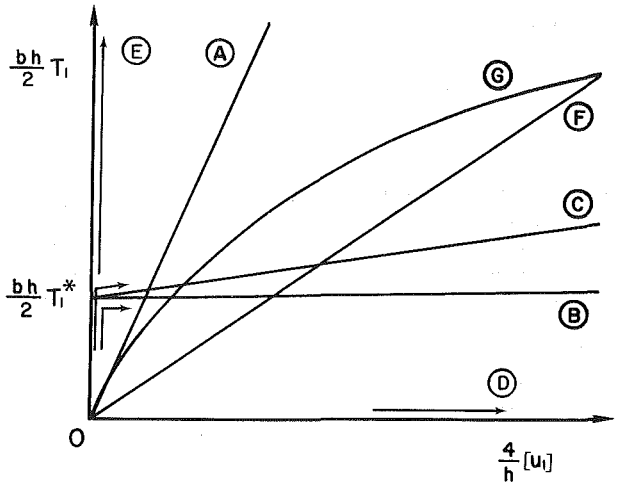


Fig. 5(*a*) Simple shear stress-slip relations

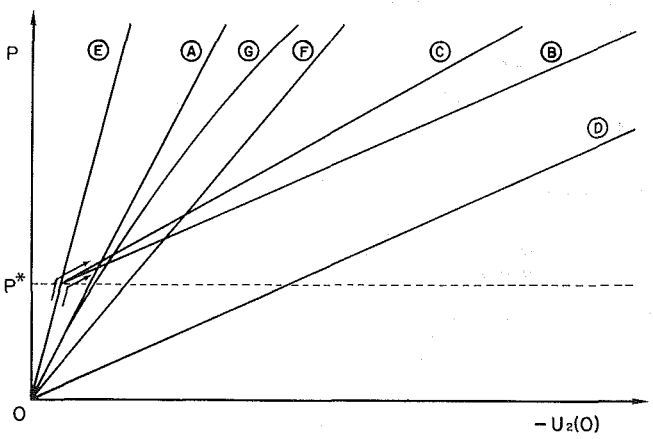


Fig. 5(*b*) Corresponding load-deflection curves ($P^* = 3/4\,hT_1{}^*$)

Fig. 5

connectors. By rewriting (63) in a different form, one of the reviewers has pointed out that for minor deterioration of interface bond quality, for the curves *A*, *G* and *F*, the stiffness softening due to the interface bond deterioration is the same order as the one due to the effect of transverse shear. Further deterioration of the interface causes total delamination and large slip, and eventually yields significant stiffness degradation of the beam structure as shown by the curves *B* and *D* which have reached a stage where interface bond may be modeled by the lubricated interface (66*b*). Finally, it is worthwhile to mention the comparison of the Bernoulli-Euler beam theory (47), (50), and (51), with experimental data obtained by Goodman and Popov [4]. They conducted experiments on a three-layered nailed wooden beam that was simply supported and loaded with a concentrated load at the center, as shown in Fig. 4. The interface shear-slip relation was measured separately for the nail connectors. Their comparison of the beam theory with the data demonstrated excellent agreement. Since the slenderness of the beam $l/h = 90/3$, the effect of transverse shear was small.

It can be stated that the present theory, which is a higher order beam theory will provide us with more accurate theoretical means to study the effect of interlayer slip in layered beams than does the Bernoulli-Euler beam theory. Furthermore, the excellent agreement between theory and experiment obtained by Goodman and Popov using the Bernoulli-Euler beam theory, guarantees experimental corroboration of the present Timoshenko beam theory with built-in interlayer slip.

Downloaded 02 May 2010 to 171.66.16.25. Redistribution subject to ASME license or copyright; see http://www.asme.org/terms/Terms_Use.cfm

5 Conclusions

A Timoshenko beam theory with interlayer slip has been presented. The theory is unique in the sense that any interface slip law can be adopted in the beam equations. The theory is superior to the Bernoulli-Euler beam theory with interlayer slip developed by Newmark et al. [1] since it includes the effect of transverse shear. Based on the principle of virtual work, well-posed boundary value problems of the proposed beam theory were defined. It was also shown that from the proposed theory, the Bernoulli-Euler beam theory with interlayer slip [1, 4] was recovered by introducing the kinematic constraint of zero transverse shear strain. Finally, to clarify the effect of bond strength on the deflection of sandwich beams, a simply supported beam subjected to a concentrated load at the center was solved with typical interface shear stress-slip relations. The results indicate that the model has the capability of simulating a wide range of bond damages from partial delamination to total delamination. Thus the model provides a tool for the study of certain kinds of failure modes of laminated beams with delamination.

Acknowledgment

The author thanks Professors E. Reissner and G. A. Hegemier for their advice and encouragement.

References

1 Newmark, N. M., Seiss, C. P., and Veist, I. M., "Tests and Analysis of Composite Beams With Incomplete Interactions," *Proceedings Society for Experimental Stress Analysis*, Vol. IX, No. 1, 1951, pp. 75–92.

2 Granholm, H., "On Sammansatta Balker Och Pelare Med Sarkid Hansyn Till Spikade Trakonstruktioner (On Composite Beams and Columns With Particular Regard to Nailed Timber Structures)," *Transactions, Chalmers Tekniska Hogskolao*, Gottenburg, Sweden, No. 88, 1949.

3 Pleshkov, P. F., "Teoriia Rascheta Dereviannykh Sostavnnykh Sterzhnei (Theoretical Studies of Composite Wood Structures)," Moscow, 1952, 192 pp.

4 Goodman, J. R., and Popkov, E. P., "Layered Beam Systems With Interlayer Slip," *Journal of the Structural Division*, ASCE, Vol. 24, No. ST11, Nov. 1968, pp. 2535–2547.

5 Goodman, J. R., "Layered Wood Systems With Interlayer Slip," *Wood Science*, Vol. 1, No. 3, 1969, pp. 148–158.

6 Henghold, W. M., and Goodman, J. R., "Static and Dynamic Behavior of Layered Beam Including Slip," *Composite Materials in Engineering Design*, Norton, R., Ed., American Society of Mechanical Engineers Technical Division and Activities, Metal Park, Ohio, 1973, pp. 81–92.

7 Vanderbilt, M. D., Goodman, J. R., and Criswell, M. E., "Service and Overload Behavior of Wood Joist Floor Systems," *Journal of the Structural Division*, ASCE, Vol. 100, No. ST 1, Jan., 1974, pp. 11–29.

8 Norris, C. B., Ericksen, S., and Kommers, W. J., "Flexural Rigidity of a Rectangular Strip of Sandwich Construction—Comparison Between Mathematical Analysis and Results of Tests," Forest Products Laboratory Report 1505A, May, 1952.

9 Kuenzi, E. W., and Wilkinson, T. L., "Composite Beams—Effect of Adhesive or Fastner Rigidity," Forest Products Laboratory, U.S. Department of Agriculture, Forest Service Research Paper, FPL 152, 1971.

10 Hoyle, R. J., and McGee, D. W., "Design Methods for Elastometric Adhesive Bonded Joint-Deck System," *Wood Fiber*, Vol. 6, No. 2, 1974.

11 Itani, R. Y., and Brito, F. A., "Elastometric Bonded Wood Beams With Transverse Gaps," *Journal of the Structural Division*, ASCE, Vol. 104, No. ST 10, Oct., 1978, pp. 1595–1609.

12 Anderson, M., "Behavior of Wood Beams Bonded With Elastometric Adhesive," Thesis presented to Washington State University, at Pullman, Wash., in 1976, in partial fulfillment of the requirements for the degree of Doctor of Philosophy.

13 Thompson, E. G., Goodman, J. R., and Vanderbilt, M. D., "Finite Element Analysis of Layered Wood Systems," *Journal of Structural Division*, ASCE, Vol. 101, No. ST12, Dec., 1975, pp. 2659–2671.

14 Itani, R. Y., and Hiremath, G. S., "Partial Composite Action in Diaphrams," *Journal of the Engineering Mechanics Div.*, ASCE, Vol. 106, No. EM4, Aug., 1980, pp. 739–751.

15 Rao, K. M., and Ghosh, B. G., "Imperfectly Bonded Unsymmetric Lamianted Beam," *Journal of the Engineering Mechanics Div.*, ASCE, Vol. 106, No. EM4, Aug., 1980, pp. 685–697.

16 Fazio, P., and Hussein, R., "Sandwich Beam-Columns With Interlayer Slips," *Journal of the Engineering Mechanics Div.*, ASCE, Vol. 108, No. EM 2, April, 1982, pp. 354–366.

17 Timoshenko, S. P., "On The Correction for Shear of the Differential Equation for Transverse Vibrations of Prismatic Bars," *Philosophical Magazine*, Series 6, Vol. 41, 1921, pp. 744–746.

18 Drucker, D. C., and Prager, W., "Soil Mechanics and Plastic Analysis or Limit Design," *Quarterly Journal of Applied Mechanics*, Vol. 10, 1952, pp. 157–165.

19 Love, A. E. H., *Mathematical Theory of Elasticity*, 4th ed., Cambridge Univ. Press, 1927.

20 Mindlin, R. D., "Influence of Rotatory Inertia and Shear on Flexural Motions of Isotropic, Elastic Plates," ASME JOURNAL OF APPLIED MECHANICS, Vol. 18, 1951, p. 31–38.

21 Cowper, G. R., "The Shear Coefficient in Timoshenko's Beam Theory," ASME JOURNAL OF APPLIED MECHANICS, Vol. 33, 1966, pp. 335–340.

22 Van Dyke, M., *Perturbation Methods in Fluid Mechanics*, The Parabolic Press, Stanford, Calif., 1964.

23 Cole, J. D., *Perturbation Methods in Applied Mathematics*, Blaisdell, Waltham, Mass., 1968.

24 Bogy, D. B., "Edge-Bonded Dissimilar Orthogonal Elastic Wedges Under Normal and Shear Loading," ASME JOURNAL OF APPLIED MECHANICS, Vol. 35, 1968, pp. 460–466.

25 Pagano, N. J., "Free Edge Stress Fields in Composite Lamiantes," *International Journal of Solids and Structures*, Vol. 14, 1978, pp. 401–406.

26 Tang, S., "Interlaminar Stresses of Uniformly Loaded Rectangular Composite Plates," *Journal of Composite Materials*, Vol. 10, 1976, pp. 69–78.

27 Bar-Yoseph, P., and Pian, T. H., "Calculation of Interlaminar Stress Concentration in Composite Laminates," *Journal of Composite Materials*, Vol. 15, 1981, pp. 225–239.

28 Ting, T. C., and Chou, S. C., "Edge Singularities in Anisotropic Composites," *International Journal of Solids and Structures*, Vol. 17, 1981, pp. 1057–1068.

29 Schmueser, D., Comninou, M., and Dundurs, J., "Frictional Slip Between Layer and and Substrate," *Journal of the Engineering Mechanics Division*, ASCE, Vol. 107, No. EM6, 1981, pp. 1103–1118.

30 Reissner, E., "On Transverse Bending of Plates Including the Effect of Transverse Shear Deformation," *International Journal of Solids and Structures*, Vol. 11, 1975, pp. 569–573.

31 Lo, K. H., Christensen, R. M., and Wu, E. M., "A High-Order Theory of Plate Deformation, Part 2: Lamianted Plates," ASME JOURNAL OF APPLIED MECHANICS, Vol. 44, 1977, pp. 669–676.

32 Pagano, N. J., "Stress Fields in Composite Laminates," *International Journal of Solids and Structures*, Vol. 14, 1978, pp. 385–400.

33 Reissner, E., "A Twelfth-Order Theory of Transverse Bending of Transversely Isotropic Plates," *Zeitschrift für Angewandte Mathematik und Mechanik*, Vol. 63, 1983, pp. 285–289.

34 Owen, D. R. J., and Hinton, E., *Finite Elements in Plasticity, Theory and Practice*, Pineridge Press Limited, Swansea, U.K., 1980.

APPENDIX

A Finite Element Implementation

To illustrate how various interface slip laws can be employed in the theory, a finite element implementation of the problem defined by (33)–(41*a*) is briefly discussed. From (15) the principle of virtual work for total field variables becomes

$$\int_0^{1/2} (\delta\,\boldsymbol{\epsilon}^T\boldsymbol{\sigma}^T + \delta\,\mathbf{u}^T\mathbf{f})\,dx = -\delta\,U_2(0)\,P/2 \qquad (A\text{-}1a)$$

in which

$$\boldsymbol{\epsilon} = \left[U_{2,1} + \Psi_1 - \frac{4}{h}[u_1], \Psi_{1,1}, -\frac{4}{h}[u_1]_1{}^T,\right.$$

$$\boldsymbol{\sigma} = [N_{12}, M_{11}, N_{11}^*]^T, N_{11}^* = N_I^{(u)} = N_{11}^{(l)},$$

$$\mathbf{u} = \left[U_2, \Psi_1, \frac{4}{h}[u_1]\right]^T, \mathbf{f} = [0,0,bh\ T_1/2]^T \qquad (A\text{-}1b,f)$$

where $(\ )^T$ denotes the transpose of $(\ )$. The incremental form of the principle of virtual work becomes

$$\int_0^{l/2} (\delta\,\boldsymbol{\epsilon}^T\Delta\boldsymbol{\sigma} + \delta\,\mathbf{u}^T\Delta\,\mathbf{f})\,dx = -\delta\,U_2(0)\,\Delta\,P/2 \qquad (A\text{-}2)$$

With the division of the domain into N_d-node finite elements, the displacement $\mathbf{u}^{(e)}$ is interpolated by nodal values $\Phi_i^{(e)}$ in each element $\Omega^{(e)}$:

$$\mathbf{u}^{(e)} = \begin{bmatrix} U_2 \\ \Psi_1 \\ \frac{4}{h}[u_1] \end{bmatrix}^{(e)} = \sum_{i=1}^{N_d}$$

Downloaded 02 May 2010 to 171.66.16.25. Redistribution subject to ASME license or copyright; see http://www.asme.org/terms/Terms_Use.cfm

$$\begin{bmatrix} N_i(x) & 0 & 0 \\ 0 & N_i(x) & 0 \\ 0 & 0 & N_i(x) \end{bmatrix}^{(e)} \begin{bmatrix} U_2^{(i)} \\ \Psi_1^{(i)} \\ \frac{4}{h}[u_1]^{(i)} \end{bmatrix}^{(e)}$$

$$= \sum_{i=1}^{N^d} \underline{\underline{N}}_i^{(e)} \Phi_i^{(i)} = \underline{\underline{N}}^{(e)} \Phi^{(e)} \quad \text{in } \Omega^{(e)} \tag{A-3a}$$

in which $N_i(x)$ is an interpolation function that satisfies

$$N_i(x_j) = \delta_{ij} \quad x_j \epsilon\, \Omega^{(e)} \tag{A-3b}$$

where x_j is the x-coordinate of the jth node of the element. The strain $\epsilon^{(e)}$ can be computed from (A-3a) and (A-1b) as follows

$$\epsilon^{(e)} = \begin{bmatrix} U_{2,1} + \Psi_1 - \frac{4}{h}[u_1] \\ \Psi_{1,1} \\ -\frac{4}{h}[u_1]_{,1} \end{bmatrix}^{(e)} = \underline{\underline{B}}^{(e)} \Phi^{(e)} \quad \text{in } \Omega^{(e)} \tag{A-4}$$

By substituting (A-3) and (A-4) into (A-1a) the discretized equilibrium equations can be obtained for arbitrary $\delta\Phi_i$ from

$$\sum_{e=1}^{N_e} \delta\Phi^{(e)^T} \int_{\Omega^{(e)}} (\underline{\underline{B}}^{(e)^T} \sigma^{(e)} + \underline{\underline{N}}^{(e)^T} \mathbf{f}^{(e)}) dx = -\delta\, \Phi_1 \frac{P}{2} \tag{A-5}$$

where $\Phi_1 \equiv U_2(0)$ and N_e is the total number of elements. Equation (A-5) is used to compute residual forces to check convergence at each iteration.

To compute the displacement increment $\Delta\, \Phi$ by the tangent stiffness method incremental constitutive relations are required.

$$\Delta\, \sigma^{(e)} = \underline{\underline{D}}_T^{(e)}\ \Delta\, \epsilon^{(e)}, \Delta \mathbf{f}^{(e)} = \underline{\underline{D}}_s^{(e)} \Delta\, \mathbf{u}^{(e)} \quad \text{in } \Omega^{(e)} \tag{A-6a}$$

where

$$\underline{\underline{D}}_T^{(e)} = \begin{bmatrix} bhC_{33} & 0 & 0 \\ 0 & I & I/3 \\ 0 & I/3 & I/6 \end{bmatrix}^{(e)}, \quad \underline{\underline{D}}_S^{(e)} = \begin{bmatrix} 0 & 0 & 0 \\ 0 & 0 & 0 \\ 0 & 0 & k_T \end{bmatrix} \tag{A-6b,c}$$

By substituting (A-3a), (A-4), and (A-6) into (A-2) one obtains

$$\sum_{e=1}^{N_e} \delta\, \Phi^{(e)^T} (\underline{\underline{K}}_T^{(e)} + \underline{\underline{K}}_s^{(e)})\, \Delta\, \Phi^{(e)} \equiv -\delta\Phi_1 \Delta\, P/2 \tag{A-7a}$$

where

$$\underline{\underline{K}}_T^{(e)} = \int_{\Omega^{(e)}} \underline{\underline{B}}^{(e)^T} \underline{\underline{D}}_T^{(e)} \underline{\underline{B}}^{(e)} dx, \underline{\underline{K}}_s^{(e)} = \int_{\Omega^{(e)}} \underline{\underline{N}}^{(e)^T} \underline{\underline{D}}_s^{(e)} \underline{\underline{N}}^{(e)} dx. \tag{A-7b,c}$$

For arbitrary variation of $\delta\Phi_i$ one can obtain the incremental equilibrium equations from (A-7a).

Starting from an initial guess $\mathbf{u} = [0, 0, 0]^T$ one uses (A-7a) to compute $\Delta\, \Phi$ for the load increment $\Delta\, P$, and compute residual force of the equilibrium equations obtained from (A-5) to check whether the equilibrium equations for Φ are satisfied to the desired accuracy, or else continue the iteration process. The numerical implementation of the foregoing process may be found in [34]. A FORTRAN program was developed using two-node elements and used to compute the load-deflection curves in Fig. 5(b).

Downloaded 02 May 2010 to 171.66.16.25. Redistribution subject to ASME license or copyright; see http://www.asme.org/terms/Terms_Use.cfm

M. M. Bernitsas
Assistant Professor.

T. Kokkinis
Graduate Student and Research Assistant.

Department of Naval Architecture and Marine Engineering,
North Campus,
The University of Michigan,
Ann Arbor, Mich. 48109

Asymptotic Behavior of Heavy Column and Riser Stability Boundaries

Columns, marine risers, pipelines, hydraulic columns, and legs of tension leg platforms can be modeled for customary Euler buckling analysis by a single model which, in its most general form, applies to risers. Previous work has shown that numerical algorithms fail to provide stability boundaries for long risers. Asymptotic analyses for long columns have been developed as early as 1941 but the results are either incomplete or incorrect. The goals of this paper are to develop a long-column buckling theory, indicate errors in holding theories, and complete the numerical data available in the literature.

Introduction

For global Euler stability analysis, marine drilling, production risers, and hydraulic columns can be modeled as open-ended tubes subject to tension exerted at their top, their own weight, and internal and external fluid static pressure forces. Several aspects of this general stability problem have been studied in the past by Willers [1], Lubinski [2], Huang and Dareing [3, 4], Plunkett [5], and Sugiyama and Ashida [6]. In these references particular attention was paid to problems related to columns, closed tubes, and drill strings which can be modeled as special cases of the general riser model [7]. Buckling loads of long columns and effects of boundary conditions were also considered for these special cases [1, 4, 5]. Finally, Bernitsas and Kokkinis [8, 9] computed the stability boundaries for the general riser case and studied the effect of internal and external variable fluid static pressure forces on riser stability.

In this paper, the problem formulation and solution are briefly reviewed in Section 1. In Section 2, the asymptotic behavior of the stability boundaries is derived theoretically for columns with movable and nonmovable boundaries and used to produce data for very long slender columns. The results for columns with movable boundaries are in agreement with those published in the literature [1, 5] and match the data for short columns derived with customary numerical methods [3, 4, 9]. However, the results for columns with nonmovable boundaries differ by as much as 84 percent from those published in [1] and do not match the data for short columns derived in [3, 4, 8]. To explain these differences a long, slender, heavy column analysis is developed in Section 3 and the results are used to verify the asymptotic analysis of Section 2 and produce data that fill in the gap between numerical methods and asymptotic theory for columns with nonmovable boundaries. Finally in Section 4 the errors in the holding theory for columns with nonmovable boundaries developed in 1941 [1] are explained.

1 Problem Formulation and Solution Methods

In this work, a riser is considered as a long, slender, open-ended, heavy tubular column with tension exerted at its top, subject to internal and external static pressure forces due to fluids in gravity field. Regular columns can be modeled as a special case of this problem if actual weight and tension are substituted for effective ones used for risers.

1.1 Problem Formulation. In dimensionless form the governing differential equatioon is [8, 9]

$$\frac{d^4U}{dp^4} - (\beta p + \tau)\frac{d^2U}{dp^2} - \beta\frac{dU}{dp} = 0, \tag{1}$$

where $0 \le p = z/L \le 1$, L is the column or riser length, z is the coordinate along the riser, $\beta = W_e L^3/EI$ is the dimensionless effective weight, W_e is the effective weight per unit length, EI is the bending rigidity, U is the lateral deflection, and $\tau = P_e(0)L^2/EI$ is the effective tension at the riser lower end ($P_e(0)$) in dimensionless form.

The general boundary conditions in dimensionless form for a riser with rotational and linear springs at both ends are at the lower end where $p = 0$

$$\frac{d^3U(0)}{dp^3} - \delta(0)\frac{dU(0)}{dp} + \frac{C_B L^3}{EI}U(0) = 0 \tag{2}$$

and

$$\frac{d^2U(0)}{dp^2} + \frac{r_B L}{EI}\frac{dU(0)}{dp} = 0 \tag{3}$$

and at the top of the riser where $p = 1$

Contributed by the Applied Mechanics Division for presentation at the Winter Annual Meeting, New Orleans, La., December 9-14, 1984 of THE AMERICAN SOCIETY OF MECHANICAL ENGINEERS.

Discussion on this paper should be addressed to the Editorial Department, ASME, United Engineering Center, 345 East 47th Street, New York, N.Y. 10017, and will be accepted until two months after final publication of the paper itself in the JOURNAL OF APPLIED MECHANICS. Manuscript received by ASME Applied Mechanics Division, March, 1983, December, 1983. Paper No. 84-APM-7.

Copies will be available until August, 1985.

Copyright © 1984 by ASME
Downloaded 02 May 2010 to 171.66.16.25. Redistribution subject to ASME license or copyright; see http://www.asme.org/terms/Terms_Use.cfm

$$\frac{d^3U(1)}{dp^3} - \delta(1)\frac{dU(1)}{dp} - \frac{C_T L^3}{EI}U(1) = 0 \tag{4}$$

and

$$\frac{d^2U(1)}{dp^2} - \frac{r_T L}{EI}\frac{dU(1)}{dp} = 0 \tag{5}$$

where C_B, C_T are the linear spring constants at the bottom and top of the riser, respectively, r_B and r_T are the rotational spring constants at the bottom and top of the riser, respectively, and δ is the dimensionless actual tension.

Equations (1)–(5) constitute an eigenvalue problem, the eigenvalues of which define the riser stability boundary in the $\beta - \tau$ plane. Two types of boundary conditions that are considered of practical importance are studied in this work (see Section 2). For all cases the appropriate boundary conditions can be derived as special cases of equations (2)–(5) by assigning the proper values to the spring constants C_B, r_B, C_T, and r_T.

1.2 Solution Methods for Low β Values. Equation (1) has been solved in four different ways. The first is based on a power series solution [8], the second on Airy functions [10] (see Section 2), the third on Bessel and Lommel functions [1] (see Section 4), and the fourth on a finite element discretization [8]. Numerical implementations with double precision arithmetic of all three solution methods yield riser stability boundaries in the $\beta - \tau$ plane for values of β up to about 1500–2500 depending on the boundary conditions and the order of the buckling mode. For higher β values, none of these methods can produce stability boundary data due to numerical instabilities. For this reason it has become necessary to develop theoretical methods for high β values which will produce such data. This need had become obvious to Willers as early as in 1941 [1]. Willers' asymptotic analysis was based on the Bessel-Lommel function solution, which is discussed in Section 4. In our effort to derive the asymptotic behavior of the stability boundaries we have considered using matched asymptotic expansions and Airy functions. Equation (1) for $\beta \to \infty$ becomes singular and the boundary value problem exhibits two boundary layers at $p = 0$ and $p = 1$ [10]. After matching the inner and outer solutions at both layers the expressions derived were too complicated to reveal the expected geometric asymptotic behavior of the stability boundaries. Consequently this solution method was abandoned in favor of the one based on the Airy function solution which is the subject of the next section.

2 Asymptotic Solution

We start this analysis by studying the behavior of the stability boundaries for $\beta \to \infty$. In this analysis two basic sets of boundary conditions are distinguished: (1) the set for columns with movable boundary at the top (or bottom), and (2) the set for columns with nonmovable boundaries. The derivation of the asymptotic behavior is fundamentally different for these two sets and will be treated separately. In both cases the final result is that the asymptotic behavior of the stability boundary is geometric of the form

$$\tau_{\text{crit}} = c\,\beta^{2/3} \tag{7}$$

where c is a negative constant depending only on the boundary condition at the lower end of the column or riser.

Integrating equation (1) once, we get

$$\frac{d^3U}{dp^3} - (\beta p + \tau)\frac{dU}{dp} = \sigma \tag{8}$$

The general solution to (8) is [10]

$$U(p) = \beta^{-2/3}\int^x y(\xi)d\xi + c_4 \tag{9}$$

where

$$y(x) = c_1 Ai(x) + c_2 Bi(x) + \pi\sigma\beta^{-2/3}\{-Ai(x)\int_{x_1}^{x} Bi(\zeta)d\zeta + Bi(x)\int_{x_1}^{x} Ai(\zeta)d\zeta\} \tag{10}$$

$$x = \beta^{1/3}p + \beta^{-2/3}\tau \tag{11}$$

c_1, c_2, c_4 are constants of integration and x_1, given by (12)

$$x_1 = x|_{p=1} = \beta^{1/3} + \beta^{-2/3}\tau \tag{12}$$

is used as a constant reference value for x.

σ can be found from boundary condition (4). Equation (8) evaluated at $p = 1$ becomes

$$\frac{d^3U(1)}{dp^3} - (\beta + \tau)\frac{dU(1)}{dp} = \sigma \tag{13}$$

Furthermore

$$\beta + \tau = \frac{w_e L^3}{EI} + \frac{P_e(0)L^2}{EI} = \frac{[w_e L + P_e(0)]L^2}{EI} = \frac{T(1)L^2}{EI} = \delta(1) \tag{14}$$

Combining (4), (13), and (14) we find

$$\sigma = \frac{C_T L^3}{EI}\cdot U(1) \tag{15}$$

In general σ, which is the dimensionless horizontal reaction at the top, is nonzero. As explained in the following, it is zero only when $C_T = 0$, that is, if the top of the heavy column or riser is unrestrained horizontally.

2.1 Movable Upper Boundary. We define the upper boundary as movable if it is completely unrestrained in the horizontal direction ($C_T = 0$) as opposed to an elastically restrained for which C_T is nonzero and finite and a nonmovable for which $C_T \to \infty$.

For movable upper boundary, equation (15) yields $\sigma = 0$ and (10) becomes

$$y(x) = c_1 Ai(x) + c_2 Bi(x) \tag{16}$$

For columns movably hinged at their upper end ($r_T = 0$) condition (5) yields

$$y'(x_1) = \beta^{1/3}[c_1 Ai'(x_1) + c_2 Bi'(x_1)] = 0 \tag{17}$$

For heavy columns and partially buoyed risers, which is the case in practice, β is positive, τ is negative, and $x_1 \to \infty$ as $\beta \to \infty$ [15]. The first derivative of the Airy function of the first kind, Ai', is bounded as $\beta \to \infty$ while that of the second kind, Bi', is unbounded. Thus condition (17) can be satisfied only if $c_2 = 0$. Therefore

$$y(x) = c_1 Ai(x) \tag{18}$$

For columns movably C_2 clamped at their upper end ($r_T \to \infty$) condition (5) and the fact that $Ai(x_1)/Bi(x_1) \to 0$ as $\beta \to \infty$ yields again equation (18).

Further condition (3) yields

$$Ai'(x_0) = 0 \tag{19}$$

for columns hinged at their lower end and

$$Ai(x_0) = 0 \tag{20}$$

for columns clamped at their lower end. Consequently the asymptotic behavior of the stability boundary for the ith buckling mode is given by equation (7) where the constant c is the ith root of either (19) or (20). Further it should be noticed that:

Downloaded 02 May 2010 to 171.66.16.25. Redistribution subject to ASME license or copyright; see http://www.asme.org/terms/Terms_Use.cfm

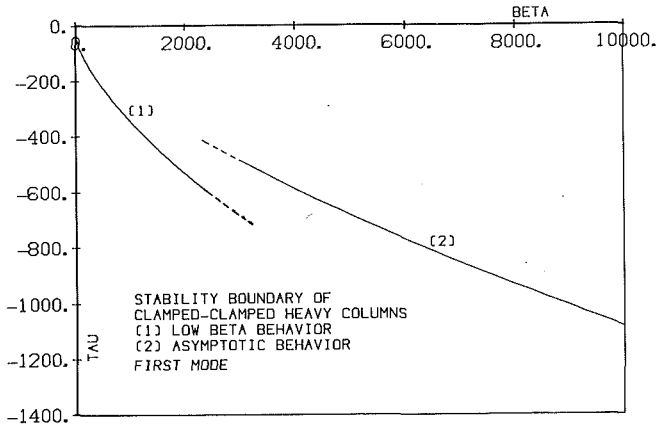


Fig. 1 Stability boundary for clamped-clamped columns. Low β, and asymptotic behavior.

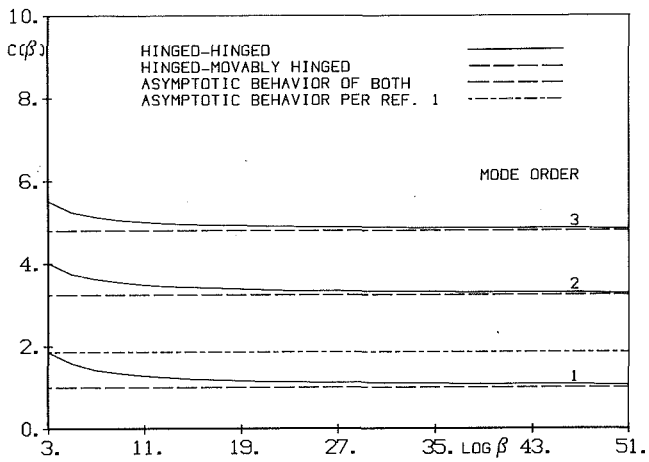


Fig. 2 Buckling load coefficient $c(\beta)$. High β and asymptotic behavior for hinged-hinged and hinged-movably hinged columns.

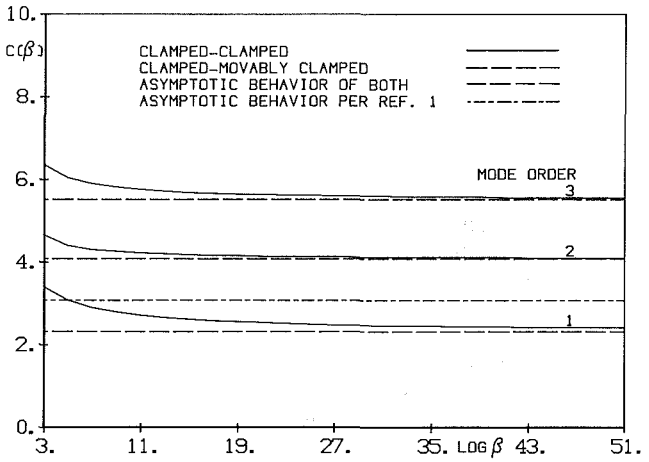


Fig. 3 Buckling load coefficient $c(\beta)$. High β and asymptotic behavior for clamped-clamped and clamped-movably clamped columns.

(a) Equations (19) and (20) show that the asymptotic behavior of the stability boundary is independent of the stiffness of the rotational spring at the top and depends only on the boundary condition at the lower end.

(b) The convergence of the stability boundaries to their asymptotic geometric behavior is very fast. It practically occurs for $\beta \cong 100$. Further, the results of the numerical methods discussed in Section 1 are valid up to $\beta \cong 2000$. Thus the entire domain of practical interest is covered.

The first roots of equations (19) and (20) are 1.018 and 2.338, respectively, which are in agreement with the results that Willers [1] and Plunkett [5] derived in a different way.

2.2 Nonmovable Boundaries. If the top support is elastically restrained in the horizontal direction, σ is nonzero because both C_T and $U(1)$ in equation (15) are nonzero and finite. In the extreme case of nonmovable support, where $C_T \to \infty$ and $U(1) \to 0$, the product $C_T U(1)$ represents the horizontal reaction and is finite and nonzero. This can become obvious by considering the heavy column in its deformed position and studying the equilibrium of external moments acting on the column with respect to the lower end support.

Long heavy columns and risers are not perfect by construction. Imperfections usually make the two end supports nonaligned but do not affect the boundary conditions. A nonmovable boundary, perfect or with small imperfections, has $C_T \to \infty$ and should not be confused in any way with the case of elastically restrained boundary or the case of movable boundary considered in the preceding section. Small imperfections do not affect the Euler buckling loads which are computed in this work. Small imperfections affect the actual buckling loads only – insignificantly in the case of stable postbuckling behavior and possibly significantly in the case of unstable postbuckling behavior.

The fact that σ is nonzero makes the derivation of the asymptotic behavior of the stability boundaries complicated. This behavior is derived in the following only for clamped-clamped columns. The solution for all other problems with nonmovable supports is similar.

Equation (5) yields

$$y(x_1) = 0 = c_1 Ai(x_1) + c_2 Bi(x_1) \tag{21}$$

For $x_1 \to \infty$, $Bi(x_1) \to \infty$, and $Ai(x_1) \to 0$ [10]. Thus equation (21) can be satisfied only if $c_2 = 0$. Therefore boundary condition (3) becomes

$$Ai(x_0)\left(c_1 + \pi\sigma\beta^{-2/3}\int_{x_0}^{0} Bi(\zeta)d\zeta + \pi\sigma\beta^{-2/3}\int_{0}^{x_1} Bi(\zeta)d\zeta\right) - Bi(x_0)$$

$$\cdot\, \pi\sigma\beta^{-2/3}\left(\int_{x_0}^{0} Ai(\zeta)d\zeta + \int_{0}^{x_1} Ai(\zeta)d\zeta\right) = 0 \tag{22}$$

Since τ and therefore x_0 are negative there are two possibilities. Either x_0 is finite or $-\infty$. In the former case the first and third integrals in (22) are obviously finite; in the latter it is shown in reference [15] that these integrals are also finite. In addition $Ai(x_0)$ and $Bi(x_0)$ are bounded and the fourth integral in (22) converges to 1/3 for $\beta \to \infty$. Thus (22) reduces to

$$Ai(x_0)\left(c_1 + \pi\sigma\beta^{-2/3}\int_{0}^{x_1} Bi(z)dz\right) = 0 \tag{23}$$

For $\beta \to \infty$ the second term in the brackets is unbounded and consequently the preceding equation can be satisfied if $\sigma = 0$ or $Ai(x_0) = 0$. The former is not true for heavy columns or risers with nonmovable supports and consequently we retrieve equation (20). Similarly (20) holds for clamped-hinged and (19) for hinged-hinged and hinged-clamped columns.

At this point we can draw the following conclusions:

(a) As in the case of columns with movable top support, equations (19) and (20) for columns with nonmovable top support show, that the asymptotic behavior of the stability

Downloaded 02 May 2010 to 171.66.16.25. Redistribution subject to ASME license or copyright; see http://www.asme.org/terms/Terms_Use.cfm

boundaries is independent of the stiffness of the rotational spring at the top.

(*b*) The foregoing conclusion further shows that the asymptotic behavior of the stability boundaries is independent of the stiffness of the linear spring at the top as well.

The convergence of the stability boundaries of heavy columns with nonmovable supports to their asymptotic geometric behavior is very slow. It practically occurs for $\beta \gtrsim 10^{50}$. On the other hand, the numerical methods discussed in Section 1 can yield results only for $\beta \lesssim 2000$. Risers currently being designed have $\beta \cong 7\times 10^4$. Risers of $L \cong 2000$m, which are going to be in operation during the next 20 years will have $\beta \cong 2\times 10^5$. Furtheremore mining risers of $L \cong 4500$m have $\beta \cong 2\times 10^7$. Therefore there is a big gap in the available data that is covered by the analysis of Section 3. This gap is due to the fact that the low β and the asymptotic solution do not match, as shown in Fig. 1. Intermediate data are derived in the next section and shown in Figs. 2 and 3.

In this work we found that the asymptotic behavior of the stability boundary of heavy columns with hinged lower end is

$$\tau_{\text{crit}} = -1.018\,\beta^{2/3} \tag{24}$$

and with clamped lower end is

$$\tau_{\text{crit}} = -2.338\,\beta^{2/3} \tag{25}$$

Willers [1] derived the same results for columns with movable top support. For columns with nonmovable support, however, his results are

$$\tau_{\text{crit}} = -1.88\,\beta^{2/3} \tag{26}$$

and

$$\tau_{\text{crit}} = -3.09\,\beta^{2/3} \tag{27}$$

respectively. The results in equations (26) and (27) differ from those in equations (24) and (25) by 84 percent and 33 percent, respectively. The method used in deriving these results is discussed and its limitations are pointed out in Section 4.

3 Complete High β Behavior of Stability Boundaries

As explained in Section 2.2, it is necessary to study the high β behavior of the stability boundaries for columns with nonmovable supports in order to fill in the gap between the low β and the asymptotic results. The general solution to equation (8) can be written as [11]

$$U(p) = \beta^{-1/3}\left\{c_1\int_0^x Ai(\xi)d\xi + c_2\int_0^x Bi(\xi)d\xi - \pi\sigma\beta^{-2/3}\int_0^x Gi(\xi)\,d\xi + c_4\right\} \tag{28}$$

where

$$Gi(x) = Bi(x)\int_x^\infty Ai(\xi)\,d\xi + Ai(x)\int_0^x Bi(\xi)d\xi \tag{29}$$

and the constants of integration c_1, c_2, c_4, and σ will be determined from boundary conditions (2)–(5).

The case of clamped-clamped heavy columns is studied here in detail. Results for other boundary conditions with nonmovable supports can be derived similarly. Boundary conditions (2)–(5) yield, respectively,

$$c_1\beta^{-1/3}\int_0^{x_0} Ai(\xi)d\xi + c_2\beta^{-1/3}\int_0^{x_0} Bi(\xi)d\xi - \pi\sigma\beta^{-1}\int_0^{x_0} Gi(\xi)d\xi + \beta^{-1/3}c_4 = 0 \tag{30}$$

$$c_1 Ai(x_0) + c_2 Bi(x_0) - \pi\sigma\beta^{-2/3}Gi(x_0) = 0 \tag{31}$$

$$c_1\beta^{-1/3}\int_0^{x_1} Ai(\xi)d\xi + c_2\beta^{-1/3}\int_0^{x_1} Bi(\xi)d\xi - \pi\sigma\beta^{-1}\int_0^{x_1} Gi(\xi)d\xi + \beta^{-1/3}c_4 = 0 \tag{32}$$

$$c_1 Ai(x_1) + c_2 Bi(x_1) - \pi\sigma\beta^{-2/3}Gi(x_1) = 0 \tag{33}$$

The system of equations (30)–(33) will have a nontrivial solution for c_1, c_2, σ, and c_4 if the determinant of their coefficients is zero. This yields the characteristic equation which has the following form [15]:

$$f(x_0, x_1) = 0 \tag{34}$$

As mentioned in Section 2 as $\beta \to \infty$, $x_1 \to \infty$, and x_0 remains finite. To simplify the characteristic equation (34), we replace all functions with argument x_1 by their asymptotic expansions.

Asymptotic expansions for $Ai(x_1)$ and $Bi(x_1)$ can be found in [11] and for

$$\int_0^{x_1} Gi(\xi)d\xi$$

in [13]. Further it can be shown [15] that

$$\int_0^z Ai(\xi)d\xi \underset{z\to\infty}{=} \frac{1}{3} - \frac{1}{2}\pi^{-1/2}z^{-3/4}\exp\left(\frac{-2z^{3/2}}{3}\right) \sum_{k=0}^{\infty}(-1)^k\left(\sum_{l=0}^{k}\left(\frac{3}{4}\right)^{k-l}\prod_{m=1}^{k-l}(2m-1)c_l\right)z^{-3k/2} \tag{35}$$

where by definition

$$\prod_{m=1}^{0}(2m-1) = 1,$$

$$\int_0^z Bi(\xi)d\xi \underset{z\to\infty}{\sim} \pi^{-1/2}z^{-3/4}\exp\left(\frac{2z^{3/2}}{3}\right) \sum_{k=0}^{\infty}\sum_{l=0}^{k}\left(\frac{3}{4}\right)^{k-l}\prod_{m=1}^{k-l}(2m-1)c_l z^{-3k/2} \tag{36}$$

and

$$Gi(z) \underset{z\to\infty}{\sim} \frac{1}{\pi}\left(\frac{1}{z} + \sum_{i=1}^{\infty}\frac{(3i-1)!}{3^{i-1}(i-1)!z^{(3i+1)}}\right) \tag{37}$$

It should be emphasized at this point that the preceding asymptotic series are divergent. All six series, however, satisfy the conditions of the optimal truncation rule for divergent series and have a finite sum for finite arguments [10, 12]. Therefore, in numerical computations the series must be truncated before they start diverging and after all significantly contributing terms have been computed. The series are truncated after the minimum term has been included in the addition or if terms smaller than the double precision error in computer arithmetic are encountered. For $\beta \gtrsim 10^5$ the absolute error in the summation of the series is of the order of the roundoff error in double precision computer arithmetic and the relative error is less than $5\cdot 10^{-11}$ percent. For $1000 \leq \beta \leq 10^5$ the maximum error occurs for $\beta = 1000$ and is less than $5\cdot 10^{-5}$ percent. The number of terms retained in the computations varies from 2 to over 100 depending on the value of β.

Based on the preceding asymptotic series we transform equation (34) to one of the following form [15]:

Downloaded 02 May 2010 to 171.66.16.25. Redistribution subject to ASME license or copyright; see http://www.asme.org/terms/Terms_Use.cfm

$$\exp X \quad f_1(x_0,x_1)+\exp(-X) \quad f_2(x_0,x_1)+f_3(x_0,x_1)=0 \qquad (38)$$

where $X = 2x^{3/2}/3$.

For large β the first term of (38) is dominant. Therefore

$$f_1(x_0,x_1)=\int_0^{x_1} Bi(\xi)\,d\xi\, Gi(x_1)Ai(x_0)$$

$$-Bi(x_1)\int_0^{x_1} Gi(\xi)d\xi \quad Ai(x_0)+\frac{1}{3}Bi(x_1)Gi(x_0)$$

$$-Bi(x_1)\int_0^{x_0} Ai(\xi)\,d\xi\, Gi(x_0)-Ai(x_0)\int_0^{x_0} Gi(\xi)\,d\xi\cong 0 \qquad (39)$$

From equation (39) we can retrieve (20) for $\beta \to \infty$. For large finite β values the stability boundary is still given by equation (7). However, c now depends on β and can be determined from equation (39). The results are shown for the three buckling modes, in Fig. 3 together with the asymptotic solution represented by the horizontal dashed lines. It can be seen that the asymptotic behavior is practically attained for $\beta \gtrsim 10^{50}$.

Results for hinged-hinged, clamped-hinged, and hinged-clamped heavy columns and risers can be derived from the following characteristic equations

$$\int_0^{x_1} Bi(\xi)d\xi\, Gi'(x_1)Ai'(x_0)$$

$$-Bi'(x_1)\int_0^{x_1} Gi(\xi)\,d\xi\, Ai'(x_0)+\frac{1}{3}Bi'(x_1)Gi'(x_0)$$

$$-Bi'(x_1)\left[\int_0^{x_0} Ai(\xi)\,d\xi \quad Gi'(x_0)\right.$$

$$\left.-Ai'(x_0)\int_0^{x_0} Gi(\xi)\,d\xi\right]\cong 0, \qquad (40)$$

$$\int_0^{x_1} Bi(\xi)\,d\xi \quad Gi'(x_1)Ai(x_0)$$

$$-Bi'(x_1)\int_0^{x_1} Gi(\xi)\,d\xi \quad Ai(x_0)+\frac{1}{3}Bi'(x_1)Gi(x_0)$$

$$-Bi'(x_1)\left[\int_0^{x_0} Ai(\xi)d\xi \quad Gi(x_0)\right.$$

$$\left.-Ai(x_0)\int_0^{x_0} Gi(\xi)\,d\xi\right]\cong 0 \qquad (41)$$

and

$$\int_0^{x_1} Bi(\xi)\,d\xi \quad Gi(x_1)Ai'(x_0)$$

$$-Bi(x_1)\int_0^{x_1} Gi(\xi)d\xi A^{I}(x_0)+\frac{1}{3}Bi(x_1)Gi'(x_0)$$

$$-Bi(x_1)\left[\int_0^{x_0} Ai(\xi)d\xi \quad Gi'(x_0)\right.$$

$$\left.-Ai'(x_0)\int_0^{x_0} Gi(\xi)\,d\xi\right]\cong 0, \qquad (42)$$

respectively. For numerical computations $Ai(x_0)$, $Bi(x_0)$, $Gi(x_0)$, and their derivatives and integrals were evaluated from series representations taken from [10, 11, 13, 14]. Figure 2 shows the results for hinged-hinged columns. The results for hinged-clamped columns are almost but not exactly identical [15]. The maximum difference occurs at $\beta = 1000$ and is 0.58 percent. Similarly, the results for clamped-hinged columns are almost identical to those for clamped-clamped columns, with maximum difference of 0.35 percent at $\beta = 1000$.

4 Willers' Asymptotic Solution [1]

The asymptotic behavior of the stability boundaries of columns with nonmovable supports was derived in [1] by transforming the governing equation (1) to a Bessel equation and writing the solution in terms of Bessel and Lommel functions. Further, for clamped end it was concluded the c in equation (7) is the root of (43)

$$\frac{\pi}{\sqrt{3}} r_0^{1/3}\frac{dJ_{1/3}(r_0)}{dr}+r_0^{1/3}\frac{ds_{0,1/3}(r_0)}{dr}=0 \qquad (43)$$

where $r_0 = 2/3\beta(-\tau)^{3/2}$.

The first root of (43) is $c = -3.09$ which differs significantly from the actual value of -2.338, which is the first root of equation (20).

For hinged lower end it was found that $c = -1.88$ which is not close to the actual value of -1.018 which is the first root of equation (19). The limitations to the validity of the analysis and results in [1] are the following:

1. The asymptotic expansions of the Bessel and Lommel functions were taken in the form of a leading asymptotic behavior multipled by a series. Only the first two terms in the series were retained which are dominant only for relatively low values of β. For higher β values, this approximation is not valid because the asymptotic series involved in the characteristic equation that yields the eigenvalues are divergent. What is required in this case is a truncation rule for the divergent series like the optimal truncation rule for the divergent asymptotic series used in Section 3.

2. One would expect then that the truncation method used in [1] would produce results valid for some intermediate β values where the asymptotic analysis assumptions hold and before the omitted terms in the series become significant. Actually this is true but since the expansions in [1] are not consistent the only way of determining the range of validity of these results is by comparing them to the correct ones in Figs. 2 and 3 and the numerical data in [15] (see Figs. 2 and 3).

3. In the range where these results seem to be close to the data in Figs. 2 and 3 the actual asymptotic behavior has not been achieved yet by the stability boundaries. The error is 84 percent for heavy columns or risers hinged at their lower end and 33 percent for those clamped at their lower end.

Summary

This work has produced complete data for the stability boundaries of heavy columns and risers with movable and nonmovable boundaries beyond the range covered by regular numerical methods. For movable boundaries the results are in agreement with those available in the open literature. For nonmovable boundaries, however, the results differ significantly and the errors in previous analyses were explained. Further, it was shown that it is incorrect to use the asymptotic behavior even for very long columns with nonmovable boundaries because the effect of the horizontal restraint of the top support persists.

Acknowledgments

This work constitutes part of the outcome of the research on global static elastic instabilities of risers undertaken by the first author at the Department of Naval Architecture and Marine Engineering at the University of Michigan for the Ocean Engineering Division of the American Bureau of Shipping.

Downloaded 02 May 2010 to 171.66.16.25. Redistribution subject to ASME license or copyright; see http://www.asme.org/terms/Terms_Use.cfm

References

1 Willers, F. A., "Das Knicken Schwerer Gestaenge," *Zeitung fuer Angewandter Mathematic und Mechanik*, Vol. 21, No. 1, 1941, pp. 43–51.

2 Lubinski, A., "A Study of the Buckling of Rotary Drilling Strings," *Drilling and Production Practice*, API, 1950, pp. 178–214.

3 Huang, T., and Dareing, D. W., "Buckling and Frequency of Long Vertical Pipes," *Journal of Engineering Mechanics Division*, Proceedings of the ASCE, Vol. 95, Feb. 1967, pp. 167–181.

4 Huang, T., and Dareing, D. W., "Buckling and Lateral Vibration of Drill Pipe," ASME *Journal of Engineering for Industry*, Vol. 90, Nov. 1968, pp. 613–619.

5 Plunkett, R., "Static Bending Stresses in Catenaries and Drill Strings," ASME *Journal of Engineering for Industry*, Vol. 89, No. 1., Feb. 1967, pp. 31–36.

6 Sugiyama, Y., and Ashida, K., "Buckling of Long Columns Under Their Own Weight," *Transactions, Japanese Society of Mechanical Engineers*, Vol. 21, No. 158, Aug. 1978, pp. 1228–1235.

7 Bernitsas, M. M., "Three-Dimensional, Nonlinear Large Deflection Model of Dynamic Response of Risers, Pipelines and Cables," *Journal of Ship Research*, Vol. 26, No. 1, Mar. 1982, pp. 59–64.

8 Bernitsas, M. M., and Kokkinis, T., "Buckling of Columns With Nonmovable Boundaries," *Journal of Structural Engineering*, ASCE Transactions, Vol. 105, No. ST9, Sept. 1983.

9 Bernitsas, M. M., and Kokkinis T., "Buckling of Columns With Movable Boundaries," *Journal of Structural Mechanics*, Vol. 11, No. 3, Oct. 1983.

10 Bender, C. M., and Orszag, S. A., *Advanced Mathematical Methods for Scientists and Engineers*, McGraw-Hill, New York, 1978, pp. 61–145.

11 Abramowitz, M., and Stegun, I. A., *Handbook of Mathematical Functions*, Dover, New York, 1970.

12 Erdelyi, A., *Asymptotic Expansions*, Dover, New York, 1956.

13 Rothman, M., "Tables of Integrals and Differential Coefficients of $Gi(+x)$, $Hi(-x)$," *Quart. Journal of Mechanics and Applied Mathematics*, Vol. 7, 1954, pp. 379.

14 Scorer, R. S., "Numerical Evaluation of Integrals of the Form $I = \int_{x_1}^{x_2} f(x)\, e^{ip(x)} dx$ and the Tabulation of the Function $Gi(z) = 1/\pi \int_0^\infty \sin(uz + 1/3u^3)du$," *Quart. Journal of Mechanics and Applied Mathematics*, Vol. 3, 1950, pp. 107–112.

15 Bernitsas, M. M., and Kokkinis, T., "Asymptotic Behavior of Riser Stability Boundaries," Department of Naval Architecture and Marine Engineering, The University of Michigan, Report #255, Dec. 1982.

16 Watson, G. N., *A Treatise on the Theory of Bessel Functions*, Cambridge University Press, 1966.

Downloaded 02 May 2010 to 171.66.16.25. Redistribution subject to ASME license or copyright; see http://www.asme.org/terms/Terms_Use.cfm

Effects of Mode Interaction on Collapse of Short, Imperfect, Thin-Walled Columns

David Hui[1]

Department of Ocean Engineering,
Massachusetts Institute of Technology,
Cambridge, Mass. 02139.
Mem. ASME

The present paper deals with the design of beneficial geometric imperfections of short, thin-walled columns in order to maximize their energy absorption. The investigation was motivated by the experimental finding that under axial compressive load, the symmetric mode (which has a higher buckling load than the antisymmetric mode) actually has a much higher energy absorption than the antisymmetric mode as measured by the area under the curve of applied load versus end-shortening curve. Thus, an attempt is made to introduce imperfections in the beneficial symmetric mode so that the mode shapes of extremely large deflection in plastic collapse will also be of the symmetric type. The two-mode stability problem is studied using Koiter's theory of elastic stability.

1 Introduction

Crashworthiness of thin-walled structures has become one of the most important and challenging applied mechanics problems due to the fact that extremely large deformation is a complex mathematical problem. Moreover, it has found increasingly widespread applications in aerospace, mechanical, and ocean engineering structures. One of the most commonly encountered structural problems is the crushing of short, thin-walled columns under axial load. The dominant modes are the symmetric and the antisymmetric buckling modes of angled columns (see Fig. 1 and references [1-4]. The influence of initial geometric imperfections on the initial postbuckling behavior of such structures and their effects on the crushing of thin-walled structures are not well established. The present study is motivated by experimental investigations [1] which found that the symmetric mode of an angle-column has a much higher energy absorption than the antisymmetric mode as measured by the area under the load versus end-shortening curve for extremely large deflection (of the order of the length of the structure). An attempt is made to introduce the geometric imperfections in the "beneficial" symmetric mode so that the structure will follow the equilibrium paths of this mode in the initial postbuckling regime as well as in the regime of large deflection and crushing of the structure.

Previous investigations on the interaction between the Euler mode (one axial half wave) and the local mode (at least several axial half waves) of thin-walled columns was investigated by Van der Neut [5, 6], Koiter and Kuiken [7], and Byskov [8]. Related studies on the postbuckling behavior of thin-walled columns were also studied by Graves Smith [9, 10], and Grimaldi and Pignataro [11]. However, the mode interactions of short, angle-shaped, thin-walled columns where the two competing modes have the same axial wavelength (Euler modes) have not been investigated. Thus, it is of interest to study the initial postbuckling behavior of geometrically imperfect columns. In contrast to all the foregoing studies, the present ultimate goal is not to design a structure with high buckling load and low imperfection-sensitivity; rather, the objective is to design a structure with high energy absorption. Thus, an attempt is made to introduce a "beneficial" geometric imperfection of specified magnitude in the shape of the "symmetric mode" so that the structure will follow the equilibrium path of this mode in the initial postbuckling as well as in the very large deflection regimes, leading to the plastic collapse of the structure. Early experimental results on these angled structures are reported by Bridget, Jerome, and Vossler [12].

The present paper aims to examine the effects of geometric imperfections on the initial postbuckling behavior of short, angle-shaped, thin-walled columns under longitudinal compression. The loaded edges are assumed to be simply supported and one of the two longitudinal edges is free. The remaining longitudinal edge may be either simply supported (antisymmetric mode) or clamped (symmetric mode). Koiter's theory of multimode postbuckling [13, 14] is used to study the interaction between these two modes. The analysis is based on a solution of the nonlinear von Karman differential equations for plates valid for moderately large deflections. To compute the postbuckling coefficients, it is necessary to solve the eigenvalue problem (for the buckling loads and buckling modes of these two modes) and three uncoupled linear boundary-value problems for the second-order fields. Based

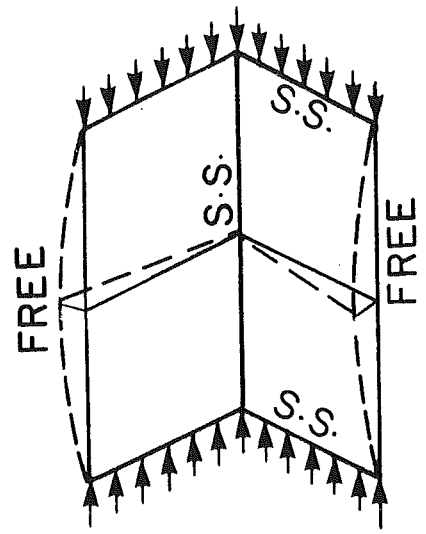
[1] Present affiliation: Assistant Professor, Department of Engineering Mechanics, The Ohio State University, Columbus, Ohio 43210.

Contributed by the Applied Mechanics Division for presentation at the Winter Annual Meeting, New Orleans, La., December 9-14, 1984 of THE AMERICAN SOCIETY OF MECHANICAL ENGINEERS.

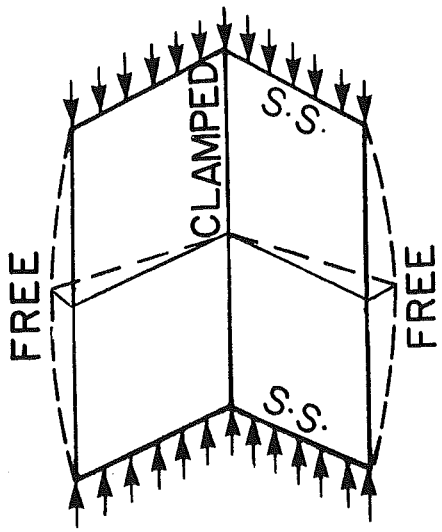
Discussion on this paper should be addressed to the Editorial Department, ASME, United Engineering Center, 345 East 47th Street, New York, N.Y. 10017, and will be accepted until two months after final publication of the paper itself in the JOURNAL OF APPLIED MECHANICS. Manuscript received by ASME Applied Mechanics Division, August, 1983; final revision, January, 1984. Paper No. 84-WA/APM-16.

Copies will be available until August, 1985.

Copyright © 1984 by ASME
Downloaded 02 May 2010 to 171.66.16.25. Redistribution subject to ASME license or copyright; see http://www.asme.org/terms/Terms_Use.cfm



ANTI-SYMMETRIC MODE



SYMMETRIC MODE

Fig. 1 Antisymmetric (simply supported at Y = 0) and symmetric (clamped at Y = 0) buckling modes of angled columns

on these postbuckling coefficients, the appropriate equilibrium paths of imperfect columns are plotted for Poisson's ratio of 0.3 and aspect ratio between 0.5 and 2.0. It is found that it is possible to design "beneficial" geometric imperfections so that the structure will follow the equilibrium paths of the symmetric mode in the large deflection regime.

2 Governing Differential Equations

The von Karman nonlinear equilibrium and compatibility equations for plates written in terms of an out-of-plane displacement W and a stress function F, valid for moderately large deflection, are

$$(D)\,(W_{,XXXX}+W_{,YYYY}+2W_{,XXYY})=F_{,YY}W_{,XX}+F_{,XX}W_{,YY}-2F_{,XY}W_{,XY} \tag{1}$$

$$[1/(Eh)](F_{,XXXX}+F_{,YYYY}+2F_{,XXYY})=(W_{,XY})^2-W_{,XX}W_{,YY} \tag{2}$$

where D is the flexural rigidity, E is Young's modulus, h is the plate thickness, and X and Y are the longitudinal and transverse in-plane coordinates. Introducing the nondimensional quantities (B is the width of the plate, $c=[3(1-\nu^2)]^{1/2}$ and ν is Poisson's ratio)

$$w=W/h,\quad f=2cF/(Eh^3),\quad (x,y)=(X,Y)\,(1/B) \tag{3}$$

the governing differential equations become

$$w_{,xxxx}+w_{,yyyy}+2w_{,xxyy}=(2c)\,[f_{,yy}w_{,xx}+f_{,xx}w_{,yy}-2f_{,xy}w_{,xy}] \tag{4}$$

$$f_{,xxxx}+f_{,yyyy}+2f_{,xxyy}=(2c)\,[(w_{,xy})^2-w_{,xx}w_{,yy}] \tag{5}$$

The plate is simply supported at the two loaded edges $x=0$ and $x=L/B$ where L is the length of the plate (see Fig. 1). Further, it is free at the edge $y=1$ so that

$$w_{,yy}(x,y=1)+\nu w_{,xx}(x,y=1)=0 \tag{6}$$

$$w_{,yyy}(x,y=1)+(2-\nu)\,w_{,xxy}(x,y=1)=0$$

Two types of boundary conditions at the intersecting edge $y=0$ are considered (Fig. 1): simply supported (i.e., antisymmetric mode) and clamped (i.e., symmetric mode). Finally, the stress resultants are related to the stress function by

$$N_x=F_{,YY},\quad N_y=F_{,XX},\quad N_{xy}=-F_{,XY} \tag{7}$$

and the in-plane boundary conditions will be examined subsequently.

Within the context of Koiter's theory of elastic stability [13], the out-of-plane displacement and the stress function for the two-mode stability problem are sought in the form (ξ_1 and ξ_2 are the amplitudes of the antisymmetric and symmetric modes, respectively)

$$w=0+(\xi_1 w_1+\xi_2 w_2)+(\xi_1{}^2 w_{11}+\xi_2{}^2 w_{22}+2\xi_1\xi_2 w_{12})=w_c+w_{II} \tag{8}$$

$$f=f_0+(\xi_1 f_1+\xi_2 f_2)+(\xi_1{}^2 f_{11}+\xi_2{}^2 f_{22}+2\xi_1\xi_2 f_{12})=f_0+f_c+f_{II}$$

It will be shown in subsequent sections that for the present problem

$$f_1=f_2=0\quad\text{and}\quad w_{11}=w_{22}=w_{12}=0 \tag{9}$$

3 Classical Buckling Load

For a rectangular plate uniformly compressed in the longitudinal direction, buckling occurs with zero in-plane displacements. The differential equation for buckling is

$$w_{,xxxx}+w_{,yyyy}+2w_{,xxyy}+(\pi^2\sigma)\,w_{,xx}=0 \tag{10a}$$

where ($\bar{\sigma}$ is the axial stress per unit cross-sectional area, positive for compression, and f_0 is the prebuckling stress function)

$$\sigma=k(\text{Timoshenko})=\bar{\sigma}hB^2/(\pi^2 D)=(-2c/\pi^2)f_{0,yy} \tag{10b}$$

Antisymmetric Mode (Simply Supported at $y=0$). The solution that satisfies the simply supported condition at the two loaded edges is

$$w_1(x,y)=w_1(y)\,\sin(M_1 x) \tag{11}$$

Downloaded 02 May 2010 to 171.66.16.25. Redistribution subject to ASME license or copyright; see http://www.asme.org/terms/Terms_Use.cfm

where $M_1 = m_1 B/L$ and m_1 is the number of axial half waves. Thus, the ordinary homogeneous differential equation is

$$w_1(y),_{yyyy} - 2M_1^2 w_1(y),_{yy} + (M_1^4 - \pi^2 \sigma M_1^2) w_1(y) = 0 \quad (12)$$

The solution that satisfies the simply supported boundary condition at $y = 0$ is [15]

$$w_1(y) = (\xi_1)[A_1 \sinh(c_1 y) + B_1 \sin(d_1 y)] \quad (13)$$

Substituting the buckling mode into the differential equation, the real positive quantities c_1 and d_1 are found to be functions of the applied load in the form

$$c_1 = [M_1^2 + \pi M_1 \sigma^{1/2}]^{1/2}, \quad d_1 = [-M_1^2 + \pi M_1 \sigma^{1/2}]^{1/2} \quad (14)$$

where $\sigma > (M_1^2/\pi^2) = (m_1 B/L)^2$. Further, by defining $w_1(y=1) = \xi_1$, the quantity ξ_1 can be considered as the amplitude of the antisymmetric buckling mode at the middle of the free edge normalized with respect to the plate thickness. Substituting $w_1(x,y)$ into the two boundary conditions at the free edge $y = 1$, one obtains

$$\begin{aligned}
&(c_1^2 - \nu M_1^2)[\sinh(c_1)]A_1 + (d_1^2 + \nu M_1^2)[-\sin(d_1)]B_1 = 0 \\
&(c_1)[c_1^2 - (2-\nu) M_1^2][\cosh(c_1)]A_1 \\
&\quad + (d_1)[d_1^2 + (2-\nu) M_1^2][-\cos(d_1)]B_1 = 0
\end{aligned} \quad (15)$$

Since the first principal minor is always positive, the condition for buckling is that the determinant should vanish, that is (using $c_1^2 - d_1^2 = 2M_1^2$),

$$(-d_1)(c_1^2 - \nu M_1^2)^2 \tanh(c_1) + (c_1)(d_1^2 + \nu M_1^2)^2 \tan(d_1) = 0 \quad (16)$$

Symmetric Mode (Clamped at $y=0$). Similarly, the symmetric mode that satisfies the boundary conditions at the loaded edges $x = 0$ and $x = L/B$ and at the intersecting edge $y = 0$ can be written in the separable form $w_2(x,y) = w_2(y) \sin(M_2 x)$ where $M_2 = m_2 \pi B/L$ and

$$\begin{aligned}
w_2(y) = (\xi_2)\Big\{ &A_2[\cos(d_2 y) - \cosh(c_2 y)] \\
&+ B_2[\sin(d_2 y) - (d_2/c_2)\sinh(c_2 y)]\Big\}
\end{aligned} \quad (17)$$

In the foregoing, the positive real quantities c_2 and d_2 are obtained by replacing M_1 by M_2 in equations (14). By imposing $w_2(y=1) = \xi_2$, the quantity ξ_2 is the amplitude of the symmetric mode at the middle of the free edge normalized with respect to the plate thickness. The two boundary conditions at the free edge $y = 1$ yield (using $c_2^2 - d_2^2 = 2M_2^2$)

$$\begin{aligned}
&[-T\cos(d_2) - S \cosh(c_2)]A_2 \\
&\quad - [T\sin(d_2) + (d_2/c_2)S \sinh(c_2)]B_2 = 0 \\
&[Sd_2 \sin(d_2) - Tc_2 \sinh(c_2)]A_2 \\
&\quad - [Sd_2 \cos(d_2) + Td_2 \cosh(c_2)]B_2 = 0
\end{aligned} \quad (18)$$

where $S = c_2^2 - \nu M_2^2$ and $T = d_2^2 + \nu M_2^2$. The vanishing of the determinant yields (one should also check the vanishing of the first principal minor)

$$\begin{aligned}
2TS + (S^2 + T^2)\cos(d_2) \cosh(c_2) \\
= [(c_2^2 T^2 - d_2^2 S^2)/(c_2 d_2)]\sin(d_2) \sinh(c_2)
\end{aligned} \quad (19)$$

4 Second-Order Fields

Within the context of Koiter's theory of elastic stability, the postbuckling behavior requires the computation of the second-order fields w_{II} and f_{II} in addition to the buckling mode w_c and f_c. Since $f_c = 0$, the differential equation for w_{II} is identical to that for w_c so that w_{II} is identically zero due to the orthogonality requirement between w_c and w_{II}. The differential equation for the stress function f_{II} is

$$\begin{aligned}
&f_{II,xxxx} + f_{II,yyyy} + 2f_{II,xxyy} \\
&\quad = (2c)[(w_{c,xy})^2 - w_{c,xx} w_{c,yy}]
\end{aligned} \quad (20)$$

Substituting $w_c = w_1(x,y)$ into equation (20), the differential equation for f_{11} which corresponds to the antisymmetric mode is

$$\begin{aligned}
&f_{11,xxxx} + f_{11,yyyy} + 2f_{11,xxyy} \\
&= (cM_1^2)\Big\{ w_1(y),_y{}^2 + w_1(y) w_1(y),_{yy} \\
&\quad + [w_1(y),_y{}^2 - w_1(y) w_1(y),_{yy}]\cos(2M_1 x)\Big\}
\end{aligned} \quad (21)$$

Thus, the solution is of the separable form

$$f_{11}(x,y) = f_\alpha(y) + f_\beta(y)\cos(2M_1 x) \quad (22)$$

The ordinary differential equation for the $f_\alpha(y)$ problem is

$$f_\alpha(y),_{yyyy} = (cM_1^2)[w_1(y),_y{}^2 + w_1(y) w_1(y),_{yy}] \quad (23)$$

while for the $f_\beta(y)$ problem, one obtains

$$\begin{aligned}
&f_\beta(y),_{yyyy} - (8M_1^2) f_\beta(y),_{yy} + (16M_1^4) f_\beta(y) \\
&\quad = (cM_1^2)[w_1(y),_y{}^2 - w_1(y) w_1(y),_{yy}]
\end{aligned} \quad (24)$$

The in-plane boundary conditions at the free edge are $N_{xy}(y=1) = 0$ and $N_y(y=1) = 0$; that is,

$$f_{\beta,y}(y=1) = 0, \quad f_\beta(y=1) = 0 \quad (25)$$

Furthermore, there is no in-plane longitudinal shear at the intersecting edge $y = 0$ due to symmetry; that is, $N_{xy}(y=0) = 0$, which implies

$$f_{\beta,y}(y=0) = 0 \quad (26)$$

From symmetry considerations, the in-plane displacement in the y direction, V, vanishes at the intersecting edge $y = 0$. Since V is related to W and F by [16, 17]

$$\begin{aligned}
(-Eh)(V,_{XX} + W,_{XX} W,_Y) &= (F,_{YY}),_Y - \nu(F,_{XX}),_Y \\
&\quad + (2+2\nu)(F,_{XY}),_X
\end{aligned} \quad (27)$$

The foregoing boundary conditions imply

$$f_{\beta,yyy}(y=0) = 0, \quad f_{\alpha,yyy}(y=0) = 0 \quad (28)$$

At the two loaded edges $x = 0$ and $x = L/B$, it can be seen that the no shear condition $N_{xy} = 0$ is satisfied exactly by the separable form of the stress function. Imposing the condition that the average second-order longitudinal stress is zero at the loaded edge, one obtains

$$\int_{y=0}^{1} \Big\{ f_\alpha(y),_{yy} + f_\beta(y),_{yy} \Big\} dy = 0 \quad (29)$$

Furthermore, integrating both sides of the differential equation for $f_\alpha(y)$ twice, one obtains

$$f_\alpha(y),_{yy} = (cM_1^2/2) w_1(y)^2 + c_\alpha \quad (30)$$

where the constant of integration c_α is found from equation (29) to be

$$c_\alpha = -cM_1^2 H_1/2 \quad \text{and} \quad H_1 = \int_0^1 w_1(y)^2 \, dy \quad (31)$$

It will be shown that it is not necessary to compute $f_\alpha(y)$ nor $f_\alpha(y),_y$ since the postbuckling coefficient depends only on $f_\alpha(y),_{yy}$.

Closed-form solution for the $f_\beta(y)$ problem is sought as the sum of a particular solution and a homogeneous solution in the form

$$f_\beta(y) = P_\beta(y) + H_\beta(y) \quad (32)$$

where

$$\begin{aligned}
P_\beta(y) = e_0 &+ e_1 \sin(d_1 y) \sinh(c_1 y) \\
&+ e_2 \cos(d_1 y) \cosh(c_1 y)
\end{aligned}$$

Downloaded 02 May 2010 to 171.66.16.25. Redistribution subject to ASME license or copyright; see http://www.asme.org/terms/Terms_Use.cfm

$$H_\beta(y) = (s_1 + ys_2)\exp(2M_1 y) + (s_3 + ys_4)\exp(-2M_1 y) \quad (33)$$

Substituting the solution form into equation (24), the constants e_0, e_1, and e_2 which satisfy the differential equation exactly are

$$e_0 = (A_1^2 c_1^2 + B_1^2 d_1^2)c/(16M_1^2) \quad (34)$$

and e_1 and e_2 can be determined from

$$\begin{bmatrix} E_{11} & E_{12} \\ E_{21} & E_{22} \end{bmatrix} \begin{bmatrix} e_1 \\ e_2 \end{bmatrix} = \begin{bmatrix} E_1 \\ E_2 \end{bmatrix} \quad (35)$$

In the foregoing,

$$(E_1, E_2) = (cM_1^2)(A_1 B_1)[d_1^2 - c_1^2, 2c_1 d_1]$$

$$E_{11} = E_{22} = (c_1^4 + d_1^4 - 6c_1^2 d_1^2) - (8M_1^2)(c_1^2 - d_1^2) + 16M_1^4 \quad (36)$$

$$E_{12} = (-1)E_{21} = (4c_1 d_1^3 - 4c_1^3 d_1) + 16c_1 d_1 M_1^2$$

Finally, the constants s_1, s_2, s_3, and s_4, which enable the total solution $P_\beta(y) + H_\beta(y)$ to satisfy the boundary conditions exactly, can be computed from

$$\begin{bmatrix} P+Q & -P+Q \\ (2M_1)(P-Q) & -(1+2M_1)P + (1-2M_1)Q \end{bmatrix} \begin{bmatrix} s_3 \\ s_4 \end{bmatrix} = \begin{bmatrix} Z_3 - (Z_5 + Z_6)P \\ Z_4 - P[2M_1 Z_5 + (1+2M)Z_6] \end{bmatrix} \quad (37)$$

where

$$P = \exp(2M_1), \quad Q = \exp(-2M_1)$$

and

$$Z_1 = -P_{\beta,y}(y=0), \quad Z_2 = -P_{\beta,yyy}(y=0)$$

$$Z_3 = -P_\beta(y=1), \quad Z_4 = -P_{\beta,y}(y=1)$$

$$Z_5 = [3Z_1/(4M_1)] - [Z_2/(16M_1^3)]$$

$$Z_6 = [Z_2/(8M_1^2)] - (Z_1/2) \quad (38)$$

The constants s_1 and s_2 can be determined from

$$s_1 = s_3 + Z_5, \quad s_2 = -s_4 + Z_6 \quad (39)$$

Similarly, the stress function $f_{22}(x,y)$, which corresponds to the symmetric mode, can be expressed in the separable form

$$f_{22}(x,y) = f_a(y) + f_b(y)\cos(2M_2 x) \quad (40)$$

The quantity $f_a(y)_{,yy}$ is found to be

$$f_a(y)_{,yy} = (cM_2^2/2)w_2(y)^2 + c_a \quad (41)$$

where

$$c_a = -cM_2^2 H_2/2 \quad \text{and} \quad H_2 = \int_0^1 w_2(y)^2\, dy \quad (42)$$

The differential equation and the boundary conditions for $f_b(y)$ are identical to that presented for $f_\beta(y)$ by replacing $f_\beta(y)$, $w_1(y)$, and M_1 by $f_b(y)$, $w_2(y)$, and M_2, respectively. Again, exact solution for $f_b(y)$ is sought in the form

$$f_b(y) = P_b(y) + H_b(y) \quad (43)$$

where $H_b(y)$ and $H_\beta(y)$ have the same form and

$$P_b(y) = k_0 + k_1 \sin(d_2 y)\cosh(c_2 y) + k_2 \cos(d_2 y)\cosh(c_2 y) + k_3 \sin(d_2 y)\cosh(c_2 y) + k_4 \cos(d_2 y)\sinh(c_2 y) \quad (44)$$

The constant k_0 is found to be

$$k_0 = [(d_2^2 - c_2^2)(A_2)^2 + 2d_2^2(B_2)^2]c/(16M_2^2) \quad (45)$$

and k_1, k_2, k_3, and k_4 can be obtained from

$$\begin{bmatrix} R_{11} & R_{12} \\ R_{21} & R_{22} \end{bmatrix} \begin{bmatrix} k_1 \\ k_2 \end{bmatrix} = (cM_2^2) \begin{bmatrix} 2c_2 d_2 A_2^2 + [c_2 d_2 - (d_2^3/c_2)]B_2^2 \\ -2d_2^2 B_2^2 - (d_2^2 - c_2^2)(A_2)^2 \end{bmatrix}$$

$$\begin{bmatrix} R_{11} & R_{12} \\ R_{21} & R_{22} \end{bmatrix} \begin{bmatrix} k_3 \\ k_4 \end{bmatrix} = (cM_2^2)(A_2 B_2) \begin{bmatrix} d_2^2 + c_2^2 \\ -c_2 d_2 - (d_2^3/c_2) \end{bmatrix} \quad (46)$$

where

$$R_{11} = R_{22} = c_2^4 + d_2^4 - 6c_2^2 d_2^2 - (8M_2^2)(c_2^2 - d_2^2) + 16M_2^4$$

$$R_{12} = (-1)R_{21} = 4c_2 d_2^3 - 4c_2^3 d_2 + 16c_2 d_2 M_2^2 \quad (47)$$

The constants s_1, s_2, s_3, and s_4 for the homogeneous solution $H_b(y)$ can be obtained from equations (37)–(39) by replacing M_1 and $P_\beta(y)$ by M_2 and $P_b(y)$, respectively.

Finally, the compatibility equation for the second-order stress function f_{12}, which corresponds to the interaction between the antisymmetric and the symmetric mode, is

$$f_{12,xxxx} + f_{12,yyyy} + 2f_{12,xxyy} = (c)[2w_{1,xy}w_{2,xy} - w_{1,xx}w_{2,yy} - w_{1,yy}w_{2,xx}] \quad (48)$$

The solution $f_{12}(x,y)$ can be written in the separable form (letting $M_1 = M_2 = M$ which is valid only for short columns $L/B < 2.3$)

$$f_{12}(x,y) = f_A(y) + f_B(y)\cos(2Mx) \quad (49)$$

In a similar manner, one obtains

$$f_A(y)_{,yy} = (cM^2/2)w_1(y)w_2(y) + c_A$$

where

$$c_A = -cM^2 H_3/2 \quad \text{and} \quad H_3 = \int_0^1 w_1(y)w_2(y)\, dy \quad (50)$$

The differential equation for $f_B(y)$ is

$$f_B(y)_{,yyyy} - (8M^2)f_B(y)_{,yy} + (16M^4)f_B(y) = (M^2)[2w_1(y)_{,y}w_2(y)_{,y} - w_1(y)w_2(y)_{,yy} - w_1(y)_{,yy}w_2(y)] \quad (51)$$

and the boundary conditions for $f_B(y)$ are identical to those applicable for $f_\beta(y)$ presented earlier. Closed-form solution for $f_B(y)$ is obtained in the form

$$f_B(y) = P_B(y) + H_B(y) \quad (52)$$

where $H_B(y)$ has the same form as $H_\beta(y)$ and the exact solution for $P_B(y)$ is

$$P_B(y) = a_1 \cosh(c_1 y)\sin(d_2 y) + a_2 \sinh(c_1 y)\cos(d_2 y) + a_3 \cosh(c_1 y)\cos(d_2 y) + a_4 \sinh(c_1 y)\sin(d_2 y) + a_5 \cosh(c_1 y)\sinh(c_2 y) + a_6 \sinh(c_1 y)\cosh(c_2 y)$$

Downloaded 02 May 2010 to 171.66.16.25. Redistribution subject to ASME license or copyright; see http://www.asme.org/terms/Terms_Use.cfm

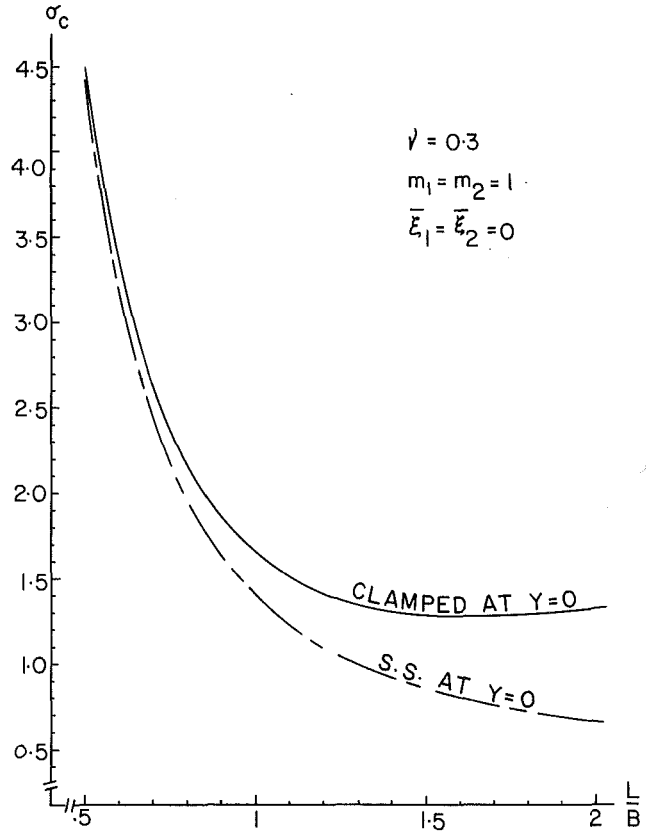


Fig. 2 Antisymmetric and symmetric buckling loads versus the aspect ratio for Poisson's ratio of 0.3

$$+a_7\cosh(c_1y)\cosh(c_2y)+a_8\sinh(c_1y)\sinh(c_2y)$$
$$+a_9\cos(d_1y)\sin(d_2y)+a_{10}\sin(d_1y)\cos(d_2y)$$
$$+a_{11}\cos(d_1y)\cos(d_2y)+a_{12}\sin(d_1y)\sin(d_2y) \quad (53)$$
$$+a_{13}\cos(d_1y)\sinh(c_2y)+a_{14}\sin(d_1y)\cosh(c_2y)$$
$$+a_{15}\cos(d_1y)\cosh(c_2y)+a_{16}\sin(d_1y)\sinh(c_2y)$$

For brevity, the lengthy expressions for the coefficients $a_1, a_2, \ldots a_{16}$ and $s_1, \ldots s_4$ will not be shown here. The solutions $f_\beta(y)$, $f_b(y)$, and $f_B(y)$ are verified independently by discretizing the differential equations using a central finite difference scheme with 101 integration points from $y=0$ to $y=1$.

5 Postbuckling Behavior

For a plate, the cubic terms of the potential energy vanish identically so that the potential energy of the present two-mode stability problem is [13]

$$P.E.=\Big\{(C_{40}\xi_1^4+C_{04}\xi_2^4+C_{22}\xi_1^2\xi_2^2)+(C_{31}\xi_1^3\xi_2+C_{13}\xi_1\xi_2^3)$$
$$+(D_1/2)[1-(\sigma/\sigma_1)]\xi_1^2+(D_2/2)[1-(\sigma/\sigma_2)]\xi_2^2$$
$$-(\sigma/\sigma_1)\bar{\xi}_1\xi_1D_1-(\sigma/\sigma_2)\bar{\xi}_2\xi_2D_2\Big\}.\ \text{constant} \quad (54)$$

In the foregoing, σ_1 and σ_2 are the classical buckling load (of the perfect system) of the antisymmetric and symmetric modes and $\bar{\xi}_1$ and $\bar{\xi}_2$ are the amplitudes of the geometric imperfections in the shapes of these two modes, respectively. The postbuckling coefficients C_{40}, C_{04}, C_{22}, C_{31}, and C_{13} are [18]

$$C_{40}=(1/4)\sigma_{11}\bullet I_2(u_1)=(1/4)\int_0^1\int_0^{L/B}[f_{11,yy}(w_{1,x})^2$$
$$+f_{11,xx}(w_{1,y})^2-2f_{11,xy}(w_{1,x}w_{1,y})]dxdy$$
$$C_{04}=(1/4)\sigma_{22}\bullet I_2(u_2)$$
$$C_{22}=(1/4)\sigma_{11}\bullet I_2(u_2)+(1/4)\sigma_{22}\bullet I_2(u_1)$$
$$+\sigma_{12}\bullet I_{11}(u_1,u_2) \quad (55)$$
$$C_{31}=(1/2)\sigma_{12}\bullet I_2(u_1)+(1/2)\sigma_{11}\bullet I_{11}(u_1,u_2)$$
$$C_{13}=(1/2)\sigma_{12}\bullet I_2(u_2)+\sigma_{22}\bullet I_{11}(u_1,u_2)$$

where, for example,

$$\sigma_{12}\bullet I_{11}(u_1,u_2)=\int_0^1\int_0^{L/B}[f_{12,yy}(w_{1,x}w_{2,x})+f_{12,xx}(w_{1,y}w_{2,y})$$
$$-f_{12,xy}(w_{1,x}w_{2,y}+w_{1,y}w_{2,x})]\,dxdy \quad (56)$$

Further, the positive quantities D_1 and D_2 are defined to be

$$D_1=(-1)f_{0,yy}(\text{at}\quad\sigma=\sigma_1)\int_0^1\int_0^{L/B}(w_{1,x})^2dx\,dy$$
$$D_2=(-1)f_{0,yy}(\text{at}\quad\sigma=\sigma_2)\int_0^1\int_0^{L/B}(w_{2,x})^2dx\,dy \quad (57)$$

Minimizing the potential energy with respect to the amplitudes of the buckling modes ξ_1 and ξ_2, the two equilibrium equations are

$$b_1\xi_1^3+b_{12}\xi_1\xi_2^2+C_{311}\xi_1^2\xi_2+C_{131}\xi_2^3$$
$$+[1-(\sigma/\sigma_1)]\xi_1=(\sigma/\sigma_1)\bar{\xi}_1$$
$$b_2\xi_2^3+b_{21}\xi_1^2\xi_2+C_{312}\xi_1^3+C_{132}\xi_1\xi_2^2$$
$$+[1-(\sigma/\sigma_2)]\xi_2=(\sigma/\sigma_2)\bar{\xi}_2 \quad (58)$$

where

$$b_1=4C_{40}/D_1\quad b_2=4C_{04}/D_2,\quad b_{12}=2C_{22}/D_1,$$
$$b_{21}=2C_{22}/D_2$$
$$C_{311}=3C_{31}/D_1\quad C_{131}=C_{13}/D_1,\quad C_{312}=C_{31}/D_2,$$
$$C_{132}=3C_{13}/D_2 \quad (59)$$

In computing these postbuckling coefficients, integration in the axial x direction can be carried out analytically while integration in the y direction is performed by computing the area using Simpson's rule.

As a check on the preceding coefficients, it can be seen that the foregoing two equilibrium equations agree with those presented by Byskov and Hutchinson [8, 18-20],

$$b_{1111}\xi_1^3+(b_{1221}+b_{2121}+b_{2211})\xi_1\xi_2^2+(b_{1121}+b_{1211}$$
$$+b_{2111})\xi_1^2\xi_2+b_{2221}\xi_2^3+[1-(\sigma/\sigma_1)]\xi_1=(\sigma/\sigma_1)\bar{\xi}_1$$
$$b_{2222}\xi_2^3+(b_{1122}+b_{1212}+b_{2112})\xi_1^2\xi_2+b_{1112}\xi_1^3$$
$$+(b_{1222}+b_{2122}+b_{2212})\xi_1\xi_2^2+[1-(\sigma/\sigma_2)]\xi_2=$$
$$(\sigma/\sigma_2)\bar{\xi}_2 \quad (60)$$

where

$$b_{ijkJ}=[\sigma_J\bullet I_{11}(u_j,u_k)+\sigma_{ij}\bullet I_{11}(u_k,u_J)]/(2D_J) \quad (61)$$

It should be noted in the isotropic plate buckling problem, $\sigma_J\bullet I_{11}(u_j,u_k)$ is zero.

In the present two-mode stability problem, it is found that $C_{13}=C_{31}=0$. For a column with a purely symmetric imperfection ($\bar{\xi}_1=0$ and $\bar{\xi}_2\neq0$), the equilibrium path will follow the mode shape of a symmetric mode until the applied load is sufficiently large such that it will intersect the stability boundary and thus, bifurcation into the antisymmetric mode will occur. This equilibrium path is governed by

Downloaded 02 May 2010 to 171.66.16.25. Redistribution subject to ASME license or copyright; see http://www.asme.org/terms/Terms_Use.cfm

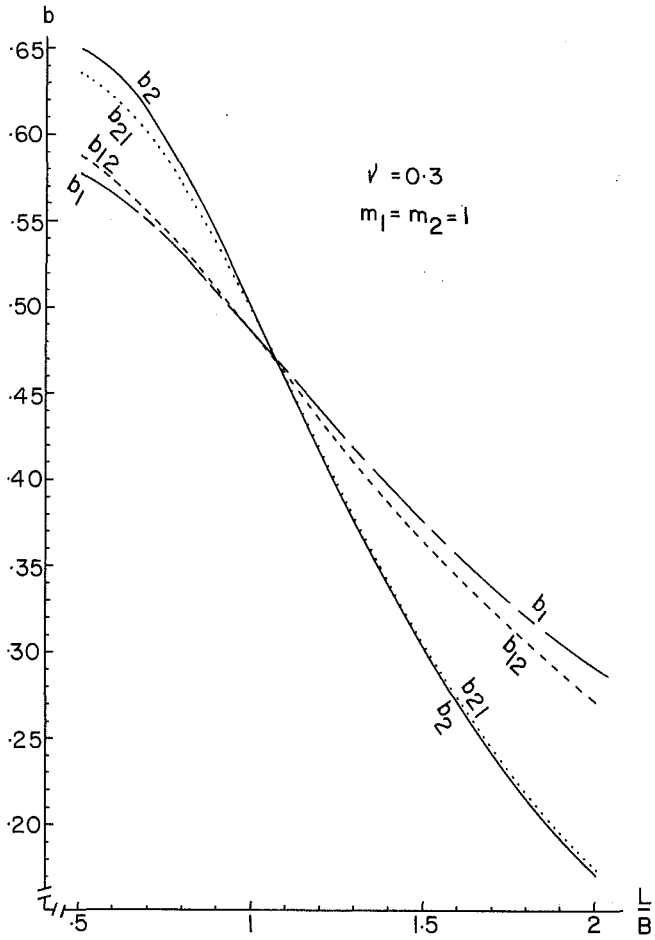


Fig. 3 The b_1, b_2, and b_{22} coefficients versus the aspect ratio for Poisson's ratio of 0.3

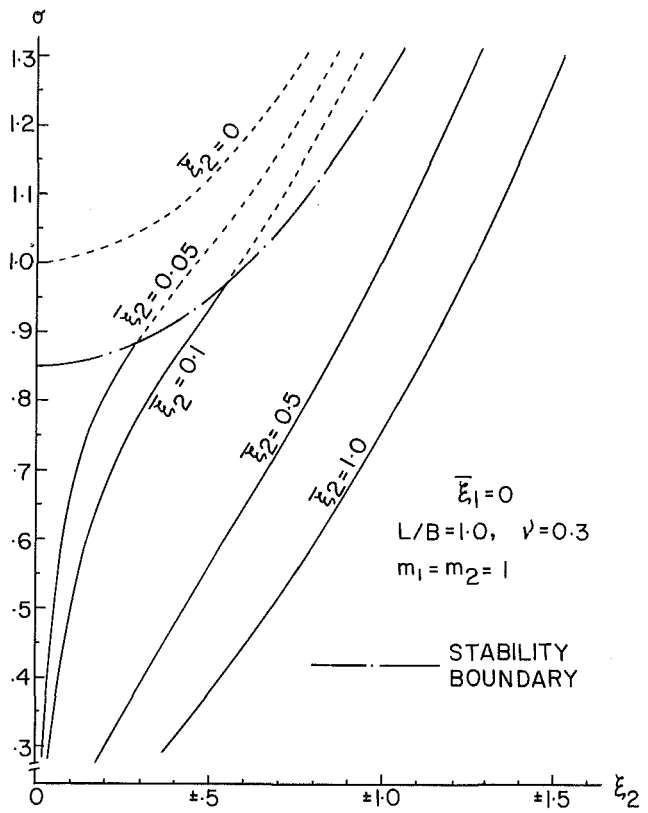


Fig. 4 Equilibrium paths of a symmetrically imperfect column with $L/B = 1.0$ and $\nu = 0.3$

$$b_2\xi_2^3 + [1-(\sigma/\sigma_2)]\xi_2 = (\sigma/\sigma_2)\bar{\xi}_2 \tag{62}$$

and the stability boundary is specified by

$$b_{12}\xi_2^2 + [1-(\sigma/\sigma_1)] = 0 \tag{63}$$

Note that this particular problem is independent of the b_1 and b_{21} coefficients.

6 Discussion of Results

Figure 2 shows a graph of the buckling load versus the aspect ratio of the plate L/B where Poisson's ratio is $\nu = 0.3$. Within the range of the values of L/B being 0.5 and 2, the classical buckling loads σ_1 and σ_2 correspond to one half sine-wave in the longitudinal direction ($m_1 = m_2 = 1$). It can be seen that the symmetric mode (clamped at $y = 0$) has a higher buckling load than the antisymmetric mode (simply supported at $y = 0$). The difference between these two buckling loads becomes smaller for shorter columns.

Figure 3 shows a plot of the postbuckling coefficients b_1, b_2, b_{12} and b_{21} versus the aspect ratio of the plate. It can be seen that all these coefficients are found to be positive so that the postbuckling problem is stable. That is, buckling will not be associated with the loss of the carrying capacity of the structure, at least in the initial postbuckling regime. These coefficients become more positive for shorter columns. It should be noted that C_{13} and C_{31} vanish for the present range of L/B being considered.

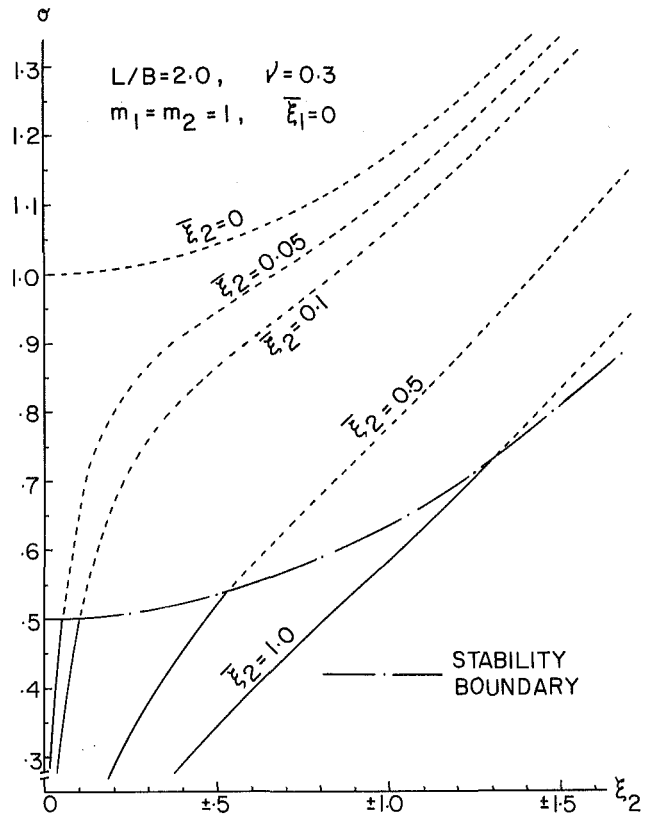


Fig. 5 Equilibrium paths of a symmetrically imperfect column with $L/B = 2.0$ and $\nu = 0.3$

Downloaded 02 May 2010 to 171.66.16.25. Redistribution subject to ASME license or copyright; see http://www.asme.org/terms/Terms_Use.cfm

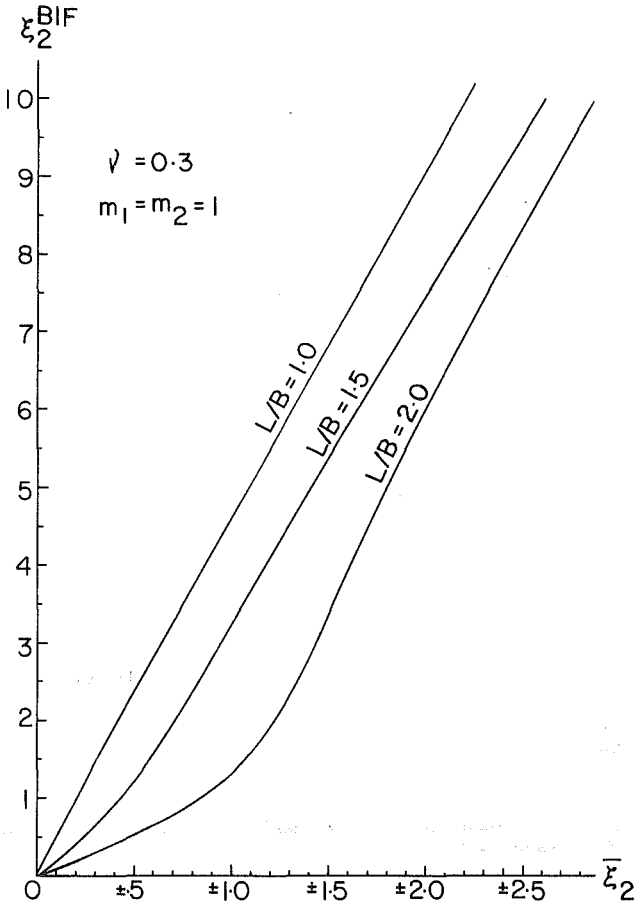


Fig. 6 Amplitude of the symmetric mode (at which bifurcation into the antisymmetric mode just occurs) versus amplitude of the symmetric imperfection

The aim of the present study is to examine the possibility of introducing a geometric imperfection in the shape of the symmetric mode so that the structure will follow the equilibrium path of this mode in the initial postbuckling regime as well as in the very large deflection stage. Thus, it is of interest to examine the equilibrium path of the column with $\bar{\xi}_1 = 0$ and $\bar{\xi}_2 \neq 0$. Figure 4 shows a graph of the applied load versus the amplitude of the symmetric mode ξ_2 for $L/B = 1$ and $\nu = 0.3$, where $\sigma_1/\sigma_2 = (1.4016/1.6525) = 0.8481$, $b_2 = 0.500$, and $b_{12} = 0.4835$. The structure is assumed to be loaded from zero so that the solid lines are of physical significance while the dotted lines are unstable equilibrium paths (physically unattainable in general). As the applied load is increased the stable equilibrium paths of an imperfect system will eventually intersect the stability boundary, at which bifurcation into the antisymmetric mode will occur.

Figure 5 shows the equilibrium path of an imperfect column ($\bar{\xi}_1 = 0$ and $\bar{\xi}_2 \neq 0$) for $L/B = 2$ and $\nu = 0.3$ where $\sigma_1/\sigma_2 = (0.6681/1.3360) = 0.500$, $b_2 = 0.1716$ and $b_{12} = 0.2719$. Since both the b_2 and b_{12} coefficients for $L/B = 2$ are smaller than those for $L/B = 1$, the perfect path $\bar{\xi}_2 = 0$ and the stability boundary opens wider. Thus, a larger value of the imperfection amplitude $\bar{\xi}_2$ is needed to avoid bifurcation into the antisymmetric mode. Note that the present Koiter-type analysis is valid only for sufficiently small values of the imperfection amplitude. However, the initial postbuckling behavior is crucial in determining the final collapse mode.

Figure 6 depicts a graph of the value of the amplitude of the symmetric mode (at which bifurcation into the antisymmetric mode just occurs) versus the symmetric imperfection amplitude $\bar{\xi}_2$ for aspect ratio L/B being 1.0, 1.5, and 2.0. As predicted from Fig. 4, a larger value of $\bar{\xi}_2$ is needed to achieve a symmetric mode shape with $\xi_2 = 10.0$ without bifurcation into the antisymmetric mode. For $L/B = 1.5$, it is found that $\sigma_1/\sigma_2 = (0.8578/1.2912) = 0.6643$, $b_2 = 0.3031$ and $b_{12} = 0.3633$.

7 Concluding Remarks

The two-mode stability problem which involved the antisymmetric and the symmetric modes for a short, thin-walled, geometrically imperfect column has been investigated. The postbuckling coefficients of this two nonsimultaneous mode problem are computed. It appears from the equilibrium paths that it is possible to introduce a geometric imperfection in the shape of a symmetric mode so that the equilibrium paths will follow the shape of a symmetric mode in the postbuckling as well as in the large deflection regimes. This design is particularly beneficial from the energy absorption point of view since the symmetric mode has a much higher energy absorption than the antisymmetric mode.

Finally, the plastic collapse analysis of short, imperfect thin-walled angled columns (taking into account plastic deformation in the postbuckling range) will be examined in a separate paper.

Acknowledgment

The author would like to thank Tomasz Wierzbicki (Professor, Department of Ocean Engineering, M.I.T.) for his comments on this work and constant encouragement.

References

1 Wierzbicki, T., Akerstrom, T., and Jernstrom, C., "Shape Optimization of Sheet Metal Structures Against Crash," *Proceedings of the 4th Vehicle Structural Mechanics (V.S.M.) Conference*, Detroit, Nov. 18-20, 1981 (also M.I.T. Dept. of Ocean Engineering Report 81-10, July, 1981).

2 Wierzbicki, T., " 'On the Formation and Growth of Folding Modes,' Collapse: The Buckling of Structures in Theory and Practice," *Proceedings of IUTAM Symposium*, Thompson, J. M.T., and Hunt, G. W., eds., August 1982, Cambridge University Press, 1983.

3 Wierzbicki, T., and Abramowicz, W., "On the Crushing Mechanics of Thin-Walled Structures," ASME JOURNAL OF APPLIED MECHANICS, Vol. 50, 1983, pp. 727-734.

4 Wierzbicki, T., "On the Crushing Mechanics of Thin-Walled Structures," ASME JOURNAL OF APPLIED MECHANICS, Vol. 50, 1983, pp. 727-734.

5 Van der Neut, A., "The Interaction of Local Buckling and Column Failure of Thin-Walled Compression Members," *Proceedings of the 12th International Congress of Applied Mechanics*, held at Stanford University, Springer-Verlag, 1969, pp. 389-399.

6 Van der Neut, A., "Mode Interaction With Stiffened Panels," *Proceedings of the IUTAM International Symposium on Buckling of Structures*, Budiansky, B., ed., Springer, New York, 1976, pp. 365-382.

7 Koiter, W. T., and Kuiken, G. D. C., "The Interaction Between Local Buckling and Overall Buckling on the Behaviour of Built-Up Columns," Delft University of Technology, WTHD 23, May 1971, 26 pp.

8 Byskov, E., " 'An Asymptotic Expansion Applied to Van der Neut's Column,' Collapse: The Buckling of Structures in Theory and Practice," *Proceedings of IUTAM Symposium*, Thompson, J. M. T., and Hunt, G. W., eds., Cambridge University Press, 1983 (also Technical University of Denmark DCAMM Report #251, October 1982).

9 Graves Smith, T. R., "The Ultimate Strength of Locally Buckled Columns of Arbitrary Length," *Thin-Walled Steel Structures, Their Design and Use in Building*, Rockey, K. C., and Hill, H. V., eds., Crosby Lockwood, 1967, pp. 35-60.

10 Graves Smith, T. R., "The Local Collapse of Elastic Thin Walled Columns," *Journal of Structural Mechanics*, Vol. 8, No. 4, 1980, pp. 471-489.

11 Grimaldi, A., and Pignataro, M., "Postbuckling Behavior of Thin-Walled Open Cross-section Compression Members," *Journal of Structural Mechanics*, Vol. 7, No. 2, 1979, pp. 143-159.

12 Bridget, F. J., Jerome, C. C., and Vosseler, A. B., "Some New Ex-

Downloaded 02 May 2010 to 171.66.16.25. Redistribution subject to ASME license or copyright; see http://www.asme.org/terms/Terms_Use.cfm

periments on Thin-Wall Construction," *ASME Transactions*, Vol. 56, 1934, pp. 569–578.

13 Koiter, W. T., "On the Stability of Elastic Equilibrium," Doctoral *Thesis, Delft, Amsterdam, 1945*; English Translations: NASA-TT-F10, 833, 1967 and AFFDL-TR-70-25, 1970.

14 Hui, D., and Hansen, J. S., "Two-Mode Buckling of an Elastically Supported Plate and Its Relation to Catastrophe Theory," ASME JOURNAL OF APPLIED MECHANICS, Vol. 47, 1980, pp. 607–612.

15 Timoshenko, S. P., and Gere, J. M., *Theory of Elastic Stability*, McGraw-Hill, New York, 1961.

16 Tvergaard, V., "Imperfection-Sensitivity of a Wide Integrally Stiffened Panel under Compression," *International Journal of Solids and Structures*, Vol. 9, 1973, pp. 177–192.

17 Hui, D., Tennyson, R. C., and Hansen, J. S., "Mode Interaction of Axially Stiffened Cylindrical Shells: Effects of Stringer Axial Stiffness, Torsional Rigidity, and Eccentricity," ASME JOURNAL OF APPLIED MECHANICS, Vol. 48, 1981, pp. 915–922.

18 Byskov, E., and Hutchinson, J. W., "Mode Interaction in Axially Stiffened Cylindrical Shells," *AIAA Journal*, Vol. 15, July, 1977, pp. 941–948.

19 Olesen, J. F., and Byskov, E., "Accurate Determination of Asymptotic Postbuckling Stresses by the Finite Element Method," Danish Center for Applied Math and Mechanics DCAMM Report No. 215, July, 1981.

20 Budiansky, B., and Hutchinson, J. W., "Dynamic Buckling of Imperfection-Sensitive Structures," *Proceedings of the 11th International Congress of Applied Mechanics*, Gortler, H., ed., Munich, 1964, Springer-Verlag, 1966, pp. 634–651.

Downloaded 02 May 2010 to 171.66.16.25. Redistribution subject to ASME license or copyright; see http://www.asme.org/terms/Terms_Use.cfm

Analysis of Clamped Plates on Elastic Foundation by the Boundary Integral Equation Method[1]

J. T. Katsikadelis
Lecturer,
Institute of Structural Analysis,
National Technical University
of Athens,
Athens, Greece

A. E. Armenàkas[2]
Professor of Aerospace Engineering,
Polytechnic Institute of New York,
Mem. ASME

In this investigation the boundary integral equation (BIE) method with numerical evaluation of the boundary integral equations is developed for analyzing clamped plates of any shape resting on an elastic foundation. A numerical technique for the solution to the boundary integral equations is presented and numerical results are obtained and compared with those existing from analytical solutions. The effectiveness of the BIE method is demonstrated.

1 Introduction

To the authors' knowledge, the boundary value problems which have been treated by the BIE method are governed by the following differential equations [1–5]:

(*a*) The Laplace or Poisson equation

(*b*) The Navier equations of equilibrium for isotropic and anisotropic linearly elastic bodies

(*c*) The Navier equations of motion

(*d*) The biharmonic equation

(*e*) The Helmholz equation

(*f*) The diffusion equation

In this investigation, the BIE method is developed for the fourth-order differential equation governing the bending of a thin elastic plate resting on a Winkler's type elastic foundation. The plate is considered clamped at the boundary. However, the procedure presented herein can be extended to plates having other boundary conditions [5].

2 Formulation of the Problem

Consider a thin elastic plate of thickness h, occupying a two-dimensional region R, bounded by a curve C and resting on a linearly elastic Winkler's foundation with stiffness k (see Fig. 1). The region R may have holes, and the boundary may have a finite number of corners. The plate is subjected to a

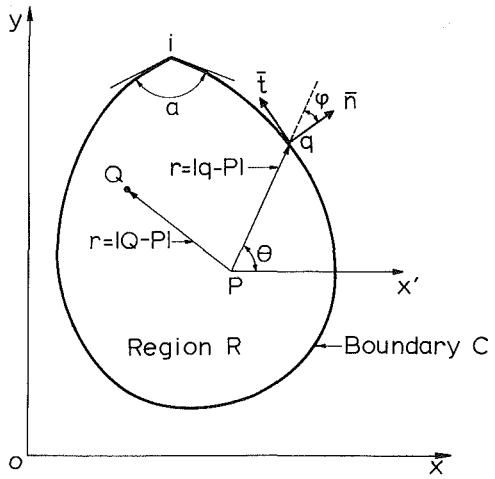


Fig. 1 Two-dimensional region *R* bounded by the curve *C*, occupied by the plate

transverse loading $f(P)$. Thus, its deflection $w(P)$ satisfies the following differential equation [6] at any point P inside the region R

$$Lw = f(P)/D \tag{1}$$

D is the flexural rigidity $[D = Eh^3/12(1-\nu^2)]$ of the plate, while the operator L is defined as

$$L = \nabla^4 + \kappa^2 \tag{2}$$

[1] Taken from the dissertation submitted to the Faculty of the Polytechnic Institute of New York in partial fulfillment of the requirements of the degree of Doctor of Philosophy, 1982.

[2] Also, Professor and Director of the Institute of Structural Analysis, National Technical University of Athens.

Contributed by the Applied Mechanics Division for presentation at the Winter Annual Meeting, New Orleans, La., December 9–14, 1984 of THE AMERICAN SOCIETY OF MECHANICAL ENGINEERS.

Discussion on this paper should be addressed to the Editorial Department, ASME, United Engineering Center, 345 East 47th Street, New York, N.Y. 10017, and will be accepted until two months after final publication of the paper itself in the JOURNAL OF APPLIED MECHANICS. Manuscript received by ASME Applied Mechanics Division, April, 1983; final revision November, 1983. Paper No. 84-WA/APM-6.

Copies will be available until August, 1985.

Copyright © 1984 by ASME
Downloaded 02 May 2010 to 171.66.16.25. Redistribution subject to ASME license or copyright; see http://www.asme.org/terms/Terms_Use.cfm

with

$$\nabla^4 = \frac{\partial^4}{\partial x^4} + 2\frac{\partial^4}{\partial x^2 \partial y^2} + \frac{\partial^4}{\partial y^4} \tag{3}$$

and

$$\kappa^2 = k/D \tag{4}$$

Moreover, the deflection w must satisfy the following boundary conditions on the clamped boundary C of the plate

$$w = 0, \quad \frac{\partial w}{\partial n} = 0 \tag{5}$$

where $\partial/\partial n$ denotes the directional derivative along the outward normal to the boundary.

The bending moments M_n and M_t, the twisting moment M_{nt} and the effective shearing force V_n acting on the boundary of the plate are related to the deflection w [5] by the following relations:

$$M_n = -D\nabla^2 w, \quad M_t = -D\nabla^2 w \tag{6a,b}$$

$$M_{nt} = 0, \qquad V_n = -D\frac{\partial}{\partial n}\nabla^2 w \tag{6c,d}$$

3 Fundamental Solution to the Differential Equation

Inasmuch as the operator L is self-adjoint, the fundamental solution to equation (1) is a singular particular solution of the following equation

$$Lv = \delta(P-Q)/D \tag{7}$$

where $\delta(P-Q)$ is the Dirac δ function, P is the field point, and Q is the source point.

The solution $v = v(P,Q)$ to equation (7) is a two-point function whose value does not change if points P and Q are interchanged. It represents the deflection, at point P, of an infinite plate resting on a linearly elastic foundation, subjected to a concentrated unit load at point Q or the deflection at point Q due to a unit concentrated load at point P. The function $v(P,Q)$ is axisymmetric with respect to the point where the concentrated force is applied, that is, it depends only on the radial distance from this point. Denoting the distance between points P and Q by $r = |P-Q|$, the solution to equation (7) is [6]

$$v = v(P,Q) = -\frac{l^2}{2\pi D} kei(\rho) \tag{8}$$

where the dimensionless coordinate ρ is defined as

$$\rho = r/l \tag{9}$$

and

$$l = \sqrt{1/\kappa} = \sqrt[4]{D/k} \tag{10}$$

$kei(\rho)$ is one of the zero-order Kelvin functions of the second kind—the other is $ker(\rho)$ [7]. They are related to the Bessel function K_0 by

$$K_0(\rho\sqrt{i}) = ker(\rho) + (i)kei(\rho), \quad (i = \sqrt{-1}) \tag{11}$$

From equation (8) it can be shown that

$$\nabla^2 v = -\frac{1}{2\pi D} ker(\rho), \quad \frac{\partial v}{\partial n} = -\frac{l}{2\pi D} kei'(\rho)\cos\varphi \tag{12a,b}$$

$$\frac{\partial}{\partial n}\nabla^2 v = -\frac{1}{2\pi l D} ker'(\rho)\cos\varphi \tag{12c}$$

where φ is the angle between $\mathbf{r}$ and $\mathbf{n}$ (see Fig. 1), and $(\ )'$ denotes differentiation of the Kelvin functions.

4 Integral Representation of the Solution

Consider two functions v and w that have continuous fourth-order derivatives inside a region R and third-order derivatives on its boundary C. The region may be simply or multiply connected while its boundary may be piecewise smooth. It can be shown that these functions satisfy the following relation [5], known as the Rayleigh-Green identity

$$\iint_R (v\nabla^4 w - w\nabla^4 v)\, d\sigma = \int_C \left[v\frac{\partial}{\partial n}\nabla^2 w - \frac{\partial v}{\partial n}\nabla^2 w - w\frac{\partial}{\partial n}\nabla^2 v + \frac{\partial w}{\partial n}\nabla^2 v \right] ds \tag{13}$$

By adding and subtracting the term $\iint_R \kappa^2 wv\, d\sigma$ to the left-hand side of equation (13) the following Green identity for the operator L is obtained

$$\iint_R [vLw - wLv] d\sigma = \int_C \left[v\frac{\partial}{\partial n}\nabla^2 w - \frac{\partial v}{\partial n}\nabla^2 w - w\frac{\partial}{\partial n}\nabla^2 v + \frac{\partial w}{\partial n}\nabla^2 v \right] ds \tag{14}$$

The fundamental solution to the differential equation (7) is chosen as the function v and the deflection of the middle surface of the plate is chosen as the function w. In this case $\partial w/\partial n$ represents the slope at the boundary of the plate, while $\nabla^2 w$ and $\partial/\partial n\ \nabla^2 w$ represent the bending moment and the effective shearing force, respectively, at the boundary of the plate multiplied by $-1/D$.

Substituting equation (7) into the Green identity (14) and taking into account the boundary conditions (5), the following integral representation for the deflection w is obtained

$$w(P) = \iint_R v(P,Q) f(Q)\, d\sigma_Q - D\int_C \left[v(P,q)\frac{\partial}{\partial n_q}\nabla^2 w(q) - \frac{\partial}{\partial n_q} v(P,q)\nabla^2 w(q) \right] ds_q \tag{15}$$

In the preceding relation, points inside the region R are denoted by Q or P, while points on the boundary C are denoted by q or p. Moreover, the subscript of the surface element $d\sigma$ and of the arc element ds denotes the point that varies during integration. Furthermore, $\partial/\partial n_q$ indicates that the normal derivative is taken at point q.

Using relations (8) and (12), relation (15) may be written as

$$w(P) = \iint_R v(P,Q) f(Q)\, d\sigma_Q - D\int_C v(P,q)\Psi(q) - \frac{\partial v(P,q)}{\partial n_q}\Phi(q)\, ds_q = \frac{l^2}{2\pi}[-F(P) + J_1(P) - J_2(P)] \tag{16}$$

where the following notation has been introduced for conciseness

$$\Phi(q) = \nabla^2 w(q), \quad \Psi(q) = \frac{\partial}{\partial n}\nabla^2 w(q) \tag{17a,b}$$

$$F(P) = \frac{1}{D}\iint_R f(Q) kei(\rho_{PQ})\, d\sigma_Q \tag{18}$$

$$J_1(P) = \int_C \Psi(q) kei(\rho_{Pq})\, ds_q \tag{19a}$$

$$J_2(P) = \int_C \Phi(q)\rho_{Pq} kei'(\rho_{Pq})\, d\theta_q \tag{19b}$$

$$\rho_{Pq} = r_{Pq}/l, \quad r_{Pq} = |P-q|, \quad \theta = \mathbf{x}, \hat{\mathbf{r}}.$$

In deriving relation (16) the following relation [5] has been used

$$\cos\varphi\, ds = r\, d\theta \tag{20}$$

Downloaded 02 May 2010 to 171.66.16.25. Redistribution subject to ASME license or copyright; see http://www.asme.org/terms/Terms_Use.cfm

5 Derivation of the Boundary Integral Equations

In equation (15) the loading function $f(Q)$ is given at every point in R. Moreover, the function $v(P,Q)$ is obtained from relation (8). However, the bending moment $M_n = -D\nabla^2 w$ and the effective shearing force $V_n = -D(\partial/\partial n)\nabla^2 w$ are not known on the points of the boundary C. In this section, two coupled boundary integral equations are derived from which these quantities can be established.

The first boundary integral equation is established from equation (16) by letting point P approach a point p on the boundary C. However, before passing the limit to the integrand of the line integrals in equation (16) their existence and continuity must be examined as $P \to p \epsilon C$. Moreover, if a line integral is not continuous as point P reaches the boundary, its jump must be established. The functions $kei(\rho)$ and $kei'(\rho)$ are not singular as $\rho \to 0$ [7]. Thus, the line integrals in equation (16) exist for $P \equiv p \epsilon C$ and they are continuous as $P \to p \epsilon C$ [5]. Consequently, the first boundary integral equation is

$$-\int_C \Phi(q)\rho_{pq} kei'(\rho_{pq})\, d\theta_q + \int_C \Psi(q) kei(\rho_{pq})\, ds_q = F(p) \tag{21}$$

The second boundary integral equation is derived by adhering to the following steps:

(*a*) The operator ∇^2 is applied to both sides of equation (16) yielding

$$-2\pi\nabla^2 w(P) = G(P) - \int_C \Psi(q) ker(\rho_{Pq})\, ds_q + \int_C \Phi(q)\rho_{Pq} ker'(\rho_{Pq})\, d\theta_q \tag{22}$$

where

$$G(P) = \frac{1}{D}\iint_R f(Q) ker(\rho_{PQ})\, d\sigma_Q \tag{23}$$

(*b*) The limits of both sides of equation (22) are established when point P approaches a point p on the boundary.

For small values of the argument ρ, the function $ker(\rho)$ behaves like $ln(\rho)$ [7]. Consequently, the first line integral on the right-hand side of equation (22) represents the logarithmic potential due to a mass distribution $\Psi(q)$ on the boundary C. This is a single-layer potential and, thus, the line integral exists and is continuous as $P \to p \epsilon C$ [8, 9]. Moreover, as $\rho \to 0$, the function $ker'(\rho)$ behaves like $1/\rho$ [7]. Consequently, the second integral on the right-hand side of equation (22) represents a double-layer potential due to a mass distribution $\Phi(q)$ on the boundary C. Hence, this integral exists when $P \to p \epsilon C$. However, it has a discontinuity as $P \to p \epsilon C$ [8, 9]. The jump of the singular line integral is obtained using the systematic procedure presented in reference [5]. It is equal to

$$\lim_{P\to p}\int_C \Phi(q) ker'(\rho_{Pq})\, d\theta_q - \int_C \Phi(q) ker'(\rho_{pq})\, d\theta_q = -(2\pi - \alpha)\Phi(p)$$

where α is the angle between the tangents at point p (see Fig. 1). If at point p the boundary is smooth $\alpha = \pi$. Thus, referring to equation (22) the second boundary integral equation is

$$-\alpha\Phi(p) - \int_C \Phi(q)\rho_{pq} ker'(\rho_{pq})\, d\theta_q + \int_C \Psi(q) ker(\rho_{pq})\, ds_q = G(p) \tag{24}$$

For any given geometry of the clamped boundary of the plate, the functions $\Phi(s)$ and $\Psi(s)$ may be obtained from the solution to the coupled boundary integral equations (21) and (24). In these equations, the terms F and G may be established from the given loading $f(Q)$. For certain types of loading such as concentrated forces or moments, F and G may be evaluated directly by representing the concentrated force by a δ-function and the concentrated moment by the derivative of the δ-function. For other types of loading, these quantities must be evaluated numerically. Once the functions Φ, Ψ are known, the solution to the boundary value problem (1) and (5) may be obtained from equation (16).

6 Numerical Analysis

The numerical integration of the boundary integral equations (21) and (24) can be carried out by dividing the boundary into a finite number of intervals referred to as boundary elements [4]. The end points of each interval are referred to as dividing points or interval points. The points on which the values of the unknown functions are evaluated are referred to as nodal points or nodes. The boundary can be approximated by straight line or curved line segments. On each interval, the unknown functions Φ and Ψ can be approximately considered either constant, or varying linearly or varying as polynomials of any desired degree, for example quadratic [10]. On intervals where a line integral of equations (21) and (24) becomes singular, its Cauchy principal value must be established using a process depending on the type of the singularity.

In this investigation the boundary is divided into M, not necessarily equal intervals, which are numbered consecutively clockwise. The centers of these intervals or other points near them are taken as their nodes (see Fig. 2). The values of the unknown functions are assumed constant on each interval (step function assumption). Moreover, the curved boundary is approximated by straight line segments.

Denoting by Φ_j and Ψ_j the values of Φ and Ψ on the j-element, equations (21) and (24) are transformed into the following set of $2M$ simultaneous linear algebraic equations

$$\mathbf{AY} = \mathbf{B} \tag{25}$$

where

$$\mathbf{Y}^T = [\Phi_1, \Phi_2 \ldots \Phi_M \mid \Psi_1, \Psi_2 \ldots \Psi_M]$$

$$\mathbf{B}^T = [F_1, F_2 \ldots F_M \mid G_1, G_2 \ldots G_M] \tag{26a,b}$$

$$\mathbf{A} = \left[\begin{array}{ccc|ccc} a_{11} & a_{12} & \ldots\ a_{1M} & b_{11} & b_{12} & \ldots\ b_{1M} \\ a_{21} & a_{22} & \ldots\ a_{2M} & b_{21} & b_{22} & \ldots\ b_{2M} \\ \vdots & \vdots & & \vdots & \vdots & \\ a_{M1} & a_{M2} & \ldots\ a_{MM} & b_{M1} & b_{M2} & \ldots\ b_{MM} \\ \hline c_{11}-\pi & c_{12} & \ldots\ c_{1M} & d_{11} & d_{12} & \ldots\ d_{1M} \\ c_{21} & c_{22}-\pi & \ldots\ c_{2M} & d_{21} & d_{22} & \ldots\ d_{2M} \\ \vdots & \vdots & & \vdots & \vdots & \\ c_{M1} & c_{M2} & \ldots\ c_{MM}-\pi & d_{M1} & d_{M2} & \ldots\ d_{MM} \end{array}\right] \tag{27}$$

and

$$a_{kj} = -\int_j \rho_{kj} kei'(\rho_{kj})\, d\theta_q, \quad b_{kj} = \int_j kei(\rho_{kj})\, ds_q \tag{28a,b}$$

$$c_{kj} = -\int_j \rho_{kj} ker'(\rho_{kj})\, d\theta_q, \quad d_{kj} = \int_j ker(\rho_{kj})\, ds_q \tag{28c,d}$$

$$F_k = \frac{1}{D}\iint_R f(Q) kei(\rho_{kQ})\, d\sigma_Q \tag{29a}$$

Downloaded 02 May 2010 to 171.66.16.25. Redistribution subject to ASME license or copyright; see http://www.asme.org/terms/Terms_Use.cfm

$$G_k = \frac{1}{D}\iint_R f(Q)\,ker(\rho_{kQ})\,d\sigma_Q \tag{29b}$$

where

$\rho_{kj} = |p_k - q|/l, \quad \rho_{kQ} = |p_k - Q|/l,$

$Q \epsilon R, \quad p_k \epsilon C, \quad q \epsilon j$-element

In relations (28), the symbol $\int_j$ denotes the line integral over the j-element; point p_k is a nodal point.

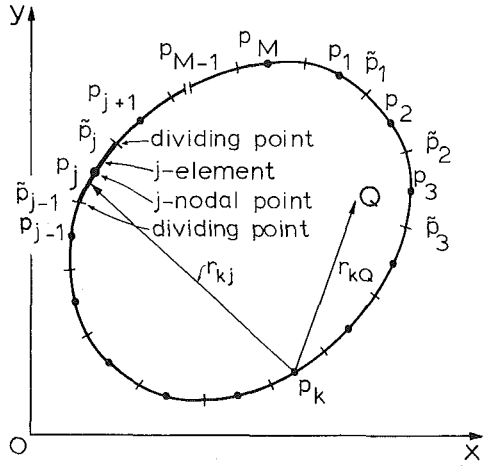


Fig. 2 Discretization of the boundary

When $k \neq j$ ($\rho \neq 0$) the line integrals (28) are not singular and since the middle point of the arc $\tilde{p}_{j-1}\tilde{p}_j$ cannot always be readily established their value is approximated using the following formula [5]:

$$I = \int_j g(s)\,ds \simeq \frac{1}{6s_1s_2}\,[(g_0 - g_1)s_2^3 + (g_0 - g_2)s_1^3 + s_1^2 s_2(2g_1 + 3g_0 + g_2) + s_1 s_2^2(g_1 + 3g_0 + 2g_2)] \tag{30}$$

where g_1, g_0, g_2 are the values of the integrand $g(s)$ at points $\tilde{p}_{j-1}, p_j, \tilde{p}_j$, respectively (see Fig. 2). Moreover, s_1 and s_2 are the distances $\tilde{p}_{j-1}, p_j$ and $p_j, \tilde{p}_j$, respectively [i.e., $s_1 = |\tilde{p}_{j-1} - p_j|$, $s_2 = |p_j - \tilde{p}_j|$]. When $s_1 = s_2$, formula (30) reduces to Simpson's rule.

When $k = j$ (ρ becomes zero for $p = q$) it can be shown [5, 7] that the integrals a_{kk}, b_{kk}, and c_{kk} are not singular and consequently they are evaluated using formula (30). Moreover, the integral d_{kk} can be written as

$$d_{kk} = \int_k ker(\rho)\,ds = \int_k [ker(\rho) + ln(\rho)]\,ds - \int_k ln(\rho)\,ds \tag{31}$$

It can be shown [5] that the first integral on the right-hand side of equation (31) is not singular and consequently it can be evaulated using formula (30). The second integral is evaluated [11] on the straight lines connecting the pairs of points $\tilde{p}_{j-1}, p_j$ and $p_j, \tilde{p}_j$. Thus,

$$\int_k ln(\rho)\,ds = [s_1(ln\rho_1 - 1) + s_2(ln\rho_2 - 1)] \tag{32}$$

where $\rho_1 = s_1/l$ and $\rho_2 = s_2/l$.

The surface integral G_k is a double improper integral, $\lim_{\rho \to 0} [ker(\rho)] = \infty$, and consequently, its numerical evaluation is a difficult task. In this investigation this integral is evaluated by a method proposed in reference [12]. In this method, the singularity of the integrand is removed by a coordinate transformation and, subsequently, the region R is divided into M sectors each having the point of singularity (point p_k) as vertex and a boundary element as base. On each sector, the integral is evaluated by techniques applicable to double integrals with regular integrand. The value of the integral on the region R is obtained as the sum of the values of the integrals evaluated on the sectors.

The integral F_k is not singular and, consequently, it can be evaluated using any technique for the evaluation of double integrals [13]. However, because its integrand exhibits a finite peak at $\rho = 0$, it was found more convenient to employ the method used for the evaluation of the integral G_k.

When the plate is subjected to a concentrated force P, acting at some point Q_0, the loading function $f(Q)$ can be represented as

$$f(Q) = P\delta(Q - Q_0) \tag{33}$$

where $\delta(Q - Q_0)$ is the Dirac δ-function. Using relation (33) the values of the integrals (18) and (23) are

$$F_k = \frac{1}{D}\iint_R P\delta(Q - Q_0)\,kei(\rho_{kQ})\,d\sigma_Q = \frac{P}{D}\,kei(\rho_{kQ_0}) \tag{34}$$

$$G_k = \frac{1}{D}\iint_R P\delta(Q - Q_0)\,ker(\rho_{kQ})\,d\sigma_Q = \frac{P}{D}\,ker(\rho_{kQ_0}) \tag{35}$$

where

$$\rho_{kQ_0} = |p_k - Q_0|/l$$

Relations (34) and (35) indicate that the BIE method is very well suited for the analysis of plates subjected to transverse concentrated forces.

7 Evaluation of the Deflections and Stress Resultants

Once the coefficients $a_{kj}, b_{kj}, c_{kj}, d_{kj}$, and the integrals F_k, G_k are established, the system of simultaneous algebraic equations (25) is solved and the values Φ_j and Ψ_j of the functions $\Phi(s)$ and $\Psi(s)$ at the nodal points are obtained. These values can be used to obtain the deflection $w(P)$ of the plate and the stress resultants. The integrals $f(P), J_1(P), J_2(P)$ in the expression (16) for the deflection $w(P)$, can be approximated by the following sums

$$J_1(P) = \sum_{j=1}^{M} \Psi_j \int_j kei(\rho_{Pj})\,ds_q \tag{36a}$$

$$J_2(P) = \sum_{j=1}^{M} \Phi_j \int_j \rho_{Pj}\,kei'(\rho_{Pj})\,d\theta_q \tag{36b}$$

The integrals $\int_j \rho kei'(\rho)\,d\theta_q$ and $\int_j kei(\rho)\,ds_q$ are not singular and consequently they are evaluated using formula (30). Moreover the integral $F(P)$ is evaluated by dividing the region R into M sectors each having point P as its vertex and the j-element as its base. On each sector the integral is evaluated using the technique presented in reference [12]. The value of the integral on the region R is obtained as the sum of the values of the integrals evaluated on the sectors. That is

$$F(P) = \frac{1}{D}\sum_{j=1}^{M}\iint_j f(Q)\,kei(\rho_{PQ})\,d\sigma_Q \tag{36c}$$

Referring to relations (6) and (17) it is apparent that the bending moments M_n, M_t and the effective shearing force V_n on the boundary of the plate are readily computed from the values of Φ and Ψ.

The bending moments M_x, M_y, the twisting moment M_{xy} and the shear forces Q_x and Q_y at any point of the plate may be expressed [6] as

Downloaded 02 May 2010 to 171.66.16.25. Redistribution subject to ASME license or copyright; see http://www.asme.org/terms/Terms_Use.cfm

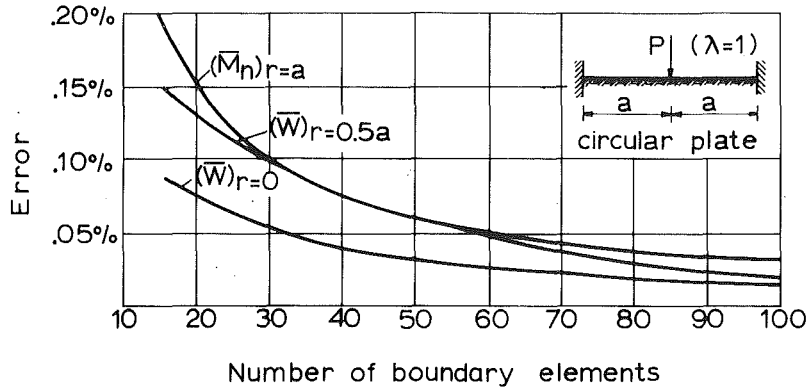


Fig. 3 Percent error in the deflection $\bar{w}$ at $r=0$, $r=0.5a$, and the bending moment $\bar{M}_n$ at $r=a$ versus the number of boundary elements

$$M_x=-D\left(\frac{\partial^2 w}{\partial x^2}+\nu\frac{\partial^2 w}{\partial y^2}\right),\quad Q_x=-D\frac{\partial}{\partial x}\nabla^2 w$$

$$M_y=-D\left(\frac{\partial^2 w}{\partial y^2}+\nu\frac{\partial^2 w}{\partial x^2}\right),\quad Q_y=-D\frac{\partial}{\partial y}\nabla^2 w$$

$$M_{xy}=-M_{yx}=D(1-\nu)\frac{\partial^2 w}{\partial x\partial y} \tag{37}$$

The second and third-order partial derivatives of the deflection w in relations (37) may be evaluated from the computed values of the deflections using numerical differentiation. However, in this investigation they are evaluated using the following combinations of the derivatives of equation (16):

$$d_i=\frac{1}{2\pi}\left[-\frac{1}{D}\iint_R fK_i(\rho)\,d\sigma+\int_C \Psi K_i(\rho)\,ds-\frac{1}{l}\int_C \Phi\Lambda_i(\rho)\,ds\right]\quad (i=1,2,3,4,5) \tag{38}$$

where

$$d_1=\frac{\partial^2 w}{\partial x^2}+\frac{\partial^2 w}{\partial y^2},\quad d_2=\frac{\partial^2 w}{\partial x^2}-\frac{\partial^2 w}{\partial y^2},\quad d_3=2\frac{\partial^2 w}{\partial x\partial y}$$

$$d_4=l\frac{\partial}{\partial x}\nabla^2 w,\quad d_5=l\frac{\partial}{\partial y}\nabla^2 w$$

$$K_1(\rho)=ker(\rho),\quad K_2(\rho)=C(\rho)\cos 2\theta,\quad K_3(\rho)=C(\rho)\sin 2\theta$$

$$K_4(\rho)=-ker'(\rho)\cos\theta,\quad K_5(\rho)=-ker'(\rho)\sin\theta$$

$$\Lambda_1(\rho)=ker'(\rho)\cos\varphi$$

$$\Lambda_2(\rho)=ker'(\rho)\cos 2\theta\cos\varphi-\frac{2}{\rho}C(\rho)\cos(2\theta-\varphi) \tag{39}$$

$$\Lambda_3(\rho)=ker'(\rho)\sin 2\theta\cos\varphi-\frac{2}{\rho}C(\rho)\sin(2\theta-\varphi)$$

$$\Lambda_4(\rho)=\frac{1}{\rho}ker'(\rho)\cos(\theta-\varphi)+kei(\rho)\cos\theta\cos\varphi$$

$$\Lambda_5(\rho)=\frac{1}{\rho}ker'(\rho)\sin(\theta-\varphi)+kei(\rho)\sin\theta\sin\varphi$$

$$C(\rho)=ker(\rho)-\frac{2}{\rho}kei'(\rho)$$

Notice that in the double integrals of relations (38) $\rho=\rho_{PQ}$, while in the line integrals $\rho=\rho_{Pq}$.

Relations (38) are approximated by following sums

$$d_i(P)=-\frac{1}{D}\sum_{j=1}^{M}\iint_j fK_i(\rho)\,d\sigma+\sum_{j=1}^{M}\Psi_j\int_j K_i(\rho)\,ds-\frac{1}{l}\sum_{j=1}^{M}\Phi_j\int_j\Lambda_i(\rho)\,ds\quad (i=1,2,3,4,5) \tag{40}$$

Inasmuch as point P, where the integrals in relation (40) are evaluated, is inside the region R, the argument ρ does not vanish and these integrals are not singular.

8 Numerical Results

A computer program has been written for the numerical evaluation of the response of clamped plates to a given loading $f(P)$ using the aforementioned numerical technique. For the numerical evaluation of the Kelvin functions, their expansion in Chebyshev series is used [5, 14]. Numerical results have been obtained for circular plates rectangular plates and a plate with composite shape, using a CDC/CYBER 171-18 computer. These results are in excellent agreement with those available from analytical solutions [6, 15, 16] for circular and rectangular plates subjected to uniformly distributed forces or to a concentrated force (see Fig. 3 and reference [5]). For rectangular plates, the results obtained using small values for the constant of the elastic foundation have been also compared to those available for rectangular plates not resting on an elastic foundation.

For the presentation of the numerical results, the following dimensionless quantity has been introduced

$$\lambda=a/l=a/\sqrt[4]{D/k} \tag{41}$$

where a is a characteristic dimension of the clamped plate (e.g., the radius of a circular plate or the half length of one side of a rectangular plate).

For usual engineering applications the constant k of an elastic foundation may vary between 0 (for clamped plates not resting on an elastic foundation) and 200MN/m^3 [6]. For these values of k, it can be shown that the dimensionless parameter λ for a plate resting on an elastic foundation varies between 0.5 (soft subgrade) and 20 (stiff subgrade). Inasmuch as there are computational difficulties for $\lambda=0$ the results for plates that do not rest on an elastic foundation are obtained using a small value of λ (say $\lambda=0.5$ to 1.0) [5]. It is not necessary to employ values of λ less than 0.5 because for these values of λ, the deflections of a plate resting on an elastic foundation vary negligibly from those of a plate that does not rest on a foundation.

Downloaded 02 May 2010 to 171.66.16.25. Redistribution subject to ASME license or copyright; see http://www.asme.org/terms/Terms_Use.cfm

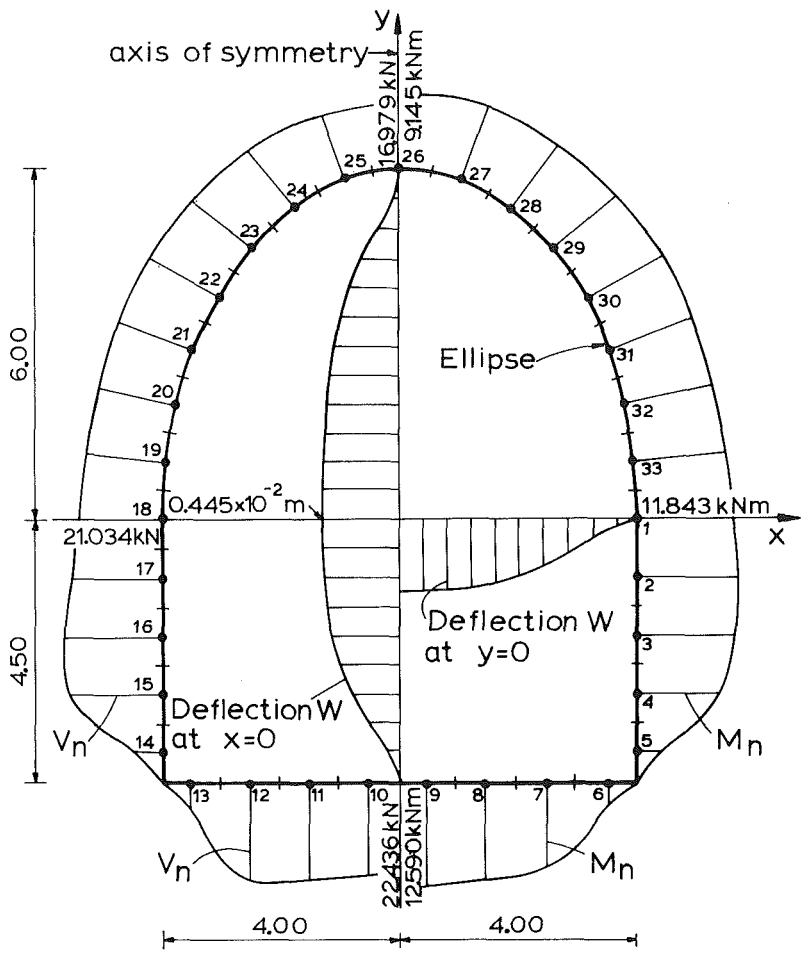


Fig. 4 Uniformly loaded clamped plate of composite geometry resting on an elastic foundation ($k = 4905\text{kN/m}^3$, $h = 0.10\text{m}$ $E = 20.601 \times 10^3\text{MPa}$, $\nu = 0.30$, $q_0 = 19.62\text{kN/m}^2$)

Table 1 Influence coefficients for a clamped rectangular ($2a \times 2b$) plate with side ratio $b/a = 1.2$ resting on an elastic foundation with $\lambda = 5$

Load position	Influence coefficients for $\overline{w} = w/(Pa^2/D)$ at $x = y = 0$				
y/b \ x/a	0	0.2	0.4	0.6	0.8
0.8	$-0.2901E-04$	$-0.3150E-04$	$-0.3344E-04$	$-0.2622E-04$	$-0.1030E-04$
0.6	$0.8551E-04$	$0.5078E-04$	$-0.1285E-04$	$-0.4209E-04$	$-0.2366E-04$
0.4	$0.8020E-03$	$0.6140E-03$	$0.2648E-03$	$0.3889E-04$	$-0.1560E-04$
0.2	$0.2706E-02$	$0.1990E-02$	$0.8795E-03$	$0.2300E-03$	$0.1802E-04$
0	$0.4992E-02$	$0.3146E-02$	$0.1292E-02$	$0.3488E-03$	$0.3978E-04$
	Influence coefficient for $\overline{M}_x = M_x/P$ at $x = y = 0$ ($\nu = 0.3$)				
y/b \ x/a	0	0.2	0.4	0.6	0.8
0.8	$-0.5082E-03$	$-0.5305E-03$	$-0.4791E-03$	$-0.2648E-03$	$-0.4790E-04$
0.6	$-0.9462E-03$	$-0.1513E-02$	$-0.2028E-02$	$-0.1427E-02$	$-0.4147E-03$
0.4	$-0.4239E-02$	$-0.4396E-03$	$-0.5245E-02$	$-0.4347E-02$	$-0.1412E-02$
0.2	$0.3900E-01$	$0.7038E-02$	$-0.1188E-01$	$-0.9410E-02$	$-0.3024E-02$
0	$0.1000E-31$	$0.6407E-02$	$-0.1839E-01$	$-0.1269E-01$	$-0.3958E-02$

In Fig. 3, the percent error in the results obtained using the BIE method as compared with those obtained from analytical solutions [15] are plotted versus the number of boundary elements for clamped circular plates resting on an elastic foundation with $\lambda = 1$, subjected to a centrally applied concentrated load. It is apparent that relatively few boundary elements (30–40) are required to obtain accurate results. Moreover, when the same number of boundary elements is used, the error in the deflection of the plate is greater at points close to the boundary.

In Fig. 4, results obtained on the basis of the BIE method using 33 boundary elements for a uniformly loaded clamped plate of composite shape, resting on an elastic foundation, are presented. These results are considered accurate because they differ very negligibly from those obtained using twice as many boundary elements.

Downloaded 02 May 2010 to 171.66.16.25. Redistribution subject to ASME license or copyright; see http://www.asme.org/terms/Terms_Use.cfm

In Table 1, the dimensionless deflection $\bar{w} = w/(Pa^2/D)$ and the bending moment $\bar{M}_x = M_x/P$ at point $x=y=0$ of a clamped rectangular plate ($2a \times 2b$) ($\epsilon = b/a = 1.2$), subjected to a concentrated force P are presented for $\lambda = 5$. Results for other values of λ for circular and rectangular clamped plates are available in reference [5].

Conclusions

The conclusions drawn from this investigation can be summarized as follows:

(*a*) The computational error of the results approaches zero as the number of boundary elements is increased.

(*b*) For plates having a smooth boundary, accurate results can be obtained using a small number of boundary elements.

(*c*) The numerical procedure presented in this investigation is well suited for computer-aided analysis of plates on an elastic foundation.

(*d*) The assumption that the unknown boundary quantitites are constant over each boundary element yields very satisfactory results.

(*e*) As it was anticipated, for small values of the constant of the elastic foundation, the results approach those of a plate not resting on an elastic foundation.

(*f*) The accuracy of the results obtained using the same number of boundary elements is greater for points located away from the boundary of the plate.

(*g*) The values of the Kelvin functions obtained from their Chebyshev series [14] are more accurate than those obtained using Lanczos' economization procedure as proposed by Burgoyne [17].

References

1 Mendelson, A., "Boundary Integral Methods in Elasticity and Plasticity," NASA, TN D-7418, 1973.

2 Cruse, T., and Rizzo, F., eds., *Boundary-Integral Equation Method: Computational Applications in Applied Mechanics*, AMD-Vol. 11, ASME, New York, 1975.

3 Brebbia, C. A., ed., *Recent Advances in Boundary Element Method*, Pentech Press, London, 1978.

4 Banerjee, P. K., and Butterfield, R., *Boundary Element Methods in Engineering Science*, McGraw-Hill, 1981.

5 Katsikadelis, J. T., "The Analysis of Plates on Elastic Foundation by the Boundary Integral Equation Method," P.hD Dissertation, Polytechnic Institute of New York, 1982.

6 Timoshenko, S., and Woinowsky-Krieger, S., *Theory of Plates and Shells*, 2nd Ed., McGraw-Hill, New York, 1959.

7 Abramowitz, M., and Stegun, I., eds., *Handbook of Mathematical Functions*, 10th Ed., Dover, New York, 1972.

8 Kellogg, O. D., *Foundations of Potential Theory*, Springer Verlag, Berlin, 1967.

9 Courant, R., and Hilbert, D., *Methods of Mathematical Physics*, Vol. II, Interscience, New York, 1953, Chapter IV.

10 Brebbia, C. A., and Nagaguma, R., "Boundary Elements in Stress Analysis," *Journal of Engineering Mechanics Division*, ASCE, EM1, 1979, pp. 55-69.

11 Jaswon, M. A., and Ponter, A. R., "An Integral Equation Solution of the Torsion Problem," *Proc. Roy. Soc.*, Series A, Vol. 273, No. 1353, 1963, pp. 237-246.

12 Katsikadelis, J. T., and Armenàkas, A. E., "Numerical Evaluation of Double Integrals With a Logarithmic or a Cauchy-type Singularity," ASME JOURNAL OF APPLIED MECHANICS, Vol. 50, 1983, pp. 682-684.

13 Stroud, A. H., *Approximate Calculation of Multiple Integrals*, Prentice-Hall, Englewood Cliffs, N.J., 1971, pp. 346-348.

14 Luke, Y. L., *Mathematical Functions and Their Approximations*, Academic Press, New York, 1975, pp. 337-341.

15 Schleicher, F., *Kreisplatten auf Elastischer Unterlage*, Springer Verlag, Berlin, 1926.

16 Fletcher, H. J., and Thorne, C. J., "Thin Rectangular Plates on Elastic Foundation," ASME JOURNAL OF APPLIED MECHANICS, Vol. 19, 1952, pp. 361-368.

17 Burgoyne, F. D., "Approximations to Kelvin Functions," *Math. Computation*, Vol. 17, 1963, pp. 295-298.

Downloaded 02 May 2010 to 171.66.16.25. Redistribution subject to ASME license or copyright; see http://www.asme.org/terms/Terms_Use.cfm

Vibrations of Thick Free Circular Plates, Exact Versus Approximate Solutions

J. R. Hutchinson
Professor,
Department of Civil Engineering,
University of California,
Davis, Calif. 95616
Mem. ASME

An exact solution for the natural frequencies of a thick free circular plate is compared to approximate solutions. The exact solution is a series solution of the general linear elasticity equations that converges to the correct natural frequencies. The approximate solutions to which this exact solution is compared are the Mindlin plate theory and a modification of a solution method proposed by Pickett. The comparisons clearly show the range of applicability of the approximate solutions as well as their accuracy. The choice of a best shear coefficient for use in the Mindlin plate theory is considered by evaluating the shear coefficient that would make the exact and modified Pickett method match the Mindlin plate solution.

Introduction

In a recent paper by this author [1] an exact solution for the vibrations of a solid isotropic linearly elastic cylinder with traction-free boundaries was developed. The flexural vibrations of thick free circular plates represents an important subset of that exact solution. In previous papers this author has compared the exact solution with Mindlin plate theory for axisymmetic flexural vibrations of circular plates [2] and compared the exact solution with the Pochhammer-Chree approximation, Timoshenko beam approximation, and the Pickett aproximation for transverse vibrations of beams [3]. In the previous papers comparisons were also made to experimental results, which clearly showed the high degree of accuracy of the solution method. This paper represents an extension of reference [2] to include nonaxisymmetric motions as well as a comparison with a modified Pickett method, which proves to be highly accurate within its range of applicability.

The vibrations of thick plates, or the higher modes of thin plates, has received much prior attention in a series of papers by Mindlin and his coworkers. In reference [4] Mindlin included shear and rotary inertia effects in a similar manner as Timoshenko did for the transverse vibrations of a beam. It is this form of solution that is referred to as Mindlin plate theory. Mindlin and Deresiewicz used this theory to consider axisymmetric flexural vibration of circular plates in reference [5] and to consider the $n = 1$ mode in reference [6]. Mindlin [4] showed two ways to determine the shear coefficient by matching the thick plate solution with the solution of the three-dimensional theory of infinite plates. In this paper another shear coefficient is evaluated by the same type of matching procedure. This new shear coefficient provides a good match for long wave lengths.

In 1945, Pickett [7] introduced an elasticity solution for both long circular rods and for circular plates. Pickett's rod solution was compared to the exact solution in reference [3] and it was shown to produce excellent results over its range of applicability. In Pickett's plate solution he satisfied the boundary conditions on the top and bottom of the plate identically and approximated the edge boundary conditions by setting the bending moment and effective shear equal to zero (i.e., the Kirchhoff boundary conditions). It was found that this procedure leads to frequencies that are significantly higher than the exact solutions. To modify Pickett's method another solution of the elasticity equations is introduced, which also identically satisfies the boundary conditions on the upper and lower surfaces and, together with Pickett's terms, allows satisfaction of zero bending moment (M_r), twisting moment ($M_{r\theta}$), and transverse shear (Q_r). This modification of Pickett's method is shown to produce good results.

It should be noted that in 1955 Mindlin [8] also developed a general methodology for obtaining plate theories of higher order, as have Bache and Hegemier [9] in 1974. In 1980 Celep [10] showed results of a higher order plate theory applied to the vibrations of free circular plates. In the present paper reference to Mindlin plate theory refers to inclusion of shear and rotary inertia effects alone and not to any higher order theories. It should also be noted that the modified Pickett solution is different than the higher order theories developed in references [8–10].

A major reason for investigating the range of applicability of the Mindlin plate theory is that it is the simplest plate theory that can be used to study wave propagation in plates. In references [11–12] this author has shown how Mindlin plate theory can be applied to the solution of impulsively loaded plates. The solution process in those references involved modal superposition of 1000 modes. It is imperative in such

Contributed by the Applied Mechanics Division for presentation at the Winter Annual Meeting, New Orleans, La., December 9–14, 1984 of THE AMERICAN SOCIETY OF MECHANICAL ENGINEERS.

Discussion of this paper should be addressed to the Editorial Department, ASME, United Engineering Center, 345 East 47th Street, New York, N.Y. 10017, and will be accepted until two months after final publication of the paper itself in the JOURNAL OF APPLIED MECHANICS. Manuscript received by ASME Applied Mechanics Division, September, 1983; final revision, January, 1984. Paper No. 84-WA/APM-19.

Copies will be available until August, 1985.

Copyright © 1984 by ASME
Downloaded 02 May 2010 to 171.66.16.25. Redistribution subject to ASME license or copyright; see http://www.asme.org/terms/Terms_Use.cfm

solutions to known the range of applicability of the plate theory being applied. For instance, in such problems the researcher must know if his 1000th mode and frequency from the Mindlin plate theory have any correspondence with the true 1000th mode and frequency.

Because of space limitations it was impossible to make this paper self-contained; thus to fully understand the exact solution one must refer to reference [1], and to fully understand the Mindlin plate theory one must refer to reference [6]. The reader is also cautioned that in the section on the "Mindlin Plate Solution" the notation of reference [6] is used; whereas, throughout the rest of the text the notation is defined in its first usage.

Exact Solution

The exact solution is described in detail in reference [1] and will only be briefly outlined in this section. What is referred to as an exact solution is a series solution in which each term identically satisfies the linear elasticity equations. These solution forms are tabulated in Table 1. The solution forms are grouped in three series. Boundary conditions on the shear stress τ_{rz} at the top, bottom, and edge of the plate and on $\tau_{\theta z}$ at the top and bottom of the plate are satisfied identically. The boundary conditions on the normal stress σ_r at the edge, σ_z and the top and bottom, and $\tau_{r\theta}$ at the edge are satisfied by orthogonality. This process leads to an infinite system of homogeneous simultaneous equations whose coefficients are transcendental functions of the natural frequency. By truncating the series and searching for the zeroes of the determinant of the coefficients the natural frequencies are found. Convergence is reached with relatively few terms in each series so that the method is practical for computational purposes. Convergence is particulary rapid when the thickness of the plate is equal to its diameter. As the plate becomes thinner, however, more terms are required for equivalent accuracy. The convergence is monotonic in either case.

In Table 1 and in the following section all values are dimensionless. The displacements u,v, and w are made dimensionless by dividing by the radius. The wave numbers α,β, and δ are made dimensionless by multiplying by the radius. All stress quantities are made dimensionless by dividing by the shear modulus and the frequency ω is made dimensionless by multiplying by the radius and dividing by the shear wave velocity.

Modified Pickett Method. In Pickett's method, terms were chosen from columns A and B of Table 1. Thus,

$$\sigma_z = [A(2\alpha^2 - \omega^2)\sin \delta z + B2\alpha^2 \sin \beta z] J_n(\alpha r) \cos n\theta \quad (1)$$

$$\tau_{rz} = \left[A2\delta \cos \delta z - B\frac{1}{\beta}(\alpha^2 - \beta^2) \times \cos \beta z\right] \alpha J_n'(\alpha r) \cos n\theta \quad (2)$$

$$\tau_{\theta z} = -\left[A2\delta \cos \delta z - B\frac{1}{\beta}(\alpha^2 - \beta^2) \times \cos \beta z\right] \frac{n}{r} J_n(\alpha r) \cos n\theta \quad (3)$$

Satisfying the boundary conditions that σ_z, τ_{rz}, and $\tau_{\theta z}$ must be zero at the top and bottom of the plate ($z = \pm h$) gives:

$$\begin{bmatrix} (2\alpha^2 - \omega^2)\sin \delta h & 2\alpha^2 \sin \beta h \\ 2\delta \cos \delta h & -\dfrac{(\alpha^2 - \beta^2)}{\beta} \cos \beta h \end{bmatrix} \begin{Bmatrix} A \\ B \end{Bmatrix} = \begin{Bmatrix} 0 \\ 0 \end{Bmatrix} \quad (4)$$

Setting the determinant of the coefficients equal to zero yields

$$(\alpha^2 - \beta^2)^2 \sin \delta h \cos \beta h + 4\alpha^2 \beta\delta \sin \beta h \cos \delta h = 0 \quad (5)$$

The relationship between A and B is

$$B = A(\beta^2 - \alpha^2)\sin \delta h / 2\alpha^2 \sin \beta h \quad (6)$$

Equation (5) was shown by Pickett to yield only two real values of α for low frequencies. Thus only those two were used by him. Pickett then satisfied zero bending moment and effective shear at the edge of the plate. When Pickett's method was tried it was found that the solution yielded poor results. It can be seen that the solution forms in column C of Table 1 can also be made to identically satisfy the boundary conditions on the top and bottom of the plate by making

$$\beta_c = (2i-1)\pi/2h; \quad i = 1,2,3 \ldots . \quad (7)$$

These forms were neglected by Pickett. For consistency with Pickett's solution only the first term ($i = 1$) will be used. Because of the two roots of α from equation (5) the $A-B$ combinations as shown in equations (1), (2), and (3) represent two forms. The additional form is C times column C where

$$\beta_c = \pi/2h \quad (8)$$

The boundary conditions at the plate's edge are

$$M_r = \int_{-h}^{h} z\sigma_r(1,z)\,dz = 0 \quad (9)$$

$$Q_r = \int_{-h}^{h} \tau_{rz}(1,z)\,dz = 0 \quad (10)$$

$$M_{r\theta} = \int_{-h}^{h} z\tau_{r\theta}(1,z)\,dz = 0 \quad (11)$$

Table 1 Solutions of elasticity equations. $J_n(\ )$ denotes the nth-order Bessel function of the first kind. Primes denote differentiation with respect to argument. The dimensionless wave numbers α, β, and δ and the frequency parameter ω are related by $\alpha^2 + \delta^2 = \omega^2(1-2\nu)/2(1-\nu)$ and $\alpha^2 + \beta^2 = 1^2$. The constant $k = \nu/(1-\nu)$, where ν is Poisson's ratio.

	A	B	C
u	$\alpha J_n'(\alpha r) \sin \delta z \cos n\theta$	$\alpha J_n'(\alpha r) \sin \beta z \cos n\theta$	$-\frac{n}{r}J_n(\alpha r) \sin \beta z \cos n\theta$
v	$-\frac{n}{r}J_n(\alpha r) \sin \delta z \sin n\theta$	$-\frac{n}{r}J_n(\alpha r) \sin \beta z \sin n\theta$	$\alpha J_n'(\alpha r) \sin \beta z \sin n\theta$
w	$\delta J_n(\alpha r) \cos \delta z \cos n\theta$	$-\frac{\alpha^2}{\beta}J_n(\alpha r) \cos \beta z \cos n\theta$	0
σ_r	$[-k\omega^2 J_n(\alpha r) + 2\alpha^2 J_n''(\alpha r)] \sin \delta z \cos n\theta$	$2\alpha^2 J_n''(\alpha r) \sin \beta z \cos n\theta$	$-\frac{2n}{r}[\alpha J_n'(\alpha r) - \frac{1}{r}J_n(\alpha r)] \sin \beta z \cos n\theta$
σ_z	$(2\alpha^2 - \omega^2)J_n(\alpha r) \sin \delta z \cos n\theta$	$2\alpha^2 J_n(\alpha r) \sin \beta z \cos n\theta$	0
$\tau_{r\theta}$	$\frac{2n}{r}[-\alpha J_n'(\alpha r) + \frac{1}{r}J_n(\alpha r)] \sin \delta z \sin n\theta$	$\frac{2n}{r}[-\alpha J_n'(\alpha r) + \frac{1}{r}J_n(\alpha r)] \sin \beta z \sin n\theta$	$\alpha^2[2J_n''(\alpha r) + J_n(\alpha r)] \sin \beta z \sin n\theta$
τ_{rz}	$2\alpha\delta J_n'(\alpha r) \cos \delta z \cos n\theta$	$-\frac{\alpha}{\beta}(\alpha^2 - \beta^2)J_n'(\alpha r) \cos \beta z \cos n\theta$	$-\frac{n\beta}{r}J_n(\alpha r) \cos \beta z \cos n\theta$
$\tau_{\theta z}$	$-\frac{2n\delta}{r}J_n(\alpha r) \cos \delta z \sin n\theta$	$\frac{n}{\beta r}(\alpha^2 - \beta^2)J_n(\alpha r) \cos \beta z \sin n\theta$	$\alpha\beta J_n'(\alpha r) \cos \beta z \sin n\theta$

Downloaded 02 May 2010 to 171.66.16.25. Redistribution subject to ASME license or copyright; see http://www.asme.org/terms/Terms_Use.cfm

Substitution of the three solution forms into the boundary conditions yields a 3 × 3 set of homogeneous simultaneous equations whose coefficients are as follows:

$$a_{1j} = 2[-k\omega^2 J_n(\alpha_j) + 2\alpha_j^2 J_n''(\alpha_j)][1 - \delta_j h \cot \delta_j h]/\delta_j^2 - 2(\alpha_j^2 - \beta_j^2) J_n''(\alpha_j)[1 - \beta_j h \cot \beta_j h]/\beta_j^2 \quad (12)$$

$$a_{2j} = (\alpha_j^2 + \beta_j^2)^2 J_n'(\alpha_j) \sin \delta_j h / \alpha_j \beta_j^2 \quad (13)$$

$$a_{3j} = 2n[J_n(\alpha_j) - \alpha_j J_n'(\alpha_j)] \times [2(1 - \delta_j h \cot \delta_j h)/\delta_j^2 - (\alpha_j^2 - \beta_j^2)(1 - \beta_j h \cot \beta_j h)/\alpha_j^2 \beta_j^2] \quad (14)$$

$$a_{13} = 4n[J_n(\alpha_c) - \alpha_c J_n'(\alpha_c)]/\beta_c^2 \quad (15)$$

$$a_{23} = -2nJ_n(\alpha_c) \quad (16)$$

$$a_{33} = 2\alpha_c^2 [2J_n''(\alpha_c) + J_n(\alpha_c)]/\beta_c^2 \quad (17)$$

where, for equations (12), (13), and (14) $j = 1,2$; α_1 and α_2 are the two roots from equation (5), and β's and δ's are from the relations expressed in Table 1. For equations (15), (16), and (17) β_c is defined by equation (8) and α_c is found from the relation expressed in Table 1.

The solution process is to choose a value for ω and find the two real roots, α_1, α_2, from equation (5). The coefficients expressed in equations (12)–(15) are determined and the determinant of those coefficient is evaluated. Values of ω that make the determinant vanish are the natural frequencies.

The Pickett solution assumes two real roots from equation (5); however, for high frequencies additional real roots emerge from the complex plane. It was shown in reference [3] that these additional real roots represented higher dispersion curves. Also in reference [3] it was noted that the range of applicability of the Pickett solution was limited to values of frequencies less than the first emergence of these additional roots. This emergence occurs when ωh equals 4.3, 4.7, and 4.4 for a Poisson's ratio of 0, 0.3, and 0.5, respectively. The modified Pickett solution can thus be considered valid for values of ωh less than these. For good matching with the exact solution it is suggested that a somewhat lower value of

$$\omega h \leq 3 \quad (18)$$

be used. This represents a good practical limit for both the modified Pickett solution and the Mindlin plate solution.

Mindlin Plate Solution. In reference [6] Mindlin and Deresiewicz derived the $n = 1$ case for vibrations of a thick circular plate and pointed out how to extend that solution to the general case for arbitrary n. Following their suggestion equations similar to equation (17) of reference [6] is

$$[a]\{A\} = \{0\} \quad (19)$$

where the coefficients of the 3×3 matrix [a] are

$$a_{1j} = (\sigma_j - 1)[\delta_j^2 J_n''(\delta_j a) + \frac{\nu}{a}\delta_j J_n'(\delta_j a) - \frac{\nu n^2}{a^2} J_n(\delta_j a)] \quad (20)$$

$$a_{2j} = (\sigma_j - 1)\frac{2n}{a}[-\delta_j J_n'(\delta_j a) + \frac{1}{a} J_n(\delta_j a)] \quad (21)$$

$$a_{3j} = \sigma_j \delta_j J_n'(\delta_j a) \quad (22)$$

$$a_{13} = \frac{n}{a}(1 - \nu)[\omega J_n'(\omega a) - \frac{1}{a} J_n(\omega a)] \quad (23)$$

$$a_{23} = -\frac{n^2}{a^2} J_n(\omega a) + \frac{\omega}{a} J_n'(\omega a) - \omega^2 J_n''(\omega a) \quad (24)$$

$$a_{33} = \frac{n}{a} J_n(\omega a) \quad (25)$$

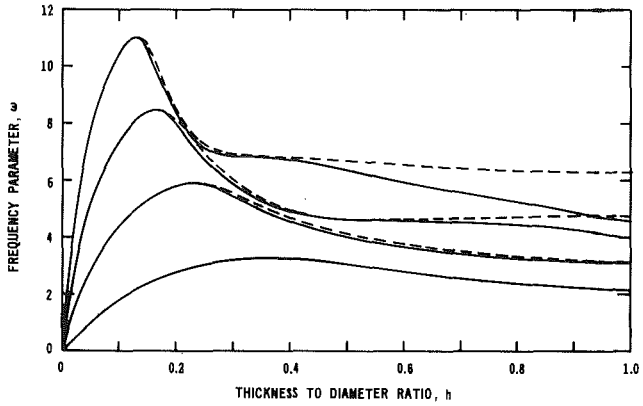


Fig. 1 Frequency parameter ω versus thickness-to-diameter ratio h from exact solution (—) and Mindlin solution (- - - - - -) for $K = 5/(6\text{-}\nu)$, $\nu = 0.3$, and $n = 1$

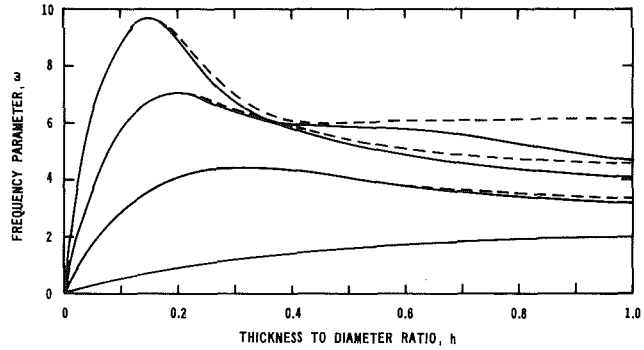


Fig. 2 Frequency parameter ω versus thickness-to-diameter ratio h from exact solution (—) and Mindlin solution (- - - - - -) for $K = 5/(6\text{-}\nu)$, $\nu = 0.3$, and $n = 2$

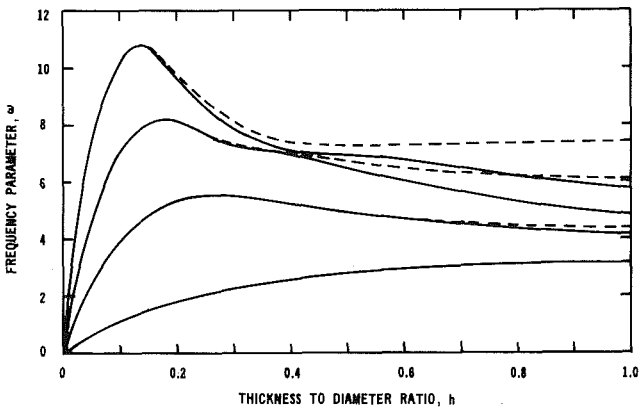


Fig. 3 Frequency parameter ω versus thickness-to-diameter ratio h from exact solution (—) and Mindlin solution (- - - - - -) for $K = 5/(6\text{-}\nu)$, $\nu = 0.3$, and $n = 3$

where, for equations (20), (21), and (22), $j = 1,2$. In equations (20)–(25) the notation of reference [6] has been used. In particular, note that ω is a wave number rather than the natural frequency as denoted in the previous sections.

The constants and the wave numbers in equations (20)–(25) are all defined in equations (6)–(9) of reference [6]. The solution process is to search for the zeros of the determinant of the coefficients in equation (19). It can be seen that this process can be carried out for determining the natural freqencies for a known shear coefficient or can be used to find the shear coefficient for a known natural frequency.

Downloaded 02 May 2010 to 171.66.16.25. Redistribution subject to ASME license or copyright; see http://www.asme.org/terms/Terms_Use.cfm

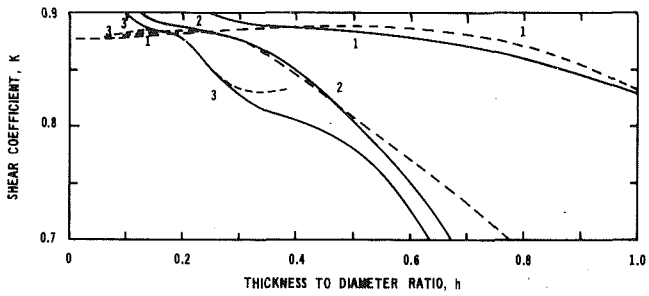


Fig. 4 Shear coefficient, K, versus thickness-to-diameter ratio, h, for $\nu = 0.3$ and $n = 0$. Exact solution (—), modified Pickett solution (- - - - - -).

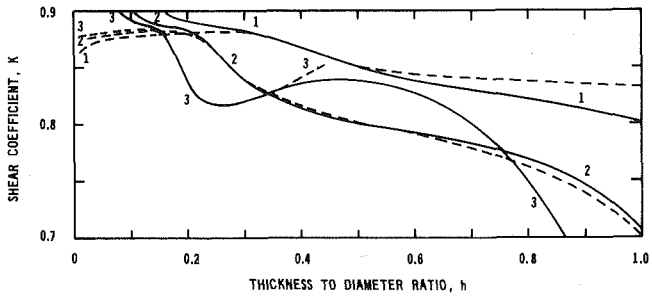


Fig. 5 Shear coefficient, K, versus thickness-to-diameter ratio, h, for $\nu = 0.3$ and $n = 1$. Exact solution (—), modified Pickett solution (- - - - - -).

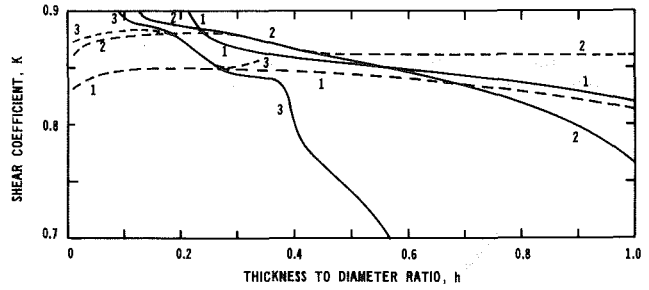


Fig. 6 Shear coefficient, K, versus thickness-to-diameter ratio, h, for $\nu = 0.3$ and $n = 2$. Exact solution (—), modified Pickett solution (- - - - - -).

Choice of an appropriate shear coefficient has been the subject of much speculation with almost as many different values as authors. Mindlin [4] indicated two ways to determine the shear coefficient by matching the thick plate solution with the solution of the three-dimensional theory for infinite plates. For matching with the thickness shear modes, Mindlin showed that a shear coefficient of $\pi^2/12$ is required. For matching with the straight-crested flexural wave Mindlin chose to match at short wave lengths, resulting in a shear coefficient that is a function of Poisson's ratio and is found by solving a cubic equation.

By matching the exact theory with the Mindlin plate theory both in reference [2] and in this work it was found that the shear coefficient was not a constant but a function of frequency. For long wave lengths, however, the shear coefficient does reach a constant value. This constant value can be determined by matching the exact infinite plate solution for straight-crested flexural waves of long wave length with the Mindlin plate solution. To find this expression Mindlin's [4] equation for long wave lengths is reduced to

$$\frac{C}{Cs} = \frac{2}{3}\left(\frac{1}{1-\nu}\right)\left(\frac{\pi h}{\lambda}\right)^2 - \left[\frac{14}{45(1-\nu)} + \frac{4}{9(1-\nu)^2}\right]\left(\frac{\pi h}{\lambda}\right)^4 \quad (26)$$

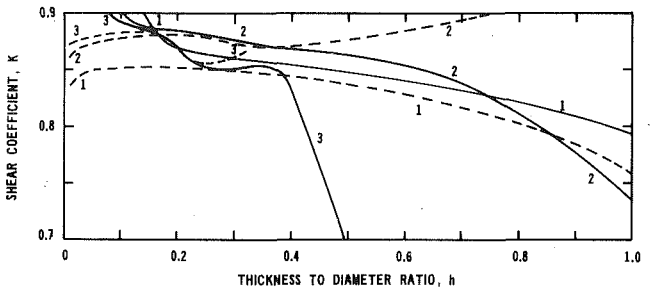


Fig. 7 Shear coefficient, K, versus thickness-to-diameter ratio, h, for $\nu = 0.3$ and $n = 3$. Exact solution (—), modified Pickett solution (- - - - - -).

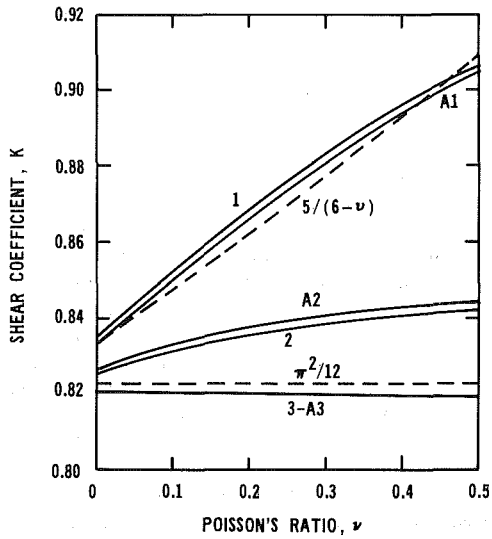


Fig. 8 Shear coefficient, K, versus Poisson's ratio, ν, for $h = 0.3$ and $n = 1$. Lines labeled, 1, 2, 3 are for the first three modes from the exact solution. Lines labeled $A1$, $A2$, $A3$ are for the first three modes from the modified Pickett solution.

The first term of this expression is the same as Mindlin's equation (41). Insertion of this expression in Mindlin's equation (46) gives the shear coefficient

$$K = 5/(6-\nu) \quad (27)$$

(Note that the shear coefficient K is denoted by κ^2 in Mindlin's work.)

Results

Figures 1–3 show the variation of frequency, ω, with the thickness to diameter ratio, h, for the four lowest frequencies for $n = 1$, 2, and 3, respectively. A similar figure for $n = 0$ appears in reference [2]. In these figures both the exact and the Mindlin solution are shown. A Poisson's ratio, ν, of 0.3 was used. For the Mindlin solution a shear coefficient of $5/(6-\nu)$ was used. The modified Pickett solution is not shown on these plots because it falls too close to the exact solution to differentiate between the two over the range of applicability defined by equation (18). It should be noted that the Mindlin solution is also close to the exact solution for the range of applicability defined by equation (18) and only for values outside that range does it diverge from the exact solution. The reason for the $n = 2$ frequencies being the lowest is that $n = 2$ is the lowest value of n for which no nodal circles appear. For $n = 0$ and $n = 1$ the fundamental modes have a nodal circle.

Figures 4–7 show the value of the shear coefficient that would allow the exact solution to match the Mindlin solution (solid lines) and the shear coefficient that would cause the Mindlin

Downloaded 02 May 2010 to 171.66.16.25. Redistribution subject to ASME license or copyright; see http://www.asme.org/terms/Terms_Use.cfm

solution to match the modified Pickett solution (broken lines). These plots show how well the modified Pickett solution works as well as show how the shear coefficient varies with thickness. It should be noted that the modified Pickett solution follows the behavior of the exact solution relatively well, and in most cases approaches the predicted shear constant of $5/(6-\nu)$ (i.e., 0.877) as h approaches zero. The reason for the exact solution being cut off for small h is twofold: first, as explained previously, as the plate becomes thinner more terms are needed for equivalent accuracy; and second, as the plate becomes thinner, greater accuracy in the frequency is necessary to compute a correct shear coefficient. Figure 8 shows the variation of shear coefficient with Poisson's ratio for the first three modes for $n=1$ and $h=0.3$. It is seen that the shear coefficient corresponding to the first mode varies as $5/(6-\nu)$ which is the value for long flexural waves in an infinite plate, whereas the shear coefficient corresponding to the third mode is close to a constant value of $\pi^2/12$, which is the value for shear waves in an infinite plate. The shear coefficient corresponding to the second mode is seen as a compromise between the values for the first and third modes.

Conclusions

The modified Pickett method gives good results for this problem; however, it does require slightly more computational effort than the Mindlin solution and is derived only for this one specific geometry. The range of applicability of both these approximate methods is about the same and is defined by equation (18).

The question of a best shear coefficient to use in application of the Mindlin theory is still left as a matter of judgment, but the shear coefficient can be seen to vary from $5/(6-\nu)$ to $\pi^2/12$, within the range of applicability, as the wave length is decreased.

References

1 Hutchinson, J. R., "Vibrations of Solid Cylinders," ASME JOURNAL OF APPLIED MECHANICS, Vol. 47, 1980, pp. 901–907.

2 Hutchinson, J. R., "Axisymmetric Flexural Vibrations of a Thick Free Circular Plate," ASME JOURNAL OF APPLIED MECHANICS, Vol. 46, 1979, pp. 139–144.

3 Hutchinson, J. R., "Transverse Vibrations of Beams, Exact Versus Approximate Solutions," ASME JOURNAL OF APPLIED MECHANICS, Vol. 48, 1981, pp. 923–928.

4 Mindlin, R. D., "Influence of Rotary Inertia and Shear on Flexural Motions of Isotropic, Elastic Plates," ASME JOURNAL OF APPLIED MECHANICS, Vol. 18, 1951, pp. 31–38.

5 Deresiewicz, H., and Mindlin, R. D., "Axially Symmetric Flexural Vibrations of a Circular Disk," ASME JOURNAL OF APPLIED MECHANICS, Vol. 22, 1955, pp. 86–88.

6 Mindlin, R. D., and Deresiewicz, H., "Thickness-Shear and Flexural Vibrations of a Circular Disk," *Journal of Applied Physics*, Vol. 25, 1954, pp. 1329–1332.

7 Pickett, G., "Flexural Vibrations of Unrestrained Cylinders and Disks," *Journal of Applied Physics*, Vol. 16, 1945, pp. 820–831.

8 Mindlin, R. D., "An Introduction to the Mathematical Theory of Vibrations of Elastic Plates," a monograph prepared for U.S. Army Signal Corps Engineering Laboratories, Fort Monmouth, N.J., 1955.

9 Bache, T. C., and Hegemier, G. A., "On Higher-Order Elastodynamic Plate Theories," ASME JOURNAL OF APPLIED MECHANICS, Vol. 41, 1974, pp. 423–4287.

10 Celep, A., "Free Vibration of Some Circular Plates of Arbitrary Thickness," *Journal of Sound and Vibration*, Vol. 70, 1980, pp. 379–388.

11 Hutchinson, J. R., "Wave Propagation Using Mindlin Plate Theory," Proceedings of the Second Cairo University MDP Conference, Dec. 27–29, 1982, Cairo, Egypt.

12 Hutchinson, J. R., Discussion of "Axisymmetric Elastic Waves Excited by a Point Source in a Plate," by R. L. Weaver and Y. H. Pao, ASME JOURNAL OF APPLIED MECHANICS, Vol. 50, 1983, pp. 699–700.

Downloaded 02 May 2010 to 171.66.16.25. Redistribution subject to ASME license or copyright; see http://www.asme.org/terms/Terms_Use.cfm

Simple Waves and Shock Waves Generated by an Incident Shock Wave in Two-Dimensional Hyperelastic Materials

Yongchi Li
Assistant Professor,
Department of Modern Mechanics,
University of Science and Technology,
of China
Hefei, Anhui, China

T. C. T. Ting
Professor of Applied Mechanics,
Department of Civil Engineering,
Mechanics and Metallurgy,
University of Illinois at Chicago,
Chicago, Ill. 60680
Mem. ASME

The reflection of an oblique plane shock wave from a boundary in a two-dimensional isotropic hyperelastic material is studied. For plane strain deformations, the strain energy function W *is a function of two invariants* p *and* q *of the deformation gradient. There are, in general, two reflected waves each of which can be a simple wave or a shock wave. For a special class of materials for which the strain energy function* W(p, q) *represents a developable surface (of which harmonic materials are particular examples), one of the reflected waves is always a shock wave. It is shown that there are materials other than harmonic materials for which the wave speeds are independent of the direction of propagation. Illustrative examples are presented to show how one can determine the reflected waves from a rigid boundary. It is also shown that for certain incident shock waves, there exists only one reflected wave.*

1 Introduction

The reflection problem of an oblique plane shock wave from a plane boundary in nonlinear elastic solids has been studied by several investigators (see [1-4], for example). Duvaut [1] studied the problem for harmonic materials while Reid [2] considered the problem for an isotropic hyperelastic material. Both of them were mainly interested in the reflected waves which are shock waves. Wright [3] further investigated the problem and offered a general procedure for combining the reflected simple waves to obtain the solution. He also looked at the cases where the incident angle exceeds the critical angle [4] and hence the regular reflection pattern breaks down.

When the incident angle does not exceed the critical angle, the reflected wave in general consists of simple waves as well as shock waves. It may also consist of a composite wave [5] in which part of the composite wave is a simple wave and the other part a shock wave. For a given incident shock wave and boundary conditions, the problem of finding the correct combination of reflected waves has been a difficult and challenging problem. A similar problem arises in one-dimensional plane waves in half space in which the correct combination of simple waves and shock waves is determined to satisfy the initial and boundary conditions [5]. The problem was solved by using the idea of "stress paths for simple waves" [6, 7] and the new idea of "stress paths for shock waves." One could apply the ideas of stress paths for simple waves and shock waves to the present problem. However, the stress paths are two-dimensional curves in [5] and four-dimensional curves here.

In this paper, we consider the reflection of an oblique shock wave in isotropic hyperelastic materials. The motion is assumed to be plane strain and hence only two (instead of three) wave speeds are present. Accordingly, there are only two reflected waves. Since each of the reflected waves can be a simple wave or shock wave, we present differential equations for simple waves in Section 2 and jump conditions for shock waves in Section 3. Differential equations for simple waves in a three-dimensional space were first formulated by Varley [8]. Here we present an alternate set of differential equations for simple waves in isotropic elastic solids and a condition under which a centered simple wave may degenerate into a shock wave. In Section 4, we briefly derive constitutive equations for a hyperelastic solid that is undergoing a plane strain deformation. The strain energy function W depends only on two invariants p and q of the deformation gradient. We also obtain the wave speeds c and the associated eigenvectors $\mathbf{r}$. A special class of isotropic materials for which the function $W(p, q)$ represents a developable surface is considered in Section 5. The harmonic materials introduced in [9] belong to this class. For this special class of materials, the reflected wave associated with c_2 cannot be a centered simple wave. It is always a shock wave. We also show that there are isotropic materials other than harmonic materials for which

Contributed by the Applied Mechanics Division for presentation at the Winter Annual Meeting, New Orleans, La., December 9-14, 1984 of THE AMERICAN SOCIETY OF MECHANICAL ENGINEERS.

Discussion on this paper should be addressed to the Editorial Department, ASME, United Engineering Center, 345 East 47th Street, New York, N.Y. 10017, and will be accepted until two months after final publication of the paper itself in the JOURNAL OF APPLIED MECHANICS. Manuscript received by ASME Applied Mechanics Division, November, 1983; final revision, January, 1984. Paper No. 84-WA/APM-12.

Copies will be available until August, 1985.

Copyright © 1984 by ASME
Downloaded 02 May 2010 to 171.66.16.25. Redistribution subject to ASME license or copyright; see http://www.asme.org/terms/Terms_Use.cfm

the wave speeds are independent of the direction of propagation.

The advantage of considering the special class of materials in the reflection problem is obvious. With one of the reflected waves known to be a shock wave, all one has to do is to investigate whether the remaining reflected wave is a simple wave, a shock wave, or a composite wave. As an illustration, we study the reflection of an oblique plane incident shock wave from a rigid boundary in a special isotropic hyperelastic material in Section 6. When the incident wave is a pressure shock wave, the reflected wave associated with c_1 changes from a simple wave to a shock wave as the incident angle decreases. When the incident wave front and the reflected shock wave front associated with c_2 are orthogonal to each other, the reflected wave associated with c_1 is absent and there exists only one reflected wave. For an incident shear shock wave, the reflected wave c_1 is a simple wave or a shock wave depending on the sign of the incident shear shock wave. Again, for certain incident shear shock waves, there exists only one reflected wave.

2 Differential Equations for Simple Waves

In a fixed rectangular coordinate system let $\mathbf{x}$ and $\mathbf{X}$ be, respectively, the position of a particle at time t and $t=0$ which is taken as the undeformed state. Assuming that

$$x_i = x_i(X_\alpha, t), \quad (i,\alpha = 1,2,3) \tag{1}$$

the equations of motion and the continuity of displacement can be written as

$$\left.\begin{aligned} T_{i\alpha,\alpha} - \rho_o \dot{v}_i &= 0 \\ v_{i,\alpha} - \dot{F}_{i\alpha} &= 0 \end{aligned}\right\} \tag{2}$$

where a comma stands for differentiation with the space variable X_α, a dot stands for differentiation with time t, $\mathbf{v}$ and $\mathbf{F}$ are, respectively, the velocity and the deformation gradient given by

$$v_i = \dot{x}_i, \quad F_{i\alpha} = x_{i,\alpha} \tag{3}$$

and repeated indices imply summation. ρ_o is the mass density in the undeformed state and $\mathbf{T}$ is the Piola-Kirchhoff stress tensor of the first kind which is assumed to be a given function of the deformation gradient $\mathbf{F}$:

$$\mathbf{T} = \mathbf{T}(\mathbf{F}) \tag{4}$$

For a simple wave solution, we assume that $\mathbf{v}$, $\mathbf{F}$, and hence $\mathbf{T}$ are constants on a one-parameter family of planes

$$N_\beta(\phi) X_\beta - c(\phi) t = g(\phi) \tag{5}$$

where ϕ is an arbitrary parameter, N_α, c, and g are functions of ϕ. In the (X_1, X_2, X_3) space, $\phi =$ constant is a plane moving at the speed c in the direction of the unit normal $\mathbf{N}$. Equation (5) defines implicitly ϕ as a function of $\mathbf{X}$ and t. Differentiation of equation (5) with respect to X_α and t yields

$$\left.\begin{aligned} \phi_{,\alpha} &= N_\alpha / K \\ \dot{\phi} &= -c/K, \\ K &= g' + c't - N'_\alpha X_\alpha \end{aligned}\right\} \tag{6}$$

where a prime stands for differentiation with respect to ϕ. Since $\mathbf{v}$, $\mathbf{F}$, and $\mathbf{T}$ are now considered functions of a single variable ϕ, equations (2) reduce to, using equation (6),

$$\left.\begin{aligned} c_{i\alpha j\beta} N_\alpha F'_{j\beta} + \rho_o c v'_i &= 0 \\ N_\alpha v'_i + c F'_{i\alpha} &= 0 \end{aligned}\right\} \tag{7}$$

where

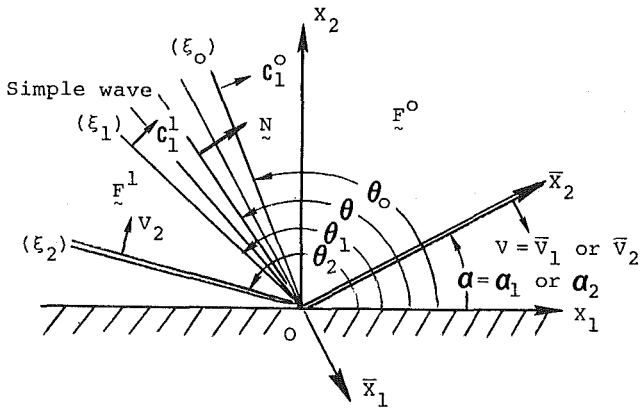


Fig. 1 Reflected simple wave c_1 and shock wave V_2 due to an incident shock wave

$$c_{i\alpha j\beta} = \partial T_{i\alpha} / \partial F_{j\beta} \tag{8}$$

is the elasticity of the material. Elimination of $F'_{j\beta}$ provides the equation for v'_j,

$$(\mathbf{Q} - \rho_o c^2 \mathbf{I})\mathbf{v}' = \mathbf{0}, \tag{9}$$

where $\mathbf{I}$ is Kronecker delta and

$$Q_{ij} = c_{i\alpha j\beta} N_\alpha N_\beta \tag{10}$$

is the acoustic tensor. A nontrivial solution for $\mathbf{v}'$ exists if

$$\|\mathbf{Q} - \rho_o c^2 \mathbf{I}\| = 0 \tag{11}$$

which furnishes the wave speeds c. Let $\mathbf{r}$ be the right eigenvector associated with the wave speed c:

$$(\mathbf{Q} - \rho_o c^2 \mathbf{I})\mathbf{r} = \mathbf{0} \tag{12}$$

We have from equations (9), (7), (4), and (8)

$$v'_i = -c\omega r_i \tag{13a}$$

$$F'_{i\alpha} = \omega r_i N_\alpha \tag{13b}$$

$$T'_{i\alpha} = \omega c_{i\alpha j\beta} r_j N_\beta \tag{13c}$$

where ω is a proportional factor which we will determine next.

For a simple wave moving in a half space $X_2 > 0$, we may choose the X_1 and X_3 axes such that the normal $\mathbf{N}$ to the plane $\phi =$ constant has the expression

$$(N_1, N_2, N_3) = (\sin\theta, -\cos\theta, 0) \tag{14}$$

where θ is the angle between the plane $\phi =$ constant and the X_1-axis, Fig. 1. Let

$$V_a \sin\theta = c \tag{15}$$

where V_a is the apparent velocity of the point of intersection of the plane $\phi =$ constant and the X_1-axis. V_a must be a constant for a steady motion of the simple wave as we will be considering later on. In general, however, V_a may depend on ϕ as long as planes associated with different ϕ do not intersect each other in the $X_2 > 0$ space. The same restriction holds on the specification of $g(\phi)$ in equation (5) and $\mathbf{N}$ in equation (14). Otherwise $\mathbf{v}$, $\mathbf{F}$, and $\mathbf{T}$ which are now functions of ϕ would not be single-valued in the $X_2 > 0$ space. Noticing that c as given by equation (11) is a function of $\mathbf{F}$ and θ, differentiation of equation (15) with ϕ and using equation (13b) lead to

$$\omega = \left\{ V'_a \sin\theta + \left(c\cot\theta - \frac{\partial c}{\partial \theta} \right) \theta' \right\} \Big/ \left(r_i N_\alpha \frac{\partial c}{\partial F_{i\alpha}} \right) \tag{16}$$

The fact that $\mathbf{r}$ as defined in equation (12) is nonunique does not affect the uniqueness of the expressions in equations (13) because ω as given by equation (16) involves $\mathbf{r}$ in the denominator.

Inasmuch as ϕ is an arbitrary parameter, we may choose ϕ

Downloaded 02 May 2010 to 171.66.16.25. Redistribution subject to ASME license or copyright; see http://www.asme.org/terms/Terms_Use.cfm

$= \theta$, c, or any component of $\mathbf{v}$, $\mathbf{F}$, and $\mathbf{T}$. In the special cases in which all planes $\phi =$ constant are parallel to each other such as in one-dimensional waves, θ is a constant and we may choose $\phi = c$. Equation (16) then reduces to, using equation (15),

$$\omega = (r_i N_\alpha \partial c/\partial F_{i\alpha})^{-1} \tag{17}$$

and the primes in equations (13) stand for d/dc. Alternately, when θ is a constant we may write equations (13) as

$$\frac{dv_1}{-cr_1} = \frac{dv_2}{-cr_2} = \frac{dv_3}{-cr_3} = \frac{dF_{11}}{r_1 N_1} = \frac{dF_{12}}{r_1 N_2} = \cdots = \frac{dT_{33}}{c_{33j\beta} r_j N_\beta} \tag{18}$$

Since the denominators depend on $\mathbf{F}$ only, not on θ, equations (18) can be integrated [6, 7, 10].

Another special case which we will be discussing in this paper is the three-dimensional "centered simple wave" in which θ is not a constant but all planes intersect at the same point on the X_1-axis, Fig. 1. For this case, $g(\phi) = 0$ and $V_a' = 0$. If we choose $\phi = \theta$, equation (16) reduces to

$$\omega = \left(c \cot\theta - \frac{\partial c}{\partial \theta}\right) \Big/ \left(r_i N_\alpha \frac{\partial c}{\partial F_{i\alpha}}\right) \tag{19}$$

and the primes in equations (13) stand for $d/d\theta$. Equation (19) is meaningless when

$$r_i N_\alpha \partial c/\partial F_{i\alpha} = 0 \tag{20}$$

In this case, a centered simple wave does not exist and we have a shock wave instead (see Section 5). When (20) holds, the system of equations is not "genuinely nonlinear" [12].

3 Plane Shock Waves

Consider a plane shock surface across which the values of $\mathbf{v}$, $\mathbf{F}$, and $\mathbf{T}$ are discontinuous. The jump conditions across the shock surface are [11]

$$\left.\begin{aligned} [T_{i\alpha}]N_\alpha + \rho_o V[v_i] = 0 \\ [v_i]N_\alpha + V[F_{i\alpha}] = 0 \end{aligned}\right\} \tag{21}$$

where V is the shock wave speed, N_α the unit normal to the shock surface, and

$$[g] = g^- - g^+ \tag{22}$$

in which g^- and g^+ are the values of g behind and in front of the shock surface, respectively. Elimination of $[v_i]$ in equations (21) yields

$$[T_{i\alpha}]N_\alpha N_\beta = \rho_o V^2 [F_{i\beta}] \tag{23}$$

Noticing that $\mathbf{T}$ is a given function of $\mathbf{F}$, equation (23) provides nine equations for $\mathbf{F}^-$ when $\mathbf{F}^+$ and V are known.

Equation (23) can be simplified when $\mathbf{N}$ is given by equation (14). First, since $N_3 = 0$, equation (23) for $\beta = 3$ gives

$$[F_{i3}] = 0, \quad (i = 1,2,3) \tag{24}$$

Next for $\beta = 1$, equation (23) can be written as

$$[T_{i1}] + \xi[T_{i2}] = \rho_o V_a^2 [F_{i1}] \quad (i = 1,2,3) \tag{25}$$

where

$$\xi = -\cot\theta, \tag{26}$$

$$V = V_a \sin\theta = V_a/(1+\xi^2)^{1/2} \tag{27}$$

Finally, for $\beta = 2$ we have

$$\xi[T_{i1}] + \xi^2[T_{i2}] = \rho_o V_a^2 [F_{i2}] \tag{28}$$

or, in view of equation (25),

$$[F_{i2}] = \xi[F_{i1}] \quad (i = 1,2,3) \tag{29}$$

We will use equations (24), (25), and (29) instead of (23) in this paper.

4 Isotropic Hyperelastic Materials in Plane Strain Deformation

For the rest of the paper will limit our attention to plane strain deformations so that

$$\left.\begin{aligned} x_1 &= x_1(X_1, X_2, t) \\ x_2 &= x_2(X_1, X_2, t) \\ x_3 &= X_3 \end{aligned}\right\} \tag{30}$$

The nonzero components of the deformation gradients are

$$\mathbf{F} = \begin{bmatrix} F_{11} & F_{12} & 0 \\ F_{21} & F_{22} & 0 \\ 0 & 0 & 1 \end{bmatrix} \tag{31}$$

For isotropic hyperelastic materials,

$$T_{i\alpha} = \partial W/\partial F_{i\alpha} \tag{32}$$

where W is the strain energy which is a function of the three principal invariants I_B, II_B, and III_B of the left Cauchy-Green tensor [11],

$$\mathbf{B} = \mathbf{F}\mathbf{F}^T \tag{33}$$

For the $\mathbf{F}$ given by equation (31), one of the principal directions of the stretch is in the X_3-direction with the principal stretch ratio being unity. Hence the three principal invariants are related by

$$1 - I_B + II_B - III_B = 0 \tag{34}$$

Therefore, for isotropic hyperelastic materials in a plane strain deformation, there is no loss of generality in assuming that[1]

$$W = W(p,q) \tag{35}$$

where

$$\left.\begin{aligned} q &= \frac{1}{2}(F_{i\alpha}F_{i\alpha} - 3) = \frac{1}{2}(I_B - 3) \\ p &= \|\mathbf{F}\| - 1 = \sqrt{III_B} - 1 \end{aligned}\right\} \tag{36}$$

It can be shown that

$$\frac{\partial p}{\partial F_{i\alpha}} = F^*_{i\alpha}, \quad \frac{\partial q}{\partial F_{i\alpha}} = F_{i\alpha} \tag{37}$$

where $\mathbf{F}^*$ is the adjoint of $\mathbf{F}$ so that

$$\mathbf{F}^T\mathbf{F}^* = \mathbf{F}^*\mathbf{F}^T = \|\mathbf{F}\|\mathbf{I} \tag{38}$$

$$\mathbf{F}^{*T} = (p+1)\mathbf{F}^{-1} \tag{39}$$

For the $\mathbf{F}$ given by equation (31), we have

$$\mathbf{F}^* = \begin{bmatrix} F_{22} & -F_{21} & 0 \\ -F_{12} & F_{11} & 0 \\ 0 & 0 & p+1 \end{bmatrix} \tag{40}$$

Equation (32) now has the expression, using equations (35) and (37)

$$T = W_q\mathbf{F} + W_p\mathbf{F}^* \tag{41}$$

where the subscripts p and q of W denote partial dif-

[1] For general three-dimensional deformations, equation (35) remains valid if deformations of order higher than the second power in $(\mathbf{F} - \mathbf{1})$ are ignored.

Downloaded 02 May 2010 to 171.66.16.25. Redistribution subject to ASME license or copyright; see http://www.asme.org/terms/Terms_Use.cfm

ferentiation with respect to these variables. Since $\mathbf{T} = \mathbf{0}$ when $\mathbf{F} = \mathbf{I}$, we must have

$$W_q(0,0) + W_p(0,0) = 0 \tag{42}$$

The results derived here agree with that obtained in [9].

To find the acoustic tensor $\mathbf{Q}$ given by equation (10), we have to determine first the elasticity $c_{i\alpha j\beta}$ defined in equation (8). It can be shown by differentiating equation (38) that

$$\partial F^*_{i\alpha}/\partial F_{j\beta} = \left\{F^*_{i\alpha}F^*_{j\beta} - F^*_{i\beta}F^*_{j\alpha}\right\}\Big/\|\mathbf{F}\| \tag{43}$$

Hence, substituting equation (41) into (8) and then (10), we have

$$\mathbf{Q} = W_q\mathbf{I} + W_{qq}\mathbf{f}\mathbf{f}^T + W_{pp}\mathbf{f}^*\mathbf{f}^{*T} + W_{pq}(\mathbf{f}\mathbf{f}^{*T} + \mathbf{f}^*\mathbf{f}^T) \tag{44}$$

where

$$\mathbf{f} = \mathbf{F}\mathbf{N}, \quad \mathbf{f}^* = \mathbf{F}^*\mathbf{N} \tag{45}$$

It is not difficult to see that $\mathbf{f}$ is in the direction of the material line in the deformed body whose undeformed line is along the $\mathbf{N}$ vector while $\mathbf{f}^*$ is in the direction normal to the deformed wave front.

For the wave speeds c and the right eigenvector $\mathbf{r}$ defined in equation (12), let

$$\mathbf{r} = \beta\mathbf{f} + \beta^*\mathbf{f}^* \tag{46}$$

where β and β^* are coefficients to be determined. Substituting equation (46) into (12) and setting the coefficient of $\mathbf{f}$ and $\mathbf{f}^*$ to zero, we obtain

$$\begin{bmatrix} (W_q - \rho_o c^2) + W_{qq}l + W_{pq}m & W_{qq}m + W_{pq}n \\ W_{pq}l + W_{pp}m & (W_q - \rho_o c^2) + W_{pq}m + W_{pp}n \end{bmatrix} \begin{bmatrix} \beta \\ \beta^* \end{bmatrix} = \mathbf{0} \tag{47}$$

where

$$\left.\begin{aligned} l &= \mathbf{f}^T\mathbf{f} = \mathbf{N}^T(\mathbf{F}^T\mathbf{F})\mathbf{N} \\ m &= \mathbf{f}^T\mathbf{f}^* = \mathbf{N}^T(\mathbf{F}^T\mathbf{F}^*)\mathbf{N} = p + 1 \\ n &= \mathbf{f}^{*T}\mathbf{f}^* = \mathbf{N}^T(\mathbf{F}^{*T}\mathbf{F}^*)\mathbf{N} \end{aligned}\right\} \tag{48}$$

From equations (31), (40), (14), and (36) it can be shown that

$$l + n = 2q + 2 \tag{49}$$

For a nonzero solution of β and β^*, the determinant must be zero. We have

$$\begin{aligned} \rho_o c^2 = W_q &+ \frac{1}{2}(W_{qq}l + 2W_{pq}m + W_{pp}n) \\ &\pm \frac{1}{2}\left\{(W_{qq}l + 2W_{pq}m + W_{pp}n)^2 \right. \\ &\left. - 4(W_{pp}W_{qq} - W^2_{pq})(ln - m^2)\right\}^{1/2} \end{aligned} \tag{50}$$

and

$$\frac{\beta}{\beta^*} = \frac{-(W_{qq}m + W_{pq}n)}{W_q - \rho_o c^2 + W_{qq}l + W_{pq}m} = \frac{W_q - \rho_o c^2 + W_{pq}m + W_{pp}n}{-(W_{pq}l + W_{pp}m)} \tag{51}$$

For the $\mathbf{F}$ and $\mathbf{T}$ given by equations (31) and (41), the shock conditions (24) and equations (29) and (25) for $i = 3$ are trivially satisfied. Equations (29) and (25) for $i = 1$ and 2 are

$$[F_{i2}] = \xi[F_{i1}], \quad (i = 1,2) \tag{52}$$

$$\begin{aligned} &[W_q(F_{i1} + \xi F_{i2})] + [W_p(F^*_{i1} + \xi F^*_{i2})] \\ &\qquad = \rho_o V_a^2[F_{i1}], \quad (i = 1,2) \end{aligned} \tag{53}$$

Using equations (27), (52), and the identity

$$[hg] = h^-[g] + g^+[h], \tag{54}$$

equation (53) for $i = 1,2$ can be rewritten as

$$\left.\begin{aligned} &[W_q](F^+_{11} + \xi F^+_{12}) + [W_p](F^+_{22} - \xi F^+_{21}) \\ &\qquad = (1 + \xi^2)(\rho_o V^2 - W^-_q)[F_{11}] \\ &[W_q](F^+_{21} + \xi F^+_{22}) - [W_p](F^+_{12} - \xi F^+_{11}) \\ &\qquad = (1 + \xi^2)(\rho_o V^2 - W^-_q)[F_{21}] \end{aligned}\right\} \tag{55}$$

For a fixed V_a and $F^+_{i\alpha}$, equations (52) and (55) provide four equations for $F^-_{i\alpha}$ $(i,\alpha = 1,2)$ with ξ as the parameter. As ξ varies, $F^-_{i\alpha}$ traces a curve in the $(F_{11},F_{12},F_{21},F_{22})$ space. This curve is called the "deformation gradient path" for shock wave [5]. One could obtain equations for the deformation gradient path without the parameter by eliminating V in equations (55). We have

$$\begin{aligned} &[W_q]\left\{(F^+_{11} + \xi F^+_{12})[F_{21}] - (F^+_{21} + \xi F^+_{22})[F_{11}]\right\} \\ &+ [W_p]\left\{(F^+_{22} - \xi F^+_{21})[F_{21}] + (F^+_{12} - \xi F^+_{11})[F_{11}]\right\} = 0 \end{aligned} \tag{56}$$

Equations (52) and (56) provide the equations for the deformation gradient path for shock waves in the $\mathbf{F}$ space.

5 Special Isotropic Hyperelastic Materials

In this section, we consider a special class of isotropic hyperelastic materials for which the strain energy $W(p,q)$ satisfies the equation

$$W_{pp}W_{qq} = W^2_{pq} \tag{57}$$

As we will see later, the harmonic material [9] is a particular case of this class of materials. In the (p,q,W) space, the surface $W = W(p,q)$ given by equation (57) is a developable surface. It is seen that W_{pp} and W_{qq} must have the same sign. Also, if any of W_{pp} or W_{qq} is zero, so is W_{pq}. We will exclude the case in which $W_{pp} = W_{qq} = W_{pq} = 0$. Let

$$\left.\begin{aligned} &\beta = \sqrt{|W_{qq}|}, \\ &\beta^* = \pm\sqrt{|W_{pp}|}, \quad \text{if } W_{pp}W_{pq} \text{ or } W_{qq}W_{pq} \gtrless 0 \end{aligned}\right\} \tag{58}$$

Then equation (44) can be written as

$$\mathbf{Q} = W_q\mathbf{I} \pm (\beta\mathbf{f} + \beta^*\mathbf{f}^*)(\beta\mathbf{f} + \beta^*\mathbf{f}^*)^T, \quad \text{if } W_{qq} \text{ or } W_{pp} \gtrless 0 \tag{59}$$

By a direct substitution, it can be verified that the following wave speed denoted by c_1 and the right eigenvector denoted by $\mathbf{r}_1$ satisfy equation (12):

$$\left.\begin{aligned} &\mathbf{r}_1 = \beta\mathbf{f} + \beta^*\mathbf{f}^* \\ &\rho_o c_1^2 = W_q \pm \mathbf{r}_1^T\mathbf{r}_1 = W_q \pm (\beta^2 l + 2\beta\beta^* m + \beta^{*2}n), \\ &\qquad\qquad \text{if } W_{qq} \text{ or } W_{pp} \gtrless 0. \end{aligned}\right\} \tag{60}$$

Similarly, the right eigenvector $\mathbf{r}_2$ and the wave speed c_2 given by

$$\mathbf{r}_2^T\mathbf{r}_1 = 0, \quad \rho_o c_2^2 = W_q \tag{61}$$

satisfy equation (12). $\mathbf{r}_2$ is orthogonal to $\mathbf{r}_1$. If $\mathbf{r}_1$ has the components $(k_1,k_2,0)$ we may choose $\mathbf{r}_2 = (k_2,-k_1,0)$. Notice that the wave speed c_2 is independent of the direction of propagation $\mathbf{N}$.

Let us consider the centered simple wave associated with c_2. Using equations (37), (45), and (58), we have

Downloaded 02 May 2010 to 171.66.16.25. Redistribution subject to ASME license or copyright; see http://www.asme.org/terms/Terms_Use.cfm

$$2\rho_o c_2 \frac{\partial c_2}{\partial F_{i\alpha}} N_\alpha = (W_{qq} F_{i\alpha} + W_{pq} F^*_{i\alpha}) N_\alpha \tag{62}$$

$$= \pm\beta(\beta f_i + \beta^* f_i^*) = \pm\beta(\mathbf{r}_1)_i, \quad \text{if } W_{qq} \gtrless 0$$

Since $\mathbf{r}_2$ associated with c_2 is orthogonal to $\mathbf{r}_1$, equation (20) is satisfied. Therefore, *a centered simple wave solution associated with the wave speed c_2 does not exist for the special class of materials considered here.*

We now consider the shock wave V_2 associated with the wave speed c_2. According to Lax [12], a necessary condition for a shock wave to be stable is

$$c_2^- \geq V_2 \geq c_2^+ \tag{63}$$

Since equation (57) is equivalent to [13]

$$G(W_p, W_q) = 0 \tag{64}$$

where G is an arbitrary function, it is seen that

$$W_p^- = W_p^+, \quad \text{if } W_q^- = W_q^+, \tag{65}$$

and vice versa. Hence

$$[W_p] = 0, \quad \text{if } [W_q] = 0 \tag{66}$$

and vice versa. We see that

$$[W_p] = [W_q] = 0 \tag{67}$$

satisfy equation (56). From equation (55) we have, with V written as V_2 and using equation (67),

$$\rho_o V_2^2 = W_q^- = W_q^+ \tag{68}$$

In view of equations (61) and (68), the stability condition (63) is satisfied. Therefore, *the shock wave V_2 is always stable for the special class of materials considered here.*

Before we close this section, we consider the following particular W's which satisfy equation (57)

$$\text{Case 1:} \quad W_{pp} = W_{qq} = W_{pq} \tag{69}$$

$$\text{Case 2:} \quad W_{pp} = W_{qq} = -W_{pq} \tag{70}$$

$$\text{Case 3:} \quad W_{pp} = W_{pq} = 0 \tag{71}$$

$$\text{Case 4:} \quad W_{qq} = W_{pq} = 0 \tag{72}$$

For these materials, equations (60) for c_1 and $\mathbf{r}_1$, equation (67) for the jump across V_2, and equation (55) for shock wave speed V_1 have simpler expressions.

***(i)* Case 1:** The general solution to equations (69) is

$$W = a(q-p) + \psi(q+p), \quad \psi(0) = \psi'(0) = 0 \tag{73}$$

where a is a constant, ψ is an abritrary function, and the prime stands for differentiation with the argument. Equations (73), which satisfy equation (42), is the harmonic material introduced in [9]. For this material, we can write $\mathbf{r}_1$ and c_1 as

$$\mathbf{r}_1 = \mathbf{f} + \mathbf{f}^*, \quad \rho_o c_1^2 = W_q + (2q + 2p + 4) W_{qq} \tag{74}$$

Hence c_1 is independent of the direction of wave propagation $\mathbf{N}$. Since

$$[W_p] = [W_q] = [\psi'(q+p)], \tag{75}$$

the jump across V_2 is, by equation (67)

$$[q+p] = 0 \tag{76}$$

If $[q+p] \neq 0$, we obtain from equation (55) the other shock wave speed V_1.

$$\left.\begin{aligned} \rho_o V_1^2 &= W_q^- + \Big\{ (F_{11}^+ + F_{22}^+) \\ &\quad - \xi (F_{21}^+ - F_{12}^+) \Big\} [\psi'(q+p)]/(1+\xi^2)[F_{11}] \\ &= W_q^- + \Big\{ (F_{21}^+ - F_{12}^+) \\ &\quad + \xi (F_{11}^+ + F_{22}^+) \Big\} [\psi'(q+p)]/(1+\xi^2)[F_{21}] \end{aligned}\right\} \tag{77}$$

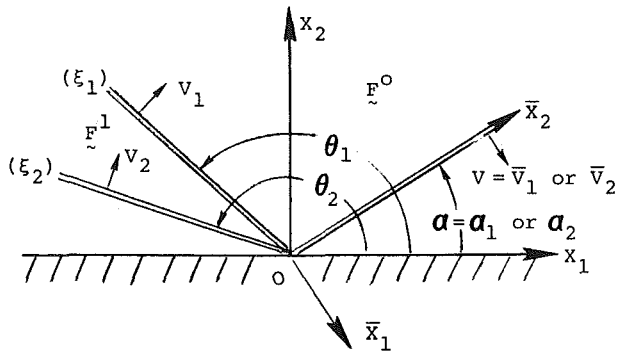


Fig. 2 Reflected shock waves V_1 and V_2 due to an incident shock wave

***(ii)* Case 2:** The general solution to equation (70) is

$$W = a(q-p) + \psi(q-p), \quad \psi(0) = 0. \tag{78}$$

We therefore can write

$$\mathbf{r}_1 = \mathbf{f} - \mathbf{f}^*, \quad \rho_o c_1^2 = W_q + (2q - 2p) W_{qq} \tag{79}$$

Again, c_1 is independent of $\mathbf{N}$. Hence there are materials other than harmonic materials for which the wave speeds c_1 and c_2 are independent of the direction of wave propagation. From equation (78), we have

$$[W_q] = -[W_p] = [\psi'(q-p)] \tag{80}$$

Therefore, across the shock wave V_2 we have

$$[q-p] = 0 \tag{81}$$

If $[q-p] \neq 0$, we obtain V_1 from equation (55):

$$\left.\begin{aligned} \rho_o V_1^2 &= W_q^- + \Big\{ (F_{11}^+ - F_{22}^+) \\ &\quad + \xi (F_{12}^+ + F_{21}^+) \Big\} [\psi'(q-p)]/(1+\xi^2)[F_{11}] \\ &= W_q^- + \Big\{ (F_{12}^+ + F_{21}^+) \\ &\quad - \xi (F_{11}^+ - F_{22}^+) \Big\} [\psi'(q-p)]/(1+\xi^2)[F_{21}] \end{aligned}\right\} \tag{82}$$

***(iii)* Case 3:** The general solution to equation (71) is

$$W = a(q-p) + \psi(q), \quad \psi(0) = \psi'(0) = 0 \tag{83}$$

and we have

$$\mathbf{r}_1 = \mathbf{f}, \quad \rho_o c_1^2 = W_q + W_{qq} I \tag{84}$$

Since

$$[W_p] = 0, \quad [W_q] = [\psi'(q)], \tag{85}$$

the jump across V_2 is

$$[q] = 0. \tag{86}$$

Across the shock wave V_1, $[q] \neq 0$ and

$$\left.\begin{aligned} \rho_o V_1^2 &= W_q^- + (F_{11}^+ + \xi F_{12}^+)[\psi'(q)]/(1+\xi^2)[F_{11}] \\ &= W_q^- + (F_{21}^+ + \xi F_{22}^+)[\psi'(q)]/(1+\xi^2)[F_{21}] \end{aligned}\right\} \tag{87}$$

***(iv)* Case 4:** The general solution to equation (72) is

$$W = a(q-p) + \psi(p), \quad \psi(0) = \psi'(0) = 0 \tag{88}$$

Hence

$$\mathbf{r}_1 = \mathbf{f}^*, \quad \rho_o c_1^2 = W_q + W_{pp} n \tag{89}$$

From

$$[W_q] = 0, \quad [W_p] = [\psi'(p)] \tag{90}$$

we see that across the shock wave V_2

$$[p] = 0 \tag{91}$$

while for shock wave V_1, $[p] \neq 0$, and

Downloaded 02 May 2010 to 171.66.16.25. Redistribution subject to ASME license or copyright; see http://www.asme.org/terms/Terms_Use.cfm

$$\rho_o V_1^2 = W_q^- + (F_{22}^+ - \xi F_{21}^+)[\psi'(p)]/(1+\xi^2)[F_{11}] \quad (92)$$
$$= W_q^- - (F_{12}^+ - \xi F_{11}^+)[\psi'(p)]/(1+\xi^2)[F_{21}]$$

6 Reflection From a Rigid Boundary

Consider a plane shock wave moving at the speed $\bar{V}$ striking obliquely on a plane boundary at an angle α, Figs. 1 and 2. In general, two waves are reflected, each of which can be a shock wave or a simple wave. It can also be a composite wave in which part of the wave is a simple wave and the other part a shock wave [5]. For the special class of materials considered in the previous section, the reflection problem is simplified considerably because one of the reflected waves is always the shock wave V_2. Therefore, all one has to determine is whether the remaining reflected wave is a simple wave, a shock wave, or a composite wave.

For an illustrative purpose, we consider the case of a rigid boundary, which means that

$$x_1(X_1,0,t) = X_1, \quad x_2(X_1,0,t) = 0 \quad (93)$$

and consider the material whose strain energy W is given by

$$W = a(q-p) + \frac{1}{2}bp^2 + \frac{1}{3}ep^3 \quad (94)$$

where a, b, and e are constants. This material belongs to Case 4 in the preceding section. The relations between the stress $\mathbf{T}$ and the deformation gradient $\mathbf{F}$ are given by equation (41) in which the nonzero elements of $\mathbf{F}$ and $\mathbf{F}^*$ are shown in equations (31) and (40) while

$$W_q = a, \quad W_p = -a + bp + ep^2 \quad (95)$$

When a plane shock wave propagates in the direction of the $\bar{X}_1$-axis, Fig. 1, with the region ahead of the shock wave being stress free, the motion behind the shock wave can be described by

$$\left.\begin{aligned} \bar{x}_1 &= \bar{X}_1 + \bar{u}_1(\bar{X}_1,t) \\ \bar{x}_2 &= \bar{X}_2 + \bar{u}_2(\bar{X}_1,t) \end{aligned}\right\} \quad (96)$$

where $\bar{u}_1$ and $\bar{u}_2$ are the displacement components behind the shock wave in the $\bar{X}_1$ and $\bar{X}_2$ direction, respectively. The deformation gradient $\bar{\mathbf{F}}$ referred to the $\bar{X}_\alpha$ coordinates is

$$\bar{\mathbf{F}} = \begin{bmatrix} 1+\epsilon & 0 & 0 \\ \gamma & 1 & 0 \\ 0 & 0 & 1 \end{bmatrix}, \quad (97)$$

$$\epsilon = \partial\bar{u}_1/\partial\bar{X}_1, \quad \gamma = \partial\bar{u}_2/\partial\bar{X}_1, \quad (98)$$

where ϵ and γ are, respectively, the extensional strain and shear strain. Hence

$$p = \bar{p} = \epsilon, \quad q = \bar{q} = \epsilon + \frac{1}{2}(\epsilon^2 + \gamma^2) \quad (99)$$

and

$$\left.\begin{aligned} \bar{T}_{11} &= (a+b)\epsilon + e\epsilon^2 \\ \bar{T}_{12} &= \gamma(a - b\epsilon - e\epsilon^2) \\ \bar{T}_{21} &= a\gamma \\ \bar{T}_{22} &= -a\epsilon + (1+\epsilon)(b\epsilon + e\epsilon^2) \end{aligned}\right\} \quad (100)$$

Comparing the linear terms in ϵ and γ with the classical elasticity, we have

$$a = \mu > 0, \quad b = \lambda + \mu > 0 \quad (101)$$

where λ and μ are the Lamé constants. We see that the relation between $\bar{T}_{21}$ and γ is linear while that between $\bar{T}_{11}$ and ϵ can be concave or convex with respect to the ϵ-axis depending on the sign of e. If the shock wave is a pressure shock involving a discontinuity in $\bar{T}_{11}$ and ϵ, it is not difficult to see that the shock wave is stable when

$$e[\epsilon] = e\epsilon > 0 \quad (102)$$

The shock wave speed will be denoted by $\bar{V}_1$ and the angle at which the shock plane makes with the boundary will be denoted by α_1. If the shock wave is a shear shock involving a discontinuity in $\bar{T}_{21}$ and γ, the corresponding shock wave speed and the angle will be denoted by $\bar{V}_2$ and α_2, respectively.

If the first reflected wave is a shock wave, the associated wave speed and the angle of inclination of the shock plane are denoted by V_1 and θ_1, respectively, Fig. 2. If it is a centered simple wave, then the wave speeds and the angles of inclination of the beginning and end of the simple wave are denoted by c_1^0, θ_0 and c_1^1, θ_1, respectively, Fig. 1. The second reflected wave is always the shock wave V_2 where

$$\rho_o V_2^2 = a \quad (103)$$

with the angle of inclination denoted by θ_2. Since the apparent wave speed V_a is the same for all waves, we have

$$V_a = \frac{\bar{V}_1}{\sin\alpha_1} = \frac{\bar{V}_2}{\sin\alpha_2} = \frac{c_1^0}{\sin\theta_0} = \frac{c_1^1}{\sin\theta_1} = \frac{V_2}{\sin\theta_2} = \frac{c_1}{\sin\theta} \quad (104)$$

where $\bar{V}_2 = V_2 = \sqrt{a/\rho_0}$. The deformation gradient behind the incident shock wave is denoted by $\mathbf{F}^0$ while that in front of the reflected V_2 shock wave is denoted by $\mathbf{F}^1$.

For the material given by equation (94), the wave speeds c_1, c_2, and the right eigenvectors $\mathbf{r}_1$, $\mathbf{r}_2$ can be written as, using equations (89) and (61)

$$\left.\begin{aligned} \rho_o c_1^2 &= a + (b+2ep)\left\{(F_{22}N_1 - F_{21}N_2)^2 + (F_{11}N_2 - F_{12}N_1)^2\right\} \\ \mathbf{r}_1 &= (F_{22}N_1 - F_{21}N_2, \quad F_{11}N_2 - F_{12}N_1) \end{aligned}\right\} \quad (105)$$

$$\left.\begin{aligned} \rho_o c_2^2 &= a = \rho_o V_2^2 \\ \mathbf{r}_2 &= (F_{11}N_2 - F_{12}N_1, \quad F_{21}N_2 - F_{22}N_1) \end{aligned}\right\} \quad (106)$$

We see that

$$c_1 \gtrless c_2 \text{ if } b + 2ep \gtrless 0 \quad (107)$$

and hence c_1 can be the fast wave or slow wave depending on the sign of $b+2ep$. For small deformations in which $p << 1$ and hence $b+2ep > 0$, c_1 is the fast wave. In the numerical examples we will consider later, c_1 is always the fast wave speed.

Using equations (13b) and (19), the differential equations for the simple wave associated with c_1 can be written as

$$\left.\begin{aligned} dF_{11}/d\xi &= -\hat{\omega}(F_{22} - \xi F_{21}) \\ dF_{12}/d\xi &= -\hat{\omega}\xi(F_{22} - \xi F_{21}) \\ dF_{21}/d\xi &= \hat{\omega}(F_{12} - \xi F_{11}) \\ dF_{22}/d\xi &= \hat{\omega}\xi(F_{12} - \xi F_{11}) \end{aligned}\right\} \quad (108)$$

where

$$\hat{\omega} = \frac{a\xi - (b+2ep)\left\{(F_{22} - \xi F_{21})F_{21} + (F_{12} - \xi F_{11})F_{11}\right\}}{e\left\{(F_{22} - \xi F_{21})^2 + (F_{12} - \xi F_{11})^2\right\}^2} \quad (109)$$

Downloaded 02 May 2010 to 171.66.16.25. Redistribution subject to ASME license or copyright; see http://www.asme.org/terms/Terms_Use.cfm

and ξ is defined in equation (26). If we know the initial conditions $\mathbf{F} = \mathbf{F}^0$ at $\xi = \xi_0$, Fig. 1, equations (108) can be integrated numerically provided that $\hat{\omega}$ is bounded.

The jump conditions associated with shock wave V_1 are obtained from equations (29) and (92).

$$\left.\begin{aligned}[F_{12}] &= \xi[F_{11}] \\ [F_{22}] &= \xi][F_{21}]\end{aligned}\right\} \tag{110a}$$

$$\left.\begin{aligned}\rho_o V_1^2 &= a + (F_{22}^+ - \xi F_{21}^+)[bp + ep^2]/(1+\xi^2)[F_{11}] \\ &= a - (F_{12}^+ - \xi F_{11}^+)[bp + ep^2]/(1+\xi^2)[F_{21}]\end{aligned}\right\} \tag{110b}$$

Using the definition for p, equation (36), and equation (110a), it can be shown that

$$[p] = [F_{11}](F_{22}^+ - \xi F_{21}^+) - [F_{21}](F_{12}^+ - \xi F_{11}^+) \tag{111}$$

Equations (110) can be solved for $[F_{11}]$, $[F_{12}]$, $[F_{21}]$, and $[F_{22}]$. The results can be written as

$$[F_{11}] = (F_{22}^+ - \xi F_{21}^+)[p]/h^+ \tag{112}$$

$$[F_{12}] = \xi[F_{11}]$$

$$[F_{21}] = -(F_{12}^+ - \xi F_{11}^+)[p]/h^+$$

$$[F_{22}] = \xi[F_{21}]$$

where

$$[p] = \left\{\rho_o V_a^2 - a(1+\xi^2) - \left(2p^+ + \frac{b}{e}\right)eh^+\right\}\Big/(eh^+) \tag{113}$$

$$h = (F_{12} - \xi F_{11})^2 + (F_{22} - \xi F_{21})^2 \tag{114}$$

The V_1 given in equation (110b) can now be written in the form

$$\rho_o V_1^2 = \rho_o (c_1^+)^2 + e[p]h^+/(1+\xi^2) \tag{115}$$

$$= \rho_o (c_1^-)^2 - e[p]h^-/(1+\xi^2)$$

where use has been made of equation (105). Using equations (110a), it can be shown that $h^+ = h^-$. For the shock wave V_1 to be stable, we must have $c_1^- \geq V_1 \geq c_1^+$ and hence

$$e[p] \geq 0 \tag{116}$$

The jump condition associated with V_2 is given in equation (91), or by equation (111),

$$[F_{11}](F_{22}^+ - \xi F_{21}^+) = [F_{21}](F_{12}^+ - \xi F_{11}^+) \tag{117}$$

If V_2 is the shock wave in which $\mathbf{F}^-$ is adjacent to the boundary as shown in Figs. 1 and 2, then by equation (93),

$$F_{11}^- = 1, \quad F_{21}^- = 0 \tag{118}$$

With this, equation (117) reduces to

$$F_{21}^1(F_{12}^1 - \xi_2 F_{11}^1) - (F_{22}^1 - \xi_2 F_{21}^1)(F_{11}^1 - 1) = 0 \tag{119}$$

where according to Figs. 1 and 2 we have set $\mathbf{F}^+ = \mathbf{F}^1$ and $\xi = \xi_2$. Notice that

$$\xi_2 = -\cot\theta_2, \quad V_a \sin\theta_2 = V_2 = \sqrt{a/\rho_o} \tag{120}$$

where V_a is the apparent wave speed.

6(a) Incident Pressure Shock Wave. If the incident shock wave is a pressure wave, the deformation gradient $\bar{\mathbf{F}}$ referred to the $\bar{\mathbf{X}}$ coordinates, Fig. 1, is given by equation (97) with $\gamma = 0$. Since $\bar{\mathbf{F}}^+ = \mathbf{I}$, and $\xi = 0$ when referred to the $\bar{\mathbf{X}}$ coordinates, equations (111) and (110b) yield

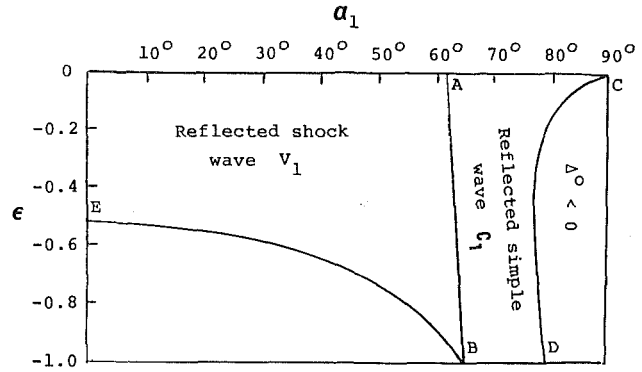


Fig. 3 Reflected fast wave is a simple wave c_1 or a shock wave V_1 depending on the angle α_1 of the incident pressure shock and its amplitude ϵ (Drawn for $b/a = 2.5$, $e/a = -1$)

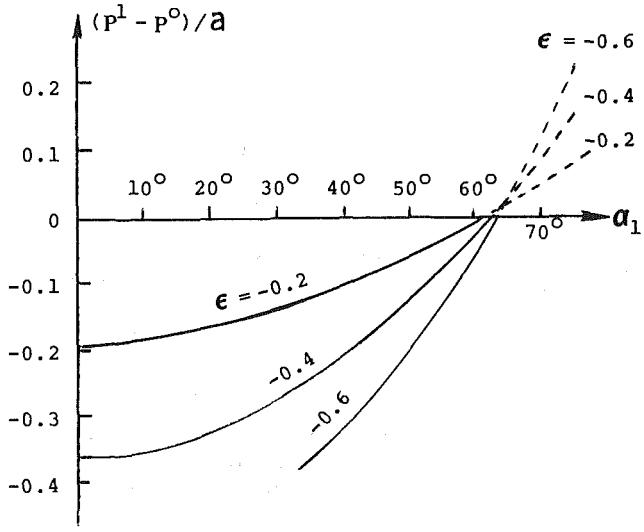


Fig. 4 Difference in pressure across reflected shock wave V_1 (solid lines) or simple wave c_1 (dotted lines) for incident pressure shock wave

$$\left.\begin{aligned}[p] &= \epsilon \\ \rho_o \bar{V}_1^2 &= a + b + e\epsilon\end{aligned}\right\} \tag{121}$$

Transforming $\bar{\mathbf{F}}$ in equation (97) to the $\mathbf{X}$ coordinates with $\gamma = 0$, we have,

$$\left.\begin{aligned}F_{11}^0 &= 1 + \epsilon\sin^2\alpha_1, \quad F_{22}^0 = 1 + \epsilon\cos^2\alpha_1 \\ F_{12}^0 &= F_{21}^0 = -\epsilon\sin\alpha_1\cos\alpha_1\end{aligned}\right\} \tag{122}$$

With $\bar{V}_1$ and α_1 known, equations (104) and (120) provide θ_2 and ξ_2. Now if the first reflected wave is a shock wave V_1, equations (112) can be used to find $\mathbf{F}^1$ when ξ is given. When $\xi = \xi_1$, $\mathbf{F}^1$ should satisfy equation (119). Hence equations (112) together with (119) form an implicit equation for ξ_1. The root ξ_1 can be determined numerically. The shock wave V_1 is stable if the inequality (116) is satisfied.

If the first reflected wave is a simple wave, equation (108) can be integrated numerically with the initial conditions $\mathbf{F} = \mathbf{F}^0$ at $\xi = \xi_0$. We used a fourth-order Runge-Kutta method [14] for the numerical integration. The value of ξ_0 can be determined by using equation (105) and the condition

$$V_a \sin\theta_0 = c_1 \tag{123}$$

The result is

$$\xi_0 = \frac{(b + 2ep^0)(F_{22}^0 F_{21}^0 + F_{12}^0 F_{11}^0) \pm \sqrt{\Delta^0}}{a + (b + 2ep^0)(F_{21}^{02} + F_{11}^{02})} \tag{124}$$

Downloaded 02 May 2010 to 171.66.16.25. Redistribution subject to ASME license or copyright; see http://www.asme.org/terms/Terms_Use.cfm

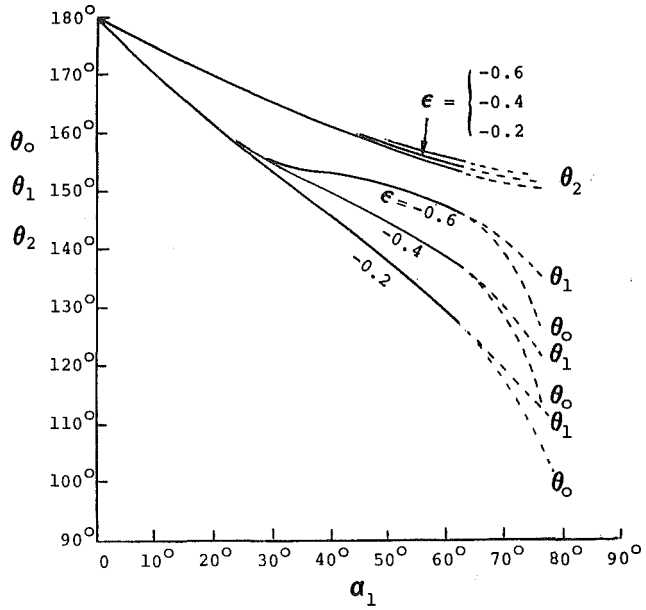


Fig. 5 Reflected angles θ_0, θ_1, and θ_2 verses incident angle α_1 for incident pressure shock wave. Solid (dotted) lines indicate that the reflected fast wave is a shock (simple) wave.

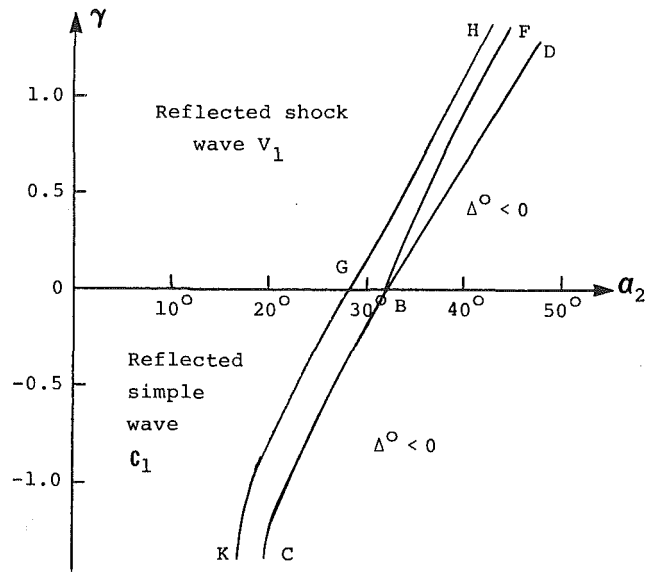


Fig. 6 Reflected fast wave is a simple wave c_1 or shock wave V_1 depending on the angle α_2 of the incident shear shock and its amplitude γ (Drawn for $b/a = 2.5, e/a = -1$)

where

$$\Delta = (b+2ep)^2(F_{22}F_{21}+F_{12}F_{11})^2 \qquad (125)$$
$$-\left\{a+(b+2ep)\left(F_{21}^2+F_{11}^2\right)\right\}\left\{a+(b+2ep)\left(F_{22}^2+F_{12}^2\right)-\rho_o V_a^2\right\}$$

For an infinitesimal incident shock, equation (124) reduces to

$$\xi_0 = \pm\left\{\frac{\rho_o V_a^2}{a+b}-1\right\}^{1/2} \qquad (126)$$

It can be shown that $-$ and $+$ correspond to the incident and reflected wave, respectively. Hence we should use the $+$ sign in equation (124). Numerical integration of equations (108) yields $\mathbf{F}$ as a function of ξ. At each increment of ξ, we check and see if equation (119) is satisfied. If it is, we have obtained ξ_1 and $\mathbf{F}^1$, Fig. 1.

The numerical results for various incident pressure shock amplitudes ϵ and the inclination angles α_1 are shown in Figs. 3–5. For numerical calculations, we chose $b/a = 2.5$ and $e/a = -1$. Figure 3 shows that if the combination of ϵ and α_1 falls in the region $OABE$, the first reflected wave is a shock wave. If it falls in the region $ABDC$, we have a simple wave. The curve EB marks the limit at which $p = -1$ behind the reflected V_1 shock wave. Since $\|\mathbf{F}\| = 1 + p > 0, p < -1$ is not permissible.

The line AB in Fig. 3 corresponds to a change over from a simple wave to a shock wave in the first reflected wave. Hence for (α_1, ϵ) values on the line AB, the first reflected wave is absent, which means $\mathbf{F}^0 = \mathbf{F}^1$, Fig. 1 or 2. We can obtain the line AB analytically by substituting $\mathbf{F}^0$ of equation (122) in place of $\mathbf{F}^1$ in equation (119). The result is

$$a+b+e\epsilon = a\tan^2\alpha_1 \qquad (127)$$

This is the curve AB. Using equations (121) and (120), we can rewrite (127) as

$$\frac{\bar{V}_1}{\sin\alpha_1} = \frac{V_2}{\cos\alpha_1} \qquad (128)$$

Comparison with equations (104) shows that

$$\theta_2 - \alpha_1 = \pi/2 \qquad (129)$$

Hence when the reflected shock wave front V_2 is orthogonal to the incident pressure shock wave $\bar{V}_1$, there is no reflected wave other than V_2.

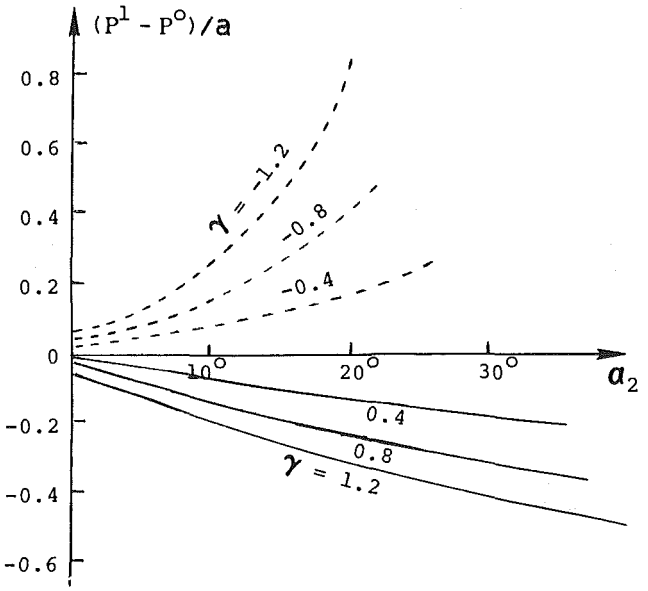


Fig. 7 Difference in pressure across reflected shock wave V_1 (solid lines) or simple wave c_1 (dotted lines) for incident shear shock wave

The curve CD is obtained by setting $\Delta^0 = 0$. From equation (124), we see that ξ_0 and hence c_1^0 does not exist if $\Delta^0 < 0$. Thus for the region to the right of the curve CD, c_1^0 does not exist. The incident angle α_1 has reached a critical angle on the curve CD and one does not have a reflection pattern given in Fig. 1 or 2.

In Fig. 4, we show the difference in the p values across the shock wave V_1 (solid lines) or across the simple wave (dotted lines) versus α_1 for certain values of ϵ. In Fig. 5 we show the reflected angles θ_0, θ_1 and θ_2 versus α_1 for three values of ϵ. Again, the solid lines (or dotted lines) indicate that the first reflected wave is a shock wave (or simple wave).

6(*b*) Incident Shear Shock Wave. When the incident shock wave is a shear shock, $\alpha = \alpha_2$ while $\bar{V} = \bar{V}_2 = V_2 = \sqrt{a/\rho_o}$. From equations (104) we have $\theta_2 = \pi - \alpha_2$. The

Downloaded 02 May 2010 to 171.66.16.25. Redistribution subject to ASME license or copyright; see http://www.asme.org/terms/Terms_Use.cfm

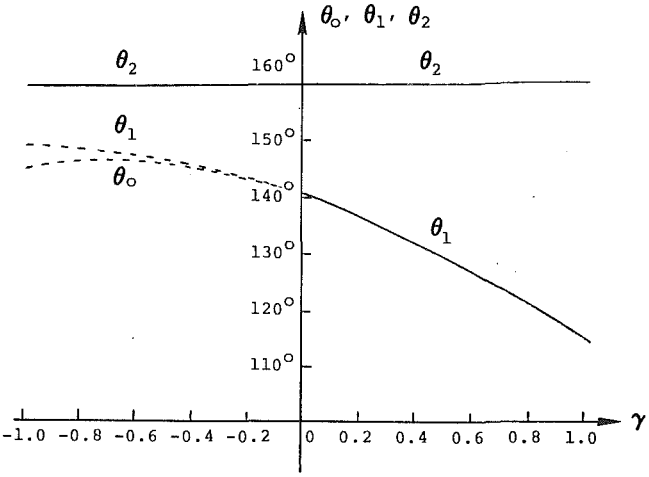


Fig. 8 Reflected angle θ_1 for shock wave V_1 (solid line) and θ_0, θ_1 for simple wave c_1 (dotted lines) verses amplitude γ of the incident shear shock wave. Incident angle is 20 deg. θ_2 is the reflected angle for shock wave V_2.

deformation gradient behind the incident shock wave is given by equation (97) with $\epsilon = 0$. If we transform $\bar{\mathbf{F}}$ to the coordinate system $\mathbf{X}$, we obtain $\mathbf{F}^0$ whose components are

$$\left.\begin{aligned} F^0_{11} &= 1+\gamma\sin\alpha_2\cos\alpha_2 \\ F^0_{12} &= -\gamma\cos^2\alpha_2 \\ F^0_{21} &= \gamma\sin^2\alpha_2 \\ F^0_{22} &= 1-\gamma\sin\alpha_2\cos\alpha_2 \end{aligned}\right\} \tag{130}$$

We also have $p^0 = 0$. The rest of the analysis is similar to the case of an incident pressure shock wave presented in Section 6(*a*) and the numerical results are presented in Figs. 6–8. In Fig. 6, we see that the first reflected wave is a shock wave (or a simple wave) when $\gamma > 0$ (or < 0). The line *CBD* is obtained from $\Delta^0 = 0$. Thus c_1^0 does not exist to the right of the line *CBD*. In the numerical calculations, we were not able to find ξ_1 for the region to the left of *BD* up to the line *BF*. We could not explain why a ξ_1 does not exist for this region. Perhaps the reflected wave is a composite wave. This problem is one of the topics for further investigation.

The line *HGK* corresponds to the combination of (γ,α_2) for which the V_2 shock wave is absent. The *GK* portion of the curve is obtained numerically. To obtain the portion *GH* analytically, we let $F^-_{11} = 1$, $F^-_{21} = 0$ in the first and third of equations (112). We have

$$\left.\begin{aligned} 1-F^0_{11} &= \left(F^0_{22}-\xi_1F^0_{21}\right)[p]/h^0 \\ -F^0_{21} &= -\left(F^0_{12}-\xi_1F^0_{11}\right)[p]/h^0 \end{aligned}\right\} \tag{131}$$

where we have replaced $\mathbf{F}^+$ by $\mathbf{F}^0$ and ξ by ξ_1. With $\mathbf{F}^0$ given by equation (130), equation (131) provide equations for the relation between γ and α_2 with ξ_1 as a parameter. Notice that if we eliminate $[p]$ between the two equations in (131), we obtain

$$\xi_1 = \frac{\tan\alpha_2-\gamma}{1+\gamma\tan\alpha_2} = \tan(\alpha_2-\tan^{-1}\gamma) \tag{132}$$

Since $\xi_1 = -\cot\theta_1 = \tan(\theta_1 - \pi/2)$, we have

$$\theta_1-\alpha_2 = \pi/2-\tan^{-1}\gamma \tag{133}$$

For a very small incident shear shock in which $\tan^{-1}\gamma \cong 1$, the reflected shock wave V_1 is almost perpendicular to the incident shock when the reflected V_2 shock is absent.

In Fig. 7 we show the difference in p^1 and p^0 values versus α_2 for various incident shear shock amplitudes γ. In Fig. 8 the angle θ_1 for reflected shock wave V_1 and θ_0 and θ_1 for reflected simple wave are plotted against the incident shock amplitude γ for $\alpha_2 = 20$ deg. The angle θ_2 of the reflected shock wave V_2 is always 160 deg. Again, the solid lines (or dotted lines) correspond to the cases in which the first reflected wave is a shock (or a simple) wave.

Acknowledgments

This work has been supported by the U.S. Army Research Office under Grant DAAG 29-80-C-0093 to the University of Illinois at Chicago.

References

1 Duvaut, M. G., "Ondes Dans les Matériaux de Type Harmonique. Réflexion Oblique D'une Onde de Choc Plane longitudinale Sur Une Paroi Fixe," *C. R. Acad. Sc. Paris*, t.266, Série *A*, 1968, pp. 246–249.

2 Reid, S. R., "The Influence of Non-Linearity Upon the Reflection of Finite Amplitude Shock Waves in Elastodynamics," *Q. J. Mech. Appl. Math.*, Vol. 25, 1972, pp. 185–206.

3 Wright, T. W., "Reflection of Oblique Shock Waves in Elastic Solids," Int. J. Solids Structures, Vol. 7, 1971, pp. 161–181.

4 Wright, T. W., "Critical Angles and Grazing Incidence: The Breakdown of Regular Shock Reflection in Solids," *J. Elasticity*, Vol. 11, 1981, pp. 81–107.

5 Li, Yongchi, and Ting, T. C. T., "Plane Waves in Simple Elastic Solids and Discontinuous Dependence of Solution on Boundary Conditions," *Int. J. Solids Structures*, Vol. 19, 1983, pp. 989–1008.

6 Clifton, R. J., "An Analysis of Combined Longitudinal and Torsional Plastic Waves in a Thin-Walled Tube," *Proc. 5th U.S. Nat. Congress Appl. Mech.*, ASME, New York, 1966, pp. 465–480.

7 Ting, T. C. T., and Nan, N., "Plane Waves Due to Combined Compressive and Shear Stresses in Half-Space," JOURNAL OF APPLIED MECHANICS, Vol. 36, 1969, pp. 189–197.

8 Varley, E., "Simple Waves in General Elastic Materials," *Arch. Rat. Mech. Anal.*, Vol. 20, 1965, pp. 309–328.

9 Stoker, J. J., "Topics in Non-Linear Elasticity," Courant Institute of Mathematical Sciences, New York University, 1964.

10 Jeffrey, A., and Taniuti, T., *Nonlinear Wave Propagation With Applications to Physics and Magnetohydrodynamics*, Academic Press, New York, 1964.

11 Truesdell, C., and Noll, W., "The Non-Linear Field Theories of Mechanics," *Handbuch der Physik*, Vol. III/3, Springer-Verlag, 1965.

12 Lax, P. D., "Hyperbolic Systems of Conservation Laws II," *Comm. Pure and Appl. Math.*, Vol. 10, 1957, pp. 537–566.

13 Courant, R., and Hilbert, D., *Methods of Mathematical Physics*, Vol. II, Interscience, 1955, p. 10.

14 Stroud, A. H., "Numerical Quadrature and Solution of Ordinary Differential Equations," *Appl. Math. Sci.*, Vol. 10, 1974, p. 223.

Downloaded 02 May 2010 to 171.66.16.25. Redistribution subject to ASME license or copyright; see http://www.asme.org/terms/Terms_Use.cfm

N. Sugimoto
Research Associate.

Y. Yamane
Graduate Student.

T. Kakutani
Professor.

Department of Mechanical Engineering,
Faculty of Engineering Science,
Osaka University,
Toyonaka, Osaka
560, Japan

Torsional Shock Waves in a Viscoelastic Rod[1]

The propagation of torsional shock waves in a thin circular viscoelastic rod is investigated theoretically. An analysis is carried out based on the approximate equations previously derived. Two typical viscoelastic models are considered, which possess, respectively, the discrete and continuous relaxation spectrum. One is the usual Maxwell-Voigt model and the other is a new model whose relaxation function is given by a power law with weak singularity. The structures of steady shock profiles are presented and compared for both types. Finally a brief discussion is included on the simplified evolution equations for a far field transient behavior.

1 Introduction

A dynamic test of a viscoelastic solid at high strain rates often utilizes the wave propagation techniques consisting of the introduction of torsional or longitudinal waves in a circular rod. The torsional waves are of primary importance in evaluating a shear response. In such viscoelastic materials as polymers, the effect of finite torsion, namely, nonlinearity, plays an essential role so that the linear theory is of no use. Nevertheless, the nonlinear dynamic theory for torsional waves has been poorly cultivated so far, even for an elastic rod. Usually the effect of nonlinearity manifests itself in formation of shock waves.[2] In particular, the propagation of steady shock waves is possible as a result of balance between both the effects of nonlinearity and viscoelasticity. One of the purposes of this paper is to clarify whether the steady torsional shock waves can propagate in a circular rod and, if possible, to obtain explicit shock profiles. Our starting point is set on the approximate equations already derived in [1] for a thin, "nearly elastic" rod. The other purpose is to introduce a new type of viscoelastic character and to compare its shock profiles with the well-known model. Since the shock profiles reflect a dynamic behavior of materials, they can provide useful information in evaluating the relevant constitutive equations at a finite strain and high strain rate.

The viscoelastic behavior is often modeled by combinations of several springs and dashpots, which are usually known as Voigt model, Maxwell-Voigt model (the standard solid), etc. Such models have succeeded in explaining intuitively the inner relaxation mechanisms involved. But they are too simple to describe the actual viscoelastic behavior of materials like polymers. For a spring-dashpot model, the constitutive equations are given in the differential form. In this case, the relaxation functions are represented by a sum of several exponential functions including the delta or step function as a limiting case. Each exponential function introduces a characteristic relaxation time associated with each element involved. In this sense, the spring-dashpot model has usually several discrete relaxation times. It is known, however, that the actual viscoelastic materials have infinitely and continuously many relaxation times resulting from the inner molecular relaxation mechanisms and consequently they exhibit a slow relaxation over a long time range [2]. To describe them properly, the idea of the relaxation spectrum is introduced, so that the constitutive equations are essentially expressed in the integral (functional) form. In this paper, we consider, as a simple but promising model of relaxation function, the power function with weak singularity. This model is proposed by assuming that the continuous relaxation spectrum is approximated by an inverse power law with respect to the relaxation time.

In what follows, the approximate equations are first presented. For the relaxation function involved there, various viscoelastic models, especially of the power function type, are discussed. The conditions for existence of steady shock waves are derived, which pose restrictions on the elastic response of materials and the relaxation character. In obtaining the shock profiles, we treat two types of relaxation functions that typify the discrete and continuous relaxation spectrum, respectively. One is the usual Maxwell-Voigt model in which the relaxation function is given by the single exponential function (Type I called hereafter). The other is the power function type proposed here (Type II). Particularly for Type II, the nonlinear integral equation with the weak singular kernel is reduced to obtain the shock profiles. The numerical method solving it is demonstrated. The explicit structures of shock profiles are compared for both types. Finally a brief discussion is included on the simplified evolution equations describing a far field behavior.

[1] A part of this paper was presented at the IUTAM symposium on "Nonlinear Deformation Waves" held at Tallinn, Estonia U.S.S.R. in 1982.

[2] The shock waves in the present context are meant not only by the first-order discontinuity of displacement but also by the smooth transition layer caused intrinsically by the nonlinearity.

Contributed by the Applied Mechanics Division for publication in the JOURNAL OF APPLIED MECHANICS.

Discussion on this paper should be addressed to the Editorial Department, ASME, United Engineering Center, 345 East 47th Street, New York, N.Y. 10017, and will be accepted until two months after final publication of the paper itself in the JOURNAL OF APPLIED MECHANICS. Manuscript received by ASME Applied Mechanics Division August; 1983, final revision, November, 1983.

Copyright © 1984 by ASME
Downloaded 02 May 2010 to 171.66.16.25. Redistribution subject to ASME license or copyright; see http://www.asme.org/terms/Terms_Use.cfm

2 Approximate Equations

The following analysis begins with the approximate equations previously derived in [1]. A finite torsional deformation couples with a longitudinal one through the normal stress effect. If the angle of torsion of a cross section and the longitudinal deformation are denoted by φ and w, respectively, the approximate equations in dimensionless form are given in terms of the axial coordinate z and the time t as

$$\frac{\partial^2\varphi}{\partial t^2} - G\frac{\partial^2\varphi}{\partial z^2} - \gamma\frac{\partial^2}{\partial z^2}\int_{-\infty}^{t} K(t-t_1)\frac{\partial}{\partial t_1}\varphi(z, t_1)dt_1$$

$$= -2\epsilon^2\left[\frac{\partial}{\partial t}\left(\Phi\frac{\partial\varphi}{\partial t}\right) - G\frac{\partial}{\partial z}\left(\Phi\frac{\partial\varphi}{\partial z}\right)\right]$$

$$+\epsilon^2\frac{\partial}{\partial z}\left\{\left[a\frac{\partial w}{\partial z} + b_1\left(\frac{\partial\varphi}{\partial t}\right)^2 + b_2\left(\frac{\partial\varphi}{\partial z}\right)^2\right]\frac{\partial\varphi}{\partial z}\right\}, \quad (1)$$

$$\frac{\partial^2 w}{\partial t^2} - E\frac{\partial^2 w}{\partial z^2} = \frac{\partial}{\partial z}\left[c_1\left(\frac{\partial\varphi}{\partial t}\right)^2 + c_2\left(\frac{\partial\varphi}{\partial z}\right)^2\right], \quad (2)$$

with

$$\Phi = -\frac{E-2G}{2G}\frac{\partial w}{\partial z} + d_1\left(\frac{\partial\varphi}{\partial t}\right)^2 + d_2\left(\frac{\partial\varphi}{\partial z}\right)^2, \quad (3)$$

where the length and time scales are already normalized, respectively, by a characteristic wavelength L (which is assumed to be sufficiently long compared with the radius of rod R) and time T $(=L/(S/\rho_0)^{1/2})$, S being a characteristic stress, and ρ_0 the density in the reference state; G and E, both normalized by S, denote, respectively, the modulus of rigidity and Young's modulus in the equilibrium state, while the constants a, b_i, c_i, and d_i $(i = 1, 2)$ are determined by G, E, and the higher order equilibrium elastic moduli (see Appendix 2 in [1]). Here the two small parameters γ and ϵ $(0 < \gamma, \epsilon << 1$, and $\epsilon^4 < \gamma << 1)$ imply, respectively, the order of weakness of viscoelasticity and that of thin rod $(\epsilon \equiv R/L)$, the latter also representing the order of torsional shear strain, i.e., nonlinearity [1]. The viscoelastic behavior is characterized by the relaxation function $K(t)$. Strictly speaking, however, we note that $G + \gamma K(t)$ represents the shear stress relaxation function in linear viscoelasticity and hence $\gamma K(t)$ is a deviation from the equilibrium state G. Accordingly $K(t)$ is assumed to vanish as t increases.

For the well-known spring-dashpot models, $K(t)$ is represented by a sum of several exponential functions as

$$K(t) = \sum_\alpha K_\alpha \exp\left(-\frac{t}{T_\alpha}\right), \quad \text{for } t \geq 0, \quad (4)$$

where T_α (>0) is called a characteristic relaxation time, while K_α is a modulus contribution. In this sense, it is said that (4) has several relaxation times. Since $K(t)$ vanishes as t increases, the special case with $T_\alpha = \infty$ is excluded here. But the other special case with T_α, say $T_1 \to 0$ with $K_1 T_1$ held constant is included to represent the delta function. For actual viscoelastic materials, however, there are continuously and infinitely many relaxation times. In this case, equation (4) is extended as

$$K(t) = \int_0^\infty H(T)\exp\left(-\frac{t}{T}\right)\frac{dT}{T}, \quad \text{for } t \geq 0, \quad (5)$$

where after the convention, $H(T)$ is called the relaxation spectrum [2, 3]. In view of this, the spring-dashpot model is said to have the discrete relaxation spectrum. In identifying the viscoelastic behavior, on the other hand, there is another approach in terms of a creep function $J(t)$ or a retardation spectrum $L(T)$ [2]. Experimentally this approach is preferable to that by a relaxation function or spectrum employed in the present theoretical treatment. But since there are interrelations among them [2–4], a transformation from one to the other is a matter of integration.

Among the models having a continuous relaxation spectrum, there are known the power function models. Caputo and Mainardi [5, 6] investigated various linear models by generalizing the Maxwell-Voigt model. Among them, we propose here, as a simple but promising model for the viscoelastic "solids," $H(T)$ approximated by the inverse power law of T:

$$H(T) = T^{-\nu}/\Gamma(\nu), \ (0 < \nu < 1), \quad (6)$$

where $\Gamma(\nu)$ is the gamma function. The resulting relaxation function from (5) with (6) is also given in the form of the inverse power function of time:

$$K(t) = t^{-\nu}, \quad \text{for } t \geq 0, \ (0 < \nu < 1). \quad (7)$$

Here we note that $K(t)$ exhibits an infinite stiffness at $t = 0$ just as the delta function in the Voigt model. But the relaxation does not cease so quickly as the delta function but rather it relaxes more slowly than the exponential function in the Maxwell-Voigt model. In the creep formulation, the creep function $J(t)$ corresponding to (7) is given by

$$J(t) = \frac{1}{G}\left\{1 - E_\nu\left[-\frac{G}{\gamma\Gamma(1-\nu)}t^\nu\right]\right\}, \quad \text{for } t \geq 0. \quad (8)$$

where $E_\nu[\ \ldots\ ]$ denotes the Mittag-Leffler function of order ν[7]. From (8), it is found that $J(t)$ increases from zero and approaches the equilibrium value G^{-1} as time elapses.

As another simple and plausible model, it is known that the creep function may be given by a power function of time [4–6]:

$$J(t) = J_0 + \gamma t^{\nu'}, \quad \text{for } t \geq 0, \ (0 < \nu' < 1), \quad (9)$$

where J_0 is a positive constant and γ is also a small positive constant for a measure of weakness of viscoelasticity. Owing to the relations between the creep function $J(t)$ and the relaxation function $K'(t)$ $(=G+\gamma K(t))$ [4–6], the corresponding $K'(t)$ is given by

$$K'(t) = \frac{1}{J_0}E_{\nu'}\left[-\frac{\gamma\Gamma(1+\nu')}{J_0}t^{\nu'}\right], \quad \text{for } t \geq 0. \quad (10)$$

Since we are concerned with the case $\gamma << 1$, equation (10) is expanded as

$$K'(t) = G - \gamma G^2 t^{\nu'} + O(\gamma^2), \quad \text{for } t \geq 0, \quad (11)$$

where $G = J_0^{-1}$ and $\gamma G^2 t^{\nu'} << G$. The first term G implies the constant elastic response and the second term gives $K(t)$ in our formulation, namely, $K(t) = -G^2 t^{\nu'}$. This model is also very simple. But is should be noted that as time elapses, (9) increases without limit and no equilibrium state can be expected. Such a model provides a good agreement with the experiments at a relatively slow strain rate and over a long time range [4]. It is not suitable, however, for a case with a high strain rate such as the propagation of shock waves. Indeed, as will be shown later, there exist no steady shock waves for this model. Therefore we are concerned here with the power function model given by (7). To compare with the usual spring-dashpot model, we first consider the exponential function type (Type I) corresponding to the well-known Maxwell-Voigt model and later the power function type (Type II):

Type I: $$K(t) = \exp(-\kappa t), \quad (12)$$

Type II: $$K(t) = t^{-\nu}, \ (0 < \nu < 1), \quad (13)$$

where κ^{-1} is the characteristic relaxation time. But we note

Downloaded 02 May 2010 to 171.66.16.25. Redistribution subject to ASME license or copyright; see http://www.asme.org/terms/Terms_Use.cfm

again that there exists no such time in Type II because of the continuous relaxation spectrum.

Before proceeding to the shock wave problem, we consider the linear dispersion ralation of (1). On neglecting the nonlinear terms, it can easily be obtained by setting $\varphi \propto \exp[i(kz-\omega t)]$, k and ω (>0) being a wave number and a frequency, respectively. For Type I, the phase velocity $c(=\omega/k)$ is given by $c = [G+\gamma/(1+i\kappa/\omega)]^{1/2}$. In this case, there exist two characteristic sound speeds, the instantaneous sound speed $c_i = (G+\gamma)^{1/2}$ as $\omega \to \infty$, and the equilibrium sound speed $c_e = G^{1/2}$ as $\omega \to 0$. For Type II, on the other hand, since the relaxation function exhibits an infinite stiffness at $t = 0$, the instantaneous sound speed becomes infinite. This can be seen from the dispersion relation $c = [G + \gamma\Gamma(1-\nu)(-i\omega)^{\nu}]^{1/2}$ that $c_i \to \infty$ as $\omega \to \infty$, although $c_e = G^{1/2}$.

3 Structure of Steady Shock Waves

Based on (1)–(3), let us investigate the steady shock waves propagating into the unstrained state far ahead ($z \to \infty$) with an equilibrium state far behind ($z \to -\infty$). Assuming φ and w depend on $\eta = t - z/\lambda$ only, λ being a positive constant representing a shock velocity, equations (1)–(3) are written as

$$(\lambda^2-G)\varphi' - \gamma\int_{-\infty}^{\eta} K(\eta-\eta_1)\frac{d\varphi'}{d\eta_1}\,d\eta_1 = -2\epsilon^2(\lambda^2-G)\Phi\varphi' + \epsilon^2\left[-\frac{a}{\lambda}\frac{dw}{d\eta} + \left(b_1+\frac{b_2}{\lambda^2}\right)\varphi'^2\right]\varphi' + \text{const.}, \tag{14}$$

$$\frac{dw}{d\eta} = -\frac{c_1\lambda^2+c_2}{\lambda(\lambda^2-E)}\varphi'^2 + \text{const.}, \tag{15}$$

with

$$\Phi = \frac{E-2G}{2G\lambda}\frac{dw}{d\eta} + \left(d_1+\frac{d_2}{\lambda^2}\right)\varphi'^2, \tag{16}$$

where $\varphi' \equiv d\varphi/d\eta$ and const. denotes an integration constant. For the boundary condition at both infinite ends of the rod, we require that φ' and $dw/d\eta \to 0$ as $\eta \to -\infty$, while as $\eta \to +\infty$, $\varphi' \to \varphi'_\infty$ (= constant), where note that $dw/d\eta$ as $\eta \to +\infty$ is then determined by (15) as $-\{(c_1\lambda^2+c_2)/[\lambda(\lambda^2-E)]\}\varphi'^2_\infty$ + const. Hence the integration constants must be chosen to be zero. We eliminate $dw/d\eta$ in (14) by (15). In (14), all quantities except ϵ^2 and γ are assumed to be of order of unity. To have a significant φ', (λ^2-G) should be of order of ϵ^2 or γ, so that λ^2 is nearly equal to G: $\lambda^2 = G + O(\epsilon^2, \gamma)$. Using this result, it follows upon retaining the lowest order of ϵ^2 and γ that

$$(\lambda^2-G)\varphi' - \gamma\int_{-\infty}^{\eta} K(\eta-\eta_1)\frac{d\varphi'}{d\eta_1}\,d\eta_1 \cong \frac{\epsilon^2}{\lambda^2}\left[\frac{a(c_1\lambda^2+c_2)}{\lambda^2-E}+b_1\lambda^2+b_2\right]\varphi'^3 \cong \frac{\epsilon^2}{G}\left[\frac{a(c_1G+c_2)}{G-E}+b_1G+b_2\right]\varphi'^3 \cong \epsilon^2 C\varphi'^3, \tag{17}$$

where C is defined by $[a(c_1G+c_2)/(G-E)+b_1G+b_2]/G$. We introduce the parameter $U = (\lambda^2-G)/\gamma$ and set $\phi = [\epsilon^2|C|/\gamma]^{1/2}\varphi'$. Then (17) and the boundary condition are rewritten in a compact form as

$$U\phi - \text{sgn}C\phi^3 = \int_{-\infty}^{\eta} K(\eta-\eta_1)\frac{d\phi}{d\eta_1}\,d\eta_1, \tag{18}$$

with $\phi \to 0$ as $\eta \to -\infty$, and $\phi \to \phi_\infty$ = constant as $\eta \to +\infty$, where the sgn C takes the value 1 for $C > 0$ and -1 for $C < 0$, and $\phi_\infty \equiv [\epsilon^2|C|/\gamma]^{1/2}\varphi'_\infty$. Here the case with $C = 0$ is excluded since no steady shock waves exist in such a "linear" case. By the cubic nonlinearity in ϕ, the solutions of (18) always have two branches $\pm\phi$ which represent the right and left twisted wave. In what follows, we are only concerned with a case $\phi_\infty > 0$. The longitudinal deformation induced, w, is obtained by integrating (15) if ϕ i.e., φ' is solved. Finally we keep it in mind that ϕ represents physically the variation of the torsional shear strain or the angular velocity of a cross section, if a proper numerical factor is introduced.

3.1 Conditions for Existence of Steady Shock Waves. Before solving (18), we check the necessary conditions for the steady shock wave solutions to exist. On assuming the existence of ϕ_∞, we multiply (18) by $d\phi/d\eta$ and integrate it over the whole range of η. Then it follows that

$$U\phi_\infty^2/2 - \text{sgn}C\phi_\infty^4/4 = (2\pi)^{1/2}\int_{-\infty}^{\infty}\hat{K}(y)\,|\hat{\phi}'(y)|^2dy \equiv A, \tag{19}$$

where $\hat{\phi}'(y)$ and $\hat{K}(y)$ are, respectively, Fourier transform of $d\phi/d\eta$ and $K(\eta)$ defined by, for example,

$$\hat{\phi}'(y) = \frac{1}{\sqrt{2\pi}}\int_{-\infty}^{\infty}\frac{d\phi}{d\eta}\exp(iy\eta)d\eta, \tag{20}$$

where $K(\eta)$ vanishes for $\eta < 0$ and therefore it is extended as $K(|\eta|)h(\eta)$, $h(\eta)$ being the unit step function. Here each explicit expression of A for Type I and Type II is given, respectively, by

$$A = \int_{-\infty}^{\infty}\frac{\kappa}{y^2+\kappa^2}|\hat{\phi}'(y)|^2dy > 0, \quad \text{for Type I,} \tag{21}$$

and

$$A = \Gamma(1-\nu)\sin\left(\frac{\pi\nu}{2}\right)\int_{-\infty}^{\infty}|y|^{\nu-1}|\hat{\phi}'(y)|^2dy > 0, \quad \text{for Type II,} \tag{22}$$

Next, on differentiating (18) with respect to η and multiplying it by ϕ, it also follows after integration that [3]

$$U\phi_\infty^2/2 - 3\,\text{sgn}\,C\phi_\infty^4/4 = -A. \tag{23}$$

Thus from (19) and (23), we should have

$$\phi_\infty^2 = U\text{sgn}\,C, \quad \text{and} \quad A = U^2\,\text{sgn}\,C/4. \tag{24}$$

Hence for ϕ_∞ to exist, A must be finite. To examine it, we must know the asymptotic behavior of $\hat{\phi}'(y)$ as $y \to 0$ and $|y| \to \infty$. For the former limit, it is easily seen from the definition (20) that $\hat{\phi}'(y) \to (2\pi)^{-1/2}\phi_\infty$ as $y \to 0$, provided ϕ_∞ be finite. For the latter limit, on the other hand, $\hat{\phi}'$ dies away at least as rapidly as $|y|^{-2}$, if ϕ and $d\phi/d\eta$ are continuous [8] (see next subsection) and hence A is found to exist. Therefore if we are looking for the continuous solutions with $d\phi/d\eta$ inclusive, we conclude from (24) that C and U must be positive. Since C is the material constant, its positiveness poses a restriction on possible types of elastic response. From $U > 0$, the equilibrium value ϕ_∞ is given by $\pm U^{1/2}$. Conversely if a strength of shock wave ϕ_∞ is given, then the velocity of shock wave λ is determined by

[3] Note that the Fourier transform of ϕ is given by $i\hat{\phi}'/y$ + const. $\delta(y)$, $\delta(y)$ being the delta function [9].

Downloaded 02 May 2010 to 171.66.16.25. Redistribution subject to ASME license or copyright; see http://www.asme.org/terms/Terms_Use.cfm

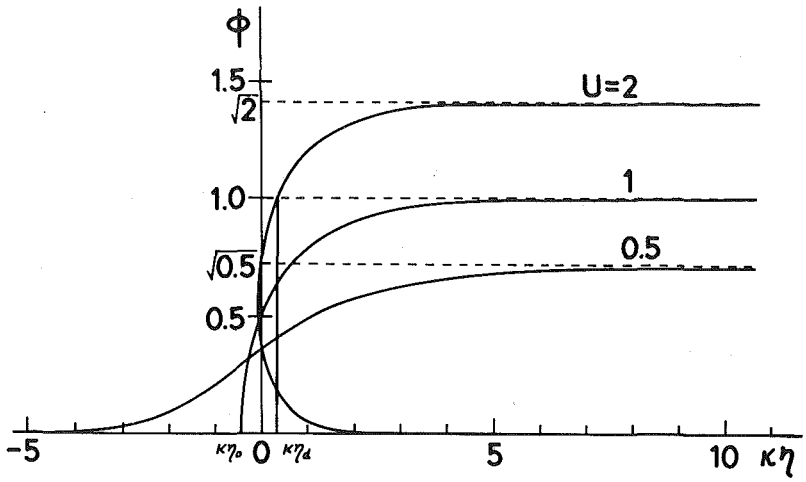


Fig. 1 Shock profiles for Type I with various values of U

$$\lambda^2 = G + \gamma U = G + \gamma\phi_\infty^2 = G + \epsilon^2 |C| \varphi_\infty'^2 > G = c_e^2. \quad (25)$$

It is thus found that λ is always greater than the equilibrium sound speed c_e and it becomes faster as ϕ_∞ increases.

Finally we observe that there exist no steady solutions for the relaxation function (11). In this case, A is given by

$$A = G^2\Gamma(1+\nu')\sin\left(\frac{\pi\nu'}{2}\right)\int_{-\infty}^{\infty} |y|^{-\nu'-1} |\hat{\phi}'(y)|^2 dy. \quad (26)$$

It is readily seen from this that A diverges near $y = 0$. Hence we ascertain no existence of steady solutions.

3.2 Discontinuous Solutions. In the preceding subsection, it was assumed that ϕ and $d\phi/d\eta$ are continuous. In addition to such smooth solutions, we check whether or not a discontinuous solution is possible. Let a discontinuity be located at $\eta = 0$ and let the unstrained state prevail in $\eta < 0$. Near $\eta = 0$, the discontinuous solution is assumed to be expressed as $\phi = \phi_0 h(\eta)$, ϕ_0 being a constant jump and $h(\eta)$ the unit step function. Evaluation of (18) at $\eta = \Delta\eta > 0$ ($\Delta\eta \to 0$) justs behind the discontinuity leads to

$$U\phi_0 - \text{sgn}\, C\phi_0^3 = \int_{-\infty}^{\Delta\eta} K(\Delta\eta - \eta_1)\phi_0\delta(\eta_1)d\eta_1$$

$$= \phi_0 K(\Delta\eta) \to \phi_0 K(0), \quad (27)$$

as $\Delta\eta$ tends to zero, where $\delta(\eta_1)$ denotes the delta function. If $K(0)$ remains finite (which is the case with Type I), there exists a discontinuous solution with a jump given by

$$\phi_0^2 = [U - K(0)]/\text{sgn}\, C = [(\lambda^2 - G)/\gamma - K(0)]/\text{sgn}\, C. \quad (28)$$

This gives the relation between the strength of discontinuity and its velocity[4]. On the other hand, if $K(0)$ is infinite (which is the case with Type II), there exists no discontinuous solution. Further, the higher order discontinuity in $d\phi/d\eta$ may similarly be examined. Here we only note the results that for $|K(0)| < \infty$, the discontinuity occurs when $U = K(0)$, whereas for $|K(0)| \to \infty$, no discontinuity occurs.

Finally we return to the conditions for existence of steady shock solutions when such a discontinuous solution is included. This is, of course, the case with Type I. If a discontinuity in ϕ is concerned, the asymptotic behavior of $\hat{\phi}'$ as $|y| \to \infty$ does not decay so quickly as $|y|^{-2}$ but it remains finite there. Even so, A is guaranteed finite and the existence of a discontinuous solution is possible.

[4] It should be remarked that near the discontinuity, the assumption of thin rod becomes invalid and a new formulation is required. Therefore the discontinuous solution should be regarded as a formal one.

3.3 Steady Shock Profiles.

3.3.1. Type I: Exponential Function Type. As is suggested from the Section 3.1., it is assumed in the following analysis that C and U are positive in (18). For Type I, equation (18) can be reduced, by differentiating with respect to η, to the first order differential equation:

$$\frac{d\phi}{d\eta} = \kappa\frac{(U-\phi^2)\phi}{1-U+3\phi^2}. \quad (29)$$

The equilibrium points of (29) are given by $\phi^2 = \phi_\infty^2 = U > 0$ and $\phi = 0$. But since $d\phi/d\eta$ becomes infinite at $\phi_B^2 = (U-1)/3$, we must pay attention to the location of ϕ_B. The solution to (29) can easily be obtained as

$$\frac{(1-U)}{2U}\log|\phi^2| - \frac{(1+2U)}{2U}\log|U-\phi^2| = \kappa(\eta - \eta_0), \quad (30)$$

where η_0 is an arbitrary integration constant. In Fig. 1, the explicit form of (30) is shown for the typcial values of U with $\phi_\infty > 0$ where η_0 is chosen so that ϕ takes $\phi_\infty/2$ at $\eta = 0$. If $0 < U < 1$, (30) exhibits a smooth and monotonic transition from $\phi = 0$ at $\eta = -\infty$ to $\phi = \phi_\infty$ at $\eta = \infty$. The velocity of this shock wave is determined by the strength of shock wave ϕ_∞ as $\lambda^2 = G + \gamma\phi_\infty^2$. Since $0 < U < 1$, λ is greater than the equilibrium sound speed, but less than the instantaneous one, i.e., $c_e < \lambda < c_i$. If $1 < U$, on the other hand, ϕ_B is always located between $\phi = 0$ and $\phi = \phi_\infty$ and both asymptotic branches of (30) as $\phi \to 0$ and $\phi \to \phi_\infty$ approach $\eta \to \infty$. Thus (30) does not satisfy the boundary condition at $\eta = -\infty$. For Type I, however, we already know that there may appear a discontinuity in the solution. Hence to fit (30) with the boundary condition, the discontinuity $\phi_0 = (U-1)^{1/2}$ given by (28) with $C > 0$ is placed at a point $\eta = \eta_d$ where ϕ_0 equals ϕ by (30). In Fig. 1, the vertical line connected with the solution for $U = 2$ at $\phi = 1$ represents this discontinuity. For $\eta < \eta_d$, the solution takes the value of zero, while for $\eta > \eta_d$, the solution takes the upper branch of (30) and the branch below $U = 1$ loses its meaning. Thus we have the discontinuous shock profile followed by the monotonic relaxation region. The velocity is then given by $\lambda^2 = G + \gamma\phi_\infty^2 > G + \gamma = c_i^2$ and is faster than the instantaneous sound speed. As a special case, if $U = 1$, (30) degenerates to

$$\phi^2 = 1 - \exp[-2\kappa(\eta - \eta_0)/3]. \quad (31)$$

This solution ceases to be valid for $\eta < \eta_0$ and the boundary condition at $\eta = -\infty$ cannot be satisfied. In this case as well, for $\eta \leqq \eta_0$, the solution takes the value of zero, and for $\eta > \eta_0$, it takes (31). Consequently $d\phi/d\eta$ becomes discontinuous

Downloaded 02 May 2010 to 171.66.16.25. Redistribution subject to ASME license or copyright; see http://www.asme.org/terms/Terms_Use.cfm

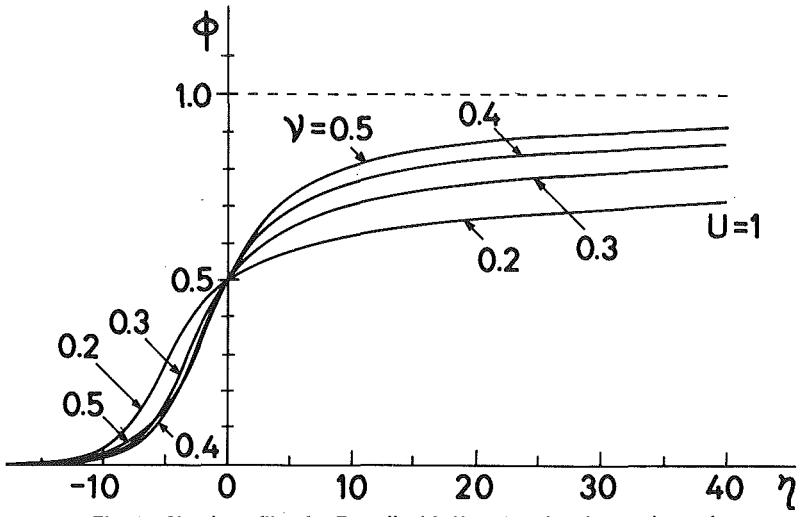


Fig. 2 Shock profiles for Type II with $U = 1$ and various values of ν

at $\eta = \eta_0$. This is known as the so-called acceleration wave, which propagates with the velocity $\lambda = c_i$.

3.3.2 Type II: Power Function Type. For this type, equation (18) remains essentially the nonlinear integral equation:

$$U\phi - \phi^3 = \int_{-\infty}^{\eta} \frac{1}{(\eta-\eta_1)^{\nu}} \frac{d\phi}{d\eta_1} d\eta_1, (0<\nu<1). \tag{32}$$

Since an analytical solution of this equation is unknown at present, it is solved numerically by the method of quadrature. To apply this method, it is advantageous to invert (32) to remove the derivative in the integrand. Equation (32) is Abel's type of integral equation, which can be rewritten as

$$\phi = \frac{1}{\Gamma(\nu)\Gamma(1-\nu)} \int_{-\infty}^{\eta} \frac{U\phi(\eta_1) - \phi^3(\eta_1)}{(\eta-\eta_1)^{1-\nu}} d\eta_1. \tag{33}$$

Here we remark on two analytical results which assist the numerical computation. First, the solution is independent of the choice of the origin of coordinate axis, as this property comes from the general characteristics of the hereditary integral in (18). Secondly, though the full explicit solution of (33) is difficult to obtain analytically, the asymptotic solution as $\eta \to -\infty$ can be easily sought as

$$\phi \sim \phi^{(1)}\exp(\alpha\eta) + \frac{1}{(1-3^{\nu})U}\phi^{(1)3}\exp(3\alpha\eta) + \frac{3}{(1-3^{\nu})(1-5^{\nu})U^2} \times \phi^{(1)5}\exp(5\alpha\eta) + \ldots, \tag{34}$$

where $\phi^{(1)}$ is a constant and $\alpha = [U/\Gamma(1-\nu)]^{1/\nu}$. We use these results to demonstrate the numerical method of treating (33).

Since the lower bound of the integration extends to infinity and moreover the integrand diverges at the upper bound (though the integral itself exists), special care should be taken. For the treatment of the infinite lower bound, we first divide the region into two regions $(-\infty, M]$ and $[M, \eta]$, where M is taken arbitrarily but fixed, say $M = 0$. Then (33) can be split into

$$\Gamma(\nu)\Gamma(1-\nu)\phi = \left(\int_{-\infty}^{M} + \int_{M}^{\eta}\right) \frac{F[\phi(\eta_1)]}{(\eta-\eta_1)^{1-\nu}} d\eta_1, \tag{35}$$

where $F[\phi(\eta_1)] \equiv F(\phi_1) \equiv U\phi(\eta_1) - \phi^3(\eta_1)$. In the first region $(-\infty, M]$, we assume that the asymptotic solution (34) is valid by using the freedom of the choice of the origin of coordinate axis, i.e.,

$$\phi \sim \phi^{(1)}\exp[\alpha(\eta-M)] + O(\phi^{(1)3}), \tag{36}$$

where $\phi^{(1)}$ is taken small $(0 < \phi^{(1)} \ll 1)$. On substituting this into the first integral, I_1, of (35), we obtain

$$I_1 = \int_{-\infty}^{M} \frac{U\phi^{(1)}\exp[\alpha(\eta_1-M)]}{(\eta-\eta_1)^{1-\nu}} d\eta_1 + O(\phi^{(1)3}) = \Gamma(1-\nu)\phi^{(1)}\exp[\alpha(\eta-M)]\Gamma[\nu,\alpha(\eta-M)] + O(\phi^{(1)3}), \tag{37}$$

where $\Gamma[\nu, \alpha(\eta-M)]$ denotes the incomplete gamma function. From the asymptotic behavior of $\Gamma[\nu, \alpha(\eta-M)] \sim [\alpha(\eta-M)]^{\nu-1}\exp[-\alpha(\eta-M)]$ as $\alpha(\eta-M) \to \infty$, the contribution of I_1 to the total integral (35) becomes small and negligible as $\alpha(\eta-M) \to \infty$.

In the second region $[M, \eta]$, on the other hand, we take the equidistant points separated by $h\ (>0)$, i.e., $\eta = \eta^{(i)} = M + h(i-1)$, $(i \geq 1)$ and evaluate the second integral in (35) by Simpson's rule. But since the integrand diverges at the upper bound, we further divide the region into two parts, $[M, \eta^{(i-2)}]$and $[\eta^{(i-2)}, \eta^{(i)}]$. In the former region, the integrand remains finite and the usual Simpson's rule can be applied. For the integral in $[\eta^{(i-2)}, \eta^{(i)}]$, however, a "modified Simpson's rule" is devised to take account of the singularity. Instead of approximating the whole integrand by the quadratic function, we approximate the numerator F by the quadratic function and calculate the integral analytically. After the strightforward calculation, we have the approximation formula,

$$\int_{\eta^{(i-2)}}^{\eta^{(i)}} \frac{F(\phi_1)}{(\eta-\eta_1)^{1-\nu}} d\eta_1 = p\left[\nu F^{(i-2)} + 4F^{(i-1)} + \frac{2-\nu}{\nu}F^{(i)}\right] + O(h^{3+\nu}), \tag{38}$$

where $p = (2h)^{\nu}/[(1+\nu)(2+\nu)]$ and $F^{(i-k)}$ $(k=0, 1, 2)$ denotes the values of F at $\eta^{(i-k)}$. Thus the scheme to calculate the unknown $\phi^{(i)}$ at $\eta = \eta^{(i)}$ from the known $\phi^{(k)}$ $(k=1, 2, 3, \ldots, i-1)$ is to solve the following cubic equation for $\phi^{(i)}$ successively:

$$\phi^{(i)3} + \left[\frac{\Gamma(\nu)\Gamma(1-\nu)\nu}{(2-\nu)p} - U\right]\phi^{(i)} - \frac{\nu}{2-\nu}\left[\nu F^{(i-2)} + 4F^{(i-1)} + \frac{1}{p}(I_1+I_2)\right] = 0, \tag{39}$$

where I_2 denotes the integral in $[M, \eta^{(i-2)}]$. Here we remark that this scheme is applied to the odd $i\ (\geq 3)$ only after giving the starting data $\phi^{(1)}$ and $\phi^{(2)}$. For the even $i\ (\geq 2)$, the starting point $i = 1$ is shifted to $i = 0$ with $\phi^{(0)} = \phi^{(1)}\exp(-\alpha h)$ and the same scheme is applied.

Downloaded 02 May 2010 to 171.66.16.25. Redistribution subject to ASME license or copyright; see http://www.asme.org/terms/Terms_Use.cfm

Here we estimate the approximation error involved. In I_1, the smaller is made the error, the smaller $\phi^{(1)}$ is taken. Simpson's rule involves the error of $O(h^5)$ in the $2h$ interval, while the "modified Simpson's rule" involves that of $O(h^{3+\nu})$.[5] Therefore as ν approaches zero, the accuracy of the "modified Simpson's rule" deteriorates to that for the trapezoidal rule. To recover it, we may take the region $[\eta^{(i-4)}\eta^{(i)}]$ and approximate F by the quartic function. By this "modified Bodes's rule," the error is improved to give the order of $h^{5+\nu}$. Choosing $h = 0.02$ and $\phi^{(1)} = 0.001$ in the present analysis, the results of two modified rules are compared, but no substantial differences are recognized.

In Fig. 2, the numerical solutions are displayed for $\phi_\infty = U^{1/2} = 1$ and $\nu = 0.2$, 0.3, 0.4, and 0.5 in which the coordinate is readjusted so that ϕ may $\phi_\infty/2$ at $\eta = 0$. It is seen that the shock profiles are smooth and monotonic. As suggested by the asymptotic solution (34), the step-up behavior is exponentially steep. But the very slow relaxation region appears in the trail. Therefore it takes a long time to attain the equilibrium value. This tendency becomes prominent as ν decreases. The asymmetric character of shock profiles with respect to $\eta = 0$ is remarkable, which should be compared with the results of Type I. For other positive values of U, the exponential step-up becomes steep as U increases and the qualitative behavior is similar.

4 Results

We summarize the results of the steady shock wave propagation. For any materials, the steady shock waves exist only if their elastic response satisfies $C > 0$. As for their viscoelastic character, the Fourier transform of the relaxation function must satisfy the criteria shown in section 3.1. Such requirements provide useful informations in evaluating the nonlinear viscoelastic behavior. The shock waves result from a balance between the nonlinearity and the viscoelasticity represented by the two parameters ϵ and γ, respectively. This is reflected in the transformation of variable $\phi = [\epsilon^2 |C|/\gamma]^{1/2}\varphi'$. The competition between them determines the magnitude of shock waves. The velocity of shock wave λ is given by the strength of shock wave ϕ_∞ $[=(\epsilon^2 |C|/\gamma)^{1/2}\varphi'_\infty]$ applied at the infinity $z = -\infty$. The velocity is always greater than the equilibrium sound speed c_e, and it becomes faster as ϕ_∞ increases, i.e., $\lambda^2 = G + \gamma\phi_\infty^2 = G + \epsilon^2 |C| \varphi'^2_\infty > G = c_e^2$.

Next we consider the specific shock profiles of ϕ for Types I and II. We again note that ϕ represents the torsional shear strain if an appropriate scale factor is introduced. As is understood from the linear dispersion relations, the viscoelastic effect brings about not only the dissipation but also the dispersion. In spite of the dispersion, however, the shock profiles are always monotonic but not oscillatory. For Type I, there is the critical speed c_i $[=(G+\gamma)^{1/2}]$ beyond which the shock profiles change remarkably. For $c_e < \lambda < c_i$, the shock profiles are smooth and monotonic. But for $c_i \leqq \lambda$, they contain the discontinuity followed by the monotonic relaxation region. In Fig. 1, we can define a sharp shock layer over which ϕ changes appreciably. The thickness of this layer, which is estimated by the characteristic relaxation time κ^{-1}, is seen to be of order of $5\lambda/\kappa$ to $10\lambda/\kappa$ for the moderate values of U. For the strong shock wave $U >> 1$, the discontinuity $(U-1)^{1/2}$ and the equilibrium value $U^{1/2}$ are nearly equal. Therefore the thickness is so thin that it is almost represented by the discontinuity. For the weak shock wave $U << 1$, on the other hand, the thickness becomes wide and is given from (30) by the order of $\lambda/(U\kappa)$.

[5] When ν approaches unity, the order of error $h^{3+\nu}$ should agree with that of Simpson's rule. Although it might appear that the order approaches h^4, the coefficient of h^4 then vanishes and the order becomes h^5. Also for the modified Bode's rule" described below, the same situation occurs and the order of error approaches h^7 as $\nu \to 1$.

For Type II, it is important that the relaxation function $K(t)$ exhibits the singularity at $t = 0$. So the instantaneous sound speed is infinitely large and also no discontinuity is allowed in the solution. From (34), there always exists for $U > 0$ the asymptotic branch emanating from $\eta = -\infty$. Consequently there is no critical speed corresponding to c_i in the case of Type I. Thus the shock profiles are always smooth, which should be compared with the results of Type I. Another important characteristic of Type II is the slow relaxation. The shock profile has a steep front but a slow relaxation region behind. Therefore the thickness of shock layer is very wide compared with Type I. This is the essential difference from Type I even if it would be extended to include many (but finite) numbers of the exponential functions.

In this paper, we have sought the explicit shock profiles by assuming relevant forms of the relaxation functions. This provides useful information as a guideline. In reality, however, the wave profiles are known and the relaxation function is required. In such a case, the inverse problem of (18) must be solved to determine $K(t)$ by using the known ϕ.

5 Simplified Evolution Equations

In concluding this paper, we briefly discuss the simplified evolution equations for a far field transient behavior. Equations (1)–(3) can describe the bidirectional wave propagation, namely, propagation along both directions of right and left. But if only a far field behavior is concerned along either one of the directions, the unidirectional wave propagation is sufficient. In this case, equations (1)–(3) are simplified considerably. Following the idea of the reductive perturbation method [10], we introduce the new variable $\xi = t - z/G^{1/2}$ moving with the equilibrium sound speed and the stretched space variable $\tau = \epsilon^2 z/G^{1/2}$. Rewriting (1)–(3) in terms of ξ and τ, and retaining the lowest order terms in γ and ϵ^2, we have the simple evolution equation for $f = -G^{-1/2}\partial\varphi/\partial\xi$:

$$\frac{\partial f}{\partial \tau} - \frac{C}{2}\frac{\partial f^3}{\partial \xi} = \frac{\gamma}{2\epsilon^2 G}\frac{\partial}{\partial \xi}\int_{-\infty}^{\xi} K(\xi-\xi_1)\frac{\partial f}{\partial \xi_1}d\xi_1,$$

with

$$-G^{-1/2}\frac{\partial w}{\partial \xi} = \frac{(c_1 G + c_2)}{G(G-E)}\left(\frac{\partial \varphi}{\partial \xi}\right)^2, \tag{40}$$

where the unstrained state is assumed ahead of wave propagation. For Type I, (40) is further reduced to the differential equation:

$$\frac{\partial f}{\partial \tau} - \frac{C}{2}\frac{\partial f^3}{\partial \xi} = -\kappa^{-1}\frac{\partial}{\partial \xi}\left(\frac{\partial f}{\partial \tau} - \frac{C}{2}\frac{\partial f^3}{\partial \xi} - \frac{\gamma}{2\epsilon^2 G}\frac{\partial f}{\partial \xi}\right). \tag{41}$$

In particular, if the rapid relaxation is assumed, i.e., $\kappa^{-1} \sim \epsilon^2/\gamma << 1$, (41) is further simplified to give "cubic Burgers equation":

$$\frac{\partial f}{\partial \tau} - \frac{C}{2}\frac{\partial f^3}{\partial \xi} = \frac{\gamma}{2\epsilon^2 G\kappa}\frac{\partial^2 f}{\partial \xi^2} + O(\kappa^{-2}). \tag{42}$$

On the other hand, if the slow relaxation is assumed, i.e., $\kappa^{-1} >> 1$, (41) is reduced to

$$\frac{\partial f}{\partial \tau} - \frac{C}{2}\frac{\partial f^3}{\partial \xi} - \frac{\gamma}{2\epsilon^2 G}\frac{\partial f}{\partial \xi} = -\frac{\gamma\kappa}{2\epsilon^2 G}f + O(\kappa^2). \tag{43}$$

After some thought, it is found that (43) describes the far field behavior moving with the instantaneous sound speed.

For Type II, equation (40) cannot be further reduced. It is called "generalized Burgers' equation" on introduction of the derivative of real order:

Downloaded 02 May 2010 to 171.66.16.25. Redistribution subject to ASME license or copyright; see http://www.asme.org/terms/Terms_Use.cfm

$$\frac{\partial f}{\partial \tau} - \frac{C}{2}\frac{\partial f^3}{\partial \xi} = \frac{\gamma \Gamma(1-\nu)}{2\epsilon^2 G}\frac{\partial^{1+\nu} f}{\partial \xi^{1+\nu}}, \tag{44}$$

with the definition given by [11],

$$\int_{-\infty}^{\xi} \frac{1}{(\xi-\xi_1)^{\nu}}\frac{\partial f}{\partial \xi_1} d\xi_1 \equiv \Gamma(1-\nu)\frac{\partial^{\nu} f}{\partial \xi^{\nu}}. \tag{45}$$

Acknowledgments

We are grateful to Professor Y. Inoue for the stimulating discussions and also to Professor F. Mainardi at University of Bologna, Italy for informing us of his papers in compiling this manuscript. We are much obliged to the associate editor, Professor Malvern and the reviewers for their suggestions, which have led to the improvement of the original manuscript.

This work has been supported partially by the Grant-in-Aid for the Scientific Research from the Ministry of Education, Science and Culture of Japan.

References

1 Sugimoto, N., Yamane, Y., and Kakutani T., "Approximate Equations for Torsional Waves in a Nonlinear Elastic Rod With Weak Viscoelasticity," to be published in *Wave Motion*.

2 Ferry, J. D., *Viscoelastic Properties of Polymers*, Wiley, New York, 1970.

3 Christensen, R. M., *Theory of Viscoelasticity: An Introduction*, Academic Press, New York, 1971.

4 Findley, W. N., Lai, J. S., and Onaran, K., *Creep and Relaxation of Nonlinear Viscoelastic Materials*, North-Holland, Amsterdam, 1976.

5 Caputo, M., and Mainardi, F., "A New Dissipation Model Based on Memory Mechanism," *Pure and Applied Geophysics*, Vol. 91, 1971, pp. 134–147.

6 Caputo, M., and Mainardi, F., "Linear Models of Dissipation in Anelastic Solids," *Rivista del Nuovo Cimento*, Vol. 1, 1971, pp. 161–198.

7 Erdelyi, A., *Higher Transcendental Functions*, Vol. III, McGraw-Hill, New York, 1955.

8 Bracewell, R. N., *The Fourier Transform and its Applications*, McGraw-Hill, New York, 1978.

9 Lighthill, M. J., *Fourier Analysis and Generalised Functions*, Cambridge University Press, Cambridge, 1970.

10 Taniuti, T., "Reductive Perturbation Method and Far Fields of Wave Equations," *Supplement of Progress of Theoretical Physics*, No. 55, 1974, pp. 1–35.

11 Riesz, M., "L'integrale de Riemann-Liouville et le probleme de Cauchy," *Acta. Mathematica*, Vol. 81, 1949, pp. 1–223.

Downloaded 02 May 2010 to 171.66.16.25. Redistribution subject to ASME license or copyright; see http://www.asme.org/terms/Terms_Use.cfm

M. J. Forrestal
Sandia National Laboratories,
Albuquerque, N.Mex. 87185
Mem. ASME

L. M. Lee

B. D. Jenrette

Ktech Corporation,
Albuquerque, N. Mex. 87110

R. E. Setchell
Sandia National Laboratories,
Albuquerque, N. Mex. 87185

Gas-Gun Experiments Determine Forces on Penetrators Into Geological Targets[1]

We developed a convenient laboratory procedure to determine forces on projectiles penetrating geological targets. Gas guns were used to accelerate foundry core targets (a simulated soft sandstone) to steady velocities, and the targets subsequently impacted 20.6-mm-dia penetrators instrumented with piezoelectric accelerometers. Rigid-body acceleration data were recorded for one ogival and two conical nose shapes for impact velocities between 0.2-1.2 km/s.

Introduction

Zukas [1] and Colp [2] present many recently developed analytical and experimental methods used to study penetration mechanics. For geological targets, investigators usually predict or measure final penetration depth or deceleration history. Examples of predictive techniques are empirical equations based on test data [3, 4], models that approximate target response by one-dimensional motion using cavity expansion methods [5, 6], and detailed wave-code solutions [7]. Time-resolved measurements for experimental confirmation of the theoretical models use displacement-time [4], velocity-time [8], and acceleration-time diagnostics [5, 9, 10].

This paper describes a laboratory procedure to determine forces on penetrators from rigid-body acceleration-time data for impact velocities to 1.2 km/s. Full-scale penetration tests into natural geological targets [5, 9] obtain acceleration data; however, field data are expensive to obtain and the maximum impact velocity is limited to about 0.5 km/s. Previous laboratory-scale experiments obtain acceleration data for carefully prepared soil targets [10]; however, the maximum impact velocity for this study is 90 m/s.

For the present study, gas guns accelerated simulated, dry porous rock targets to impact velocities between 0.2-1.2 km/s. After targets impacted instrumented penetrators, acceleration data were measured for about two nose lengths of penetration. These laboratory-scale experiments were devised to complement the full-scale field work conducted at the Sandia Tonopah Test Range, Nevada [9]. Since the natural rock targets at this site are dry, porous tuff with densities ranging from 1.6–2.0 Mg/m^3, the man-made targets for the present study were made to a density of about 1.8 Mg/m^3. Data for the three nose shapes showed a substantial increase in penetration resistance for velocities greater than 0.5 km/s, the current upper limit for full-scale tests.

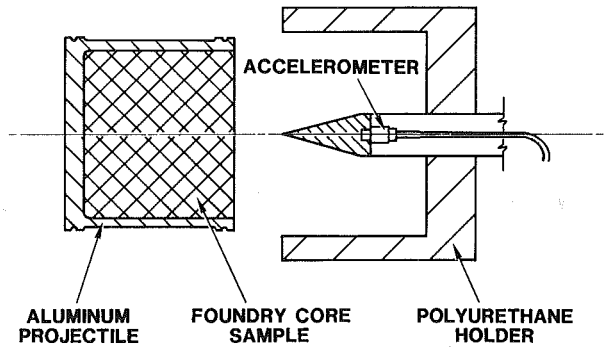


Fig. 1 Schematic for the reverse ballistic experiments

Description of Experiments

The penetration experiments were conducted at three gas gun facilities: the Sandia National Laboratories 63.5-mm-bore (2.5 in.) gas gun, the Air Force Weapons Laboratory 102-mm-bore (4.0 in.) gas gun, and the University of Dayton Research Institute 178-mm-bore (7.0 in.) gas gun. Foundry core material property data were obtained from triaxial tests conducted at the TerraTek Laboratory. More details for these experiments are reported in [11–15].

Reverse Ballistic Experiments. A schematic of the reverse ballistic experiments is shown in Fig. 1. Foundry core samples, contained within hollow projectiles, were accelerated to steady velocities with compressed-gas guns after which the targets impacted instrumented 20.6-mm-dia penetrators. Feasibility experiments were conducted with the 63.5-mm-dia

[1] This work was supported by the U.S. Department of Energy under contract DE-AC04-76DP00789.

Contributed by the Applied Mechanics Division for presentation at the Winter Annual Meeting, New Orleans, La., December 9-14, 1984 of THE AMERICAN SOCIETY OF MECHANICAL ENGINEERS.

Discussion on this paper should be addressed to the Editorial Department, ASME, United Engineering Center, 345 East 47th Street, New York, N.Y. 10017, and will be accepted until two months after final publication of the paper itself in the JOURNAL OF APPLIED MECHANICS. Manuscript received by ASME Applied Mechanics Division, April, 1983; final revision, September, 1983. Paper No. 84-WA/APM-3.

Copies will be available until July, 1985.

Copyright © 1984 by ASME
Downloaded 02 May 2010 to 171.66.16.25. Redistribution subject to ASME license or copyright; see http://www.asme.org/terms/Terms_Use.cfm

gun, but the majority of the data were obtained with the 102-mm-dia gun. Several experiments were also conducted with the 178-mm-dia gun to demonstrate that sample size and confinement did not significantly affect penetration resistance.

The instrumented penetrators were supported in polyurethane holders designed to ensure penetrator alignment for normal impact and to allow negligible axial constraint. Impact velocity was obtained from a series of electrical contact pins mounted in the final section of the gun barrel and could be measured to within 0.2 percent accuracy. The 63.5-mm-dia and 102-mm-dia guns used aluminum projectiles to hold the foundry core targets and the 178-mm-dia gun used structural urethane foam projectiles.

Instrumented Penetrator Designs. Experiments were conducted with one ogival and two conical nose shapes, all with 20.6-mm-dia afterbodies. The penetrator designs are shown in Fig. 2 and basically consist of a tungsten alloy[2] nose with density 18.7 Mg/m^3, a PCB[3] Model 305A quartz accelerometer, range 10^5 g, and a 0.25 mm (0.01 in.) wall steel tube with length[4] 0.16 m (6.25 in.). A high density nose material was required to have enough mass to keep the accelerations within the transducer capacity and still maintain a body diameter that was relatively small compared with the target size. For most experiments, the accelerometer was screwed into the penetrator nose after applying a light coat of epoxy on the threads and this provided the rigid connection illustrated in Fig. 2(*b*). A few experiments, however, were conducted with the design shown in Fig. 2(*c*). This penetrator contained a 0.76 mm (0.03 in.) pad of rubber[5] between the nose and the accelerometer; the pad was designed to act as a mechanical filter and to reduce the amplitude of high-frequency excitation delivered to the accelerometer. In both designs, the accelerometer cable was attached to the accelerometer with a light coat of epoxy in order to provide a tight, bounce-free connection. The steel tube was shrink-fitted to the nosepiece and the accelerometer and cable were encapsulated with about 0.006 kg of Hysol 2038 epoxy.[6]

Target Material. The foundry core targets and material test samples were made at the Sandia foundry with nearly the same process as that used for making molds for metal castings. This material is primarily silica sand (90 percent by weight) and is combined with sufficient binder ingredients such that when oven fired, the material resembles a low-density cemented sandstone. Different sample sizes required for the gas gun reverse ballistics and triaxial material tests could be conveniently made and the sample-to-sample density variations were usually within 2 percent.

Penetration experiments with foundry core targets have been previously reported [8], but the density of those targets was very low (1.46 Mg/m^3). As previously mentioned, the current experiments were devised to complement the full-scale tests conducted into natural dry porous tuff targets [9] which have densities between 1.6 and 2.0 Mg/m^3. Thus, the samples for the current study were tamped sufficiently before oven firing such that nominal densities were raised to 1.82 Mg/m^3 and porosity was about 30 percent.

Triaxial material tests were conducted on foundry core samples and results are shown in Figs. 3(*a*,*b*). For these tests, cylindrical samples were first loaded with hydrostatic pressure ($\sigma_1 = \sigma_c$, where σ_1 is axial stress and σ_c is the radial or confining stress) and the sample volume change was measured.

[2] Kennertium W-2, Kennametal, Inc., Latrobe, Pa. 15650.

[3] PCB Piezotronics, Inc., 3425 Walden Ave., Depew, N.Y. 14043.

[4] The four experiments conducted with conical-nosed ($\tan\theta = 1/4$) penetrators and the 63.5-mm-bore gun had length 0.08 m (3.0 in.).

[5] RTV630, General Electric Co., Silicon Product Dept., Waterford, N.Y. 12188.

[6] Hysol Div., The Dexter Corp., Industry, Calif. 91744.

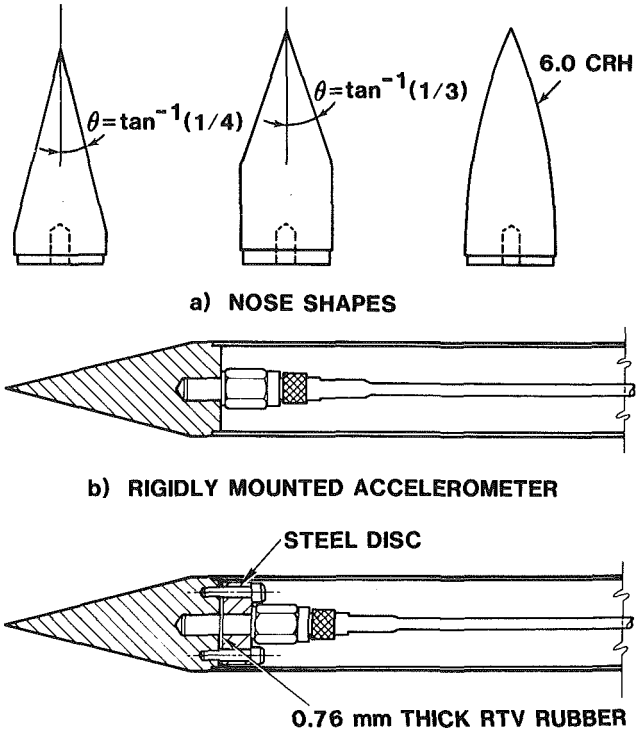


Fig. 2 Instrumented penetrator designs. All diameters 20.6 mm (0.81 in.).

These data are commonly called the hydrostat and are shown in Fig. 3(*a*). The samples were also subjected to triaxial compression tests. For these tests samples were loaded in hydrostatic compression to some fixed pressure; next, the lateral stress or confining pressure, σ_c, was held fixed and the axial stress was increased beyond the confining pressure, $\sigma_1 > \sigma_c$. Stress difference versus strain difference data for these tests are shown in Fig. 3(*b*). As typical for dry porous geological materials, shear resistance increases significantly with confining pressure. A comparison of the foundry core and Antelope tuff data [9] show many similarities.

Penetration Response Data. As typical with transient acceleration measurements, many high frequency components are present in the data. The unwanted high frequency signals can be minimized or eliminated by electronically or mechanically filtering the data. Scope traces showing unfiltered and electronically filtered data appear in Fig. 4 for both penetrator designs. The accelerometer has a fundamental resonance at about 60 kHz, and the 20 kHz filter removes this and higher modes. Comparison of the traces with the 50 kHz and 20 kHz filters indicate that the rise time during nose entry is somewhat distorted by the 20 kHz filter.

Several experiments were also conducted with a thin rubber pad between the nose and the accelerometer. This pad was inserted in an attempt to reduce the amplitude of high frequency mechanical input to the acclerometer, and thus to reduce spurious contributions to output due to accelerometer resonances. As indicated by the data in Fig. 4 from experiments conducted at nearly the same impact velocity, the rubber pad did not substantially reduce the amplitudes of the unwanted high frequency components in the acclerometer signal.

For this study, forces from penetration were determined from rigid-body, acceleration-time profiles which are the data shown in Fig. 4, filtered at 20 kHz. Rigid-body, acceleration-time profiles for sufficiently slender nose shapes of the type

Downloaded 02 May 2010 to 171.66.16.25. Redistribution subject to ASME license or copyright; see http://www.asme.org/terms/Terms_Use.cfm

Table 1 Data summary for the conical-nosed penetrators with $\theta = \tan^{-1}(1/4)$. All afterbody diameters were 20.6 mm (0.810 in.). The asterisk denotes an experiment conducted with the rubber shock isolation pad.

Impact velocity (km/s)	Target density (Mg/m^3)	Target diameter, length (mm)	Penetrator mass (kg)	Peak acceleration (g)	Peak force (kN)
0.233	1.83	90,90	0.150	29,000	43
0.282	1.76	165,90	0.148	34,000	50
0.302	1.82	90,90	0.149	34,000	50
0.310	1.80	90,90	0.150	34,000	50
0.449	1.82	90,90	0.151	41,000	61
0.584	1.85	60,67	0.147	45,000	65
0.585	1.85	60,67	0.147	43,000	62
0.610	1.81	90,90	0.155	53,000	81
0.620	1.81	90,90	0.155	49,000	74
0.904	1.80	90,90	0.152	79,000	117
1.03	1.83	90,90	0.152	89,000	133
1.18	1.87	60,67	0.141	123,000	170
1.20	1.83	60,67	0.137	137,000	184
0.995*	1.83	90,90	0.168	99,000	163

Table 2 Data summary for the conical-nosed penetrators with $\theta = \tan^{-1}(1/3)$. All afterbody diameters were 20.6 mm (0.810 in.). The asterisk denotes an experiment conducted with the rubber shock isolation pad.

Impact velocity (km/s)	Target density (Mg/m^3)	Target diameter, length (mm)	Penetrator mass (kg)	Peak acceleration (g)	Peak force (kN)
0.200	1.85	90,90	0.231	24,000	55
0.280	1.76	165,90	0.235	23,000	54
0.292	1.76	165,90	0.232	24,000	56
0.295	1.84	90,90	0.233	27,000	63
0.400	1.84	90,90	0.234	30,000	70
0.505	1.84	90,90	0.235	39,000	89
0.614	1.83	90,90	0.235	48,000	110
0.779	1.83	90,90	0.236	69,000	159
1.00	1.84	90,90	0.235	96,000	222
0.987*	1.81	90,90	0.251	86,000	212

Table 3 Data summary for the six CRH-nosed penetrators. All afterbody diameters were 20.6 mm (0.810 in.). The asterisk denotes an experiment conducted with the rubber shock isolation pad.

Impact velocity (km/s)	Target density (Mg/m^3)	Target diameter, length (mm)	Penetrator mass (kg)	Peak acceleration (g)	Peak force (kN)
0.236	1.81	90,90	0.227	21,000	47
0.272	1.76	165,90	0.227	20,000	44
0.280	1.76	165,90	0.232	20,000	46
0.314	1.82	90,90	0.224	22,000	48
0.452	1.80	90,90	0.228	21,000	48
0.604	1.81	90,90	0.231	25,000	57
0.715	1.81	90,90	0.229	32,000	72
0.917	1.79	90,90	0.230	43,000	97
1.08	1.82	90,90	0.231	51,000	115
1.23	1.82	90,90	0.225	68,000	150
1.18*	1.83	90,90	0.247	66,000	160

examined in this study and the full-scale tests reported in [5, 9] are similar to those shown in Fig. 4. All these profiles have a monotonic rise for about the time fo nose entry followed by a nearly flat plateau for the time corresponding to two or three additional nose lengths. Peak values of rigid-body acceleration given in the data summarizes of Tables 1, 2, and 3 are the acceleration magnitudes corresponding to the plateaus of the data filtered at 20 kHz. Peak values of force are the total penetrator mass times this peak acceleration.

As shown in Fig. 1, the thin afterbody tube held the penetrator forward of the base of the polyurethane holding fixture. The first experiments were conducted with conical-nosed ($\tan\theta = 1/4$) penetrators and the 63.5-mm-bore gun; for these experiments the tube had length 0.08 m (3.0 in.) and mass 0.01 kg, which is about 7 percent of the total penetrator mass. The other experiments on the $\tan\theta = 1/4$ nose were conducted with the 102-mm-bore gun and used a tube length of 0.16 m (6.25 in.) with mass 0.02 kg which is about 14 percent of the total penetrator mass. The $\tan\theta = 1/3$ and 6.0 CRH-nosed penetrators used the 0.16 m afterbody tube, which is about 9 percent of the total penetrator masses. Total penetrator masses for all experiments are recorded in Tables 1, 2, and 3. As was discussed, we measured rigid-body acceleration and calculated penetration forces from the total penetrator mass. We recorded over time intervals of 100–500 μs for impact velocities between 0.2–1.2 km/s. Since we measured rigid-body acceleration at the back of the nosepiece, several wave transits through the nose material were required. Typical nose transit times were about 10 μs, and a transit time down the 0.16 m-long afterbody shell is about 30 μs. Since a

Downloaded 02 May 2010 to 171.66.16.25. Redistribution subject to ASME license or copyright; see http://www.asme.org/terms/Terms_Use.cfm

complex stress wave interaction process occurs between the nosepieces and the shells during the recording time, the force estimate based on rigid-body acceleration data and total penetrator mass had some uncertainty.

The reviewers also suggested a procedure to calculate the force due to penetration from the rigid-body acceleration data. For this estimate, the nosepiece was taken as rigid and was acted on by the force due to penetration and the force from the afterbody tubes. The particle velocity imparted to the tube was calculated by integrating the acceleration trace, idealized as a ramp pulse. The rise time of the pulse was taken as the time of nose entry and the plateau was taken as the data presented in Tables 1, 2, and 3. These post test calculations indicated that the cold drawn steel tubes were stressed beyond static yield strength, taken as 330 MPa (54,000 psi), during the rise portion of the pulse for all experiments. Thus, for this procedure the peak force due to penetration was calculated as the effective mass (total penetrator mass minus the tube mass) times the peak rigid-body acceleration plus the force from the shell corresponding to the tube yield stress. For this design the force was 6.0 kN. This calculation estimated forces that were lower than those presented in Tables 1, 2, and 3; however, both calculational procedures produced nearly identical results for all but a few experiments. Calculations were within 5 percent agreement for all experiments except those for the $\tan\theta = 1/4$ nose at impact velocities of $V = 0.904$ and 1.02 km/s given in Table 1, and the calculated forces for these experiments differed by only 9 percent.

Experimental Results

Summaries of the data for each of the three nose shapes are presented in Tables 1, 2, and 3. The first experiments were conducted with the Sandia 63.5-mm-dia gun on conical nose shapes with $\theta = \tan^{-1}(1/4)$; the target dimensions (diameter, length) noted in Table 1 for these experiments were 60, 67 mm (2.4, 2.5 in.). Once feasibility of the technique was demonstrated, most of the data were obtained with the larger bore Air Force Weapons Laboratory 102-mm-dia gun; target dimensions (diameter, length) for these experiments were 90, 90 mm (3.5, 3.5 in.). For both sets of experiments, the foundry core targets were contained within hollow aluminum projectiles.

To demonstrate that simple size and confinement did not significantly affect penetration resistance, five experiments were conducted with the University of Dayton Research Institute 178-mm-dia gun. These experiments used 165 mm (6.5 in.) diameter, 90 mm (3.5 in.) long targets which were supported within structural urethane foam projectiles. Thus, the foundry core targets for the largest bore gas-gun experiments not only had a much larger diameter, but were supported in a more flexible projectile. Comparison of the data in Tables 1, 2, and 3 indicates that penetration resistance from the larger diameter targets is within the experimental scatter of the other data. It is, therefore, concluded that the target samples with diameter and length 90 mm have adequate size for the parametric range covered in this study.

Along with target sizes, the density of each target is given in Tables 1, 2, and 3. The average densities for the 60, 90, and 165 mm diameter targets are 1.85, 1.82, and 1.76 Mg/m^3, respectively. As previously mentioned, the targets were tamped before oven firing to achieve densities higher than those of foundry core molds for metal castings. The density variations for the three sample sizes indicate that the smaller samples offered more constraint for a nearly constant tamping procedure. These density variations, however, are considered small for a simulated geological target.

Experimental data and a least-squares quadratic fit to the data for the six CRH ogival nose shape are shown in Fig. 5. Quadratic fits to the data for the conical nose shapes are also

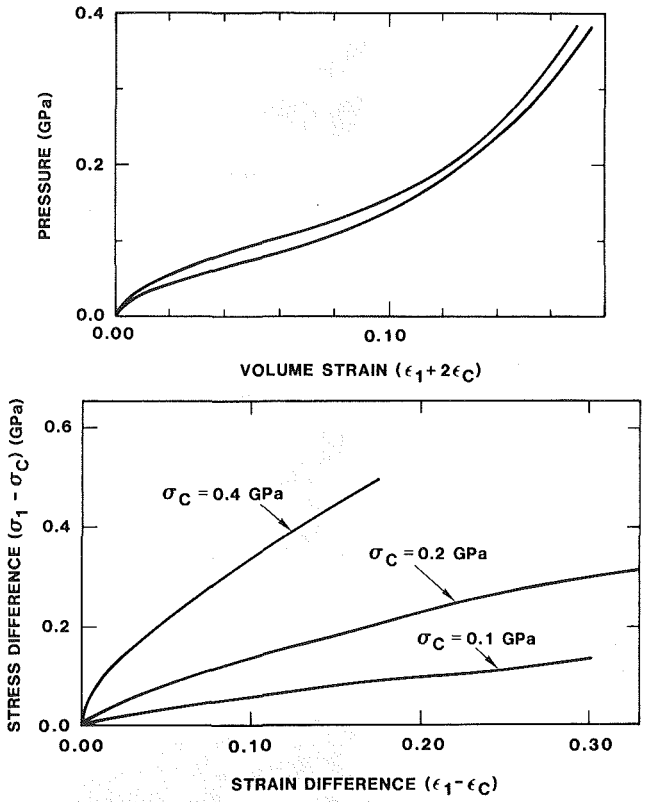


Fig. 3 Triaxial material test data: (a) Data from two hydrostatic compression tests ($\sigma_1 = \sigma_C$), and (b) triaxial compression test data ($\sigma_1 > \sigma_C$).

presented in Fig. 5 to compare the resistances offered by the three shapes. The quadratic data fits have root mean relative errors of 3.3, 6.1, and 4.7 percent for the six CRH, $\theta = \tan^{-1}(1/4)$ and $\theta = \tan^{-1}(1/3)$ nose shapes, respectively. Data scatter for the conical nose shapes is similar to that shown for the ogival nose shape; however, these data, which are given in Tables 1 and 2, were not included in Fig. 5 to avoid clutter. As expected, the blunter conical nose shape has more penetration resistance. The ogival nose shape has less resistance than the conical nose shapes and qualitative arguments for this effect are given by Hill [16].

Data and linear fits to the data for the six CRH ogival nose shape are also presented on a log-log plot in Fig. 6. The data indicate an increased resistance relationship for $V > 0.5$ km/s which is about the velocity limit for current field tests with onboard recording systems. Empirical models are widely used as predictive tools [3, 4, 17], and the ogival nose shape data can be described conveniently in the form

$$F = KV^n, \quad 0.5 < V < 1.2 \text{km/s}$$

where $K = 109$, $n = 1.29$, and F, V have units of kN, km/s. Data for the conical nose shapes also show an increased resistance relationship for $V > 0.5$. Figure 7 presents data and linear fits for the three nose shapes in this higher impact velocity region. For $\theta = \tan^{-1}(1/3)$ over $0.5 < V < 1.1$, $K = 221$, $n = 1.36$; and for $\theta = \tan^{-1}(1/4)$ over $0.5 < V < 1.2$, $K = 136$, $n = 1.32$.

Discussion

We developed a convenient laboratory procedure to determine forces on projectiles penetrating geological targets and obtained new data for three nose shapes for impact velocities to 1.2 km/s. Data in Fig. 6 show a substantial increase in penetration resistance for impact velocities greater than 0.5 km/s, the current limit for full-scale tests. Full-scale

Downloaded 02 May 2010 to 171.66.16.25. Redistribution subject to ASME license or copyright; see http://www.asme.org/terms/Terms_Use.cfm

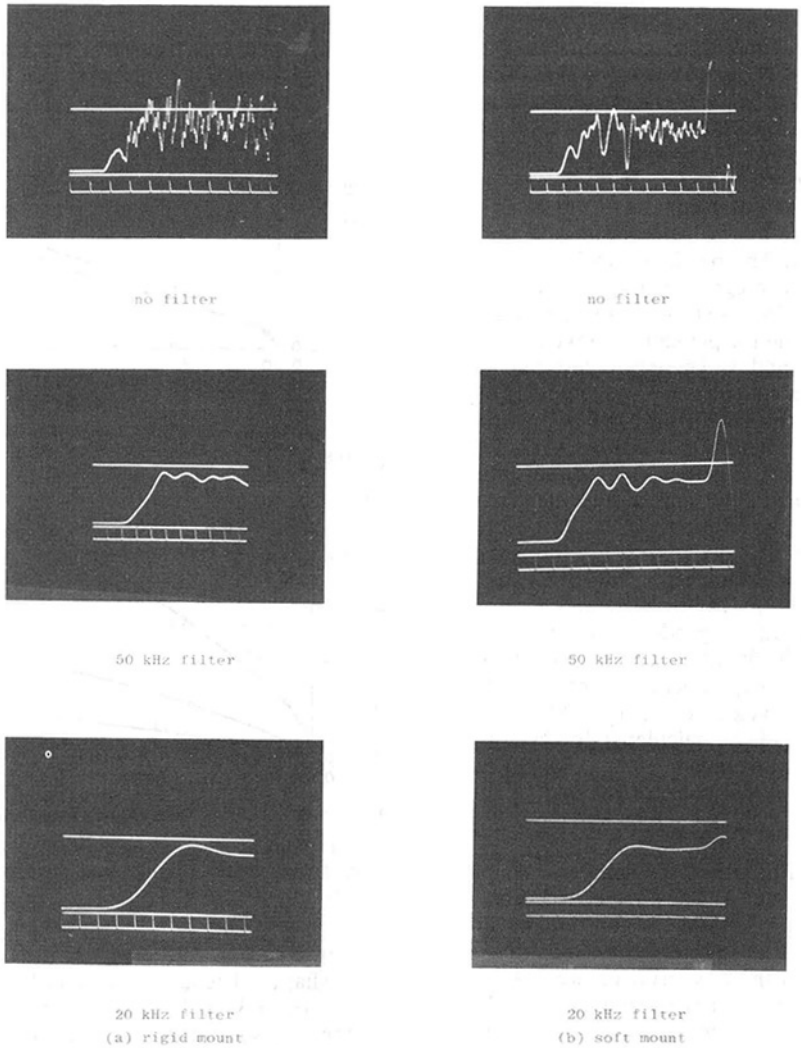


Fig. 4 Acceleration time for $\theta = \tan^{-1}(1/3)$ nose shapes. All traces have 5.0 V calibration and 10 μs timing marks. Rigid mount experiment had impact velocity 1.00 km/s and accelerometer sensitivity 0.0450 m V/g. Soft mount experiment had impact velocity 0.987 km/s and accelerometer sensitivity 0.0396 m V/g.

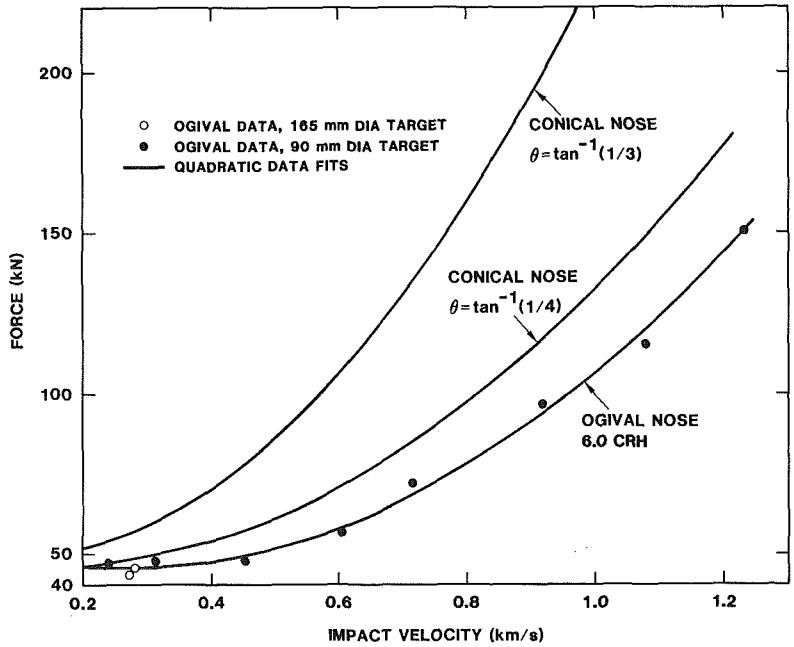


Fig. 5 Least-squares quadratic fits to the data for three nose shapes and data for the six CRH ogival-nose shape

Downloaded 02 May 2010 to 171.66.16.25. Redistribution subject to ASME license or copyright; see http://www.asme.org/terms/Terms_Use.cfm

tests are required for total systems design verification; however, these laboratory-scale experiments can complement field-test programs.

As discussed throughout this paper, research on penetration into geological targets consists of a mix of analytical, experimental, and field-test work. We try to march in parallel with these approaches; however, one approach always leads the others. Our current predictive models [5, 9] have elastic-plastic constitutive laws with fixed, pressure-dependent yield surfaces; in contrast, the foundry core data show that stress difference increases monotonically with strain difference and does not reach a plateau. So, our penetration theories are not directly applicable to the foundry core targets. Since many natural geological materials behave similar to foundry core, the data in this paper suggest new analytical areas for study.

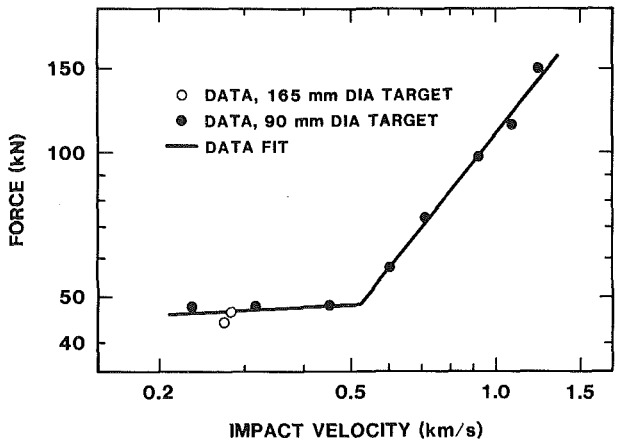


Fig. 6 Data and power law fit for the six CRH ogival-nose shape

Acknowledgments

D. L. Paisley and S. J. Hanchak performed the gas gun experiments conducted at the University of Dayton Research Institute, C. Cooley guided the triaxial material test programs conducted at TerraTek, and D. K. Overmier of Sandia offered many helpful suggestions related to acceleration measurements.

References

1 Zukas, J. A., et al., *Impact Dynamics*, Wiley, New York, 1982.

2 Colp, J. L., ed., Proceedings, *Rapid Penetration of Terrestrial Materials*, Texas A & M University, Feb. 1972.

3 Young, C. W., "Depth Prediction for Earth Penetrating Projectiles," ASCE *Journal of Soil Mechanics and Foundation*, May 1969, pp. 803–817.

4 Allen, W. A., Mayfield, E. B., and Morrison, H. I., "Dynamics of a Projectile Penetrating Sand," *Journal of Applied Physics*, Vol. 28, No. 3, Mar. 1957, pp. 370–376.

5 Forrestal, M. J., and Longcope, D. B., "Closed-Form Solutions for Forces on Conical-Nosed Penetrators Into Geological Targets With Constant Shear Strength," *Mechanics of Materials*, Vol. 1, 1982, pp. 285–295.

6 Bishop, R. F., Hill, R., and Mott, N. F., "The Theory of Indentation and Hardness Tests," *The Proceedings of the Physical Society*, Vol. 57, Part 3, May 1945, pp. 147–159.

7 Ito, Y. M., Nelson, R. B., Ross-Perry, F. W., and Cheng, L. Y., "Earth Penetrator Yawed Impact Sensitivity Investigation," DNA-5835F, California Research and Technology, Inc., Woodland Hills, Calif., Feb. 1980.

8 Forrestal, M. J., and Grady, D. E., "Penetration Experiments for Normal Impact Into Geological Targets," *International Journal of Solids and Structures*, Vol. 18, No. 3, 1982, pp. 229–234.

9 Longcope, D. B., and Forrestal, M. J., "Penetration of Targets Described by a Mohr-Coulomb Failure Criterion With a Tension Cutoff," ASME JOURNAL OF APPLIED MECHANICS, Vol. 50, No. 2, June 1983, pp. 327–333.

10 Murff, J. D., and Coyle, H. M., "A Laboratory Investigation of Low Velocity Penetration," Proceedings, *Rapid Penetration of Terrestrial Materials*, Colp, J. L., ed., Texas A & M University, Feb. 1972.

11 Setchell, R. E., and Guzman, J. A., "Laboratory Simulation of Projectile Penetration," SAND81-2029, Sandia National Laboratories, Albuquerque, N. Mex., Jan. 1983.

12 Lee, L. M., and Jenrette, B. D., "Scaled Model Penetrator Impact Test Program," AFWL-TR-82-72, Air Force Weapons Laboratory, Kirtland Air Force Base, N. Mex.

13 Lee, L. M., and Jenrette, B. D., "Penetration Experiments Into Foundry Core," AFWL-TR-82-83, Air Force Weapons Laboratory, Kirtland Air Force Base, N. Mex.

14 Paisley, D. L., and Hanchak, S. J., "Sandia One-Sixth Scale Penetrator Impact Into Foundry Core," UDR-TR-82-137, University of Dayton Research Institute, Nov. 1982.

15 Smith, R. H., "Testing Program on Tamped Foundry Core," Terra Tek, Salt Lake City, Utah, letter report to M. J. Forrestal, Dec. 1981.

16 Hill, R., "Cavitation and the Influence of Headshape in Attack of Thick Targets by Non-Deforming Projectiles," *Journal of the Mechanics and Physics of Solids*, Vol. 28, 1980, pp. 249–263.

17 Longcope, D. B., and Forrestal, M. J., "Closed-Form Approximations for Forces on Conical Penetrators Into Dry Porous Rock," ASME JOURNAL OF APPLIED MECHANICS, Vol. 48, Dec. 1981, pp. 971–972.

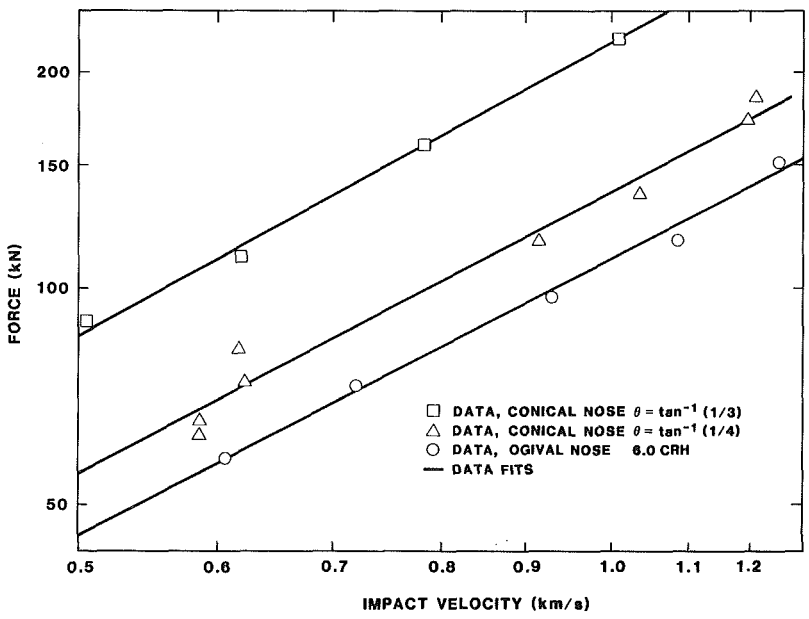


Fig. 7 Data and power law fits for V > 0.5 km/s

Downloaded 02 May 2010 to 171.66.16.25. Redistribution subject to ASME license or copyright; see http://www.asme.org/terms/Terms_Use.cfm

On the Nonlocal Theory of Wave Propagation in Elastic Plates[1]

J. L. Nowinski
H. Fletcher Brown Professor Emeritus,
Department of Mechanical and
Aerospace Engineering,
University of Delaware,
Newark, Del. 19716

Propagation of longitudinal waves in isotropic homogeneous elastic plates is studied in the context of the linear theory of nonlocal continuum mechanics. To determine the nonlocal moduli, the dispersion equation obtained for the plane longitudinal waves in an infinite medium is matched with the parallel equation derived in the theory of atomic lattice dynamics. Using the integroalgebraic representation of the stress tensor and the Fourier transform, the system of two coupled differential field equations is solved in the standard manner giving the frequency equations for the symmetric and antisymmetric wave modes. It is found that the short wave speed in the Poisson medium differs by about 13 percent from the speed established in the classical theory. A numerical example is given.

Introduction

As is commonly known, one of the principal postulates of the traditional mechanics of continuous media is the principle of local action. This principle excludes the action at a distance, and attributes changes occurring at a point of the medium to thermoenergetic factors acting at the point. Of necessity then, the classical theory, by restricting the response of the continuum to strictly local actions, constitutes a so-called *local* theory. A familiar example is provided by the conventional theory of elasticity, in which, when determining the stress at a point, one disregards the deformation and the temperature fields outside an arbitrarily small neighborhood at the point.

In contrast to this local approach, of zero-range internal interactions, the modern *nonlocal* continuum mechanics, originated and developed in the last two decades, postulates that the local state at a point is influenced by the action of all particles of the body. As a result, the stress at a point, say, while remaining a function of motion and temperature at the point, simultaneously becomes a functional in the just two named factors extended over the entire volume of the body. Such a situation is well illustrated by the form of the stress-strain relation for the nonlocal elastic medium,

$$\tau_{ij} = 2\mu e_{ij} + \lambda e_{kk}\delta_{ij} + \int_V (2\mu' e'_{ij} + \lambda' e'_{kk}\delta_{ij})\, dv', \qquad (0.1)$$

derived by Eringen ([1], p. 245) on the basis of the general theory of constitutive equations.[2] Here the prime refers to an arbitrary point of the body, V is the volume of the body, μ and λ are Lamé constants, and μ' and λ' are nonlocal elastic moduli (influence functions) depending on the distance between an arbitrary point of the body and the point under observation. Although problems of a nonlocal character emerged occasionally in the past, the new and promising discipline of nonlocal continuum mechanics, based on rigorous theoretical foundations, was established (as already mentioned) quite recently. We owe it for the most part to the efforts of Green and Rivlin, Kroener, Eringen, Edelen and Kunin.

Certain connections between the micropolar continuum mechanics and the nonlocal interactions were first noted by Green and Rivlin in 1965 [2]. Slightly later, in 1966, Kroener analyzed continuum mechanics in the context of the atomic cohesion forces [3]. This supplemented his novel ideas expounded earlier in [23]. Regarding the nonlocalities, Kroener and Datta made an attempt to derive the nonlocal elastostatics from the theory of crystal lattices [24], and Kroener discussed other implications of the long-range forces [25]. In a unified theory of materials published in 1966, Eringen gave a thought to the role of nonlocalities [4]; some of his papers, [7–10], are briefly mentioned, but additional citations are his analysis of the nonlocal Rayleigh waves [16], the theory of nonlocal electromagnetic elasticity [19], and most recently the theory of the nonlocal plasticity [20]. Edelen's early work, 1969, involved a class of nonlocal bodies which he called protoelastic [5]. In 1976 he published a treatise in which he gave a rigorous comprehensive analysis of the foundations of nonlocal theories (in particular, of the constitutive postulates), and, in this context, discussed variational and thermodynamic questions [12]. Kunin's early work on nonlocal interactions [26*a*] was published in 1967. Later, in a series of papers such as [6] and [26*b*–26*d*], he (in part with his co-workers) developed an original approach to a general theory of elastic media encompassing continuous and discrete systems, as well as strong (wave length of the order of the lattice spacing) and weak nonlocalities (oriented, micropolar, micromorphic, and other media). A synthesis of Kunin's work is presented in his books [27, 28].

[1] Prepared with partial support of the University of Delaware.

[2] In equation (0.1), and throughout this text, we apply the summation convention over the repeated indices.

Contributed by the Applied Mechanics Division for publication in the JOURNAL OF APPLIED MECHANICS.

Discussion on this paper should be addressed to the Editorial Department, ASME, United Engineering Center, 345 East 47th Street, New York, N.Y. 10017, and will be accepted until two months after final publication of the paper itself in the JOURNAL OF APPLIED MECHANICS. Manuscript received by ASME Applied Mechanics Division June, 1983; final revision, December, 1983.

Copyright © 1984 by ASME
Downloaded 02 May 2010 to 171.66.16.25. Redistribution subject to ASME license or copyright; see http://www.asme.org/terms/Terms_Use.cfm

While the literature on the fundamental aspects of the nonlocal continuum mechanics is relatively extensive, applications of the theory are not too numerous. The results, however, of those concrete problems that were solved display a rather remarkable agreement with experimental evidence. This is so, for example, with a nonlocal approach to the crack problem, which leads to a finite stress at the crack tip, and predicts the cohesive stress for various materials close to that obtained in the atomic lattice dynamics [7, 8]. Likewise, a nonlocal study of the secondary flow of viscous fluid in a pipe furnishes a streamline pattern similar to the one obtained experimentally by Nikuradze [9]. Other examples of the effectiveness of the nonlocal approach are: prediction of the dispersive character of elastic waves demonstrated experimentally (and lacking in the classical theory) [10]; and calculation of the velocity of short Love waves whose nonlocal estimates agree better with seismological observations than the local ones [11][3].

With regard to the undulatory motions in plates—the subject of the present study—the investigations have a rather long history, inasmuch as the Rayleigh-Lamb dispersion equation (generalized in Section 2 to the nonlocal case) was derived in 1889. Later Lamb analyzed the fundamental symmetric and antisymmetric modes [29]. A modern review of the problem[4] as well as a comprehensive investigation of symmetric and antisymmetric modes we owe to Mindlin [34, 35], who in cooperation with Onoe was able to calculate the curves for the real and imaginary roots for the first 12 modes (up to the fairly short waves) [38]. The papers of Meeker and Meitzler [36], Agarwal and Shaw [37], and Sherwood [39] also deserve mention. Interesting associations of phase and group velocities of opposite sign with the second symmetric and third antisymmetric modes and long waves were discussed by Tolstoy and Usdin [40]. Their results for the first two modes calculated up to $kh = 8$ (k = wave number, $2h$ = plate thickness) and for the Poisson material (Poisson ratio $\nu = 1/4$) are extended in Section 3 to short waves, and compared with their nonlocal counterparts. We end this sketchy survey by mentioning a general analysis of Gogoladze for arbitrary values of Lamé constants [42].

With the hope of shedding more light on the subject this paper examines the nonlocal aspect of the longitudinal waves in isotropic homogeneous elastic plates. To determine the nonlocal moduli, the dispersion equation of longitudinal waves in an infinite medium is compared with the corresponding equation obtained in the theory of lattice dynamics. Solution of two coupled integrodifferential field equations leads to the frequency equations for the symmetric and antisymmetric wave modes. It is found that, while the long wave speeds in the nonlocal and local theories are (as one may have expected) the same, the speed in the Poisson medium of the short waves is, in the nonlocal case, by about 13 percent less than the speed found in the local theory. A numerical example illustrates this result.

1 Plane Longitudinal Waves

For future reference let us first recall some results involving propagation of plane longitudinal waves in an infinite medium with nonlocal properties.[5] Let the waves propagate in the x_1-direction of a rectangular coordinate system $x = (x_1, x_2, x_3)$. Since in the case considered, the only nonzero displacement component is $u_1 \equiv u = u(x_1, t)$, then, in the framework of the linear theory, $e_{11} = \partial u/\partial x_1$ becomes the only nonzero strain component.

Using the representation (0.1) we arrive at the equation

$$\frac{\tau_{11}}{2\mu+\lambda} = \frac{\partial u}{\partial x_1} + \int_{-\infty}^{\infty} [2\mu'(|x_1 - x_1'|) + \lambda'(|x_1 - x_1'|)] \frac{\partial u'}{\partial x_1'} \Big] dx_1', \tag{1.1}$$

with all of the remaining stress components vanishing or immaterial for our purposes.

In casting the stress τ_{11} in the foregoing form we used the argument of Edelen (see [11], Appendix), by which, for λ' and μ' as functions of $|x - x'|$ vanishing at infinity, one is permitted to reduce the three-dimensional problem, such as the one under discussion, to a one-dimensional independent of the (unprimed) coordinates x_2 and x_3.

By appeal to the derivations of Erigen in [10] and [43], we arrive at the final result

$$\frac{c^2}{c_1^2} = 1 + \sqrt{2\pi}\frac{2\bar{\mu}'(k) + \bar{\lambda}'(k)}{2\mu+\lambda}, \tag{1.2}$$

where k is the wave number, ω the frequency, $c = \omega/k$ the actual speed of longitudinal waves in their nonlocal aspect, $c_1 = (2\mu+\lambda/\rho)^{1/2}$ the speed of these waves in the classical theory, and an overbar indicates a Fourier transform:

$$\bar{u}(k,t) = \frac{1}{\sqrt{2\pi}}\int_{-\infty}^{\infty} u(x_1,t)e^{ikx_1}dx_1. \tag{1.3}$$

Combining equation (1.2) with the dispersion equation derived in the atomic lattice dynamics of Born-von Kármán [14] for longitudinal waves in a monoatomic lattice,

$$c^2 = \frac{4(\lambda+2\mu)}{\rho a^2 k^2}\sin^2\frac{ka}{2}, \tag{1.4}$$

where a is the lattice spacing, one obtains

$$\frac{2\bar{\mu}'(k) + \bar{\lambda}'(k)}{2\mu+\lambda} = \frac{1}{\sqrt{2\pi}}\left[\frac{\sin^2\frac{ka}{2}}{\left(\frac{ka}{2}\right)^2} - 1\right]. \tag{1.5}$$

We note that, in analogy to the classical case, we introduce the nonlocal longitudinal and shear wave pseudospeeds,

$$c_1^* = \left(\frac{2\mu+\lambda+2\bar{\mu}'+\bar{\lambda}'}{\rho}\right)^{1/2}, \quad \text{and} \quad c_2^* - \left(\frac{\mu+\bar{\mu}'}{\rho}\right)^{1/2}. \tag{1.6}$$

The variation of the wave number is restricted to the positive half of the so-called first Brillouin zone $(-(\pi/a) \le k \le (\pi/a)$; this guarantees the single-valuedness of the wave length associated with the given frequency, [14].

2 Wave Propagation in Plates

We now return to the main subject of this study, that is, to the propagation of longitudinal waves in an infinite plate. Let the middle plane of the plate of thickness $2h$ coincide with the plane x_1 x_3 of a Cartesian rectangular coordinate system x_1, x_2, x_3, and let the waves in question proceed in the direction of the x_1-axis.

We set

$$u_1 = u_1(x_1,x_2;t), \quad u_2 = u_2(x_1,x_2;t), \quad u_3 = 0, \tag{2.1}$$

and conclude that

$$e_{11} = u_{1,1}, e_{22} = u_{2,2}, e_{12} = \frac{1}{2}(u_{1,2} + u_{2,1}). \tag{2.2}$$

[3] Historical reviews on the subject and extensive bibliographies are found in the treatises by Edelen [12], Eringen [1], and Kunin [27, 28].

[4] Some interim reviews and analyses may be found in [30–33].

[5] This problem was examined by Erigen in [43]; see also [1], p. 248.

Downloaded 02 May 2010 to 171.66.16.25. Redistribution subject to ASME license or copyright; see http://www.asme.org/terms/Terms_Use.cfm

Consequently, the associated nonvanishing stress components become

$$\left.\begin{aligned}
\tau_{11} &= (2\mu+\lambda)u_{1,1} + \lambda u_{2,2} + \int_{-h}^{h}\int_{-\infty}^{\infty}[(2\mu'+\lambda')u'_{1,1} \\
&\quad + \lambda' u'_{2,2}]dx_1' dx_2', \\
\tau_{22} &= (2\mu+\lambda)u_{2,2} + \lambda u_{1,1} + \int_{-h}^{h}\int_{\infty}^{\infty}[(2\mu'+\lambda')u'_{2,2} \\
&\quad + \lambda' u'_{1,1}]dx_1' dx_2', \\
\tau_{12} &= \mu(u_{1,2}+u_{2,1}) \\
&\quad + \int_{-h}^{h}\int_{\infty}^{\infty}\mu'(u'_{1,2}+u'_{2,1})dx_1' dx_2'.
\end{aligned}\right\} \quad (2.3)$$

We note that u'_i, $i = 1, 2$, are functions of x_1', x'_2, and t, and $\mu' = \mu'(|x_1' = x_1|, |x'_2 - x_2|)$ and $\lambda' = \lambda'(|x'_1 - x_1|, |x'_2 - x_2|)$ are functions of $|x_i' - x_i|$, $i = 1, 2$. A Fourier double transformation with respect to x_1 and t of the two identically nonzero equations of motion,

$$\begin{aligned}
\tau_{11,1} + \tau_{12,2} - \rho\ddot{u}_1 &= 0, \\
\tau_{12,1} + \tau_{22,2} - \rho\ddot{u}_2 &= 0,
\end{aligned} \quad (2.4)$$

gives

$$\begin{aligned}
-ik\,\bar{\tau}_{11} + \bar{\tau}_{12,2} + \rho\omega^2\bar{u}_1 &= 0, \\
-ik\,\bar{\tau}_{12} + \bar{\tau}_{22,2} + \rho\omega^2\bar{u}_2 &= 0,
\end{aligned} \quad (2.5)$$

where the transformed quantities are now functions of the Fourier parameters k and ω as well as of the coordinates x_2. With this in mind, a transformation of the equations (2.3) after lengthy but standard calculations leads to

$$\left.\begin{aligned}
\bar{\tau}_{11} &= -ik(2\mu+\lambda)\bar{u}_1 + \lambda\bar{u}_{2,2} \\
&\quad + \int_{-h}^{h}[-ik(2\bar{\mu}_*' + \bar{\lambda}_*')u_1' + \bar{\lambda}_*'\bar{u}'_{2,2}]dx_2', \\
\bar{\tau}_{22} &= (2\mu+\lambda)u_{2,2} - ik\lambda\bar{u}_1 \\
&\quad + \int_{-h}^{h}[(2\bar{\mu}_*' + \bar{\lambda}_*')\bar{u}'_{2,2} - ik\bar{\lambda}_*'\bar{u}_1']dx_2', \\
\bar{\tau}_{12} &= \mu(\bar{u}_{1,2} - ik\bar{u}_2) \\
&\quad + \int_{-h}^{h}\bar{\mu}_*'(\bar{u}'_{1,2} - ik\bar{u}_2')dx_2'.
\end{aligned}\right\} \quad (2.6)$$

Here $\bar{\mu}_*' = \bar{\mu}_*'(k, |x_2' - x_2|)$ and $\bar{\lambda}_*' = \bar{\lambda}_*'(k, |x_2' - x_2|)$ are transforms of the moduli $\mu'(|x_1' - x_1'|, |x_2' - x_2|)$ and $\lambda'(|x_1' - x_1|, |x_2 - x_2|)$, respectively. It is worth noting that $\bar{u}_i$ and $\bar{u}_i'$, $i = 1, 2$, now depend on the parameters k and ω as well as on the variables x_2 and x_2', respectively. In arriving at the equations (2.6) we assume that it is permissible to change the order of integration; we also applied the double Faltung theorem in combination with the substitution $\eta = x_1 - x_1'$.

What now remains is to substitute equations (2.6) into the equations (2.5) and to solve the resulting system of two coupled integrodifferential equations for the functions $\bar{u}_i$, $i = 1, 2$, provided that the values of the nonlocal moduli are known. It seems obvious that a rigorous solution of such problem encounters serious if not unsurmountable mathematical difficulties, and one has to resort to an approximate procedure. In the given problem, the appropriate numerical procedure seems to spring quite naturally from the hypothesis of the attenuating neighborhood underlying the theory of nonlocal continua. According to this hypothesis, the influence of the particles of the body, on the thermoenergetic state at the particle under observation, subsides rather rapidly with an increasing distance from the particle. In the classical theory, the function that characterizes the particle interactions is the Dirac delta function since in this theory the actions are assumed to have a zero range. In nonlocal theories the intermolecular forces may be represented by a variety of functions as long as their values decrease rapidly with the distance. In the present study, as adequate functions we decide to select the terms, $\delta_n(x_2' - x_2)$, $n = 1, 2. \ldots$, of the so-called δ-sequences. A δ-sequence, as generally known, is a sequence whose limit, for the index n increasing infinitely, is (in the present case a one-dimensional) Dirac delta function, $\delta(x_2' - x_2)$. With respect to the terms of the adopted delta sequence we accept the following simplifying assumptions: (*a*) For a sufficiently large l (as compared with the sphere of interactions of the particles), it is permissible to make the replacement

$$\int_0^l f(x_2')\delta_n(x_2' - x_2)dx_2' \approx \int_{-\infty}^{\infty} f(x_2')\delta(x_2' - x_2)dx_2'. \quad (2.7a)$$

(*b*) As a consequence of the foregoing, the terms $\delta_n(x_2' - x_2)$, $n >> 1$, acquire the shifting properly characteristic of the Dirac function,

$$\int_0^l f(x_2')\delta_n(x_2' - x_2')dx_2' \approx f(x_2). \quad (2.7b)$$

We now set

$$\bar{\mu}_*' = \bar{\mu}'(k)\cdot\delta_n(x_2' - x_2), \bar{\lambda}_*' = \bar{\lambda}'(k)\cdot\delta_n(x_2' - x_2), \quad (2.8)$$

where $\bar{\mu}'(k)$ and $\bar{\mu}'(k)$ are functions of the wave number k introduced earlier in Section 1. Inserting (2.8) into (2.3) yields

$$\left.\begin{aligned}
\bar{\tau}_{11} &= ik\Gamma_1\bar{u}_1 + \Gamma_2\bar{u}_{2,2}, & \Gamma_1 &= 2\mu+\lambda+2\bar{\mu}'(k)+\bar{\lambda}'(k), \\
\bar{\tau}_{22} &= \Gamma_1\bar{u}_{2,2} - ik\,\Gamma_2\bar{u}_1, & \Gamma_2 &= \lambda+\bar{\lambda}'(k), \\
\bar{\tau}_{12} &= \Gamma_3(\bar{u}_{1,2} - ik\bar{u}_2), & \Gamma_3 &= \mu+\bar{\mu}'(k).
\end{aligned}\right\} \quad (2.9)$$

Again setting, $\bar{u}_1 = U_1(k,\omega)e^{-\alpha x_2}$, $\bar{u}_2 = U_2(k,\omega)e^{-\alpha x_2}$, we substitute these expressions into (2.9) and the result into (2.5). We find

$$\left.\begin{aligned}
U_1\left(\alpha^2 - k^2\frac{\Gamma_1}{\Gamma_3} + \rho\frac{\omega^2}{\Gamma_3}\right) + U_2 i\alpha k\left(\frac{\Gamma_1}{\Gamma_3} - 1\right) &= 0, \\
U_1 i\alpha k\left(\frac{\Gamma_1}{\Gamma_3} - 1\right) + U_2\left(\alpha^2\frac{\Gamma_1}{\Gamma_3} - k^2 + \rho\frac{\omega^2}{\Gamma_3}\right).
\end{aligned}\right\} \quad (2.10)$$

A nontrivial solution to the foregoing system of algebraic equations calls for the vanishing of the determinant of the system. This gives after some calculations,

$$\left.\begin{aligned}
\bar{u}_1 &= A\sinh\nu_1 x_2 + B\cosh\nu_1 x_2 \\
&\quad + C\sinh\nu_2 x_2 + D\cosh\nu_2 x_2, \\
\bar{u}_2 &= B\kappa_1\sinh\nu_1 x_2 - A\kappa_1\cosh\nu_1 x_2 \\
&\quad - D\kappa_2\sinh\nu_2 x_2 - C\kappa_2\cdot \\
&\quad \cdot\cosh\nu_2 x_2
\end{aligned}\right\} \quad (2.11)$$

where

Downloaded 02 May 2010 to 171.66.16.25. Redistribution subject to ASME license or copyright; see http://www.asme.org/terms/Terms_Use.cfm

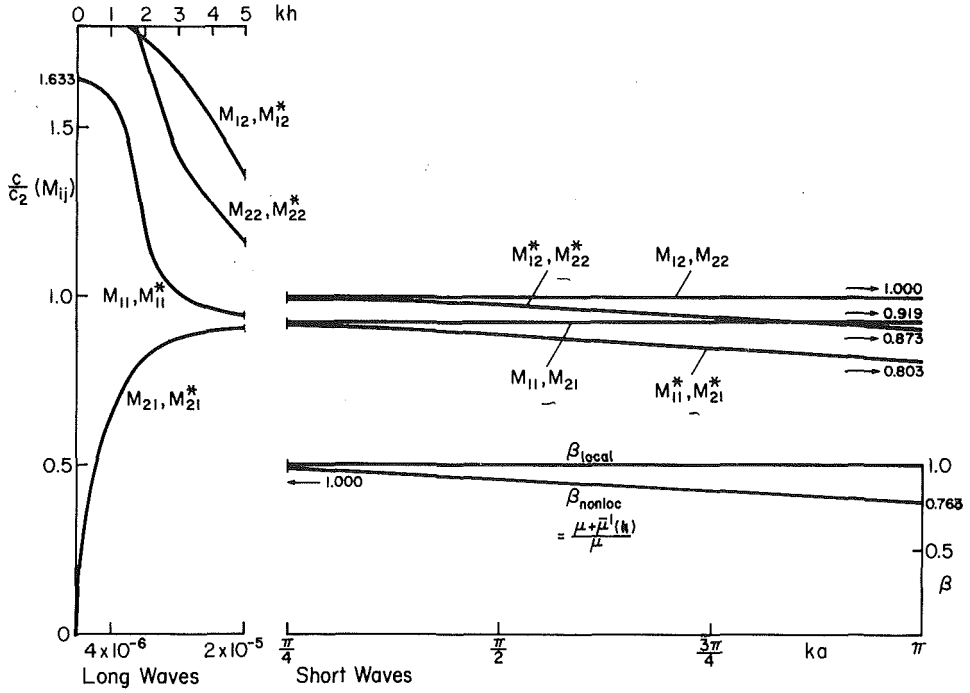


Fig. 1 Relative velocity versus relative wave number for symmetric (M_{11}, M_{12}) and antisymmetric (M_{21}, M_{22}) modes. An asterisk denotes the nonlocal case.

$$\left.\begin{aligned} &\nu_1 = \left(k^2 - \rho\frac{\omega^2}{\Gamma_3}\right)^{1/2}, \qquad \nu_2 = \left(k^2 - \rho\frac{\omega^2}{\Gamma_1}\right)^{1/2}, \\ &\kappa_n = \frac{i\alpha_n(\Gamma_1 - \Gamma_3)}{\alpha^2\Gamma_1 - k^2\Gamma_3 + \rho\omega^2}, \qquad n = 1, 2, \alpha_1 = \nu_1, \ \alpha_2 = \nu_2. \end{aligned}\right\} \tag{2.12}$$

We subsequently find the stress components

$$\left.\begin{aligned} \bar{\tau}_{22} = {} & A\sinh\nu_1 x_2(\Gamma_1 - \Gamma_2)ik + B\cosh\nu_1 x_2(\Gamma_1 - \Gamma_2)ik \\ & + C\sinh\nu_2 x_2\left(\Gamma_1\frac{i\nu_2^2}{k} - ik\Gamma_2\right) + D\cosh\nu_2 x_2 \\ & \cdot\left(\Gamma_1\frac{i\nu_2^2}{k} - ik\Gamma_2\right), \end{aligned}\right\} \tag{2.13}$$

$$\left.\begin{aligned} \bar{\tau}_{12} = {} & \Gamma_3\left[A\cosh\nu_1 x_2\left(\nu_1 + \frac{k^2}{\nu_1}\right) + B\sinh\nu_1 x_2\left(\nu_1 + \frac{k^2}{\nu_1}\right)\right. \\ & \left. + C\cosh\nu_2 x_2 \cdot 2\nu_2 + D\sinh\nu_2 x_2 \cdot 2\nu_2\right], \end{aligned}\right\} \tag{2.14}$$

and assume that the faces of the plate are free from external tractions. This leads to four boundary conditions,

$$\bar{\tau}_{22}\Big|_{z=\pm h} = 0, \quad \bar{\tau}_{12}\Big|_{z=\pm h} = 0, \tag{2.15}$$

from which it is not difficult to arrive at the following frequency equations generalizing the classical, local, *Rayleigh-Lamb* equations[6]:

for the symmetric wave mode M_1,

$$\frac{\tanh\nu_1 h}{\tanh\nu_2 h} = \frac{4\nu_1\nu_2 k^2}{(\nu_1^2 + k^2)^2}; \tag{2.16a}$$

or the antisymmetric wave mode M_2,

$$\frac{\tanh\nu_1 h}{\tanh\nu_2 h} = \frac{(\nu_1^2 + k^2)^2}{4\nu_1\nu_2 k^2}. \tag{2.16b}$$

Just as in the local theory, the preceding equations reveal dispersive character of the wave propagation in plates. In contrast to the local theory, however, the dispersion is both of the configurational and of the physical type.

A general discussion of either of the transcendental equations (2.16) presents considerable difficulties even in the classical case.[7] In the nonlocal case, it is even more complicated because of the dependence of the moduli on the wave number. To obtain tangible results one has to appeal to a numerical procedure using a high-potency computer. This is done in Section 3, which follows. First let us examine the following limiting cases.

Symmetric Mode. In the *long-wave* approximation, the wave number is small ($\Lambda = 2\pi/k$), and for $c = \omega/k$ finite and ρ/Γ_3 small there is $\nu_i \approx k$, $i = 1,2$. Since in this case $\tanh x \approx x$, we find from (2.16*a*) that

$$c^2 = 4(c_2^*)^4\left(\frac{1}{(c_2^*)^2} - \frac{1}{(c_1^*)^2}\right). \tag{2.17}$$

However, as seen from Fig. 1, for k tending to zero, the nonlocal modulus $\bar{\mu}'(k)$ tends to zero, so that in the limiting case the nonlocal long-wave velocity coincides with that provided by the classical theory.[8]

In the case of *short waves*, the wave parameter becomes

[6] Compare, e.g., [15], p. 560.

[7] According to the observation of Mindlin, equations (2.16) are "deceivingly simple in appearance."

[8] Compare, e.g., [15], equation (7.9.12). This sui generis "correspondence principle" seems to be a counterpart in the nonlocal theory of the well-known Bohr's correspondence principle in quantum mechanics.

Downloaded 02 May 2010 to 171.66.16.25. Redistribution subject to ASME license or copyright; see http://www.asme.org/terms/Terms_Use.cfm

large, and so are the parameters ν_i, $i = 1,2$. We than have $\tanh x \approx 1$, and equation (2.16a) reduces to

$$\left(2-\frac{c^2}{(c_2^*)^2}\right)^4 - 16\left(1-\frac{c^2}{(c_1^*)^2}\right)\left(1-\frac{c^2}{(c_2^*)^2}\right)=0. \qquad (2.18)$$

The just written equation turns out to be the dispersion equation associated with the Rayleigh wave; it was derived directly in [16] for the nonlocal medium. For the generalized Poisson material, i.e., for $\lambda = \mu$, and $\bar{\lambda}' = \bar{\mu}'$, it is found that the speed of the Rayleigh waves in the nonlocal continuum equals 0.873 of the speed of these waves in the classical case.

Antisymmetric Mode. The analysis of the long and short-wave limits in the antisymmetric mode is essentially the same as in the symmetric mode. It seems, therefore, that there is no need to repeat the argument, and instead to give Table 1 listing wave speeds.

With regard to the data in the following table, this writer was unable to conclusively[9] establish whether the short-wave speed in plates obtained from the nonlocal theory agrees better (or less) with the experimental evidence than the speed obtained in the classical theory. Some indirect conclusions may be drawn from the fact that (as seen from the table) the short-wave speed in plates coincides with the speed of Rayleigh waves. So far as the latter is concerned, Eringen [16] found a close agreement between the nonlocal theory and the theory of lattice dynamics, in which the dispersion equations obtained agree very well with the data of experiments.[10] Final conclusions in this matter must, of course, be left to further studies. Whatever the outcome, an analysis of the nonlocal wave propagation in plates should contribute to a better understanding of the phenomena that are of such a considerable importance in several areas of research such as performance of structures under high rates of loading, geophysics, earthquake predictions, prospective techniques, and nuclear detection.

3 Illustrative Example

To arrive at some more specific results, let us examine a plate of thickness[11] $2h = 2.10^{-2}$ cm made of aluminum for which $a \approx 4.10^{-8}$ cm. The results of the solution to equations (2.16) are displayed in Fig. 1 for the first two of the symmetric (M_{11}, M_{12}) and the first two of the antisymmetric (M_{21}, M_{22}) modes, the asterisks referring to the corresponding modes as predicted by the nonlocal theory. Inasmuch as in the long-wave range the values of the phase velocities decrease rapidly to their short-wave (and close to their asymptotic) values, it was necessary to depict the short and long-wave curves using two different scales. However, Fig. 1 encompasses the entire positive part of Brillouin zone,[12] $0 \le ka \le \pi$. The long-wave portions of the curves M_{11}, M_{12}, M_{21}, and M_{22} coincide, as they should, with the corresponding curves displayed in [40],[13] and there is no appreciable difference between the starred and unstarred modes in this wave range. Likewise, indistinguishible from each other (in the scale of Fig. 1) are the modes of the pairs M_{11} M_{21}, M_{11}^* M_{21}^*, M_{12} M_{22}, and M_{12}^* M_{22}^*. The greatest difference between the wave velocities in the local and nonlocal case occurs at the limit $ka = \pi$ for the modes M_{12} and M_{12}^* as well as M_{22} and M_{22}^*, and amounts to about 13 percent.

[9] It is possible that the search was not extensive enough.

[10] Compare, e.g., [17], pp. 238 a. 243, and [18], pp. 301 a. 302.

[11] This is close to the plate thickness used in the experiments by Press and Oliver [44].

[12] As noted, one of the features of the first Brillouin zone is that it removes the ambiquity in wave length associated with the given frequency. The minimum wave length is, of course, set equal to two atomic spacings.

[13] The long-wave curves are displayed in [40] for the range limited to $0 \le ha \le 8$.

Table 1 Wave speed $c = \omega/k$ for the Poisson material

Mode	Wave length	Continuum theory	Nonlocal theory
Symmetric	Long	$\sqrt{8/3}\,c_2$	$\sqrt{8/3}\,c_2\left(1+\frac{\bar{\mu}'}{\mu}\right)^{1/2}$ for $\frac{\bar{\mu}'}{\mu}\to 0$
	Short	$0.9194\,c_2$	$0.9194\,c_2\left(1+\frac{\bar{\mu}'}{\mu}\right)^{1/2}$ for $\frac{\bar{\mu}'}{\mu}\to -0.235$
Antisymmetric	Long	$\frac{2}{3}\sqrt{2}kh\,c_2$	$\frac{2}{3}\sqrt{2}khc_2\left(1+\frac{\bar{\mu}'}{\mu}\right)^{1/2}$ for $\frac{\bar{\mu}'}{\mu}\to 0$
	Short	$0.9194\,c_2$	$0.9194\,c_2\left(1+\frac{\bar{\mu}'}{\mu}\right)^{1/2}$ for $\frac{\mu'}{\mu}\to -0.235$

References

1 Eringen, A. C., "Nonlocal Polar Field Theories," *Continuum Physics*, Vol. 4, Eringen, A. C., ed., Academic Press, New York, 1976, pp. 205-267.

2 Green, A. E., and Rivlin, R. S., "Multipolar Continuum Mechanics: Functional Theory I," *Proceedings of the Royal Society*, London, Series *A*, Vol. 284, 1965, p. 303.

3 Kroener, E., "Continuum Mechanics and Range of Atomic Cohesion Forces," *Proceedings, International Conference on Fracture*, Vol. 1, Japanese Society for Fracture of Materials, Sendai, 1966.

4 Eringen, A. C., "A Unified Theory of Thermo-Mechanical Materials," *International Journal of Engineering Science*, Vol. 4, 1966, pp. 179-202.

5 Edelen, D. G. B., "Protoelastic Bodies With Large Deformations," *Archive for Rational Mechanics and Analysis*, Vol. 34, 1969, p. 283.

6 Vaisman, A. M., and Kunin, I. A., "Boundary Value Problems in Nonlocal Theory of Elasticity" (in Russian), *Journal of Applied Mathematics and Mechanics*, Vol. 33, 1969, pp. 784-796.

7 Eringen, A. C., and Kim, B. S., "On the Problem of Crack in Non-Local Elasticity," *Continuum Mechanics Aspects of Geodynamics and Rock Fracture Mechanics*, Thoft-Christensen, P., ed., D. Reider, Dordrecht, Holland, 1974, pp. 107-113.

8 Eringen, A. C., and Kim, B. S., "Relation Between Non-Local Elasticity and Lattice Dynamics," *Crystal Lattice Defects*, Vol. 7, 1977, pp. 51-57.

9 Eringen, A. C., "Continuum Mechanics at the Atomic Scale," *Crystal Lattice Defects*, Vol. 7, 1977, pp. 109-130.

Downloaded 02 May 2010 to 171.66.16.25. Redistribution subject to ASME license or copyright; see http://www.asme.org/terms/Terms_Use.cfm

10 Eringen, A. C., "Linear Theory of Non-Local Elasticity and Dispersion of Plane Waves," *International Journal of Engineering Science*, Vol. 10, 1972, pp. 425-435.

11 Nowinski, J. L., "On the Nonlocal Aspects of the Propagation of Love Waves," *International Journal of Engineering Science*, 1983, in press.

12 Edelen, D. G. B., "Nonlocal Field Theories," *Continuum Physics*, Vol. 4, Eringen, A. C., ed., Academic Press, New York, 1976, pp. 75-204.

13 Sneddon, I. N., *Fourier Transforms*, McGraw-Hill, New York, 1951.

14 Kittel, C., *Introduction to Solid Physics*, Wiley, New York, 1975.

15 Eringen, A. C., and Suhubi, E. S., *Elastodynamics*, Vol. 1a.2, Academic Press, New York, 1975.

16 Eringen, A. C., "On Rayleigh Surface Waves With Small Wave Lengths," *Letters in Applied and Engineering Sciences*, Vol. 1, 1973, pp. 11-17.

17 Maradudin, A. A., et al., *Theory of Lattice Dynamics in the Harmonic Approximation*, Academic Press, New York, 1971.

18 Krumhansl, J. A., "Some Considerations of the Relation Between Solid State Physics and Generalized Continuum Mechanics," *Proceedings of the IUTAM Symposium on the Generalized Cosserat Continuum and the Continuum Theory of Dislocations With Applications*, Kroener, E., ed., Springer-Verlag, New York, 1968, pp. 298-311.

19 Eringen, A. C., "Theory of Nonlocal Electromagnetic Elastic Solid," *Journal of Mathematics and Physics*, Vol. 14, 1973, pp. 733-740.

20 Eringen, A. C., "On Nonlocal Plasticity," *International Journal of Engineering Science*, Vol. 19, 1981, pp. 1461-1474.

21 Eringen, A. C., and Edelen, D. G. B., "On Nonlocal Elasticity," *International Journal of Engineering Science*, Vol. 10, pp. 233-248.

22 Edelen, D. G. B., Green, A. E., and Laws, N., "Nonlocal Continuum Mechanics," *Archive for Rational Mechanics and Analysis*, Vol. 43, 1971, pp. 36-44.

23 Kroener, E., "Continuum Theory of Dislocations and Self-Stresses" (in German), *Ergebnisse der Angewandten Mathematik*, Vol. 51, Springer, Berlin, 1958.

24 Kroener, E., and Datta, B. K., "Nonlocal Elastostatic: Derivation from the Lattice Theory" (in German), *Zeitschrift fuer Physik*, Vol. 196, 1966, pp. 203-211.

25 Kroener, E., "Elasticity Theory With Long Range Cohesive Forces," *International Journal of Solids and Structures*, Vol. 3, 1967, pp. 731-742.

26*a* Kunin, I. A., "Nonhomogeneous Elastic Medium With Nonlocal Interactions" (in Russian), *Prikladnaya Mekhanika i Tekhnicheskaya Fizika*, No. 3, 1967, pp. 60-66.

26*b* Kunin, I. A., "Theories of Elastic Media With Microstructure," *Proceedings of Vibration Problems*, Vol. 9, 1968, pp. 323-336.

26*c* Kunin, I. A., and Weisman, A. M., "On Problems of the Non-Local Theory of Elasticity," *Conference Proceeedings*, Vol. 2, Nat. Bur. Stand., Washington, D.C., 1970, pp. 747-759.

26*d* Kunin, I. A., "Model of an Elastic Medium of Simple Structure With a Spatial Dispersion" (in Russian), *Prikladnaya Matematika i Mekhanika*, Vol. 30, 1966, pp. 542-550.

27 Kunin, I. A., *Theory of Elastic Media With Microstructure* (in Russian), Nauka, Moscow, 1975.

28 Kunin, I. A., *Elastic Media With Microstructure*, Vols. 1 and 2, Springer, Berlin, 1982 and 1983.

29 Lamb, H., "On Waves in an Elastic Plate," *Proceedings of the Royal Society*, London, Series *A*, Vol. 93, 1917, pp. 114-128.

30 Miklowitz, J., "Elastic Wave Propagation," in *Applied Mechanics Surveys*, Abramson, H. N., Liebowitz, H., Crowley, J. M., and Juhasz, S., eds., Spartan Books, Washington, D.C., 1966, pp. 809-839.

31 Pfeiffer, F., "Elastokinetik," *Handbuch der Physik*, Vol. 6, Springer, Berlin, 1928.

32 Schoch, A., "Schallreflexion, Schallbrechung und Schallbeugung," *Ergebnisse der Exacten Naturwissenschaften*, Vol. 23, 1950, pp. 127-234.

33 Davies, R. M., "Stress Waves in Solids," *Applied Mechanics Review*, Vol. 6, 1953, pp. 1-3.

34 Mindlin, R. D., "An Introduction to the Mathematical Theory of Vibrations of Elastic Plates," U.S. Army Signal Corps Eng. Labs., Fort Monmouth, N.J., Contract DA-36-039, Sc. 56772, 1955.

35 Mindlin, R. D., "Waves and Vibrations in Isotropic, Elastic Plates," *Structural Mechanics Proceedings, First Symposium on Naval Structural Mechanics*, Pergamon, New York, 1960, pp. 199-232.

36 Mecker, T. R., and Meitzler, A. H., "Guided Wave Propagation in Elongated Cylinders and Plates," *Physical Acoustics*, Mason, W. P., ed., Vol. 1, Part A, Academic Press, New York, 1964, pp. 111-167.

37 Agarwal, R. R., and Shaw, "Axially Symmetric Vibrations of a Finite Isotropic Disk," *Journal of the Acoustical Society of America*, Vol. 26, 1954, pp. 259-265.

38 Mindlin, R. D., and Onoe, M., "Mathematical Theory of Vibrations of Elastic Plates," *Proceedings, Annual Symposium on Frequency Control*, 11th U.S. Army Signal Corps Eng. Labs., Fort Monmouth, N.J., 1957, pp. 17-40.

39 Sherwood, J. W. C., "Propagation in an Infinite Elastic Plate," *Journal of the Acoustical Society of America*, Vol. 30, 1958, pp. 979-984.

40 Tolstoy, L., and Usdin, E., "Dispersive Properties of Stratified Elastic and Liquid Media," *Geophysics*, Vol. 18, pp. 844-870.

41 Ewing, W. M., Jardetzky, W. S., and Press, E., *Elastic Waves on Layered Media*, McGraw-Hill, New York, 1957.

42 Gogoladze, V. G., "Dispersion of Rayleigh Waves in a Layer" (in Russian), *Publications of the Seismological Institute, Academy of Sciences of URSS*, Vol. 119, 1947, pp. 27-38.

43 Eringen, A. C., "Nonlocal Elasticity and Waves," *Continuum Mechanics Aspects of Geodynamics and Rock Fracture Mechanics*, Thoft-Christensen, P., ed., D. Reider, Dordrecht, Holland, 1974, pp. 81-105.

44 Press, F., and Oliver, J., "Model Study of Air-Coupled Flexural Waves," *Journal of the Acoustical Society of America*, Vol. 27, 1955, pp. 43-46.

Downloaded 02 May 2010 to 171.66.16.25. Redistribution subject to ASME license or copyright; see http://www.asme.org/terms/Terms_Use.cfm

Finite Element Eigenfunction Method (FEEM) for Elastic Wave Scattering by Arbitrary Three-Dimensional Axisymmetric Scatterers

J. H. Su[1]
Graduate Student.

V. V. Varadan[2]
Associate Professor.

V. K. Varadan[2]
Associate Professor.
Mem. ASME

Wave Propagation Group,
Department of Engineering Mechanics,
The Ohio State University,
Columbus, Ohio 43210

A finite element eigenfunction method (FEEM) is formulated for elastic wave scattering by bounded three-dimensional axisymmetric regions (cavity, homogeneous, or inhomogeneous) for harmonic waves incident at arbitrary angles. The solutions are hence three-dimensional and no longer axisymmetric. The scattering region is enclosed within a sphere. The scattered field outside the sphere is expanded in outgoing vector spherical functions. Within the sphere, basis-functions are generated by a finite element technique applying the vector spherical harmonics as boundary conditions. The field inside the sphere is then written as a superposition of these basis functions with unknown coefficients which are then solved by matching with the exterior field. Numerical results are obtained for a variety of scatterers and comparisons made with available results.

Introduction

In the last 10 years several numerical methods have been developed for the solution of elastic wave scattering problems which find application in diverse fields such as Ultrasonic Nondestructive Evaluation (NDE) of flaws in structural parts, sonar and underwater acoustics, geophysics, medical uses of ultrasound for diagnostic purposes, etc. The main aim of these methods has been an attempt to solve scattering problems involving arbitrary shaped obstacles, layered obstacles, multiple obstacles, etc., with or without the presence of nearby boundaries for a wide range of frequencies and scattering geometries. Some of the methods which are currently in use for elastic wave problems are the T-matrix or null field method, boundary integral method, and hybrid finite element method. Of these, the T-matrix method has been applied to the widest class of problems. All of these methods encounter difficulty when truly arbitrary or complex geometries are involved and they are all inapplicable to problems involving material inhomogeneity. Some of the methods are not very convenient for the evalutation of near or surface fields.

In this paper a Finite Element Eigenfunction Method (FEEM) has been developed to overcome these difficulties and applied to three-dimensional problems. "Three-dimensional problems" here means an arbitrary axisymmetric geometry and material properties subjected to a general elastic incident wave at an arbitrary angle. In this method of analysis, the scatterer is enclosed within an imaginary sphere. The scattered field outside this sphere can be represented by vector outgoing wave functions that satisfy radiation conditions at infinity. Guided by the solution of the scattered field, the solution inside the sphere is also assumed to be expanded by a series of basis functions that satisfy appropriate conditions at the physical boundary of the scatterer. They are generated through the standard finite element technique by imposing suitable boundary conditions on the sphere. Then the coefficients of the scattered field for a given incident wave and those of the interior field are found by means of a least square fit by imposing continuity conditions across the sphere. The solution obtained thereby is considered complete in the sense that both the scattered and the near fields are solved simultaneously.

Hunt, et al. [1] presented a finite element approach to acoustic scattering from elastic structure in 1974, which was an extension of their earlier work [2]. Essentially, they used the expression given by Zienkiewicz, et al. [3] for a vibrating elastic body immersed in an acoustic medium of finite volume

[1] Presently, Project Engineer, Structural Mechanics Consultants Corporation, Warren, Mich.

[2] Presently at the Department of Engineering Science and Mechanics, The Pennsylvania State University, University Park, Pa. 16802.

Contributed by the Applied Mechanics Division and presented at the 1984 PVP Conference and Exhibition, Joint with Applied Mechanics Division and Materials Division, San Antonio, Texas, June 17-21, 1984 of THE AMERICAN SOCIETY OF MECHANICAL ENGINEERS.

Discussion on this paper should be addressed to the Editorial Department, ASME, United Engineering Center, 345 East 47th Street, New York, N.Y. 10017, and will be accepted until two months after final publication of the paper itself in the JOURNAL OF APPLIED MECHANICS. Manuscript received by ASME Applied Mechanics Division, January, 1983; final revision, October, 1983. Paper No. 84-APM-37.

Copies will be available until February, 1985.

Copyright © 1984 by ASME
Downloaded 02 May 2010 to 171.66.16.25. Redistribution subject to ASME license or copyright; see http://www.asme.org/terms/Terms_Use.cfm

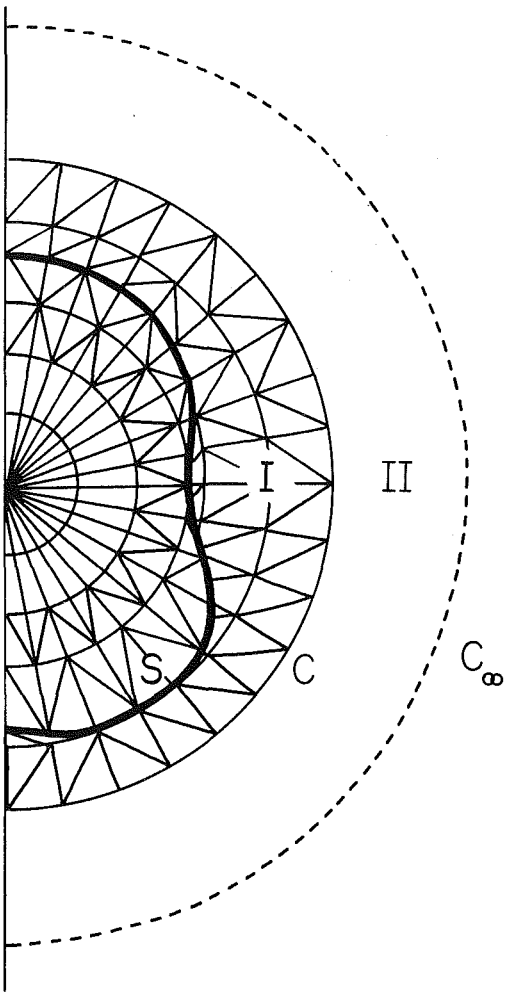


Fig. 1 Rotationally symmetric scatterer with surface S enclosed within a sphere C. C∞ is the surface at infinity on which radiation conditions are satisfied.

and the surface Helmholtz Integral Equation. The numerical results presented in their paper was only for the axisymmetric case, i.e., incidence along the symmetry axis. Mei [4] proposed the "Unimoment Method" for solving antenna and electromagnetic scattering problems in the same year. Afterward, Mei et al. [5-8] applied this method, which makes use of numerical methods such as finite difference and finite element for a finite domain, and coupled these solutions with analytical outgoing wave functions on an imaginary surface, to various electromagnetic wave scattering problems involving inhomogeneous media, two, and three-dimensional geometries. Goetchel [9] adapted a global-local finite element method [GLFEM] to axisymmetric scattering of elastic waves which showed the capability of handling plane waves incident along the axis of rotational symmetry only. More recently, Su, Varadan, and Varadan [10-12] gave a formulation based on reference [5] for *SH*-wave scattering problems.

This method is similar to the eigenfunction expansion method except for the introduction of an imaginary boundary and the basis functions in the interior are obtained by a finite element method. Therefore, this method is named Finite Element Eigenfunction Method (FEEM). Its effectiveness as well as validity are demonstrated by good comparisons with exact analysis and the *T*-matrix method. This new method is exceptionally general. Once a computer program has been written for this method it is easy to handle a great variety of scatterers and boundary conditions. This program can solve, in addition to the complicated geometry of scatterers, rigid obstacles, cavities, inclusions, inhomogeneous inclusions, cavities surrounded by inhomogeneous materials, and a finite number of scatterers in a rotationally symmetric configuration.

FEEM Formulation

A bounded scatterer with surface S (see Fig. 1) is embedded in an infinite, homogeneous, isotropic, and linearly elastic medium. The scatterer is either a void or filled with a different material that is assumed to be perfectly bounded to its host material on S.

The formulation presented is for an axisymmetric bounded region, although the methodology can be applied to any arbitrary three-dimensional bounded region. The material inside this bounded region can be inhomogeneous. A steady monchromatic general elastic wave with frequency ω and time dependence $\exp(-i\omega t)$ is incident on this bounded region at an arbitrary angle of incidence. Since the incident wave has time dependence $\exp(-i\omega t)$, all field quantities will have the same time dependence and in the sequel this time factor is suppressed.

The Finite Element Eigenfunction Method (FEEM) separates this local inhomogeneity from the infinite domain, region *II* by enclosing an imaginary sphere C, around it. Finite Element Approximation (FEA) will be used for the region I inside C. Outside the region of FEA, vector spherical functions are used to expand the incident and scattered fields. These are given by

$$\begin{matrix} Ou \\ Re \end{matrix} \Psi_{1lm\sigma} = \left(\frac{k_p}{k_s}\right)^{1/2} \nabla \left\{ \begin{matrix} h_l(k_p r) \\ j_l(k_p r) \end{matrix} \right\} Y_{lm\sigma}(\theta,\phi) \tag{1}$$

$$\begin{matrix} Ou \\ Re \end{matrix} \Psi_{2lm\sigma} = \frac{1}{k_s} \nabla x \left(\mathbf{r} \left\{ \begin{matrix} h_l(k_s r) \\ j_l(k_s r) \end{matrix} \right\} Y_{lm\sigma}(\theta,\phi) \right) \tag{2}$$

$$\Psi_{3lm\sigma} = \frac{1}{k_s} \nabla \times \psi_{2lm\sigma} \tag{3}$$

where j_l, h_l are the spherical Bessel and Hankel functions, $Y_{lm\sigma}$ are normalized spherical harmonics, k_p and k_s and the P and S- wavenumbers, and r, θ, ϕ are polar coordinates, Ou stands for functions outgoint at infinity, and Re for functions angular at the origin.

The incident field which is usually a plane wave or due to a harmonic point source may be written as

$$\mathbf{U}^i(\mathbf{r}) = \sum_{\tau=1}^{3} \sum_{l=0}^{\infty} \sum_{m=0}^{l} \sum_{\sigma=e}^{o} a_{\tau lm\sigma} Re \Psi_{\tau lm\sigma}(\mathbf{r}) ; \quad \begin{matrix} e \rightarrow \text{even} \\ o \rightarrow \text{odd} \end{matrix} \tag{4}$$

where the coefficients $a_{\tau lm\sigma}$ are assumed to be known.

The scattered field must satisfy radiation conditions at infinity and hence

$$U^s(\mathbf{r}) = \sum_{\tau} \sum_{l} \sum_{m} \sum_{\sigma} f_{\tau lm\sigma} Ou \Psi_{\tau lm\sigma}(\mathbf{r}) \; ; \; \mathbf{r} \in \text{region } II \tag{5}$$

where $f_{\tau lm\sigma}$ are to be determined.

Within C, a finite element approximation is invoked for the description of the displacement field. In a standard FEM procedure, the displacement field is completely described by the values that it assumes at certain nodal points. These nodal values are calculated by the FEM. In our case, C is only a mathematical boundary and hence the nodal value will depend on what displacements are prescribed at C. We observe that the angular behavior of the incident and scattered fields is a superposition of the vector spherical harmonics $\mathbf{A}_{\tau lm\sigma}$. This results from equations (1)-(3) and the definition of $\mathbf{A}_{\tau lm\sigma}$ as

$$\mathbf{A}_{1lm\sigma} = \hat{r}\, Y_{lm\sigma}(\theta,\phi) \tag{6}$$

Downloaded 02 May 2010 to 171.66.16.25. Redistribution subject to ASME license or copyright; see http://www.asme.org/terms/Terms_Use.cfm

$$\mathbf{A}_{2lm\sigma} = \frac{r}{\sqrt{l(l+1)}} \nabla Y_{lm\sigma}(\theta,\phi) \tag{7}$$

and

$$\mathbf{A}_{3lm\sigma} = \hat{r} \times \mathbf{A}_{2lm\sigma}. \tag{8}$$

For three-dimensional problems, these are a convenient series of boundary conditions to impose on C. We remark that for the corresponding two-dimensional *SH*-wave problem, the trignometric functions cos $m\phi$, sin $m\phi$ were the appropriate boundary conditions. Application of one of the vector spherical harmonics, results in a certain response at each nodal point, not the nodal value for the scattering problem in general. However, the response or basis functions resulting from each vector spherical harmonic can be superposed with proper weighting coefficients $\alpha_{\tau lm\sigma}$ to generate what is conventionally called the nodal value of the displacement. Thus at the nodal point *NP*,

$$\mathbf{U}^{NP}(\mathbf{r}_{NP}) = \sum_{\tau} \sum_{lm\sigma} \alpha^{NP}_{\tau lm\sigma} \mathbf{U}^{NP}_{\tau lm\sigma}(\mathbf{r}_{NP}) \tag{9}$$

If the scatterer is rotationally symmetric, we know that cos $m\phi$ and sin $m\phi$ are sufficient to describe the ϕ-dependence of the displacement. It is convenient to use rectangular coordinates in the FEM, hence the index τ in equation (9) refers to the cylindrical components R, ϕ, z and are not the same as in equations (1)–(3). The rotational symmetry results in further simplifications. The azimuthal indices m are uncoupled i.e., a particular m value say $m=5$ in the vector spherical harmonic prescribed on C will make the ϕ-dependence within C, cos 5ϕ or sin 5ϕ. Further, the problem of parallel polarization is uncoupled from that of perpendicular polarization. In other words, if the incident wave is polarized and propagates in a certain plane which may be taken as the x-z plane (no loss of generality), then the expansions in equations (4), (5), and (9) must be qualified by the following conditions

$$\delta_{\tau 1}\delta_{\sigma e}; \delta_{\tau 2}\delta_{\sigma 0}; \delta_{\tau 3}\delta_{\sigma e} \tag{10}$$

This is the problem of parallel polarization. If the incident wave is propagating in the x-z plane but is polarized in the y-direction, then equation (10) changes to

$$\delta_{\tau 1}\sigma_{\sigma 0}; \delta_{\tau 2}\delta_{\sigma e}; \delta_{\tau 3}\delta_{\sigma 0} \tag{11}$$

This is the problem of perpendicular polarization and a simple relationship exists between the two solutions [13]. The physical reason for the foregoing conditions is that if the incident wave is in the x-z plane, then the ϕ components of the scattered field displacement must be antisymmmetric with respect to the x-z plane so that boundary conditions can be satisfied. The bottom line is that in the FEM, 6 degrees of freedom at each nodal point, namely (R, z, ϕ) with an even or odd index attached to each component of the field reduces to three. This simplifies the calculations enormously.

In what follows, we consider the problem of parallel polarization only, since the perpendicular case can also be obtained without additional calculation. Thus in equations (4), (5), and (9) the summation on σ is removed in accordance with equation (10). To proceed with the evaluation of the *three sets of basis functions* at each nodal point namely, $U^{NP}{}_{Rlme}, U^{NP}{}_{\phi lmo}$, and $U^{NP}{}_{zlme}$, we must construct a functional whose first variation is zero everywhere within C. The functional can generally be taken to be the Lagrangian density L such that

$$\delta \int_{V_c} L \, dV_c = 0 \tag{12}$$

Equation (12) will be true if the equation of motion, namely Navier's equation is satisfied, as well as boundary conditions on S and C. We recall that $L = T - V$, the difference between the kinetic and strain energy densities which in turn are quadratic functions of the displacement. Equation (12) will

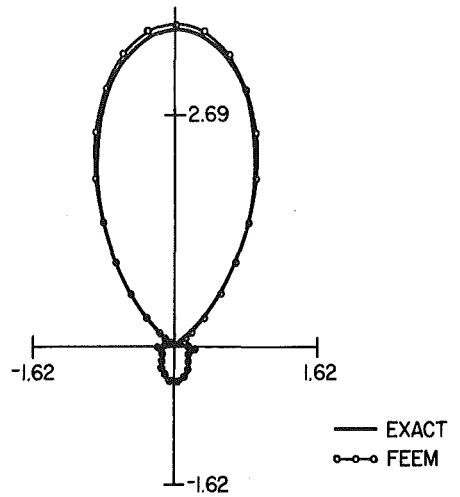


Fig. 2(a) Comparison of FEEM with exact results for the compressional wave scattering cross section of a spherical cavity for an incident plane *P*-wave with $k_p a = 3.0$ at $\theta_0 = 0$ deg

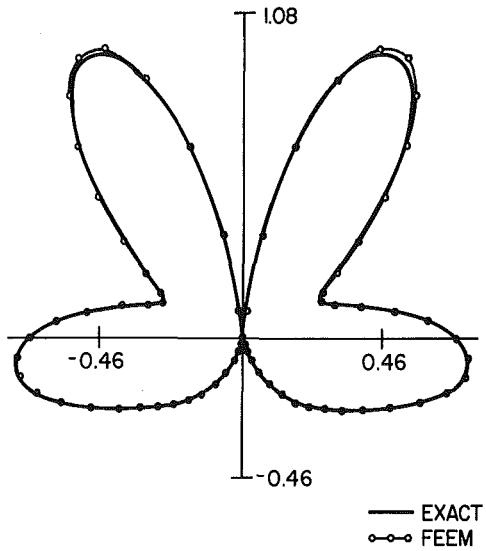


Fig. 2(b) Comparison of FEEM with exact results for the shear wave scattering cross section of a spherical cavity for an incident plane *P*-wave with $k_p a = 3.0$ at $\theta_0 = 0$ deg

Fig. 2

then result in a set of linear algebraic equations for the basis functions $\mathbf{U}^{NP}_{\tau lm\sigma}$ which may be solved by standard methods. The exact form of the functional itself and the resulting "stiffness matrix" are very lengthy and are included in Appendix A. The interested reader is referred to reference [12].

The solution to the problem is still not complete. At this point we only know the basis functions at each nodal point within C. To complete the solution we must determine the coefficients $\alpha_{\tau lm\sigma}$ within C and $f_{\tau lm\sigma}$ of the scattered field. This can be done by demanding continuity of the field and its partial derivatives across C. The partial derivatives with respect to θ and ϕ are automatically satisfied by the manner in which the basis functions were generated. Hence the continuity conditions reduce to

$$\mathbf{U}_I(\mathbf{r}) = \mathbf{U}_{II}(\mathbf{r}); \; \mathbf{r} \epsilon C \tag{13}$$

$$\frac{\partial \mathbf{U}_I}{\partial r}\bigg|_{\mathbf{r}\epsilon C} = \frac{\partial \mathbf{U}_{II}}{\partial r}\bigg|_{\mathbf{r}\epsilon C} \tag{14}$$

Downloaded 02 May 2010 to 171.66.16.25. Redistribution subject to ASME license or copyright; see http://www.asme.org/terms/Terms_Use.cfm

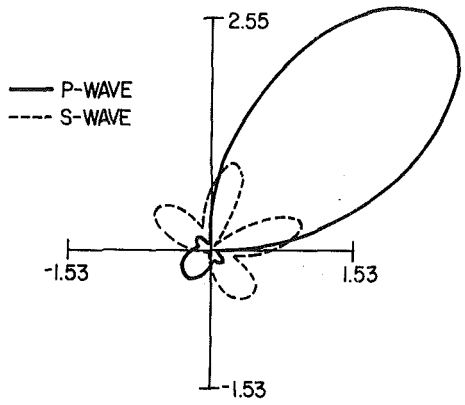


Fig. 3 Polar plot of the scattering cross sections of a spherical cavity for an incident plane *P*-wave with $k_p a = 3.0$ at $\theta_0 = 45$ deg using FEEM

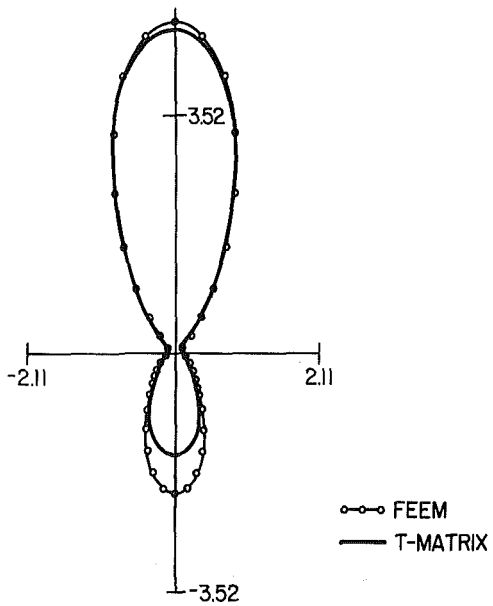


Fig. 4 Polar plot of the compressional wave scattering cross section of an oblate cavity for an incident plane *P*-wave with $k_p a = 4.0$ at $\theta_0 = 0$ deg

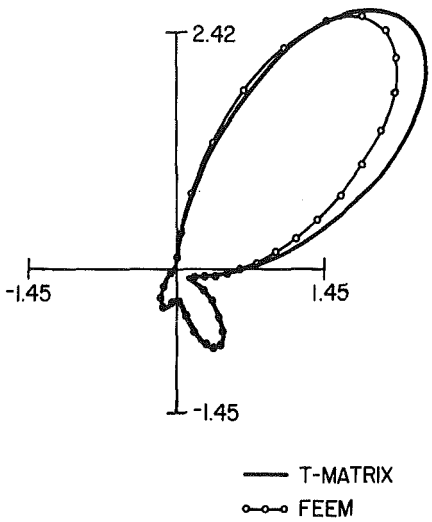


Fig. 5 Polar plot of the compressional wave scattering cross section of an oblate cavity for an incident plane *P*-wave with $k_p a = 4.0$ at $\theta_0 = 45$ deg

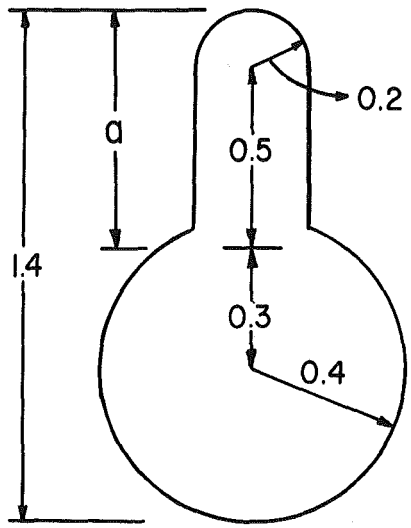


Fig. 6(*a*)



Fig. 6(*b*)

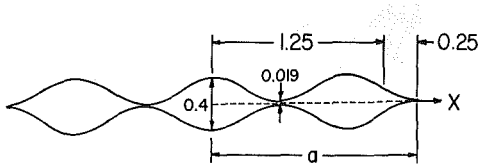


Fig. 6(*c*)

Fig. 6 Geometry of three flaw shapes relevant to NDE applications (all voids)

To conveniently apply equations (13) and (14), the cylindrical coordinates used to express U_I are first transformed to spherical coordinates. Then equations (13) and (14) are enforced at the nodal points on C. Depending on the truncation size $NTOT$ used for the expansion of $U_{II} = U^i + U^s$ and U_I, the number of nodal points on C, $NC \geq NTOT$ for each azimuthal index. If $NC > NTOT$, then the resulting system of equations can be solved by a least squares method. The value $NTOT$ is determined by trial to insure convergence. In any event, solution of the system of coupled equations (13) and (14) will yield the coefficients $\alpha_{\tau lm\sigma}$ of U_I and $f_{\tau lm\sigma}$ of U^s. The solution is now complete in the sense that we have determined the displacement field at all nodal points within, on, and outside C.

The amplitude of the scattered displacement field, equation [5], at distances far from the scatterer is obtained using the asymptotic forms of the basis functions, equations (1)–(3) as in [15]

$$U^s(\mathbf{r}) \underset{kr\to\infty}{\to} \hat{r}\, f_p(\theta,\phi)\exp(ik_p r)/r + [\hat{\theta} f_{s1}(\theta,\phi) + \hat{\phi} f_{s2}(\theta,\phi)]\exp(ik_s r)/r. \quad (15)$$

where

$$f_p(\theta,\phi) = \left(\frac{k_p}{k_s}\right)^{1/2} \sum_{m=0}^{\infty} \sum_{l=m}^{\infty} \xi_{lm} i^{-l} P_l^m(\cos\theta) f_{1lm} \cos m\phi \quad (16a)$$

Downloaded 02 May 2010 to 171.66.16.25. Redistribution subject to ASME license or copyright; see http://www.asme.org/terms/Terms_Use.cfm

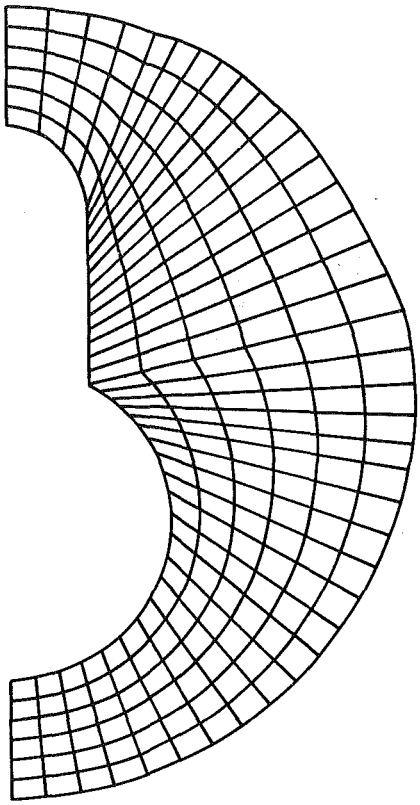


Fig. 7(a) Finite element mesh for flaw shape in Fig. 6(a)

$$f_{s1}(\theta,\phi)=\sum_{m=0}^{\infty}\sum_{l=m}^{\infty}\xi_{lm}[l(l+1)]^{-1/2}i^{-l}\times$$

$$\left[-im\frac{P_l^m}{\sin\theta}(\cos\theta)f_{2lm}\sin m\phi+\frac{d}{d\theta}P_l^m(\cos\theta)f_{3lm}\cos m\phi\right] \quad (16b)$$

$$f_{s2}(\theta,\phi)=\sum_{m=0}^{\infty}\sum_{l=m}^{\infty}\xi_{lm}[l(l+1)]^{-1/2}i^{-l}\times$$

$$\left[i\frac{d}{d\theta}P_l^m(\cos\theta)f_{2lm}\cos m\phi+\frac{mP_l^m(\cos\theta)}{\sin\theta}f_{3lm}\sin m\phi\right] \quad (16c)$$

The differential scattering cross section, which is proportional to the rate at which energy is scattered into a small solid angle in the direction defined by the angle (θ,ϕ), is given by

$$\sigma^{p}=|f_p(\theta,\phi)|^2$$
$$\sigma^{s1}=|f_{s1}(\theta,\phi)|^2 \quad (17b)$$

and

$$\sigma^{s2}=|f_{s2}(\theta,\phi)|^2 \quad (17c)$$

An incident plane P- wave propagating at an angle θ_0 in the x-z plane is considered. The coefficients $a_{\tau lm\sigma}$ of equation (4) take the form

$$a_{\tau lm\sigma}=\frac{4\pi}{k_p}\left(\frac{k_s}{k_p}\right)^{1/2}\xi_{lm}i^{l-1}P^m_{l(\cos\theta_0)}\delta_{\tau 1}\delta_{\sigma e} \quad (18)$$

where in equations (16)–(18)

$$\epsilon_{lm}=\sqrt{\epsilon_m\frac{(2l+1)}{4\pi}\frac{(l-m)!}{(l+m)!}}$$

and ϵ_m is the Neumann factor $\epsilon_0=1$, $\epsilon_m=2$, $m>0$.

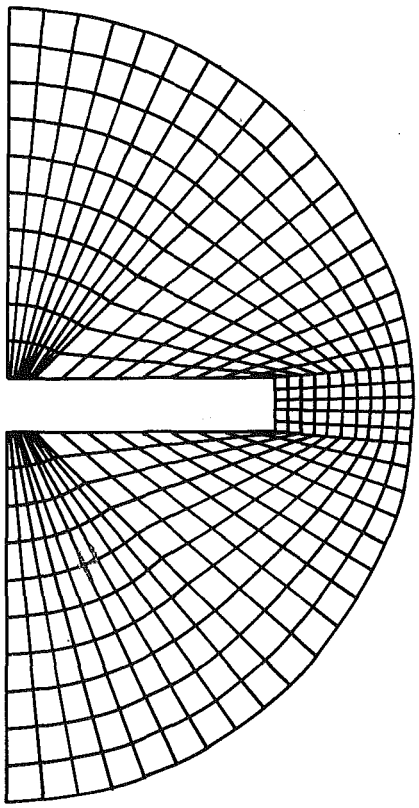


Fig. 7(b) Finite element mesh for flaw shape in Fig. 6(b)

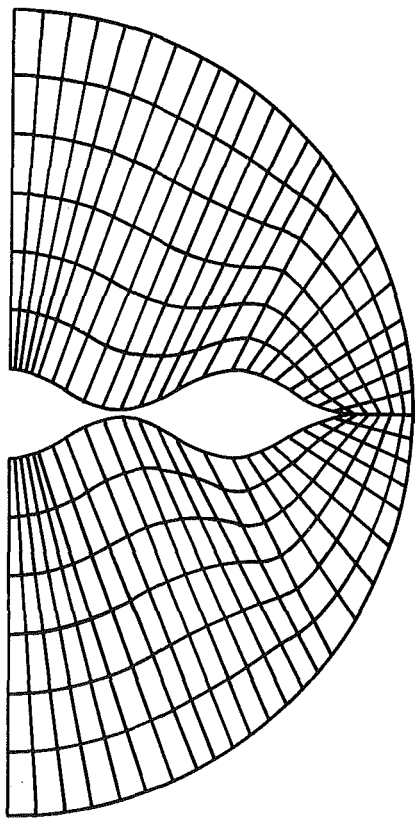


Fig. 7(c) Finite element mesh used for flaw shape in Fig. 7(c)

Fig. 7

Downloaded 02 May 2010 to 171.66.16.25. Redistribution subject to ASME license or copyright; see http://www.asme.org/terms/Terms_Use.cfm

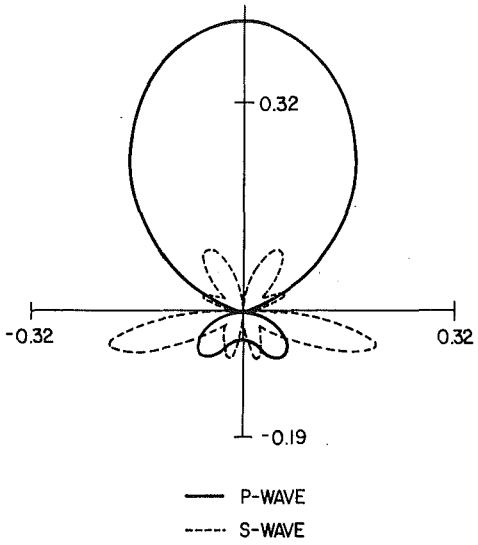


Fig. 8 Polar plot of the scattering cross sections of flaw in Fig. 6(*a*) for an incident plane *P*-wave with $k_p a = 3.0$ at $\theta_0 = 0$ deg

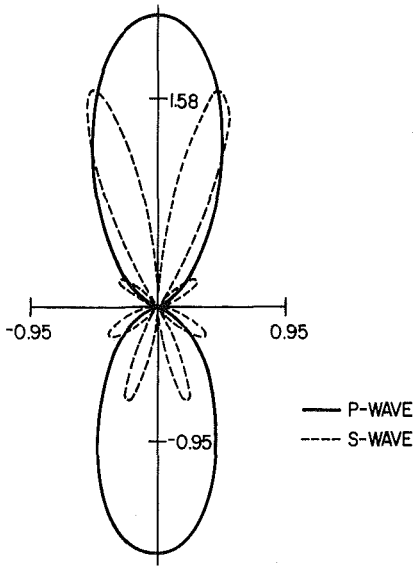


Fig. 9 Polar plot of the scattering cross sections of flaw in Fig. 6(*b*) for an incident plane *P*-wave with $k_p a = 3.0$ at $\theta_0 = 0$ deg

Numerical Results

The formulation presented here has been implemented in a Fortran program. No commercial finite element codes were used. This has resulted in an efficient compact code that is customized for scattering problems. The program is quite general and it can handle a variety of different geometries, boundary conditions, etc., without extensive modification.

Quadrilateral elements [4] were used for all computations. The purpose of presenting calculations is to verify the method and computer code by comparing with available results for simple shapes and also presenting results for complex shapes that cannot be handled by existing methods. The computations were performed on an AMDAHL 470 computer and a typical computation time for one frequency say $k_p a = 3.0$, 72 elements, 111 nodal points, and several angles of observation was 60 sec. The time involved is more if the number of elements is increased. The accuracy of the computation for a given truncation size and number of elements is very much machine-dependent, since double precision on an IBM System is roughly equal to only single precision on a CDC System.

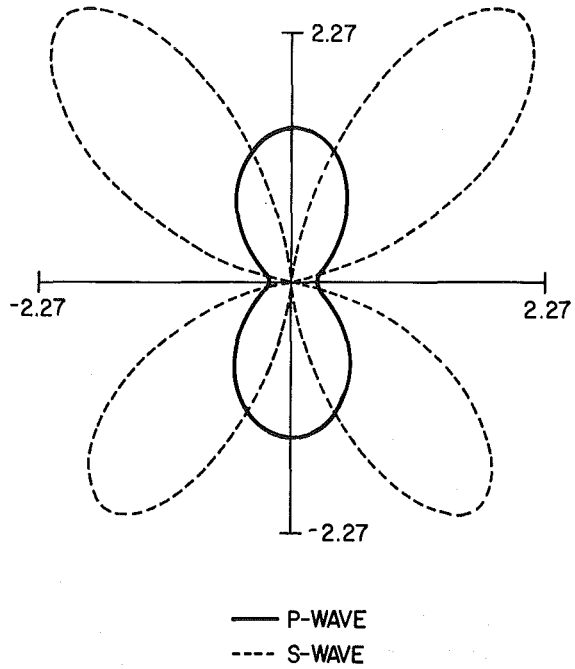


Fig. 10 Polar plot of the scattering cross sections of the flaw in Fig. 6(c) for an incident plane *P*-wave with $k_p a = 1.0$ at $\theta_0 = 0$ deg

The cost of the computation is very much dependent on the changing algorithm. At the Ohio State University, where the computations were performed, 60 sec of cpu time during peak hours costs roughly $10. The computations were limited basically by the limits of the system and finances. Memory requirements never exceeded 2 megabytes for the computations shown here. No particular difficulties were encountered at frequencies close to an eigenfrequency of the scatterer but this may be fortuitous and further studies are needed in this regard.

The calculations were carried out for the plane $\phi = 0$ and π only. The host medium is chosen to be Titanium (Ti) with longitudinal and shear wave speeds given by $c_p = 6340$ m/s and $c_s = 3030$ m/s. Let $k_p a$ be the nondimensional compressional wavenumber and a the maximum radius of the scatterer.

A polar plot of the differential scattering cross section for a spherical cavity is compared for $k_p a = 3.0$ and incident angles equal to 0 deg and 45 deg with the exact solutions [16] and is shown in Figs. 2(*a*), 2(*b*), and 3. Figure 3 is simply a rotation of Figs. 2(*a*) and 2(*b*) by 45 deg since a sphere "looks" the same in all directions. Thus the numerical computation for obliquely incident waves on a rotationally symmetric scatterer is shown to be correct. In these calculations 72 elements and 111 nodal points were used and both the incident and the scattered field expansions were truncated at $l = 10$ and $m = 0$ for 0 deg incidence and $m = 7$ for 45 deg incidence. Coefficients $a_{\tau lm\sigma}$ and $f_{\tau lm\sigma}$ decrease rapidly as the indices l and m increase resulting in rapid convergence.

In Figs. 4 and 5, polar plots are presented for $P \rightarrow P$ scattering from an oblate spheroidal void for both normal (θ deg = 0 deg) and oblique (θ deg = 45) incidence. The FEEM results show good agreement with *T*-matrix results [15].

To demonstrate the generality of this formulation some additional complex shapes were considered. Three practical models of flaws for NDE applications are shown in Figs. 6(*a*), 6(*b*), and 6(*c*), respectively. Figs. 7(*a*), 7(*b*), and 7(*c*) show the meshes used in the computation. Polar plots of differential scattering cross sections are presented in Figs. 8 and 9 for flaws shown in Figs. 6(*a*) and 6(*b*), respectively, when a plane

Downloaded 02 May 2010 to 171.66.16.25. Redistribution subject to ASME license or copyright; see http://www.asme.org/terms/Terms_Use.cfm

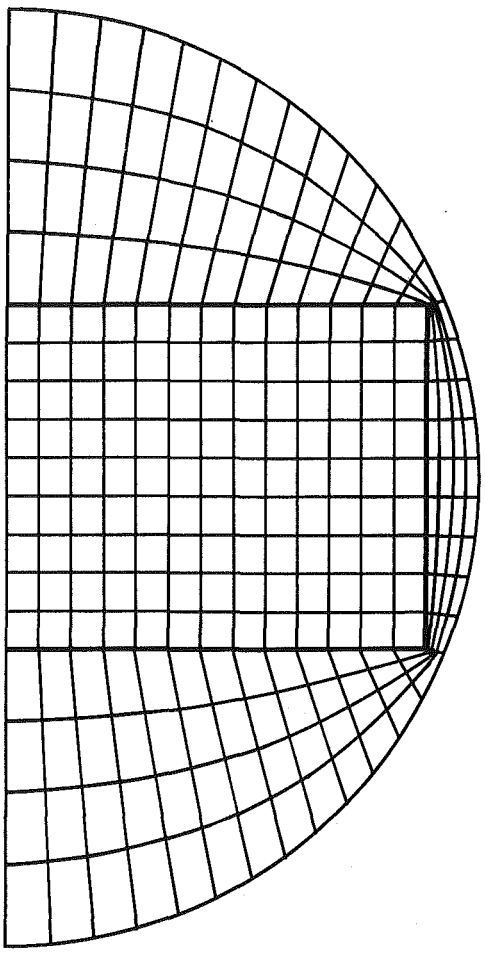


Fig. 11 Mesh for a finite right circular cylindrical inclusion with height/diameter = 0.4216

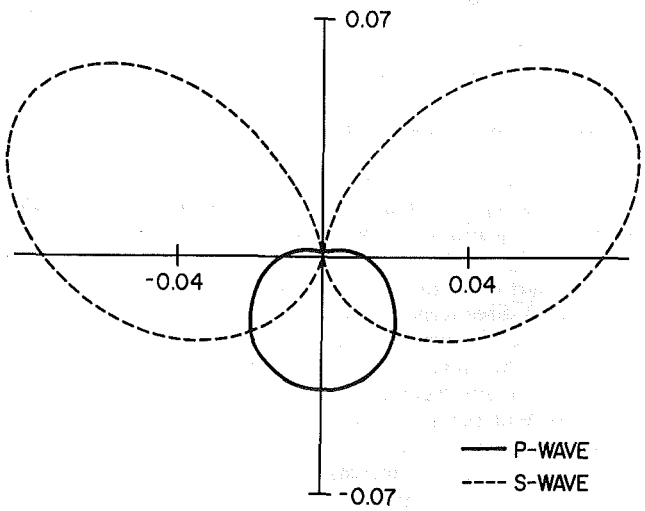


Fig. 12 Polar plot of the scattering cross sections of the right circular cylinder (WC) in Ti for an incident plane P-wave with $k_p a = 1.0$ at $\theta_0 = 0$ deg

P-wave with $k_p a = 3.0$ is incident at 0 deg. For the flaw shown in Fig. 6(*c*) the polar plot of differential scattering cross section is presented in Fig. 10 for a plane *P*-wave incident at 0 deg with $k_p a = 1.0$.

In Fig. 11 the mesh used for a right circular cylindrical inclusion with aspect ratio, height/diameter = 0.4216 is shown. The inclusion material was Tungsten Carbide (WC), $c_p = 6660$ m/s, and $c_s = 3980$ m/s and density $\rho = 13.8$ gm/cc. The host material was Titanium. In Fig. 12, a polar plot of the differential scattering cross section is shown for *P*-waves incident along the rotational axis of symmetry for $k_P a = 1.0$. The truncation size for this calculation was $l = 11$ and 276 elements were needed for convergence.

Conclusions

In this paper we have presented a finite element eigenfunction method (FEEM) for the solution of elastic wave scattering problems involving scatterers of truly arbitrary shape, oblique angle of incidence, and wavelengths comparable to scatterer size. For both spherical and nonspherical geometries, good agreement is obtained with existing results. This method is very general and has unlimited application for problems of practical interest.

Acknowledgment

Initial phases of this work were supported by the Center for Advanced NDE operated by the Ames Laboratory, USDOE for DARPA and AFWAL/ML under contract No. W-7405-ENG-82. Helpful discussions with Dr. K. Eswaran and Professor J. K. Lee are gratefully acknowledged.

References

1 Hunt, J. T., Knittel, M. R., and Barach, D., "Finite Element Approach to Acoustic Scattering from Elastic Structures," *Journal of the Acoustical Society of America*, Vol. 57, 1975, pp. 287–299.

2 Hunt, J. T., Knittel, M. R., and Barach, D., "Finite Element Approach to Acoustic Radiation from Elastic Structures," *Journal of the Acoustical Society of America*, Vol. 55, 1974, pp. 269–280.

3 Zienkiewicz, O. C., and Newton, R. E., "Coupled Vibrations of a Structure Submerged in a Compressible Fluid," *Proceedings of the International Symposium on Finite Element Techniques*, Int. Assoc. for Ship Structures, Stuttgart, Germany, June 10–12, 1969.

4 Mei, K. K., "Unimoment Method of Solving Antenna and Scattering Problems," *IEEE Trans. Antenna Propagat.*, Vol. *AP*-22, 1974, pp. 760–766.

5 Chang, S. K., and Mei, K. K., "Application of the Unimoment Method to Electromagnetic Scattering of Dielectric Cylinders," *IEEE Transactions on Antennas and Propagation*, Vol. *AP*-24, 1976, pp. 35–42.

6 Morgan, M. A., "Numerical Computation of Electromagnetic Scattering by Inhomogeneous Dielectric Bodies of Revolution," Ph.D. Dissertation, University of California, Berkeley, 1976.

7 Stoval, R. E., "A Uni-moment Technique for the Solution of Radiation and Scattering Problems Involving Inhomogeneous Media," Ph.D. Dissertation, University of California, Berkeley, 1975.

8 Morgan, M. A., and Mei, K. K., "Finite-Element Computation of Scattering by Inhomogeneous Penetrable Bodies of Revolution," URSI International Electromagnetic Symposium, Palo Alto, Calif., June 1977.

9 Goetschel, D. B., "Analysis of Steady State Elastic Wave Scattering by Global Local Finite Elements," Ph.D. Dissertation, University of California, Los Angeles, 1980.

10 Su, J. H., Varadan, V. V., and Varadan, V. K., "Finite Element Eigenfunction Method (FEEM) for Elastic (SH-) Wave Scattering," *Journal of the Acoustical Society of America*, submitted.

11 Su, J. H., Varadan, V. V., and Varadan, V. K., "The Unimoment Method for Elastic Wave Scattering Problems," DARPA/AF, *Review of Progress in Quantitative NDE*, Vol. 1, Thompson, D. O., and Chimenti, D. E., eds., Pergamon Press, New York, 1982.

12 Su, J. H., "Finite Element Eigenfunction Method (FEEM) for Elastic Wave Scattering Problems," Ph.D. Dissertation, The Ohio State University, Columbus, 1982.

13 Varadan, V. K., and Varadan, V. V., eds., *Acoustic, Electromagnetic and Elastic Wave Scattering—Focus on the T-Matrix Approach*, Pergamon Press, New York, 1980.

14 Zienkiewicz, O. C., *Finite Element Method*, McGraw-Hill, London, 1977.

15 Varadan, V. V., and Varadan, V. K., "Scattering Matrix for Elastic Waves, III. Application to Spheroids," *J. Acoust. Soc. Am.*, Vol. 65, 1979, pp. 896–905.

16 Eringen, A. C., and Suhubi, E. S., *Elastodynamics, Vol. II*, Academic Press, New York, 1975.

APPENDIX *A*

Finite Element Equations for Region *II*

Within the sphere bounded by the surface *C*, the finite

Downloaded 02 May 2010 to 171.66.16.25. Redistribution subject to ASME license or copyright; see http://www.asme.org/terms/Terms_Use.cfm

element approximation is made and displacements are given by values taken at the nodal points. For rotationally symmetric scatterers the ϕ dependence, i.e., angular dependence in the x-y plane is given in terms of cos $m\phi$ and sin $m\phi$. The basis functions which result from a given application of the boundary condition on C may be written in cylindrical polar coordinates (R,z,ϕ) as

$$\begin{matrix} U_R \\ z \\ \phi \end{matrix}(\mathbf{r}) = \sum_{m=0}^{\infty} \sum_{i=1}^{NEN} \begin{matrix} U_{Rmi} \\ z \\ \phi \end{matrix} N_i(R,z) \begin{matrix} \cos\ m\phi \\ \sin\ m\phi \end{matrix} \tag{A1}$$

where NEN stands for number of nodes per element and N_i are interpolation functions or interpolants that depend on the particular element used.

The Lagrangian can be written as

$$L = \int_{V_I} \left[-\frac{1}{2}\rho_\omega{}^2 U_i U_i + \frac{1}{2}\lambda(\epsilon_{kk})^2 + \mu\epsilon_{ij}\epsilon_{ij} \right] dV \tag{A2}$$

where ϵ_{ij} is the strain tensor, U_i are components of the displacement λ, μ are Lamé constants, and ρ is the density. The preceding volume integral must be subdivided if region I is inhomogeneous or includes an inclusion of different material properties.

By substituting (A1) into (A2) and setting the first variation $\delta L = 0$, we obtain the following set of algebraic equations for the nodal values of the displacement for a given applied boundary condition on C(as discussed in the main text).

$$\begin{bmatrix} & & \\ & 0 & \\ & & \\ & K_{ij} & \\ & & \\ 0 & & \end{bmatrix} \begin{bmatrix} U^c_{Rm1} \\ U^c_{zm1} \\ U^s_{\phi m1} \\ \cdot\cdot \\ \cdot\cdot \\ \cdot\cdot \\ U^c_{RmN}{}^{TP} \\ U^c_{zmN_{TP}} \\ \\ U^s_{\phi mN}TP \end{bmatrix} = 0; \quad i,j = 1,2,3 \tag{A3}$$

where K_{ij} is the "Stiffness Matrix," U^c_{Rmj}, U^c_{zmj}, and $U^S_{\phi mj}$ are the R,z,ϕ components of the displacement at node j for a given boundary condition on C. As discussed in the text, we will only consider the problem of parallel polarization. For axisymmetric scatterers, the R and z components of the displacement have a ϕ dependence of the form cos $m\phi$ and the ϕ component of the displacement has a sin $m\phi$ dependence on ϕ. The stiffness matrix K_{ij} is a sparse banded matrix whose elements are of the form

$$\begin{aligned} K_{3i-2,3j-1} &= K_{3j-1,3i-2} &&= S^2_{ij} \\ K_{3i-2,3j} &= K_{3j,3i-2} &&= S^3_{ij} \\ K_{3i-1,3j} &= K_{3j,3i-1} &&= S^4_{ij} \\ K_{3i-2,3j-2} &= K_{3j-2,3i-2} &&= S^1_{ij} + S^1_{ji} \\ K_{3i-1,3j-1} &= K_{3j-1,3i-1} &&= S^5_{ij} + S^5_{ji} \\ K_{3i,3j} &= K_{3j,3i} &&= S^6_{ij} + S^6_{ji} \end{aligned} \tag{A4}$$

and hence K_{ij} is symmetric.

The elements s^k_{ij} are as follows:

$$s^1_{ij} = \iint_e \left(R\left[-k_s^2 N_i N_j + (c_p/c_s)^2 \frac{\partial N_i}{\partial R} + 2((c_p/c_s)^2 - 2)N_j/_R) \frac{\partial N_i}{\partial R} + ((c_p/c_s)^2 + m^2)N_i/R\ N_j/R + \frac{\partial N_i}{\partial Z}\frac{\partial N_j}{\partial z} \right] \right) dRdz, \tag{A5}$$

$$s^2_{ij} = \iint_e (2R[(c_p/c_s)^2 - 2)\left(\frac{\partial N_i}{\partial R} + \frac{N_i}{R} \right) \frac{\partial N_j}{\partial z} + \frac{\partial N_i}{\partial z}\frac{\partial N_j}{\partial R} \right]) dRdz, \tag{A6}$$

$$s^3_{ij} = \iint_e (2mR\left[((c_p/c_s)^2 + 1)N_i/R + \left((c_p/c_s)2 - 2\frac{\partial N_i}{\partial R} \right) N_j/R - N_i/R\frac{\partial N_j}{\partial R} \right]) dRdz, \tag{A7}$$

$$s^4_{ij} = \iint_e (2mR\left[(c_p/c_s)^2 - 2) \frac{\partial N_i}{\partial Z} N_j/R - N_i/R\frac{\partial N_j}{\partial z} \right]) dRdZ, \tag{A8}$$

$$s^5_{ij} = \iint_e \left(R\left[-k_s^2 N_i N_j + (c_p/c_s)^2 \frac{\partial N_i}{\partial z}\frac{\partial N_j}{\partial Z} + m^2 N_i/R N_j/R + \frac{\partial N_i}{\partial R}\frac{\partial N_j}{\partial R} \right] \right) dRdz, \tag{A9}$$

$$s^6_{ij} = \iint_e \left(R\left[-k_s^2 N_i N_j + (m^2(c_p/c_s)^2 + 1)\frac{N_i}{R}\frac{N_j}{R} + \left(\frac{\partial N_j}{\partial R}\frac{\partial N_j}{\partial R} - 2\frac{\partial N_i}{\partial R}\frac{N_j}{R} + \frac{\partial N_i}{\partial z}\frac{\partial N_j}{\partial Z} \right) \right] \right) dRdz, \tag{A10}$$

where c_p and c_s are the longitudinal and shear wave speeds and e denotes area of element.

In equation (A3), NTP is the total number of nodal points in region II. Of there, NC nodal points lie on the surface C, and these nodal values are prescribed by the vector spherical harmonics. Hence the unknown nodal values which are $NT-NC$ in number can be solved from equation (A3) by standard techniques. The general solution for the displacement in region II is then a superposition of such basis functions with weighting coefficients. These unknown coefficients are solved by matching with the wave-function expansion in the exterior region (region I) as described in the text.

Downloaded 02 May 2010 to 171.66.16.25. Redistribution subject to ASME license or copyright; see http://www.asme.org/terms/Terms_Use.cfm

An Elastic Punch Moving Across the Surface of a Semi-Infinite Solid

G. G. Adams
Associate Professor.
Assoc. Mem. ASME

I. Zeid
Assistant Professor.
Assoc. Mem. ASME

Department of Mechanical Engineering,
Northeastern University,
Boston, Mass. 02115

An elastic punch, modeled as a semi-infinite strip, moves with constant speed over the surface of a semi-infinite elastic body. Using the plane strain theory of elasticity, we obtain the resulting stress distribution along the interface of the contacting bodies for different material combinations and a range of sliding velocity and frictional coefficients. It is found that both the stress intensity factor and the order of the singularity depend on sliding velocity as well as on the other parameters. Speed-dependent composite material parameters are defined which determine the orders of the singularities.

Introduction

When one elastic body slides along the surface of another, the resulting stress distribution can cause wear of the contacting bodies as well as other undesirable effects. The determination of the stress distribution at the interface of the sliding bodies has generally been limited to problems involving rigid punches. The problem of a frictionless rigid punch moving along the surface of a semi-infinite body was solved by Galin [1] and independently by Radok [2]. Suhubi [3, 4] then treats a moving rigid punch in which the effect of friction is included. Sve and Keer [5] solve the problem of an elastic layer acted upon by a pair of moving punches. In [1–4] the complex variable method is used whereas in [5] the solution is obtained using integral transform techniques.

The assumption of a rigid, rather than an elastic punch has been motivated more for mathematical ease rather than for physical realism. Recently a solution was obtained by Bogy [6], using integral transform methods, for the stress distribution acting on the end of a semi-infinite elastic strip with arbitrary end conditions. This solution was utilized by Adams and Bogy [7] to study the static problem of a semi-infinite elastic strip pressed against an elastic half plane for both smooth and bonded contact.

In the present paper we determine the stress distribution at the end of a semi-infinite elastic strip that is pressed against, and moving along, the surface of a semi-infinite elastic solid. After formulating the problem, we obtain a solution for an arbitrary load distribution moving with constant speed along the surface of an elastic half plane. This solution is then matched with Bogy's semi-infinite strip solution [6] and a set of singular integral equations is obtained. An asymptotic analysis, using the method of Muskhelishvili [8], determines the order of the singularities at the punch corners. It is found that the order of the singularity depends on sliding velocity as well as on material combination and frictional coefficient.

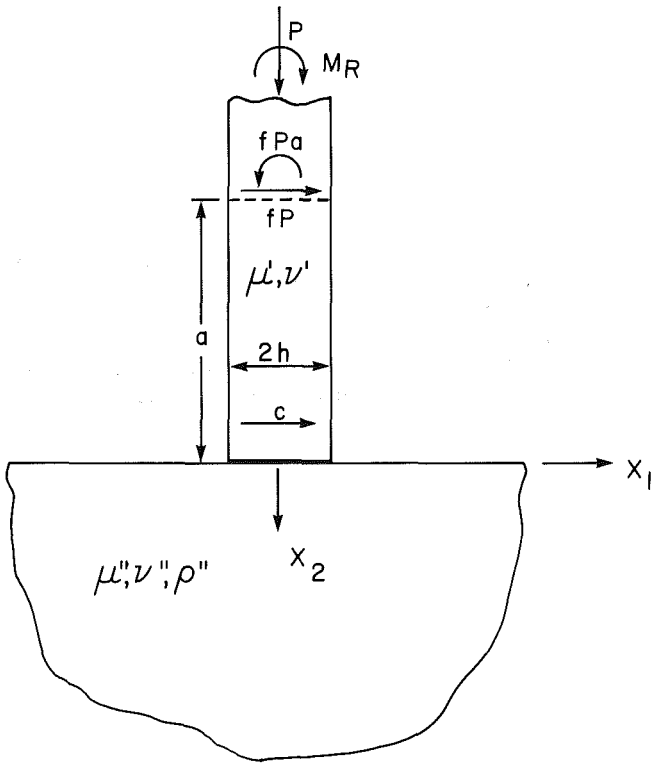


Fig. 1 An elastic punch moving steadily across the surface of a semi-infinite elastic solid

Contributed by the Applied Mechanics Division for presentation at the Winter Annual Meeting, New Orleans, La., December 9–14, 1984 of THE AMERICAN SOCIETY OF MECHANICAL ENGINEERS.

Discussion on this paper should be addressed to the Editorial Department, ASME, United Engineering Center, 345 East 47th Street, New York, N.Y. 10017, and will be accepted until two months after final publication of the paper itself in the JOURNAL OF APPLIED MECHANICS. Manuscript received by ASME Applied Mechanics Division, September, 1982; final revision, November, 1983. Paper No. 84-WA/APM-2.

Copies will be available until August, 1985.

Copyright © 1984 by ASME
Downloaded 02 May 2010 to 171.66.16.25. Redistribution subject to ASME license or copyright; see http://www.asme.org/terms/Terms_Use.cfm

Speed-dependent composite material parameters are defined which determine the order of the singularities at the punch corners, thus giving a reduced dependence on the elastic constants. Finally the system of singular integral equations is solved numerically and the stress intensity factors and stress distributions along the interface are determined and presented graphically.

Problem Formulation

Using the two-dimensional (plane strain) theory of elasticity, we deal with a semi-infinite elastic strip whose end is pressed against and moving along the surface of an elastic half plane. Referring to Fig. 1, we note that the strip has width $2h$ and moves to the right at constant speed c with a frictional coefficient f between the strip and half plane. The strip is pushed against the semi-infinite body with a resultant force P but is otherwise clamped sufficiently far away from the interface.

The appropriate displacement of motion in terms of body fixed coordinates are

$$\mu\nabla^2 u_i + (\lambda+\mu)\frac{\partial v}{\partial x_i} = \rho\frac{\partial^2 u_i}{\partial t^2}, \quad i=1,2 \tag{1}$$

where λ, μ, ρ, u_i are the Lamé's constant, shear modulus, mass density, and components of displacement, respectively, and the dilation v is given by

$$v = \frac{\partial u_1}{\partial x_1} + \frac{\partial u_2}{\partial x_2} \tag{2}$$

We observe that although the half plane sees a steadily moving load distribution, the semi-infinite strip sees a stationary load distribution. Hence for the semi-infinite strip, u_i is independent of time and the right-hand side of (1) vanishes in a coordinate system attached to the strip. However, the equations of motion for the half plane require a transformation into a moving coordinate system where

$$x_1^* = x_1 - ct, \quad u_i^*(x_1^*, x_2) = u_i(x_1, x_2, t), \tag{3}$$

which leads to

$$(\delta^2-\beta_2^2)\frac{\partial^2 u_1}{\partial x_1^2} + \frac{\partial^2 u_1}{\partial x_2^2} + (\delta^2-1)\frac{\partial^2 u_2}{\partial x_1 \partial x_2} = 0,$$

$$\delta^2\frac{\partial^2 u_2}{\partial x_2^2} + (1-\beta_2^2)\frac{\partial^2 u_2}{\partial x_1^2} + (\delta^2-1)\frac{\partial^2 u_1}{\partial x_1 \partial x_2} = 0, \tag{4}$$

where

$$\beta_i = c/c_i, \ \delta = c_1/c_2, \ c_1 = \sqrt{(\lambda+2\mu)/\rho}, \ c_2 = \sqrt{\mu/\rho}. \tag{5}$$

In (4) and in what follows, we omit the superscript (*) which is assumed. Hence the coordinate system for both bodies are the same and move to the right with constant speed c.

The boundary and continuity conditions to be satisfied are

$$\sigma''_{11}(x_1,x_2), \sigma''_{12}(x_1,x_2), \sigma''_{22}(x_1,x_2) \to 0 \quad \text{as} \quad x_1^2 + x_2^2 \to \infty \tag{6}$$

$$\sigma''_{12}(x_1,0) = f\sigma''_{22}(x_1,0), \quad |x_1| < \infty, \tag{7}$$

$$\sigma''_{22}(x_1,0) = 0 \quad |x_1| > h, \tag{8}$$

$$\sigma''_{i2}(x_1,0) = \sigma'_{i2}(x_1,0), \quad |x_1| < h, \quad i=1,2, \tag{9}$$

$$u''_2(x_1,0) = u'_2(x_1,0), \quad |x_1| < h, \tag{10}$$

$$\sigma'_{11}(\pm h, x_2) = 0, \quad -\infty < x_2 < 0, \tag{11}$$

$$\sigma'_{12}(\pm h, x_2) = 0, \quad -\infty < x_2 < 0, \tag{12}$$

where ($'$) and ($''$) refer to the semi-infinite strip and half plane, a respectively. Finally the stresses and displacements of the strip must approach those of the corresponding St. Venant solution as $x_2 \to -\infty$. We note from Fig. 1 that there is a compressive force P and an unknown couple moment M_R both at $x_2 = -\infty$. Furthermore, at $x_2 = -a$, there is a transverse force fP and a couple moment fPa as shown. We then take the limit as the distance a approaches infinity, leaving a finite bending moment at the interface.

Half-Plane Solution

Applying the exponential Fourier transform (with respect to x_1) to (4), we obtain

$$u''_1(x_1,x_2) = \frac{1}{\sqrt{2\pi}}\int_{-\infty}^{\infty} \{B_1 e^{-|\lambda_1| x_2} + B_2 e^{-|\lambda_2| x_2}\} e^{i\omega x_1}\, d\omega, \tag{13}$$

$$u''_2(x_1,x_2) = \frac{i}{\sqrt{2\pi}}\int_{-\infty}^{\infty} \{B_1\kappa_1 e^{-|\lambda_1| x_2} + \frac{B_2}{\kappa_2} e^{-|\lambda_2| x_2}\} \operatorname{sgn}(\omega)\, e^{i\omega x_1}\, d\omega \tag{14}$$

where

$$\kappa_i = \sqrt{1-\beta_i^2}, \quad \lambda_i = \omega\kappa_i, \quad i=1,2$$

and $B_1(\omega)$, $B_2(\omega)$ are yet to be determined. Using (7) we obtain

$$B_2(\omega) = \frac{-2\kappa_1 \operatorname{sgn}(\omega) - if(\beta_2^2-2)}{(2-\beta_2^2)\operatorname{sgn}(\omega)/\kappa_2 - 2if} B_1(\omega) \tag{15}$$

and condition (8) yields

$$B_1(\omega) = \frac{-2f\kappa_2 \operatorname{sgn}(\omega) - i(1+\kappa_2^2)}{\sqrt{2\pi}\mu''[4\kappa_1\kappa_2 - (1+\kappa_2^2)^2]\omega}\int_{-h}^{h} \sigma''_{22}(x_1,0) e^{-i\omega x_1}\, d\omega \tag{16}$$

Finally we compute the slope of the surface of the half plane in the region $(-h, h)$ using (14), (15), and (16) obtaining

$$\frac{du''_2}{dx_1}(x_1,0) = -fP_1\sigma''_{22}(x_1,0) - P_2\int_{-h}^{h}\frac{\sigma''_{22}(t,0)}{t-x_1}\, dt \tag{17}$$

where

$$P_1 = (1-2\kappa_1\kappa_2+\kappa_2^2)/\mu''\Delta, \quad P_2 = \kappa_1\beta_2^2/\pi\mu''\Delta, \quad \Delta = 4\kappa_1\kappa_2 - (1+\kappa_2^2)^2. \tag{18}$$

In determining (17) it was necessary to use the identities

$$\frac{d}{dx}\int_{-\infty}^{\infty}\frac{1}{\omega} e^{i\omega(x-t)} d\omega = 2\pi i\delta(x-t),$$

$$\frac{d}{dx}\int_{-\infty}^{\infty}\frac{\operatorname{sgn}\omega}{\omega} e^{i\omega(x-t)} d\omega = \frac{2}{t-x},$$

which were determined from [9, section 1.5, equation (1), section 2.6, equation (1)], and where $\delta(\ )$ is the dirac delta function. Summarizing, equations (17) and (18) give the slope of the surface of the half plane in terms of an arbitrary moving normal and shear load (subject to (7)) in the region $(-h, h)$.

Semi-Infinite Strip Solution

Using the solution of Bogy [6] for a semi-infinite elastic strip with arbitrary end conditions we have

$$\sum_{j=1}^{2}\int_{-h}^{h}\left[\frac{a_{ij}^S}{t-x_1} + k_{ij}^S(x_1,t)\right]\phi_j^S(t)\, dt = g_i^S(x_1), \quad i=1,2, \quad -h < x_1 < h,$$

Downloaded 02 May 2010 to 171.66.16.25. Redistribution subject to ASME license or copyright; see http://www.asme.org/terms/Terms_Use.cfm

$$\sum_{j=1}^{2}\int_{-h}^{h}\left[\frac{a_{ij}^{A}}{t-x_1}+k_{ij}^{A}(x_1,t)\right]\phi_j^{A}(t)\quad dt$$
$$=g_i^{A}(x_1),\quad i=1,2,\ -h<x_1<h \tag{19}$$

in which the superscripts S and A refer to the symmetric and antisymmetric end problems [6], and where

$$\begin{aligned}
\phi_1^{S}(t) &= -\hat{\sigma}_{12}'(t,0)/\pi(1-\nu'),\quad \phi_1^{A}(t)=\hat{\sigma}_{22}'(t,0)/\pi(1-\nu'),\\
\phi_2^{S}(t) &= 2\mu'\frac{d\hat{u}_2'(t,0)}{dt}/\pi(1-\nu'),\quad \phi_2^{A}(t)\\
&= -2\mu'\frac{d\hat{u}_1(t,0)}{dt}/\pi(1-\nu'),\\
g_1^{S}(x_1) &= -2\mu'\frac{d\hat{u}_1(x_1,0)}{dx_1},\quad g_1^{A}(x_1)=2\mu'\frac{d\hat{u}_2(x_1,0)}{dx_1},\\
g_2^{S}(x_1) &= \hat{\sigma}_{22}'(x_1,0),\quad g_2^{A}(x_1)=\hat{\sigma}_{12}'(x_1,0).
\end{aligned} \tag{20}$$

The a_{ij}^{S} and a_{ij}^{A} are constants defined in [6] and the kernels k_{ij}^{S} and k_{ij}^{A} have generalized Cauchy singularities as well as regular parts (see [6] for details). In (20) $\hat{u}_i$ and $\hat{\sigma}_{ij}$ are the residual displacement and stress on the end of the strip to which the corresponding St. Venant solutions must be added:

$$\begin{aligned}
u_1'(x_1,0) &= \hat{u}_1'(x_1,0)+(P/4h\mu')\nu' x_1\\
&\quad +(3M_R/8h^3\mu')\nu'(x_1^2-h^2),\\
u_2'(x_1,0) &= \hat{u}_2'(x_1,0)+(3Pf/8\mu' h^3)(2-\nu')x_1^3/3,\\
\sigma_{12}'(x_1,0) &= \hat{\sigma}_{12}'(x_1,0),\quad \sigma_{22}'(x_1,0)=\hat{\sigma}_{22}'(x_1,0)\\
&\quad -P/2h-(3M_R/2h^3)x_1,
\end{aligned} \tag{21}$$

to obtain the complete solution. (We note that the use of the (ˆ) notation to represent the residual solution is different from that in [6]).

Continuity at Interface

It is now necessary to match the half-plane solution and the semi-infinite strip solution using the continuity conditions (9) and (10). We recognize, however, that the semi-infinite strip solution is given in terms of certain symmetric and antisymmetric parts and so our half-plane solution must be decomposed according to

$$\frac{du_2''^{S}(x_1,0)}{dx_1}=-fP_1\sigma_{22}''^{A}(x_1,0)-P_2\int_{-h}^{h}\frac{\sigma_{22}''^{S}(t,0)}{t-x_1}\,dt, \tag{22}$$

$$\frac{du_2''^{A}(x_1,0)}{dx_1}=-fP_1\sigma_{22}''^{S}(x_1,0)-P_2\int_{-h}^{h}\frac{\sigma_{22}''^{A}(t,0)}{t-x_1}\,dt. \tag{23}$$

Applying (9) and (10) to (19)–(23), we finally obtain a system of singular integral equations:

$$\sum_{j=1}^{4}\int_{-h}^{h}\left\{\frac{b_{ij}}{t-x_1}+L_{ij}(x_1,t)\right\}\psi_j(t)dt+\sum_{j=1}^{4}c_{ij}\psi_j(t)=f_i(x_1),\quad i=1,2,3,4,\quad -h<x_1<h \tag{24}$$

where

$$\begin{aligned}
&b_{11}=a_{22}^{S},b_{13}=a_{21}^{S},b_{22}=Q_2,b_{33}=a_{21}^{A},\\
&\qquad b_{34}=a_{22}^{A},b_{43}=a_{11}^{A}+Q_3,b_{44}=a_{12}^{A},\\
&b_{12}=b_{14}=b_{21}=b_{23}=b_{24}=b_{31}=b_{32}=b_{41}=b_{42}=0,\\
&c_{12}=-1,c_{21}=1,c_{23}=fQ_1,c_{32}=-f,c_{42}=fQ_1,c_{11}\\
&=c_{13}=c_{14}=c_{22}=c_{24}=c_{31}=c_{33}=c_{34}=c_{41}=c_{43}=c_{44}=0,\\
&L_{11}(x_1,t)=k_{22}^{S}(x_1,t),L_{13}(x_1,t)\\
&=k_{21}^{S}(x_1,t),L_{33}(x_1,t)=k_{21}^{A}(x_1,t),\\
&L_{34}(x_1,t)=k_{22}^{A}(x_1,t),L_{43}(x_1,t)\\
&=K_{11}^{A}(x_1,t),L_{44}(x_1,t)=K_{12}^{A}(x_1,t),\\
&L_{12}=L_{14}=L_{21}=L_{22}=L_{23}=L_{24}=L_{31}=L_{32}=L_{41}=L_{42}=0,\\
&f_1(x_1)=P/2h,\ f_2(x_1)=0,\\
&f_3(x_1)=1.5f(P/2h)(1+x_1^2/h^2)-\frac{1.5M_R}{\pi(1-\nu')h^3}\\
&\qquad\int_{-h}^{h}\{k_{21}^{A}(x_1,t)+\nu' k_{22}^{A}(x_1,t)\}\ t\ dt,\\
&f_4(x_1)=-1.5f(P/2h)(2-\nu')(x_1^2/h^2-1/3)\\
&-\frac{1.5M_R}{\pi(1-\nu')h^3}\int_{-h}^{h}\{k_{11}^{A}(x_1,t)+\nu' k_{12}^{A}(x_1,t)\}t\,dt,\\
&\psi_1(t)=\phi_2^{S}(t),\ \psi_2(t)=g_2^{S}(t)-(P/2h),\\
&\psi_3(t)=\phi_1^{A}(t)-\frac{1.5M_R x_1}{\pi(1-\nu')h^3},\quad \psi_4(t)=\phi_2^{A}(t)-\frac{1.5M_R\nu' x_1}{\pi(1-\nu')h^3}
\end{aligned} \tag{25}$$

$$Q_1=2\mu' P_1,\ Q_2=\frac{2\mu' P_2}{\pi(1-\nu')},\quad Q_3=2\mu'\pi(1-\nu')P_2.$$

Finally, the following resultant conditions are necessary

$$\begin{aligned}
&\int_{-h}^{h}\psi_1(t)dt=0,\int_{-h}^{h}\psi_2(t)dt=-P,\int_{-h}^{h}\psi_3(t)dt=0,\\
&\int_{-h}^{h}\psi_4(t)dt=0,\int_{-h}^{h}\psi_3(t)dt=-M_R/\pi(1-\nu').
\end{aligned} \tag{26}$$

The extra resultant condition $(26)_5$ is necessary to determine the unknown M_R.

Analysis of Singular Integral Equations

It is now necessary to perform an asymptotic analysis of the singular integral equations (24), to determine the orders of the singularities at the leading and trailing corners of the punch. We recognize that (24) contains Cauchy singularities (b_{ij} terms), generalized Cauchy singularities (L_{ij} terms), and free terms (c_{ij} terms). Proceeding as in [8] we define $\bar{\psi}_j(t)$ according to

$$\psi_j(t)=\bar{\psi}_j(t)/(h^2-t^2)^{\gamma} \tag{27}$$

and it follows that

$$\begin{aligned}
&\frac{1}{\pi}\int_{-h}^{h}\frac{\psi_j(t)}{t-x}dt=\bar{\psi}_j(-h)(2h)^{-\gamma}(h+x)^{-\gamma}\\
&\cot\pi\gamma-\bar{\psi}_j(h)(2h)^{-\gamma}(h-x)^{-\gamma}\cot\pi\gamma+F_1(x),\\
&\frac{1}{\pi}\int_{-h}^{h}\psi_j(t)(h-x)^{k}\frac{d^k(t+x-2h)^{-1}}{dx^k}\,dt\\
&=-\bar{\psi}_j(h)(2h)^{-\gamma}\gamma(\gamma+1)\ldots(\gamma+k-1)(h-x)^{-\gamma}\csc\pi\gamma\\
&\qquad+F_2(x),\\
&\frac{1}{\pi}\int_{-h}^{h}\psi_j(t)(h+x)^{k}\frac{d^k(t+x-2h)^{-1}}{dx^k}\,dt\\
&=\bar{\psi}_j(-h)(2h)^{-\gamma}(-1)^k\gamma(\gamma+1)\ldots(\gamma+k-1)(h+x)^{-\gamma}\csc\pi\gamma\\
&\qquad+F_3(x),
\end{aligned} \tag{28}$$

where $F_1(x)$, $F_2(x)$, and $F_3(x)$ are bounded functions of x. We note that although the singularities at the leading and trailing corners of the punch will in general be of different order, the functions $\psi_j(t)$ will have singularities of the same order at each end. This is because the $\psi_j(t)$ defined by (25) and (20) are either the symmetric or antisymmetric parts of the stresses and displacement gradients. Thus if the stresses and displacement gradients have different order singularities at each end, the $\psi_j(t)$ will have both singularities occurring at each end. The power γ appearing in (27) represents the greater of the two singularities.

Downloaded 02 May 2010 to 171.66.16.25. Redistribution subject to ASME license or copyright; see http://www.asme.org/terms/Terms_Use.cfm

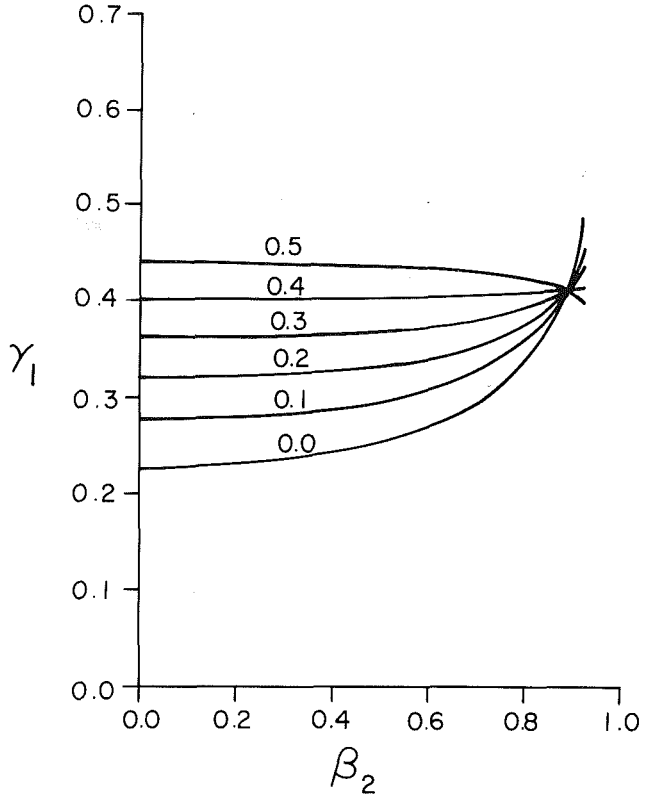


Fig. 2 Order of the leading edge singularity (γ_1) versus dimensionless speed (β_2) for composite *A* and various values of the friction coefficient *f*

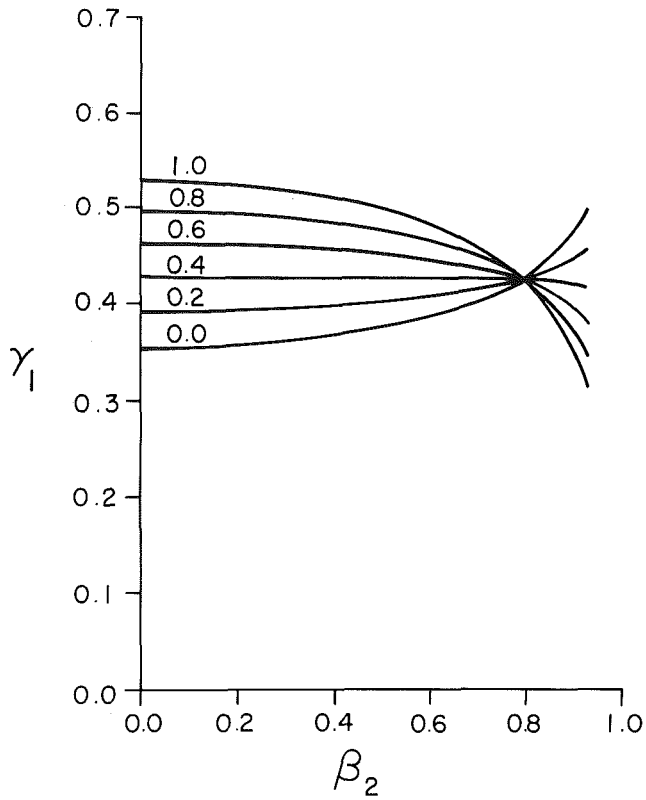


Fig. 3 Order of the leading edge singularity (γ_1) versus dimensionless speed (β_2) for composite *B* and various values of the friction coefficient *f*

The condition that the sum of the singular terms appearing in (24) is bounded, enables us to determine the order of the singularity. Applying (27) and (28) to (24), yields a system of four homogeneous linear algebraic equations whose determinant must vanish

$$|d_{ij}|=0 \tag{29}$$

where

$$\begin{aligned}
d_{11} &= \frac{1}{2}\cos\pi\gamma-\frac{1}{2}(1-4\gamma+2\gamma^2),\\
d_{12} &= f\Big[\frac{1}{2}(1-2\nu')\cos\pi\gamma+\frac{1}{2}(1-4\gamma+2\gamma^2)\\
&\quad +(1-\nu')(3-2\gamma)\Big],\\
d_{13} &= 0, d_{14}=-(1/\pi)\sin\pi\gamma,\ d_{21}=0,\\
d_{22} &= \frac{1}{2}(1-2\nu')\cos\pi\gamma-\frac{1}{2}(1-4\gamma+2\gamma^2)\\
&\quad +(1-\nu')(1-2\gamma)\qquad (30)\\
d_{23} &= \frac{1}{2}\cos\pi\gamma+\frac{1}{2}(1-4\gamma+2\gamma^2),\ d_{24}=-(f/\pi)\sin\pi\gamma,\\
d_{31} &= (1/\pi)\sin\pi\gamma,\ d_{32}=-(fQ_1/\pi)\sin\pi\gamma,\ d_{33}=0,\\
&\quad d_{34}=-Q_2\cos\pi\gamma,\\
d_{41} &= 0,\ d_{42}=-(3/2-2\nu'+Q_3)\cos\pi\gamma\\
&\quad -\frac{1}{2}(1-4\gamma+2\gamma^2)+2(1-\nu')(1-2\nu'),
\end{aligned}$$

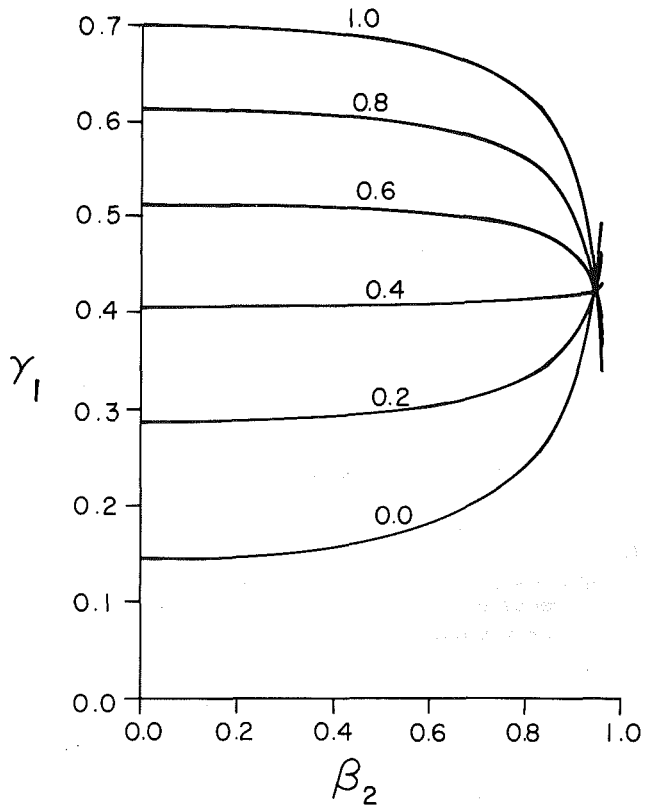


Fig. 4 Order of the leading edge singularity (γ_1) versus dimensionless speed (β_2) for composite *C* and various values of the friction coefficient *f*

Downloaded 02 May 2010 to 171.66.16.25. Redistribution subject to ASME license or copyright; see http://www.asme.org/terms/Terms_Use.cfm

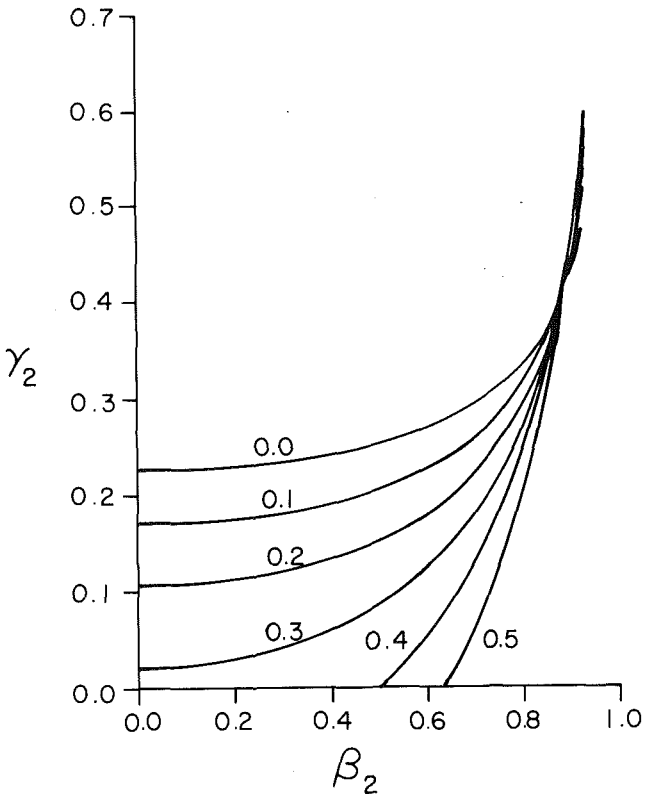


Fig. 5 Order of the trailing edge singularity (γ_2) versus dimensionless speed (β_2) for composite *A* and various values of the friction coefficient *f*

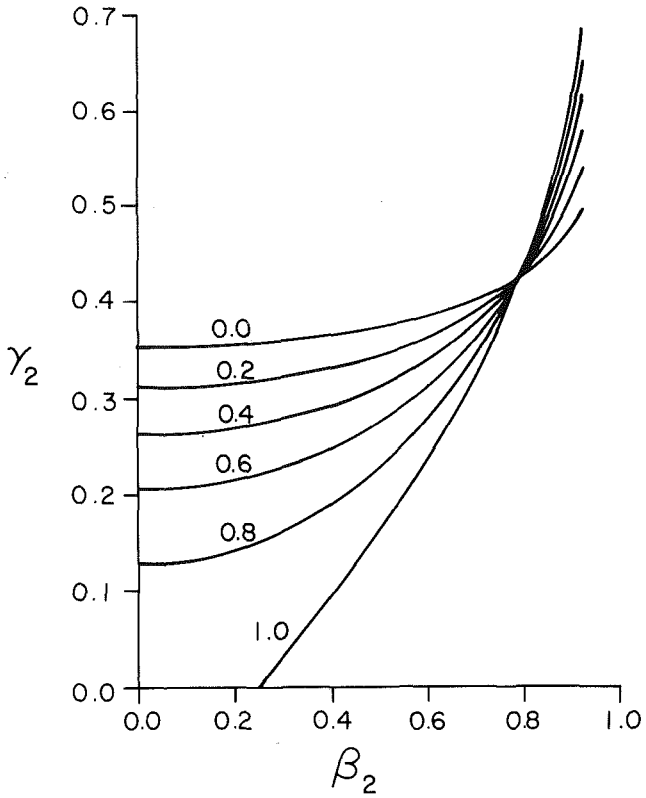


Fig. 6 Order of the trailing edge singularity (γ_2) versus dimensionless speed (β_2) for composite *B* and various values of the friction coefficient *f*

$$d_{43} = \frac{1}{2}(1-2\nu')\cos\pi\gamma + \frac{1}{2}(1-4\gamma+2\gamma^2) + (1-\nu')(3-2\gamma),\ d_{44} = (fQ/\pi)\sin\pi\gamma.$$

After considerable algebra, equation (29) reduces to

$$A_1\alpha^* + A_2\beta^* + A_3 = 0 \tag{31}$$

where

$$\begin{aligned} A_1 &= -1+(1-4\gamma+2\gamma^2)\cos\pi\gamma \pm 2f(1-\gamma)(2-\gamma)\sin\pi\gamma, \\ A_2 &= \pm f[\sin 2\pi\gamma - 2(1-4\gamma+2\gamma^2)\sin\pi\gamma] \\ A_3 &= -\cos 2\pi\gamma + (1-4\gamma+2\gamma^2)\cos\pi\gamma \mp 2f(1-\gamma)(2-\gamma)\sin\pi\gamma \end{aligned} \tag{32}$$

and

$$\alpha^* = \frac{Q_2 - 2/\pi}{Q_2 + 2/\pi}, \quad \beta^* = -(1-\alpha^*)(1-2\nu'-Q_1)/4(1-\nu'), \tag{33}$$

which agrees with the results of a wedge/half-plane analysis currently in progress.

The α^*, β^* appearing in (31) and defined in (33) are speed-dependent composite material parameters. By taking an asymptotic expansion for small speeds we can show that α^*, β^* approach the corresponding α, β defined by Dundurs [10] for stationary contact given as

$$\alpha = \frac{k(1-\nu'')-(1-\nu')}{k(1-\nu'')+(1-\nu')}, \quad \beta = \frac{k(1-2\nu'')-(1-2\nu')}{2k(1-\nu'')+2(1-\nu')}, \quad k = \mu'/\mu''. \tag{34}$$

The α^*, β^* along with f, determine the order of the singularity, but do not, by themselves, determine the overall state of stress. Furthermore, the results given by (31) agree with the static wedge results of Gdoutos and Theocaris [11] in

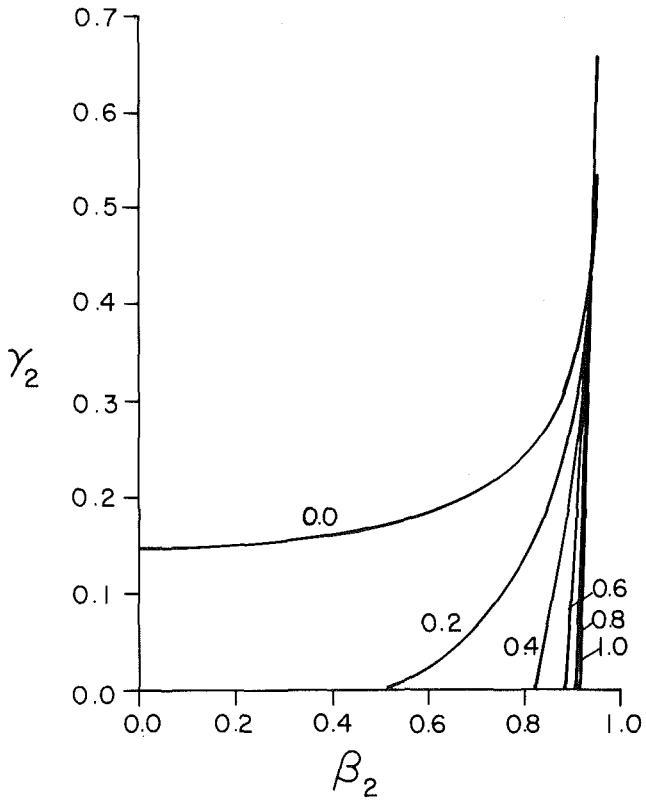


Fig. 7 Order of the trailing edge singularity (γ_2) versus dimensionless speed (β_2) for composite *C* and various values of the friction coefficient *f*

Downloaded 02 May 2010 to 171.66.16.25. Redistribution subject to ASME license or copyright; see http://www.asme.org/terms/Terms_Use.cfm

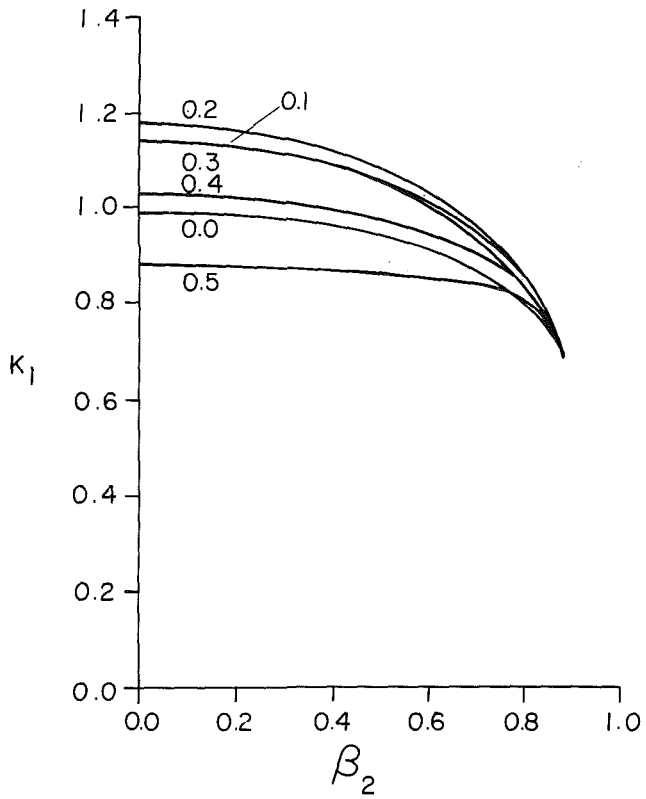


Fig. 8 Stress intensity factor (K_1) at the leading edge versus dimensionless speed (β_2) for composite *A* and various values of the friction coefficient *f*

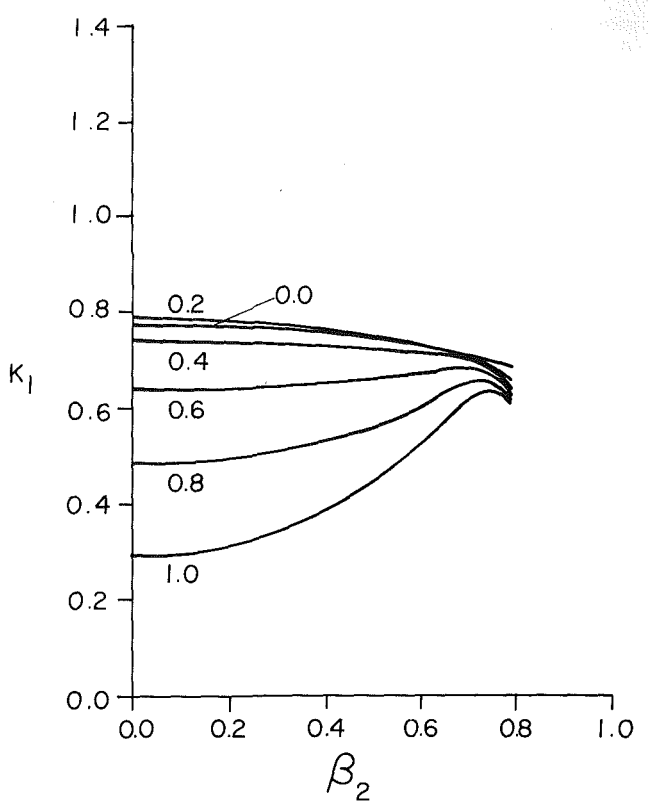


Fig. 9 Stress intensity factor (K_1) at the leading edge versus dimensionless speed (β_2) for composite *B* and various values of the friction coefficient *f*

the limit as the speed becomes small. The $\pm f$ terms appearing in (32) are due to the presence of two singularities, with the upper sign corresponding to the leading edge.

Numerical Solution

With the order of the singularity determined from (31), we now proceed to solve the system of singular integral equations (24), along with the resultant conditions (26). Applying the numerical method of Erdogan and Gupta [12], we obtain

$$\sum_{j=1}^{4}\sum_{J=1}^{N}\left\{\frac{b_{ij}}{\tau_J - y_K} + hL_{ij}(hy_K, h\tau_J)\right\}A_J\bar{\psi}_j^*(\tau_J) + \sum_{j=1}^{4} C_{ij}\bar{\psi}_j^*(\tau_J)/(1-y_K^2)^{\gamma} = f_i(hy_K),$$

$$i = 1,2,3,4, \quad K = 1,2, \ldots N-1 \tag{35}$$

$$\sum_{J=1}^{N} A_J\bar{\psi}_j^*(\tau_J) = 0, j = 1,3,4, \sum_{J=1}^{N} A_J\bar{\psi}_2^*(\tau_J) = -P/h,$$

$$\sum_{J=1}^{N} A_J\tau_J\bar{\psi}_3^*(\tau_J) = -M_R/h^2\pi(1-\nu'), \tag{36}$$

where

$$\bar{\psi}_j^*(\tau) = \psi_j(h\tau)(1-\tau^2)^{\gamma} = \bar{\psi}_j(h\tau)/h^{2\gamma}, \tag{37}$$

$$A_J = -\frac{2(N-\gamma+1)\Gamma^2(N-\gamma+1)2^{-2\gamma}}{(N+1)!(N-2\gamma+1)\Gamma(N-2\gamma+1)P_N'^{(-\gamma,-\gamma)}(\tau_J)P_{N+1}^{(-\gamma,-\gamma)}(\tau_J)}$$

$$P_N^{(\gamma,\gamma)}(\tau) = \frac{\Gamma(\gamma+N+1)}{\Gamma(2\gamma+N+1)}\sum_{K=0}^{N}\frac{\Gamma(2\gamma+N+K+1)(\tau-1)^K}{K!(N-K)!2^K\Gamma(\gamma+K+1)}, \tag{38}$$

$\tau_J, (J = 1,2, \ldots N)$ are N roots of $P_N^{(-\gamma,-\gamma)}(\tau) = 0$,

$y_K, (K = 1,2, \ldots N-1)$ are $N-1$ roots of $P_{N-1}^{(1-\gamma,1-\gamma)}(y) = 0$.

Since the system of $4N+1$ linear algebraic equations, (35) and (36), involves both $\bar{\psi}_j^*(\tau_J)$ and $\bar{\psi}_j^*(y_K)$, there are a total of $8N-3$ unknowns. Following the procedure of [7] we reduce the number of unknowns to $4N+1$ by expanding $\bar{\psi}_j^*$ in terms of Jacobi of Polynomials

$$\bar{\psi}_j^*(\tau) = \sum_{I=0}^{N+1} G_{jI}P_I^{(-\gamma,-\gamma)}(\tau). \tag{39}$$

Substituting (39) into (35) and (36) we finally obtain a system of $4N+1$ linear equations which can be solved for the $4N+1$ unknowns G_{jI} and M_R. Having obtained G_{jI}, we can now find the ψ_j from (37) and (39).

Finally the normal stress, calculated as described in the foregoing, must be compressive everywhere in the contact region. All of the results shown in the next section satisfy that condition.

Results and Discussion

In Figs. 2-4 are graphs of the order of the leading edge singularity (γ_1) versus dimensionless speed (β_2) for various values of the frictional coefficient (f) and for different material combinations. The range of β_2 is from zero to the Rayleigh wave speed of the half plane. Related results corresponding to the trailing edge singularity (γ_2) are shown in Figs. 5-7. Perhaps the most striking feature is that for a given material pair the curves corresponding to different friction coefficients all cross at the same point. Said differently, for any material combination there exists a certain dimensionless speed (β_2) at which the order of the singularity is independent of the coefficient of friction. We note that the trailing edge singularity may be viewed as a special case of the leading edge singularity with negative friction and hence the

Downloaded 02 May 2010 to 171.66.16.25. Redistribution subject to ASME license or copyright; see http://www.asme.org/terms/Terms_Use.cfm

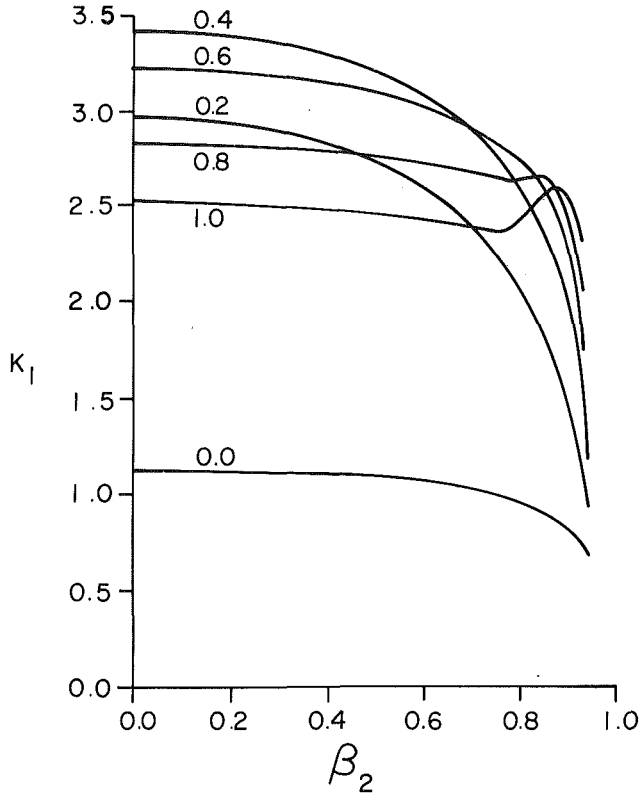


Fig. 10 Stress intensity factor (K_1) at the leading edge versus dimensionless speed (β_2) for composite C and various values of the friction coefficient f

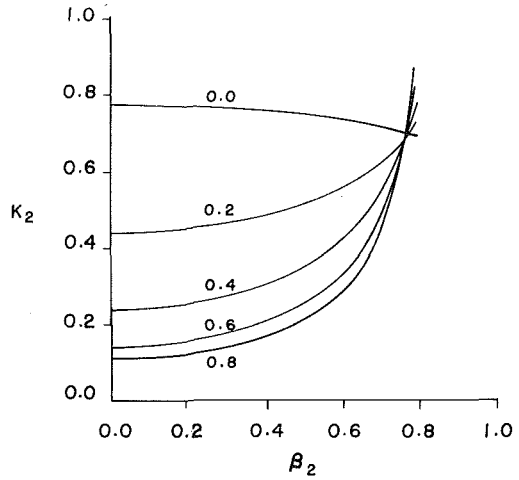


Fig. 11 Stress intensity factor (K_2) at the trailing edge versus dimensionless speed (β_2) for composite B and various values of the friction coefficient f

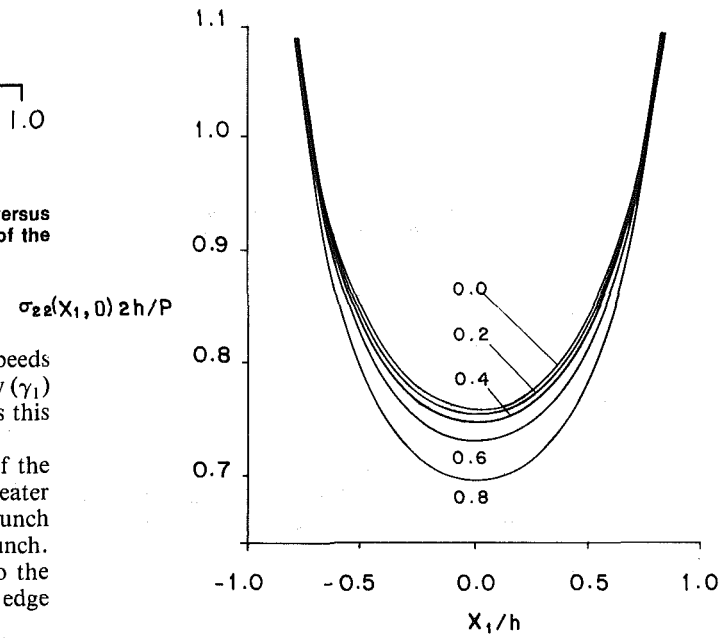


Fig. 12 Normal stress versus position for composite B with f = 0.2 and at different speeds (β_2)

cross-over points are the same for both corners. For speeds less than the cross-over speed, the leading edge singularity (γ_1) is greater than the trailing edge singularity (γ_2), whereas this behavior is reversed above the cross-over speed.

It is also interesting to note that, at low speeds, all of the material combinations shown in Figs. 2–7 have γ_1 greater than γ_2. This trend is the reverse of that for the rigid punch problem [3] and is due to the elasticity of the punch. Specifically the leading edge singularity is insensitive to the composite material parameter (α) but the trailing edge singularity is very sensitive to α.

To compare the results obtained for the different composites, we refer to the following table

Composite	Figs.	μ'/μ''	ν'	ν''	α	β
A	2,5	1.0	0.3	0.3	0	0
B	3,6	3.0	0.3	0.3	1/2	1/7
C	4,7	1.0	0.0	0.5	−1/3	−1/3

which gives the properties of the various composites including the static composite material parameters (α,β). We note that for negative values of α,β (Composite *C*) the dependence of γ_1 and γ_2 on friction is much greater than it is for $\alpha=\beta=0$ (Composite *A*) or for positive values of α,β (Composite *B*). In fact even for moderate values of the friction coefficient, the trailing edge of composite *C* does not have a power singularity until the speed becomes very high at which point γ_2 increases extremely rapidly. This behavior is not nearly as pronounced in composites *A* and *B*.

Also of interest is the behavior near the Rayleigh wave speed. By taking the limit as the speed approaches the Rayleigh wave speed, we can show from (31)–(33) that γ_1 and γ_2 approach that obtained in the rigid punch problem [3] at the Rayleigh wave velocity. Hence γ does not, in that case, depend on the properties of the punch.

The stress intensity factor at the leading edge (K_1) of Composites *A*, *B*, *C* are shown in Figs. 8–10, respectively, where

$$K_1 = -\lim_{x\to h} (h^2 - x^2)^{\gamma}\sigma''_{22}(x,0). \tag{40}$$

The stress intensity factor at the trailing edge (K_2) for Composite *B* is given in Fig. 11. The normal stress in the contact region is shown in Fig. 12 for various values of the dimensionless speed (β_2) and for fixed friction coefficient ($f = 0.2$).

The range of β_2 is from zero to the cross-over speed. Note that for low and even moderate speeds, the stress-intensity factor does not vary monotonically with the coefficient of friction; the stress field near the leading edge being dominated by γ_1. However as the cross-over speed is approached, the variation of K_1 with f becomes monotonic as the values of γ_1, for different f, become equal. We further note that we have

Downloaded 02 May 2010 to 171.66.16.25. Redistribution subject to ASME license or copyright; see http://www.asme.org/terms/Terms_Use.cfm

solved this system of singular integral equations with two singularities. This is a potential source of inaccuracies; however the results for large values of the stiffness ratio (k) approach those for the rigid punch problem [3] even when γ_1 and γ_2 are close to each other. This given us confidence in our numerical results.

References

1 Galin, L. A., *Contact Problems in the Theory of Elasticity*, Gostechizdat, 1953.

2 Radok, J. R. M., "On the Solution of Problems of Dynamic Plane Elasticity," *Quarterly Journal of Applied Mathematics*, Vol. 14, 1956, pp. 289–298.

3 Suhubi, E. S., "Moving Rough Punch on an Elastic Half-Plane," *Letters in Applied and Engineering Sciences*, Vol. 1, 1972, pp. 119–128.

4 Suhubi, E. S., "Moving Rough Punch on an Elastic Half Space," MAE Applied Mathematics Division, Report No. 16, 1972.

5 Sve, C., and Keer, L. M., "Indentations of an Elastic Layer by Moving Punches," *International Journal of Solids and Structures*, Vol. 5, 1969, pp. 795–816.

6 Bogy, D. B., "Solution of the Plane End Problem for a Semi-Infinite Elastic Strip," *ZAMP*, Vol. 26, 1975, pp. 749–769.

7 Adams, G. G., and Bogy, D. B., "The Plane Elastic Contact Problem of a Semi-Infinite Strip and Half-Plane," ASME JOURNAL OF APPLIED MECHANICS, Vol. 43, 1976, pp. 603–607.

8 Muskhelishvili, N. I., *Singular Integral Equations*, P. Noordhoff, 1958.

9 Erdelyi, A., et al., *Tables of Integral Transforms*, Vol. 1, McGraw-Hill, New York, 1954.

10 Dundurs, J., "Effect of Elastic Constants on Stress in a Composite Under Plane Deformation," *Journal of Composite Materials*, Vol. 1, 1967, pp. 310–322.

11 Gdoutos, E. E., and Theocaris, P. S., "Stress Concentrations at the Apex of a Plane Indenter Acting on an Elastic Half Plane," ASME JOURNAL OF APPLIED MECHANICS, Vol. 42, 1975, pp. 688–692.

12 Erdogan, F., and Gupta, G. D., "On the Numerical Solution of Singular Integral Equations," *Quarterly of Applied Mathematics*, Vol. 29, 1972, pp. 525–534.

Downloaded 02 May 2010 to 171.66.16.25. Redistribution subject to ASME license or copyright; see http://www.asme.org/terms/Terms_Use.cfm

Axisymmetric Solutions in Elastostatics and Elastic Wave Propagation by Ascent Methods[1]

F. R. Norwood
Computational Physics and Mechanics
Division II, 1533
Sandia National Laboratories,
Albuquerque, N.M. 87185
Mem. ASME

In the present paper a method of ascent for axisymmetric problems is developed. It is shown that, for problems where the vector or scalar Laplacian operator specifies the space behavior of the potential functions, the three-dimensional axisymmetric problems may be solved by operating on the solution to an associated two-dimensional problem. Hence, the theoretical results presented here may be applied to heat transfer problems, to problems in elastostatics, and to elastic wave propagation problems.

1 Introduction

The present paper was motivated by the recent publications of Bragg [1], Zukas et al. [2], and Brown [3] and is intended for problems where axial symmetry exists. This includes not only the impact problems treated in references [2] and [3], but also a larger class of problems in areas as diverse as penetration technology and heat transfer. As reported in [2], the application of the technique will reduce computer costs. Bragg [1] established the ascent method for solving abstract Cauchy problems involving the wave and Euler-Poisson-Darboux equations. Thus, his results apply to initial value problems where the required function and its time derivative are given at the beginning of time. His general results are shown to reduce to the standard solutions for the classical wave problems for the case of two or three space variables. Whereas Bragg obtained fairly general results for the Cauchy problem, results for boundary value problems require a more specific approach. Hence, in the present work, results will be obtained for elastic half spaces acted upon by normal loads. This will reveal some complexities found in using an ascent method for boundary value problems which are not found in the Cauchy problem. Zukas et al. [2] made a study "to determine the feasibility" of using the plane strain mode of a two-dimensional code in lieu of a three-dimensional code for an oblique kinetic energy penetration problem. The results were compared with experimental data and very good agreement was found at early times. Brown [3] was also interested in applying the numerical results from a two-dimensional wavecode to the problem of impact of a spherical projectile onto a target surface. He was able to obtain approximate peak pressures for the spherical impactor from a numerical plane-strain solution.

The ascent method has been used in elastic wave propagation to solve two limited classes of problems. In the first class, the correspondence between point sources and line sources has been discussed in several papers [3–5], where emphasis has been placed on the corresponding displacements. In the second class, investigators [7–9] have used the method developed by Smirnov and Sobolev for self-similar problems. Since the original derivation of the method [10] required functional invariants, the technique was employed only to solve problems where the load could be expressed in terms of such invariants. In elastostatics, the method of ascent seems to have been used only by Weber [11]. Other previous work on axisymmetric mechanics problems has dealt only with either specific sources (see for example reference [12]) or with sources leading to self-similar problems [13].

In the use of computer codes to solve problems in fluid and solid mechanics, fully three-dimensional problems are more expensive to solve than two-dimensional problems [2]. Consequently, at least for axisymmetric problems, it seems advantageous to develop a technique for using two-dimensional codes combined with an ascent method to deduce the desired solution to a three-dimensional problem. However, for a general purpose code, the requirement of self-similar loads is too restrictive, and therefore, the present work deals with more general sources than those treated in [4–9], and for these new sources axisymmetry will be the main restriction.

It is of interest to note that, although the interest is in axisymmetric problems, a cylindrical coordinate system is not employed in the main part of the analysis. Instead, the basic equations are referred to a Cartesian coordinate system. The advantage of this is that the spectral representation of the solution is in terms of algebraic and trigonometric expressions rather than Bessel functions.

[1]This work performed at Sandia National Laboratories supported by the U.S. Department of Energy under contract number DE-AC04-76DP00789.

Contributed by the Applied Mechanics Division for presentation at the Winter Annual Meeting, New Orleans, La., December 9–14, 1984 of the AMERICAN SOCIETY OF MECHANICAL ENGINEERS.

Discussion on this paper should be addressed to the Editorial Department, ASME United Engineering Center, 345 East 47th Street, New York, N.Y. 10017, and will be accepted until two months after final publication of the paper itself in the JOURNAL OF APPLIED MECHANICS. Manuscript received by ASME Applied Mechanics Division, April, 1983. Paper No. 84-WA/APM-4.

Copies will be available until August, 1985.

Copyright © 1984 by ASME
Downloaded 02 May 2010 to 171.66.16.25. Redistribution subject to ASME license or copyright; see http://www.asme.org/terms/Terms_Use.cfm

2 Statement of the Problem

In a rectangular coordinate system, consider the problem of an axisymmetric, but otherwise arbitrary, load applied to the bounding surface $z=0$. The governing wave equations are

$$c_1^2 \nabla^2 \phi = \frac{\partial^2 \phi}{\partial t^2}, \quad c_2^2 \nabla^2 \psi = \frac{\partial^2 \psi}{\partial t^2}, \quad \Delta \cdot \psi = 0. \tag{1}$$

The potentials ϕ and ψ are related to the displacements $\mathbf{U}$ through

$$\mathbf{U} = \nabla \phi + \nabla \times \psi, \tag{2}$$

where c_1 and c_2 are the wave speeds, $\rho c_1^2 = \lambda + 2\mu$, $\rho c_2^2 = \mu$, λ and μ are the Lame constants and ρ is the material density. The stress-strain relations for the medium are

$$\tau_{ij} = \lambda \nabla^2 \phi \delta_{ij} + 2\mu \epsilon_{ij}, \quad \epsilon_{ij} = \frac{1}{2}\left(\frac{\partial U_i}{\partial x_j} + \frac{\partial U_j}{\partial x_i}\right), \tag{3}$$

where δ_{ij} is the Kronecker delta. The initial conditions are taken as

$$\phi(x,y,z,0) = \frac{\partial \phi}{\partial t}(x,y,z,0) = \psi(x,y,z,0) = \frac{\partial \psi}{\partial t}(x,y,z,0) = 0, \tag{4}$$

representing quiescence at $t=0$. The boundary conditions for the problems are

$$\tau_{zz}(x,y,0,t) = \mu g(x,y,t) H(t),$$
$$\tau_{yz}(x,y,0,t) = \tau_{xz}(x,y,0,t) = 0, \tag{5}$$

where $g(x,y,t)$ is the loading function assumed to be Fourier and/or Laplace transformable in all three variables and $H(t)$ is the Heaviside unit function. By the assumption of symmetry,

$$g(x,y,t) = G(r,t), \quad r^2 = x^2 + y^2, \tag{6}$$

for some function G. The potentials ϕ and ψ and the space derivatives of the potentials are required to vanish at infinity; that is, they must satisfy the radiation condition

$$\lim_{|x|,|y|,|z| \to \infty} [\phi(x,y,z,t), \psi(x,y,z,t), \text{etc.}] = 0. \tag{7}$$

3 Preliminaries-Method of Ascent for the Scalar Wave Equation

Before proceeding to the solution of the posed problem, it seems pertinent to illustrate the technique with the simplest possible case for the governing equations. Hence, consider the scalar wave equation for ϕ, with the initial conditions (4) and the conditions (7). The boundary condition for this function is

$$\phi(x,y,0,t) = Q(x,y,t) H(t). \tag{8}$$

In view of the initial, boundary, and radiation conditions, by the results in [14], the appropriate respresentation of the solution may be obtained by using Laplace and Fourier transforms defined, respectively, by the equations

$$f^L(x,y,z,p) = \int_0^\infty f(x,y,z,t) e^{-pt} dt, \tag{9a}$$

$$f(x,y,z,t) = (1/2\pi i) \int_{c-i\infty}^{c+i\infty} f^L(x,y,z,p) e^{pt} dp, \tag{9b}$$

$$f^{LFF}(k,v,z,p) = \int\int_{-\infty}^{\infty} f^L(x,y,z,p) e^{p(kx+vy)} dx\, dy, \tag{10a}$$

$$f^L(x,y,z,p) = (1/2\pi)^2 \int\int_{-\infty+i\epsilon}^{\infty+i\epsilon} f^{LFF}(k,v,z,p) e^{-i(x\xi+y\omega)} d\xi d\omega, \tag{10b}$$

where p, ξ, and ω are transform parameters, $k = i\xi/p$, $v = i\omega/p$, and c is chosen to the right of any singularity of $f^L(x,y,z,p)$. In accordance with Lerch's theorem [15], it is sufficient to assume in equations (9) and (10) that p is a real positive number, for this guarantees the existence of a unique inverse. In equation (10*b*), ϵ lies within the strip of convergence [16]. By applying these transforms in sequence to equation (1), in conjunction with the initial conditions, boundary condition, and radiation conditions, one finds the ordinary differential equation and its solution:

$$\frac{d^2 \phi^{LFF}}{dz^2} = p^2 \eta_1^2(k,v) \phi^{LFF},$$
$$\phi^{LFF}(k,v,z,p) = A(k,v,p) e^{-p\eta_1(k,v)z}, \tag{11}$$

where $\eta_1(k,v) = (a_1^2 - k^2 - v^2)^{1/2}$, $a_1 c_1 = 1$, and $Re\, \eta_1(k,v) \geq 0$; Re denotes the real part. Also,

$$A(k,v,p) = \int\int_{-\infty}^{\infty} Q^L(x,y,p) e^{p(kx+vy)} dx dy. \tag{12}$$

From equation (11) several special solutions may be obtained as follows. If Q is independent of y, then

$$Q(x,y,t) = q_2(x,t), \tag{13}$$

and

$$A(k,v,p) = 2\pi\delta(\omega) A_2(k,p),$$
$$A_2(k,p) = \int_{-\infty}^{\infty} q_2^L(x,p) e^{pkx} dx, \tag{14}$$

where the subscript 2 denotes a two-dimensional problem. In the case when the boundary condition is independent of time, that is, $\phi(x,y,t) = Q(x,y)$, then, for equation (11),

$$A(k,v,p) = 2\pi i \delta(p) Q^{FF}(k,v)^*, \tag{15}$$

where the subscript * means evaluated at $p=1$, and therefore

$$\phi^{LFF}(k,v,z,p) = 2\pi i \delta(p) Q^{FF}(k,v)^* e^{-p\eta_1(k,v)z}. \tag{16}$$

The inverse of this function satisfies Laplace's equation.

Assuming that Q depends only on t and the radial coordinate r defined by equation (6), then

$$Q(x,y,t) = q(r,t). \tag{17}$$

For the present purposes, it is necessary to find, when equation (17) is valid, a special form of ϕ showing its dependence on r and z. By rotating the axes of integration in equation (12) according to the equations

$$\nu x = Xk - Yv, \quad \nu y = Yk + Xv, \tag{18}$$

where $\nu = (k^2 + v^2)^{1/2} = i(\xi^2 + \omega^2)^{1/2}/p$, one finds that $r^2 = X^2 + Y^2$ and

$$A(k,v,p) = \int\int_{-\infty}^{\infty} q^L(r,p) e^{\nu p X} dX dY = B(\sqrt{k^2 + v^2}, p). \tag{19}$$

Hence A depends only on k and v through the combination $k^2 + v^2$. This result will be used in the sequel. For symmetric loads, the real axis lies within the strip of convergence and therefore ϵ in equation (10) may be set equal to zero. Thus, it follows from equation (11) that

$$\phi^L(x,y,z,p) = (1/2\pi)^2 \int\int_{-\infty}^{\infty} B(\sqrt{k^2 + v^2}, p) e^{-p\eta_1(k,v)z} e^{-i(x\xi+y\omega)} d\xi d\omega. \tag{20}$$

Now, by letting $x = r\cos\alpha$ and $y = r\sin\alpha$, and changing to cylindrical coordinates defined by

$$\xi = \sigma\cos\theta, \quad \omega = \sigma\sin\theta, \tag{21}$$

equation (20) may be written as

$$\phi^L(x,y,z,p) = (1/2\pi)^2 \int_0^{2\pi} \int_0^{\infty}$$

Downloaded 02 May 2010 to 171.66.16.25. Redistribution subject to ASME license or copyright; see http://www.asme.org/terms/Terms_Use.cfm

$$B(i\sigma/p,p)\,e^{-p\eta_1(i\sigma/p,0)z}e^{-i\tau\sigma\cos(\theta-\alpha)}\,\sigma d\sigma d\theta. \tag{22}$$

Since the limits of integration for θ are 0 and 2π, then α may be set equal to zero and equation (22) may be reduced to

$$\phi^L(x,y,z,p)=(1/2\pi^2)\int_0^{\pi}\int_0^{\infty} B(k,p)\,e^{-p\eta_1(k,0)z}\,\xi\cos(\xi r\cos\theta)d\xi d\theta, \tag{23}$$

where the dummy variable of integration has been changed from σ to ξ and $k=i\xi/p$. This is the special form needed for the ascent method.

Consider now the two-dimensional case when q_2 in equation (13) is an even function of x. Then, by the second of equations (14), it follows that A_2 is an even function of k. The solution to this symmetric two-dimensional problem is obtained by substituting the first of equations (14) into equation (11) and finding the inverse transform. This leads to the two-dimensional solution

$$\phi_2(x,z,p)=(1/2\pi)\int_{-\infty}^{\infty} A_2(k,p)\,e^{-p\eta_1(k,0)z}e^{-i\xi x}d\xi, \tag{24}$$

where the subscript 2 denotes a two-dimensional solution. However, since both A_2 and η_1 are even functions of k, $k=i\xi/p$, one finds that

$$\phi_2(x,z,p)=(1/\pi)\int_0^{\infty} A_2(k,p)e^{-p\eta_1(k,0)z}\cos\xi x d\xi. \tag{25}$$

By comparing equations (23) and (25), it follows that

$$\phi_3^L(r,z,p)=\phi^L(x,y,z,p)=(1/2\pi)\int_0^{\pi}\phi_2(r\cos\theta,z,p)d\theta, \tag{26}$$

provided that A_2 be related to B through

$$A_2(k,p)=\xi B(k,p), \tag{27}$$

and the subscript 3 denotes an axisymmetric solution. Since A_2 was assumed to be an even function of k, then, by this equation, B is required to be an odd function of k. The case requiring B as an even function of k will be treated in another section. By taking the inverse transform on time of equation (26), one finds that

$$\phi_3(r,z,t)=L_1\phi_2(x,z,t)=(1/2\pi)\int_0^{\pi}\phi_2(r\cos\theta,z,t)d\theta, \tag{28}$$

where the integral operator L_1 is defined by this equation.

Hence, given an axisymmetric source $q(r,t)$, the solution for ϕ_3 may be obtained by finding the corresponding solution for $\phi_2(x,z,t)$ and then using equation (28) to find ϕ_3.

It is important to note that this derivation assumed only an axisymmetric source which was Laplace transformable. By this assumption, it was possible to find the relation (27) for the associated two-dimensional problem. By direct differentiation of equation (28), the requirement that the source possess a Laplace transform may be removed, and thus the technique is more general than the methods in references [7–10, 17, and 18], which required self-similar solutions.

Equation (28) is readily invertible by the following process. Let $q=r\cos\theta$, and then let $q^2=u$, $r^2=s$. Equation (28) becomes an Abel integral equation [16] which leads to the solution

$$\phi_2(\sqrt{u},z,t)=2\sqrt{u}\,\frac{d}{du}\int_0^u\frac{\phi_3(\sqrt{s},z,t)ds}{(u-s)^{1/2}}. \tag{29}$$

The results in equations (28) and (29) may be generalized as indicated by the following results:

Result 1. If $\phi_2(x,z,t)$ is an even function of x and satisfies the equation

$$\frac{\partial^2\phi_2}{\partial x^2}+\frac{\partial^2\phi_2}{\partial z^2}=L(\phi_2,\partial\phi_2/\partial t,\partial^2\phi_2/\partial t^2,\text{etc.}), \tag{30}$$

where L is a linear combination of its arguments, then ϕ_3, given by equation (28), satisfies the equation

$$\frac{\partial^2\phi_3}{\partial r^2}+\frac{1}{r}\frac{\partial\phi_3}{\partial r}+\frac{\partial^2\phi_3}{\partial z^2}=L(\phi_3,\partial\phi_3/\partial t,\partial^2\phi_3/\partial t^2,\text{etc.}). \tag{31}$$

Result 2. If ϕ_2 satisfies the conditions of Result 1, then the function Ω_3, defined by

$$\Omega_3(r,z,t)=L_2\phi_2(x,z,t)=(1/2\pi)\int_0^{\pi}\phi_2(r\cos\theta,z,t)\cos\theta d\theta, \tag{32}$$

satisfies the equation

$$\frac{\partial^2\Omega_3}{\partial r^2}+\frac{1}{r}\frac{\partial\Omega_3}{\partial r}-\frac{\Omega_3}{r^2}+\frac{\partial^2\Omega_s}{\partial z^2}=L(\Omega_3,\partial\Omega_3/\partial t,\partial^2\Omega_3/\partial t^2,\text{etc.}). \tag{33}$$

The integral operator L_2 is defined by equation (32). Result 2 may be easily obtained by differentiating equations (28) and (31) with respect to r and defining Ω_3 as $\Omega_3=\partial\phi_s/\partial r$.

When L involves only the second time derivative, then equations (30), (31), and (33) are the equations satisfied by the elasticity displacement potentials of equation (1) in Cartesian and cylindrical coordinates [19]. Based on the analysis of this section, the problem posed by equations (1)–(7) will now be treated.

4 Three-Dimensional General Solution

Formal Solution. The application of (9) and (10) to the second of equations (1), using the indicated initial conditions, leads to the ordinary differential equation for ψ^{LFF} and its solution (see equation (11)):

$$\psi_j^{LFF}(k,v,z,p)=B_j(k,v,p)\,e^{-p\eta_3(k,v)z},\quad j=x,y,z, \tag{34}$$

where $\eta_2(k,v)=(a_2^2-k^2-v^2)^{1/2}$, $a_2c_2=1$ and $Re\,\eta_2(k,v)\geq 0$. Using this equation, and also equation (11), in the third of equations (1) and also in equations (2) and (3), one finds that

$$\eta_2\psi_z^{LFF}+k\psi_x^{LFF}+v\psi_y^{LFF}=0, \tag{35}$$

$$u_x^{LFF}=-pk\phi^{LFF}-pv\psi_z^{LFF}+p\eta_2\psi_y^{LFF}, \tag{36}$$

$$u_y^{LFF}=-pv\phi^{LFF}-p\eta_2\psi_x^{LFF}+pk\psi_z^{LFF}, \tag{37}$$

$$u_z^{LFF}=-p\eta_1\phi^{LFF}-pk\psi_y^{LFF}+pv\psi_x^{LFF}, \tag{38}$$

$$\tau_{zz}^{LFF}/\mu p^2=(a_2^2-2k^2-2v^2)\phi^{LFF}+2\eta_2(k\psi_y^{LFF}-v\psi_x^{LFF}), \tag{39}$$

$$\tau_{xz}^{LFF}/\mu p^2=(2k^2+v^2-a_2^2)\psi_y^{LFF}+2k\eta_1\phi^{LFF}+v\eta_2\psi_z^{LFF}-kv\psi_x^{LFF}, \tag{40}$$

$$\tau_{yz}^{LFF}/\mu p^2=(a_2^2-k^2-2v^2)\psi_x^{LFF}+2v\eta_1\phi^{LFF}+kv\psi_y^{LFF}-k\eta_2\psi_z^{LFF}, \tag{41}$$

where the dependence on k, v, z, and p is to be understood.

Application of the Boundary Conditions. By equations (5), it follows that

$$\tau_{zz}^{LFF}(k,v,0,p)=\mu g^{LFF}(k,v,p),\quad \tau_{xz}^{LFF}(k,v,0,p)=\tau_{yz}^{LFF}(k,v,0,p)=0. \tag{42}$$

Using these conditions and equation (35) to find A and B_j, one deduces that

$$p^2R(k,v)A(k,v,p)=(a_2^2-2k^2-2v^2)g^{LFF}(k,v,p), \tag{43}$$

$$p^2R(k,v)B_x(k,v,p)=-2v\eta_1(k,v)g^{LFF}(k,v,p), \tag{44}$$

$$p^2R(k,v)B_y(k,v,p)=2k\eta_1(k,v)g^{LFF}(k,v,p), \tag{45}$$

$$B_z(k,v,p)=0, \tag{46}$$

Downloaded 02 May 2010 to 171.66.16.25. Redistribution subject to ASME license or copyright; see http://www.asme.org/terms/Terms_Use.cfm

where $R(k,v)$ is the Rayleigh characteristic function defined by

$$R(k,v) = (a_2^2 - 2k^2 - 2v^2)^2 + 4(k^2+v^2)\eta_1(k,v)\eta_2(k,v). \quad (47)$$

These results are valid for an arbitrary load $g(x,y,t)$ which will be restricted in another section to the axisymmetric case given by equation (6).

5 Two-Dimensional Plane Strain Solution

Equations (1)–(5) of the three-dimensional case also apply for the plane-strain solution. However, it is now assumed that u_y vanishes everywhere and that u_x and u_z are independent of y. These assumptions yield the plane strain case in which, by the second of equations (3),

$$\epsilon_{iy} = \frac{1}{2}\left(\frac{\partial U_i}{\partial_y} + \frac{\partial U_y}{\partial x_i}\right) = 0 \quad (48)$$

for all i. Therefore $\tau_{xy} = \tau_{zy} = 0$ everywhere. Also, by these assumptions, the function g must be independent of y. Hence, if

$$g(x,y,t) = g_2(x,t), \quad (49)$$

then it immediately follows that

$$g^{LFF}(k,v,p) = 2\pi\delta(\omega) g_2^L(k,p). \quad (50)$$

Equations (11) and (34)–(47), with the special form of g^{LFF} in equation (50), apply directly in the plane-strain case. From equation (44), for a normal load, one finds that

$$B_x(k,v,p) = 0. \quad (51)$$

Considering now the case when g_2 is an even function of x, then g_2^L is an even function of k. The results in this case may be written in terms of the two functions F and I defined by

$$F(k,v,z,p) = \frac{(a_2^2 - 2k^2 - 2v^2)}{p^2 R(k,v)} g_2^L(k,v) e^{-p\eta_1(k,v)z}, \quad (52)$$

$$I(k,v,z,p) = \frac{2\eta_1(k,v)}{p^2 R(k,v)} g_2^L(k,v) e^{-p\eta_2(k,v)z}. \quad (53)$$

By the inversion of the Fourier transforms, it follows that

$$\phi_2^L(x,z,p) = \frac{1}{\pi}\int_0^\infty F(k,0,z,p)\cos(\xi x)d\xi, \quad (54)$$

$$\psi_{y2}^L(x,z,p) = \frac{1}{\pi i}\int_0^\infty kI(k,0,z,p)\sin(\xi x)d\xi, \quad (55)$$

where, as in equations (24) and (25), the subscript 2 denotes two-dimensional solutions, and $k = i\xi/p$. In a similar manner, one deduces that

$$u_{x2}^L(x,z,p) = \frac{1}{\pi i}\int_0^\infty pk[-F(k,0,z,p) + \eta_2(k,0)I(k,0,z,p)]\sin\xi x d\xi, \quad (56)$$

$$u_{z2}^L(x,z,p) = -\frac{1}{\pi}\int_0^\infty p[\eta_1(k,0)F(k,0,z,p) + k^2 I(k,0,z,p)]\cos\xi x d\xi, \quad (57)$$

$$\tau_{zz2}^L(x,z,p) = \frac{\mu p^2}{\pi}\int_0^\infty [(a_2^2 - 2k^2)F(k,0,z,p) + 2k^2\eta_2(k,0)I(k,0,z,p)]\cos\xi x d\xi, \quad (58)$$

$$\tau_{xz2}^L(x,z,p) = \frac{\mu p^2}{\pi i}\int_0^\infty k[2\eta_1(k,0)F(k,0,z,p) - (a_2^2 - 2k^2)I(k,0,z,p)]\sin\xi x d\xi. \quad (59)$$

6 Three-Dimensional Axisymmetric Solution

In this case, g is given by equation (6) and consequently g^{LFF} depends on k and v only through the combination $k^2 + v^2$; that is,

$$g^{LFF}(k,v,p) = Q(\sqrt{k^2+v^2}, p). \quad (60)$$

Corresponding to equations (52) and (53), the functions L and M are defined by

$$L(k,v,z,p) = \frac{(a_2^2 - 2k^2 - 2v^2)}{p^2 R(k,v)} Q(\sqrt{k^2+v^2}, p) e^{-p\eta_1(k,v)z}, \quad (61)$$

$$M(k,v,z,p) = \frac{2\eta_1(k,v)}{p^2 R(k,v)} Q(\sqrt{k^2+v^2}, p) e^{-p\eta_2(k,v)z}. \quad (62)$$

It seems appropriate at this point to introduce the usual cylindrical coordinate system such that $x = r\cos\alpha$ and $y = r\sin\alpha$, $z = z$. The components of the vector potential, the displacement vector, and the stress tensor will be referred to this coordinate system. For example,

$$\psi_\alpha = \psi_y\cos\alpha - \psi_x\sin\alpha. \quad (63)$$

The details of the Fourier transform inversion employed in going from equation (20)–(23), when applied to this case, lead to the equations

$$\phi_3^L(r,z,p) = \frac{1}{2\pi^2}\int_0^\pi\int_0^\infty L(k,0,z,p)\xi\cos(\xi r\cos\theta)d\xi d\theta, \quad (64)$$

$$\psi_{\alpha 3}^L(r,z,p) = \frac{1}{2i\pi^2}\int_0^\pi\cos\theta\int_0^\infty k\xi M(k,0,z,p)\sin(\xi r\cos\theta)d\xi d\theta, \quad (65)$$

$$[\psi_{r3}, \mu_\alpha, \tau_{\alpha z3}](r,z,t) = 0, \quad (66)$$

$$u_{r3}^L(r,z,p) = \frac{1}{2i\pi^2}\int_0^\pi\cos\theta\int_0^\infty pk[-L(k,0,z,p) + \eta_2(k,0)M(k,0,z,p)]\xi\sin(\xi r\cos\theta)d\xi d\theta, \quad (67)$$

$$u_{z3}^L(r,z,p) = -\frac{1}{2\pi^2}\int_0^\pi\int_0^\infty p[\eta_1(k,0)L(k,0,z,p) + k^2 M(k,0,z,p)]\xi\cos(\xi r\cos\theta)d\xi d\theta, \quad (68)$$

$$\tau_{zz3}^L(r,z,p) = \frac{\mu p^2}{2\pi^2}\int_0^\pi\int_0^\infty [(a_2^2 - 2k^2)L(k,0,z,p) + 2k^2\eta_2(k,0)M(k,0,z,p)]\xi\cos(\xi r\cos\theta)d\xi d\theta, \quad (69)$$

$$\tau_{rz3}^\Sigma(r,z,p) = \frac{\mu p^2}{2i\pi^2}\int_0^\pi\int_0^\infty k[2\eta_1(k,0)L(k,0,z,p) - (a_2^2 - 2k^2)M(k,0,z,p)]\xi\sin(\xi r\cos\theta)d\xi d\theta. \quad (75)$$

From these equations it is easy to see the following result:

Result 3. If g_2^L in equations (50)–(59) is selected as

$$g_2^L(k,p) = \xi Q(k,p), \quad (71)$$

where Q is an odd function of k, then the axisymmetric solution is given by

$$[\phi_3, U_{z3}, \tau_{zz3}](r,z,t) = L_1[\phi_2, U_{z2}, \tau_{zz2}](x,z,t), \quad (72,73,74)$$

$$[\psi_{\alpha 3}, U_{r3}, \tau_{rz3}](r,z,t) = L_2[\psi_{y2}, U_{x2}, \tau_{zz2}](x,z,t), \quad (75,76,77)$$

$$[\psi_{r3}, U_{\alpha 3}, \tau_{\alpha z3}](r,z,t) = 0, \quad (78)$$

where α is the angular coordinate.

Equations (72–78) correspond to those found by Smirnov and Sobolev. However, the restriction of self-similarity was not imposed in their derivation. Nevertheless, the requirement

Downloaded 02 May 2010 to 171.66.16.25. Redistribution subject to ASME license or copyright; see http://www.asme.org/terms/Terms_Use.cfm

that Q in equation (71) be an odd function of k means that these equations do not represent the most general solution. The case when Q is an even function of k will be treated next.

7 Extension of the Preceding Results

An arbitrary axisymmetric three-diemensional load may be decomposed into the sum of an even and an odd function of r. This may be seen as follows. For the load $\tau(r,t)$, if $\tau_1(r,t) = [\tau(r,t) - \tau(-r,t)]/2$, $\tau_2(r,t) = [\tau(r,t) + \tau(-r,t)]/2$, then it follows that τ_1 is an odd function of r, τ_2 is an even function of r, and $\tau(r,t) = [\tau_1(r,t) + \tau_2(r,t)]$. Since the previous results hold only for loads that are odd functions of r, corresponding results need to be derived for loads that are even functions of r. Equivalently, the previous results must now be extended to the case when $Q(k,p)$ is an even function of k. As was done in the preceding sections, the analysis will be done first for the scalar wave equation. In this manner, the necessary steps required in deriving the results will be clearly illustrated.

Preliminaries. Suppose that B in equation (23) is an even function of k, and consider the identity for the Bessel function J_0 [20,21] given by

$$J_0(\sigma r) = \frac{1}{\pi}\int_0^{\pi} \cos(\sigma r\cos\theta)d\theta = \frac{2}{\pi}\int_0^{\infty} \sin(\sigma r\cosh u)\,du. \tag{79}$$

By using this identity in equation (23), by expressing the sine in terms of exponentials, by a simple change of variable and from the assumption that B is an even function of k, it follows that

$$\phi^L(x,y,z,p) = \frac{i}{2\pi^2}\int_0^{\infty}\int_{-\infty}^{\infty} \xi B(k,p)\,e^{-p\eta_1(k,0)z}e^{-i\xi r\cosh u}\,d\xi\,du. \tag{80}$$

By comparing this equation with equation (24), and finding the inverse Laplace transform, one obtains the result

$$\phi_3(r,z,t) = L_3\phi_2(x,z,t) = (1/\pi)\int_0^{\infty} \phi_2(r\cosh u,z,t)du, \tag{81}$$

provided that

$$A_2(k,p) = i\xi B(k,p). \tag{82}$$

This equation imposes the requirement that A_2 be an odd function of k. Equation (81) serves as the definition of the integral operator L_3.

Results 1 and 2 remain valid when equation (28) is replaced by equation (81); and equation (32), by the equation

$$\Omega_3(r,z,t) = L_4\phi_2(x,z,t) = (1/\pi)\int_0^{\infty} \phi_2(r\cosh u,z,t)\cosh u\,du. \tag{83}$$

The integral operator L_4 is defined by this equation.

Axisymmetric Solution. To derive the results corresponding to equation (71)–(78), the identity for the Bessel function J_1 given by

$$J_1(\sigma r) = \frac{1}{\pi}\int_0^{\pi} \sin(\sigma r\cos\theta)\cos\theta\,d\theta = -\frac{2}{\pi}\int_0^{\infty} \cos(\sigma r\cosh u)\cosh u\,du$$

is required. By the assumption that $Q(k,p)$ in equations (60)–(71) is an even function of k, corresponding to equation (71), one finds that equations (64)–(75) may be used in this case by the following replacements:

$$\frac{1}{2\pi^2}\int_0^{\pi}\int_0^{\infty} (\cdots)\cos(\xi r\cos\theta)d\xi d\theta \to \frac{i}{2\pi^2}\int_0^{\infty}\int_{-\infty}^{\infty} (\cdots)e^{-i\xi r\cosh u}d\xi\,du, \tag{84}$$

$$\frac{1}{2i\pi^2}\int_0^{\pi}\cos\theta\int_0^{\infty} (\cdots)\sin(\xi r\cos\theta)d\xi d\theta \to \frac{i}{2\pi^2}\int_0^{\infty}\cosh u\int_{-\infty}^{\infty} (\cdots)e^{-i\xi r\cosh u}d\xi\,du. \tag{85}$$

For example, from equation (65),

$$\psi^L_{\alpha 3}(r,z,p) = \frac{i}{2\pi^2}\int_0^{\infty}\cosh u\int_{-\infty}^{\infty} k\xi M(k,0,z,p)e^{-i\xi r\cosh u}d\xi\,du, \tag{86}$$

and a further example is provided by the pair of equations (23) and (80).

Plane-Strain Solution. The required form for the present case is obtained directly from equations (54)–(59) by disregarding the assumption that g_2^L is an even function of k and making the following changes

$$\frac{1}{\pi}\int_0^{\infty} (\cdots)\cos\xi x d\xi \to \frac{1}{2\pi}\int_{-\infty}^{\infty} (\cdots)e^{-i\xi x}d\xi, \tag{87}$$

$$\frac{1}{\pi i}\int_0^{\infty} (\cdots)\sin\xi x d\xi \to \frac{1}{2\pi}\int_{-\infty}^{\infty} (\cdots)e^{-i\xi x}d\xi. \tag{88}$$

For example, from equation (55) one obtains

$$\psi^L_{y2}(x,z,p) = \frac{1}{2\pi}\int_{-\infty}^{\infty} kI(k,0,z,p)e^{-i\xi x}d\xi. \tag{89}$$

By the process indicated in equations (84)–(89), the following result is obtained:

Result 4. If g_2^L is selected such that

$$g_2^L(k,p) = i\xi Q(k,p), \tag{90}$$

where Q is an even function of k, then the axisymmetric solution is given by

$$[\phi_3, U_{z3}, \tau_{zz3}](r,z,t) = L_3[\phi_2, U_{z2}, \tau_{zz2}](x,z,t), \tag{91,92,93}$$

$$[\psi_{\alpha 3}, U_{r3}, \tau_{rz3}](r,z,t) = L_4[\psi_{y2}, U_{x2}, \tau_{xz2}](x,z,t), \tag{94,95,96}$$

$$[\psi_{r3}, U_{\alpha 3}, \tau_{\alpha z3}](r,z,t) = 0. \tag{97}$$

Since multiplying the Fourier transform by $-i\xi$ corresponds to differentiating with respect to x, then Result 5 is obtained:

Result 5. If g_2^L is selected such that

$$g_2^L(k,p) = Q(k,p), \tag{98}$$

where Q is an even function of k, then the axisymmetric solution is given by

$$[\phi_3, U_{z3}, \tau_{zz3}](r,z,t) = -L_3[\phi_2, U_{z2}, \tau_{zz2}]'(x,z,t), \tag{99,100,101}$$

$$[\psi_{\alpha 3}, U_{r3}, \tau_{rz3}](r,z,t) = -L_4[\psi_{y2}, U_{x2}, \tau_{xz2}]'(x,z,t), \tag{102,103,104}$$

$$[\psi_{r3}, U_{\alpha 3}, \tau_{\alpha z3}](r,z,t) = 0, \tag{105}$$

where the prime denotes differentiation with respect to x. For example,

$$\phi_3(r,z,t) = -(1/\pi)\int_0^{\infty} \frac{\partial\phi_2(x,z,t)}{\partial x}\bigg|_{z=r\cosh u} du.$$

8 Discussion

In the preceding sections, an ascent method was developed for using two-dimensional solutions as the basis for finding axisymmetric solutions. The generality of the development made it possible to generate new results and to extend the

Downloaded 02 May 2010 to 171.66.16.25. Redistribution subject to ASME license or copyright; see http://www.asme.org/terms/Terms_Use.cfm

validity of previous results. Thus, equations (28) and (30)–(33) extend the results in [10] from self-similar dynamic solutions to arbitrary dynamic or static solutions, subject only to the restriction in equation (27). Result 4 is a new result, while Result 5 is an extension of the work in [3,22,23] which relates dynamic line sources and point sources. However, this result holds also for static solutions as will now be shown. For a point load, by equations (6) and (60), one has

$$g(x,y,t) = f(t)\,\delta(x)\,\delta(y), \quad Q(\sqrt{k^2+v^2},p) = f^L(p).$$

For a line load, by equations (49) and (50),

$$g(x,y,t) = f(t)\,\delta(x), \quad g_2^L(k,p) = f^L(p).$$

Hence, equation (98) holds and, for both the dynamic and the static case, equations (99)–(105) apply. For the dynamic displacements, this is a well-known result [3–5,22,23]. But, for the other dynamic quantities and for the static case, this is a new result which may be verified by taking the solution for a line load [24, Article 33]:

$$[\tau_{zz2}, \tau_{xz2}](x,z) = -\frac{2P}{\pi}\,\frac{z^2}{(x^2+z^2)^2}\,[z,x].$$

By equations (101) and (104), it follows that

$$[\tau_{zz3}, \tau_{rz3}](r,z) = -\frac{3P}{2\pi}\,\frac{z^2}{(r^2+z^2)^{5/2}}\,[z,r].$$

These are precisely the formulas derived in [24, Article 123] by a different method.

Although this paper dealt only with loads applied to the surface of a half space, it is important to note that the results can be extended to more general boundary value problems, as has been done for self-similar problems [7–10,25,26] which represent special cases of the present theory. For the required two-dimensional self-similar problem, the solution technique in [27] would be directly applicable.

References

1 Bragg, L. R., "The Ascent Method for Abstract Wave Problems," *J. Differential Equations*, Vol. 38, 1980, pp. 413–421.

2 Zukas, J. A., Jonas, G. H., and Misey, J. J., "On the Utility of Plane Strain Approximations for Oblique Impact Computations," Memorandum Report ARBRL-MR-02969, Ballistic Research Laboratory, Aberdeen Proving Ground, Md., 1979.

3 Brown, W. T., "Numerical Modeling of Oblique Impact Using Two-Dimensional Plane Strain Models," *Shock Waves in Condensed Matter—1981* (Menlo Park), AIP Conference Proceedings No. 78, Nellis, W. J., Seaman, L., and Graham, R. A., eds., American Institute of Physics, 1982.

4 Thau, S. A., and Pao, Y.-H., "On the Derivation of Point Source Responses From Line Source Solutions," *Inter. J. Eng. Sci.*, Vol. 8, 1970, pp. 207–218.

5 Thau, S. A., and Pao, Y.-H., "Comments on Two and Three-Dimensional Wave Propagation," *Bull. Seism. Soc. America*, Vol. 63, 1973, p. 329.

6 Norwood, F. R., "Remarks on the Paper by C. N. G. Dampney 'The Relationship Between Two- and Three-Dimensional Elastic-Wave Propagation,'" *Bull. Seism. Soc. America*, Vol. 63, 1973, pp. 1173–1174.

7 Nikitin, L. V., and Odintsev, V. N., "Axisymmetric Self-Similar Dynamic Problems for an Elastic Half-Space With Mixed Moving Boundary Conditions," *Archiwum Mechaniki Stosowanej*, Vol. 25, 1973, pp. 351–363.

8 Robinson, A. R., and Thompson, J. C., "Transient Stresses in an Elastic Half Space Resulting from the Frictionless Indentation of a Rigid Axially Symmetric Conical Die," *Proc. Camb. Phil. Soc.*, Vol. 76, 1974, pp. 369–379.

9 Zvolinskii, N. V., "Reflected and Head Waves Emerging at a Plane Interface of Two Elastic Media—I," *Bull. Acad. Sci. USSR, Geophys. Ser. (English Transl.)*, Vol. 10, 1957, pp. 1–21.

10 Smirnov, V., and Sobolev, S., "Sur L'Application de la Methode Nouvelle a L'Etude des Vibrations Elastiques dans L'Espace a Symetrie Axiale," *Trudy Seismologicheskobo Instituta*, No. 29, 1933, pp. 1–49.

11 Weber, C., "Zur Umwandlung von rotationssymmetrischen Problemen in zweidimensionale und umgekert," *Z. angew. Math. Mech.*, Vol. 20, 1940, pp. 117–118.

12 Aggarwal, H. R., and Ablow, C. M., "Disturbance From a Circularly Symmetric Load Spreading over an Acoustic Half-Space," *Bull. Seism. Soc. America*, Vol. 55, 1965, pp. 673–691.

13 Craggs, J. W., "On Axially Symmetric Waves, III. Elastic Waves in a Half-Space," *Proc. Camb. Phil. Soc.*, Vol. 59, 1963, pp. 803–809.

14 Freidman, B., *Principles and Techniques of Applied Mathematics*, Wiley, New York, 1956.

15 Carslaw, H. S., and Jaeger, J. C., *Operational Methods in Applied Mathematics*, Oxford University Press, London, 1941.

16 Van Der Pol, B., and Bremmer, H., *Operational Calculus Based on the Two-Sided Laplace Integral*, Cambridge University Press, London, 1964.

17 Atkinson, C., "On Axially Symmetric Expanding Boundary Value Problems in Classical Elasticity," *Int. J. Engrg. Sci.*, Vol. 6, 1968, pp. 27–35.

18 Willis, J. R., "Self-Similar Problems in Elastodynamics," *Phil. Trans. Roy. Soc. London*, Vol. 274, 1973, pp. 435–491.

19 Achenbach, J. D., *Wave Propagation in Elastic Solids*, North Holland, Amsterdam, 1976.

20 Abramowitz, M., and Stegun, I. A., *Handbook of Mathematical Functions*, National Bureau of Standards, U.S. Government Printing Office, Washington, D.C., 1964.

21 Watson, G. N., *A Treatise on the Theory of Bessel Functions*, Cambridge University Press, London, 1966.

22 Ewing, W. M., Jardetzky, W. S., and Press, F., *Elastic Waves in Layered Media*, McGraw-Hill, New York, 1957.

23 Lloyd, J. R., "Wave Propagation in an Elastic Plate Resting on an Elastic Foundation," Ph.D. Thesis, California Institute of Technology, 1962.

24 Timoshenko, S., and Goodier, J. N., *Theory of Elasticity*, McGraw-Hill, New York, 1951.

25 Zaitsev, L. P., and Zvolinskii, N. V., "Investigation of a Head Wave Emerging at the Plane Interface of Two Elastic Liquids," *Izv. Akad. Nauk SSSR, Ser. Geofiz.*, No. 1, 1951.

26 Zaitsev, L. P., and Zvolinskii, N. V., "Investigation of a Line-Symmetric Head Wave Emerging at a Plane Interface of Two Elastic Liquids," *Izv. Akad. Nauk SSSR, Ser. Geofiz.*, No. 5, 1951.

27 Norwood, F. R., "Similarity Solutions in Plane Elastodynamics," *Int. J. Solids Structures*, Vol. 9, 1973, pp. 789–803.

Downloaded 02 May 2010 to 171.66.16.25. Redistribution subject to ASME license or copyright; see http://www.asme.org/terms/Terms_Use.cfm

Thermoelastic Displacements and Stresses Due to a Heat Source Moving Over the Surface of a Half Plane

J. R. Barber
Department of Mechanical Engineering
and Applied Mechanics,
University of Michigan,
Ann Arbor, Mich. 48109

A solution is given for the surface displacement and stresses due to a line heat source that moves at constant speed over the surface of an elastic half plane. The solution is obtained by integration of previous results for the instantaneous point source. The final results are expressed in terms of Bessel functions for which numerically efficient series and asymptotic expressions are given.

Introduction

If two thermally conducting bodies are in sliding contact, the frictional heat generated at the interfaces causes thermoelastic distortion which profoundly influences the extent of the contact area and the distribution of contact stress [1]. This phenomenon – now known as thermoelastic instability – has been observed experimentally in a wide range of practical sliding systems [2, 3].

Several theoretical solutions have been obtained to problems of this kind, e.g., [4–6], but most make the assumption that one of the bodies is either rigid or a nonconductor or both, thus ensuring that the temperature field is stationary in the deformable solid.

In the more general problem, the contact area and hence the temperature field will move with respect to both solids. One way to treat problems of this kind is to use the Green's function for a moving heat source on the surface of the body. The two-dimensional Green's function for a heat source moving over the surface of an elastic half plane was first investigated by Ling and Mow [7], who used Fourier transformation to obtain a simplified solution in which conduction of heat in the direction of motion is neglected. This approximation is justified at large Peclet number – i.e., when

$$\frac{Vx_0}{k} >> 1 \qquad (1)$$

where V is the source velocity, x_0 is a characteristic length for the problem and k is the thermal diffusivity of the material.

More recently, Kilaparti and Burton [8] have developed an exact Fourier series solution for a periodic strip heat input. Their series is rather unwieldly, but at large Vx_0/k, it reduces to a form [9] that is simpler than that of Ling and Mow [7].

Contributed by the Applied Mechanics Division for presentation at the Winter Annual Meeting, New Orleans, La., December 9–14, 1984 of THE AMERICAN SOCIETY OF MECHANICAL ENGINEERS.

Discussion on this paper should be addressed to the Editorial Department, ASME, United Engineering Center, 345 East 47th Street, New York, N.Y. 10017, and will be accepted until two months after final publication of the paper itself in the JOURNAL OF APPLIED MECHANICS. Manuscript received by ASME Applied Mechanics Division, May, 1983, Paper No. 84-WA/APM-17.

Copies will be available until August, 1985.

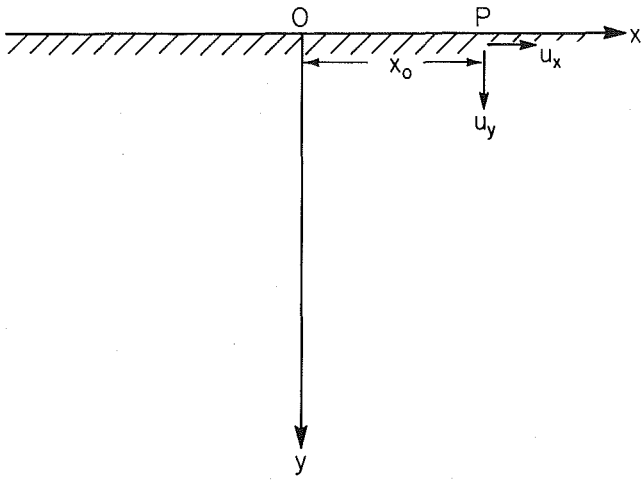


Fig. 1 The heat source is moving to the right at speed *V* and has just reached 0. Stresses and displacements are to be found at *P*.

Tseng and Burton [10] have extended this solution to give the tangential surface stress due to a moving heat source.

In this paper, we shall develop the Green's function for the problem of Kilaparti and Burton, by superposition of previously published results for the instantaneous point heat source [11]. The results obtained are expressed in a simple form and are exact for all values of Vx_0/k in the context of quasi-static, uncoupled thermoelasticity.

Solution

The fundamental problem is illustrated in Fig. 1. A line heat source, q per unit length per unit time, moves from left to right at constant speed V on the traction-free surface of an elastic half plane. We wish to find the components of displacement, u_x, u_y and stress σ_{xx} at the point $P(x_0,0)$ on the surface when the source has reached the origin 0. Plane-strain conditions are assumed.

The moving source can be considered as a sequence of instantaneous sources of strength $q\ \delta t$ at time $(-t)$ and

Copyright © 1984 by ASME
Downloaded 02 May 2010 to 171.66.16.25. Redistribution subject to ASME license or copyright; see http://www.asme.org/terms/Terms_Use.cfm

position $(-Vt, 0)$ as t takes all the values in the range $0<t<\infty$.

The surface displacements at $(x, 0)$ due to an instantaneous source Q at $(0, 0)$ are given in [11] as

$$u_x = \frac{\alpha Q(1+\nu)}{\pi\rho c(kt)^{1/2}} \frac{(1-e^{-X^2})}{X} \tag{2}$$

$$u_y = -\frac{\alpha Q(1+\nu)}{\pi\rho c(kt)^{1/2}} F_1(R) \tag{3}$$

where

$$F_1(R) = \frac{2}{\pi^{1/2}} \frac{e^{-R^2}}{R} \int_0^R e^{S^2}\, dS \tag{4}$$

$$X = x/(4kt)^{1/2} \tag{5}$$

$$R = |X| \tag{6}$$

and α, ν, ρ, c are the coefficient of thermal expansion, Poisson's ratio, density, and specific heat, respectively, for the material.

If follows that the displacement components for the moving source are

$$u_x = \frac{\alpha(1+\nu)q}{\pi\rho c k^{1/2}} \int_0^\infty \frac{(1-e^{-X^2})}{X} \frac{dt}{t^{1/2}} \tag{7}$$

$$u_y = -\frac{\alpha(1+\nu)q}{\pi\rho c k^{1/2}} \int_0^\infty F_1(R) \frac{dt}{t^{1/2}} \tag{8}$$

where

$$X = (x_0 + Vt)/(4kt)^{1/2} \tag{9}$$

We shall evaluate the integrals (7) and (8) by substituting for t in terms of X (or R). It is convenient to consider the cases $x_0 > 0$, $x_0 < 0$ separately.

(i) $x_0 > 0$. The results for $x_0 > 0$ correspond to points P which have not yet been passed by the source. We note from equations (9) and (6) that $R = X$ and that $X \to \infty$ at both ends of the range of integration ($t \to \infty$, $t \to 0$). There is therefore a time t_0 at which X is a minimum, which occurs when

$$\frac{dX}{dt} = \frac{Vt - x_0}{2t(4kt)^{1/2}} = 0 \tag{10}$$

i.e.,

$$t = t_0 = x_0/V. \tag{11}$$

Substituting in equation (9), we find the minimum value of X is

$$X_0 = (Vx_0/k)^{1/2} \tag{12}$$

Solving equation (9) for t, we find

$0 < t < t_0$

$$t = t_1 = k\{2X^2 - X_0^2 - 2\sqrt{X^2(X^2 - X_0^2)}\}/V^2 \tag{13}$$

$t > t_0$

$$t = t_2 = k\{2X^2 - X_0^2 + 2\sqrt{X^2(X^2 - X_0^2)}\}/V^2 \tag{14}$$

and hence we can rewrite equation (7) in the form

$$u_x = \frac{\alpha(1+\nu)q}{\pi\rho c k^{1/2}} \left[\int_0^{t_0} \frac{(1-e^{-X^2})}{X} \frac{dt_1}{t_1^{1/2}} + \int_{t_0}^\infty \frac{(1-e^{-X^2})}{X} \frac{dt_2}{t_2^{1/2}}\right] \tag{15}$$

$$= \frac{\alpha(1+\nu)q}{\pi\rho c k^{1/2}} \int_{X=X_0}^{X=\infty} \frac{(1-e^{-X^2})}{X} \left\{\frac{dt_2}{t_2^{1/2}} - \frac{dt_1}{t_1^{1/2}}\right\} \tag{16}$$

Finally, differentiating (13) and (14) and substituting for t_1, t_2 into (16) we find

$$\left\{\frac{dt_2}{t_2^{1/2}} - \frac{dt_1}{t_1^{1/2}}\right\} = \frac{4k^{1/2}dX}{V\sqrt{1 - X_0^2/X^2}} \tag{17}$$

and hence

$$u_x = \frac{4\alpha(1+\nu)q}{\pi\rho c\, V} \int_{X_0}^\infty \frac{(1-e^{-X^2})dX}{\sqrt{X^2 - X_0^2}} \tag{18}$$

Similarly, from equations (8) and (17)

$$u_y = -\frac{4\alpha(1+\nu)q}{\pi c\rho V} \int_{X_0}^\infty \frac{XF_1(X)dX}{\sqrt{X^2 - X_0^2}} \tag{19}$$

(ii) $x_0 < 0$. When the source has passed P and $x_0 < 0$, there is no minimum value of X as defined by equation (10) and X varies monotonically from $-\infty$ to $+\infty$ through the range of integration. Solving equation (9) for t, we find

$0 < t < t_0$, $X < 0$

$$t = t_1 = k\{2X^2 + X_0^2 - 2\sqrt{X^2(X^2 + X_0^2)}\}/V^2 \tag{20}$$

$t > t_0$, $X < 0$

$$t = t_2 = k\{2X^2 + X_0^2 + 2\sqrt{X^2(X^2 + X_0^2)}\}/V^2 \tag{21}$$

where we now redefine

$$t_0 = -x_0/V \tag{22}$$

$$X_0 = (-V x_0/k)^{1/2} \tag{23}$$

Notice that X_0 is *not* now the minimum value of X – in fact $X \to 0$ as $t \to t_0$, as can be seen on substituting (22) into (9). The time $t = t_0$ corresponds in this case to the instant when the source is passing the point P.

Equation (15) now takes the form

$$u_x = \frac{\alpha(1+\nu)q}{\pi\rho c k^{1/2}} \int_{X=-\infty}^{X=0} \left[\frac{(1-e^{-X^2})}{X} \frac{dt_1}{t_1^{1/2}} + \int_{X=0}^{X=+\infty} \frac{(1-e^{-X^2})}{X} \frac{dt_2}{t_2^{1/2}}\right] \tag{24}$$

and since $(1-e^{-X^2})/X$ is odd in X, the two integrals can be combined to give

$$u_x = \frac{\alpha(1+\nu)q}{\pi\rho\, ck^{1/2}} \int_{X=0}^{X=\infty} \frac{(1-e^{-X^2})}{X} \left\{\frac{dt_2}{t_2^{1/2}} + \frac{dt_1}{t_1^{1/2}}\right\} \tag{25}$$

After substitution from equations (20) and (21), this reduces to

$$u_x = \frac{4\alpha(1+\nu)q}{\pi\rho c\, V} \int_0^\infty \frac{(1-e^{-X^2})dX}{\sqrt{X^2 + X_0^2}} \tag{26}$$

We follow a similar procedure to determine u_y, but, since $F_1(X)$ an even function, we find

$$u_y = -\frac{\alpha(1+\nu)q}{\pi\rho c k^{1/2}} \int_{X=0}^{X=\infty} F_1(X) \left\{\frac{dt_2}{t_2^{1/2}} - \frac{dt_1}{t_1^{1/2}}\right\} \tag{27}$$

$$= -\frac{4\alpha(1+\nu)q}{\pi\rho c\, V} \int_0^\infty F_1(X)\, dX \tag{28}$$

after substitution.

Notice that equation (28) is independent of X_0. In other words, the normal displacement u_y remains constant once the source has passed P.

(iii) **Stress at the Surface.** We anticipate that the maximum thermal stress due to the moving source will occur at the surface and hence we calculate the component σ_{xx} (the other two components σ_{xy}, σ_{yy} being zero because of the zero traction condition). Expressions for σ_{xx} are not given in [11],

Downloaded 02 May 2010 to 171.66.16.25. Redistribution subject to ASME license or copyright; see http://www.asme.org/terms/Terms_Use.cfm

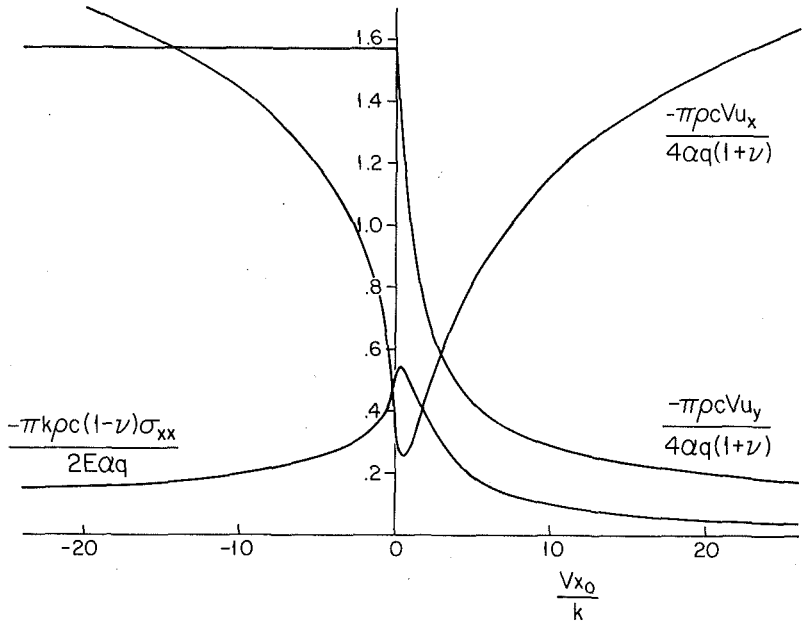


Fig. 2 Displacement u_x, u_y and tangential stress σ_{xx} as functions of Vx_0/k. The source is at 0 and is moving to the right at speed V.

but they are easily obtained in the same manner as the displacement components by superposition of an axisymmetric thermal stress field and an isothermal correction field to leave surface free of traction. The contribution from the axisymmetric field is given by equations (3) and (4) of [11].

If a half plane is subjected to a purely normal traction σ_{yy}, it can be shown that the stress σ_{xx} induced at the surface is everywhere equal to σ_{yy} (except for a possible additive constant). Hence, the corrective traction that cancels the component $\sigma_{\theta\theta}$ (equation (4) of [11]) leaves behind a stress

$$\sigma_{(xx=0)} = \sigma_{rr} - \sigma_{\theta\theta} = -\frac{\alpha QE}{2\pi\rho c(1-\nu)kt}\left[\frac{(1-e^{-R^2})}{R^2} - e^{-R^2}\right] \tag{29}$$

Following the same procedure as in the preceding section, we find that the moving source produces a surface stress

$$\sigma_{xx} = -\frac{\alpha Eq}{2\pi\rho c(1-\nu)k}\int_0^\infty\left[\frac{1-e^{-R^2}}{R^2} - e^{-R^2}\right]\frac{dt}{t} \tag{30}$$

The integrand is even in R and hence the substitution process is similar to that used for u_y in section (*ii*). For $X_0 > 0$,

$$\sigma_{xx} = -\frac{\alpha Eq}{2\pi\rho c(1-\nu)k}\int_{X=X_0}^{X=\infty}\left[\frac{1-e^{-X^2}}{X^2} - e^{-X^2}\right]\left(\frac{dt_2}{t_2} - \frac{dt_1}{t_1}\right) \tag{31}$$

$$= \frac{2\alpha Eq}{\pi\rho c(1-\nu)k}\int_{X_0}^\infty\left[\frac{1-e^{-X^2}}{X^2} - e^{-X^2}\right]\frac{dX}{\sqrt{X^2-X_0^2}} \tag{32}$$

while for $x_0 < 0$,

$$\sigma_{xx} = -\frac{\alpha Eq}{2\pi\rho c(1-\nu)k}\int_{X=0}^{X=\infty}\left[\frac{1-e^{-X^2}}{X^2} - e^{-X^2}\right]\left(\frac{dt_2}{t_2} - \frac{dt_1}{t_1}\right) \tag{33}$$

$$= -\frac{2\alpha Eq}{\pi\rho c(1-\nu)k}\int_0^\infty\left[\frac{1-e^{-X^2}}{X^2} - e^{-X^2}\right]\frac{dX}{\sqrt{X^2+X_0^2}} \tag{34}$$

In each case, definitions of t_1, t_2, and X_0 are as in the appropriate part of section (11).

Results

The integrals in equations (18), (19), (26), (28), (30), and (34) are evaluated in Appendix I, giving the results

$$u_x = -\frac{2\alpha q(1+\nu)}{\pi\rho c\ V}\left\{\log\left|\frac{Vx_0}{k}\right| + e^{-Vx_0/2k}K_0\left(\frac{Vx_0}{2k}\right)\right\} + C \tag{35}$$

$$u_y = -\frac{2\alpha q(1+\nu)}{\rho c\ V}e^{-Vx_0/2k}I_0\left(\frac{Vx_0}{2k}\right); x_0 > 0 \tag{36}$$

$$= -\frac{2\alpha q(1+\nu)}{\rho c\ V}; \quad x_0 < 0 \tag{37}$$

$$\sigma_{xx} = -\frac{2\alpha qE}{\pi\rho c(1-\nu)k}\left\{\frac{k}{Vx_0} - \frac{1}{2}e^{-Vx_0/2k}K_1\left(\frac{Vx_0}{2k}\right)\right\}. \tag{38}$$

Equations (35) and (38) are valid for all values of x_0 provided we interpret $K_0(-x) = K_0(x)$, $K_1(-x) = -K_1(x)$.

The expression for u_x is unbounded as $x_0 \to \pm\infty$ and hence the tangential displacement cannot be referred to the point at infinity. For this reason, it might be more convenient in some applications to use the derivative

$$\frac{\partial u_x}{\partial x} = -\frac{2\alpha q(1+\nu)}{\pi\rho ck}\left\{\frac{k}{Vx_0} - \frac{1}{2}e^{-Vx_0/2k}\left[K_1\left(\frac{Vx_0}{2k}\right) + K_0\left(\frac{Vx_0}{2k}\right)\right]\right\} \tag{39}$$

We also record here the surface temperature due to the moving source which is

$$T = \frac{q}{\pi k\rho c}e^{-Vx_0/2k}K_0\left(\frac{Vx_0}{2k}\right) \tag{40}$$

(see Carslaw and Jaeger [12] Section 10.7).

The results for u_x, u_y, and σ_{xx} are plotted in Fig. 2. Notice that the maximum (compressive) value of σ_{xx} and the minimum u_x occur just ahead of the heat source, while the normal displacement u_y is constant behind the source.

Downloaded 02 May 2010 to 171.66.16.25. Redistribution subject to ASME license or copyright; see http://www.asme.org/terms/Terms_Use.cfm

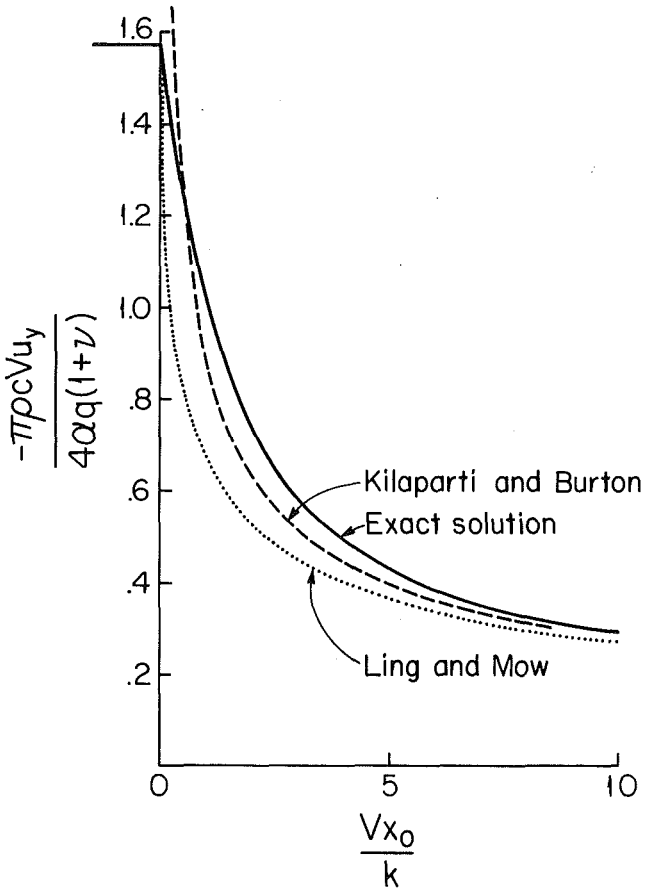


Fig. 3 Comparison of the solution for u_y – equation (36), with the approximate solution of Ling and Mow [7] and the one-term asymptotic expression of Kilaparti and Burton [9]

Numerical Evaluation and Convergence. The principal use of these results is as a Green's function for thermoelastic contact with moving heat sources. Such problems tend to involve extensive numerical computations and it is therefore important to find representations that can be easily and efficiently evaluated numerically.

The Bessel functions I_0, K_0, K_1, occurring in equations (35)–(40) can be expanded in convergent series when Vx_0/k is small and in asymptotic expansions when it is large. The appropriate expressions are given in Appendix II. Notice that the singular terms in equations (35), (38) are (39) cancel corresponding terms in the Bessel function expansions, leaving a bounded result at $Vx_0/k = 0$.

In all cases, the ranges of the two forms overlap to give good accuracy throughout the range. The series for u_y (equations (36), (A22)) is particularly convergent. For example, four-digit accuracy throughout the range can be obtained by using just the first six terms of (A22) for $0 < Vx_0/k < 8$ and six terms of the asymptotic expansion (A26) for $Vx/k > 8$. By contrast, Kilaparti and Burton [9] used 1000 terms to evaluate their Fourier expansion solution for u_y and Tseng and Burton [10] needed 5000 terms for convergence of their expansion of σ_{xx}.

Comparison With Previous Approximate Solutions. In Fig. 3, Ling and Mow's approximate solution [7] for u_y is compared with the exact solution (equation (36)). Ling and Mow's analysis is restricted to large Peclet number, which for the moving point source is equivalent to $|Vx_0/k| >> 1$. As we would expect, an asymptotic expansion of their result has the same leading term as equations (36), and (A26) except for a factor of 2 error in [7], noted already by Kilaparti and Burton [9]. This leading term was also extracted by Kilaparti and Burton [9, equation (25)] and is plotted in Fig. 3. It actually turns out to be a better approximation to the exact solution than Ling and Mow's expression except for $Vx_0/k < 0.4$.

Acknowledgement

The author gratefully acknowledges support from the U.S. Army under contract DAAG 29-82-K-0001.

References

1 Barber, J. R., "Thermoelastic Instabilities in the Sliding of Conforming Solids," *Proc. Roy. Soc.*, Series *A*, Vol. 312, 1969, pp. 381–394.

2 Burton, R. A., ed., "Thermal Deformation in Frictionally Heated Systems," Proceedings of a workshop held at Annapolis Md., June 1979; *Wear*, Vol. 59 1980.

3 Dow, T. A., ed., "Thermomechanical Effects in Wear, "Proceedings of workshop held at Columbus, Ohio, June 1981, *Wear*, Vol. 79, 1982.

4 Burton, R. A., Kilaparti, S. R., and Nerlikar, V., "A Limiting Stationary Configuration With Partially Contacting Surfaces," *Wear*, Vol. 24, 1973, pp. 199–206.

5 Barber, J. R., "Some Thermoelastic Contact Problems Involving Frictional Heating," *Q. J. Mech. Appl. Math*, Vol. 29, 1976, pp. 1–13.

6 Burton, R. A., and Nerlikar, V., "Large Disturbance Solutions for Initially Flat, Frictionally Heated Thermoelastically Deformed Surfaces," ASME *Journal of Lubrication Technology*, Vol. 97, 1975, pp. 539–545.

7 Ling, F. F., and Mow, V. C., "Surface Displacement of a Convective Elastic Half-Space Under an Arbitrarily Distributed Fast-Moving Heat Source," ASME *Journal of Basic Engineering*, Vol. 87, 1965, pp. 729–734.

8 Kilaparti, S. R., and Burton, R. A., "A Moving Hot-Spot Configuration for a Seal-Like Geometry, With Frictional Heating, Expansion and Wear," ASLE *Trans.*, Vol. 20, 1977, pp. 64–70.

9 Kilaparti, S. R., and Burton, R. A., "The Thermoelastic Patch Contact Problem for Large Peclet Number," ASME *Journal of Lubrication Technology*, Vol. 100, 1978, pp. 65–69.

10 Tseng, M. L., and Burton, R. A., "Thermal Stress in a Two-Dimensional (Plane Stress) Half-Space for a Moving Heat Input," *Wear*, Vol. 79, 1982, pp. 1–9.

11 Barber, J. R., and Martin-Moran, C. J., "Green's Functions for Transient Thermoelastic Contact Problems for the Half-Plane," *Wear*, Vol. 79, 1982, pp. 11–19.

12 Carslaw, H. S., and Jaeger, J. C., *Conduction of Heat in Solids*, 2nd Ed., Clarendon Press, Oxford, 1959.

13 Gradshteyn, I. S., and Ryzhik, I. M., (GR), *Tables of Integrals Series and Products*, Academic Press, New York, 1980.

APPENDIX I

Evaluation of Integrals

In this appendix, we evaluate the integrals in equations (18), (19), (26), (28), (30), and (34) in terms of Bessel functions.

(*i*) The integral

$$I_1 = \int_{X_0}^{\infty} \frac{(1-e^{-X^2})dX}{\sqrt{X^2-X_0^2}} \tag{A1}$$

from equation (18) is unbounded becuase of the behavior of the integrand at infinity. However, we can write $I_1 = J_1 + J_2$ where

$$J_2 = -\int_{X_0}^{\infty} \frac{e^{-X^2}\,dX}{\sqrt{X^2-X_0^2}} \tag{A2}$$

and is bounded, and

$$\frac{dJ_1}{dX_0} = \underset{c\to\infty}{Lt} \frac{d}{dX_0}\int_{X_0}^{c} \frac{dX}{\sqrt{X^2-X_0^2}} = -\frac{1}{X_0}. \tag{A3}$$

Substituting $X = X_0\, ch(y)$ in (A2), we find

$$J_2 = e^{-X_0^2/2}\int_0^{\infty} e^{-\frac{1}{2}R_0^2\, ch(2y)}\,dy = -1/2\; e^{-\frac{X_0^2}{2}} K_0\left(\frac{X_0^2}{2}\right) \tag{A4}$$

by G R, Section 3.547 [13].

Hence, we can write

Downloaded 02 May 2010 to 171.66.16.25. Redistribution subject to ASME license or copyright; see http://www.asme.org/terms/Terms_Use.cfm

$$I_1 = -\log X_0 - \frac{1}{2} e^{-\frac{x_0^2}{2}} K_0(X_0^2/2) + \text{constant} \quad (A5)$$

(*ii*) From equation (19),

$$I_2 = \int_{X_0}^{\infty} \frac{XF_1(X)dX}{\sqrt{X^2 - X_0^2}} = \frac{2}{\pi^{1/2}} \int_{X_0}^{\infty} \int_0^X \frac{e^{S^2 - X^2} dSdX}{\sqrt{X^2 - X_0^2}} \quad (A6)$$

$$= \frac{2}{\pi^{1/2}} \int_0^{\pi/2} \int_0^{X_0/\cos\theta} \frac{e^{(S^2 - X_0^2/\cos^2\theta)} dS\, d\theta}{\cos\theta} \quad (A7)$$

where $\cos\theta = X_0/X$.

Treating S, θ as polar coordinates and reducing to rectangular coordinates through $X = S\cos\theta$, $Y = S\sin\theta$, we obtain

$$I_2 = \frac{2}{\pi^{1/2}} e^{-X_0^2} \int_0^{X_0} \frac{e^{X^2}}{X} \int_0^{\infty} e^{-(X_0^2/X^2 - 1)Y^2} dY\, dX \quad (A8)$$

$$= \int_0^{X_0} \frac{e^{(X^2 - X_0^2)} dX}{\sqrt{X_0^2 - X^2}} = \frac{1}{2} \int_0^{\pi} e^{-X_0^2/2(1-\cos\phi)} d\phi \quad (A9)$$

$$= \pi/2 e^{-X_0^2/2} I_0(X_0^2/2) \quad (A10)$$

by G R, Section 8.431 [13].

(*iii*) From equation (26),

$$I_3 = \int_0^{\infty} \frac{(1 - e^{-X^2})dX}{\sqrt{X^2 + X_0}}$$

$$= -\log X_0 - \frac{1}{2} e^{X_0^2} K_0(X_0^2/2) + \text{constant} \quad (A11)$$

by a similar procedure to (*i*) in the foregoing, using the substitution $X = X_0\, sh(y)$ and G R, Section 3.547.4 [13].

(*iv*) From equation (28)

$$I_4 = \int_0^{\infty} F_1(X)dX = \pi/2 \quad (A12)$$

(see [11], equation (14)).

(*v*) From equation (32)

$$I_5 = \int_{X_0}^{\infty} \left[\frac{1 - e^{-X^2}}{X^2} - e^{-X^2} \right] \frac{dX}{\sqrt{X^2 - X_0^2}} = \frac{1}{X_0^2} - J_1 - J_2 \quad (A13)$$

where

$$J_1 = \int_{X_0}^{\infty} \frac{e^{-X^2} dX}{X^2 \sqrt{X^2 - X_0^2}}; \quad J_2 = \int_{X_0}^{\infty} \frac{e^{-X^2} dX}{\sqrt{X^2 - X_0^2}} \quad (A14)$$

Integrating by parts,

$$\int \frac{e^{-X^2} dX}{\sqrt{X^2 - X_0^2}} = \frac{\sqrt{X^2 - X_0^2}}{X} e^{-X^2} + \int \sqrt{X^2 + X_0^2} e^{-X^2}\, dX + \int \frac{\sqrt{X^2 + X_0^2} e^{-X^2} dX}{X^2} \quad (A15)$$

It follows that

$$J_2 = 2\int_{X_0}^{\infty} \sqrt{X^2 - X_0^2} e^{-X^2}\, dX + \int_{X_0}^{\infty} \frac{\sqrt{X^2 - X_0^2} e^{-X^2} dX}{X^2} \quad (A16)$$

$$= 2\int_{X_0}^{\infty} \sqrt{X^2 - X_0^2} e^{-X^2}\, dX + J_2 - X_0^2 J_1 \quad (A17)$$

and hence

$$J_1 = \frac{2}{X_0^2} \int_{X_0}^{\infty} \sqrt{X^2 - X_0^2} e^{-X^2}\, dX. \quad (A18)$$

The integrals J_1, J_2 can now be evaluated as in (*i*), in the foregoing using the substitution $X = X_0\, ch(y)$, giving

$$I_5 = \frac{1}{X_0^2} - \frac{1}{2} e^{-\frac{X_0^2}{2}} K_1(X_0^2/2) \quad (A19)$$

(*vi*) We use the same procedure for the integral

$$I_6 = \int_0^{\infty} \left[\frac{1 - e^{-X^2}}{X^2} - e^{-X^2} \right] \frac{dX}{\sqrt{X^2 + X_0^2}} \quad (A20)$$

from equation (34), obtaining

$$I_6 = -\frac{1}{X_0^2} + \frac{1}{2} e^{\frac{X_0^2}{2}} K_1(X_0^2/2). \quad (A21)$$

APPENDIX II

Series and Asymptotic Forms for Bessel Functions

For small arguments (positive or negative) we can use the convergent series

$$I_0(x) = \sum_{k=0}^{\infty} \frac{(x/2)^{2k}}{(k!)^2} \quad (A22)$$

$$K_0(x) = \sum_{k=0}^{\infty} \frac{(x/2)^{2k}}{(k!)^2} [\psi(k+1) - \log|x/2|] \quad (A23)$$

$$K_1(x) = \frac{1}{x} + \sum_{k=0}^{\infty} \frac{(x/2)^{2k+1}}{k!(k+1)!} \left[\frac{1}{2(k+1)} + \log|x/2| - \psi(k+2) \right] \quad (A24)$$

where

$$\psi(k+1) = -c + \sum_{i=1}^{k} \frac{1}{i} \quad (A25)$$

and $c = 0.577215\ldots$ is Euler's constant.
(see Gradshteyn and Ryzhik [13], Sections 8.447, 8.486.18, 8.365.4, and 9.73).

Asymptotic expansions for large positive arguments are

$$I_0(x) = \frac{e^x}{(2\pi x)^{1/2}} \left[1 + \frac{1^2}{8x} + \frac{1^2 \cdot 3^2}{2!(8x)^2} + \frac{1^2 \cdot 3^2 \cdot 5^2}{3!(8x)^3} + \ldots \right] \quad (A26)$$

$$K_0(x) = \left(\frac{\pi}{2x}\right)^{1/2} e^{-x} \left[1 - \frac{1^2}{8x} + \frac{1^2 \cdot 3^2}{2!(8x)^2} - \frac{1^2 \cdot 3^2 \cdot 5^2}{3!(8x)^3} + \ldots \right] \quad (A27)$$

$$K_1(x) = \left(\frac{\pi}{2x}\right)^{1/2} e^{-x} \left[1 + \frac{(4 - 1^2)}{8x} + \frac{(4 - 1^2)(4 - 3^2)}{2!(8x)^2} + \ldots \right] \quad (A28)$$

(see [12], Appendix III).

Downloaded 02 May 2010 to 171.66.16.25. Redistribution subject to ASME license or copyright; see http://www.asme.org/terms/Terms_Use.cfm

Propagation and Scattering of SH-Waves in Semi-Infinite Domains Using a Time-Dependent Boundary Element Method

J. M. Rice

M. H. Sadd
Mem. ASME

Department of Mechanical Engineering
and Applied Mechanics,
University of Rhode Island,
Kingston, R.I. 02881

The propagation and scattering of SH-waves of general form is investigated using the boundary element method. Attention is focused on semi-infinite regions containing subsurface cavities. The analysis is carried out within the context of linear elastodynamic theory formulated as an integral equation. Using a time-dependent Green's function for the half space, the boundary integral equation is developed and is discretized into a finite set of algebraic relations. A time-stepping algorithm is constructed for the solution of general boundary value—initial value problems. Results of this solution technique are presented for the two-dimensional case of transient waves scattering off of buried stress-free cavities.

1 Introduction

The scattering of elastic waves by cavities and cracks has been the subject of numerous investigations during the past several years. Early studies have dealt with the cases of cavities in infinite media, while more recent work [1–9] has been directed at scattering problems in semi-infinite domains. For semi-infinite regions, the presence of the free surface influences the scattered wave field, and this phenomena becomes important in a wide variety of dynamic geomechanics problems including seismology, blast loading, sensing, etc.

The solution method presented in this work is a numerical technique based on the development of an integral formulation of the elastodynamic equations. Integral formulations in elasticity theory have a long history dating back to the 19th century. However, although such formulations have been known for quite some time, their application for developing numerical algorithms for use in problem solution is relatively new. Recently many investigators have been employing integral formulations with numerical methods (including finite element concepts) to solve a broad class of both static and dynamic elasticity problems. These methods have become known as the Boundary Integral Equation Method (BIE or BIEM) or the Boundary Element Method (BEM). The recent texts by Brebbia [10], Brebbia and Walker [11], and Banerjee and Butterfield [12] provide general background for these methods as they are applied to a large variety of engineering science problems.

The principal advantages of the BIE method lie primarily in the reduction of the number of spatial dimensions of the problem by one, and by formulating the problem directly in terms of the boundary values. Since discretization is carried out only on the boundary of the body under study, the number of unknowns in the numerical problem is reduced, and the need to create space-filling three-dimensional grids is eliminated. For many cases, problems involving infinite domains can be handled in a very direct and simple manner using appropriate Green's functions.

With regard to elastodynamic problems, Cruse and Rizzo [13] and Cruse [14] developed a BIE approach in conjunction with Laplace transformation. Niwa [15, 16] used BIE methods for the steady state solution and then reconstructed the transient response by Fourier synthesis. Cole, Kosloff, and Minster [17] have developed a time-dependent formulation which eliminates the need for Laplace transformation and/or Fourier synthesis. Manolis [18] has recently compared these three BIE methods on a scattering problem in an infinite medium, and found that all three methods gave good results.

The basis for an integral equation formulation in elastodynamics was first developed by Kupradze [19], De Hoop [20], and Wheeler and Sternberg [21], while Eringen and Suhubi [22] provide a concise review of this classical work. The integral equation formulation is the dynamic extension of Betti's reciprocal theorem which relates two different dynamic states for a given elastic body. An apparent choice for one of the two elastodynamic states is the desired solution to the problem, while the other state is normally chosen to be an appropriate Green's function that satisfies the governing equation of motion in the region under study. Using these choices, the dynamic equivalent to Somigliana's

Contributed by the Applied Mechanics Division for presentation at the Winter Annual Meeting, New Orleans, La., December 9–14, 1984 of THE AMERICAN SOCIETY OF MECHANICAL ENGINEERS.

Discussion on this paper should be addressed to the Editorial Department, ASME, United Engineering Center, 345 East 47th Street, New York, N.Y. 10017, and will be accepted until two months after final publication of the paper itself in the JOURNAL OF APPLIED MECHANICS. Manuscript received by ASME Applied Mechanics Division, June, 1983; final revision, January, 1984. Paper No. 84-WA/APM-9.

Copies will be available until August, 1985.

Copyright © 1984 by ASME
Downloaded 02 May 2010 to 171.66.16.25. Redistribution subject to ASME license or copyright; see http://www.asme.org/terms/Terms_Use.cfm

identity can be derived, and through a limiting process a boundary integral equation is developed which forms the basis of the BIE method.

This paper is specifically concerned with developing a BIE technique using a time-dependent approach similar to that of Cole, et al. [17]. Furthermore, the Green's function solution for the half-space geometry will be selected for use. This choice will eliminate the need to discretize the free surface of the half space itself, thus reducing still further the number of required unknown variables. Telles and Brebbia [23] have successfully used this concept of half-space Green's functions for static elasticity problems. Attention will be directed to SH-waves propagating in a half space with cavities or inclusions. The wave forms, cavity shape, size, and number are all arbitrary.

The next section outlines the problem formulation using a direct boundary integral equation method. Numerical discretization of the boundary integral is then presented which transforms the problem into a set of algebraic relations. Results of using the proposed method are given for a two-dimensional transient scattering problem from a subsurface circular cavity.

2 Problem Formulation

The direct boundary integral equation method will be used to approximate the solution of the antiplane strain case for transient elastodynamic waves in an isotropic, homogeneous half space. Antiplane strain is characterized by a displacement field of the form $\mathbf{u} = \{0,0,w(x_1,x_2)\}$. The nonzero component w satisfies the classical wave equation

$$w_{,ii} = \frac{1}{\beta^2}\ddot{w} \tag{2.1}$$

where $\beta = \sqrt{\mu/\rho}$ is the shear wave speed. Equation (2.1) possesses a time-dependent Green's function $G(\mathbf{r},t;\mathbf{r}_o,t_o)$, which is the fundamental singular solution of the displacement field at $\mathbf{r}$ and t due to a concentrated impulsive force at $\mathbf{r}_o$ and t_o.

Employing such a Green's function, relation (2.1) can be put into the following integral form

$$cw(\mathbf{r},t) = \int_{t_o}^{\infty}\int_{\partial S}[G\tau(\mathbf{r}_o,t_o) - w(\mathbf{r}_o,t)\mathbf{K}\cdot\mathbf{n}]dS_o dt_o \tag{2.2}$$

where the body forces and the initial conditions are equal to zero, $\mathbf{K}$ is the stress field derived from Hooke's law, associated with G, w and τ are the displacement and traction components on the boundary ∂S, $\mathbf{r}_o$ and t_o are the space and time positions of the source, $\mathbf{r}$ and t are the space and time positions of the receiver, and $\mathbf{n}$ is the unit normal vector to the surface. Subscripts o refer to the source quantities, and the coefficient c is given by

$$c = \begin{cases} 1/2, \mathbf{r} \in \text{smooth boundary } \partial S \\ 1, \quad \mathbf{r} \in \text{interior of } \partial S \end{cases}$$

For the antiplane strain case, the infinite space Green's function is, see e.g., Cole, et al. [17],

$$G(\mathbf{r},t;\mathbf{r}_o,t_o) = \frac{1}{2\pi\mu}\frac{H(t-t_o-R/\beta)}{[(t-t_o)^2 - R^2/\beta^2]^{1/2}} \tag{2.3}$$

where $R = |\mathbf{r}_o - \mathbf{r}|$ and $H(t-t_o-R/\beta)$ is the Heaviside function.

The stress field associated with this Green's function is given by

$$\mathbf{K}(\mathbf{r},t;\mathbf{r}_o,t_o) = \frac{R}{2\pi\beta^2}\frac{H(t-t_o-R/\beta)}{[(t-t_o)^2 - R^2/\beta^2]^{3/2}}\frac{\partial R}{\partial \mathbf{n}} \tag{2.4}$$

For the antiplane strain half-space problem, the method of images can be used to construct a half-space Green's function

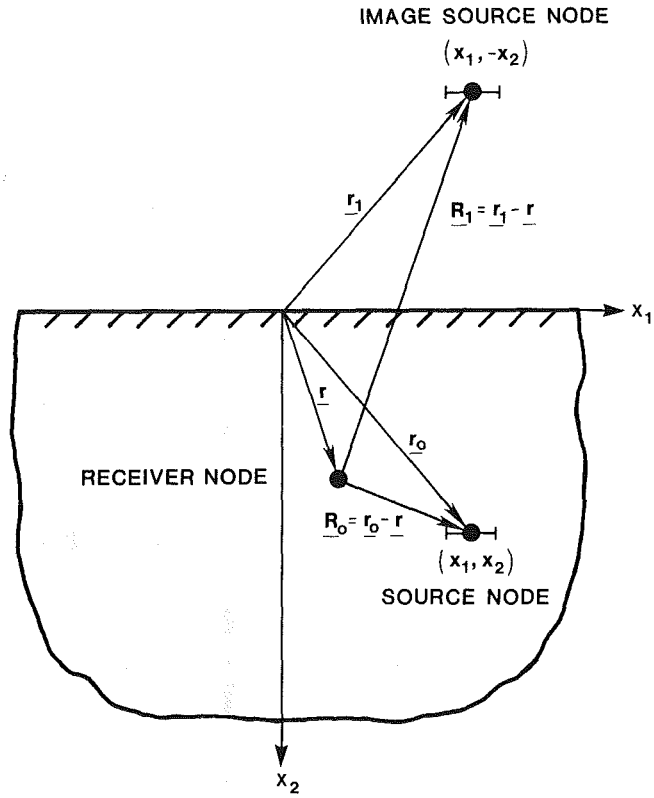


Fig. 1 Geometry of source and image for the construction of a half-space Green's function

from the infinite space Green's function, see e.g., Hudson [24]. The half-space Green's function follows from the infinite space function through the superposition of a virtual infinite space function of equal amplitude at an image point relative to the free surface. The associated stress field can be derived as in (2.4). The results are

$$G = G_o + G_1 = \frac{1}{2\pi\mu}\left[\frac{H(t-t_o-R_o/\beta)}{[(t-t_o)^2 - R_o^2/\beta^2]^{1/2}} + \frac{H(t-t_o-R_1/\beta)}{[(t-t_o)^2 - R_o^2/\beta^2]^{1/2}}\right] \tag{2.5}$$

$$\mathbf{K} = \mathbf{K}_0 + \mathbf{K}_1 = \frac{1}{2\pi\beta^2}\left[\frac{R_o H(t-t_o-R_o/\beta)}{[(t-t_o)^2 - R_o^2/\beta^2]^{3/2}}\frac{\partial R_o}{\partial \mathbf{n}} + \frac{R_1 H(t-t_o-R_1/\beta)}{[(t-t_o)^2 - R_1^2/\beta^2]^{3/2}}\frac{\partial R_1}{\partial \mathbf{n}}\right] \tag{2.6}$$

where R_o and R_1 are shown in Fig. 1.

The advantage of this superposition in the BIE method is that the boundary of the free surface will not have to be discretized, thus simplifying the problem. The boundary condition on $x_2 = 0$ is already accounted for by this half-space Green's function.

Results (2.5) and (2.6) can now be used with equation (2.2) to construct a boundary integral equation to solve for the displacements and tractions on the boundaries. With the boundary data determined, equation (2.2) can be reapplied to find the displacements and stresses at any interior points. To solve for the stress at interior points, equation (2.2) is substituted into Hooke's law yielding

$$\tau_{3i} = \mu\left[\int_{t_o}^{\infty}\int_{\partial S}[G\tau(\mathbf{r}_o,t_o) - w(\mathbf{r}_o,t_o)\mathbf{K}\cdot\mathbf{n}]dS_o dt_o\right]_{,i} \tag{2.7}$$

3 Numerical Discretization

The integral equation (2.2) must now be discretized in some

Downloaded 02 May 2010 to 171.66.16.25. Redistribution subject to ASME license or copyright; see http://www.asme.org/terms/Terms_Use.cfm

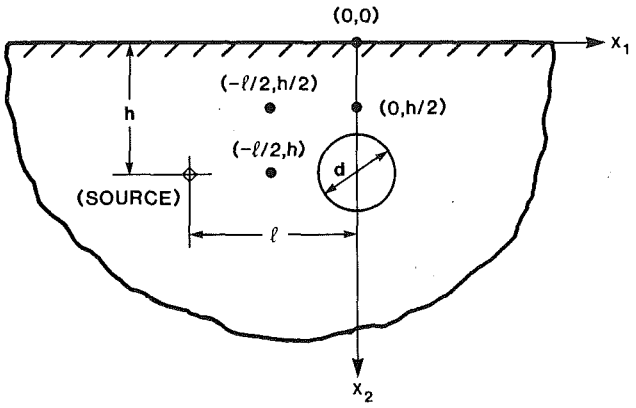


Fig. 2 Schematic of buried hole problem

manner in order to model a physical problem. For this study, the boundary to be integrated over was divided into elements with a node at the center of each. Each individual element is assumed to possess a constant displacement and a constant traction with respect to space. Integration over time was constant for the displacement kernel and linear for the stress kernel. This is essentially the same scheme used by Cole [25]. It is possible to interpolate the variation of the dynamic variables over an element with any order of shape function (e.g., constant, linear, quadratic, etc.). The Green's function used here is the solution to a hyperbolic partial differential equation and possess propagating singularities. Elliptic or parabolic equations have Green's functions that are singular only at a single point. This propagating singularity has an effect on the shape function used. Cole [25] found that for the wave equation, low-order shape functions gave better results than high-order shape functions—with the opposite being true for parabolic or elliptic equations. The reason for this behavior lies in the fact that low-order shape functions preserve the impulsive nature of the influence coefficients and averages out the singularity of this kernel.

For a receiver point on the boundary, equation (2.2) becomes

$$\frac{1}{2} w_i^m + \sum_{n=1}^{m} \sum_{j=1}^{H} \int_{t_n} \int_{\Gamma_j} \mathbf{K}\cdot\mathbf{n}\, \phi_j^n(\mathbf{r}_o,t_o)\, w_j^n \quad d\Gamma_o dt_o$$

$$= \sum_{n=1}^{m} \sum_{j=1}^{H} \int_{t_n} \int_{\Gamma_j} G\, \psi_j^n(\mathbf{r}_o,t_o)\, \tau_j^n\, d\Gamma_o\, dt_o \tag{3.1}$$

where H is the total number of elements, and M is the total number of time increments. The receiver time is incremented by m, i.e., $t_m = m\Delta t$, $m = 1,2. \ . \ .M$, while the source time is incremented by n, $t_n = n\Delta t$, $n = 1,2. \ . \ .M$. Note that since a source time t_n cannot be greater than the receiver time, n is summed only up to m. The source boundary has H elements, Γ_j, $j = 1,2, \ . \ . \ .H$ and there are H receiver elements. ϕ_j^n and ψ_j^n are the interpolation functions for displacement and traction, respectively.

Defining the discrete kernels or influence coefficients

$$IG_{ij}^{mn} = \int_{t_n} \int_{\Gamma_j} G\, d\Gamma_o\, dt_o$$

$$IK_{ij}^{mn} = \int_{t_n} \int_{\Gamma_j} \left[1 - \frac{|t_o - t_m|}{\Delta t}\right] \mathbf{K}\cdot\mathbf{n}\, d\Gamma_o\, dt_o,$$

equation (3.1) can be written as

$$-\frac{1}{2} w_i^m + \sum_{n=1}^{m} \sum_{j=1}^{H} IG_{ij}^{mn}\, \tau_j^n = \sum_{n=1}^{m} \sum_{j=1}^{H} IK_{ij}^{mn} w_j^n \tag{3.2}$$

Equation (3.2) will yield a set of H linear algebraic equations to be solved at each time step. The final result of this will be the tractions and displacements of all the boundary elements at all the time steps.

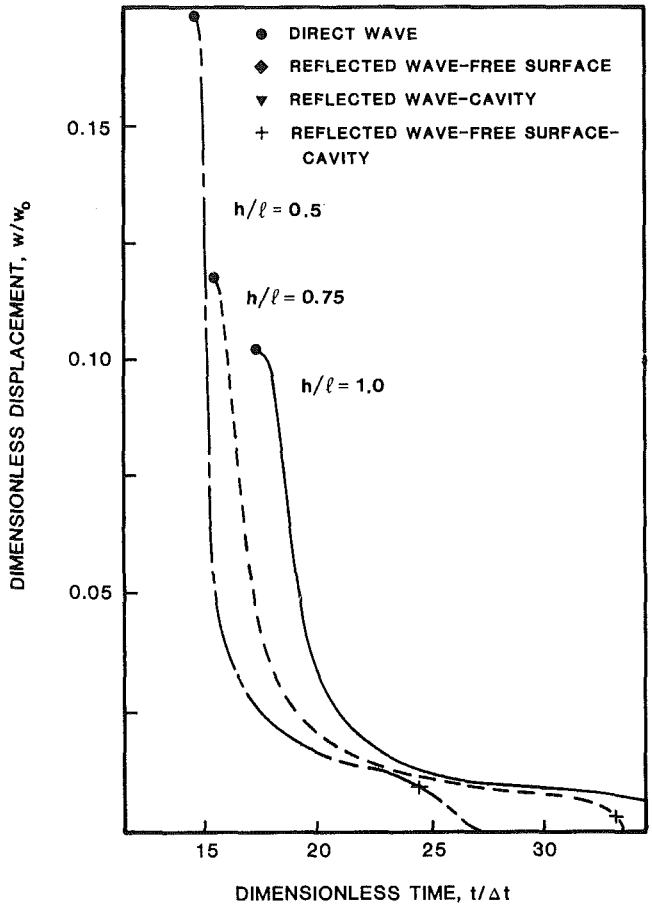


Fig. 3 Displacement response at (0, 0) for the buried hole problem; $l = 10d = 0.1$ m, $\beta = 3{,}200$ m/s, $\mu = 8.1 \times 10^{10}$ N/m^2, $\rho = 7{,}800$ kg/m^3

Although there are $2H^2M^2$ possible kernels, not all need to be calculated as the Green's function has the time translation properties,

$$G(\mathbf{r},t;r_o,t_o) = G(\mathbf{r},t+\Delta t;\mathbf{r}_o,t_o+\Delta t)$$

and the causality properties

$$G(\mathbf{r},t;r_o,t_o) = 0 \quad \text{for} \quad \beta(t-t_o) < |\mathbf{r}-\mathbf{r}_o|$$

These properties greatly reduce the number of nonzero kernels in a given computational problem. Furthermore, it is interesting to note that this discretization scheme can be implicit or explicit depending on the time spacing and the size of the elements. If $\beta\Delta t \leq \Delta\, h/2$, where Δh is the smallest element length, the coefficient matrix of the linear algebraic system to be solved will be diagonal, and the discretization scheme will be explicit. If $\beta\Delta t > \Delta h/2$, the matrix will no longer be diagonal and the discretization scheme will be implicit.

In the case of an interior point, the displacement and stress can be solved for directly, once the boundary data is known, i.e.,

$$w_p^m = -\sum_{n=1}^{m} \sum_{j=1}^{H} IK_{pj}^{mn} w_j^n + \sum_{n=1}^{m} \sum_{j=1}^{H} IG_{pj}^{mn} \tau_j^n$$

$$\tau_{p(L)}^m = -\mu\left[\sum_{n=1}^{m} \sum_{j=1}^{H} IK_{pj}^{mn} w_j^n\right]_{,L} + \left[\sum_{n=1}^{m} \sum_{j=1}^{H} IG_{pj}^{mn} \tau_j^n\right]_{,L} \tag{3.3}$$

$$(L = 1,2)$$

Downloaded 02 May 2010 to 171.66.16.25. Redistribution subject to ASME license or copyright; see http://www.asme.org/terms/Terms_Use.cfm

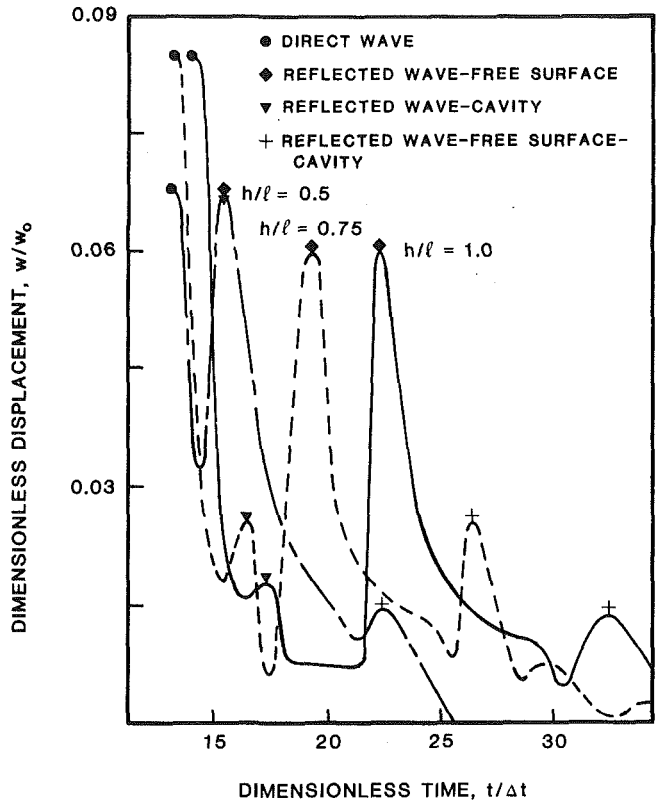


Fig. 4 Displacement response at (0, *h*/2) for the buried hole problem; *l* = 10*d* = 0.1m, β = 3,200 m/s, μ = 8.1 × 10^{10} N/m^2, ρ = 7,800 kg/m^3

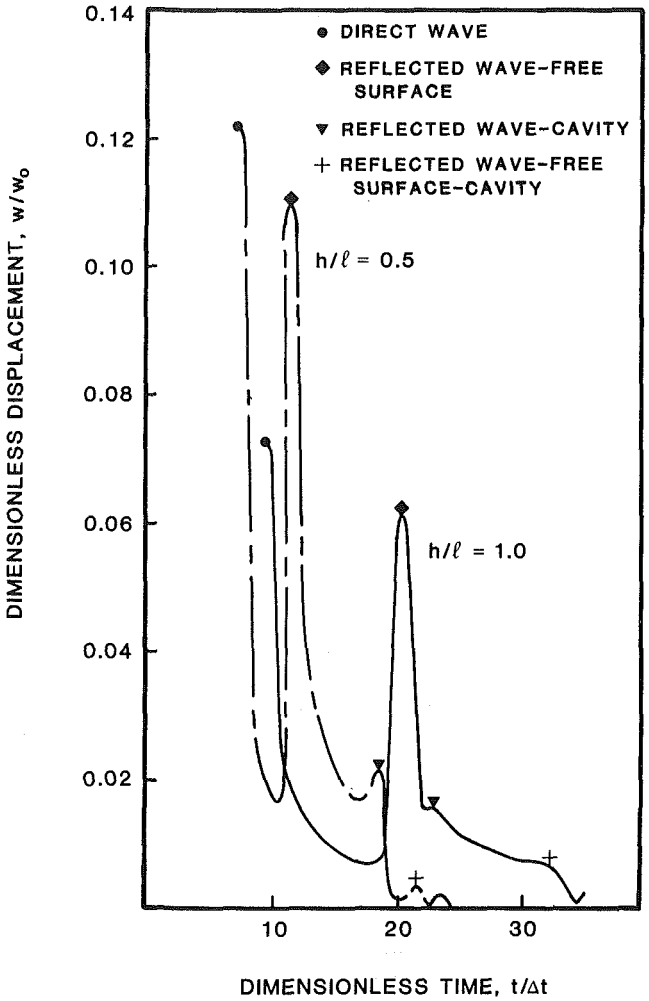


Fig. 5 Displacement response at (−*l*/2 *h*/2) for the buried hole problem; *l* = 10*d* = 0.1m, β = 3,200 m/s, μ = 8.1 × 10^{10} N/m^2, ρ = 7,800, kg/m^3

where, p is related to the interior point and L is the normal direction to the surface the stress is on.

4 Results

An example problem that will employ the solution method is shown in Fig. 2, and contains a wave source and a stress-free circular cavity embedded in an isotropic, homogeneous half space. The geometry of the source was a four-sided square and the cavity was modeled as a 12-sided hole. The distance between the source and cavity was held constant (l = 0.1 m) while the depth of the source and cavity was varied (h = 0.05, 0.075, 0.1 m). The size of the source was 0.001 m wide and the cavity was 0.01 m in diameter. The material properties used corresponded to a wave speed of 3,200 m/s and a shear modules of 8.1 × 10^{10} N/m^2. The time increment was 2.5 × 10^{-6}s. Each configuration was run with the same input condition of an impulsive step displacement pulse of 0.01 m over the whole source boundary with a duration of one time increment.

The resulting displacements from the preceding example were computed at four field receiver points (shown in Fig. 2). Figure 3 illustrates the displacement-time response of the receiver point on the surface of the half space at the coordinates (0,0). There is a distinct peak as the wave reaches this point. The closer the source to the receiver the greater the magnitude of the peak.

In Fig. 4 the receiver point is halfway between the cavity and the free surface at coordinates (0, h/2). In addition to the peaks from the direct wave there are now peaks from the reflection from the free surface, reflection from the cavity and reflection from the free surface via the cavity. Note, at h/l = 0.5 the events of the reflection from the free surface and refelction from the cavity should occur at approximately the same time according to ray theory. In general the longer the ray path the smaller the peak magnitude of the event. This, however, may not be the case near the free surface of the cavity or near the surface of the half space. Figure 5 corresponds to the receiver point at coordinates (−l/2, h/2), and again illustrates several wave arrivals.

In Fig. 6 the receiver point is located between the source and the cavity at coordinates (−l/2,h). The direct waves for the various h/l cases all occur at the same time with essentially identical magnitudes. For the h/l = 1.0 and 0.75 cases, the reflections from the cavity both occur at the same time with approximately the same magnitude. Reflections from the cavity for the h/l = 0.5 case are associated with a larger displacement magnitude because of the presence of the free surface reflected wave.

In summary, the BIE method employing a time-dependent Green's function gave good results for the examples considered. These computer runs were made on a Prime 750 minicomputer, and a typical run used a total of 16 elements with 4 output points and 40 time steps. This resulted in a total run time of 6.5 cpu(s).

One disadvantage of the method is that since all previous time steps are required for the solution, large amounts of computer storage are necessary. Another disadvantage is while the method is good for transient problems, application to the steady-state harmonic problem reveals solution error propagation. This is due to the large number of time steps required and the need of all information from the previous time steps. Dominant errors in the method arise from integrating the Green's function over the singularity as there is a

Downloaded 02 May 2010 to 171.66.16.25. Redistribution subject to ASME license or copyright; see http://www.asme.org/terms/Terms_Use.cfm

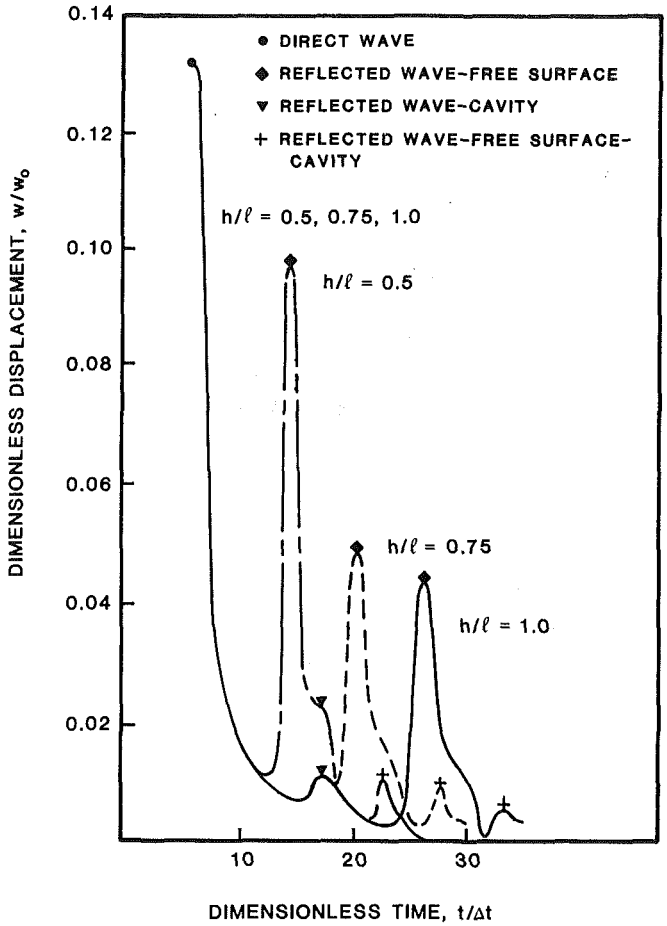


Fig. 6 Displacement response at ($-l/2$, h) for the buried hole problem; $l = 10d = 0.1$m, $\beta = 3{,}200$ m/s, $\mu = 8.1 \times 10^{10}$ N/m^2, $\rho = 7{,}800$ kg/m^3

very strong variation here. The steady-state harmonic problems have been successfully solved using Laplace and Fourier transform methods [13–16], and it appears that these methods may be more appropriate for the steady state case.

Acknolwedgment

This research was supported by the Army Research Office under contract DAAG29-82-K-0012.

References

1 Datta, S. K., "Diffraction of SH-Waves by an Edge Crack," ASME Journal of Applied Mechanics, Vol. 46, 1979, pp. 101–106.

2 Stone, S. F., Shosh, M. L., and Mal, A. K., "Diffraction of Antiplane Shear Waves by an Edge Crack," ASME Journal of Applied Mechanics, Vol. 47, 1980, pp. 359–362.

3 Mendelsohn, D. A., Achenbach, J. D., and Kerr, L. M., "Scattering of Elastic Waves by a Surface-Breaking Crack," *Wave Motion*, Vol. 2, 1980, pp. 277–292.

4 Achenbach, J. D., and Brind, R. J., "Scattering of Surface Waves by a Sub-Surface Crack," *J. Sound and Vib.*, Vol. 76, 1981, pp. 43–56.

5 Datta, S. K., and El-Akily, N., "Diffraction of Elastic Waves in a Half-Space 1: Integral Representation and Matched Asymptotic Expansions," in *Modern Problems in Elastic Wave*, Miklowitz, J., and Achenbach, J. D., eds., Wiley, New York, 1978, pp. 197–218.

6 Shah, A. H., Wong, K. C., and Datta, S. K., "Diffraction of Plane SH-Waves in a Half-Space," *Earth. Eng. Str. Dyn.*, Vol. 10, 1982, p. 519.

7 Abduljabbar, Z., Datta, S. K., and Shah, A. H., "Diffraction of Horizontally Polarized Shear Waves by Normal Edge Cracks in a Plate," *J. Appl. Phys.*, Vol. 54, No. 2, 1983, pp. 461–472.

8 Datta, S. K., and El-Akily, N., "Diffraction of Elastic Waves by a Cylindrical Cavity in Half-Space," *J. Acoust. Soc. Amer.*, Vol. 64, 1978, pp. 1692–1699.

9 Datta, S. K., "Diffraction of SH-Waves by an Elliptic Elastic Cylinder," *Int. J. Solids Structures*, Vol. 10, 1974, pp. 123–133.

10 Brebbia, C. A., *The Boundary Element Method for Engineers*, Halsted Press, New York, 1978.

11 Brebbia, C. A., and Walker, S., 1980, *Boundary Element Techniques in Engineering*, Newnes-Butterworths, London.

12 Banerjee, P. K., and Butterfield, R., 1981, *Boundary Element Methods in Engineering Science*, McGraw-Hill, England.

13 Cruse, T. A., and Rizzo, F. J., 1968, "A Direct Formulation and Numerical Solution of the General Transient Elastodynamic Problem, I," *J. Math. Anal. Appl.*, Vol. 22, pp. 244–259.

14 Cruse, T. A., 1968, "A Direct Formulation and Numerical Solution of the General Transient Elastodynamic Problem, II," *J. Math. Anal. Appl.*, Vol. 22, pp. 341–355.

15 Niwa, Y., Kobayashi, S., and Azuma, N., 1975, "An Analysis of Transient Stresses Produced Around Cavities of Arbitrary Shape During the Passage of Travelling Waves," *Memoirs Fac. Eng. Kyoto Univ.*, Vol. 37, Part 2, pp. 28–46.

16 Niwa, Y., Kobayashi, S., and Fukui, T., 1976, "Applications of Integral Equation Methods to some Geomechanical Problem," *Numerical Methods in Geomechanics*, Desui, C. S., ed., ASCE, New York, pp. 120–131.

17 Cole, D. M., Kosloff, D. D., and Minster, J. B., 1978, "A Numerical Boundary Integral Equation Method for Elastodynamics, I," *Bull. Seism. Soc. America*, Vol. 68, No. 5, pp. 1331–1357.

18 Manolis, G. D., 1983, "A Comparative Study on Three Boundary Element Method Approaches to Problems in Elastodynamics," *Numerical Methods in Engineering*, Vol. 19, pp. 73–91.

19 Kupradze, V. D., "Dynamic Problems in Elasticity," Vol. III, North-Holland, Amsterdam, 1963.

20 DeHoop, A. Y., "Representation Theorems for the Displacement in an Elastic Solid and their Application to Elasto-Dynamic Diffraction Theory," Doctoral Dissertation, Tech. Hogesehole, Delft, 1958.

21 Wheeler, L. T., and Sternberg, E., "Some Theorems in Classical Elastodynamics," *Arch. Rat. Mech. Anal.*, Vol. 31, 1968, pp. 51–90.

22 Eringen, A. C., and Suhubi, E. S., *Elastodynamics*, Academic Press, New York, 1975.

23 Telles, J. C. F., and Brebbia, C. A., 1981, "Boundary Element Solution for Half-Plane Problems," *Int. J. Solids Str.*, Vol. 7, pp. 1149–1158.

24 Hudson, J. A., The Excitation and Propagation of Elastic Waves, Cambridge University Press, Cambridge, 1980.

25 Cole, D. M., "A Numerical Boundary Integral Equation Method for Transient Motions," Doctoral dissertation, California Institute of Technology, Pasadena, Calif., 1980.

Downloaded 02 May 2010 to 171.66.16.25. Redistribution subject to ASME license or copyright; see http://www.asme.org/terms/Terms_Use.cfm

Scattering of Elastic Waves by a Plane Crack of Finite Width

J. H. M. T. van der Hijden[1]

F. L. Neerhoff

Delft University of Technology,
Department of Electrical Engineering,
Laboratory of Electromagnetic Research,
P.O. Box 5031,
2600 GA Delft, The Netherlands

A rigorous theory of the diffraction of time-harmonic elastic waves by a cylindrical, stress-free crack embedded in an elastic medium is presented. The incident wave is taken to be either a P-wave or an SV-wave. The resulting boundary-layer problem for the unknown jump in the particle displacement across the crack is solved by employing an integral-equation approach. The jump is expanded in a complete sequence of Chebyshev polynomials, and, writing the Green's function as a Fourier integral, a system of algebraic equations is obtained. Numerical results are presented in the form of dynamic stress intensity factors, scattering cross sections, and normalized power-scattering characteristics. Some of them deviate from earlier published results.

Introduction

This paper deals with the scattering that results from the interaction of incident elastic waves with a crack. The results of this research are of interest to the quantitative nondestructive evaluation of structures. We investigate a two-dimensional model configuration where the crack geometry is uniform in one direction. Recently, we have investigated the diffraction of *SH*-waves by a crack in a semi-infinite elastic solid [1], which in turn is related to [2–5].

The diffraction of *P/SV*-waves by a crack in an elastic medium has been discussed in the literature, see e.g., [6]. Stress intensity factors for a crack near a surface that is subjected to surface tractions were discussed in [7]. The problem of normally incident *P*-waves on a crack in an unbounded medium was solved in [8]. The asymptotic solution to this problem using ray theory was presented in [9]. However, an overall solution, from which the stress intensity factors also follow very naturally, has never been presented; furthermore, our results show significant deviation from those presented in [6].

In this paper, we consider the scattering of elastic waves by a cylindrical, stress-free crack of finite width that is embedded in an unbounded elastic medium. The incident time-harmonic wave is taken to be either a *P*-wave or an *SV*-wave. First, we formulate the boundary-value problem. The jump in the particle displacement across the crack can be regarded as the fundamental unknown quantity in the problem. For it, an integral equation is derived. Then, we expand the unknown quantity in a complete sequence of Chebyshev polynomials. By writing the Green's function, occurring in the integral equation, as a Fourier integral, we arrive at an infinite system of linear, algebraic equations for the expansion coefficients. The elements of the matrix of coefficients of this system of algebraic equations are infinite integrals. Finally, we present numerical results for the normalized power scattering characteristics, the scattering cross sections of the crack, as well as for the dynamic stress intensity factors at the crack tips. This is done for a range of frequencies and geometrical parameters. It appeared that already sufficient accuracy is obtained with a limited number of expansion functions. As a consequence, the computation time is rather restricted. Reciprocity relations as well as the power balance [10] are used as checks on the computer program.

Formulation of the Problem

We consider a cylindrical stress-free crack of width $2a$, embedded in an isotropic, linear, homogeneous, and perfectly elastic medium with Lamé constants λ, μ, and volume mass-density ρ. A Cartesian coordinate system (with unit vectors $\mathbf{i}_1$, $\mathbf{i}_2$, $\mathbf{i}_3$) is introduced such that the x_1-coordinate points along the crack. The crack is cylindrical in the x_2-direction and has a cross section Σ (see Fig. 1). Time-harmonic compressional waves (*P*-waves) and vertically polarized shear-waves (*SV*-waves), propagating in the x_1,x_3-plane are present. Using the summation convention for repeated Greek subscripts ranging over 1 and 3, and omitting the complex time-factor $\exp(-i\omega t)$, the governing equation of elastic motion is given by [10]

$$\partial_\beta \sigma_{\alpha\beta} + \rho\omega^2 u_\alpha = -f_\alpha, \tag{1}$$

where $\sigma_{\alpha\beta}$ are components of the stress tensor, u_α denotes the x_α-component of the particle displacement, f_α denotes the applied body force, while ∂_β denotes the partial derivative with respect to x_β. The stress is related to the displacement by the constitutive relation

$$\sigma_{\alpha\beta} = C_{\alpha\beta\gamma\delta}\partial_\gamma u_\delta, \tag{2}$$

[1] Present address: Schlumberger-Doll Research, P.O. Box 307, Ridgefield, Conn. 06877.

Contributed by the Applied Mechanics Division for presentation at the Winter Annual Meeting, New Orleans, La., December 9–14, 1984 of THE AMERICAN SOCIETY OF MECHANICAL ENGINEERS.

Discussion on this paper should be addressed to the Editorial Department, ASME, United Engineering Center, 345 East 47th Street, New York, N.Y. 10017, and will be accepted until two months after final publication of the paper itself in the JOURNAL OF APPLIED MECHANICS. Manuscript received by ASME Applied Mechanics Division, June, 1983; final revision, January, 1984. Paper No. 84-WA/APM-13.

Copies will be available until August, 1985.

Copyright © 1984 by ASME

Downloaded 02 May 2010 to 171.66.16.25. Redistribution subject to ASME license or copyright; see http://www.asme.org/terms/Terms_Use.cfm

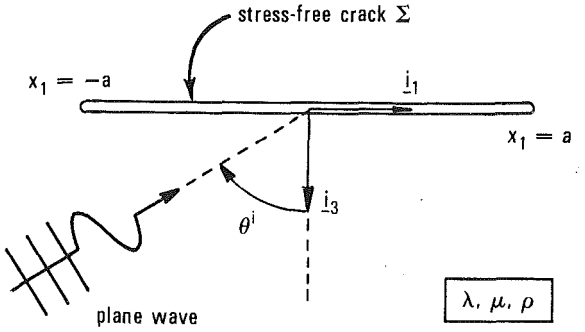


Fig. 1 Geometry of the crack Σ in the unbounded elastic medium

with the stiffness tensor $C_{\alpha\beta\gamma\delta} = \lambda\delta_{\alpha\beta}\delta_{\gamma\delta} + \mu(\delta_{\alpha\gamma}\delta_{\beta\delta} + \delta_{\alpha\delta}\delta_{\beta\gamma})$, where $\delta_{\alpha\beta}$ is the Kronecker delta. The total field $\{u_\alpha, \sigma_{\alpha\beta}\}$ is given by

$$\{u_\alpha, \sigma_{\alpha\beta}\} = \{u^i_\alpha, \sigma^i_{\alpha\beta}\} + \{u^{sc}_\alpha, \sigma^{sc}_{\alpha\beta}\}, \tag{3}$$

in which $\{u^i_\alpha, \sigma^i_{\alpha\beta}\}$ represents the incident field, while $\{u^{sc}_\alpha, \sigma^{sc}_{\alpha\beta}\}$ represents the scattered field.

In addition, the field satisfies the boundary conditions on the crack

$$\lim_{x_3 \downarrow 0} \sigma_{\alpha 3} = 0, \quad \lim_{x_3 \downarrow 0} \sigma_{\alpha 3} = 0 \quad \text{for} \quad -a < x_1 < a. \tag{4}$$

The particle displacement jumps across the crack by a finite amount

$$\Psi_\alpha = \lim_{x_3 \downarrow 0} u_\alpha - \lim_{x_3 \downarrow 0} u_\alpha. \tag{5}$$

Moreover, the field has to satisfy the edge condition at the tips of the crack [11]

$$\Psi_\alpha = O(\epsilon^{1/2}) \quad \text{as} \quad \epsilon \downarrow 0, \tag{6}$$

in which ϵ denotes the distance to a crack tip. Finally, the radiation condition is of course required.

Integral Equation for the Jump in the Particle Displacement Across the Crack

In this section we will derive a suitable (differential) integral equation for Ψ_α. Therefore, we first derive an integral representation for the scattered field u^{sc}_α. To this end we use the Betti-Rayleigh theorem [12]. In this reciprocity relation, we employ two different elastodynamic states. One of these is taken to be the Green's elastodynamic state $\{u^G_{\alpha;\gamma}, \sigma^G_{\alpha\beta;\gamma}\}$ (see Appendix *B*). By employing the scattered field as the other state, we arrive at the integral representation for u^{sc}_α

$$u^{sc}_\gamma(\mathbf{x}_\mathcal{P}) = \int_\Sigma \Psi_\alpha(x_1)\sigma^G_{\alpha 3;\gamma}(x_1, 0; \mathbf{x}_\mathcal{P})\, dx_1, \tag{7}$$

in which $\mathbf{x}_\mathcal{P} = (x_{1\mathcal{P}}, x_{3\mathcal{P}})$ denotes the position vector of a point $\mathcal{P}$. From (7), the particle displacement everywhere in the elastic medium can be calculated, provided that Ψ_α on Σ is known, which motivates the fact that Ψ_α is the fundamental unknown quantity.

To arrive at an integral equation for Ψ_α, we substitute (7) in the constitutive relation (2). Next, we multiply both the left and the right-hand side of the result by the unit vector $\mathbf{i}_3$ and in the result we subsequently let $\mathcal{P}$ approach Σ. Then, using (3) and taking into account the boundary condition (4), we arrive at

$$-\sigma^i_{\eta 3}(x_{1\mathcal{P}}, 0) = \Big[\lambda\delta_{\eta 3}\partial_{\gamma\mathcal{P}} \int_{-a}^{a} \Psi_\alpha \sigma^G_{\alpha 3;\gamma} dx_1 \tag{8}$$

$$+ \mu\partial_{\eta\mathcal{P}} \int_{-a}^{a} \Psi_\alpha \sigma^G_{\alpha 3;3} dx_1 + \mu\partial_{3\mathcal{P}} \int_{-a}^{a} \Psi_\alpha \sigma^G_{\alpha 3;\eta} dx_1 \Big]_{x_{3\mathcal{P}} \to 0}$$

$$\text{if} \quad -a < x_{1\mathcal{P}} < a,$$

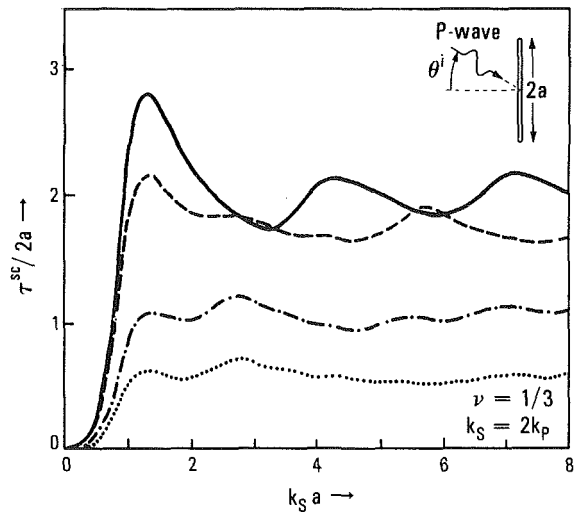


Fig. 2 Normalized plane wave scattering cross section for the scattering of a *P*-wave by a crack of finite width: $\theta^i = 0$ deg (—), $\theta^i = 30$ deg (– – –), $\theta^i = 60$ deg (–·–·–), and $\theta^i = 90$ deg (· · · · ·)

in which $\partial_{\delta\mathcal{P}}$ operates on $x_{\delta\mathcal{P}}$. Equation (8) is the desired (differential) integral equation for the yet unknown quantity Ψ_α on Σ.

Method of Solution of the Integral Equation

To solve the differential-integral equation (8), we first expand Ψ_α in a complete sequence of Chebyshev polynomials, being the eigenfunctions of Laplace's equation in elliptic coordinates. In view of the edge condition (6) this yields [13]

$$(i/4)\Psi_\alpha(x_1) = \sum_{n=1}^{\infty} a_{\alpha;n}\psi_n(x_1), \tag{9}$$

in which

$$\psi_n(x_1) = \begin{cases} \cos\,(n \arcsin(x_1/a)) & \text{if} \quad n = \text{odd}, \\ i \sin\,(n \arcsin(x_1/a)) & \text{if} \quad n = \text{even}, \end{cases} \tag{10}$$

with the property

$$\int_{-a}^{a} \psi_m(x_1)\exp(-i\,c\,x_1)dx_1 = \pi\, m\, c^{-1} J_m(ca), \tag{11}$$

in which J_m denotes the Bessel function of the first kind and c denotes some (complex) constant. As a second step, we use the Fourier integral representation of $\sigma^G_{\alpha 3;\gamma}$ (as an integral along the contour Γ in the complex k-plane, see Appendix *B*) in (8). Next, both the left and right-hand side of (8) are multiplied by the complex conjugate of a member of (10) and the result is integrated along the crack Σ. Then, we interchange the order of integration along the contour Γ and the crack. Finally, the differentiation $\partial_{\alpha\mathcal{P}}$ is carried out and, taking the limit $x_{3\mathcal{P}} \to 0$ and using (9) and (11), we arrive at the infinite system of linear algebraic equations

$$b^i_{\alpha;m} = \sum_{n=1}^{\infty} \delta_{\alpha\beta} K_{\alpha;mn}\, mn\, a_{\beta;n} \quad (m = 1, 2, \ldots). \tag{12}$$

In (12), the left-hand side is given by (see also Appendix *A*)

$$b^i_{\alpha;m} = -(\mu\pi)^{-1} \int_{-a}^{a} \sigma^i_{\alpha 3}(x_1, 0)\psi^*_m(x_1)dx_1, \tag{13}$$

in which the asterisk denotes complex conjugate. The coefficients $K_{\alpha;mn}$ of the system are given by

$$K_{1;mn} = \frac{(-1)^{m+n}}{k_S^2} \int_\Gamma \frac{\Delta}{\gamma_S k^2} J_m(ka) J_n(ka)\, dk, \tag{14}$$

Downloaded 02 May 2010 to 171.66.16.25. Redistribution subject to ASME license or copyright; see http://www.asme.org/terms/Terms_Use.cfm

Table 1 Substitutions that are used in the integral along the real axis in the k-plane

$0 \le k \le k_P$	$k = k_P \sin\xi$	$0 \le \xi \le \pi/2$	$dk = \gamma_P d\xi$
$k_P \le k \le k_S$ [a]	$k^2 = \frac{1}{2}(k_S^2 + k_P^2) - \frac{1}{2}(k_S^2 - k_P^2)\cos\zeta$	$0 \le \zeta \le \pi$	$dk = -\frac{1}{2}ik^{-1}\gamma_P\gamma_S d\zeta$
$k_S \le k \le \infty$	$k = k_S \cosh\chi$	$0 \le \chi \le \infty$	$dk = -i\gamma_S d\chi$

[a] de Hoop, A. T., "Representation Theorems for the Displacement in an Elastic Solid and Their Application to Elastodynamic Diffraction Theory," Thesis, Delft University of Technology, The Netherlands, 1958, p. 73.

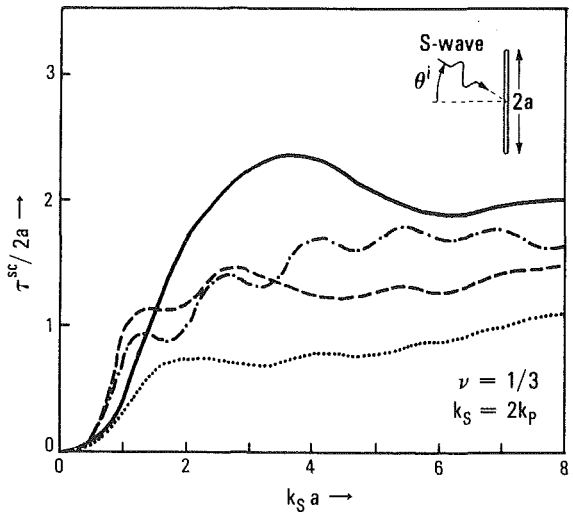


Fig. 3 Normalized plane wave scattering cross section for the scattering of an SV-wave by a crack of finite width: $\theta^i = 0$ deg (—), $\theta^i = 30$ deg (- - -), $\theta^i = 60$ deg (-•-•-), and $\theta^i = 90$ deg (• • • •)

$$K_{3;mn} = \frac{(-1)^{m+n}}{k_S^2} \int_\Gamma \frac{\Delta}{\gamma_P k^2} J_m(ka) J_n(ka)\, dk,$$

in which

$$\Delta(k) = 4k^2\gamma_P\gamma_S + (k_S^2 - 2k^2)^2. \tag{15}$$

The (uncoupled) systems of linear algebraic equations (12) hold for an arbitrary incident field. It is remarked that the integrals occurring in (14) can be rewritten as integrals over a finite range of integration [14]. However we found that evaluation of the more complicated integrand of the finite integrals was less efficient than using (14) together with the numerical techniques that are discussed in the next section.

Discussion of the Numerical Techniques

Since the jump in the particle displacement Ψ_α is expected to be represented with sufficient accuracy by a finite number of expansion functions, we truncate the infinite system (12) at $n = N$. As a consequence, we obtain a finite system of linear, algebraic equations with unknowns $a_{\alpha;n}$ $(n = 1,2, \ldots, N)$.

Let us now consider the right-hand side of (14) in some more detail. Then, it is first remarked that γ_P and γ_S are even functions of the variable of integration k and, by making use of the properties of Bessel functions with negative argument, it is easily shown that the range of integration $-\infty < k < \infty$ can be reduced to $0 < k < \infty$ without additional computing effort. Secondly, we consider the behavior of the integrands of (14) for $k \to \infty$. Then, it is observed that the integrands behave as

$$2i(k_S^2 - k_P^2)k^{-1} J_m(ka) J_n(ka) \quad \text{if} \quad k \to \infty. \tag{16}$$

To accelerate the rate of convergence of the integrals at hand, we subtract (16) numerically from the integrand. Next, this term is integrated analytically and the results are put together again. The two square-root singularities at k_P and k_S are dealt with by introducing the substitutions that are listed in Table 1.

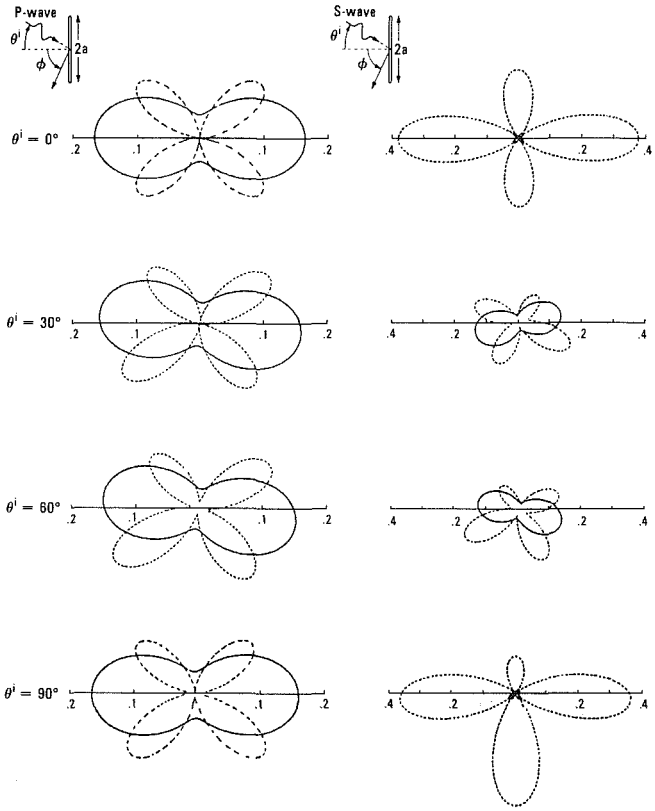


Fig. 4 Normalized power scattering characteristics for the scattering of plane P/SV-waves by a crack of finite width: $D^P(\phi)/2\pi$ (—), $D^S(\phi)/2\pi$ (- - -). Four angles of incidence are considered and $k_S a = 1.5$.

Numerical Results

In this section, we present results for the scattering of plane elastic waves by a crack in an unbounded solid. All computations have been carried out for a Poisson's ratio $\nu = 1/3$, i.e., $k_S = 2k_P$. The far-field amplitude radiation characteristic $G^{P,S}(\phi)$ of the particle displacement is given by

$$\begin{aligned} u_\alpha^{sc}(r,\phi) \approx\ & (i/4)(2/\pi k_P r)^{\frac{1}{2}} \exp(ik_P r - i\pi/4) G^P(\phi)\hat{x}_{\alpha\mathcal{P}} \\ & + (i/4)(2/\pi k_S r)^{\frac{1}{2}} \exp(ik_S r - i\pi/4) G^S(\phi)\epsilon_{\alpha\gamma 2}\hat{x}_{\gamma\mathcal{P}} \\ & \text{as} \quad r \to \infty, \end{aligned} \tag{17}$$

in which r denotes the distance from the origin to the point of observation $\mathcal{P}$, while ϕ is defined by $x_{1\mathcal{P}} = -r\sin\phi$, $x_{3\mathcal{P}} = r\cos\phi$ with $-\pi < \phi < \pi$. Further $\hat{\mathbf{x}}_{\mathcal{P}}$ is defined as the unit vector along $\mathbf{x}_{\mathcal{P}}$. Then, using (7), (B1), (9), and (11), we arrive at

$$\begin{aligned} G^P(\phi) = \frac{-4\pi\mu}{k_P k(\lambda + 2\mu)} \sum_{n=1}^{\infty} (-1)^n n \\ \{2k\gamma_P a_{1;n} - (k_S^2 - 2k^2) a_{3;n}\} J_n(ka), \end{aligned} \tag{18}$$

with $k = k_P \sin\phi$ and

$$G^S(\phi) = \frac{-4\pi}{k_S k} \sum_{n=1}^{\infty} (-1)^n n$$

Downloaded 02 May 2010 to 171.66.16.25. Redistribution subject to ASME license or copyright; see http://www.asme.org/terms/Terms_Use.cfm

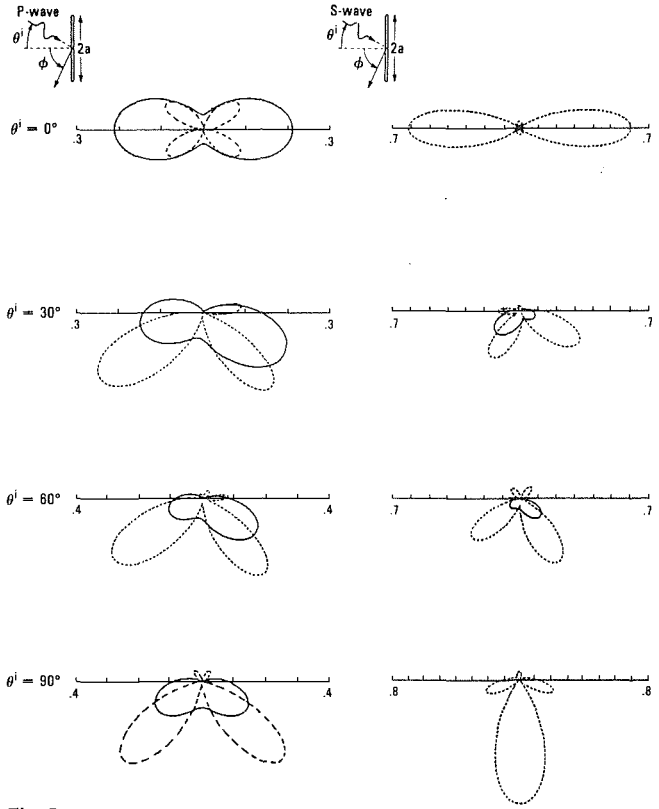


Fig. 5 Normalized power scattering characteristics for the scattering of plane *P/SV*-waves by a crack of finite width: $D^P(\phi)/2\pi$ (——), $D^S(\phi)/2\pi$ (- - -). Four angles of incidence are considered and $k_S a = 3$.

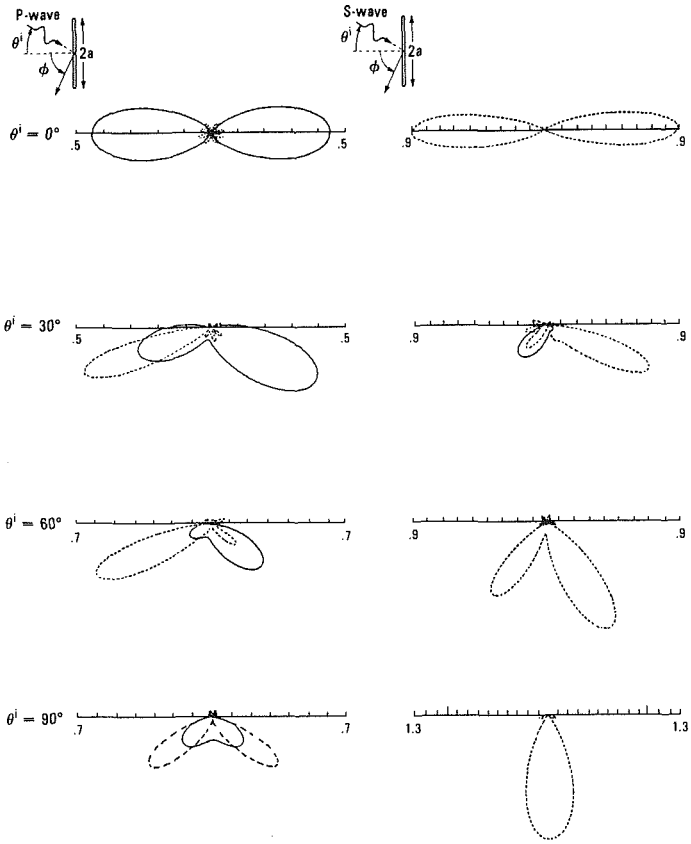


Fig. 6 Normalized power scattering characteristics for the scattering of plane *P/SV*-waves by a crack of finite width: $D^P(\phi)/2\pi$ (——), $D^S(\phi)/2\pi$ (- - -). Four angles of incidence are considered and $k_S a = 6$.

$$\{(k_S^2 - 2k^2)a_{1;n} + 2k\gamma_S a_{3;n}\} J_n(ka), \tag{19}$$

with $k = k_S \sin\phi$.

The total time-averaged power $<P>$ scattered by the crack, is given by [10]

$$<P> = \frac{\omega(\lambda+2\mu)}{16\pi}\int_{-\pi}^{\pi} |G^P(\phi)|^2 d\phi + \frac{\omega\mu}{16\pi}\int_{-\pi}^{\pi} |G^S(\phi)|^2 d\phi. \tag{20}$$

We introduce the directive gains $D^P(\phi)$ and $D^S(\phi)$ as

$$D^P(\phi) = \frac{\omega(\lambda+2\mu)}{8<P>}|G^P(\phi)|^2$$

$$\text{and} \quad D^S(\phi) = \frac{\omega\mu}{8<P>}|G^S(\phi)|^2, \tag{21}$$

respectively. The scattering cross section τ^{sc} of the crack is defined as the outward power-flow of the scattered field normalized at the intensity of the incident field. When the incident wave is a plane P or SV-wave, τ^{sc} is directly related to either G^P or G^S by [10]

$$\tau^{sc} = k_{P,S}^{-1} Im\{G^{P,S}(\theta^i \pm \pi)\}. \tag{22}$$

In Fig. 2, we present the normalized plane-wave scattering cross section $\tau^{sc}/2a$ for a P-wave at four different angles of incidence. Our results for normal incidence ($\theta^i = 0$ deg) differ significantly from the results presented by Tan [6] who used sine functions to expand the jump in the particle displacement across the crack. The strong oscillation around $k_S a = 1.5$, which was not found by Tan, was independently confirmed by unpublished results, by the use of spectral theory. In Fig. 3, the same quantities are shown for SV-wave incidence. In Figs. 4, 5, and 6 the corresponding normalized power scattering characteristics $D^P/2\pi$ and $D^S/2\pi$ are shown for both P and SV-waves at four angles of incidence and $k_S a = 1.5$, 3, and 6.

The dynamic in-plane stress near the crack tips can be expressed in terms of the stress intensity factors $k_1^{\pm}$ and $k_2^{\pm}$ (opening and sliding motion), where the plus and minus sign refer to the crack tip at $x_1 = a$ and $x_1 = -a$, respectively. The relation between the jump in the particle displacement near the crack tips and the stress intensity factors is then given by [15]

$$\Psi_3\{\pm(a-\epsilon)\} = 2\bar{k}_1^{\pm}\mu^{-1}(2\epsilon)^{1/2}(1-\nu), \tag{23}$$
$$\Psi_1\{\pm(a-\epsilon)\} = 2\bar{k}_2^{\pm}\mu^{-1}(2\epsilon)^{1/2}(1-\nu).$$

From (9), (10), and (23) we conclude that

$$\bar{k}_{1,2}^{\pm} = 2i\mu(1-\nu)^{-1}a^{-1/2}\sum_{n=1}^{\infty}(\pm i)^{n+1} n a_{3,1;n}. \tag{24}$$

Before plotting these values, $\bar{k}_{1,2}^{\pm}$ are normalized according to [16] as

$$|k_{1,2}^{\pm}| = \mu^{-1}a^{-1/2}k_S^{-1}|\bar{k}_{1,2}^{\pm}|, \tag{25}$$

for an incident SV-wave. For an incident P-wave, the normalization is obtained from (25) by replacing μ by $(\lambda+2\mu)$ and S by P.

Figure 7 depicts the variations of the normalized dynamic stress intensity factors $|k_{1,2}^{\pm}|$ with the normalized wave number $k_S a$, for both P and SV-waves incident at different angles. In [16], results were presented for $|k_{1,2}^{-}|$ and $0 < k_S a < 1.4$, which agree perfectly with our results. For a P-wave, incident at $\theta^i = 90$ deg and $\nu = 0.25$ stress intensity factors were presented in [17]. Except for a normalization factor and of course the difference due to the change in Poisson's ratio there is a good agreement with our results.

The curves in Fig. 7 show that for all nonzero angles of

Downloaded 02 May 2010 to 171.66.16.25. Redistribution subject to ASME license or copyright; see http://www.asme.org/terms/Terms_Use.cfm

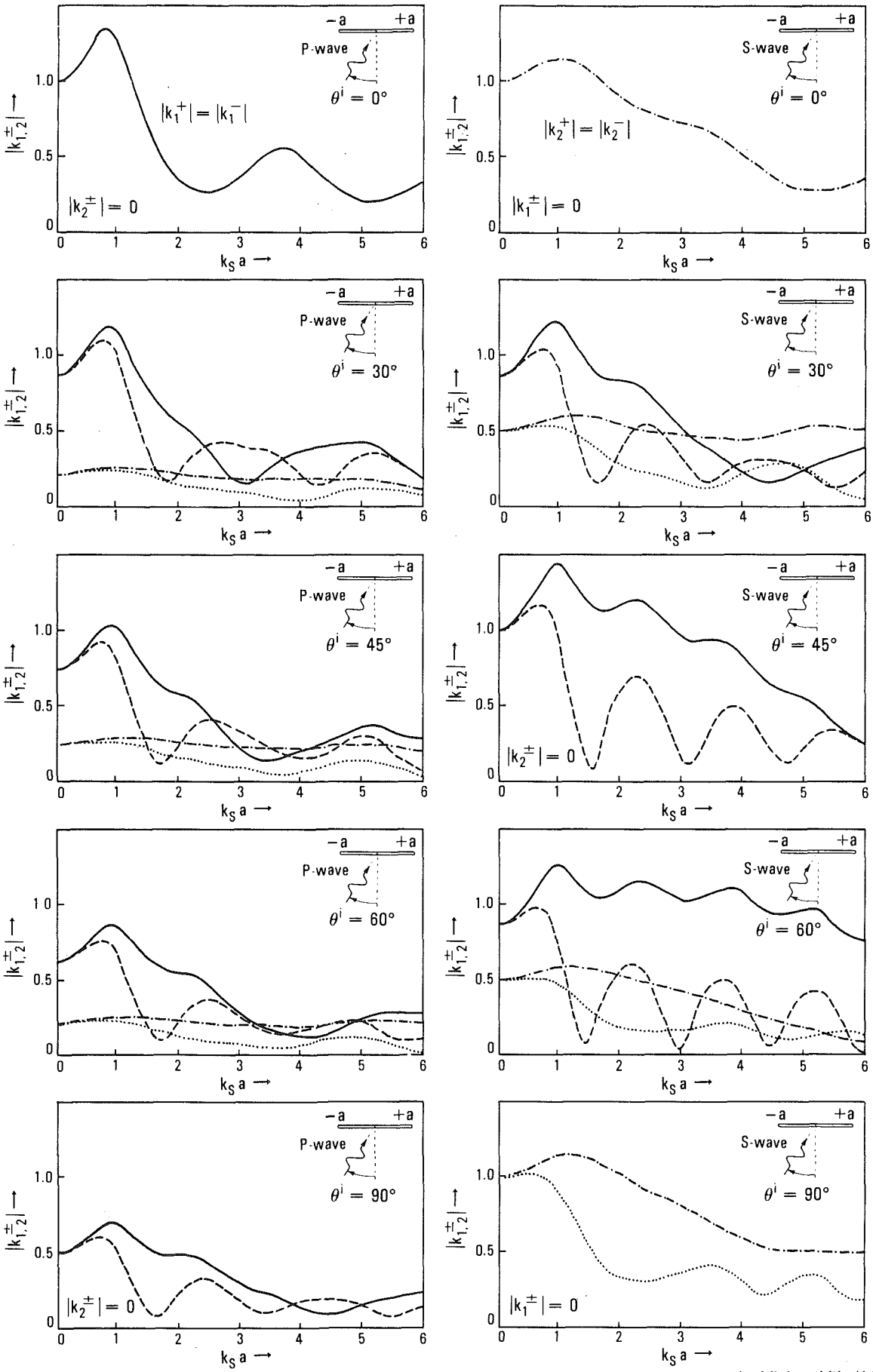


Fig. 7 Normalized dynamic stress intensity factors versus frequency for *P/SV*-waves incident on a crack of finite width: $|k_1^+|$ (——), $|k_1^-|$ (– – –), $|k_2^+|$ (–·–·–) and $|k_2^-|$ (· · · · ·)

Downloaded 02 May 2010 to 171.66.16.25. Redistribution subject to ASME license or copyright; see http://www.asme.org/terms/Terms_Use.cfm

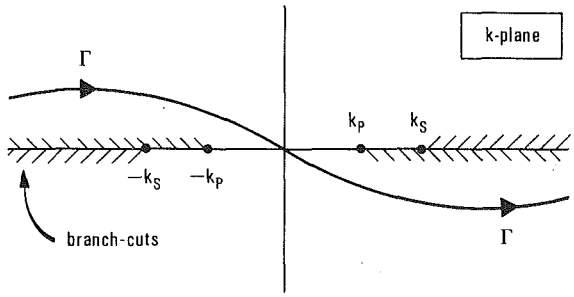


Fig. 8 Location of the path of integration Γ in the *k*-plane

incidence and almost all frequencies the stress intensity factors $|k_{1,2}^{+}|$ at the "rear" crack tip (at $x = +a$) are greater than the stress intensity factors $|k_{1,2}^{-}|$ at the "front" crack tip ($x = -a$). This implies that a crack inside a solid will always grow in a direction *away* from the source of elastodynamic wave motion.

We would like to stress that our method is exact in the sense that any desired accuracy can be reached. The edge condition is satisfied analytically, since each element of the sequence of expansion functions satisfies condition (6). The remaining error in our results is determined by the discretization of the integral (14), together with the number N of expansion functions. An accuracy of 1 percent is obtained if $N \approx 2k_S a$. The computing time to calculate the system's matrix $K_{\alpha;mn}$ varies from 0.5 s for small wave numbers to 5 s for $k_S a = 6$. Even at very large wave numbers no numerical instability sets in, but of course it becomes more efficient to use asymptotic methods in that case.

References

1 Neerhoff, F. L., and van der Hijden, J. H. M. T., "Diffraction of Elastic Waves by a Subsurface Crack (Antiplane Motion)," accepted for publication in *Journal of Sound and Vibration*, Vol. 94, May 1984.

2 Stone, S. F., Ghosh, M. L., and Mal, A. K., "Diffraction of Antiplane Shear Waves by an Edge Crack," ASME JOURNAL OF APPLIED MECHANICS, Vol. 47, 1981, pp. 359-362.

3 Datta, S. K., "Diffraction of SH Waves by an Edge Crack," ASME JOURNAL OF APPLIED MECHANICS, Vol. 46, 1980, pp. 101-106.

4 Mal, A. K., "Diffraction of SH Waves by a Near-Surface Crack," in *Review of Progress in Quantitative Nondestructive Evaluation*, Vol. 1, Thompson, D. O., and Chimunti, D. E., eds., Plenum Press, 1981, pp. 499-509.

5 Neerhoff, F. L., "Diffraction of Love Waves by a Stress-Free Crack of Finite Width in the Plane Interface of a Layered Composite," *Applied Scientific Research*, Vol. 35, 1979, pp. 265-315.

6 Tan, T. H., "Scattering of Plane, Elastic Waves by a Plane Crack of Finite Width," *Applied Scientific Research*, Vol. 33, 1977, pp. 75-88.

7 Achenbach, J. D., and Brind, R. J., "Elastodynamic Stress-Intensity Factors for a Crack Near a Free Surface," ASME JOURNAL OF APPLIED MECHANICS, Vol. 48, 1981, pp. 539-542.

8 Mal, A. K., "Interaction of Elastic Waves With a Griffith Crack," *International Journal of Engineering Science*, Vol. 8, 1970, pp. 763-776.

9 Achenbach, J. D., Gautesen, A. K., and McMaken, H., *Ray Methods for Waves in Elastic Solids*, Pitman, London, 1982.

10 Tan, T. H., "Diffraction of Time-Harmonic Elastic Waves by a Cylindrical Obstacle," *Applied Scientific Research*, Vol. 32, 1976, pp. 97-144.

11 Karal, F. C., and Karp, S. N., "Stress Behaviour in the Neighborhood of Sharp Corners," *Geophysics*, Vol. 29, 1964, pp. 360-369.

12 Kupradze, V. D., *Progress in Solid Mechanics*, Vol. III, Sneddon, I. N., and Hill, R., eds., North-Holland, Amsterdam, 1963.

13 de Hoop, A. T., "Variational Formulation of Two-Dimensional Diffraction Problems With Application to Diffraction by a Slit," *Proceedings Koninklijke Nederlandse Academie Van Wetenschappen*, Vol. B58-5, 1955, pp. 401-411.

14 van den Berg, P. M., "Scattering of Two-Dimensional Elastodynamic Waves by a Rigid Plane Strip or a Plane Crack of Finite Width: The Transition Matrix," *J. Acoust. Soc. Am.*, Vol. 72, 1982, pp. 1038-1045.

15 Sih, G. C., and Liebowitz, H., *Fracture, An Advanced Treatise (Volume II), Mathematical Theories of Brittle Fracture*, Liebowitz, H., ed., Academic Press, New York, 1968.

16 Chen, E. P., and Sih, G. C., *Mechanics of Fracture 4, Elastodynamic Crack Problems*, Sih, G. C., ed., Noordhoff International, Leyden, 1977, p. 145.

17 Luong, W. C., Keer, L. M., and Achenbach, J. D., "Elastodynamic Stress Intensity Factors of a Crack Near an Interface," *Int. J. Solids Structures*, Vol. 11, 1975, pp. 919-925.

APPENDIX *A*

Incident Fields

In this appendix the coefficients $b^i_{\alpha;m}$ (conform to (13)) are derived. The particle displacement for an incident P or SV-wave of unit amplitude is obtained as

$$u^i_\alpha(\mathbf{x}) = k^P_\alpha k_P^{-1} \exp(ik^P_\alpha x_\alpha),$$
$$u^i_\alpha(\mathbf{x}) = \epsilon_{\alpha\gamma 2} k^S_\gamma k_S^{-1} \exp(ik^S_\alpha x_\alpha), \tag{A1}$$

in which $\mathbf{k}^{P,S} = (k, -\gamma_{P,S})$, where $k = k_{P,S}\sin\theta^i$ (with θ^i the angle of incidence, see Fig. 1) while

$$\gamma_{P,S} = (k^2_{P,S} - k^2)^{1/2}$$
$$\text{with} \quad \mathrm{Re}(\gamma_{P,S}) \geq 0 \quad \text{and} \quad \mathrm{Im}(\gamma_{P,S}) \geq 0, \tag{A2}$$
$$k_P = \omega[\rho/(\lambda+2\mu)]^{1/2} \quad \text{and} \quad k_S = \omega(\rho/\mu)^{1/2}. \tag{A3}$$

The tensor ϵ_{ijk} denotes the complete antisymmetric unit tensor of rank three. To obtain $b^i_{\alpha;m}$, we first substitute (A1) in the constitutive relation (2). Then, on account of (11), we obtain from (13)

$$\begin{bmatrix} b^i_{1;m} \\ b^i_{3;m} \end{bmatrix} = \frac{im}{k_P k} \begin{bmatrix} 2k\gamma_P \\ -(k_S^2 - 2k^2) \end{bmatrix} J_m(ka), \tag{A4}$$

for an incident P-wave, and

$$\begin{bmatrix} b^i_{1;m} \\ b^i_{3;m} \end{bmatrix} = \frac{im}{k_S k} \begin{bmatrix} (k_S^2 - 2k^2) \\ 2k\gamma_S \end{bmatrix} J_m(ka), \tag{A5}$$

for an incident SV-wave.

APPENDIX *B*

The Green's Elastodynamic State

In this appendix we present a spectral representation for $\sigma^G_{\alpha 3;\gamma}(x_1, 0; \mathbf{x}_\mathcal{P})$ which occurs in (7). The Green's state $\{u^G_{\alpha;\gamma}, \sigma^G_{\alpha\beta;\gamma}\}$ corresponds to the field that originates from a line source of strength f_γ placed at $\mathcal{P}$. Then, the Green's particle displacement in terms of Hankel functions is given by (see [10], Appendix *A*)

$$u^G_{\alpha;\gamma}(\mathbf{x};\mathbf{x}_\mathcal{P}) = \frac{i}{4\rho\omega^2}[\partial_\alpha\partial_\gamma(H^{(1)}_0(k_S R) - H^{(1)}_0(k_P R)) + \delta_{\alpha\gamma} k_S^2 H^{(1)}_0(k_S R)], \tag{B1}$$

where $R = |\mathbf{x} - \mathbf{x}_\mathcal{P}|$.

To arrive at the spectral representation, we write the Hankel functions as a spatial Fourier transform with respect to the translated coordinate $(x_1 - x_{1\mathcal{P}})$

$$H^{(1)}_0(k_{P,S}R) = \pi^{-1}\int_\Gamma \gamma^{-1}_{P,S} \exp(i\gamma_{P,S}|x_3 - x_{3\mathcal{P}}|)\exp(ik(x_1 - x_{1\mathcal{P}}))dk, \tag{B2}$$

in which Γ is the path of integration in the complex k-plane as shown in Fig. 8, while $\gamma_{P,S}$ is given by (A2). Finally, in view of (2), we have $\sigma^G_{\alpha 3;\gamma} = C_{\alpha 3\delta\eta}\partial_\delta u^G_{\eta;\gamma}$.

Downloaded 02 May 2010 to 171.66.16.25. Redistribution subject to ASME license or copyright; see http://www.asme.org/terms/Terms_Use.cfm

J. L. Tassoulas
Assistant Professor,
Department of Civil Engineering,
The University of Texas at Austin,
Austin, Texas 78712

T. R. Akylas
Assistant Professor,
Department of Mechanical Engineering,
Massachusetts Institute of Technology,
Cambridge, Mass. 02139
Assoc. Mem. ASME

On Wave Modes With Zero Group Velocity in an Elastic Layer

A study is made of time-harmonic wave modes in an elastic layer in plane strain with traction-free surfaces. It is demonstrated that, at points of the Rayleigh-Lamb frequency spectrum where the group velocity vanishes, there exist nonseparable time-harmonic modes in which the amplitudes of the displacements vary linearly in the direction along the layer. These modes are used to explain the terrace-like structure of the free-vibration frequency spectrum of a circular disk.

Introduction

Wave propagation in an elastic layer has received intensive study in the last three decades owing to its fundamental significance in engineering and seismology. Most of the theoretical work has centered on wave modes that are harmonic in time and space and are obtained by separating variables in the governing equations; as in any linear wave system, more general wave disturbances can be synthesized in terms of such modes. For the simple case of an elastic layer in plane strain and with traction-free surfaces, the wave-mode frequencies are related to the wave numbers through a dispersion relation, known as the Rayleigh-Lamb frequency spectrum (see, for example, [1, 4]).

Mindlin [6] first pointed attention to the fact that the wave modes obtained by separation of variables are not the only possible time-harmonic modes consistent with the Rayleigh-Lamb frequency spectrum: he demonstrated that, at frequencies corresponding to zero wave numbers (the so-called cut-off frequencies), there exist modes in which the amplitude of one of the displacements varies linearly in the direction along the layer. However, no physical significance was attached to such modes; in fact, for a layer of infinite length unbounded disturbances are not physically relevant.

The goal of the present paper is twofold: first, a generalization of Mindlin's findings [6] concerning the special modes at cut-off frequencies is given: it is shown that modes with linearly varying amplitudes occur at any point of the frequency spectrum where the group velocity vanishes (the cut-off frequencies being a special case in which this requirement is fulfilled). These modes, which are nonseparable, are obtained by taking the derivative of the usual separable modes with respect to wave number, and are akin to the so-called generalized eigenvectors found in the hydrodynamic stability of parallel flows by Di Prima and Habetler [2]. Secondly, the free-vibration frequency spectrum of a circular disk is studied. It is demonstrated that the nonseparable modes of the infinite layer play a particular role: they are associated with the terrace-like structure of the frequency spectrum.

Elastic Layer in Plane Strain

Consider time-harmonic vibrations of frequency ω in an elastic layer of thickness $2h$, $-h \le z \le h$. Under plane-strain conditions, the governing equations are

$$(\lambda+2G)\frac{\partial^2 u}{\partial x^2}+(\lambda+G)\frac{\partial^2 w}{\partial x \partial z}+G\frac{\partial^2 u}{\partial z^2}+\omega^2\rho u=0 \quad (1a)$$

$$(\lambda+2G)\frac{\partial^2 w}{\partial z^2}+(\lambda+G)\frac{\partial^2 u}{\partial x \partial z}+G\frac{\partial^2 w}{\partial x^2}+\omega^2\rho w=0 \quad (1b)$$

where u and w denote the amplitudes of the horizontal and vertical displacements, respectively, λ and G are the Lamé moduli, and ρ is the mass density. The surfaces $z = -h$, $z = h$ are taken to be traction-free:

$$\sigma_z=\tau_{xz}=0 \quad (z=\pm h) \qquad (2)$$

with

$$\sigma_z=(\lambda+2G)\frac{\partial w}{\partial z}+\lambda\frac{\partial u}{\partial x}, \quad \tau_{xz}=G\left(\frac{\partial u}{\partial z}+\frac{\partial w}{\partial x}\right) \qquad (3)$$

In general, solutions of the equations (1), subject to the conditions (2), are expressed as linear combinations of the separable solutions (normal modes):

$$u(x,z)=U(z)\exp(-ikx) \qquad (4a)$$

$$w(x,z)=W(z)\exp(-ikx) \qquad (4b)$$

which are readily found by separating variables (see, for example, [1, 4]). As is well known, there is an infinity of eigenfunctions (mode shapes) U, W with corresponding eigenvalues k; they are related to the frequency ω through the Rayleigh-Lamb frequency equations, one for symmetric modes, and another for antisymmetric modes (symmetry, or antisymmetry of the displacement field with respect to the plane $z = 0$).

Contributed by the Applied Mechanics Division for presentation at the Winter Annual Meeting, New Orleans, La., December 9-14, 1984 of THE AMERICAN SOCIETY OF MECHANICAL ENGINEERS.

Discussion on this paper should be addressed to the Editorial Department, ASME, United Engineering Center, 345 East 47th Street, New York, N.Y. 100176, and will be accepted until two months after final publication of the paper itself in the JOURNAL OF APPLIED MECHANICS. Manuscript received by ASME Applied Mechanics Division, July, 1983; final revision, February, 1984. Paper No. 84-WA/APM-18.

Copies will be available until August, 1985.

Copyright © 1984 by ASME
Downloaded 02 May 2010 to 171.66.16.25. Redistribution subject to ASME license or copyright; see http://www.asme.org/terms/Terms_Use.cfm

The Rayleigh-Lamb frequency spectrum has been studied extensively by Mindlin and his coworkers [8]. Particular attention has been paid to those frequencies for which one of the wave numbers is equal to zero, and they are usually referred to as cut-off frequencies. The corresponding modes can be divided to longitudinal:

$$u(x,z)=0, \quad w(x,z)=W(z) \tag{5}$$

for

$$\omega h/C_L = n\pi/2, \quad n=1,2,3, \ldots \tag{6}$$

and transverse:

$$u(x,z)=U(z), \quad w(x,z)=0 \tag{7}$$

for

$$\omega h/C_T = m\pi/2, \quad m=1,2,3, \ldots \tag{8}$$

C_L, C_T being the velocities of longitudinal and transverse waves, respectively. For odd values of n in (6), or even values of m in (8), the modes (5) and (7) are symmetric; antisymmetric modes (5) and (7) are obtained for even values of n, or odd values of m.

Mindlin [6] has pointed out, however, that (5) and (7) are not the only possible modes at a cut-off frequency: in addition, there exist symmetric or antisymmetric waves in which w varies linearly with x:

$$u(x,z)=U(z), \quad w(x,z)=xW(z) \tag{9}$$

where W is the same as in (5), and U is easily determined. Similarly, there exist symmetric or antisymmetric waves in which u varies linearly with x:

$$u(x,z)=xU(z), \quad w(x,z)=W(z) \tag{10}$$

where U is the same as in (7), and W is easily calculated. The modes (9) and (10) exist unless a coincidence of cut-off frequencies occurs, i.e., if $C_L/C_T = [(2-2\nu)/(1-2\nu)]^{1/2} = m/n$, $m = 2, 4, 6. \ldots, n = 1,3,5, \ldots$ for symmetric waves, or $C_L/C_T = m/n$, $m = 1, 3, 5, \ldots, n = 2, 4, 6, \ldots$ for antisymmetric waves, ν being Poisson's ratio. Equivalently, the modes (9), (10) found by Mindlin [6] are possible, if and only if the group velocity $d\omega/dk$ vanishes at $k = 0$; for it has also been shown [5] that, for all branches of the frequency spectrum, $d\omega/dk = 0$ at $k = 0$, except if there is a coincidence of cut-off frequencies. Then, $d\omega/dk \neq 0$.

Mindlin's findings [6], regarding the exceptional modes (9) and (10), can be readily generalized to modes that do not correspond to cut-off frequencies. In fact, it will be shown that the occurrence of exceptional modes is directly related to the vanishing of the group velocity ($d\omega/dk = 0$), the cut-off frequencies being special instances at which this condition is met. To this end, consider a point (ω, k) of the frequency spectrum, such that $d\omega/dk = 0$, for the branch of the spectrum through (ω, k); the exceptional mode is the derivative of the usual mode (4) with respect to the wave number:

$$u(x,z) = -ixU\exp(-ikx) + \frac{dU}{dk}\exp(-ikx) \tag{11a}$$

$$w(x,z) = -ixW\exp(-ikx) + \frac{dW}{dk}\exp(-ikx) \tag{11b}$$

Substitution of the proposed solution (11) in the equations (1) and the boundary conditions (2) yields

$$-ix[-k^2(\lambda+2G)U - ik(\lambda+G)W' + GU'' + \omega^2\rho U]$$
$$+\left[-k^2(\lambda+2G)\frac{dU}{dk} - ik(\lambda+G)\frac{dW'}{dk} + G\frac{dU''}{dk} + \omega^2\rho\frac{dU}{dk}\right]$$
$$+[-2k(\lambda+2G)U - i(\lambda+G)W'] = 0 \tag{12a}$$
$$-ix[-k^2GW - ik(\lambda+G)U' + (\lambda+2G)W'' + \omega^2\rho W]$$
$$+\left[-k^2G\frac{dW}{dk} - ik(\lambda+G)\frac{dU'}{dk} + (\lambda+2G)\frac{dW''}{dk} + \omega^2\rho\frac{dW}{dk}\right]$$
$$+[-2kGW - i(\lambda+G)U'] = 0 \tag{12b}$$
$$-ix[(\lambda+2G)W' - ik\lambda U] + \left[(\lambda+2G)\frac{dW'}{dk} - ik\lambda\frac{dU}{dk}\right] + [-i\lambda U] = 0$$
$$(z=\pm h) \tag{13a}$$
$$-ix[-ikW + U'] + \left[-ik\frac{dW}{dk} + \frac{dU'}{dk}\right] + [-iW] = 0$$
$$(z=\pm h) \tag{13b}$$

where primes indicate derivatives with respect to z. The terms in brackets multiplying x in (12) and (13) vanish, since this is precisely the condition for mode (4) to be a solution. Accordingly, these terms are equal to zero for all wave numbers along the branch of the spectrum through (ω, k), so that, upon differentiation with respect to wave number, one obtains

$$\left[-k^2(\lambda+2G)\frac{dU}{dk} - ik(\lambda+G)\frac{dW'}{dk} + G\frac{dU''}{dk} + \omega^2\rho\frac{dU}{dk}\right]$$
$$+[-2k(\lambda+2G)U - i(\lambda+G)W'] + 2\omega\frac{d\omega}{dk}\rho U = 0 \tag{14a}$$
$$\left[-k^2G\frac{dW}{dk} - ik(\lambda+G)\frac{dU'}{dk} + (\lambda+2G)\frac{dW''}{dk} + \omega^2\rho\frac{dW}{dk}\right]$$
$$+[-2kGW - i(\lambda+G)U'] + 2\omega\frac{d\omega}{dk}\rho W = 0 \tag{14b}$$
$$\left[(\lambda+2G)\frac{dW'}{dk} - ik\lambda\frac{dU}{dk}\right] + [-i\lambda U] = 0 \quad (z=\pm h) \tag{15a}$$
$$\left[-ik\frac{dW}{dk} + \frac{dU'}{dk}\right] + [-iW] = 0 \quad (z=\pm h) \tag{15b}$$

Since $d\omega/dk = 0$ at the point (ω, k) under consideration, (14) and (15) imply that (12) and (13) are satisfied. Thus (11) is another mode at (ω, k).

It is easily seen that $d\omega/dk = 0$ at (ω, k) renders k a double root of the frequency equation $f(\omega, k) = 0$, at the frequency ω. Indeed, differentiating with respect to k along any branch of the spectrum,

$$\frac{\partial f}{\partial k} + \frac{\partial f}{\partial \omega}\frac{d\omega}{dk} = 0 \tag{16}$$

it is immediately concluded that $\partial f/\partial k = 0$ at (ω, k), since $d\omega/dk = 0$ there. The vanishing of f and its derivative $\partial f/\partial k$ at (ω, k) implies that modes of the form (11) exist at points where the frequency equation has degenerate roots and do not correspond necessarily to cut-off frequencies, since there are points of the spectrum with $k \neq 0$ and $d\omega/dk = 0$. Such a point is (ω_0, k_0), indicated in Fig. 1, at which the complex arm (not shown) of the second branch intersects the real arm, and a frequency minimum occurs for the real arm of the branch. An application, where the mode of the form (11) at (ω_0, k_0) found here plays a crucial role, is described in the next section.

Symmetric Vibrations of a Circular Disk

It is interesting to consider how the mode (11) obtained by differentiating (4) with respect to the wave number may combine with other modes (4) to yield free symmetric vibrations of a circular disk. Such vibrations were investigated experimentally by Shaw [9] and subsequently analyzed by Gazis and Mindlin [3] using an approximate

Downloaded 02 May 2010 to 171.66.16.25. Redistribution subject to ASME license or copyright; see http://www.asme.org/terms/Terms_Use.cfm

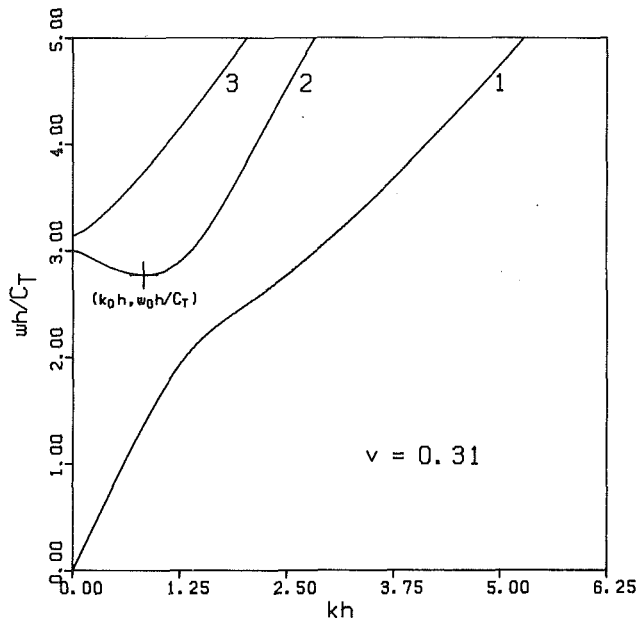


Fig. 1 Real arms of the first three branches of the Rayleigh-Lamb frequency spectrum

theory developed by Mindlin and Medick [7]. The analytical study [3] was focused on the edge vibrations observed in the experiments [9]. It was shown that modes of the infinite plate (layer) with complex wave numbers (complex arm of the second branch of the spectrum corresponding to symmetric modes) coupled with the mode having real wave number (first branch of the spectrum) lead, in the presence of the circular cylindrical boundary, to vibrations that are large near the edge of the disk and decay rapidly toward the center, in agreement with the experimental results. However, the analysis underestimated the frequency of the edge vibrations, which is virtually independent of the radius of the disk. The discrepancy was attributed [3] to the fact that the approximate theory [7] does not reproduce the details of the complex arm accurately. Apparently, these details are significant [3] in the neighborhood of the frequency of edge vibrations. Furthermore, both the analytical calculations [3] and the experiments [9] indicated another frequency, independent of the radius of the disk, at which free vibrations occur with vanishing error as the radius tends to infinity. This is the frequency minimum of the real arm of the second branch (Fig. 1). As mentioned earlier, a mode (11) appears at this frequency. The question thus arises as to how the appearance of such a mode leads to the above result.

Let R, $2h$ denote the radius and thickness of the disk, respectively. The circular cylindrical boundary $r = R$ is assumed to be traction-free, i.e.,

$$\sigma_r = \tau_{rz} = 0 \quad (r = R) \tag{17}$$

with

$$\sigma_r = \lambda\epsilon + 2G\frac{\partial u}{\partial r}, \quad \tau_{rz} = G\left[\frac{\partial u}{\partial z} + \frac{\partial w}{\partial r}\right] \tag{18}$$

where u, w are now the amplitudes of the radial and axial displacements, respectively, and ϵ is the dilatation

$$\epsilon = \frac{\partial u}{\partial r} + \frac{u}{r} + \frac{\partial w}{\partial z} \tag{19}$$

In general, the modes of vibration of the disk are linear combinations of layer modes

$$u(r,z) = U(z)J_1(kr) \tag{20a}$$

$$w(r,z) = iW(z)J_0(kr) \tag{20b}$$

It is well known [1, 4] that the eigenfunctions U, W and corresponding wave numbers k are the same as those appearing in the modes of vibration in plane strain (4). They can be conveniently calculated numerically by the finite element method. A mesh of N finite elements (subintervals) $[z_j, z_{j+1}]$, $1 \le j \le N$, is taken on the interval $[-h, h]$ so that

$$-h = z_1 < z_2 < \ldots < z_j < z_{j+1} < \ldots < z_N < z_{N+1} = h \tag{21}$$

An algebraic eigenvalue problem

$$[\mathbf{k}^2\mathbf{A} + ik\mathbf{B} + \mathbf{G} - \omega^2\mathbf{M}]\boldsymbol{\Delta} = \mathbf{0} \tag{22}$$

is easily obtained [10], assuming linear interpolation of U, W in each element (any other interpolation may be used as well). $\mathbf{A}$, $\mathbf{B}$, $\mathbf{G}$, and $\mathbf{M}$ are real block tridiagonal matrices, $\mathbf{A}$, $\mathbf{G}$, and $\mathbf{M}$ are symmetric; $\mathbf{B}$ is skew-symmetric [10]. The components of the eigenvector $\boldsymbol{\Delta}$ are the values of U, W at the nodes of the mesh:

$$\Delta_{2j-1} = U_j = U(z_j)$$

$$\Delta_{2j} = W_j = W(z_j)$$

$$1 \le j \le N+1 \tag{23}$$

The eigenvalue problem (22) yields $4N+4$ eigenvalues k and corresponding eigenvectors $\boldsymbol{\Delta}$. Thus $2N+2$ linearly independent semidiscrete modes

$$u_j(r) = U_jJ_1(kr) \tag{24a}$$

$$w_j(r) = iW_jJ_0(kr) \tag{24b}$$

$$1 \le j \le N+1$$

corresponding to (20) are obtained ($2N+2$ eigenvalues are the negatives of the other $2N+2$). At the boundary $r = R$, consistent nodal forces may be calculated (integrals of tractions multiplied by nodal shape functions) for each semidiscrete mode (24). The amplitudes of nodal displacements at $r = R$ corresponding to such a mode are readily available (24). For any linear combination of the semidiscrete modes (24), the nodal forces $\mathbf{F}$ and nodal displacements $\mathbf{U}$ at $r = R$ are related as [10]

$$\mathbf{F} = \mathbf{K}\,\mathbf{U} \tag{25}$$

$\mathbf{K}$ being a symmetric $(2N+2)\times(2N+2)$ matrix (dynamic stiffness matrix). For a mode of vibration of the disk, the homogeneous boundary conditions (17) require that $\mathbf{F} = \mathbf{0}$. Thus, the calculation of the frequency spectrum of the disk is reduced to finding the frequencies ω, for a given R, or, the radii R, for a given ω, which render $\mathbf{K}$ singular. The vector $\mathbf{U}$ is easily calculated for such a combination of ω, R, the participation factors of the modes (24) are then determined, and, finally, a semidiscrete mode of vibration of the disk is obtained. It should be noted that the computational effort involved in the procedure briefly described in the foregoing is dependent on N but not on R.

The highest frequency of interest in the present study is only slightly higher than the frequency minimum of the real arm of the second branch. For frequencies below such a level, only the layer modes corresponding to the first three branches of the spectrum contribute significantly to the modes of vibration of the disk [3]. This was verified in a preliminary convergence study which further indicated that working with $N = 20$ finite elements of equal thickness provides sufficiently accurate results. Figure 1 shows the real arms of the first three branches of the spectrum corresponding to symmetric modes ($\nu = 0.31$) as obtained from the albebraic eigenvalue problem (22). To test the validity of the numerical technique, the frequency of edge vibrations was calculated by trial and error. It was found to be approximately equal to $2.31C_T/h$ in excellent agreement with the experimental results obtained by Shaw [9]. Thus, the explanation by Gazis and Mindlin [3] of the discrepancy between experiments and the second-order

Downloaded 02 May 2010 to 171.66.16.25. Redistribution subject to ASME license or copyright; see http://www.asme.org/terms/Terms_Use.cfm

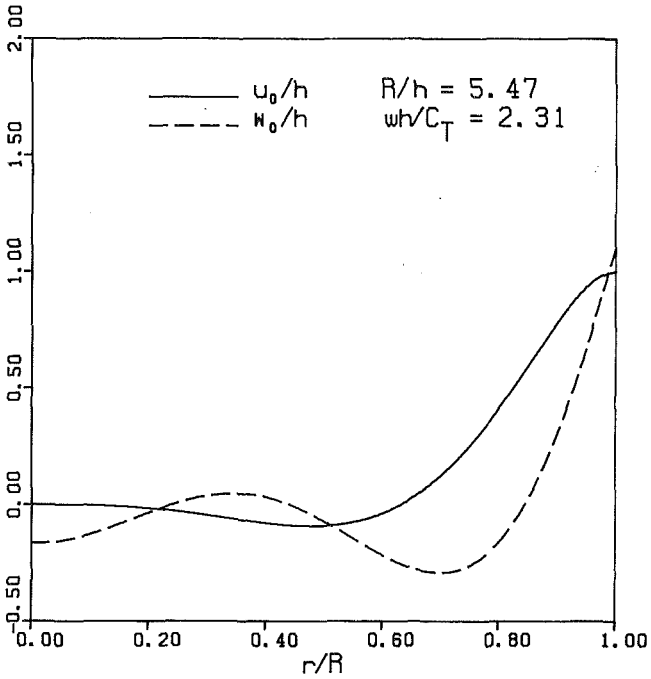


Fig. 2 Edge vibrations of the circular disk

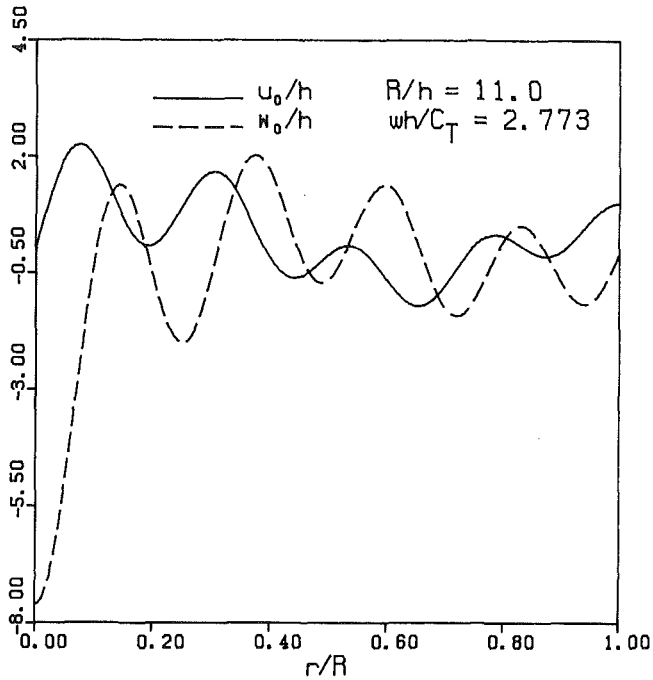


Fig. 3(*a*) Mode of vibration of the circular disk at ω_0

theory with respect to the frequency of edge vibrations is appropriate. Figure 2 shows the amplitudes of the displacements at $z = h$ (one of the faces of the disk) for a disk of radius $R = 5.47h$. The contribution of the two modes with complex wave numbers is dominant at the frequency of edge vibrations [3], and the rapid decay of displacements toward the center of the disk is clearly seen.

The frequency minimum ω_0 of the real arm of the second branch (Fig. 1) was calculated approximately equal to $2.773C_T/h$, and the real wave numbers k_0 (double root, second branch), $\hat{k}$ (first branch) at this frequency are $0.828/h$, $2.495/h$, respectively. Apart from the usual modes (20) corresponding to k_0, $\hat{k}$, there is another mode at (ω_0, k_0):

$$u(r,z) = \frac{dU}{dk} J_1(k_0 r) + rUJ_0(k_0 r) - \frac{1}{k_0} UJ_1(k_0 r) \tag{26a}$$

$$w(r,z) = i\frac{dW}{dk} J_0(k_0 r) - irWJ_1(k_0 r) \tag{26b}$$

This is the derivative of (20) with respect to the wave number. Working as in the case of plane strain and remembering that $d\omega/dk = 0$ at (ω_0, k_0), it may be shown that (26) satisfies the governing differential equations and the homogeneous boundary conditions. Figures 3 and 4 show the amplitudes of the displacements ($z = h$) at ω_0 for $R = 11.0h$, $19.83h$ and the contribution u_0, w_0 of the two modes with wave number k_0. The mild growth of u_0, w_0 with r, as seen in Fig. 4(*b*), confirms the presence of (26). It is important to notice that w and w_0 at $r = R$ are, to a very good approximation, equal to zero. This holds for $-h \le z \le h$, and for all values of R at ω_0 obtained by the numerical technique. Since the mode (20) with wave number $\hat{k}$ is the only other mode contributing significantly to the free vibrations of the disk at ω_0, it is readily concluded that $\hat{k}R$ must be very close to a zero of J_0. A quick calculation establishes this beyond any doubt. The radial stress at $r = R$ due to the mode (26) is:

$$-RJ_1(k_0 R)[(\lambda+2G)k_0 U + i\lambda W'] + 0(R^{-1/2}), \quad R \to \infty \tag{27}$$

while that due to (20) with wave number k_0:

$$J_0(k_0 R)[(\lambda+2G)k_0 U + i\lambda W'] + 0(R^{-3/2}), \quad R \to \infty \tag{28}$$

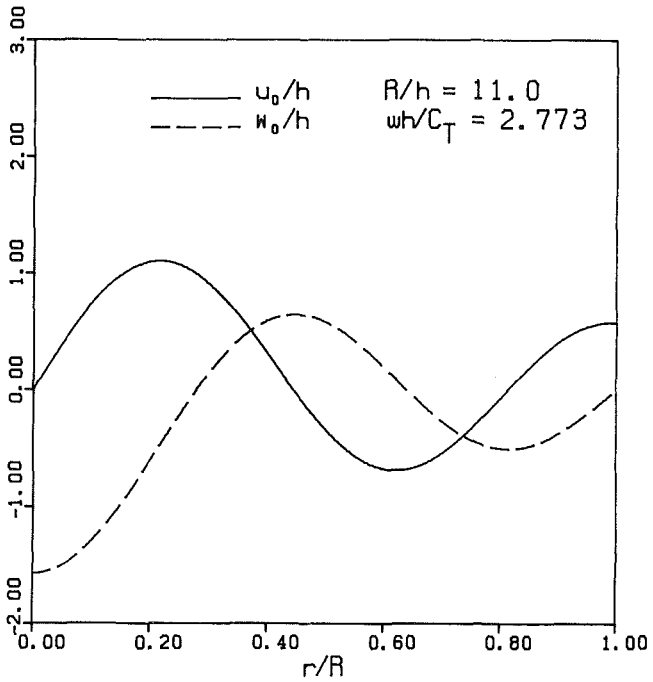


Fig. 3(*b*) Contribution of the two modes corresponding to (ω_0, k_0)

Thus, the condition (17*a*) can be satisfied with vanishing error as $R \to \infty$, if the mode (20) with wave number k_0 is multiplied by $RJ_1(k_0R)/J_0(k_0R)$ and added to the mode (26), as suggested by (27) and (28). That such a combination occurs is also supported by the fact that w_0 is almost equal to zero at $r = R$. Indeed, the axial displacement at $r = R$ due to the mode (26) is:

$$-RJ_1(k_0 R)[iW] + 0(R^{-1/2}), \quad R \to \infty \tag{29}$$

and that corresponding to (20) with wave number k_0:

$$J_0(k_0 R)[iW] \tag{30}$$

Again, the combination indicated in the foregoing annihilates

Downloaded 02 May 2010 to 171.66.16.25. Redistribution subject to ASME license or copyright; see http://www.asme.org/terms/Terms_Use.cfm

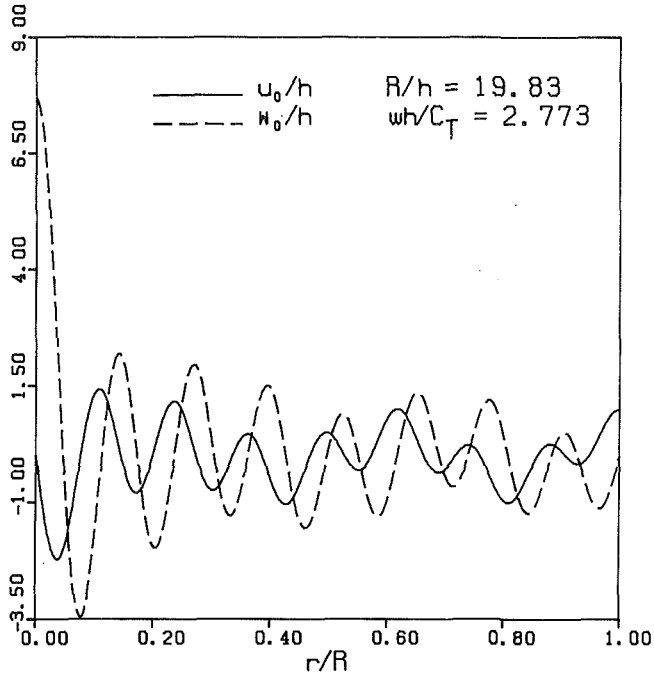


Fig. 4(*a*) Mode of vibration of the circular disk at ω_0

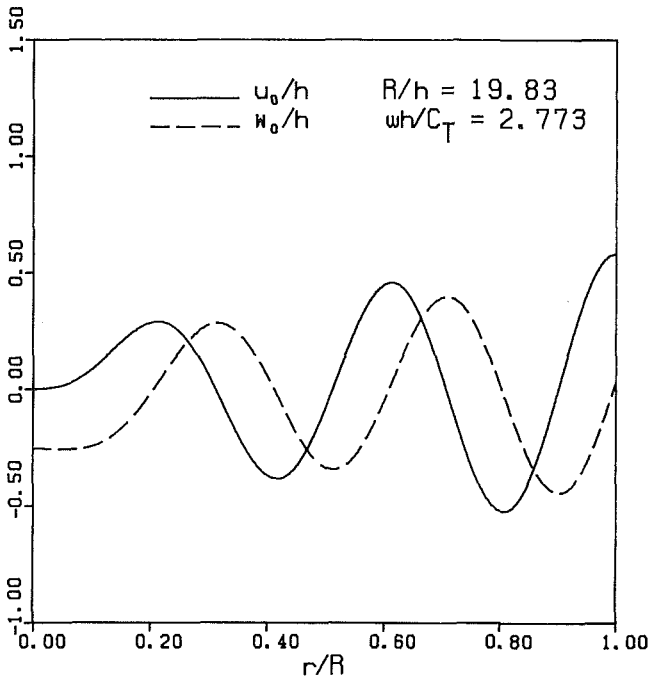


Fig. 4(*b*) Contribution of the two modes corresponding to (ω_0, k_0)

w_0 with error going to zero as $R \to \infty$. The shear stress at $r = R$ due to the combination of the two modes is given by:

$$R\frac{J_0^2(k_0R)+J_1^2(k_0R)}{J_0(k_0R)}G[U'+ikW]+0(R^{-1/2}), \quad R\to\infty \qquad (31)$$

Thus, the shear stress is $0(R^{1/2})$, $R \to \infty$, although it is equal to zero at $z = -h, 0, h$. For the boundary condition (17*b*) to be satisfied, the mode (20) with wave number $\hat{k}$ must be introduced. The participation factor of the mode must be $0(R)$, $R \to \infty$, in view of (31). However, introduction of this mode also brings about more radial stress at $r = R$:

$$J_0(\hat{k}R)[(\lambda+2G)\hat{k}\hat{U}+i\lambda\hat{W}']+0(R^{-3/2}), \quad R\to\infty \qquad (32)$$

$\hat{U}, \hat{W}$ being the eigenfunctions corresponding to $\hat{k}$. Clearly, this stress is equal to zero with vanishing error as $R \to \infty$, if $\hat{k}R$ is one of the zeroes of J_0.

The combination of the three modes at ω_0, as described in the foregoing, is consistent with all the numerical calculations. If the frequency is slightly lower or higher than ω_0, two modes with slightly differing wave numbers appear in the place of the mode (20) with wave number k_0 and (26) which, however, combine in essentially the same way as the two modes at ω_0. The other real wave number also undergoes a small change that implies a large change in R, as $R \to \infty$, so that the product of the wave number and the radius remains close to a zero of J_0. This explains the terrace-like appearance of the frequency spectrum of the disk at ω_0[3, 9].

It should be mentioned that, since the participation factors of the modes (20) with wave numbers k_0, $\hat{k}$ are $0(R)$, $R \to \infty$, while that of (26) is only 0(1), $R \to \infty$, the mode of vibration of the disk at ω_0 exhibits large displacements in a neighborhood of the center (Figs. 3(*a*), 4(*a*)). The growth implied by (26) can be seen in Fig. 4(*b*) because the participation factor of the mode (20) with wave number k_0 is approximately equal to zero for that value of the radius, i.e., k_0R is close to one of the zeroes of J_1.

The preceding analysis has demonstrated that nonseparable modes play a significant role in the free-vibration spectrum of a circular disk. Although explicit results were presented only for the point (ω_0, k_0) in Fig. 1, it is anticipated that similar conclusions should be appropriate at other frequencies where $d\omega/dk = 0$.

References

1 Achenbach, J. D., *Wave Propagation in Elastic Solids*, North Holland, 1973.

2 Di Prima, R. C., and Habetler, G. J., "A Completeness Theorem for Non-self-Adjoint Eigenvalue Problems in Hydrodynamic Stability," *Archive for Rational Mechanics and Analysis*, Vol. 34, 1969, pp. 218–227.

3 Gazis, D. C., and Mindlin, R. D., "Extensional Vibrations and Waves in a Circular Disk and a Semi-Infinite Plate," ASME JOURNAL OF APPLIED MECHANICS, Vol. 27, 1960, pp. 541–547.

4 Miklowitz, J., *The Theory of Elastic Waves and Waveguides*, North Holland, 1978.

5 Mindlin, R. D., "Mathematical Theory of Vibrations of Elastic Plates," *Proceedings, Eleventh Annual Symposium on Frequency Control*, U.S. Army Signal Corps Engineering Laboratories, Fort Monmouth, N.J., 1957, pp. 1–40.

6 Mindlin, R. D., "Vibrations of an Infinite Elastic Plate at its Cut-Off Frequencies," *Proceedings, Third U.S. National Congress of Applied Mechanics*, 1958, pp. 225–226.

7 Mindlin, R. D., and Medick, M. A., "Extensional Vibrations of Elastic Plates," ASME JOURNAL OF APPLIED MECHANICS, Vol. 26, 1959, pp. 561–569.

8 Mindlin, R. D., "Waves and Vibrations in Isotropic, Elastic Plates," in *Structural Mechanics*, Goodier, J. N., and Hoff, N. J., eds., Pergamon Press, New York, 1960, pp. 199–232.

9 Shaw, E. A. G., "On the Resonant Vibrations of Thick Barium Titanate Disks," *Journal of the Acoustical Society of America*, Vol. 28, No. 1, Jan. 1956, pp. 38–50.

10 Waas, G., "Linear Two-Dimensional Analysis of Soil Dynamics Problems in Semi-Infinite Layered Media," Ph.D. Dissertation, University of California, Berkeley, Calif., 1972.

Downloaded 02 May 2010 to 171.66.16.25. Redistribution subject to ASME license or copyright; see http://www.asme.org/terms/Terms_Use.cfm

The Improved Frequency Response Function and its Effect on Modal Circle Fits

K. B. Elliott
Instructor of Mechanical Engineering.
Assoc. Mem. ASME

L. D. Mitchell
Professor of Mechanical Engineering.
Mem. ASME

Department of Mechanical Engineering,
Virginia Polytechnic Institute
and State University,
Blacksburg, Va. 24061

When structures are excited by random force excitation the circle fits of the data around resonance are usually poor. The structural parameter estimates, which result from this fit, are usually erroneous. No matter how elegant the circle or the multimodal fit, the results will be poor if the frequency response function (FRF) is a poor representation of the actual structural response. In general for the random excitation case, this is the case. The conventional fast Fourier transform (FFT) method which is used to estimate the frequency response function, is given by $H_1(f) = G_{xy}/G_{xx}$. *This produces poor results when the coherence of the data falls in the resonance region. A drop in the coherence usually indicates noise at the input of the structure for this case.* $H_1(f)$ *is quite sensitive to such noise giving erroneous estimates. This paper investigates an alternative method for computing the frequency response function,* $H_2(f) = G_{yy}/G_{yx}$, *and its impact on the accuracy of the circle fit procedure used in modal analysis. This new estimator is not sensitive to input noise like the currently used* $H_1(f)$. $H_2(f)$ *provides the best estimate at or around resonance even in the presence of noise on the input signal. If one defines the average percentage fit error in the circle fit operation as 100 times the average radial deviation of the data points from the radius of the statistically fit circle divided by the fit circle radius, one can compute the circle fit accuracy for each of the proposed methods of data treatment. Typically, the percentage fitting error for* $H_1(f)$ *might be 10 percent while the fitting error for* $H_2(f)$ *using exactly the same data will be 0.5 percent. Thus, the proposed method eliminates long-standing system analysis errors through the use of a simple revision of the way the data are treated in the FFT processor around the resonance regions.*

Introduction

The frequency response function as computed by most fast Fourier transform systems today [1-3] is given as

$$H_1(f) = \frac{G_{xy}}{G_{xx}} = \frac{G_{uv}}{G_{xx}} \tag{1}$$

Refer to Fig. 1 for a definition of the terminology. The true frequency response function is

$$H_0(f) = \frac{G_{uv}}{G_{uu}} \tag{2}$$

where u and v denote the true inputs and outputs of the system, not the measured values. If $n(t)$ and $m(t)$ are the respective input and output noises in the measurement system and if one follows Bendat's [4] lead, one can show that

$$G_{xx} = G_{uu} + G_{nn} \tag{3}$$

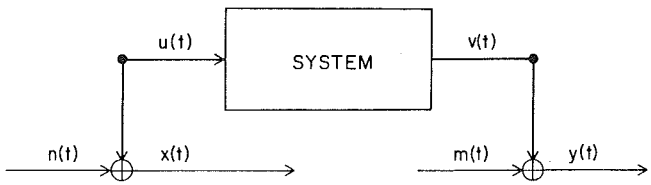


Fig. 1 System measurement model

Substitution of equation (3) into equation (1) yields

$$H_1(f) = \frac{G_{uv}}{G_{uu} + G_{nn}} = \frac{H_0(f)}{1 + \dfrac{G_{nn}}{G_{uu}}} \tag{4}$$

Bendat and Piersol [5] prove that $H_1(f)$ given in equation (4) is an optimal estimator of $H_0(f)$ provided that G_{nn} is zero. In real-world testing this is not the case and is particularly evident in the resonance and antiresonance regions. Mitchell [6] next showed that there was an alternate way of estimating the frequency response function as

Contributed by the Applied Mechanics Division for publication in the JOURNAL OF APPLIED MECHANICS.

Discussion on this paper should be addressed to the Editorial Department, ASME, United Engineering Center, 345 East 47th Street, New York, N.Y. 10017, and will be accepted until two months after final publication of the paper itself in the JOURNAL OF APPLIED MECHANICS. Manuscript received by ASME Applied Mechanics Division, August 1983; final revision, January, 1984.

Copyright © 1984 by ASME
Downloaded 02 May 2010 to 171.66.16.25. Redistribution subject to ASME license or copyright; see http://www.asme.org/terms/Terms_Use.cfm

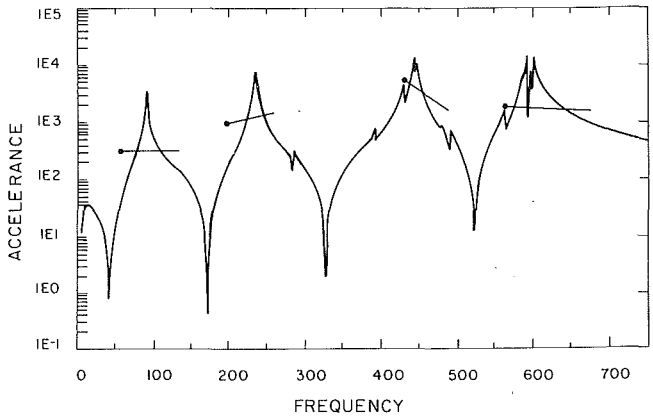


Fig. 2 Frequency response of the center of a square plate with superimposed switching criteria

$$H_2(f) = \frac{G_{yy}}{G_{yx}} = H_0(f)\left(1 + \frac{G_{mm}}{G_{vv}}\right) = \frac{H_1(f)}{\gamma_{xy}^2} \qquad (5)$$

This form of the frequency response estimator provides an estimate that is larger than the true H_0 in the presence of *output* noise. It is, however, more important that this estimator is not sensitive to input noise as in equation (4).

Random excitation usually causes a low level of the ture input power spectrum near the resonances. This is true because the impedance of the test structure is dropping drastically. This begins to effectively short circuit the shaker system. The shaker goes through large excursions and has a drastic drop in the impedance of the electromagnetic shaker input circuit at the frequency of the large excursions. Thus, the power amplifier become grossly mismatched with respect to the electromagnetic shaker load. Very little power is delivered to the shaker at these resonance frequencies. The input power spectrum drops toward the measurement system noise G_{nn} and the frequency response calculations become erroneous under the methods given in equation (1). Equation (5) remains uneffected. In addition, at resonance the true output signal is very large compared to the output noise. Thus, the ratio of the output noise to the true input power spectra, which leads to erroneous estimates when using equation (5), is very small compared to 1. Equation (5) then yields almost a perfect estimate of the true H_0 in the region of resonance.

On the other hand, at antiresonance, the output power spectrum drops toward output noise G_{mm} while the input power spectrum remains high with respect to the input noise power spectrum. Under these conditions equation (5) fails to yield acceptable results because of its sensitivity to output noise. The conventional method of computing a frequency response function (equation (4)) is best near or at an antiresonance. For this case the ratio of G_{nn} to G_{uu} is small. Thus, equation (4) becomes an excellent estimator of H_0. Further information on this topic may be obtained from reference [6].

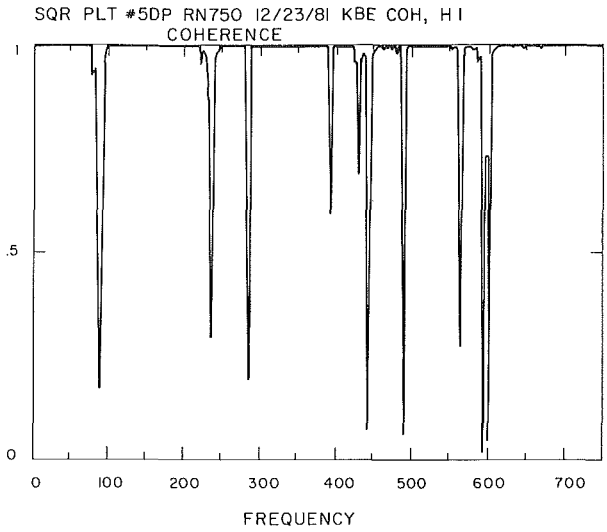


Fig. 3 Coherence function for Fig. 2 data

The Best of Both Worlds

One can conclude from the foregoing discussion that frequency response calculations should be done differently in different regions of the frequency response function. H_1 should be used in the antiresonance regions and H_2 should be used in the resonance regions. This kind of method selection would cause a high computational overhead if implemented in a general laboratory two-channel FFT processor. Moreover, the processor would have a difficult time discerning resonance from antiresonance without making a preliminary set of calculations concerning the slopes and rates if changes of slopes. These will be used to look for relative minima or maxima. This procedure would slow the frequency response function calculation greatly. However, a post-processing scheme can provide the accuracy desired when the need arises. This, of course, is the case when one is attempting to extract modal parameters from experimental data via circle or multimode fitting techniques.

An interactive post-processor has been developed which allows the user to select the regions of the frequency response function that are to be enhanced by the use of equation (5),

Nomenclature

FFT = Fast Fourier transform
FRF = Frequency response function
G_{mm} = The autospectrum of the output noise
G_{nn} = The autospectrum of the input noise
G_{xx} = Autospectrum of the system input
G_{xy} = Cross-power spectral density between input and output = G_{yx}^* where * indicates the complex conjugate
G_{yy} = Autospectrum of the system output
$H_0(t)$ = The "true" frequency response function (FRF)
$H_1(f)$ = Conventional estimator of the frequency response function (FRF) – output divided by input
$H_2(f)$ = Improved (inverse) estimator of the frequency response function (FRF) – output divided by input
$m(t)$ = The uncorrelated noise in the output
$n(t)$ = The uncorrelated noise in the input
$u(t)$ = The "true" input's signal to the measured system
$v(t)$ = The "true" output of the system being measured
$x(t)$ = The input signal measured by the FFT analyzer – sum of the "true" input plus uncorrelated noise
$y(t)$ = The output signal measured by the FFT analyzer – sum of the "true" output plus uncorrelated noise
γ_{xy}^2 = Coherence function between the input and output

Downloaded 02 May 2010 to 171.66.16.25. Redistribution subject to ASME license or copyright; see http://www.asme.org/terms/Terms_Use.cfm

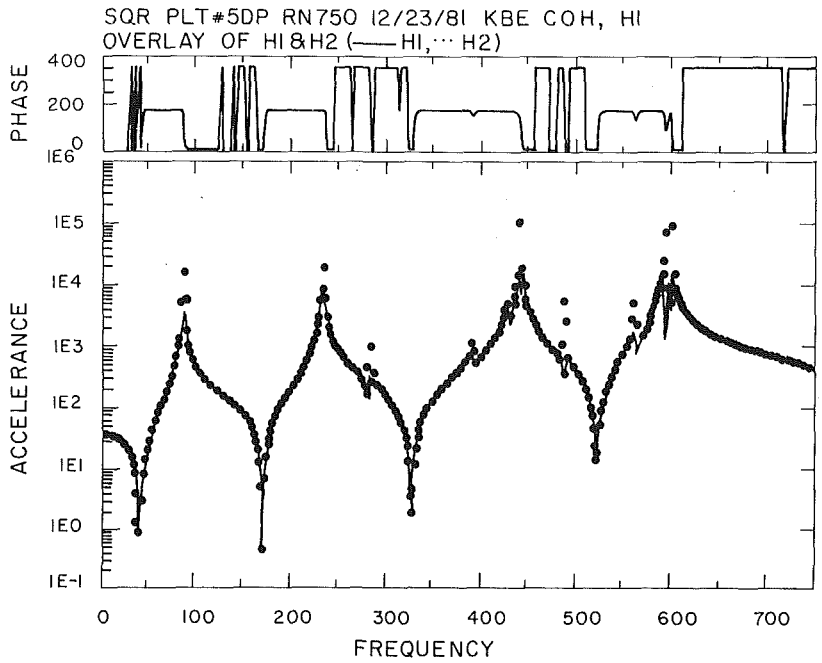


Fig. 4 Overlay of H_1 and H_2 where H_2 is computed from coherence

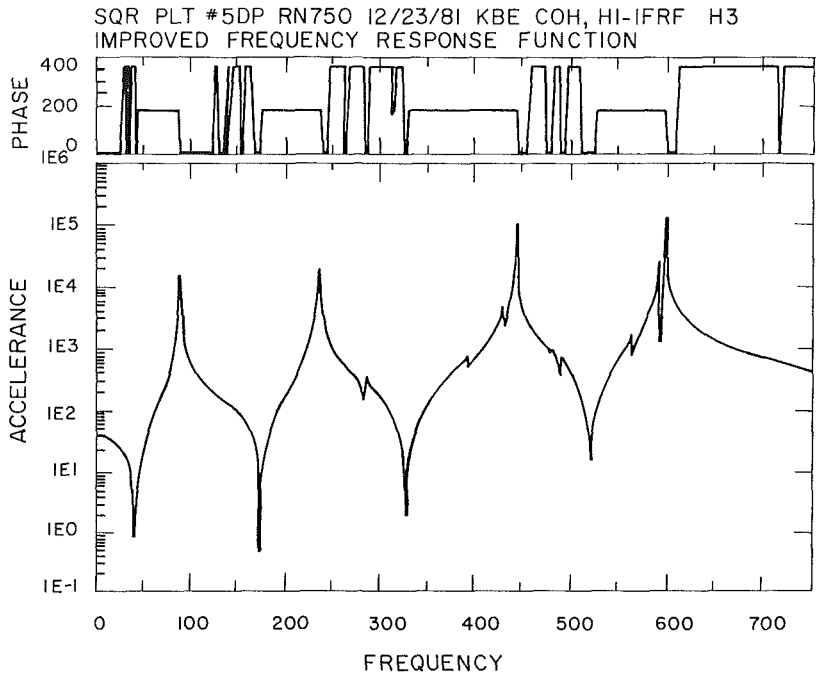


Fig. 5 Composite enhanced frequency response function

$H_2(f)$. This enhancement routine was developed for several reasons. They are

1. To illustrate the errors that the engineering community has been living with for a number of years.

2. To provide a means of improving modal parameter estimates via an improvement of the data going into the estimates.

3. To provide a means of illustrating the large errors in modal parameter estimates that have resulted from the use of $H_1(f)$.

Figure 2 shows a typical frequency response function at the central driving point of a 46 × 46 cm (18 × 18 in.) square 0.32 cm (0.125 in.) thick plate. The regions near resonance have poor coherence (See Fig. 3) and are in need of enhancement. These regions could have been enhanced through the use of band limited white noise that would concentrate its power in the regions of each resonance. An analysis would have to be done in each region and the results pieced together to get the total result. This, of course, will be very time-consuming and will require specialized excitation equipment. The use of zoom would be helpful in the patching of various sections together.

In lieu of this procedure a post-processing routine prompts the user to select the regions where the computations will be switched from the $H_1(f)$ to the $H_2(f)$ equation. The sloped

Downloaded 02 May 2010 to 171.66.16.25. Redistribution subject to ASME license or copyright; see http://www.asme.org/terms/Terms_Use.cfm

Table 1 Effective parameters for the conventional and inverse methods-baseband data

Item	H_1, Conventional	H_2, Inverse	Ratio, H_1/H_2
Mass	$6.471E-003$	$1.328E-002$	0.487
Stiffness	$1.850E+003$	$4.067E+003$	0.455
Damping	$1.18E-001$	$2.120E-002$	5.274
Percent critical damping	1.62 percent	0.14 percent	11.570

Table 2 Effective parameters for the conventional and inverse methods-zoomed data

Item	H_1, Conventional	H_2, Inverse	Ratio, H_1/H_2
Mass	$1.032E-002$	$8.961E-003$	1.152
Stiffness	$1.450E+005$	$1.260E+005$	1.151
Damping	$4.668E-002$	$3.995E-002$	1.168
Percent critical damping	0.06 percent	0.06 percent	1.000

lines crossing the various resonance peaks are the user selected switching criteria. As one proceeds from left to right and cross the first switching line while approaching the first resonance the computations switch from the $H_1(f)$ to $H_2(f)$. As one recesses from the first resonance and recrosses the switching line the computations switch back to the $H_1(f)$ procedure. This procedure is repeated at any of the resonances selected by the user.

There are two ways to compute the new $H_2(f)$ as indicated by equation (5). These are selectable by the user. The coherence method has an advantage in that the computation involves a simple scalar division of a complex number, a computationally efficient procedure. However, one can not just divide the individual $H_1(f)$'s by its corresponding coherence function since poor coherence at antiresonances are possible. This latter case would result in the frequency response function to be computed by the inverse method, $H_2(f)$, when this is inappropriate and highly erroneous. This reinforces the need for the interactive switching shown in Fig. 2. The second method of computation of the frequency response function by the inverse estimator method involves the use of the cross-spectrum and the autospectrum as given in equation (5). This calculation is more time-consuming in that it will involve a scalar divided by a complex number. Many more operations are needed than that required for the coherence method. This second method will be termed the cross-spectrum method. This method has the advantage that the data used are as close to the original data as possible and therefore minimize the errors that are introduced by the lack of precision in the FFT processor compared to the 13-digit precision of the post-processing routines. It does have one disadvantage. That is, the estimate of the output power spectrum, G_{yy}, will be excessively low at low levels of output power if the FFT's averaging process includes a numeric truncation procedure. The larger the number of averages the greater the round-down effect and the more in error the output power spectrum. Again this problem can be eliminated by the process of interactive development of switching criteria by the user. The reader is reminded that the inverse method is not be used in the regions around the antiresonance. This is the region where the output autospectrum gets small and the truncation error becomes significant. The use of the conventional frequency response function calculational method in these regions eliminates the need for the use of the potentially poorly estimated G_{yy}.

In the following discussion the plots that were processed by the coherence method will have COH in their captions; those that resulted from the cross-spectrum method will be labeled X-SPEC, AUTO-SPEC. Those plots that are labeled as ($H1$), ($H2$), and ($H3$) are, respectively, the frequency response function estimates obtained by equations (1), (5), and a combination of these equations as specified by the user

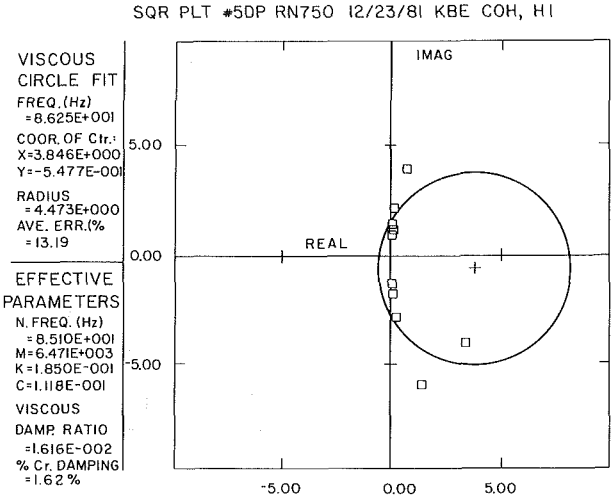


Fig. 6 Circle fit of the first resonance in Fig. 2

definable switching criteria. Thus, ($H3$) is a composite of the best of both worlds of computational methods for estimating H_0.

Errors Caused by $H_1(f)$

Figure 2 shows a result produced by a typical FFT processor. If one computes the inverse estimator of H_0 by the coherence method and overlays the result as dots on the graph of the standard $H_1(f)$, one gets Fig. 4. Notice that the data around resonance is up 10 times bigger than that of the standard estimate. Theory would say that the dotted curve is by far the most accurate estimator of the H_0. Errors of this nature have plagued the modal analysis people for years in that the coherence was poor in the region of resonance. A lot of effort has been expended in each of these experimental cases to try to improve test conditions in order to improve the coherence of the data. When all else failed, the remaining poor coherence was blamed on the leakage of signal from one FFT frequency bin to an adjacent bin. This leakage is caused by the finite width and side-lobing of the resultant frequency domain filter as caused by the time-domain filter that is applied to the data in order to force it to be periodic in the FFT's time window. From the evidence that will be presented later one will find that even these errors as well as the residual noise in the signal processing can be eliminated from the signal analysis procedure through the proper combination of user-defined switching and the inverse frequency response function computational methods.

If the switching criteria shown in Fig. 2 are used, one can

Downloaded 02 May 2010 to 171.66.16.25. Redistribution subject to ASME license or copyright; see http://www.asme.org/terms/Terms_Use.cfm

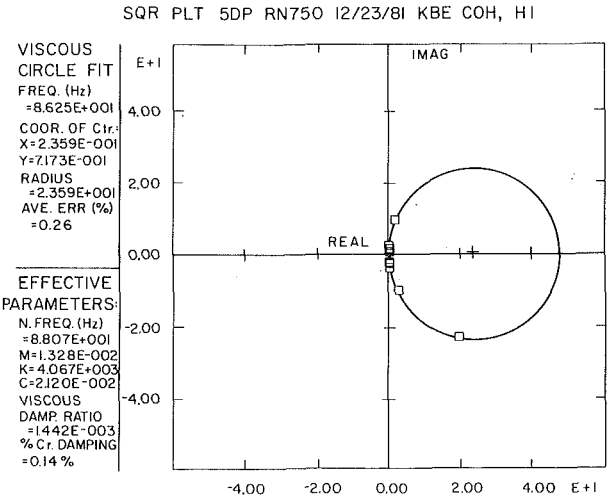


Fig. 7 Circle fit of the first resonance in Fig. 5 using the composite frequency response function

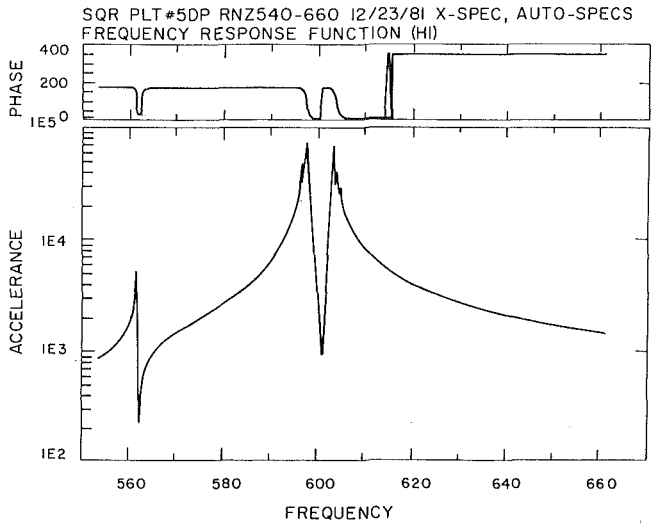


Fig. 8 Zoomed frequency response calculated by the conventional method H_1

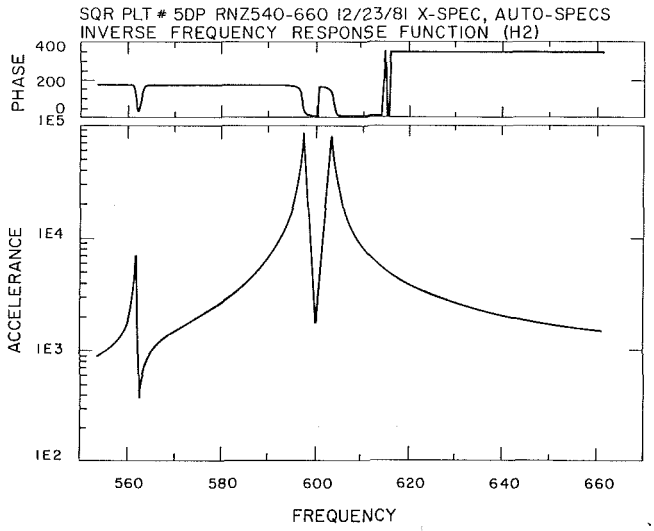


Fig. 9 Zoomed frequency response function calculated by the inverse method, H_2

generate a composite frequency response function. Such a figure would show those areas computed by the $H_1(f)$ method in solid line form and those areas computed by the $H_2(f)$ method in dotted line form. When the user is satisfied that the composite frequency response function is acceptable the user may save the enchance frequency response function data on digital media for future processing. Future retrieval and plotting of this data will result in a solid line plot labeled as $H3$ as shown in Fig. 5. This is the best of both worlds form of the frequency response function estimator.

Improved Circle Fits

If the first resonance peak (86.25 Hz) in Fig. 2 is circle fit, the plot shown in Fig. 6 results. The diamonds are the data points and the solid line circle a regressional attempt to fit this data. The local effective parameter of mass, stiffness, and damping are shown. These are related to the true modal parameter via modal vector [7]. Visually the fit is poor. The data does not seem to fit a circle! The average circle fitting error is given as 13.19 percent. The validity of the effective local parameter cannot be assessed without additional information.

Next one uses the composite frequency response function of Fig. 5 at the frequency of 86.25 Hz to carry out the circle fit. Figure 7 results. Remember this is exactly the same basic FFT data processed in the new inverse way (See Fig. (5)). Amazingly the data points now seem well behaved and conform to an approximate circle! Notice that the average circle fitting error is now 0.26 percent! This fitting error has been reduced by a factor of more than 50. This is the most convincing argument for the use of the inverse computational method around resonance. Next, compare the local effective parameters for the two methods as summarized in Table 1.

It is obvious from Table 1 that the source for the modal parameter, the local effective parameters are in error by factors of 2 and 5! The percent of critical damping is more than 10 times the actual value. This means that the severity of the resonance is being underestimated by this same factor. An engineer never wants to be working with an underestimate of the severity of a particular design situation. This situation is, of course, unacceptable.

The need for accurate modal parameter is becoming more critical as one begins to consider the possibility of using the modal database for modification of the structure on the computer before actual physical changes are to be made to the test prototype. An accurate data base is necessary so that accurate predictions may be made of the changes in resonance frequencies when user-defined structural changes are made in the modal model. Here the actual local stiffness is more than twice that determined by the conventional method for computing the frequency response function $H_1(f)$. Remember all randomly excited data processed by all commercially available FFT processors gives one these types of results when the specialized narrow-band random noise excitations are not used.

$H_3(f)$ and its Effect on Zoomed Data

When one encounters problems of low coherence one will often attempt to analyze the frequency response function by zooming in on the resonance regions of difficulty. The thought is that the increased resolution will reduce the noncoherent leakage that can cause low coherence around very sharp resonance regions. Figure 8 shows a zoomed version of the double peak in the region of 600 Hz previously shown in Fig. 2. Notice the ragged nature of the data around the peak regions. The response is certainly cleaner than that shown in Fig. 2, but is visually about the same as that shown in Fig. 5. If one uses the cross-spectrum method of computing

Downloaded 02 May 2010 to 171.66.16.25. Redistribution subject to ASME license or copyright; see http://www.asme.org/terms/Terms_Use.cfm

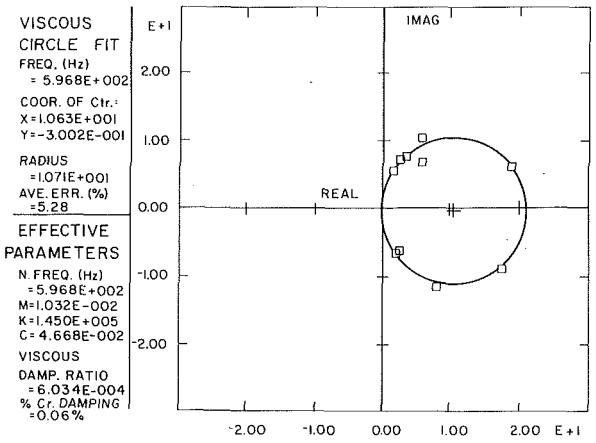


Fig. 10 Circle fit of the first of the double peaks in Fig. 8 – conventional method, H_1

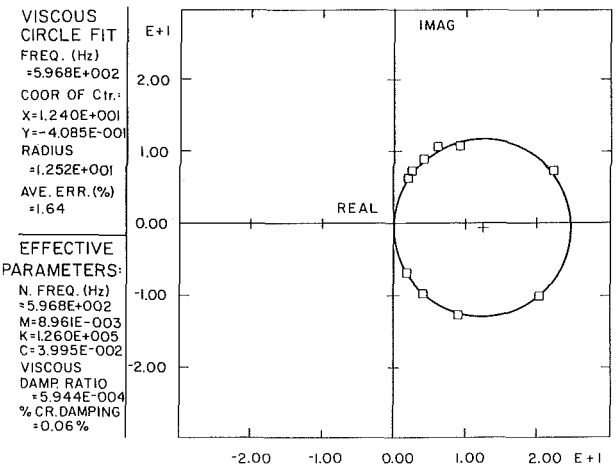


Fig. 11 Circle fit of the first of the double peaks in Fig. 9 – inverse method, H_2

the $H_2(f)$ estimate, one finds the frequency response function shown in Fig. 9. Notice the improved continuity of the zoomed frequency response functions. One suspects from these results that indeed the composite frequency response estimation methods can even improve zoomed data.

The real test of the validity of the enchancement procedure is to compare the results of circle fits of the data from Figs. 8 and 9. These circle fits are shown in Figs. 10 and 11, respectively. Notice that the data in Fig. 11 fits the statistical circle more closely and has a fitting error of 1.64 percent compared to the fitting error from Fig. 10 of 5.28 percent. Thus, the enchancement procedures even help clean up zoomed data. In this case the fitting error is reduced to less than one-third of that of the conventional method. Table 2 shows a comparison of the various local parameter for the conventional and the inverse method of computing the frequency response function around the resonance. Like the case of the baseband data, the newer inverse method improves the circle fits and the resultant parameter estimation. However, the change of the estimates is of the order of 15 percent. This is not a great change in the parameter estimation but there may be much more difficulty measuring problems that will not yield so easily to zoom technique and will require the refinement of the inverse computation technique. Moreover, if the data analysis is critical enough to warrant the use of zoom techniques it certainly warrants the use of the best method for the computation of the frequency response function to be used to carry out the circle fits.

Summary and Conclusion

In this paper the inverse method for the computation of the frequency response function is merged with the standard method for such computations. The technique used to merge these methods is the use of a user-defined switching system. The computational methods are automatically switched into use according to the user's specification.

Next, the composite frequency response function was used to provide data for circle fit procedures. The results of this effort showed that with the use of baseband data the circle fitting error could be reduced by factors of up to 50. The local modal parameter were changed by as much as a factor of 5.

Zoomed data was processed in the same way. This effort showed that in a typical case the circle fitting error was reduced by a factor of three while the effective local parameters were only changed by about 15 percent.

From these efforts and observations one concludes:

1. The inverse method of computing the frequency response function is superior to the conventional method in the vicinity of resonances.

2. The conventional method of computing the frequency response function is superior to the inverse method in the vicinity of antiresonances.

3. For optimality reasons it is proposed that the computation of critical frequency response functions be computed by a proper intermix of the two different methods.

4. The use of the composite frequency response function enhances the circle fitting of baseband data greatly. In fact, data that has yielded to no other techniques has been found to yield to this technique. The results have been almost perfect circle fits.

5. The system effective local parameters are best estimated by the composite frequency response function circle fits. These parameters vary by a factor of as much as five from the estimates obtained for the conventional methods. Modeling parameters that are off by a factor of five can yield very poor results when one attempts to carry out structural modifications via a mathematical model that has been constructed from these poor parameter estimates.

6. The percent of critical damping is in greatest error. The estimate of this damping is many times a factor of 10 or more too high, when baseband data is used.

7. Zoomed data that is sourced in a composite frequency response function, when circle fit, shows small improvements to the effective local parameter, but does have circle fit errors that are a factor of three lower, when the composite frequency response function is used.

8. All in all there is no theoretical reason why the composite frequency response function should not be used for all FFT-based calculations. However, practically speaking, the computational overhead and its associated memory and time requirements make the everyday usage in a standard FFT impractical. However, where modal analysis and structural modification is concerned these techniques are very important in providing an accurate database from which to work.

9. The preceding statement will soon become obsolete with the advent of the use of array processors as an integral part of future FFT processors. The speed acquired through the use of this hardware can and will allow one to do the necessary slope and slope rate of change preprocessing so that the machine will be able to automatically ascertain which of the two

Downloaded 02 May 2010 to 171.66.16.25. Redistribution subject to ASME license or copyright; see http://www.asme.org/terms/Terms_Use.cfm

methods should be used for each frequency response calculation in the frequency domain.

The authors feel that one of the neglected keys to sound modal analysis and structural modification prediction is the development of a sound database from which the modal model may be built. Small improvements in this area have occurred in the past. The methods presented here provide major improvements in one's abilities to obtain valid data from baseband FFT data. Incremental improvements were obtained in the processing of zoomed data.

Acknowledgments

The authors acknowledge the support of this effort by the Zonic Corporation, Milford, Ohio.

References

1 Spectral Dynamics Corporation, "SD360 Digital Signal Processor," Sales Brochure, Spectral Dynamics Corp., San Diego, Calif. 1975.

2 Zonic Corporation, "Signal Processing Language Reference," *Zonic 6080 System Manual*, Zonic Corporation, Milford, Ohio, 1980, pp. 3-70; 3-73C.

3 Nicolet Scientific Corporation "Dual-Channel FFT Analyzer," Sales Brochure for Model 660, Nicolet Scientific Corporation, Northvale, N. J., undated.

4 Bendat, J. S., and Piersol, A. G., *Random Data: Analysis and Measurement Procedures*, Wiley-Interscience, New York, 1971.

5 Bendat, J. S., and Piersol, A. G., *Engineering Applications of Correlation and Spectral Analysis*, Wiley-Interscience, New York, 1980, pp. 98-100.

6 Mitchell, L. D., "Improved Methods for the Fast Fourier Transform (FFT) Calculation of the Frequency Response Function," ASME *Journal of Mechanical Design*, Vol. 104, 1982, pp. 277-279.

7 Luk, Y. W., "System Modeling and Modification via Modal Analysis," Ph.D. dissertation submitted to the faculty of the Department of Mechanical Engineering of Virginia Polytechnic Institute and State University, Blacksburg, Va., Aug. 1981.

Downloaded 02 May 2010 to 171.66.16.25. Redistribution subject to ASME license or copyright; see http://www.asme.org/terms/Terms_Use.cfm

Observation and Evolution of Chaos for an Autonomous System

E. H. Dowell
Dean,
School of Engineering,
Duke University,
Durham, N. C. 27706
Mem. ASME

Time histories, phase plane portraits, power spectra, and Poincare maps are used as descriptors to observe the evolution of chaos in an autonomous system. Although the motions of such a system can be quite complex, these descriptors prove helpful in detecting the essential structure of the motion. Here the principal interest is in phase plane portraits and Poincare maps, their methods of construction, and physical interpretation. The system chosen for study has been previously discussed in the literature, i.e., the flutter of a buckled elastic plate in a flowing fluid.

Introduction

Several authors including Holmes [1], Holmes and Marsden [2], Thompson [3], and Dowell [4] have discussed the complicated motion that may occur due to the flutter of buckled plates. Indeed chaotic motions are now known to occur for a variety of relatively simple derterministic systems [3–5]. In the present paper the flutter of a buckled plate is again considered, and various means for observing the evolution of chaos are employed.

In particular, the Poincare maps which are presented are the first obtained for the particular example studied and among the few extant for *any autonomous* system. A simple physical motivation is provided for the manner in which the Poincare maps are constructed. Also an interpretation of their physical significance is given.

In the following, a general discussion of observation and evolution of chaos is presented first and then the example of flutter of a buckled plate is considered in some detail.

Observation of Chaos

To observe chaos, and to better understand it, several descriptors are available. Among these are:

Time histories;

Phase plane portraits;

Power spectral densities (or their Fourier transforms, correlation functions);

Poincare maps

The first three are standard and require no further elaboration here. The last is not and a few words of explanation are in order. Also see Reference [5].

A (two-dimensional) Poincare map is a plot in the (two-dimensional) phase plane at chosen discrete instants of time. For example, one might plot a displacement coordinate versus its velocity. However one might also plot two coordinates versus each other for systems of third or higher order. The *crucial* question, however, is the choice of the discrete instants of time. A normal phase plane plot, of course, is for all (continuous) instants of time.

For a nonautonomous system an appropriate choice is rather obvious. The system is forced by an input of prescribed frequency and, hence, period. Thus to construct a Poincare map one normally chooses to plot data in the phase plane at instants of time separated by equal time intervals corresponding to a period of the input. For an autonomous system, however, which is our interest here, the choice is less obvious. Nevertheless Poincare maps may also be constructed for such systems and the method for doing so may be considered a generalization of that used for nonautonomous systems.

The key concept is that of a clock for the Poincare map based on the occurrence of an event. In general, these events will *not* occur at *equal* time intervals. Indeed they may occur at *chaotic* time intervals. For example, and to be concrete, consider an elastic plate whose deflection, W, depends on one (or more) spatial variable(s) and time. Choose a point on the plate and observe the plate deflection and its velocity there. Define the event as being the passage of the velocity of the plate at that point through zero (or through any constant value, although some values of velocity will not occur and hence are inappropriate choices). Now, at those time instants (which may occur periodically or chaotically) when the plate velocity is zero, plot the deflection of the selected point on the plate versus the deflection at some other selected point on the plate. The result is a Poincare map. There are (infinitely) many variations on this same idea, of course. For example, plotting the deflection versus velocity of some selected point on the plate at those time instants when the velocity of some *other* selected point on the plate is zero would give a more conventional (chaotically stroboscopic) phase plane plot which is another Poincare map. Indeed, for technical reasons,

Contributed by the Applied Mechanics Division for presentation at the Winter Annual Meeting, New Orleans, La., December 9-14, 1984 of THE AMERICAN SOCIETY OF MECHANICAL ENGINEERS.

Discussion on this paper should be addressed to the Editorial Department, ASME, United Engineering Center, 345 East 47th Street, New York, N.Y. 10017, and will be accepted until two months after final publication of the paper itself in the JOURNAL OF APPLIED MECHANICS. Manuscript received by ASME Applied Mechanics Division, April, 1983; final revision, December, 1983. Paper No. 84-WA/APM-15.

Copies will be available until August, 1985.

Copyright © 1984 by ASME
Downloaded 02 May 2010 to 171.66.16.25. Redistribution subject to ASME license or copyright; see http://www.asme.org/terms/Terms_Use.cfm

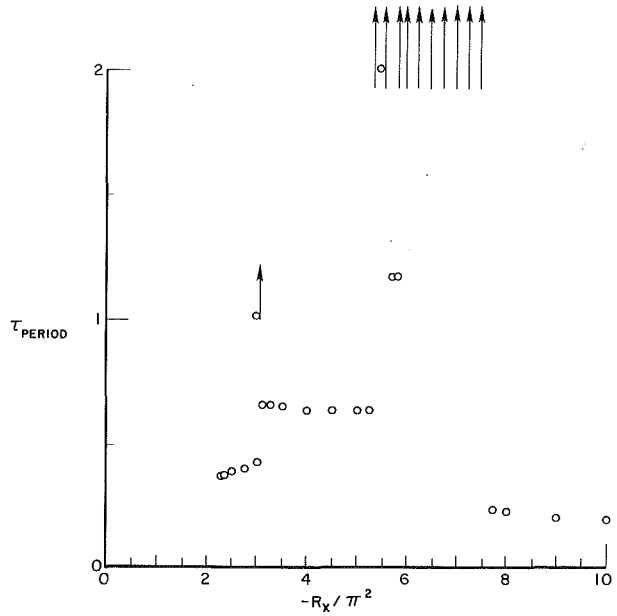


Fig. 1 Period of motion versus in-plane load

in some applications, yet other choices of Poincare map coordinates may be desirable. This will be discussed further. Also, of course, higher (than two) dimensional Poincare maps may be constructed. Indeed in the mathematical literature, a Poincare map of dimension less than N-1 where N is the order of the system is referred to as a reduced Poincare map [6]. The unifying feature of all such maps, however, is the concept of a (stroboscopic) clock based on the occurrence of an event.

Using the four descriptors listed in the foregoing, including the Poincare map, one may observe and better understand the evolution of chaos.

Evolution of Chaos

There are several distinct phenomena that occur during the evolution of chaos. While the compilation discussed in this section is not thought to be exhaustive for all examples that may be of interest, it does appear reasonably complete for the example discussed in detail in the following section. Moreover, and perhaps more importantly, because of their intrinsic quality, these phenomena are likely to appear in many other examples as well.

It is convenient to divide the evolution of chaos into three phases; the beginning, the onset, and the maturing process.

The Beginning. It is presumed that a limit cycle of a dominant single frequency has been established. (Often the motion will be nearly simple harmonic in time.) This may be a result of a Hopf Bifurcation, for example [5]. As some parameter in the governing equations of motion is changed, several characteristic changes in the motion occur. These include:

large changes in motion frequency or period near some parameter values for small changes in the parameter; the period generally becomes larger as chaos is approached.

changes in the number of maxima and minima in the time history of the motion during one period of motion; the number may increase as chaos is approached.

In the beginning (by definition), the motion remains periodic.

The Onset. The onset of chaos may be identified in several ways:

The failure of the time history to repeat itself over any finite time interval. Operationally this may be tedious to determine.

The diffusion of the phase plane plot [ideally diffusing from a curve of infinitesimal thickness that represents periodic motion to a set of points that nearly (completely) fills a finite region of the phase space when the motion is observed over a very large (infinite) time]. This is usually readily observed.

The broadening of the power spectral peaks (ideally from delta functions which are characteristic of periodic motion to a continuous distribution characteristic of chaotic motion). This is usually readily observed.

The Maturing Process. It is in the maturing process that Poincare maps become of special interest. Well beyond the onset of chaos, diffusion in the phase plane has become so pronounced that now a phase plane portrait is only indicative of the minima and maxima of the chaotic motion. However Poincare maps may be used to detect order in the chaos, though eventually such maps may undergo diffusion as well.

One interpretation of a Poincare map is as a form of conditional probability. That is, it answers the questions, given some event and the value of one system coordinate, what is the likely value of another system coordinate? Not surprisingly, at least in retrospect, the answer to this question possesses considerably more structure than the answer one would obtain if the coordinates were observed at *any* choice of *equal* time intervals rather than at those instants determined by the occurrence of an event. Choosing instants of equal time intervals would simply produce conventional phase plane portraits, unless such time intervals should happen to correspond to an *event*, e.g., the (periodic) input force reaching a maximum for a nonautonomous system. Note that using the concept of a Poincare map based on the occurrence of an event, in the nonautonomous case it is the force achieving a certain value (occurrence of an event), rather than the passage of a certain time interval, which triggers the clock of the Poincare map.

An Example

The autonomous system chosen for study is that of reference [4], hereafter referred to as Part I. Briefly, the physical system consists of an elastic plate embedded in an otherwise rigid surface and the adjacent fluid that flows over the top of the plate. A (compressive) in-plane load is applied to the plate.

The behavior of this system is governed by a (set of) partial differential equation(s) which here and in Part I is considered in its simplest form. More elaborate mathematical-physical models are considered in reference [7]. For simplicity, in the present paper the plate geometry is taken to be one-dimensional and the plate deflection, w is therefore a function of a single spatial position variable, x, and time, t. The nonlinear partial differential equation is reduced to a set of nonlinear ordinary differential equations (NODE) in time by expanding w in a set of chosen spatial functions, e.g.,

$$w(x,t) = \sum_{n=1}^{N} a_n(\tau) \sin \frac{n\pi x}{a} \tag{1}$$

where a is the plate length. The a_n satisfy a set of N NODE. These equations are solved by a numerical time marching algorithm. For further details see Part I. τ is a non-

Downloaded 02 May 2010 to 171.66.16.25. Redistribution subject to ASME license or copyright; see http://www.asme.org/terms/Terms_Use.cfm

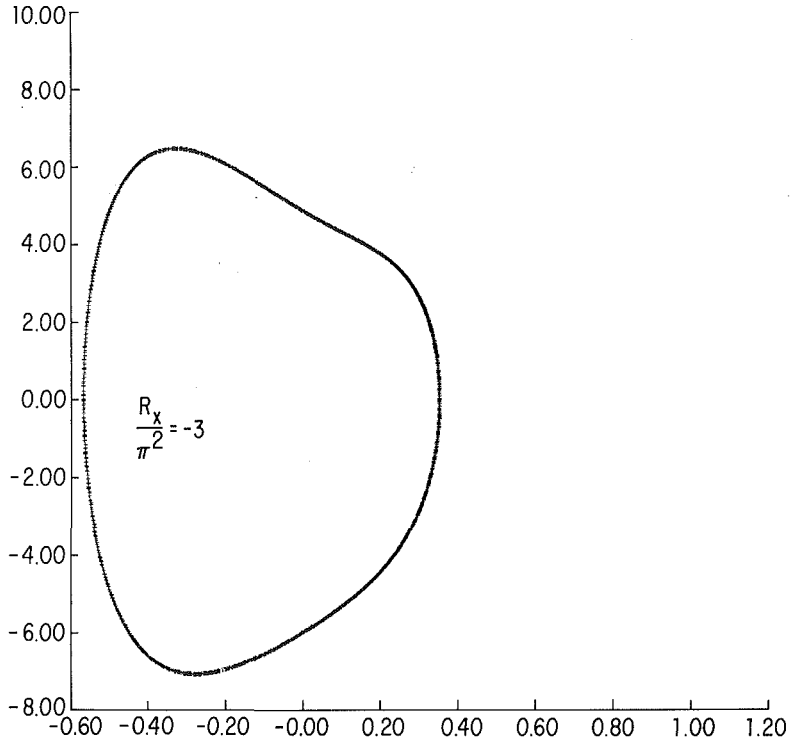


Fig. 2(*a*)

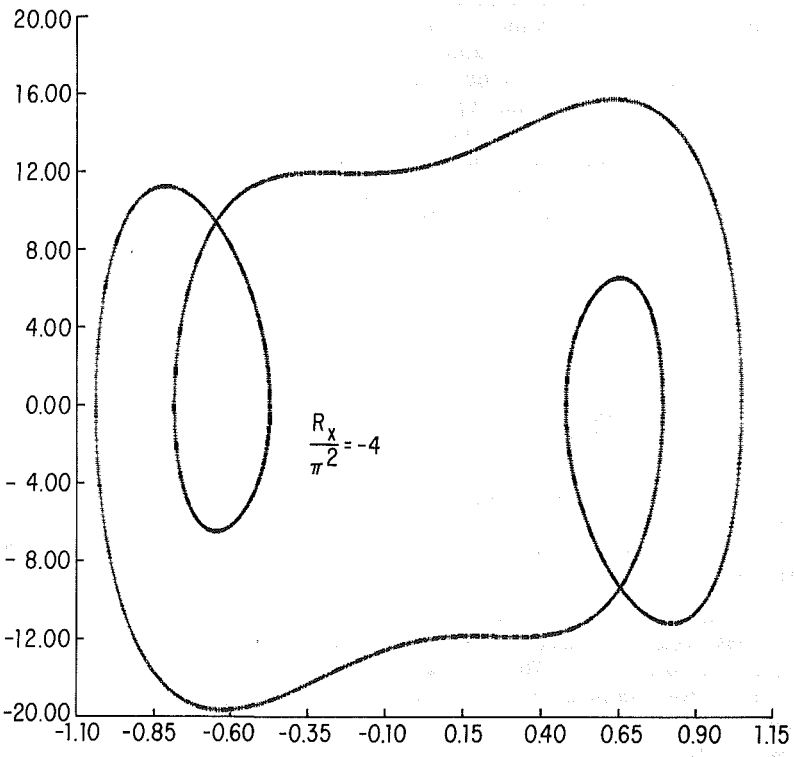


Fig. 2(*b*)

dimensional time. For the convenience of the reader, the equations that govern the a_n are given in the Appendix.

There are two important (control) parameters in the equations. λ is a nondimensional flow velocity and R_x a nondimensional mechanical in-plane load. Negative values of R_x denote an applied *compressive* load. It is known that certain values of λ, R_x will lead to chaotic motion, see Part I. It is our purpose here to observe the evolution of chaos in some detail. Before reading further, a reader interested in more detail about the mathematical-physical model, the solution techniques, and the global behavior of the system in $\lambda - R_x$ space should consult Part I.

We will consider, in turn, the four descriptors; time histories, phase plane diagrams, power spectra, and Poincare maps in order to view the beginning, onset, and maturing of chaos.

Downloaded 02 May 2010 to 171.66.16.25. Redistribution subject to ASME license or copyright; see http://www.asme.org/terms/Terms_Use.cfm

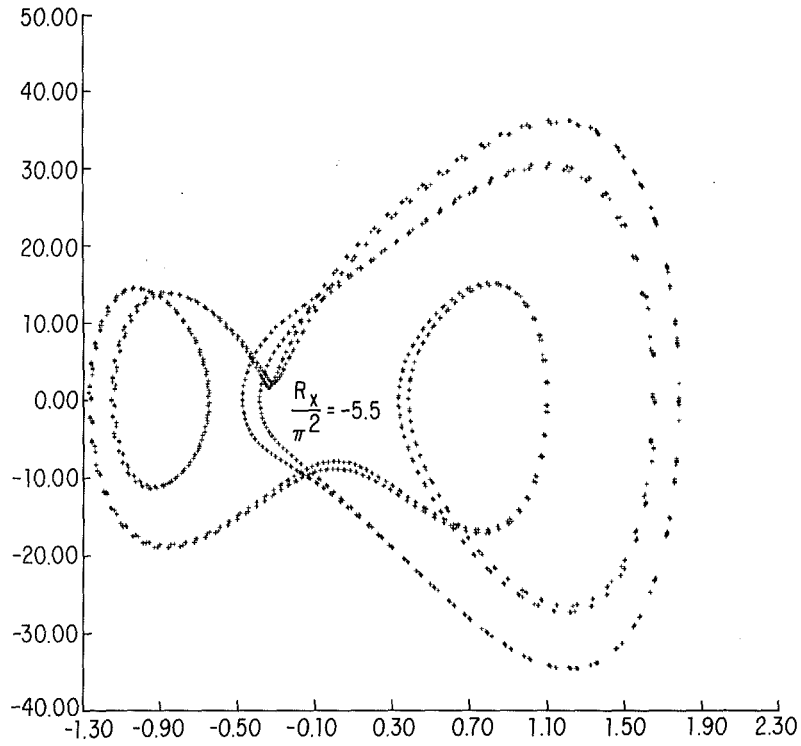


Fig. 2(c)

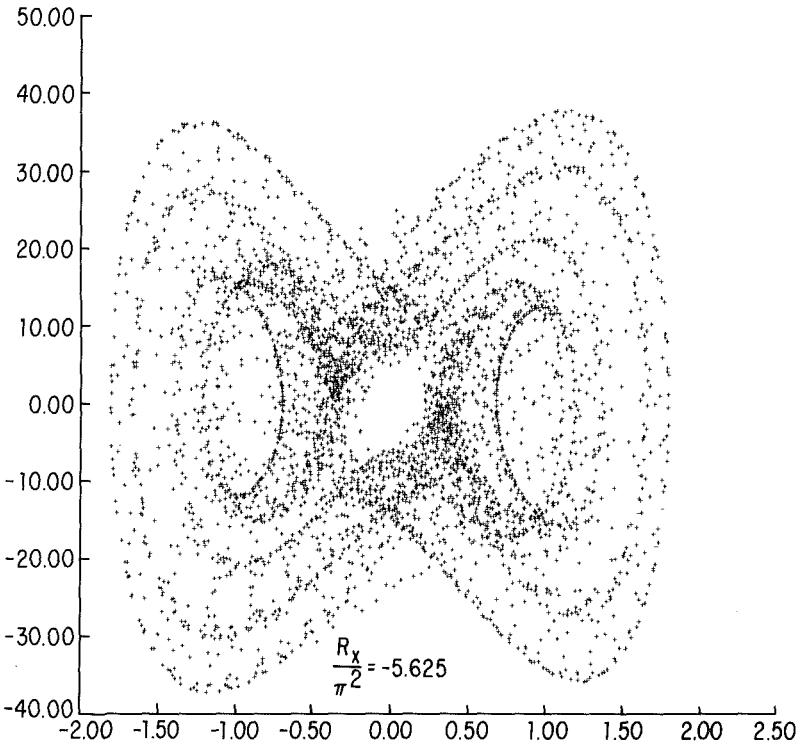


Fig. 2(d)

Time Histories

For a fixed value of λ, R_x/π^2 was varied over a range of values from -3 to -8. Only two terms were retained in equation (1), i.e., $N=2$. The time histories were computed for one period of motion, except of course where periodic motion does not exist. For brevity, the time histories per se are not shown.

It is of interest to summarize the information contained in the time histories by presenting the period of the motion versus R_x. This is done in Fig. 1. The vertical arrows indicate the period is very large, certainly in excess of $\tau = 200$, and probably infinite. This motion is called chaotic. For $-R_x/\pi^2$ less than 2.3 no (steady state) motion exists because the system is dynamically stable. Between 2.3 and 3, a predominantly single frequency limit cycle occurs which is a result of a Hopf bifurcation [1–4]. Near 3, a sudden increase in the period of

Downloaded 02 May 2010 to 171.66.16.25. Redistribution subject to ASME license or copyright; see http://www.asme.org/terms/Terms_Use.cfm

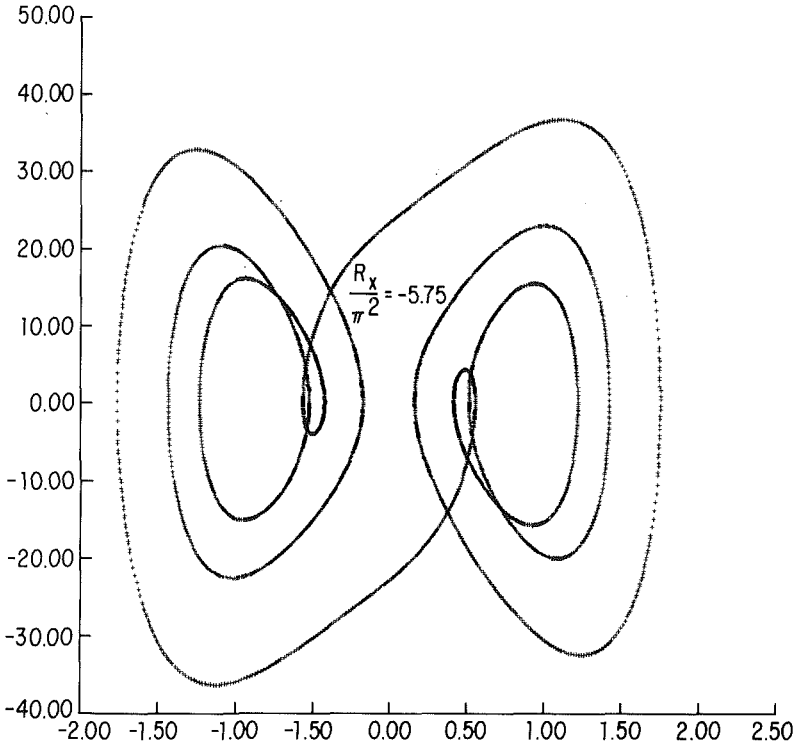


Fig. 2(e)

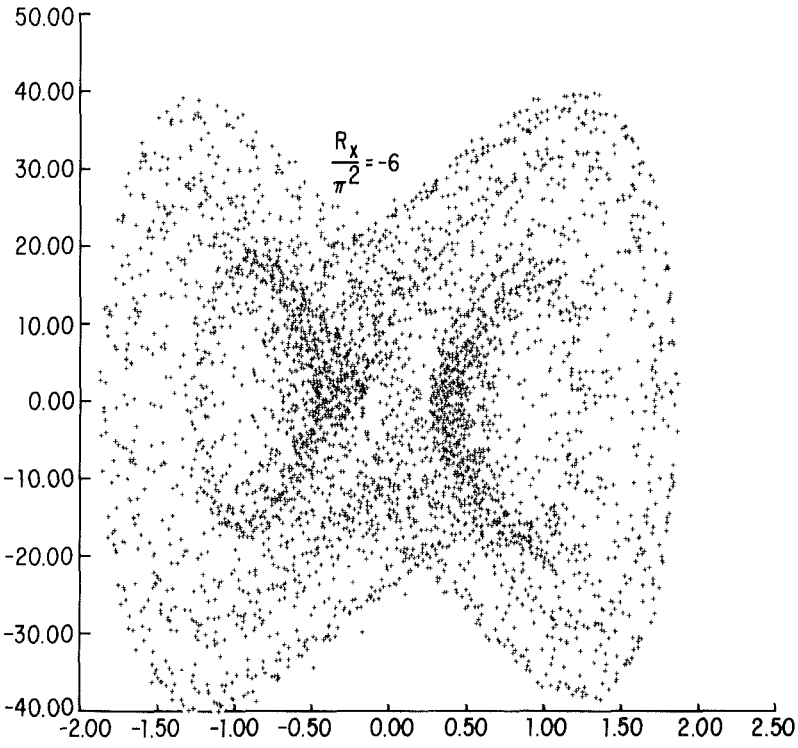


Fig. 2(f)

Fig. 2 Phase plane diagram, velocity versus displacement

the motion occurs and the motion now contains two dominant frequencies. The two frequencies are in the ratio 1:3 as one might expect with a cubic nonlinearity. For a very small interval near $-R_x/\pi^2 = 3$, the frequencies are not strictly in the ratio 1:3 and the motion is aperiodic. From 3 to 5.25 the motion retains two dominant frequencies. At $-R_x/\pi^2 = 5.5$, the motion has another dramatic increase in its period and additional frequency components become significant. These appear to be, in addition to the first and third harmonics, fifth and seventh harmonics as well. At 5.625 chaos appears;

Downloaded 02 May 2010 to 171.66.16.25. Redistribution subject to ASME license or copyright; see http://www.asme.org/terms/Terms_Use.cfm

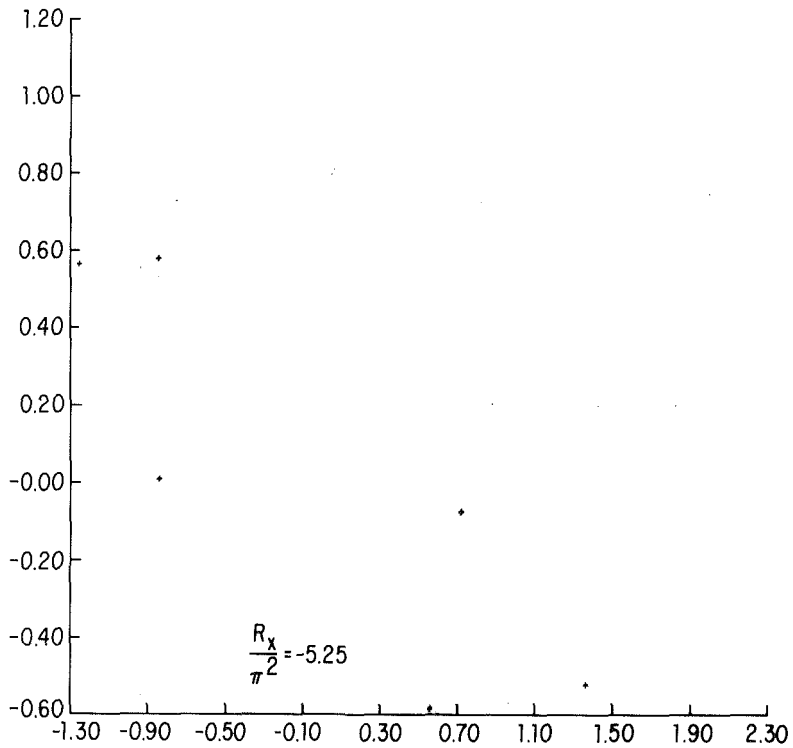


Fig. 3(a)

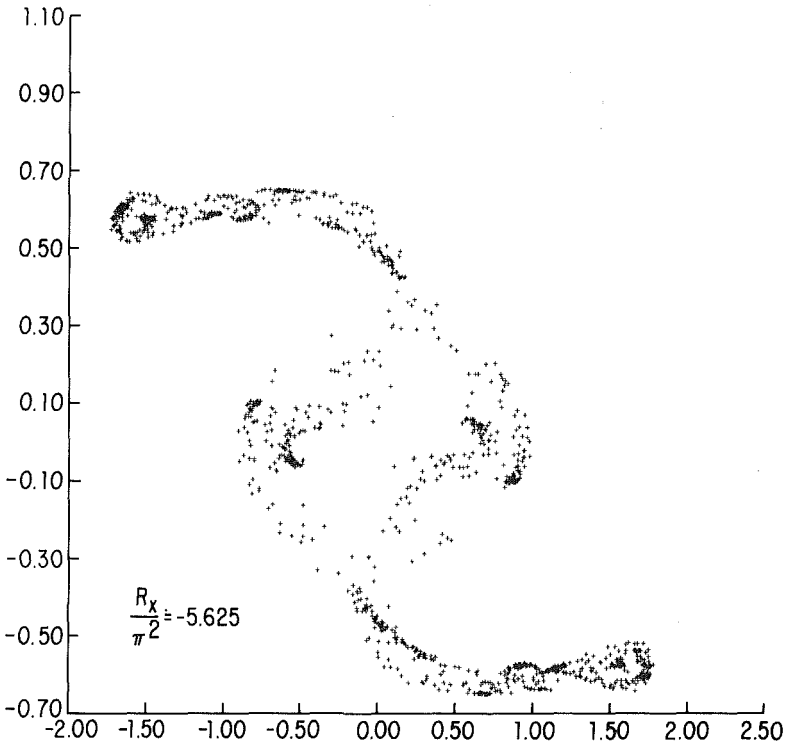


Fig. 3(b)

at 5.75 it disappears; it reappears at 5.875 and disappears at 7.75. Beyond 7.75 there is no chaos until at least 12 where computations were halted.

In these calculations $\lambda = 150$ and the mass ratio parameter, μ/M, was selected as 0.1. See Part I and the Appendix.

Phase Plane Portraits

These are shown in Fig. 2 for selected R_x. As expected, the portraits become increasingly complex as $-R_x/\pi^2 = 2.5 \rightarrow 5$ with many loops appearing immediately prior to the onset of chaos. Of course chaos appears at 5.625, disappears at 5.75, reappears at 5.875, and disappears again at 7.75. Although the portraits are quite diffuse when chaos occurs, one may sometimes detect the "shadows" of periodic motion. For example, compare the results for 6 and 5.75.

Typically the (chaos and/or) periodic motion reaches a (statistical) steady state at $\tau = 10$ or so. However when chaos

Downloaded 02 May 2010 to 171.66.16.25. Redistribution subject to ASME license or copyright; see http://www.asme.org/terms/Terms_Use.cfm

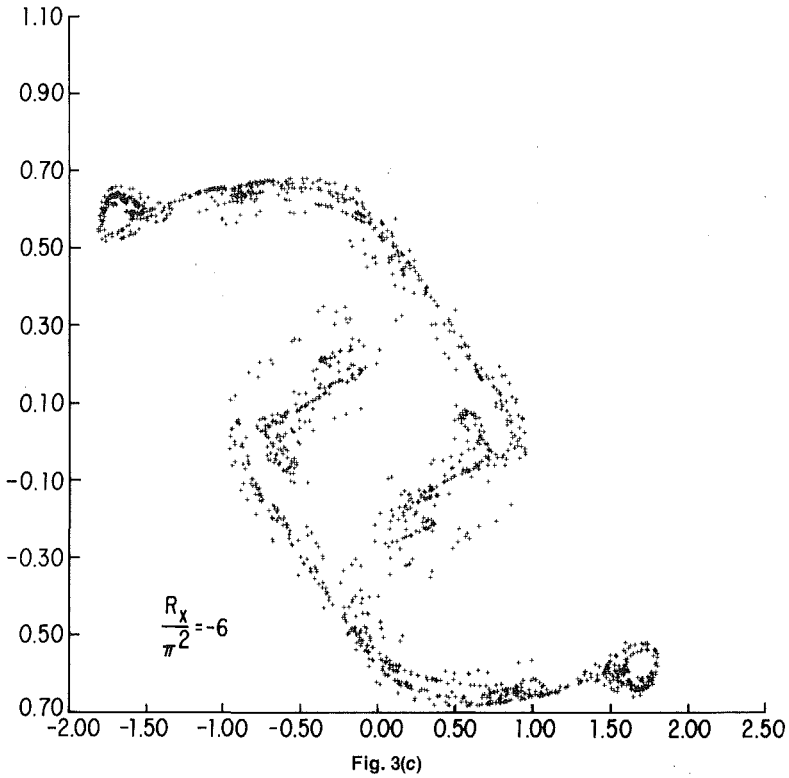


Fig. 3(c)

Fig. 3 Poincare map, second versus first Fourier coefficient, $N = 2$

appeared at 6 and then subsequently disappeared at 7.75 the emergence of the periodic motion sometimes took a remarkably long time; a "chaotic" transient of the order of $\tau \simeq 100$ might occur before the periodic motion established itself. For example, the transient for $-R_x/\pi^2 = 10$ persisted until approximately $\tau = 105$. (The phase plane portraits represent points plotted for $\tau = 100 \rightarrow 140$ for time intervals of 0.01.) One is tempted to associate this behavior with the concept of "intermittency" where both periodic and chaotic motions exist over extended periods of time.

The maturing of the chaos may be observed by noting the diffusion of the phase plane portraits. See particularly the results for $-R_x/\pi^2 = 5.625$ and 6.0. However additional structure of the motion may be observed by considering the corresponding power spectra and Poincare maps.

The phase plane portraits presented here are in terms of velocity versus displacement for a representative point on the plate, i.e., $x = 3/4a$.

Power Spectra

Power spectra have been presented in Part I and the reader is referred to that discussion. As noted previously, periodic motion will be characterized by sharp peaks and chaotic motion by broad band behavior. Consider now Poincare maps.

Poincare Maps

Various Poincare maps may be constructed based on:

The definition of the event that determines those instants of time when the coordinates are selected for plotting;

The choice of coordinates themselves.

Here the event selected is the vanishing of the velocity of a selected point on the plate, namely $x = 3/4\,a$. The coordinates selected for the map are the first two Fourier coefficients of equation (1) (nondimensionalized as discussed in Part I). The Poincare maps are presented in Fig. 3 for selected R_x.

For periodic motion, a Poincare map will consist of a finite number of (local) extrema over one period of motion. Thus for $-R_x/\pi^2 = 2.5 \rightarrow 5.5$, only a finite number of discrete points appear in the Poincare map.

However when chaos appears at, for example, $-R_x/\pi^2 = 5.625$ [6] a more complicated but still ordered Poincare map is formed. As discussed before, the Poincare map may be used to answer the question, given some event (the vanishing of the plate velocity at some point on the plate) and the value of one system coordinate, what is the likely value of another system coordinate? Clearly, as seen from Fig. 3, the range of likely values is rather limited.

The order apparent in the Poincare maps may be called "large-scale structure" by analogy to the term sometimes employed in hydrodynamic turbulence.

Some modest diffusion of the Poincare map does occur as $-R_x/\pi^2$ increases from 6 to 7, say. This, of course, corresponds to an increase in the range of possible coordinate values. The diffusion is more pronounced, however, if one considers a higher order representation of the system dynamics. For example, consider now $N = 6$ in equation (1). All previous results were for $N = 2$. Results (not shown) were also obtained for $N = 4$.

In Fig. 4 Poincare maps are presented for $-R_x/\pi^2 = 6$, 9, 12, and $N = 6$. Note the systematic increase in the diffusion of the map as $6 \rightarrow 9 \rightarrow 12$. By examining higher dimensional Poincare maps, further order might be perceived even for these relatively diffuse Poincare maps. However no such attempt is made here.

Note also that chaos occurs for $-R_x/\pi^2 = 12$ and $N = 6$ while for $N = 2$ no chaos appears. Examining the results for $N = 2$, 4, 6, it is concluded that an increase in N leads to a larger range of R_x for which chaos appears. It is expected that as $-R_x/\pi^2$ increases N must increase to obtain convergence

Downloaded 02 May 2010 to 171.66.16.25. Redistribution subject to ASME license or copyright; see http://www.asme.org/terms/Terms_Use.cfm

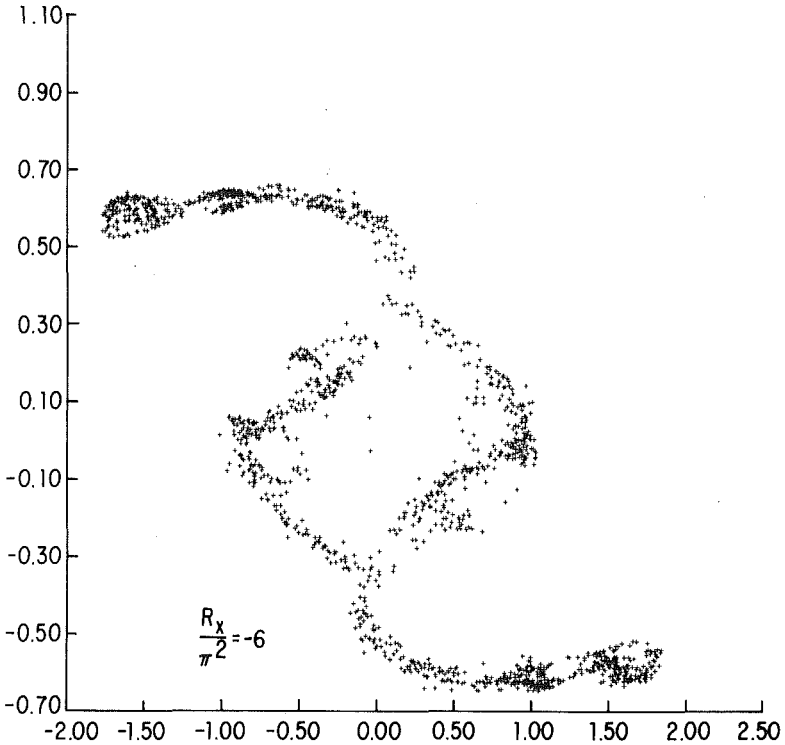


Fig. 4(*a*)

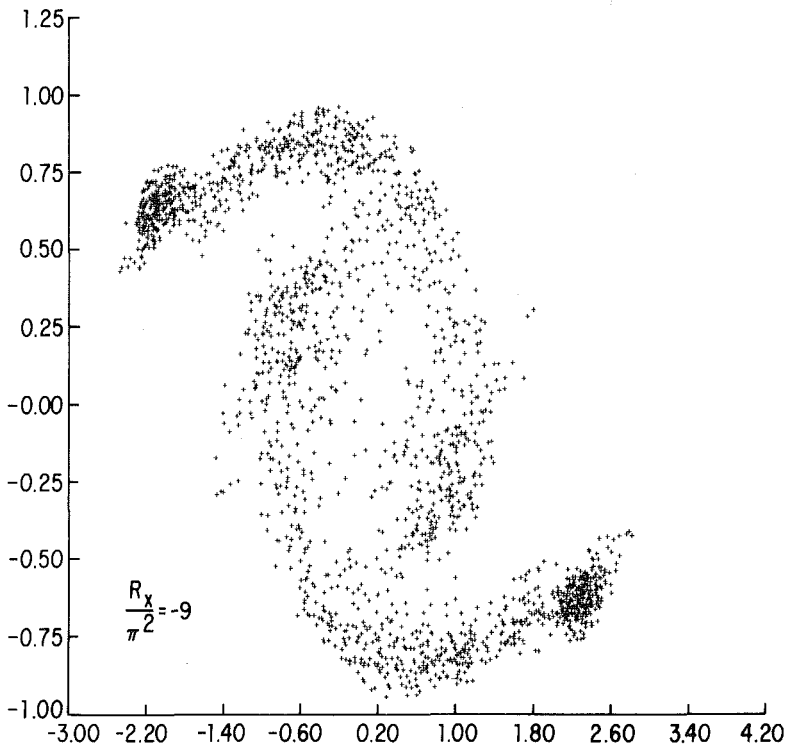


Fig. 4(*b*)

of the series in equation (1). For the range of parameters examined $N = 6$ is sufficient to give good convergence, as can be established by examining the magnitudes of the a_n that appear in equation (1). The results for $N = 2$ are not well converged quantitatively, but are qualitatively comparable to those for $N = 6$.

Temporal Statistics of An Event

When chaotic motion occurs, it is of interest to examine the temporal statistics of an event. For example, consider a certain (long) time interval. Within this interval a (large) number of events will occur. One can measure the (small) time between two successive events, and plot the numbers of events that occur versus the (small) times between two successive events. Then this graph can be normalized by dividing by the total number of events. The result is a probability density function which allows one to determine the likelihood of an event occurring within a certain (small) interval of time given the occurrence of a previous event.

Downloaded 02 May 2010 to 171.66.16.25. Redistribution subject to ASME license or copyright; see http://www.asme.org/terms/Terms_Use.cfm

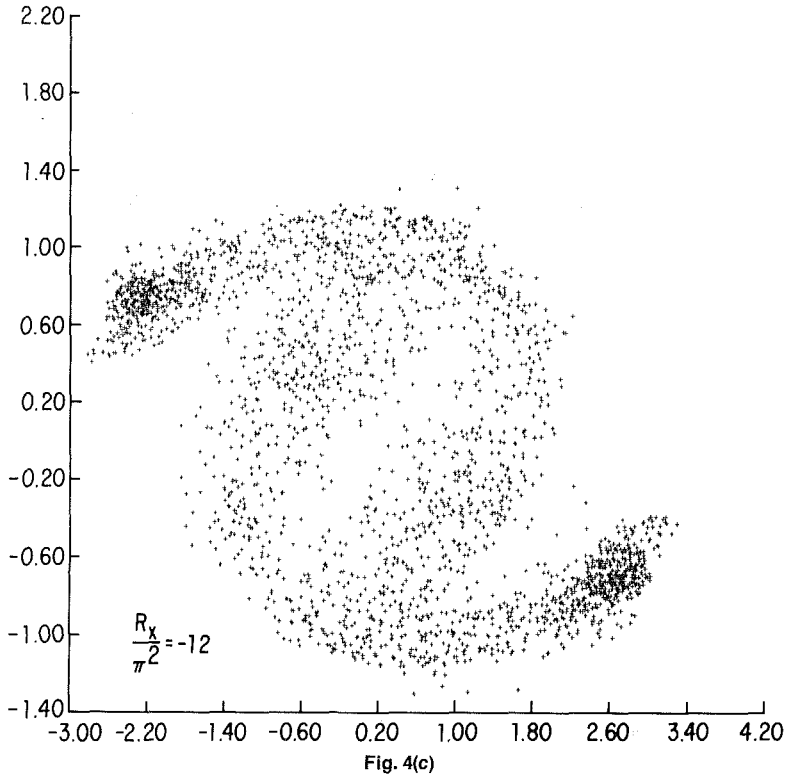


Fig. 4(c)

Fig. 4 Poincare map, second versus first Fourier coefficient, $N = 6$

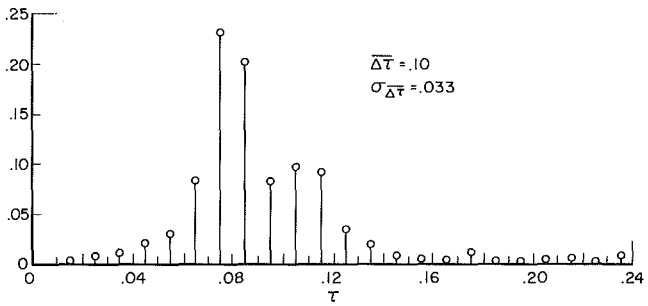


Fig. 5 Probability density of an event

In Fig. 5 such a probability density function is displayed for the case $R_x/\pi^2 = -6$ and $N = 2$. The total (long) time interval considered was $\tau = 29.4131 \rightarrow 66.3981$ and the total number of events occurring was 403. To obtain a discrete representation of the probability density function, the total time interval was divided into small time intervals of duration, 0.01. The numbers of successive events occurring in selected time intervals, $0 \rightarrow 0.01$, $0.01 \rightarrow 0.02$, $0.02 \rightarrow 0.03$, etc. was plotted.

Using Fig. 5 one can calculate the probability of an event occurring within a certain time interval given the occurrence of a previous event. For example, the probability of an event occurring between $\tau_1 = 0.10$ and $\tau_2 = 0.12$ is $0.097 + 0.092 = 0.189$ while the probability of an event occurring between $\tau_3 = 0.18$ and $\tau_4 = 0.20$ is $0.0025 + 0.0025 = 0.005$. Also shown in Fig. 5 is the average time between successive events, $\Delta\bar{\tau}$, and the variance, $\sigma_{\Delta\bar{\tau}}$.

It should be emphasized that Fig. 5 is a discrete representation (delta function) of the probability density. To obtain a (an approximate) continuous representation, one divides the ordinates of Fig. 5 by the selected (small) time interval, in this case, 0.01. In the limit as the total (long) time interval goes to infinity and the selected (small) time interval goes to zero a continuous probability density representation is obtained. An approximation to this continuous probability density function based on a selected (small) time interval of 0.01 is thus obtained by connecting the ordinate points of Fig. 5 and dividing the vertical scale by 0.01. Integrating the resulting curve between two times one computes the probability of an event occurring between these two times given the occurrence of a previous event.

Other statistics can be obtained, of course, by returning to the raw event data. For example, given the occurrence of two events within one time interval, one could deduce the probability of the occurrence of a third event during another subsequent time interval.

By examining the temporal statistics of an event, further insight may be gained concerning the essence of the chaotic motion. For example, Fig. 5 displays the relatively narrow range of probable time elapse between two successive events.

Concluding Remarks

By using several descriptive techniques, a rich variety of dynamical behavior can be observed for systems that undergo chaos. As the transition from simple harmonic, to periodic, to chaotic motion occurs, the descriptors of most value change from time histories, to phase plane portraits, to power spectra and Poincare maps. The temporal statistics of an event which defines the Poincare map proves to be a useful descriptor as well.

What remains as an open challenge is to translate the information obtained from these descriptors into an improved understanding of why apparently relatively simple systems behave in the complex manner that they do. As Simon [8] has emphasized, "the central task of a natural science is to make the wonderful commonplace: to show that complexity, correctly viewed, is only a mask for simplicity; to find pattern hidden in apparent chaos." Nevertheless, in a sense, it is encouraging that relatively simple mathematical models can give rise to complex behavior including "intermittency" and

Downloaded 02 May 2010 to 171.66.16.25. Redistribution subject to ASME license or copyright; see http://www.asme.org/terms/Terms_Use.cfm

"large scale (chaotic) structures." Perhaps other physical phenomena exhibiting similar complex behavior may prove to be governed by relatively simple models as well. See, for example, reference [9].

Finally a few comments are appropriate to relate the work on the present set of equations (see the Appendix for their explicit form) to that which has been carried out on the well-known Lorenz equations [10, 11]. In the Lorenz model, above a certain parameter value (analogous to R_x for our equations) the trivial static equilibrium becomes unstable and two new *static* equilibria exist. These are stable until for a yet higher parameter value they also become unstable. Thus, for a sufficiently high parameter value, three static equilibria exist all of which are unstable (too small perturbations). Above this parameter value, chaos occurs. Chaos appears to be the result of all equilibria solutions being unstable to infinitesimal perturbation; nevertheless the global solutions are still bounded (through understandably chaotic). For parameter values slightly below that at which chaos occurs, long chaotic transients occur [11]. These are similar to those that have been found here for the present equation.

Consider now the present equations and their behavior. As a parameter $(-R_x)$ increases, the trivial static equilibrium becomes unstable. Either two new static equilibria exist or a dynamic limit cycle equilibrium exists. As the parameter increases, further chaos or a long chaotic transient exists and, for further parameter increases, chaos is fully established. What remains to be done for the present equations is to determine whether the appearance of chaos directly follows on the instability (to infinitesimal perturbations) of all possible static and dynamic equilibria. This is a far more formidable task for the present equations than the corresponding one for the Lorenz equations, because of the more complicated equilibria which occur prior to the onset of chaos. For the Lorenz equation there are three *static* equilibria at most prior to chaos. For the present equations, these equilibria are dynamic with multiple frequency content. Indeed it is not clear whether the number of equilibria prior to chaos is finite. However, though tedious, it would appear desirable to systematically find the equilibria and evaluate their stability in the hope that the number of equilibria prior to chaos is finite, as is the case for the Lorenz equations. If it should prove to be the case that chaos begins when all equilibria are unstable with respect to infinitesimal disturbance, then a strong circumstantial case would exist for providing an explanation of the creation of chaos.

Acknowledgment

This work was supported by NSF Grant MEA-8119883, Mechanical Systems, Division of Mechanical Engineering and Applied Mechanics, Dr. Elbert L. Marsh, Program Director.

References

1 Holmes, P. J., "Bifurcations to Divergence and Flutter in Flow-Induced Oscillations: A Finite Dimensional Analysis," *J. Sound Vibration*, Vol. 53, No. 4, 1977, pp. 471–503.

2 Holmes, P. J., and Marsden, J., "Bifurcations to Divergence and Flutter in Flow-Induced Oscillations: An Infinite Dimensional Analysis," *Automatica*, Vol. 14, No. 4, 1978, pp. 367–384.

3 Thompson, J. M. T., *Instabilities and Catastrophies in Science and Engineering*, Wiley, New York, 1982.

4 Dowell, E. H., "Flutter of a Buckled Plate as an Example of Chaotic Motion of a Deterministic Autonomous System," *J. Sound Vibration*, Vol. 85, No. 3, 1982, pp. 333–344.

5 Marsden, J., and McCracken, M., "The Hopf Bifurcation and Its Applications," *Springer Applied Mathematics Series*, No. 19, Springer, Berlin, 1976.

6 Guckeheimer, J., and Holmes, P., *Nonlinear Oscillations, Dynamical Systems and Bifurcations of Vector Fields*, Springer-Verlag, New York, 1983.

7 Dowell, E. H., *Aeroelasticity of Plates and Shells*, Martinus Nijhoff, Leyden and Boston, 1975.

8 Simon, H. A., *The Sciences of the Artificial*, M.I.T. Press, Cambridge, Mass., 1969, p. 1.

9 Fenstermacher, P. R., Swinney, J. L., and Collub, J. P., "Dynamic Instabilities and the Transition to Chaotic Taylor Vortex Flow," *J. Fluid Mechanics*, Vol. 94, Part 1, 1979, pp. 103–128.

10 Lorenz, E. N., "Deterministic Nonperiodic Flow," *J. Atmospheric Science*, Vol. 20, No. 3, 1963, pp. 130–141.

11 Yorke, J. A., and Yorke, E. D., "Metastable Chaos: The Transition to Sustained Chaotic Behavior in the Lorenz Model," *J. Statistical Physics*, Vol. 21, No. 3, 1979, pp. 263–277.

APPENDIX

Ordinary Differential Equations of Motion

A set of ordinary differential equations is obtained from the governing partial differential equation [4] by using Galerkin's method with the modal expansion,

$$w = \Sigma a_n(t) \sin \frac{n\pi x}{a}$$

The result is (in non-dimensional notation)

$$A_n(n\pi)^4/2 + 6(1-\nu^2)[\sum_r A_r^2(r\pi)^2/2]A_n(n\pi)^2/2 + R_x A_n(n\pi)^2/2 + A_n''/2 + \lambda\{\sum_m [nm/(n^2-m^2)][1-(-1)^{n+m}]A_m + (\mu/M\lambda)^{1/2}A_n'\} = 0$$

$n = 1, 2, \ldots, \infty$

where

$A_n \equiv a_n/h$ and $W \equiv w/h$

$\lambda \equiv \rho_\infty U_\infty{}^3 a^3/MD$

$\mu \equiv \rho_\infty a/m$

$R_x \equiv N^E{}_x a^2/D$

$\tau \equiv t(D/ma^4)^{1/2}$

$' \equiv \partial(\ )/\partial\tau$

- w – plate transverse deflection
- x – streamwise spatial coordinate
- t – time
- D – $Eh^3/12(1-\nu^2)$, plate bending stiffness
- $N^E{}_x$ – externally applied in-plane load; positive in tension
- E – modulus of elasticity
- ν – Poisson's ratio
- a – plate length
- h – plate thickness
- m – mass/per unit length
- ρ_∞ – flow density
- U_∞ – flow velocity
- M – flow Mach number

These equations may be numerically integrated to obtain time histories of motion. These are used to construct phase plane plots and Poincare plots in terms of $W(\tau)$.

Downloaded 02 May 2010 to 171.66.16.25. Redistribution subject to ASME license or copyright; see http://www.asme.org/terms/Terms_Use.cfm

An Integral Equation Method for the First-Passage Problem in Random Vibration

P. H. Madsen

S. Krenk

Risø National Laboratory,
Roskilde, Denmark

The first-passage problem for a nonstationary stochastic process is formulated as an integral identity, which produces known bounds and series expansions as special cases, while approximation of the kernel leads to an integral equation for the first-passage probability density function. An accurate, explicit approximation formula for the kernel is derived, and the influence of uni or multi modal frequency content of the process is investigated. Numerical results provide comparisons with simulation results and alternative methods for narrow band processes, and also the case of a multimodal, nonstationary process is dealt with.

1 Introduction

A central problem in the analysis of random response of a system or structure is the evaluation of the probability that some characteristic property of the response remains within some specified limits for a given time. Alternatively this may be considered as the problem of finding the probability density function for the time until the first passage of these limits. The difficulty of the problem arises from the need to account for the full history up to the time of the first passage to assure that it is indeed the first. It is therefore hardly surprising that exact solutions are only known to special cases where the memory is of Markov type, i.e., a weak memory where the distant past is fully represented by the immediate past. Here, as in numerous other publications devoted to this subject, the ambition is merely to formulate an approximate method of analysis. However, special emphasis is given to the memory as described by the correlation function.

Let failure be the first upcrossing of the curve $\xi(t)$ by a stochastic process $X(t)$ for $t \geq 0$. The probability of failure in the time interval $[0, t]$ is called $P_f(t)$, and the probability of survival at time t then is

$$1 - P_f(t) = P\{N(t) = 0 \mid X(0) < \xi(0)\} P\{X(0) < \xi(0)\} \tag{1.1}$$

where $N(t)$ is the number of barrier crossings in the interval $[0, t]$. The last factor represents the probability of avoiding instant failure.

The relation between the failure probability $P_f(t)$ and the probability density function $f_1(t)$ of the time to the first barrier crossing conditional on $X(0) < \xi(0)$ follows from consideration of a time increment in (1.1).

$$\frac{d}{dt} P_f(t) = f_1(t) P\{X(0) < \xi(0)\} \tag{1.2}$$

The problem of finding the failure probability $P_f(t)$ is therefore equivalent to finding the probability density function $f_1(t)$ of the first passage conditional on $X(0) < \xi(0)$.

A convenient starting point for a discussion of the function $f_1(t)$ is an integral identity expressing the fact that a barrier crossing at time t must either be the first, or the first crossing must have occurred at some previous time τ. Thus the total upcrossing rate $\nu_\xi^X(t)$ is the sum of two contributions.

$$\nu_\xi^X(t) = f_1(t) + \int_0^t K(t \mid \tau) f_1(\tau) d\tau \tag{1.3}$$

where $K(t \mid \tau)$ is the upcrossing rate at t conditional on the first crossing having occurred at τ. The identity (1.3) may be considered as an integral equation for the unknown function $f_1(t)$, but the kernel $K(t \mid \tau)$ is still unknown.

Although the integral relation (1.3) is merely a restatement of the problem, it turns out to be useful both in establishing bounds and approximations for $f_1(t)$. As the integral is a probability and therefore non-negative

$$f_1(t) \leq \nu_\xi^X(t) \tag{1.4}$$

and $\nu_\xi^X(t)$ is seen to provide an upper bound on $f_1(\tau)$. A lower bound on $f_1(\tau)$ is obtained by considering the joint upcrossing rate $\nu_{\xi\xi}^X(t, \tau_1)$, and observing that for $\tau_1 < t$ the upcrossing at τ_1 is the first, or the first has occurred at some previous time τ_2. This gives the identity

$$\nu_{\xi\xi}^X(t, \tau_1) = K(t \mid \tau_1) f_1(\tau_1) + \int_0^{\tau_1} K(t, \tau_1 \mid \tau_2) f_1(\tau_2) d\tau_2 \tag{1.5}$$

similar to (1.3). Elimination of the integral in (1.3) by (1.5) gives

$$f_1(t) = \nu_\xi^X(t) - \int_0^t \nu_{\xi\xi}^X(t, \tau_1) d\tau_1 + \int_0^t \int_0^{\tau_1} K(t, \tau_1 \mid \tau_2) f_1(\tau_2) d\tau_2 d\tau_1 \tag{1.6}$$

Contributed by the Applied Mechanics Division for publication in the JOURNAL OF APPLIED MECHANICS.

Discussion on this paper should be addressed to the Editorial Department, ASME, United Engineering Center, 345 East 47th Street, New York, N.Y. 10017, and will be accepted until two months after final publication of the paper itself in the JOURNAL OF APPLIED MECHANICS. Manuscript received by ASME Applied Mechanics Division, October, 1983; final revision, January, 1984.

Copyright © 1984 by ASME
Downloaded 02 May 2010 to 171.66.16.25. Redistribution subject to ASME license or copyright; see http://www.asme.org/terms/Terms_Use.cfm

The integrals are non-negative providing a lower bound.

$$f_1(t) \geq \nu_\xi^X(t) - \int_0^t \nu_{\xi\xi}^X(t,\tau)d\tau \tag{1.7}$$

Continuation of this procedure leads to the formal series representation

$$f_1(t) = \nu_\xi^X(t) + \sum_{j=1}^{\infty} (-1)^j \int_0^j \cdots \int_0^{\tau_{j-1}} \nu_{\xi \cdots \xi}^X(t,\tau_1, \ldots \tau_j)d\tau_1 \ldots d\tau_j \tag{1.8}$$

This is the inclusion-exclusion series of Rice [1]. It provides upper and lower bounds upon truncation after an odd or even number of terms, respectively. Series representations of ths type have been used by Longuet-Higgins [2] to study intervals between zero-crossings and by Roberts [3] to study first-passage of transient response of a linear system.

The series (1.8) suffers the disadvantage that if n upcrossings are at all likely to occur at least n terms must be included in the series. This often leads to an increasing number of necessary terms for increasing t, while initial behavior of $f_1(t)$ may be predicted well by only a few terms. This problem is avoided, if the relation (1.3) is retained as an integral equation, and an approximation is provided for the kernel $K(t|\tau)$. Special cases of this procedure were considered by Bernard and Shipley [4, 5], while the general nature of the procedure was pointed out by Nielsen [6].

The simplest approximation of this type follows from assuming that the crossing rate at t is independent of a prior first upcrossing at τ,i.e., $K(t|\tau) = \nu_\xi^X(t)$. In this case (1.3) has the explicit solution

$$f_1(t) = \nu_\xi^X(t) \exp\left(-\int_0^t \nu_\xi^X(\tau)d\tau\right) \tag{1.9}$$

The corresponding survival probability is

$$1 - P_f(t) = F(\xi(0)) \exp\left(-\int_0^t \nu_\xi^X(\tau)d\tau\right) \tag{1.10}$$

where $F(x)$ is the distribution function of the initial value $X(0)$. These expressions for $f_1(t)$ and $P_f(t)$ are based on complete lack of memory, the Poisson assumption, and they are therefore not representative for the narrow band response of lightly damped systems where crossings are likely to occur at periodic intervals. The necessary incorporation of memory via an improved representation of the kernel $K(t|\tau)$ is our particular concern in the following.

2 Initial Conditions and Crossing Rates

Stochastic processes with a finite probability of exceeding the barrier level initially present a particular problem, because the upcrossing rates $\nu_\xi^X(t)$ and $K(t|\tau)$ to be used in the integral equation are then conditional on $X(0) < \xi(0)$. In particular this problem illustrates some properties of narrow band processes.

Let $X(t)$ be a normal process with expectation $\mu(t)$ and variance $\sigma(t)^2$. The first-passage problem for the curve $\xi(t)$ is then conveniently formulated in terms of the normalized variables

$$Y(t) = \frac{X(t) - \mu(t)}{\sigma(t)}, \quad \eta(t) = \frac{\xi(t) - \mu(t)}{\sigma(t)} \tag{2.1}$$

The correlation function of the process $X(t)$ is

$$\rho(t_1, t_2) = E[Y(t_1)Y(t_2)] \tag{2.2}$$

As a consequence of the normalization, $Y(t)$ and $\dot{Y}(t)$ are uncorrelated, and the upcrossing rate follows simply from Rice's formula [1] in factored form

$$\nu_\xi^X(t) = \nu_\eta^\nu(t) = \omega\phi(\eta)\Psi(\dot{\eta}/\omega) \tag{2.3}$$

Here $\omega(t)$ is the standard deviation of $\dot{Y}(t)$,

$$\omega(t)^2 = \frac{\partial^2}{\partial t_1 \partial t_2}\rho(t,t) \tag{2.4}$$

$\phi(\eta)$ is the normal density function, and $\Psi(\zeta)$ is an integral of the normal distribution function $\Phi(\zeta)$,

$$\Psi(\zeta) = \int_\zeta^\infty (z - \zeta)\phi(z)dz = \phi(\zeta) - \zeta\Phi(-\zeta) \tag{2.5}$$

This definition implies $\Psi'(\zeta) = -\Phi(-\zeta)$.

To illustrate the influence of the initial condition $X(0) < \xi(0)$ we now consider a normalized stationary process with correlation function $\rho(t_1 - t_2)$, and $\omega_s^2 = -\ddot{\rho}(0)$. First the initial condition $X(0) = x_0$ is imposed, whereby the conditional expectation and covariance become

$$\mu(t) = \rho(t)x_0 \tag{2.6}$$

$$c(t_1 t_2) = \rho(t_1 - t_2) - \rho(t_1)\rho(t_2) \tag{2.7}$$

The upcrossing rate conditional on $X(0) = x_0$ then follows from (2.3) with the parameters

$$\omega_0(t) = \omega_s \frac{(1 - \rho^2 - \dot{\rho}^2/\omega_s^2)^{1/2}}{1 - \rho^2} \tag{2.8}$$

$$\eta = \frac{\xi - \rho x_0}{\sqrt{1 - \rho^2}}$$

$$\dot{\eta} = \frac{\dot{\rho}(\rho\xi - x_0)}{(1 - \rho^2)^{3/2}} \tag{2.9}$$

The upcrossing rate conditional on $X(0) < \xi(0)$ follows by use of the probability density function $\phi(x_0)/\Phi(\xi)$, $x_0 < \xi$ for the initial value $X(0)$.

$$\nu_{\xi|x_0<\xi}^X(t) = \frac{\omega}{\Phi(\xi)} \int_{-\infty}^{\xi} \phi(x_0)\phi(\eta)\Psi(\dot{\eta}/\omega_0)dx_0 \tag{2.10}$$

By rearranging the integral and integrating by parts the result is obtained in the form

$$\nu_{\xi|x_0<\epsilon}^X(t) = \frac{\omega_s}{2\pi} \frac{e^{-\xi^2/2}}{\Phi(\xi)} \times \left\{\Phi\left(\frac{\omega_s}{\omega}\frac{\xi}{1+\rho}\right) - \frac{\dot{\rho}/\omega_s}{\sqrt{1-\rho^2}} \times \exp\left(-\frac{1-\rho}{1+\rho}\frac{\xi^2}{2}\right)\Phi\left(\frac{1}{\sqrt{1-\rho^2}}\frac{\dot{\rho}}{\omega}\frac{\xi}{1+\rho}\right)\right\} \tag{2.11}$$

The asymptotic behavior is

$$\nu_{\xi|x_0<\xi}^X \sim \begin{cases} \nu_\xi^X/\Phi(\xi) & t << 1/\omega_s \\ \nu_\xi^X & t >> 1/\omega_s \end{cases} \tag{2.12}$$

The factor $\Phi(\xi)^{-1}$ is explained by the fact that while the number of upcrossings immediately after $t = 0$ is not changed by the initial condition $X(0) < \xi$, the ensemble of sample functions $X(t)$ is reduced by the factor $\Phi(\xi)$. A reformulation of (1.10) in which the conditional upcrossing frequency is replaced by the scaled, unconditional upcrossing frequency $\nu_\xi^X/\Phi(\xi)$ has been used by Ditlevsen [7], who found good agreement with simulation results for broad band processes.

For narrow band processes the Poisson assumption of independent upcrossings becomes invalid after the first "period" $t = 2\pi/\omega$. This is illustrated in Fig. 1 showing the conditional upcrossing frequency (2.11) for the basic level $\xi = 2\sigma_x$. The correlation function is that of response of a viscous spring-mass system excited by white noise.

Downloaded 02 May 2010 to 171.66.16.25. Redistribution subject to ASME license or copyright; see http://www.asme.org/terms/Terms_Use.cfm

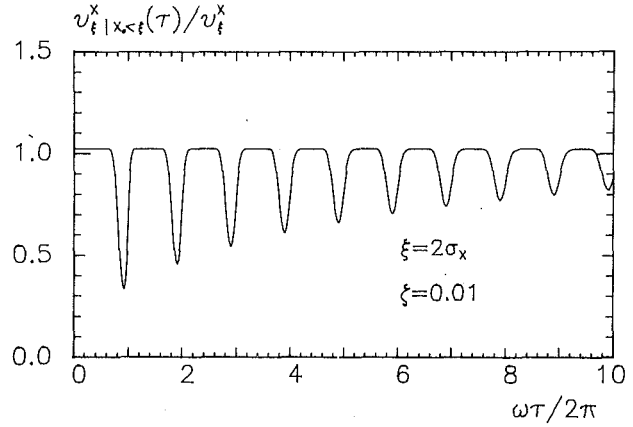


Fig. 1 The normalized crossing rate $\nu^X_{\xi|x_0<\xi}/\nu^X_\xi$, $\xi=2\sigma_X$, $\zeta=0.01$

$$\rho(t)=e^{-\omega\zeta t}\left[\cos(t\omega\sqrt{1-\zeta^2})+\frac{\zeta}{\sqrt{1-\zeta^2}}\sin(t\omega\sqrt{1-\zeta^2})\right] \quad (2.13)$$

ω is the natural angular frequency of the system and ζ is the damping ratio. Figure 1 corresponds to a lightly damped system, $\zeta=0.01$, and it is seen that the upcrossing rate is nearly constant except just before each full period $t=2\pi/\omega$. The narrow band response appears as a modulated oscillation. The initial condition has removed the sample functions crossing immediately before $t=0$, and the contributions of these are therefore missing at nearly periodic intervals.

Now it may be shown by a simple argument that $f_1(t)$ in the present problem is a nonincreasing function of t, Rice and Beer [8]. For any sample function satisfying the initial condition the point $t=0$ lies in an interval between a downcrossing and an upcrossing. Let the length of this interval be τ. The position of the origin is arbitrary, and the first-passage time conditional on τ therefore has the uniform density

$$f_1(t\,|\,\tau)=\frac{1}{\tau}, \quad 0\le t<\tau \quad (2.14)$$

The probability of finding the origin in an interval of length τ is proportional with τ, and therefore

$$f_{\tau_0}(\tau)=\frac{\tau}{\mu_\tau}f_\tau(\tau) \quad (2.15)$$

where the parameter μ_τ is seen to be the expected length of intervals in which $X(t)<\xi$. This gives the following expression for the unconditional first-passage probability of a stationary process with the initial condition $X(0)<\xi$.

$$\begin{aligned} f_1(t) &= \int_0^\infty f_1(t\,|\,\tau)f_{\tau_0}(\tau)d\tau \\ &= \frac{1}{\mu_\tau}\int_t^\infty f_\tau(\tau)d\tau \\ &= \frac{1}{\mu_\tau}[1-F_\tau(t)] \end{aligned} \quad (2.16)$$

$F_\tau(t)$ is the distribution function of the interval length τ between a downcrossing and the following upcrossing, and thus $f_1(t)$ is nonincreasing in the present case. As a consequence of this property and the bound (1.4) an upper bound on $f_1(t)$ is obtained from $\nu^X_{\xi|x_0<\xi}(t)$ by extending the first minimum value to infinity. Thus the values of $\nu^X_{\xi|x_0<\xi}(t)$ outside the first period do not appear to have any direct relation to the first-passage time. The next section describes an integral equation, in which the Poisson assumption of independent crossings is replaced by an approximate representation of the correlation between crossings.

3 The Integral Equation

In the case of narrow band processes a considerable improvement over the results of the previous section, based on the Poisson hypothesis, can be obtained by using an improved approximation for the kernel $K(t\,|\,\tau)$. This improved approximation represents $K(t\,|\,\tau)$ as the upcrossing rate at t conditional on a prior upcrossing at τ. Thus the condition that the upcrossing at τ should be the first is dropped, and the approximation reads

$$K(t\,|\,\tau)=\frac{\nu^X_{\xi\xi}(t,\tau)}{\nu^X_\xi(\tau)} \quad (3.1)$$

Details are now given concerning the evaluation of (3.1) in the case of a nonstationary process $X(t)$ and a variable barrier $\xi(t)$, when the initial condition can be neglected, as in typical cases of transient response.

First the process and the barrier level are replaced by their normalized equivalents $Y(t)$ and $\eta(t)$ defined in (2.1). By a straightforward generalization of Rice's formula the joint upcrossing rate is

$$\nu^Y_{\eta\eta}=\int_{\dot\eta_1}^\infty\int_{\dot\eta_2}^\infty f_{\dot{\mathbf{Y}}\mathbf{Y}}(\mathbf{z},\boldsymbol{\eta})(z_1-\dot\eta_1)(z_2-\dot\eta_2)dz_1dz_2 \quad (3.2)$$

$f_{\dot{\mathbf{Y}}\mathbf{Y}}(\dot{\mathbf{y}},\mathbf{y})$ is the joint normal density function of $\dot{\mathbf{Y}}=(\dot Y(t_1),\dot Y(t_2))$ and $\mathbf{Y}=(Y(t_1),\,Y(t_2))$, and the covariance matrix is given in terms of the correlation function $\rho(t_1,t_2)$.

$$\mathbf{c}=\begin{bmatrix} \mathbf{c}_{\dot{\mathbf{Y}}\dot{\mathbf{Y}}} & \mathbf{c}_{\dot{\mathbf{Y}}\mathbf{Y}} \\ \mathbf{c}_{\mathbf{Y}\dot{\mathbf{Y}}} & \mathbf{c}_{\mathbf{Y}\mathbf{Y}} \end{bmatrix}=\begin{bmatrix} \omega_1^2 & \rho_{,12} & 0 & \rho_{,1} \\ \rho_{,12} & \omega_2^2 & \rho_{,2} & 0 \\ 0 & \rho_{,2} & 1 & \rho \\ \rho_{,1} & 0 & \rho & 1 \end{bmatrix} \quad (3.3)$$

Here

$$\rho_{,1}=\left(\frac{\partial}{\partial t_1}\right)\rho(t_1,t_2)\ \text{etc.}$$

It is advantageous to write (3.2) in terms of the conditional probability density function $f_{\dot{\mathbf{Y}}|\mathbf{Y}}(\dot{\mathbf{y}}\,|\,\boldsymbol{\eta})$ for $\dot{\mathbf{Y}}$ given $\mathbf{Y}=\boldsymbol{\eta}$.

$$\nu^{\mathbf{Y}}_{\eta\eta}=f_{\mathbf{Y}}(\boldsymbol{\eta})\int_{\dot\eta_1}^\infty\int_{\dot\eta_2}^\infty f_{\dot{\mathbf{Y}}|\mathbf{Y}}(z\,|\,\boldsymbol{\eta})(z_1-\dot\eta_1)(z_2-\dot\eta_2)dz_1dz_2 \quad (3.4)$$

The first factor is simply the joint normal density with correlation ρ.

$$f_{\mathbf{Y}}(\boldsymbol{\eta})=\frac{1}{2\pi\sqrt{1-\rho^2}}\exp\left(-\frac{1}{2(1-\rho^2)}(\eta_1^2-2\rho\eta_1\eta_2+\eta_2^2)\right) \quad (3.5)$$

The conditional density $f_{\dot{\mathbf{Y}}|\mathbf{Y}}(z\,|\,\eta)$ is also joint normal with mean and covariance given by

$$\boldsymbol{\mu}=\boldsymbol{\mu}_{\dot{\mathbf{Y}}|\eta}=\mathbf{c}_{\dot{\mathbf{Y}}\mathbf{Y}}\mathbf{c}_{\mathbf{Y}\mathbf{Y}}^{-1}\boldsymbol{\eta}=\frac{1}{1-\rho^2}\begin{Bmatrix}(\eta_2-\rho\eta_1)\rho_{,1}\\(\eta_1-\rho\eta_2)\rho_{,2}\end{Bmatrix} \quad (3.6)$$

and

$$\mathbf{c}_{\dot{\mathbf{Y}}|\eta}=\mathbf{c}_{\dot{\mathbf{Y}}\dot{\mathbf{Y}}}-\mathbf{c}_{\dot{\mathbf{Y}}\mathbf{Y}}\mathbf{c}_{\mathbf{Y}\mathbf{Y}}^{-1}\mathbf{c}_{\mathbf{Y}\dot{\mathbf{Y}}}=\begin{Bmatrix}\lambda_1^2 & \kappa\lambda_1 & \lambda_2\\ \kappa\lambda_1\lambda_2 & \lambda_2^2\end{Bmatrix} \quad (3.7)$$

The parameters in the covariance matrix (3.7) follow from (3.3).

$$\lambda_1^2=\omega_1^2-\frac{(\rho_{,1})^2}{1-\rho^2} \quad (3.8)$$

$$\lambda_2^2=\omega_2^2-\frac{(\rho_{,2})^2}{1-\rho^2} \quad (3.9)$$

$$\kappa\lambda_1\lambda_2=\rho_{,12}+\frac{\rho\rho_{,1}\rho_{,2}}{1-\rho^2} \quad (3.10)$$

Downloaded 02 May 2010 to 171.66.16.25. Redistribution subject to ASME license or copyright; see http://www.asme.org/terms/Terms_Use.cfm

In terms of these parameters

$$f_{\dot{\mathbf{Y}}|\eta}(\mathbf{z},\eta)=\frac{1}{2\pi\lambda_1\lambda_2\sqrt{1-\kappa^2}}\exp\Big\{-\frac{1}{2(1-\kappa^2)}\Big(\Big(\frac{z_1-\mu_1}{\lambda_1}\Big)^2 -2\Big(\frac{z_1-\mu_1}{\lambda_1}\Big)\Big(\frac{z_2-\mu_2}{\lambda_2}\Big)+\Big(\frac{z_2-\mu_2}{\lambda_2}\Big)^2\Big)\Big\} \tag{3.11}$$

The double integral in (3.4) can not generally be evaluated in closed form, but a reduction to a single integral in the variable κ can be accomplished by use of the easily verified identity

$$\frac{\partial}{\partial\kappa}f_{\dot{\mathbf{Y}}|\eta}(\mathbf{z}|\eta)=\lambda_1\lambda_2\frac{\partial^2}{\partial z_1\partial z_2}f_{\dot{\mathbf{Y}}|\eta}(\mathbf{z}|\eta) \tag{3.12}$$

This identity gives $f_{\dot{\mathbf{Y}}|\eta}(\mathbf{z}|\eta)$ in the form

$$f_{\dot{\mathbf{Y}}|\eta}(\mathbf{z}|\eta;\kappa)=f_{\dot{\mathbf{Y}}|\eta}(\mathbf{z}|\eta;0)+\int_0^\kappa\frac{\partial}{\partial k}f_{\dot{\mathbf{Y}}|\eta}(\mathbf{z}|\eta;k)dk$$

$$=\frac{1}{\lambda_1}\phi\Big(\frac{z_1-\mu_1}{\lambda_1}\Big)\frac{1}{\lambda_2}\phi\Big(\frac{z_2-\mu_2}{\lambda_2}\Big) +\lambda_1\lambda_2\int_0^\kappa\frac{\partial^2}{\partial z_1\partial z_2}f_{\dot{\mathbf{Y}}|\eta}(\mathbf{z}|\eta;k)dk \tag{3.13}$$

Substitution of this representation into (3.2) and integration by parts twice gives the desired result.

$$\nu^Y_{\eta\eta}=\lambda_1\lambda_2 f_{\mathbf{Y}}(\eta)\Big\{\Psi\Big(-\frac{\mu_1-\dot{\eta}_1}{\lambda_1}\Big)\Psi\Big(-\frac{\mu_2-\dot{\eta}_2}{\lambda_2}\Big) +\kappa\,\Phi\Big(\frac{\mu_1-\dot{\eta}_1}{\lambda_1}\Big)\Phi\Big(\frac{\mu_2-\dot{\eta}_2}{\lambda_2}\Big) +\lambda_1\lambda_2\int_0^\kappa(\kappa-k)f_{\dot{\mathbf{Y}}|\eta}(\dot{\eta}|\eta;k)dk\Big\} \tag{3.14}$$

An explicit, approximate formula for the integral in (3.14) can be obtained by reference to the problem of a constant barrier level and a stationary narrow band process. In that case $\ddot{\rho}\simeq-\omega_s^2\rho$, and it follows that ρ appears as a factor in the expression for κ. Thus the integral vanishes twice within each period, namely for $\tau=t_1-t_2\simeq n\pi/\omega_s$. In each of these intervals there is a point at which $\rho_{,1}=-\rho_{,2}=0$, whereby $\mu_1=-\mu_2=0$. At these points the exponential function takes unit value, and the integral is of simple algebraic type. Both of these exact results for particular parameter combinations are contained within an approximation that assumes that the maximum value of the algebraic factor at $k=0$ makes it permissible to use the value $k=0$ in the argument of the exponential. This assumption leads to the explicit approximation formula

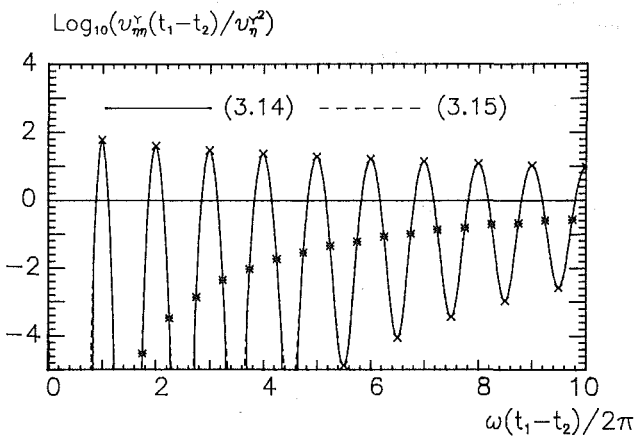


Fig. 2 Crossing frequency $\nu^Y_{\eta\eta}(t_1, t_2)$, as given by (3.14) and (3.15), $\eta=2.0$, $\zeta=0.01$

$$\nu^Y_{\eta\eta}\simeq\lambda_1\lambda_2 f_{\mathbf{Y}}(\eta)\Big\{\Psi\Big(-\frac{\mu_1-\dot{\eta}_1}{\lambda_1}\Big)\Psi\Big(-\frac{\mu_2-\dot{\eta}_2}{\lambda_2}\Big) +\kappa\Phi\Big(\frac{\mu_1-\dot{\eta}_2}{\lambda_1}\Big)\Phi\Big(\frac{\mu_2-\dot{\eta}_2}{\lambda_2}\Big) +\phi\Big(\frac{\mu_1-\dot{\eta}_1}{\lambda_1}\Big)\phi\Big(\frac{\mu_2-\dot{\eta}_2}{\lambda_2}\Big)\Big(\sqrt{1-\kappa^2}-1+\kappa\arcsin(\kappa)\Big)\Big\} \tag{3.15}$$

Figure 2 shows a comparison between the exact expression (3.14) for the joint upcrossing rate and the approximate (3.15) for a constant barrier level $\eta=2.0$ and a stationary process with correlation function (2.13) and damping ratio $\zeta=0.01$. The general agreement is very good, and points indicate exact values. It is notable that the joint upcrossing rate changes with several orders of magnitude within each period, and that the special parameter combinations of the exact points define the range well.

For constant barrier levels and stationary processes the approximation (3.15) also reproduces the theoretical limit of $\nu^Y_{\eta\eta}$ for $\tau=t_1-t_2\to0$. The correlation function (2.13) for white noise response gives the finite limit

$$\nu^Y_{\eta\eta}(\tau)\simeq\frac{\zeta\omega_s^2}{18\pi^2}(3\sqrt{3}-\pi)e^{-\eta^2/2} \tag{3.16}$$

This agrees with the result of Longuet-Higgins [2] for $\eta=0$. When the second derivative of the stochastic process is continuous $\nu^Y_{\eta\eta}\to0$.

The integral equation (1.3) with the kernel (3.1) can be written in the form

$$f_1(t)=\nu^Y_\eta(t)\Big\{1-\int_0^t\frac{\nu^Y_{\eta\eta}(t,\tau)}{\nu^Y_\eta(t)\nu^Y_\eta(\tau)}f_1(\tau)d\tau\Big\} \tag{3.17}$$

In this form the integral equation is easily solvable numerically, when the approximate formula (3.15) is used for $\nu^Y_{\eta\eta}$. It is seen that both of the bounds (1.4) and (1.7) are satisfied by the solution to (3.17). Before turning to numerical examples and a discussion of the relation between the integral equation (3.17) and other methods in current use, it appears worthwhile to derive a discretized form of (3.17) applicable in the case of a narrow band process.

4 Localized Kernel Representation

In the case of a narrow band process the kernel in the integral equation (3.17) varies by several orders of magnitude within each period. This is illustrated in Fig. 2, and the regularity of the variation suggests replacing the joint upcrossing rate $\nu^Y_{\eta\eta}$ with a series of delta functions located at $t-\tau=2n\pi/\omega_0$. Thus for any fixed value of t

$$\nu^X_{\xi\xi}(t,\tau)\simeq\sum_{n=1}^\infty a_n(t)\delta(t-\tau-2n\pi/\omega_0),\quad t>\tau \tag{4.1}$$

This localized representation of the kernel leads to the explicit recurrence formula

$$f_1(t)=\begin{cases}\nu^X_\xi(t), & 0<t<\dfrac{2\pi}{\omega_0}\\[2ex] \nu^X_\xi(t)\Big[1-\displaystyle\sum_n\frac{a_n(t)}{\nu^X_\xi(t)\nu^X_\xi(t-\tau_n)}f_1(t-\tau_n)\Big], & \dfrac{2\pi}{\omega_0}<t\end{cases}$$

$$\tau_n=2\pi n/\omega_0<t \tag{4.2}$$

The coefficients $a_n(t)$ represent the integral of $\nu^X_{\xi\xi}$ over one period, i.e.,

$$a_n(t)=\int_{(2n-1)\pi/\omega_0}^{(2n+1)\pi/\omega_0}\nu^X_{\xi\xi}(t,t-\tau)d\tau \tag{4.3}$$

Downloaded 02 May 2010 to 171.66.16.25. Redistribution subject to ASME license or copyright; see http://www.asme.org/terms/Terms_Use.cfm

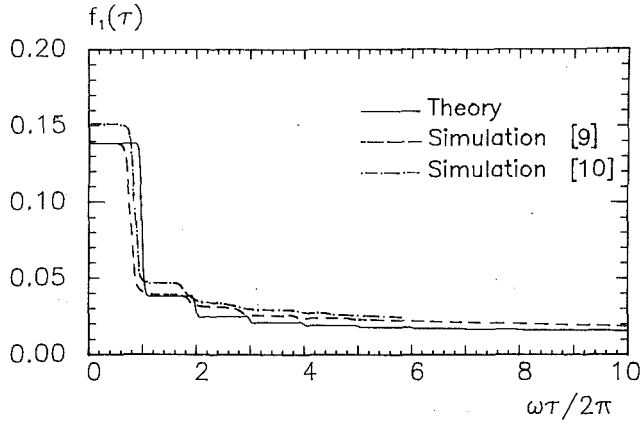


Fig. 3 First-passage probability density function $f_1(t)$ from the integral equation (3.17) and simulations from [9] and [10], $\eta = 2$, $\zeta = 0.01$

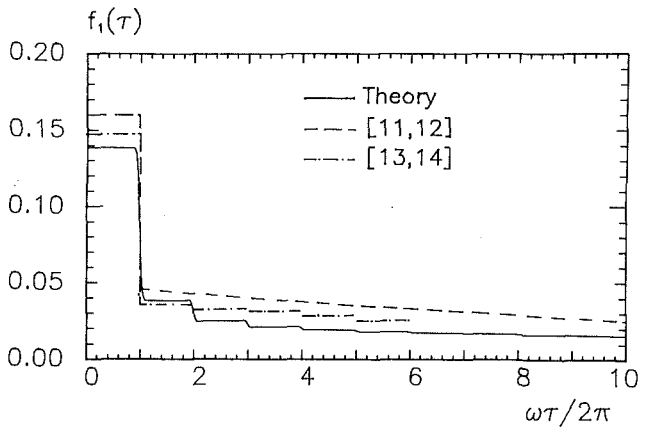


Fig. 4 First-passage probability density function $f_1(t)$ from the integral equation (3.17) and from the methods of Vanmarcke [11, 12] and Yang and Shinozuka [13, 14], stationary response, $\eta = 2$, $\zeta = 0.01$

This integral can be evaluated approximately by extracting the rapid variation of $\nu^X_{\xi\xi}$ is an exponential factor.

$$\nu^X_{\xi\xi}(t,t-\tau) = e^{h(t,t-\tau)} G(t,t-\tau) \tag{4.4}$$

In the neighborhood of points τ_n where $(\partial/\partial\tau)h = 0$ the exponent can be represented by

$$h(t,t-\tau) \simeq h(t,t-\tau_n) + \frac{1}{2}\frac{\partial^2}{\partial\tau^2} h(t,t-\tau_n)(\tau-\tau_n)^2 \tag{4.5}$$

Within this approximation the integral is

$$a_n(t) \simeq \nu^X_{\xi\xi}(t,t-\tau_n)\sqrt{\frac{2\pi}{-h_n''}}\left[2\phi\left(\frac{\pi}{\omega_0}\sqrt{-h_n''}\right) - 1\right] \tag{4.6}$$

The key parameter is seen to be $(\partial^2/\partial\tau^2)h(t,t-\tau_n)$, and the accuracy of (4.4) depends on the ability to extract the essential variation in the function $h(t,t-\tau)$. Most of the variation of $\nu^X_{\xi\xi}$ is contained in the factors in front of the braces in (3.14), whereby

$$h(t_1,t_2) = -\left[\frac{3}{2} ln(1-\rho^2) + \frac{1}{2(1-\rho^2)}(\eta_1^2 - 2\rho\eta_1\eta_2 + \eta_2^2)\right] \tag{4.7}$$

When the variation of $h(t_1,t_2)$ due to the time dependence of the normalized level η_2 is neglected

$$h_n'' = \frac{\partial^2}{\partial\tau^2} h(t,t-\tau_n) \simeq \frac{1}{1-\rho^2}\frac{\partial^2\rho}{\partial\tau^2}$$
$$\left\{3\rho + \frac{1-\rho}{1+\rho}\eta_1\eta_2 - \frac{\rho}{1-\rho^2}(\eta_1-\eta_2)^2\right\} \tag{4.8}$$

Results from the localized kernel approach are compared with solutions to the full integral equation (3.17) in the next section.

5 Examples and Discussion

Figure 3 shows a numerical solution of the integral equation (3.17) together with simulated results from [9, 10] for a stationary process with $\rho(\tau)$ given by (2.13) and the parameters $\eta = 2$ and $\zeta = 0.01$. The asymptotic form $\nu^X_\xi/\Phi(2)$ was used in the first term of (3.17) to obtain the correct limit for $t \to 0$. The calculated curve is seen to reproduce the simulation from [9] remarkably well, while the simulation from [10] gives systematically high values, and for $t \to 0$ exceeds the upper bound (1.4). It is seen that the present form of the integral equation makes the first step too wide. This is a consequence of the relaxation of the initial condition $X(0) < \xi$ as may be seen by comparison with $\nu^X_{\xi|x_0<\xi}$ from Fig. 1.

The sudden decrease in $f_1(t)$ at the end of the first period is caused by the narrow band property of the process $X(t)$ which makes the upcrossings occur in groups. This effect can be dealt with in a semiempirical way by use of an envelope that represents an instantaneous amplitude. A procedure based on envelope crossings has been developed by Vanmarcke [11, 12]. It is based on the Poisson assumption regarding independent upcrossings in connection with an effective envelope upcrossing rate. The resulting failure probability follows from (1.10) by replacing $F(\xi(0))$ with the corresponding expression for the envelope and $\nu^X_\xi(\tau)$ with the effective envelope upcrossing rate

$$\nu^R_{\xi,\text{eff}} = \nu^X_\xi[1 - \exp(-\nu^R_\xi/\nu^X_\xi)] \tag{5.1}$$

This formula provides an interpolation between the original upcrossing rate ν^X_ξ at high levels and the envelope upcrossing rate ν^R_ξ at low levels.

A discrete, envelope based procedure has been developed by Yang and Shinozuka [13, 14]. The extremes of the process are assumed to occur at equal intervals and their magnitude is determined by the envelope. By introducing a Markov assumption to limit the memory to the previous extremum a simple recurrence formulation is obtained, closely resembling a discretized form of the continuous envelope method of Vanmarcke.

The results of these two procedures are compared with those of the integral equation (3.17) in Fig. 4. While all three methods agree on the general features some differences are present.

Transient response, i.e., the response of a system excited by a stationary input from $t = 0$, represents an extreme case of nonstationarity, and therefore constitutes an important reference case. Furthermore, particularly simple expressions are available for the covariance function [15, 16]. Thus the transient equivalent to (2.13) for stationary white noise response is

$$c(t_1,t_2) = \sigma_s^2[\rho_s(t_1-t_2) - \rho_s(t_1)\rho_s(t_2) - \dot\rho_s(t_1)\dot\rho_s(t_2)\omega_s^2] \tag{5.2}$$

where $\sigma_s^2, \rho_s(\ )$ and ω_s refer to the stationary case. The various approximations to the first-passage probability density for $\xi/\sigma_s = 2$, $\zeta = 0.02$ are shown in Fig. 5. It is well established that the Poisson approximation gives too large values of $f_1(t)$, but it also appears from the figure that both of the simple envelope based approximations give larger values than the intergral equation method. No single barrier simulation results appear to be available, but supplementary calculations for symmetric barriers in [17] show superior agreement between simulation results from [10] and the integral equation results.

Downloaded 02 May 2010 to 171.66.16.25. Redistribution subject to ASME license or copyright; see http://www.asme.org/terms/Terms_Use.cfm

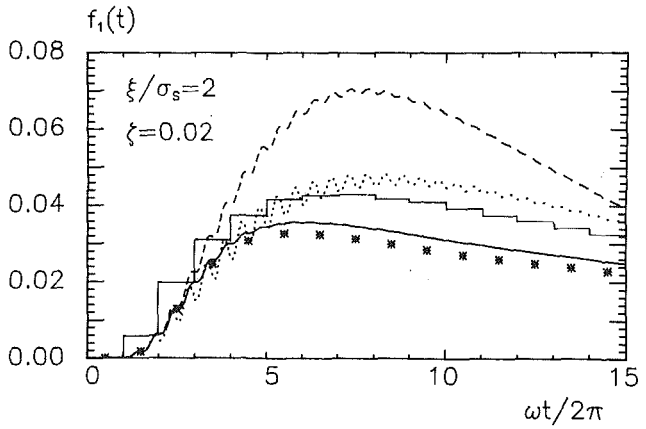


Fig. 5 First-passage probability density function $f_1(t)$ from the integral equation (3.17) (full line), the localized kernel approximation (*), and from the Poisson-type approximations (1.9) (dashed line), (5.1) (dotted line), and Yang and Shinozuka [12, 14] (step function). Transient response, $\xi_s = 2$, $\zeta = 0.02$.

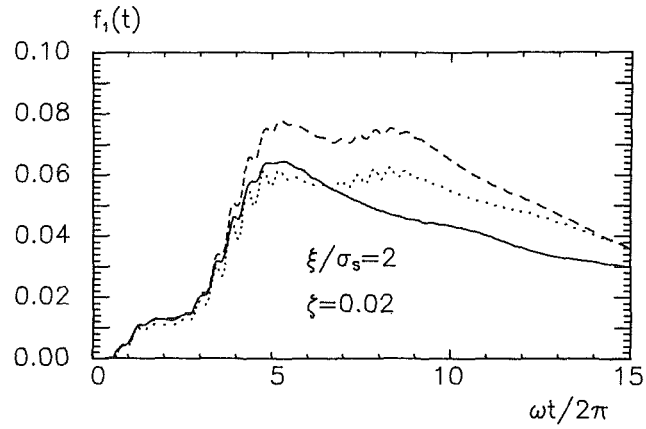


Fig. 6 First-passage probability density function $f_1(t)$ from the integral equation (3.17) (full line) and from the Poisson-type approximations (1.9) (dashed line), (5.1) (dotted line). Transient response of two-mode system, $\omega_2 = 1.25\,\omega_1$, $\xi/\sigma_s = 2$, $\zeta = 0.02$.

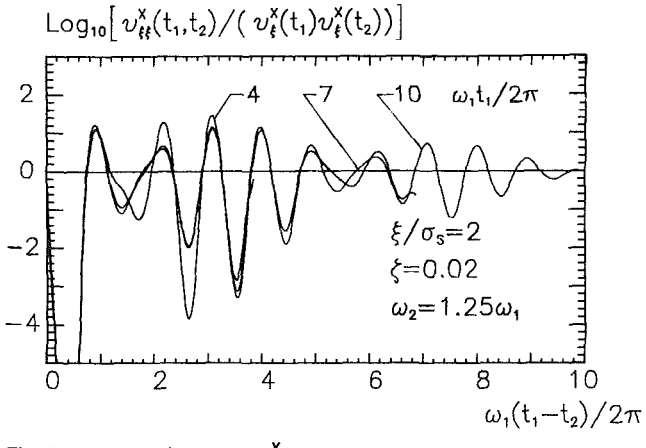


Fig. 7 Crossing frequency $\nu^X_{\dot\xi\dot\xi}(t_1, t_2)$ for a two-mode system as given by (3.14), $\omega_2 = 1.25\,\omega_1$, $\xi_s = 2$, $\zeta = 0.02$

The computational work is increased considerably by nonstationarity, and it becomes attractive to use the localized kernel formulation of the previous section. These results are also included in Fig. 5, and they are seen to fall below the more accurate solution to the integral equation. The localized kernel method is similar to an extension of the point process method in which the correlation is extended beyond neighboring points, and it has been observed that this extension leads to unconservative results, [18].

In many cases of practical interest the stochastic process under consideration is a sum of narrow band components and exhibits pronounced multimodal behavior. Figure 6 shows results for the case in which $X(t)$ is the sum of the responses from two linear systems with $\omega_1 = 1.25\,\omega_2$ and $\zeta_1 = \zeta_2 = 0.02$. The normalized level is $\xi/\sigma_s = 2$ as in Fig. 5. While both the Poisson approximation and its continuous envelope modification are seen to display secondary maxima at $t = 8\omega_1/2\pi$, the integral equation solution decreases smoothly. While no simulation results for this case are available it should be noted that only the integral equation retains a memory exceeding that of a locally determined hazard function. The influence of mode interference on the kernel of the integral equation is shown in Fig. 7. Apart from a certain development with time, the interference is clearly visible as "beats."

6 Conclusion

The integral equation of Bernard and Shipley for the first-passage probability density has been rederived in a simple and more general way, and an accurate, explicit approximation formula has been obtained for the kernel. The oscillatory behavior of the kernel for uni and multimodal processes has been investigated. The results of the integral equation method have been found to agree well with available data as well as with alternative methods for the narrow band case. At present it appears as the only available first-passage method that is able to account explicitly for the structure of multimodal stochastic processes.

References

1 Rice, S. O., "Mathematical Analysis of Random Noise," in *Selected Papers on Noise and Stochastic Processes*, Wax, N., ed., Dover, New York, 1954.

2 Longuet-Higgins, M. S., "The Distribution of Intervals Between Zeros of a Stationary Random Function," *Phil. Trans. Roy. Soc.*, Vol. A254, 1962, pp. 557–599.

3 Roberts, J. B., "An Approach to the First Passage Problem in Random Vibration," *J. Sound Vib.*, Vol. 8, 1968, pp. 301–328.

4 Bernard, M. C., and Shipley, J. W., "The First Passage Problem for Stationary Random Structural Vibration," *J. Sound Vib.*, Vol. 24, 1972, pp. 121–132.

5 Shipley, J. W., and Bernard, M. C., "The First Passage Problem for Structural Systems," ASME JOURNAL OF APPLIED MECHANICS, Vol. 39, 1972, pp. 911–917.

6 Nielsen, S. K., "Probability of Failure of Structural Systems Under Random Vibration," Institute of Building Technology and Structural Engineering, AUC, Aalborg; Report 8001, 1980.

7 Ditlevsen, O., "*Extremes and First Passage Times*," Dissertation, Copenhagen, 1971.

8 Rice, J., and Beer, F., "First-Occurrence Time of High-Level Crossings in a Continuous Random Process," *J. Acoust. Soc. Am.*, Vol. 39, 1965, pp. 323–335.

9 Christensen, J. K., and Sørensen, J. D., "Simulation of Gaussian Processes to Determine Failure," (in Danish), Institute of Building Technology and Structural Engineering, AUC, Aalborg, Report 8007, 1980.

10 Crandall, S. H., Chandiramani, K. L., and Cook, R. G., "Some First-Passage Problems in Random Vibration," ASME JOURNAL OF APPLIED MECHANICS, Vol. 33, 1966, pp. 532–538.

11 Vanmarcke, E. H., "First Passage and Other Failure Criteria in Narrow-Band Random Vibration: A Discrete State Approach," Department of Civil Engineering, M.I.T. Research Report No. R69-68, 1969.

12 Vanmarcke, E. H., "On the Distribution of the First-Passage Time for Normal Stationary Random Processes," ASME JOURNAL OF APPLIED MECHANICS, Vol. 42, 1975, pp. 215–220.

13 Yang, J. -N., and Shinozuka, M., "On the First Excursion Probability in Stationary Narrow-Band Random Vibration," ASME JOURNAL OF APPLIED MECHANICS, Vol. 30, 1971, pp. 1017–1022

14 Yang, J. -N., "First Excursion Probability in Nonstationary Random Vibration," *J. Sound Vib.*, Vol. 27, 1973, pp. 165–182.

15 Krenk, S., "Nonstationary Narrow-Band Response and First-Passage Probability," ASME JOURNAL OF APPLIED MECHANICS, Vol. 46, 1979, pp. 919–924.

16 Madsen, P. H., and Krenk, S., "Stationary and Transient Response Statistics," *J. Eng. Mech. Div.*, Proc. ASCE, Vol. 108, No. EM4, 1982, pp. 622–635.

17 Madsen, P. H., "*Stochastic Response Analysis and First-Passage Probabilities*," Risø National Laboratory, Report R-485, 1983.

18 Yang, J. -N., "Approximation to First Passage Probability," *J. Eng. Mech. Div.*, Proc. ASCE, Vol. 102, No. EM4, 1975, pp. 361–372.

Downloaded 02 May 2010 to 171.66.16.25. Redistribution subject to ASME license or copyright; see http://www.asme.org/terms/Terms_Use.cfm

Wheelset Mechanics During Wheelclimb Derailment

A. Karmel
Mechanical Research Department,
General Motors Research Laboratories,
Warren, Mich. 48090

L. M. Sweet
Manager, Control Theory
and Systems Program,
General Electric Co.,
Corporate Research and Development,
Schenectady, N.Y. 12345

An analysis of the mechanics and dynamics of a railroad vehicle wheelset during flange contact and wheelclimb derailment is presented. The theoretical model includes wheelset lateral, vertical, roll, yaw, and axle rotation degrees of freedom, plus lateral displacement of the truck frame. The equations of motion are based on the kinematics and dynamics of the wheelset subject to constraints imposed by wheel/rail contact geometry. These constraints are used to compute creepages and normal forces at the wheel/rail contact points, needed as inputs to the Kalker Simplified Theory of rolling contact. Computational methods for simulation of the nonlinear dynamic model are discussed. Results of the simulation demonstrate the significance of the various degrees of freedom on wheelset motion and on predicted values of the derailment quotient (Q/P).

Introduction

Numerous theoretical models for wheelset dynamics are available in the literature [1–4]. For large-amplitude wheelset motions, the mechanics and dynamics become highly nonlinear, due to the effects of contact geometry and rolling friction creep forces. For motions during which tread contact is maintained on both wheels, whether the wheel profiles are conical or curved, the wheelset dynamic equations include many terms of approximately equal magnitude. Under conditions of severe flange contact leading to derailment, the relative magnitudes of these various dynamic terms differ considerably from their values in the tread contact case, leading to conclusions different in certain respects from those of the cited references.

Compared to the rather rigorous analytical models of preceding references, theories used for analysis of derailment mechanics have been simplified. Equilibrium models for wheels and rails in flange contact by Gilchrist and Brickle [5], Sweet [6], and Yokose and Arai [7] have successfully predicted quasisteady derailment limits. Dynamic wheelclimb models by Sweet [8] and Yokose [7, 9, 10] on the other hand, have all been based on certain assumptions that have not been fully verified by simulation or experiment.

In this study a detailed model for wheelset derailment has been developed. The wheelset motion includes three independent degrees of freedom: lateral displacement, yaw angle, and axle rolling angular velocity, and the truck motion includes a single degree of freedom: the lateral displacement of the truck frame.

While nearly all analyses include the first two motions of the wheelset, only more recent papers by Clark [11] and Duffek [12] have accounted for the deviation of the rolling velocity from the nominal value of V/r_0 expected when the wheelset is centered and rolls with zero slip. As shown in [6], during steady flange contact and axle speed drops by about 3 percent which should have a significant effect on calculation of the longitudinal creepage.

If wheel/rail contact is maintained on both wheels, the wheelset vertrical and roll degrees of freedom are not independent and may be expressed as a function of the lateral motion. Imposition of these kinematic constraints leads to generation of significant dynamic components in the equations of motion. A wheelset kinematic model is developed in this paper to account for these dynamic effects, as well as for computation of lateral creepages in the contact zones as a function of the velocity of the wheelset center of mass.

A digital computer program for solving the resulting equations of motion is described. The program is compatible with published programs used for computation of contact geometry and creep force functions.

Kinematics of Wheelset Motion

Kinematic Model: Careful representation of the kinematics of wheelset motion is needed for determination of the creepages at the wheel/rail interfaces and the coupling of the vertical, lateral, and roll motions. The kinematic analysis employs three sets of coordinate systems, as illustrated in Fig. 1. The contact zone creepages depend on the relative velocities of the contact points of the wheels with respect to the rails. The wheelset kinematic model is used to determine these relative velocities in terms of the velocity of the wheelset center of mass, utilizing the geometrical constraints imposed by the rails on the wheelset motion. The model is also used to compute the wheelset vertical and roll accelerations, as functions of its lateral velocity and acceleration.

Contributed by the Applied Mechanics Division for publication in the JOURNAL OF APPLIED MECHANICS.
Discussion on this paper should be addressed to the Editorial Department, ASME, United Engineering Center, 345 East 47th Street, New York, N.Y. 10017, and will be accepted until two months after final publication of the paper itself in the JOURNAL OF APPLIED MECHANICS. Manuscript received by ASME Applied Mechanics Division, January, 1982; final revision, February, 1984.

Copyright © 1984 by ASME
Downloaded 02 May 2010 to 171.66.16.25. Redistribution subject to ASME license or copyright; see http://www.asme.org/terms/Terms_Use.cfm

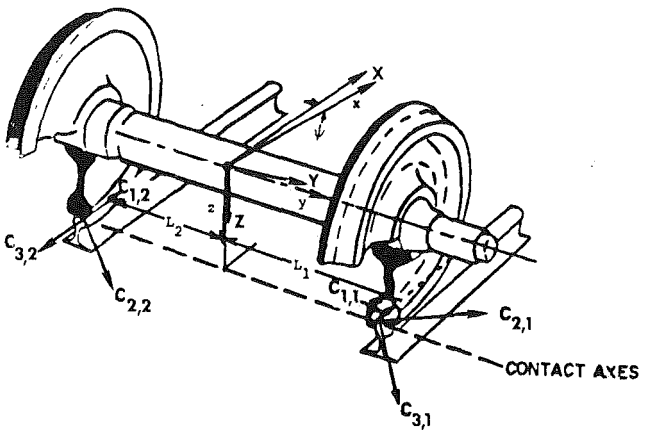


Fig. 1 Definition of coordinate systems for wheelset and contact zones

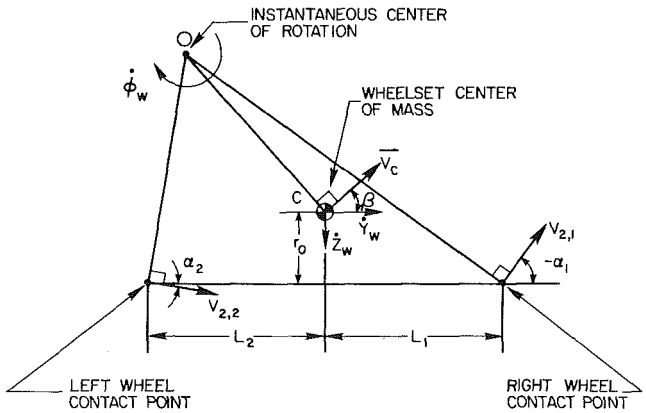


Fig. 2 Velocities defined by wheelset kinematic model

The wheelset kinematic model is illustrated in Fig. 2. A two-dimensional, planar motion model is used to derive the relationships between lateral, vertical, and roll motions. The instantaneous center of rotation, point O, is assumed to be in the YZ plane, with its location depending on the contact angles and contact points. The kinematic relationships are derived by first determining the position of the wheelset center of mass, point C, relative to the instantaneous center:

$$\overline{OC}^2 = \frac{L_2^2}{\cos^2\gamma_1} + \frac{(L_1+L_2)^2\cos^2\alpha_1}{\sin^2(|\alpha_1|+\alpha_2)} - \frac{2L_2(L_1+L_2)\cos\alpha_1\sin(\gamma_1+\alpha_2)}{\sin(|\alpha_1|+\alpha_2)\cos\gamma} \tag{1}$$

where $\gamma_1 = \tan^{-1}(r_0/L_2)$

$$\gamma_2 = \sin^{-1}[L_2\cos(\gamma_1+\alpha_2)/\overline{OC}\cos\gamma_1] \tag{2}$$

$$\beta = \gamma_2 - \alpha_2 \tag{3}$$

From equations (1)–(3) the instantaneous relationships between vertical, lateral, and roll motions for the wheelset (subscript w) are computed:

$$\frac{\partial Z_w}{\partial Y_w} = -\tan\ \beta \tag{4}$$

$$\frac{\partial \Phi_w}{\partial Y_w} = -\frac{1}{\overline{OC}\cos\ \beta} \tag{5}$$

Contact Zone Velocities. The lateral velocity in the contact plane at each contact point is determined by:

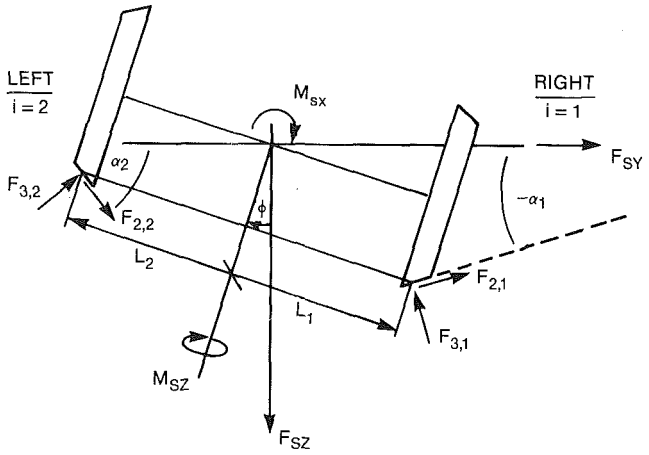


Fig. 3 External forces and moments applied to the wheelset

$$V_{2,1} = \frac{(L_1+L_2)\cos\alpha_2}{\sin(|\alpha_1|+\alpha_2)}\frac{\partial\Phi_w}{\partial Y_w}\dot{Y}_w \tag{6a}$$

$$V_{2,2} = \frac{(L_1+L_2)\cos\alpha_1}{\sin(|\alpha_1|+\alpha_2)}\frac{\partial\Phi_w}{\partial Y_w}\dot{Y}_w \tag{6b}$$

Creepages for a wheelset, with rolling radii $r_{v,i}$ traveling at forward velocity V and rolling speed Ω, are defined using the model of Gilchrist and Brickle [5], with extensions to include dynamic effects. Sign conventions have been modified for consistency with Kalker Theory. The subscript i equals 1 for the right wheel, 2 for the left.

For longitudinal creepage (nondimensional):

$$\gamma_{1,i} = \frac{\Omega r_{v,i}\cos\psi + V}{V} + (-1)^i\frac{\dot{\psi}L_i}{V} \tag{7}$$

For lateral creepage (nondimensional):

$$\gamma_{2,i} = -\frac{\sin\psi}{\cos\alpha_i} + \frac{V_{2,i}}{V} \tag{8}$$

For spin creepage (dimensional):

$$\omega_{3,i} = \frac{\sin\alpha_i}{r_{v,i}} \tag{9}$$

Similar expressions were developed by Elkins and Gostling [13], although they used the wheelset c.m. lateral velocity Y_w instead of $V_{2,i}$. The spin creepage defined in equation (9) is a function of contact geometry only, for a given value of wheelset lateral displacement. The effects of yaw velocity and slip on spin creepage have been neglected. For nonzero values of yaw angle ψ_w the wheelset contact geometry and kinematics become three-dimensional, with the longitudinal displacements of the contact points probably being the most important three-dimensional effect. These effects have not been included in the present analysis.

Vertical and Roll Accelerations. The normal forces at the wheel/rail contact points depend on the vertical and roll velocities and accelerations of the wheelset. These quantities are found readily through application of the chain rule, which relates them to the wheelset lateral velocity and acceleration. For roll,

$$\dot{\Phi}_w = \frac{\partial\Phi_w}{\partial Y_w}\dot{Y}_w \tag{10}$$

$$\ddot{\Phi}_w = \frac{\partial\Phi_w}{\partial Y_w}\ddot{Y}_w + \frac{\partial^2\Phi_w}{\partial Y_w^2}\dot{Y}_w^2 \tag{11}$$

Similar expressions hold for vertical displacement Z_w.

Downloaded 02 May 2010 to 171.66.16.25. Redistribution subject to ASME license or copyright; see http://www.asme.org/terms/Terms_Use.cfm

The first partial derivatives are given by equations (4) and (5). Both the first and second derivatives are functions of contact geometry only, and may be precomputed and stored as functions of wheelset lateral displacements.

Creep Forces Derived From Kalker Theory

Geometry of Contact Zone. The Kalker Simplified Theory of rolling contact is used to model the creepage forces at the wheel/rail interface. It is based on the Hertzian contact assumption [14], which expresses the contact zone shape and dimension in terms of the local geometry constraints of the wheel and rail. The contact ellipse semiaxes a_i and b_i are given by:

$$a_i = a(\theta_i)\sqrt[3]{\frac{F_{3,i}\rho_i}{n}} \quad b_i = b(\theta_i)\sqrt[3]{\frac{F_{3,i}\rho_i}{n}} \tag{12}$$

where

$$\rho_i = \frac{4}{\frac{1}{R_{1,i}} + \frac{1}{R'_{2,i}} + \frac{1}{R'_{1,i}}} \qquad n = \frac{4E}{3(1-\epsilon^2)}$$

$$\cos\theta_i = \frac{B_i}{A_i} \qquad A_i = \frac{2}{\rho_i}$$

$$B_i = \frac{1}{2}\sqrt{\left(\frac{1}{R_{1,i}}\frac{1}{R'_{1,i}}\right)^2 + \left(\frac{1}{R'_{2,i}}\right)^2 - 2\left(\frac{1}{R_{1,i}} - \frac{1}{R'_{1,i}}\right)\frac{1}{R'_{2,i}}\cos 2\delta}$$

$$\delta = 90 \text{ deg} - \psi_w$$

Material properties are defined by elastic modulus E and Poisson's ratio ϵ. The quantites R_{ji} and R'_{ji} represent curvatures of the contouring bodies.

Normalization of Creepages. Given the contact zone shape and dimension, and the associated creepages and spin, Kalker forms the nondimenisonal creep parameters:

$$\xi_i = \gamma_{1,i}\frac{\rho_i}{\mu\, c_i} \tag{13}$$

$$\eta_i = \gamma_{2,i}\frac{\rho_i}{\mu\, c_i} \tag{14}$$

$$\chi_i = \omega_{3,i}\frac{\rho_i}{\mu} \tag{15}$$

where μ is the friction coefficient and $c_i = \sqrt{a_i b_i}$ (the geometrical mean of the contact ellipse semiaxes).

For any combination of a/b ratio and spin parameter χ, Kalker's Simplified Theory predicts the nondimensional longitudinal and lateral creep forces $f_{1,i}$ and $f_{2,i}$. The dimensional creep forces applied by the rails on the rolling wheel along the contact zone system axes are:

$$F_{1,i} = -f_{1,i}\mu\ F_{3,i} \quad F_{2,i} = -f_{2,i}\mu\ F_{3,i} \tag{16}$$

In addition to these forces, a pure moment is transmitted, but of negligible magnitude.

The angular velocity of the wheelset (moving forward) will produce positive spin on the left contact zone, and negative on the right. To account for negative spin, the following relationships are used, based on arguments of symmetry [14],

$$\begin{aligned} f_1(\xi,\eta,\chi) &= -f_1(-\xi,\eta,\chi) = +f_1(\xi,-\eta,-\chi) \\ &= -f_1(-\xi,-\eta,-\chi) \\ f_2(\xi,\eta,\chi) &= +f_2(-\xi,\eta,\chi) = -f_2(\xi,-\eta,-\chi) \\ &= -f_2(-\xi,-\eta,-\chi) \end{aligned} \tag{17}$$

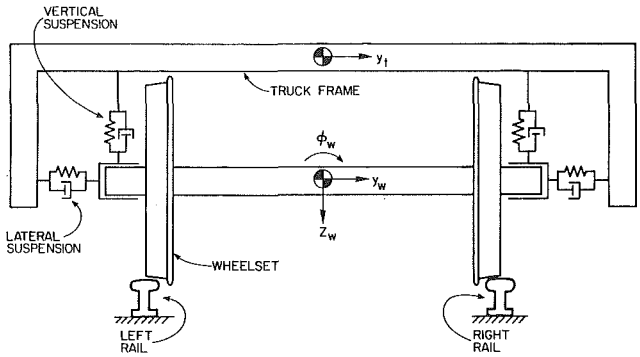


Fig. 4 Wheelset and truck frame model

Analysis of Wheelset Dynamics

Wheelset Equations of Motion. The following assumption are employed in deriving the wheelset equations of motion. Roll and yaw angles are assumed to be small. Gravity and suspension forces are applied to the wheelset along the XYZ rail coordinates axes. The longitudinal and lateral axes of the contact ellipse are assumed to coincide with the X axis and YZ plane, respectively. The equations of motion are derived in [15] by Newtonian methods using Euler Angles for calculation of the gyroscopic terms.

The translational equations of motion are derived in the XYZ rail coordinate system (see Fig. 3). Forces and moments transmitted to the wheelset from the truck frame through the primary suspension are represented by vectors $\bar{F}_s$ and $\bar{M}_s$, respectively.

$$m_w \ddot{Y}_w = \sum_i F_{3,i}(\mu f_{2,i}\cos\alpha_i + \sin\alpha_i) + F_{SY} \tag{18}$$

In the Z-directions:

$$m_w \ddot{Z}_w = \sum_i F_{3,i}(\mu f_{2,i}, \sin\alpha_i - \cos\alpha_i) F_{SZ} \tag{19}$$

The rotational equations of motion are derived in the rotating xyz system.
About the x axis:

$$\begin{aligned} \sum_i F_{3,i}[(-1)^i(\cos\alpha_i - \mu f_{2,i}\sin\alpha_i)L_i \\ -(\sin\alpha_i + \mu f_{2,i}\cos\alpha_i)r_{v,i}] + M_{sx} = \\ I_{xx}\ddot{\Phi}_w + (I_{zz} - I_{yy})\dot{\psi}_w^2 w\Phi w + I_{yy}\Omega\dot{\psi}_w \end{aligned} \tag{20}$$

About the y axis:

$$\begin{aligned} \mu\sum_i f_{1,i}F_{3,i}r_{v,i} = -I_{yy}\dot{\Omega} + I_{yy}(\ddot{\psi}_w\Phi_w + \dot{\psi}_w\dot{\Phi}_w) \\ +(I_{xx} - I_{zz})\dot{\Phi}_w\dot{\psi}_w - M_{sy} \end{aligned} \tag{21}$$

About the z axis:

$$\begin{aligned} \mu\sum_i (-1)^i f_{1,i}F_{3,i}L_i = I_{zz}\ddot{\psi}_w + \dot{\psi}_w\dot{\phi}_w\dot{\Phi}_w(I_{yy} - I_{xx} - I_{zz}) \\ -\Omega\dot{\Phi}_w I_{yy} - M_{sz} \end{aligned} \tag{22}$$

Downloaded 02 May 2010 to 171.66.16.25. Redistribution subject to ASME license or copyright; see http://www.asme.org/terms/Terms_Use.cfm

Application of the Geometrical Constraints. The geometrical constraints of the single point, continuous contact assumption can be used to express the normal forces at the contact zone by solving equation (19) and (20).
Denote:

$$A = M_w \ddot{Z}_w - F_{sz} \tag{23}$$

$$B = I_{xx}\ddot{\Phi}_w + (I_{zz} - I_{yy})\dot{\psi}_w{}^2\Phi_w + I_{yy}\Omega\dot{\psi}_w - M_{sx} \tag{24}$$

$$F_{3,1} = \frac{L_2 A + B + \bar{r}(F_{SY} - m_w \ddot{Y}_w)}{(L_1 + L_2)(\cos\alpha_1 - \mu f_{2,1}\sin\alpha_1)} \tag{25}$$

$$F_{3,2} = \frac{L_1 A - B - \bar{r}(F_{SY} - m_w Y_w)}{(L_1 + L_2)(\cos\alpha_2 - \mu f_{2,2}\sin\alpha_2)} \tag{26}$$

where $\bar{r} = (r_{v,1} + r_{v,2})/2$

Coupling to Truck Frame. Loads from the truck frame are transmitted to the wheelset through the primary suspension (Fig. 4). To obtain reasonable results for computed normal forces, the truck frame lateral displacement must be included in the simulation model. In this study, the truck yaw and roll angles and vertical displacement are treated as fixed, but these variables are included in the equations following for generality and ease of extension to future complete truck models.

For a passenger car, the primary suspension is linear so that for truck displacements (subscript t):

$$\begin{aligned} F_{SY} &= K_y(Y_t - Y_w) + B_y(\dot{Y}_t - \dot{Y}_w) \\ F_{SZ} &= K_z(Z_t - Z_w) + B_z(\dot{Z}_t - \dot{Z}_w) \\ M_{sz} &= K_n(\psi_t - \psi_w) + B_\psi(\dot{\psi}_t - \dot{\psi}_w) \\ M_{sx} &= K_\phi(\Phi_t - \Phi_w) + B_\phi(\dot{\Phi}_t - \dot{\Phi}_w) \end{aligned} \tag{27}$$

For fixed truck roll, yaw, and vertical displacements, the suspension forces reduce to:

$$\begin{aligned} F_{SZ} &= -K_z Z_w - B_z \dot{Z}_w + F_{ZO} \\ M_{sz} &= -K_\psi \psi_w - B_\psi \dot{\psi}_w + M_{zzo} \\ M_{sx} &= -K_\phi \Phi_w - B_\phi \dot{\Phi}_w + M_{xxo} \end{aligned} \tag{28}$$

where F_{ZO}, M_{zzo}, and M_{xxo} are the steady axle load, steering moment, and roll moment, respectively.

Coupling between wheelset and truck dynamic motions is represented by the following equation for truck lateral displacement:

$$m_t \ddot{Y}_t = -F_{SY} + F_{YO} \tag{29}$$

where F_{YO} is an external force applied to the truck frame via the secondary suspension. For freight trucks the primary suspension is not linear. Equations (27) and (28) may be modified readily for this case.

Moments about the y-axis are produced by drag, traction, and braking forces. In this study these moments are set to zero, but for general safety assessments they should be considered, as pointed out by Gilchirst [5].

Numerical Simulation for Wheelclimb Derailment Processes

Program Description. The computer program that simulates the dynamic model is named WHSET. Figure 5 shows a flow chart for the computational model. WHSET and its associated subroutines compute the lateral, yaw, and axle rotation motions of a wheelset and the lateral displacement of a truck traveling at a constant forward speed on a track with or without irregularities. These motion are

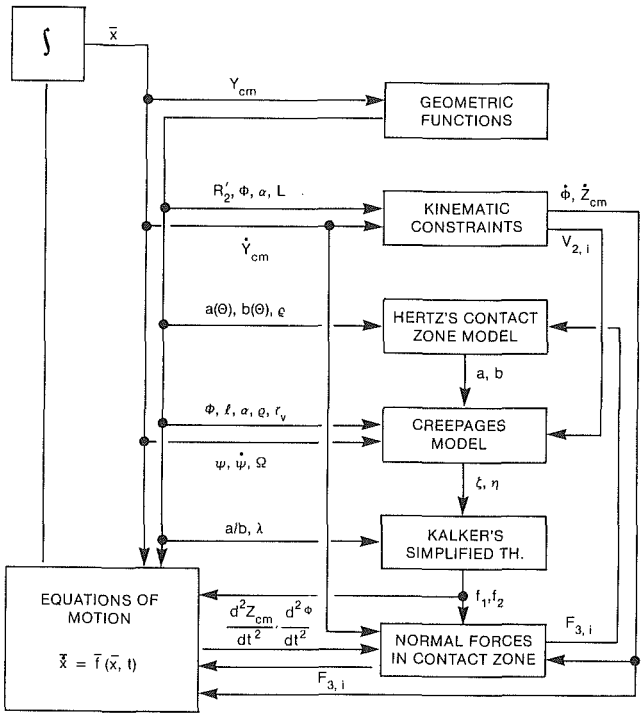


Fig. 5 Block diagram of wheelset dynamic model

computed as functions of initial conditions and external excitations. The main program calls a number of subroutines that evaluate the first derivatives of a set of simultaneous nonlinear state equations, and then integrates them numerically. The program is written in FORTRAN (IBM extension to FORTRAN ANS), and is compatible with the IBM G and H compilers.

The numerical integration is performed using DERK, a program based on the sixth-order Runge Kutta method, which is included in the IBM library of scientific programs [16]. DERK finds approximations to the solution of a system of first-order ordinary differential equations of the form $\mathbf{x}' = f(\mathbf{x}, t)$ with initial conditions.

The derivatives of the state variables depend on the contact geometry parameters (which are functions of the wheelset lateral displacement), the creep forces (which are functions of the wheelset velocities, the contact geometry and the normal forces), the wheel/rail contact normal forces, and the externally applied loads. To reduce computation time, the contact geometry functions and creep force/creepage relationships are precomputed and stored as data files for use by WHSET. These data files are generated by computer programs previously developed under U.S. DOT sponsorship, known as WHRAILA and FORCES, and are widely available to researchers in the rail vehicle dynamics area.

Contact Geometry Functions. The program WHRAILA, developed by R. Heller and N. Cooperrider [17], solves for the following contact geometry parameters as functions of the wheelset lateral position: the wheel/rail contact angles α, the wheelset roll angle ϕ_w, the wheelset c.m. vertical displacement Z_w, the rolling radii of each wheel r_v, the distance between the wheelset c.m. and the contact points of the wheels L, and the lateral radii of curvature of the rails R_2'. WHRAILA has been supplemented by additional routines which calculate the values of the elliptic integrals $a(\theta)$ and $b(\theta)$, the nondimensional spin parameter, χ, the geometric parameter ρ, the contact ellipse axes ratio a/b, and the partial derivatives defined in equations (4) and (5). WHRAILA accepts as inputs specific wheel and rail profiles, gauge, flange clearance, cant angles, and rail heights. The numerical results presented here

Downloaded 02 May 2010 to 171.66.16.25. Redistribution subject to ASME license or copyright; see http://www.asme.org/terms/Terms_Use.cfm

Table 1 Simulated Parameters

Symbol	Value	Symbol	Value
m_w	1464 kg	K_z	2×10^6 n/m
m_t	2928 kg	K_ϕ	7.4×10^3 n-m/rad
I_{xx}, I_{zz}	680 kg-m^2	K_y	1.17×10^7 n/m
I_{yy}	136 kg-m^2	B_z	4×10^4 n-s/m
μ	0.3	B_y	5.84×10^4 n-s/m
ϵ	0.3	B_ϕ	1.5×10^2 n-m-s/rad
E	2×10^{11} n/m^2	K_ψ	5.43×10^4 n-m/rad
F_{Z0}	1.36×10^5 n	B_ψ	2.17×10^2 n-m-s/rad
ψ_t	0	M_{xxo}, M_{zzo}	0
V	50 m/s		

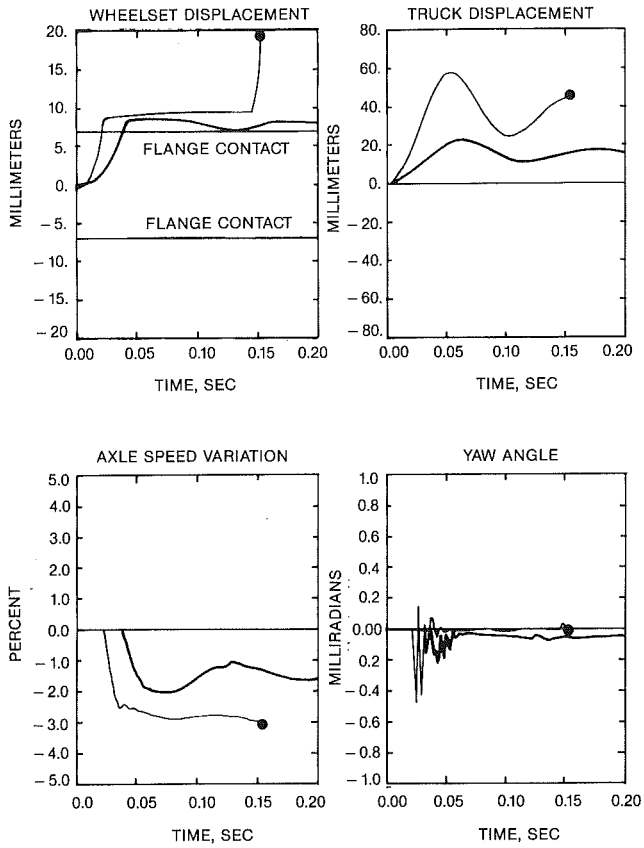


Fig. 6 Simulated response to step input lateral force applied to truck frame. Nonderailment case-bold line; derailment case-light line with circles at derailment point.

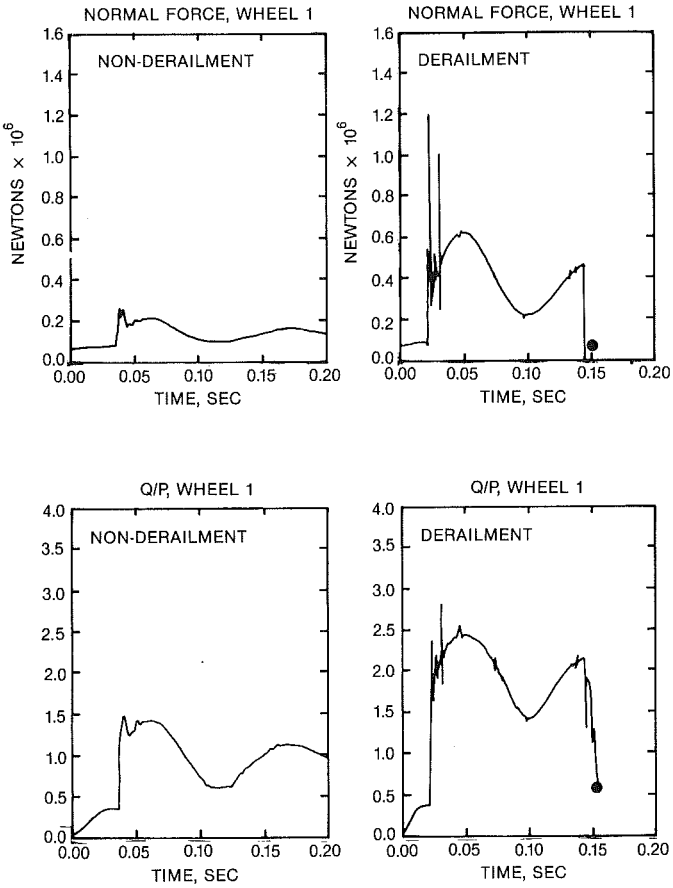


Fig. 7 Simulated normal force and derailment quotient on climbing wheel

are for new AAR profile wheels running on rails similar to 132 lb CF and I unworn profile. The program assumes that single point contact is sustained on both wheels and that yaw angle effects may be neglected. Since these functions depend on lateral displacement alone, they do not have to be computed at each time step using WHRAILA. Instead, the values precomputed at intervals of 0.51 mm are used as inuts to an interpolation routine. The program WHSET uses the IBM library program IVP, based on the Aiken's Lagrange method of interpolation [16].

Creep Force Calculation. The second data file represents the relationships between nondimensional creep forces (f_1 and f_2) and nondimensional creepages. The program FORCES [18] is used to precompute nondimensional creep forces using the Kalker Simplified Theory. It takes as input the contact ellipse dimensions, nondimensional spin and creep parameters, and Poisson's ratio. For every contact ellipse ratio a/b and nondimensional spin parameter χ, a different table is generated for the creep coefficients as functions of the nondimensional creep parameters in polar form.

The contact ellipse ratio and the nondimensional spin parameter are determined by the contact geometry alone, the latter depending on the lateral displacement of the wheelset. Consequently, these two variables can be precomputed for the full range of the lateral motion. A survey of numerical results over the displacement range has been conducted, and 21 pairs have been distinguished so that the contact ellipse ratio and the nondimensional spin parameter at any given displacement are within 10 percent tolerance of at least one of these 21 pairs. The program FORCES was run repeatedly for these pairs resulting in 21 table sets stored as data files.

At each lateral displacement, WHSET calls a subroutine to determine which of the 21 data files is to be used. It then interpolates the data in tables of this file, returning the lateral and the longitudinal creep forces as functions of the creepages.

Downloaded 02 May 2010 to 171.66.16.25. Redistribution subject to ASME license or copyright; see http://www.asme.org/terms/Terms_Use.cfm

Program Outputs. The following output variables are generated by the simulation program:

1. Wheelset lateral displacement;
2. Truck lateral displacement;
3. Wheelset axle rolling velocity;
4. Wheelset yaw angle;
5. Normal force at each contact point;
6. Derailment quotient for each wheel.

The derailment quotient, the ratio of lateral-to-vertical wheel/rail forces, is the most frequently used measure of proneness to derailment [5-10, 19]. In the literature it is designated by either (L/V) or (Q/P). Following the latter convention:

$$\left(\frac{Q}{P}\right)_i = \frac{\mu f_{2,i}\cos\alpha_i + \sin\alpha_i}{\mu f_{2,i}\sin\alpha_i - \cos\alpha_i} \tag{30}$$

Simulation Results

Definition of Simulation Conditions. The parametric values for the simulation are selected for a typical high-speed passenger car described in [20], and are a summarized in Table 1. All other values for parameters in the equations of motion are provided by programs WHRAILA and FORCES, with extensions as described previously.

Some comments are needed regarding inclusion of the truck lateral degree of freedom. In many previous, studies, and in the initial phases of this investigation, the dynamics of the wheelset alone were simulated. The dynamic excursions in normal force during derailment simulations that result from "wheelset-only" models are unrealistically large, due to high wheelset accelerations. Adding the truck mass to the model yields much more natural behavior. Although the dynamics of a complete truck with secondary suspension, two axles, etc., are not modeled here, the present simulations do exhibit the important characteristics of wheelsets during derailment.

The simulation program accepts as inputs any combination of forces and moments applied to the truck frame and wheelset, plus track irregularities. For clarity in presentation, in the simulation results that follow the only input is lateral force applied to the truck frame.

Simulation Results. Representative simulation results are shown in Figs. 6 and 7. Starting with the wheelset and truck frame in the track center position, the lateral force applied to the truck frame produces a damped sinusoidal truck lateral displacement. The wheelset lateral displacement lags, sharply decelerating after the initial flange contact.

In the derailment case, the wheelset first climbs the rail, falls slightly, then climbs again to complete derailment as the truck frame displacement reaches its second peak. Depending on initial conditions, the wheelset may derail on initial impact or later, emphasizing the importance of the dynamic coupling between wheelset and truck frame. Even though the derailment quotient exceeded the quasisteady limit (2.0 for $\psi_w = 0$) for about 0.05 sec (the JNR limit), the wheelset does not derail at this point.

After flange contact occurs, the axle speed drops, as expected from quasisteady theory. There is no fundamental difference between the derailment and nonderailment cases.

The drop in axle speed results in longitudinal creep force imbalance and a yaw moment that steers the wheelset in the negative direction. Due to the rather stiff primary suspension, the magnitude of the resulting steering angle is quite small (less than 0.5 milliradians, or 0.03 deg). These small yaw angles considerably reduce the coupling between the longitudinal and lateral dynamics of the wheelset.

Figure 7 shows the normal force and derailment quotient for the climbing wheel. In the nonderailment case, the normal force starts at a level close to one-half the axle load. During flange contact, the normal force is much larger due to the increasing contact angle. The rapid deceleration of the wheelset results in a sharp peak in the normal force. Terms due to wheelset lateral, vertical, and roll accelerations all contribute to the increased normal force on the climbing wheel while decreasing it on the opposite wheel. The initial peak in normal force is also seen in the Q/P response.

In the derailment case, the peaks in normal force and derailment quotient are much larger. These peaks may be unrealistically large, due to the assumption of rigid rails. They are not critical to the simulation, however, due to their extremely short duration. Peaks shown after initial flange contact are due to large values of partial derivative terms in equations (10) and (11).

Just prior to derailment, the normal force goes to zero for a short time. Physically, the wheel is beginning to lose contact while the contact angles decreases. The large excursions in normal force and loss of contact prior to derailment have been confirmed experimentally in tests at JNR [10].

Discussion of Modeling Effects. The computer program was altered to study the effect of model complexity on the simulation results. The first simplification was to set the axle speed to V/r_o. Exclusion of this degree of freedom was found to have almost no effect on the simulation of the other dynamic variables as a result of the stiff suspension and the negligible steering effects. As a consequence, the value of the truck yaw angle ψ_t is very important to derailment safety, since the derailment limit falls from 2.0 to 0.8 as ψ_w increases from 0 to 50 milliradians. This result, predicted from quasisteady derailment theory, is verified by the dynamic simulation model. Passenger trucks with softer yaw suspensions and freight trucks may exhibit different behavior.

The acceleration terms in equations (11)–(26) are significant in terms of their effects on wheelset motion, derailment quotient, and derailment proneness. In contrast, gyroscopic terms are not significant and may be omitted.

Discussion and Concluding Remarks

The simulation model presented in this paper represents a successful extension of contemporary understanding on wheel/rail contact phenomena and wheelset dynamics to the wheelclimb derailment regime. Through the use of this detailed model, it has been determined that the following elements are necessary for simulation of wheelclimb derailment of a typical high-speed passenger car with a stiff yaw suspension:

1. Wheelset and truck lateral displacement degrees of freedom;
2. Wheel/rail contact geometry parameters determined as functions of wheel and rail profiles;
3. Creep forces determined by Kalker Simplified Theory;
4. Wheel/rail normal forces computed from kinematic constraints resulting from continuous two-wheel, single-point contact, including acceleration effects;
5. Creepages determined by wheelset kinematics;
6. Truck yaw angle.

For freight trucks or passenger trucks with soft primary suspensions, wheelset angle and axle rotational speed should be included as additional degrees of freedom. Gyroscoptic terms are not critical to wheelclimb simulation.

The reduction in necessary degrees of freedom associated with stiff yaw suspension trucks results in significant reductions in computation time, which will be particularly important in multiple axle, complete vehicle simulations.

Large excursions in normal force result from:

Downloaded 02 May 2010 to 171.66.16.25. Redistribution subject to ASME license or copyright; see http://www.asme.org/terms/Terms_Use.cfm

1. Significant impact force due to rapid wheelset deceleration after initial flange contact;

2. Short duration force peaks due to changes in curvature of wheel and rail profiles leading to discontinuous contact geometry funcitons.

Acknowledgments

This research was supported by the U.S. Department of Transportation under contract DOT-TSC-1603. Computer programs FORCES and WHRAILA cited in the paper were provided by E. H. Law and R. Heller of Clemson University. H. C. Curtiss, Jr. of Princeton University assisted with the final formulation of the dynamic analysis. Final computer program development and simulations were performed while Dr. Sweet was a Guggenheim Fellow at the JNR Railway Technical Research Institute, Tokyo, Japan. Technical suggestions from numerous JNR staff are appreciated.

References

1 Burton, T. D., "Influence of Wheel/Rail Contact Geometry on Large Amplitude Wheelset Equations of Motion," ASME *Journal of Dynamic Systems, Measurement, and Control*, Vol. 103, 1981, pp. 211-218.

2 Moelle, D., Steinborn, H., and Gasch, R., "Computation of Limit Cycle of a Wheelset Using a Galerkin Method," in *The Dynamic of Vehicles on Roads and on Railway Tracks*, Willumeit, H. P., ed., Swets and Zeitlinger B. V., Lisse, 1980, pp. 323-336.

3 Burton, T. D., and Whitman, A. M., "Nonlinear Kinematics of Wheel-Rail Contact," ASME JOURNAL OF APPLIED MECHANICS, Vol. 45, 1978, pp. 664-668.

4 Hauschild, W., "The Application of Quasilinearization to the Limit Cycle Behavior of the Nonlinear Wheel-Rail System," in *The Dynamics of Vehicles on Roads and on Railway Tracks*, Willumeit, H. P., ed., Swets and Zeitlinger, B. V., Lisse, 1980, pp. 146-165.

5 Gilchrist, A. O., and Brickle, B. V., "A Re-Examination of the Proneness to Derailment of a Railway Wheel-Set," *J. Mech. Eng. Sci.*, Vol. 18, No. 3, 1976, pp. 131-141.

6 Sweet, L. M., and Sivak, J. A., "Nonlinear Wheelset Forces in Flange Contact-Part 1: Steady State Analysis and Numerical Results," ASME *Journal of Dynamic Systems, Measurement, and Control*, Vol. 101, 1979, pp. 238-246.

7 Arai, S., and Yokose, K., "Simulation of Lateral Motion of 2-Axle Railway Vehicle in Running," in *The Dynamics of Vehicles on Roads and Railway Tracks*, Pacejka, H., ed., Swets and Zeitlinger, B. V. Amsterdam, 1976, pp. 345-368.

8 Sweet, L. M., Karmel, A., and Moy, P., "Wheelclimb Derailment Criteria Under Steady Rolling and Dynamic Loading Conditions," in *Dynamics of Vehicles on Roads and Railway Tracks*, Willumeit, H. P., ed., Swets and Zeitlinger, B. V. Lisse, 1980, pp. 496-510.

9 Yokose, K., "A Theory of the Derailment of Wheelset," *JNR Quart. Rep.*, Vol. 7, No. 3, 1966, pp. 30-34.

10 Matsudaira, T., and Yokose, K., "On the Derailment Induced by Lateral Impact of Wheelset," In *Research on Tokaido Shinkansen JNR Rail. Tech. Res. Inst. Report*, 1962 (in Japanese), Vol. 3, pp. 235-244.

11 Clark, R. A., et al., "Prediction of the Dynamic Response Vehicles to Lateral Track Irregularities," in *The Dynamics of Vehicles on Roads and on Railway Tracks*, Wickens, A., ed., Swets and Zeitlinger, B. V. Lisse, 1980, pp. 535-548.

12 Duffek, W., and Jaschinski, A., "Efficient Implementation of Wheel Rail Contact Mechanics in Dynamic Curving," in *The Dynamics of Vehicles on Roads and on Railway Tracks*, Wickens, A., ed., Swets and Zeitlinger, B. V. Lisse, 1982, pp. 441-454.

13 Elkins, J. A., and Gostling, R. J., "A General Quasisteady Curving Theory for Railway Vehicles," in *The Dynamic of Vehicles on Roads and on Tracks*, Slibar, A., and Springer, H. eds., Swets and Zeitlinger, B. V., 1978, pp. 388-406.

14 Kalker, J. J., "Simplified Theory of Rolling Contact," *Delft Prog., Rep. Series C: Mechanical and Aeronautical Engineering and Shipbuilding* 1, 1973, pp. 1-10.

15 Karmel, A., "Analytical and Experimental Studies of Derailment Processes of Railway Vehicles," Ph.D Thesis, Princeton University, MAE Department, Princeton, N.J., Sept. 1981.

16 IBM SL-Math Scientific Subroutine Package.

17 Heller, R., and Cooperrider, N. K., "User's Manual for Asymmetric Wheel/Rail Contact Characterization Program," DOT Report FRA/ORD-78/05, Dec. 1977.

18 Goree, J. G., and Law, E. H., "User's Manual for Kalker's Simplified Theory," DOT Report FRA/ORD-78/06, Dec. 1977.

19 Sweet, L. M., and Karmel, A., "Evaluation of Time-Duration Dependent Wheel Load Criteria for Wheelclimb Derailment," ASME *Journal of Dynamic Systems, Measurement, and Control*, Vol. 103, 1981, pp. 219-227.

20 Hedrick, J. K., et al, "Performance Limits of Rail Passenger Vehicles: Conventional, Radial and Innovative Trucks," Final Report, U.S. DOT Contract DOT-OS-70052, Sept. 1980.

Downloaded 02 May 2010 to 171.66.16.25. Redistribution subject to ASME license or copyright; see http://www.asme.org/terms/Terms_Use.cfm

Journal of Applied Mechanics

Brief Notes

A Brief Note is a short paper that presents a specific solution of technical interest in mechanics but which does not necessarily contain new general methods or results. A Brief Note should not exceed 1500 words *or equivalent* (a typical one-column figure or table is equivalent to 250 words; a one line equation to 30 words). Brief Notes will be subject to the usual review procedures prior to publication. After approval such Notes will be published as soon as possible. The Notes should be submitted to the Technical Editor of the JOURNAL OF APPLIED MECHANICS. Discussions on the Brief Notes should be addressed to the Editorial Department, ASME, United Engineering Center, 345 East 47th Street, New York, N. Y. 10017, or to the Technical Editor of the JOURNAL OF APPLIED MECHANICS. Discussions on Brief Notes appearing in this issue will be accepted until two months after publication. Readers who need more time to prepare a Discussion should request an extension of the deadline from the Editorial Department.

Determination of Near-Surface Plastic Deformation in Sliding Contacts[1]

F. E. Kennedy, Jr.[2] and L. P. Grotelueschen[3]

1 Introduction

Whenever two solid bodies slide against each other without lubrication, substantial plastic deformation occurs on and near the contact surfaces. This deformation plays an important role in the tribological behavior of the sliding contact [1, 2]. The purpose of this work was the development of an analytical model to predict the near-surface plastic deformation resulting from a single pass of one metallic surface over another. Recent metal forming studies [3, 4] have shown that viscoplastic techniques are most suitable for studying high strain-rate plastic flow of this sort.

2 Analytical Procedure

Since elastic strains are negligible in comparison with the large plastic strains [2], the strain-rate stress relations for a von Mises-type yield function take the form [4]:

$$\dot{\epsilon}_{ij} \approx \dot{\epsilon}_{ij}^{(p)} = \frac{\sqrt{3}}{\sqrt{J_2}} S_{ij}\ \phi(\sqrt{3J_2} - Y) \tag{1}$$

where S_{ij} is a deviatoric stress component, J_2 is the second invariant of the stress deviator, Y is the yield strength, and ϕ is a plastic constitutive function valid for $\sqrt{3J_2} \geq Y$. It has been found that the viscoplastic behavior of tellerium-doped free machining copper [5] and many other metals can be modeled by:

$$\sqrt{3J_2} = C\dot{\bar{\epsilon}}^m \tag{2}$$

where m is a strain rate sensitivity exponent, C is a material parameter that gives a measure of strain hardening, and $\dot{\bar{\epsilon}}$ is the equivalent plastic strain rate. For this study strain-hardening effects were not included, so $C \approx Y$.

Using (2) in (1) the strain-rate stress relations for the material become

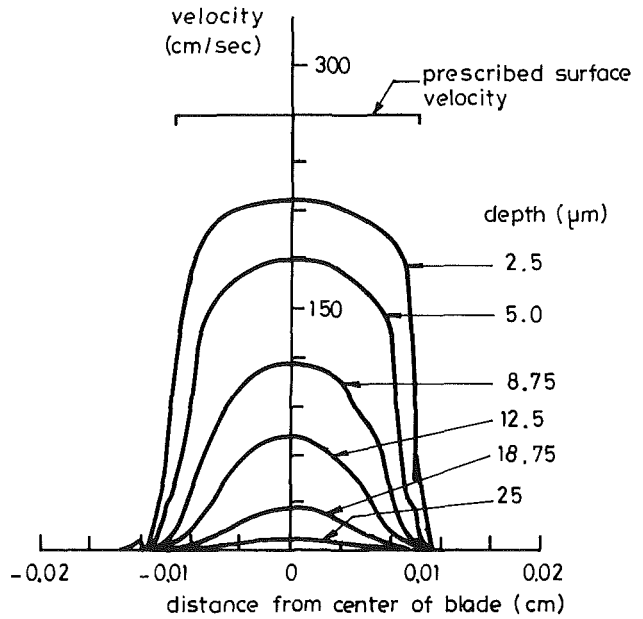


Fig. 1 Velocity distribution in copper specimen subjected to a 270 cm/s velocity on a 200 μm contact width. Only the velocity component in the rub direction is shown.

$$\dot{\epsilon}_{ij} = \frac{1}{2\sqrt{J_2}} \left(\frac{\sqrt{3J_2}}{Y} \right)^{1/m} S_{ij} \tag{3}$$

A finite element viscoplasticity program was written relating nodel velocities to forces in two-dimensional domain, using (3) in the development. Because of the similarity of (3) to the equations for linear elasticity [4], a modified form of the finite element techniques used to solve elasticity problems was used in this case. A penalty function approach [3], with Poisson's ratio $\nu = 0.4999$ was employed to permit analysis of incompressible viscoplastic flow. Reduced integration (2 × 2 Gauss) was used, with nine-node isoparametric Lagrangian quadrilaterals, to provide the necessary relaxation of constraints. As interactive solution technique was necessary, owing to the nonlinear form of equations (3).

The program was applied to the study of plastic deformation during a single pass of a hardened tool steel slider over a tellerium copper rub specimen. Experimental measurements of residual plastic deformation in such a system had been obtained in our laboratory using a pendulum-type rub apparatus [2, 6]. Since the exact boundary conditions within the contact region of such a sliding contact are not known, it was

[1] Presented at the Ninth U.S. National Congress of Applied Mechanics, Ithaca, N.Y., June 1982.

[2] Associate Professor, Thayer School of Engineering, Dartmouth College, Hanover, N.H. 03755. Mem. ASME.

[3] Engineer, Union Carbide Corp., Indianapolis, Ind. 46224.

Manuscript received by ASME Applied Mechanics Division, November, 1982; final revision, December, 1983.

Copyright © 1984 by ASME
Downloaded 02 May 2010 to 171.66.16.25. Redistribution subject to ASME license or copyright; see http://www.asme.org/terms/Terms_Use.cfm

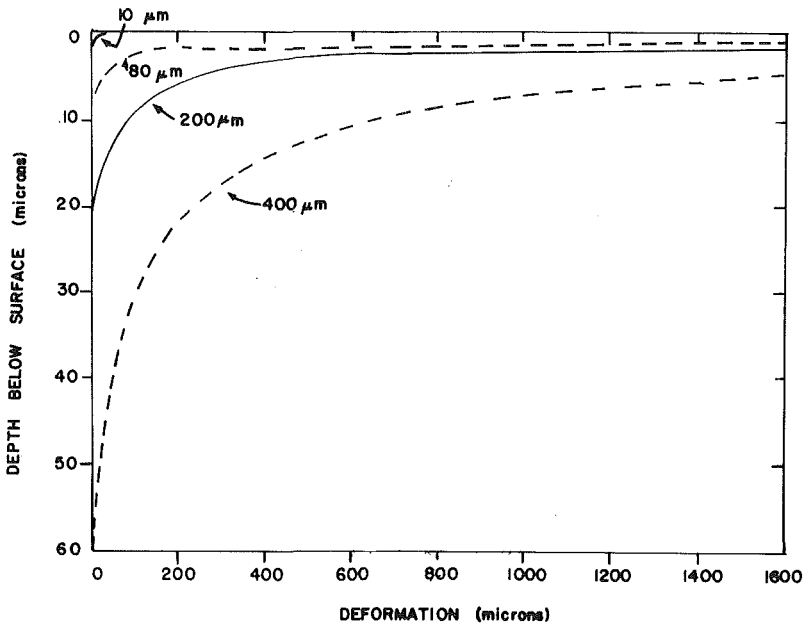


Fig. 2 Total predicted plastic deformation in rub direction as function of depth below rub surface for four different assumed contact widths. Entire contact width assumed to be moving at 270 cm/s.

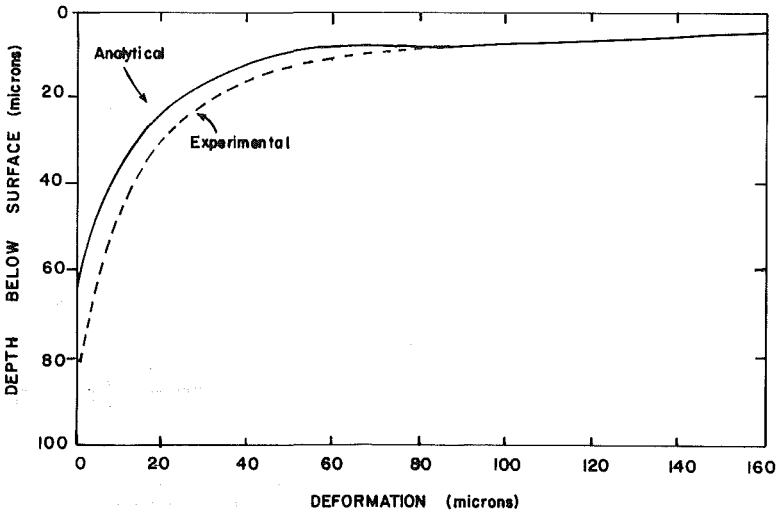


Fig. 3 Comparison between predicted and experimental plastic deformation component in rub direction for 400 μm nominal contact width. Experimental velocity 270 cm/s. Assumed average surface velocity for analytical prediction 27 cm/s.

assumed that the contacting portion of the copper surface was moving in the sliding direction at the same velocity as the moving slider (2.7 m/s) but had no motion in the normal direction. This assumption implies that the tool steel slider was perfectly rigid and that perfect adhesion occurred between slider and copper over the entire nominal contact width. As will be discussed, that assumption was later modified based on experimental measurements.

A finite element mesh was constructed which had eight thin (5μm thick) quadrilateral elements across the contact width. The mesh was expanded or contracted to enable the study of four different contact widths ranging from 10 μm to 400μm.

3 Analytical Results and Discussion

It was found that essentially the only material set in motion by the slider was directly under the contact zone. Horizontal velocity components were generally at least an order of magnitude greater than the vertical components, indicating that flow lines are approximately parallel to the sliding surface. The only notable material flow in the direction perpendicular to sliding occurred on the contact surface, just ahead of the slider, where a "bulge" appeared to form.

A typical distribution of horizontal velocities is shown in Fig. 1. The flow velocity is nearly symmetrical about the contact centerline and diminishes rapidly from 2.7 m/s at the 200μm wide contact zone to about 10 percent of that value at a depth of 18.75 μm. Results for other contact widths showed that the plastic zone decreased in size and the velocity gradient within the zone increased as the contact width decreased.

To convert velocities into deformations, the flow lines were assumed to be horizontal and it was assumed that the instant at which the analysis was performed was typical of all instants during the traversal of the slider. This enabled the velocities to be integrated along the flow lines to obtain the total displacement at a point for a single pass of slider over the specimen surface. The resulting deformations are shown in Fig. 2 for four different contact widths.

Downloaded 02 May 2010 to 171.66.16.25. Redistribution subject to ASME license or copyright; see http://www.asme.org/terms/Terms_Use.cfm

Two conclusions can be drawn from Fig. 2. First both magnitude and depth of the plastic deformation are significantly influenced by contact width. A very narrow contact zone, which would result from a low applied normal force [1] or possibly from a very sharp slider, would have a smaller amount of plastic deformation, both in volume and magnitude, than a wider contact. The second conclusion is that, in comparison with the experimentally determined deformation values, the predicted deformation is too large. A comparison of the curve in Fig. 2 for a 400μm contact width with the experimental data for a single pass [2] showed that the predicted deformations are an order of magnitude too high, but the depth of the plastic zone is approximately correct.

To resolve the discrepancy between analysis and experiment the assumed boundary conditions were reevaluated. It can be seen from Fig. 2 that a diminution of the contact zone would indeed produce smaller, more correct, deformations, but a smaller plastic zone would also result. The surface velocity, on the other hand, primarily affects the flow velocities and resulting deformations, since the strain rate sensitivity is too small to affect the contact zone depth significantly. A new analysis was performed, this time with an assumed average surface velocity of 27 cm/s, 10 percent of the value used in Fig. 2. Results for a 400μm contact width are shown in Fig. 3, along with single pass experimental results for a similar contact width. Agreement between analysis and experiment is reasonably good. If rate-independent strain hardening had been taken into account, it is expected that the plastic zone would have been driven slightly deeper, resulting in even better agreement between analysis and experiment.

The analysis has therefore shown, that if the entire contact patch adheres to, and travels at the same velocity as the moving slider, the predicted deformations are higher than those measured experimentally, whereas if the contact surface travels at an average velocity substantially less than that of the slider the predicted deformations are of the right order of magnitude.

Acknowledgment

This work was supported by NASA Grant NSG 3253 to Dartmouth College. Mr. A. F. Kaszak of NASA Lewis Research Center was the project's technical monitor.

References

1 Kragelskii, I. V., *Friction and Wear*, Butterworth's, London, 1965.

2 Kennedy, F. E., "Single Pass Rub Phenomena-Analysis and Experiment," ASME *Journal of Lubrication Technology*, Vol. 104, 1982, pp. 582–588.

3 Zienkiewicz, O. C., and Godpole, P. N., "A Penalty Function Approach to Problems of Plastic Flow of Metals With Large Surface Deformation," *J. Strain Analysis*, Vol. 10, 1975, pp. 180–185.

4 Zienkiewicz, O. C., Jain, P. C., and Onate, E., "Flow of Solids During Forming and Extrusion: Some Aspects of Numerical Solutions," *Int. J. Solids & Structures*, Vol. 14, 1978, pp. 15–38.

5 Senseny, P. E., Richman, M. H., and Duffy, J., "The Influence of Annealing Temperature on the Strain Rate Sensitivity of Copper in Torsion," JOURNAL OF APPLIED MECHANICS, Vol. 42, 1975, pp. 245–246.

6 Grotelueschen, L. P., "Investigation of Single Pass Rub Phenomena Towards Improved Gas Path Seal Materials," Master of Engineering Thesis, Thayer School of Engineering, Dartmouth College, Hanover, N.H., June 1982.

On the Buckling of Ring-Stiffened Circular Plates

J. N. Rossettos[1] and W. H. Miller[2]

Introduction

The buckling of unstiffened circular plates under the action of axisymmetric in-plane loading has been studied and discussed in [1–4]. Stiffened circular plates have received some, although limited, attention. The analysis in [5] treats the stability of circular plates that are stiffened in the circumferential and radial directions by many stiffeners, and an averaging technique is used to obtain appropriate constitutive relations. Other work [6, 7] has been concerned with the stability of circular plates that are reinforced at their edge by ring stiffeners.

In the present work a single discrete ring stiffener is symmetrically attached to the plate and the problem of symmetric buckling is treated. It is shown in what way certain parameters that specify the relative stiffness and radius of the ring influence the critical load. The stiffener radius that maximizes the buckling load is determined and depends, of course, on whether the plate is clamped or simply supported. For small stiffener sizes, buckling will occur in the first symmetric mode. However, for sufficiently large stiffeners relative to the plate, the buckling mode will become asymmetric, and this is discussed.

Analysis

Under consideration is a circular plate of radius, a and thickness, t, which is acted on by a uniform in-plane radial compressive edge stress resultant, N_r. For the plate in a slighlty buckled state, the differential equation governing the rotation, ϕ, of the normal to the plate midsurface (see Fig. 1; plate center at $r = 0$) is given [3] by

$$u^2 d^2\phi/du^2 + u d\phi/du + (u^2+1)\phi = 0 \tag{1}$$

where

$$u = \lambda r \quad \lambda^2 = N_r/D$$

The quantity, D, is the flexural rigidity of the plate. The ring stiffener is attached symmetrically to the plate at a radius $r = r_1$ as shown in Fig. 1. It is assumed that the ring cross section rotates with the plate at $r = r_1$ as a rigid body by an angle $\phi(r_1)$. This presumes a ring depth that is sufficiently small compared to the plate radius, and the other dimensions are such that there is negligible distortion of the ring cross section.

The solutions to (1) which are valid in the region of the plate inside the ring and outside the ring are, respectively,

$$\phi = \phi_1 = C_1 J_1(u) \quad (0 \le u \le \lambda r_1) \tag{2}$$

$$\phi = \phi_2 = C_2 J_1(u) + C_3 Y_1(u) \quad (\lambda r_1 \le u \le \lambda a) \tag{3}$$

where J_1 and Y_1 are Bessel functions. Appropriate continuity and boundary conditions are given as follows. The continuity conditions at the stiffener location $r = r_1$ are

$$\phi_1(r_1) = \phi_2(r_1) \tag{4}$$

$$M_2 - M_1 = K_r \phi(r_1) \quad \text{where} \quad K_r = EI/r_1^2 \tag{5}$$

The factor K_r is obtained [8] from the strain energy per unit length of ring due to the rotation $\phi(r_1)$, and I is the moment

[1] Professor, Department of Mechanical Engineering, Northeastern University, Boston, Mass. 02115. Mem. ASME.

[2] Graduate Student, Department of Mechanical Engineering, Northeastern University, Boston, Mass. 02115. Assoc. Mem. ASME. Currently at Bell Laboratories, Homdel, N.J.

Manuscript received by ASME Applied Mechanics Division, March 1983; final revision, January, 1984.

Downloaded 02 May 2010 to 171.66.16.25. Redistribution subject to ASME license or copyright; see http://www.asme.org/terms/Terms_Use.cfm

Two conclusions can be drawn from Fig. 2. First both magnitude and depth of the plastic deformation are significantly influenced by contact width. A very narrow contact zone, which would result from a low applied normal force [1] or possibly from a very sharp slider, would have a smaller amount of plastic deformation, both in volume and magnitude, than a wider contact. The second conclusion is that, in comparison with the experimentally determined deformation values, the predicted deformation is too large. A comparison of the curve in Fig. 2 for a 400μm contact width with the experimental data for a single pass [2] showed that the predicted deformations are an order of magnitude too high, but the depth of the plastic zone is approximately correct.

To resolve the discrepancy between analysis and experiment the assumed boundary conditions were reevaluated. It can be seen from Fig. 2 that a diminution of the contact zone would indeed produce smaller, more correct, deformations, but a smaller plastic zone would also result. The surface velocity, on the other hand, primarily affects the flow velocities and resulting deformations, since the strain rate sensitivity is too small to affect the contact zone depth significantly. A new analysis was performed, this time with an assumed average surface velocity of 27 cm/s, 10 percent of the value used in Fig. 2. Results for a 400μm contact width are shown in Fig. 3, along with single pass experimental results for a similar contact width. Agreement between analysis and experiment is reasonably good. If rate-independent strain hardening had been taken into account, it is expected that the plastic zone would have been driven slightly deeper, resulting in even better agreement between analysis and experiment.

The analysis has therefore shown, that if the entire contact patch adheres to, and travels at the same velocity as the moving slider, the predicted deformations are higher than those measured experimentally, whereas if the contact surface travels at an average velocity substantially less than that of the slider the predicted deformations are of the right order of magnitude.

Acknowledgment

This work was supported by NASA Grant NSG 3253 to Dartmouth College. Mr. A. F. Kaszak of NASA Lewis Research Center was the project's technical monitor.

References

1 Kragelskii, I. V., *Friction and Wear*, Butterworth's, London, 1965.

2 Kennedy, F. E., "Single Pass Rub Phenomena-Analysis and Experiment," ASME *Journal of Lubrication Technology*, Vol. 104, 1982, pp. 582–588.

3 Zienkiewicz, O. C., and Godpole, P. N., "A Penalty Function Approach to Problems of Plastic Flow of Metals With Large Surface Deformation," *J. Strain Analysis*, Vol. 10, 1975, pp. 180–185.

4 Zienkiewicz, O. C., Jain, P. C., and Onate, E., "Flow of Solids During Forming and Extrusion: Some Aspects of Numerical Solutions," *Int. J. Solids & Structures*, Vol. 14, 1978, pp. 15–38.

5 Senseny, P. E., Richman, M. H., and Duffy, J., "The Influence of Annealing Temperature on the Strain Rate Sensitivity of Copper in Torsion," JOURNAL OF APPLIED MECHANICS, Vol. 42, 1975, pp. 245–246.

6 Grotelueschen, L. P., "Investigation of Single Pass Rub Phenomena Towards Improved Gas Path Seal Materials," Master of Engineering Thesis, Thayer School of Engineering, Dartmouth College, Hanover, N.H., June 1982.

On the Buckling of Ring-Stiffened Circular Plates

J. N. Rossettos[1] and W. H. Miller[2]

Introduction

The buckling of unstiffened circular plates under the action of axisymmetric in-plane loading has been studied and discussed in [1–4]. Stiffened circular plates have received some, although limited, attention. The analysis in [5] treats the stability of circular plates that are stiffened in the circumferential and radial directions by many stiffeners, and an averaging technique is used to obtain appropriate constitutive relations. Other work [6, 7] has been concerned with the stability of circular plates that are reinforced at their edge by ring stiffeners.

In the present work a single discrete ring stiffener is symmetrically attached to the plate and the problem of symmetric buckling is treated. It is shown in what way certain parameters that specify the relative stiffness and radius of the ring influence the critical load. The stiffener radius that maximizes the buckling load is determined and depends, of course, on whether the plate is clamped or simply supported. For small stiffener sizes, buckling will occur in the first symmetric mode. However, for sufficiently large stiffeners relative to the plate, the buckling mode will become asymmetric, and this is discussed.

Analysis

Under consideration is a circular plate of radius, a and thickness, t, which is acted on by a uniform in-plane radial compressive edge stress resultant, N_r. For the plate in a slighlty buckled state, the differential equation governing the rotation, ϕ, of the normal to the plate midsurface (see Fig. 1; plate center at $r = 0$) is given [3] by

$$u^2 d^2\phi/du^2 + u d\phi/du + (u^2+1)\phi = 0 \tag{1}$$

where

$$u = \lambda r \quad \lambda^2 = N_r/D$$

The quantity, D, is the flexural rigidity of the plate. The ring stiffener is attached symmetrically to the plate at a radius $r = r_1$ as shown in Fig. 1. It is assumed that the ring cross section rotates with the plate at $r = r_1$ as a rigid body by an angle $\phi(r_1)$. This presumes a ring depth that is sufficiently small compared to the plate radius, and the other dimensions are such that there is negligible distortion of the ring cross section.

The solutions to (1) which are valid in the region of the plate inside the ring and outside the ring are, respectively,

$$\phi = \phi_1 = C_1 J_1(u) \quad (0 \le u \le \lambda r_1) \tag{2}$$

$$\phi = \phi_2 = C_2 J_1(u) + C_3 Y_1(u) \quad (\lambda r_1 \le u \le \lambda a) \tag{3}$$

where J_1 and Y_1 are Bessel functions. Appropriate continuity and boundary conditions are given as follows. The continuity conditions at the stiffener location $r = r_1$ are

$$\phi_1(r_1) = \phi_2(r_1) \tag{4}$$

$$M_2 - M_1 = K_r \phi(r_1) \quad \text{where} \quad K_r = EI/r_1^2 \tag{5}$$

The factor K_r is obtained [8] from the strain energy per unit length of ring due to the rotation $\phi(r_1)$, and I is the moment

[1] Professor, Department of Mechanical Engineering, Northeastern University, Boston, Mass. 02115. Mem. ASME.

[2] Graduate Student, Department of Mechanical Engineering, Northeastern University, Boston, Mass. 02115. Assoc. Mem. ASME. Currently at Bell Laboratories, Homdel, N.J.

Manuscript received by ASME Applied Mechanics Division, March 1983; final revision, January, 1984.

Copyright © 1984 by ASME
Downloaded 02 May 2010 to 171.66.16.25. Redistribution subject to ASME license or copyright; see http://www.asme.org/terms/Terms_Use.cfm

of inertia of ring cross section about the plate midsurface (Fig. 1). The relation between the moment, M, and ϕ in the plate is

$$M = D(d\phi/dr + \nu\phi/r) = D\lambda(d\phi/du + \nu\phi/u) \quad (6)$$

On using (6), equation (5) is written in terms of ϕ. Appropriate expressions for the derivatives of Bessel functions are next used, and the final expression for (5) can be written as

$$C_1A_1 - C_2A_2 - C_3A_3 = 0 \quad (7)$$

where

$$A_1 = J_0(\lambda aB) = J_1(\lambda aB)/\lambda aB + \nu J_1(\lambda aB)/\lambda aB + (\alpha/B)J_1(\lambda aB)/\lambda aB$$

$$A_2 = J_0(\lambda aB) - J_1(\lambda aB)/\lambda aB + \nu J_1(\lambda aB)/\lambda aB$$

$$A_3 = Y_0(\lambda aB) = Y_1(\lambda aB)/\lambda aB + \nu Y_1(\lambda aB)/\lambda aB$$

$$\alpha = EI/aD, \quad B = r_1/a \quad (8)$$

The condition given by (4) can also be written as

$$C_1J_1(u_1) = C_2J_1(u_1) + C_3Y_1(u_1) \quad (9)$$

For a clamped edge, the slope must vanish, so that on using (3), get

$$C_2J_1(\lambda a) + C_3Y_1(\lambda a) = 0 \quad (10)$$

Equations (7), (9), and (10) comprise three homogeneous algebraic equations in which λ is an eigenvalue parameter, and the corresponding characteristic equation is

$$J_1(\lambda aB)[A_1Y_1(\lambda a) + A_3J_1(\lambda a) - A_2Y_1(\lambda a)] - Y_1(\lambda aB)J_1(\lambda a)A_1 = 0 \quad (11)$$

In addition to λ the two other parameters of interest are $\alpha = EI/aD$, a measure of the ring stiffness relative to that of the plate, and $B = r_1/a$, the nondimensional ring radius. If the ring and plate have the same Young's modulus then α can be expressed as $\alpha = 12(1 - \nu^2)I/at^3$. This means that for a given plate radius, the value of α can be governed by either the ring cross section as it affects I, or, if I is fixed, by the plate thickness, t.

For the simply supported plate, the moment at the edge must vanish, so that

$$M(\lambda a)/\lambda D = d\phi(\lambda a)/du + \nu\phi(\lambda a)/u = 0 \quad (12)$$

which, on using (3), leads to

$$C_2[J_0(\lambda a) - (1-\nu)J_1(\lambda a)/\lambda a] + C_3[Y_0(\lambda a) - (1-\nu)Y_1(\lambda a)/\lambda a] = 0 \quad (13)$$

In this case, (7), (9), and (13) lead to another appropriate characteristic equation which is not written here for purposes of brevity.

Results and Discussion

The characteristic equations are evaluated numerically [8], and critical values of the buckling parameter $\lambda^2a^2 = N_ra^2/D$ are determined. In Fig. 1, N_ra^2/D is plotted against r_1/a for the clamped plate for several values of α. The lower dashed line represents the first symmetric mode of the unstiffened plate for which $N_ra^2/D = 14.68$. The buckling parameter increases with α and it is also clearly indicated that the optimum value of ring radius, to maximize the buckling load, occurs in the vicinity of $r_1/a = 0.55$. Note that the buckling mode will be the first symmetric mode for a range of values of α (α increases as the ring size increases or as the plate thickness decreases). Beyond a certain value of α the buckling mode will become asymmetric. In [8] the first asymmetric mode buckling load for the unstiffened plate was determined and gave a value of $N_ra^2/D = 26.38$ (represented by the dash-dot curve in Fig. 1). Similar results for the simply supported plate in Fig. 2 give an optimum value of ring radius of $r_1/a =$ 0.71, and again it is clear that asymmetric buckling will occur for sufficiently large values of α. Analysis of asymmetric buckling of the ring-stiffened circular plate will very likely indicate that for certain values of α and r_1/a, a coalescence will occur between the symmetric and asymmetric buckling mode eigenvalues.

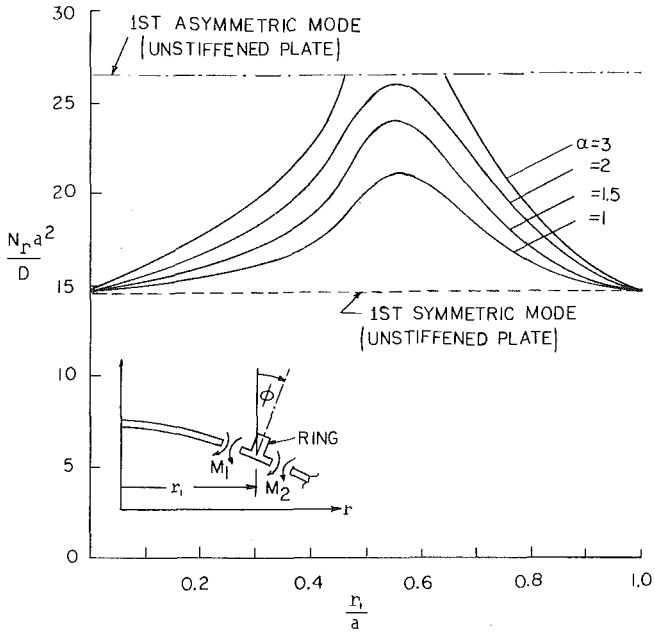


Fig. 1 Critical buckling load parameter, N_ra^2/D, versus nondimensional ring radius, r_1/a, for various values of ring stiffness parameter α; clamped plate

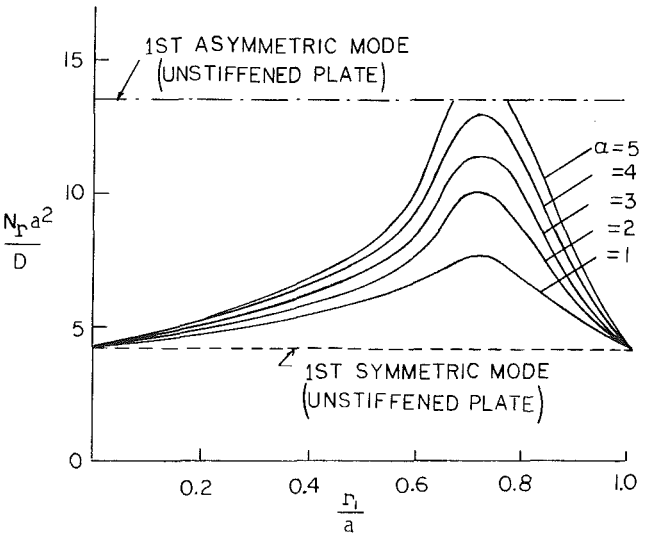


Fig. 2 Critical buckling load parameter, N_ra^2/D, versus nondimensional ring radius, r_1/a, for various values of ring stiffness parameter α; simply supported plate

References

1 Bryan, G. H., "Bucklin of Plates," *Proc. London Math. Soc.*, Vol. 22, 1891, pp. 54-67.

2 Prescott, J., *Applied Elasticity*, Dover, New York, 1961, pp. 483-492.

3 Timoshenko, S. P., and Gere, J. M., *Theory of Elastic Stability*, 2nd Ed., McGraw-Hill, New York, 1961, pp. 389-392.

4 Gerard, G., and Becker, H., "Handbook of Structural Stability, Parts I-V," NACA TN 3781-85, 1957.

Downloaded 02 May 2010 to 171.66.16.25. Redistribution subject to ASME license or copyright; see http://www.asme.org/terms/Terms_Use.cfm

5 Simitses, G. J., and Blackmon, C. M., "Buckling of Eccentrically Stiffened Thin Circular Plates," *AIAA Journal*, Vol. 7, 1969, pp. 1200–1202.
6 Amon, R., and Widera, O. E., "Stability of Edge-Reinforced Circular Plate," *Proc. Am. Soc. Civil Eng.*, Vol. 97, No. EM 5, 1971, pp. 1597–1601.
7 Reisman, H., "Bending and Buckling of an Elastically Restrained Circular Plate," ASME JOURNAL OF APPLIED MECHANICS, Vol. 19, 1952, pp. 167–172.
8 Miller, W. H., "The Buckling of Ring Stiffened Circular Plates" M.S. Thesis, Department of Mechanical Engineering, Northeastern University, Boston, Mass., Aug. 1982.

On Laminar Thin-Film Flow Along a Vertical Wall

T. R. Roy[1]

An accelerating laminar thin-film flow along a vertical wall is investigated in this paper. Using a cubic polynomial for the velocity profile inside the boundary layer the momentum integral equation is solved by a Runge-Kutta method to determine the boundary layer thickness. The corresponding film-thickness is then calculated for the entrance region. These results are compared with the existing results obtained by using a parabolic velocity profile.

Introduction

Thin-film liquid flow along a vertical wall under the influence of gravitational force, which is very often found in trickling filters, in chemical-process packing towers etc., has been investigated by a number of authors. Hassan [1], Haugen [2], and Yang and Yarbrough [3] have applied the momentum integral technique in their investigations using either a cubic or a parabolic polynomial to represent the velocity distribution in the main direction of flow. Cerro and Whitaker [4] have used a finite difference technique in their investigation.

Hassan [1] has neglected the existence of the inviscid and accelerating core inside the liquid film and hence the velocity profile and the results that he has presented do not appear to be convincing for the entrance region. Again, while Haugen [2] and Yang and Yarbrough [3] have incorporated the idea of the inviscid core within the film, they have slipped out the boundary condition, $\nu\partial^2 u/\partial y^2 = -g$ at the wall. Keeping these observations in view a modified analysis of the foregoing problem is presented in this work. Here the surface effects and the pressure gradients are neglected. The film is also assumed to have finite initial thickness h_0 and initial uniform velocity u_0.

Solution for Entrance Region

Neglecting the pressure gradient in the main direction of flow and using the usual boundary layer approximations the corresponding Navier-Stokes equation is reduced to equation (1). Substituting the no-slip conditions at the wall, equations (2), in equation (1) we get an additional no slip condition (3)

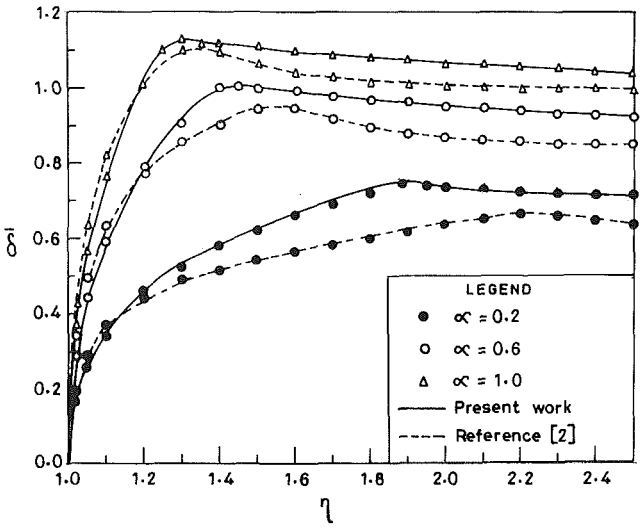


Fig. 1 Comparative presentation of dimensionless boundary layer thickness

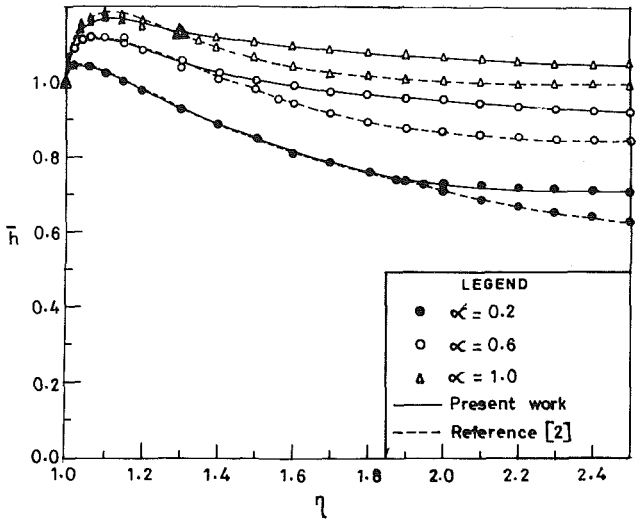


Fig. 2 Comparative presentation of dimensionless film-thickness

$$u\frac{\partial u}{\partial x} + v\frac{\partial u}{\partial y} = g + \nu\frac{\partial^2 u}{\partial y^2} \tag{1}$$

$$u = v = 0 \quad \text{at } y = 0 \tag{2}$$

$$\nu\frac{\partial^2 u}{\partial y^2}\Big]_w = -g \tag{3}$$

where u and v are velocity components in the x and y-directions, respectively, g is the gravitational acceleration in the x-direction, and ν is the kinematic viscosity. The subscript w stands for the value at the wall.

Further, the corresponding momentum integral equation and the integral form of continuity equation are, respectively, given by

$$-\frac{d}{dx}\int_0^{\delta(x)} u^2(x,y)dy + u_s\frac{d}{dx}\int_0^{\delta(x)} u(x,y)dy + g\delta(x) = \nu\frac{\partial u}{\partial y}\Big]_w \tag{4}$$

and

$$\int_0^{\delta(x)} u(x,y)dy + u_s(h(x) - \delta(x)) = \text{const.} = u_0 h_0 \tag{5}$$

where u_s is the inviscid core velocity, h and δ are the film-thickness, and the boundary layer thickness, respectively.

[1]U. G. C. Research Associate, Department of Mechanical Engineering, Institute of Technology, Banaras Hindu University, Varanasi-221 005, India.

Manuscript received by ASME Applied Mechanics Division, May 1983; final revision, December, 1983.

Downloaded 02 May 2010 to 171.66.16.25. Redistribution subject to ASME license or copyright; see http://www.asme.org/terms/Terms_Use.cfm

5 Simitses, G. J., and Blackmon, C. M., "Buckling of Eccentrically Stiffened Thin Circular Plates," *AIAA Journal*, Vol. 7, 1969, pp. 1200–1202.
6 Amon, R., and Widera, O. E., "Stability of Edge-Reinforced Circular Plate," *Proc. Am. Soc. Civil Eng.*, Vol. 97, No. EM 5, 1971, pp. 1597–1601.
7 Reisman, H., "Bending and Buckling of an Elastically Restrained Circular Plate," ASME JOURNAL OF APPLIED MECHANICS, Vol. 19, 1952, pp. 167–172.
8 Miller, W. H., "The Buckling of Ring Stiffened Circular Plates" M.S. Thesis, Department of Mechanical Engineering, Northeastern University, Boston, Mass., Aug. 1982.

On Laminar Thin-Film Flow Along a Vertical Wall

T. R. Roy[1]

An accelerating laminar thin-film flow along a vertical wall is investigated in this paper. Using a cubic polynomial for the velocity profile inside the boundary layer the momentum integral equation is solved by a Runge-Kutta method to determine the boundary layer thickness. The corresponding film-thickness is then calculated for the entrance region. These results are compared with the existing results obtained by using a parabolic velocity profile.

Introduction

Thin-film liquid flow along a vertical wall under the influence of gravitational force, which is very often found in trickling filters, in chemical-process packing towers etc., has been investigated by a number of authors. Hassan [1], Haugen [2], and Yang and Yarbrough [3] have applied the momentum integral technique in their investigations using either a cubic or a parabolic polynomial to represent the velocity distribution in the main direction of flow. Cerro and Whitaker [4] have used a finite difference technique in their investigation.

Hassan [1] has neglected the existence of the inviscid and accelerating core inside the liquid film and hence the velocity profile and the results that he has presented do not appear to be convincing for the entrance region. Again, while Haugen [2] and Yang and Yarbrough [3] have incorporated the idea of the inviscid core within the film, they have slipped out the boundary condition, $\nu\partial^2 u/\partial y^2 = -g$ at the wall. Keeping these observations in view a modified analysis of the foregoing problem is presented in this work. Here the surface effects and the pressure gradients are neglected. The film is also assumed to have finite initial thickness h_0 and initial uniform velocity u_0.

Solution for Entrance Region

Neglecting the pressure gradient in the main direction of flow and using the usual boundary layer approximations the corresponding Navier-Stokes equation is reduced to equation (1). Substituting the no-slip conditions at the wall, equations (2), in equation (1) we get an additional no slip condition (3)

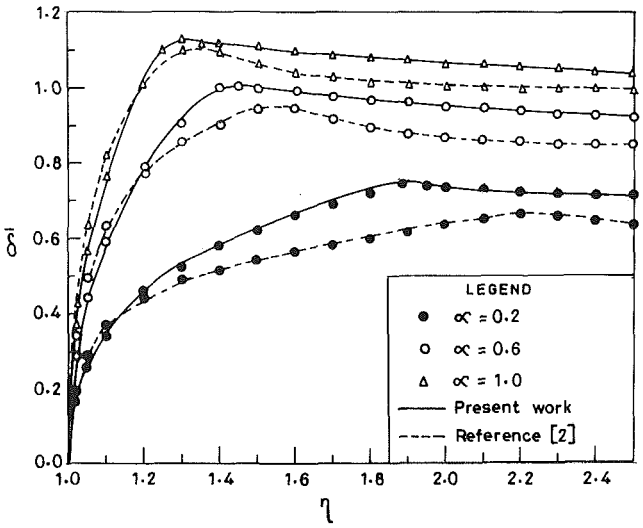


Fig. 1 Comparative presentation of dimensionless boundary layer thickness

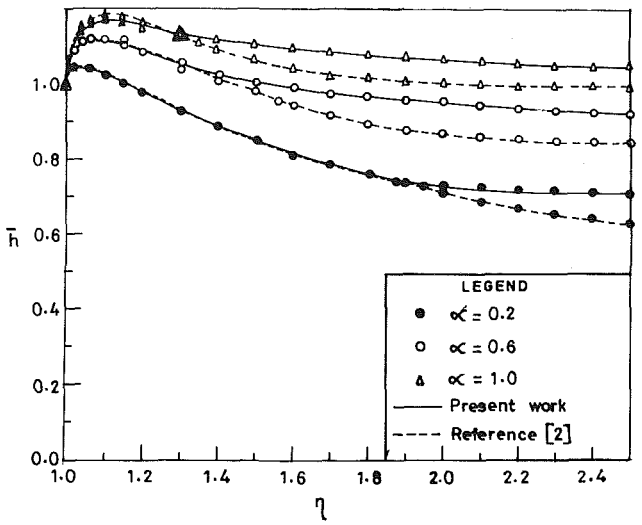


Fig. 2 Comparative presentation of dimensionless film-thickness

$$u\frac{\partial u}{\partial x} + v\frac{\partial u}{\partial y} = g + \nu\frac{\partial^2 u}{\partial y^2} \tag{1}$$

$$u = v = 0 \quad \text{at } y = 0 \tag{2}$$

$$\nu\frac{\partial^2 u}{\partial y^2}\Big]_w = -g \tag{3}$$

where u and v are velocity components in the x and y-directions, respectively, g is the gravitational acceleration in the x-direction, and ν is the kinematic viscosity. The subscript w stands for the value at the wall.

Further, the corresponding momentum integral equation and the integral form of continuity equation are, respectively, given by

$$-\frac{d}{dx}\int_0^{\delta(x)} u^2(x,y)dy + u_s\frac{d}{dx}\int_0^{\delta(x)} u(x,y)dy + g\delta(x) = \nu\frac{\partial u}{\partial y}\Big]_w \tag{4}$$

and

$$\int_0^{\delta(x)} u(x,y)dy + u_s(h(x) - \delta(x)) = \text{const.} = u_0 h_0 \tag{5}$$

where u_s is the inviscid core velocity, h and δ are the film-thickness, and the boundary layer thickness, respectively.

[1]U. G. C. Research Associate, Department of Mechanical Engineering, Institute of Technology, Banaras Hindu University, Varanasi-221 005, India.

Manuscript received by ASME Applied Mechanics Division, May 1983; final revision, December, 1983.

Copyright © 1984 by ASME
Downloaded 02 May 2010 to 171.66.16.25. Redistribution subject to ASME license or copyright; see http://www.asme.org/terms/Terms_Use.cfm

Table 1 Dimensionless values of entrance length and film-thickness at the beginning of fully developed flow

α (dimensionless)	Values obtained from present investigation		Values obtained from numerical solution of Haugen's equations [2]	
	η^* (dimensionless)	$\bar{\delta}^*$ (dimensionless)	η^* (dimensionless)	$\bar{\delta}^*$ (dimensionless)
0.2	1.88200	0.74190	2.24100	0.66937
0.6	1.41100	1.01183	1.56000	0.96179
1.0	1.27600	1.13885	1.33600	1.12350

The velocity profile appearing in equation (4) may be considered to be a cubic polynomial, equation (7), which satisfies the no slip conditions (2), (3), and the boundary conditions (6*a*,*b*)

$$u = u_s \text{ at } y = \delta \quad \text{and} \quad \frac{\partial u}{\partial y} = 0 \text{ at } y = \delta \qquad (6a,b)$$

$$\frac{u}{u_s} = \left(\frac{g\delta^2}{4\nu u_s} - \frac{1}{2}\right)\left(\frac{y}{\delta}\right)^3 - \frac{g\delta^2}{2\nu u_s}\left(\frac{y}{\delta}\right)^2 + \left(\frac{3}{2} + \frac{g\delta^2}{4\nu u_s}\right)\frac{y}{\delta} \qquad (7)$$

Hence, with the usage of the dimensionless variables, equations (8), along with the velocity profile, equation (7), the momentum integral equation (4) is simplified to equation (9)

$$\eta = \frac{u_s}{u_0} = \left(1 + \frac{2gx}{u_0^2}\right)^{1/2}, \quad \Delta^{1/2} = \bar{\delta} = \frac{\delta}{h_0} \quad \text{and} \quad \alpha = \frac{3\nu u_0}{gh_0^2} \qquad (8)$$

$$\frac{d\Delta}{d\eta} = \frac{560\alpha^3\eta^2 - 452\alpha^2\eta\Delta + 76\alpha\Delta^2}{78\alpha^2\eta^2 - 9\alpha\eta\Delta - 15\Delta^2} \qquad (9)$$

The preceding ordinary differential equation is now solved numerically using the initial condition $\Delta]_{\eta=1} = 0$.

The dimensionless film-thickness, defined by $\bar{h} = h/h_0$, is next calculated following the relation

$$\bar{h} = \eta^{-1} + \frac{3}{8}\bar{\delta} - \frac{1}{16\alpha}\eta^{-1}\bar{\delta}^3 \qquad (10)$$

Since at the onset of fully developed flow, the film-thickness becomes equal to the boundary layer thickness, the values η and $\bar{\delta}$ at that point, denoted by η^* and $\bar{\delta}^*$, respectively, are related by the expression

$$\eta^* = \frac{8}{5}(\bar{\delta}^*)^{-1} - \frac{(\bar{\delta}^*)^2}{10\alpha} \qquad (11)$$

Solution for Fully Developed Flow Region

The cubic polynomial for the velocity distribution in this region, represented by equation (13), may be determined using the conditions (2), (3), (6*a*), and continuity equation (12)

$$\int_0^{\delta(x)} u\, dy = \text{const.} = u_0 h_0 \qquad (12)$$

$$u = \left(\frac{4g\delta^2}{15\nu} - \frac{4u_0 h_0}{5\delta}\right)\left(\frac{y}{\delta}\right)^3 - \frac{g\delta^2}{2\nu}\left(\frac{y}{\delta}\right)^2 + \left(\frac{g\delta^2}{5\nu} + \frac{12u_0 h_0}{5\delta}\right)\frac{y}{\delta} \qquad (13)$$

The corresponding momentum integral equation (14) is identical to the equation derived by Hassan [1]. But here equation (14) is meant for the fully developed flow region only, not for the entire nonuniform flow region, as suggested by Hassan [1].

$$\left(\frac{g^2\delta^4}{525\nu^2} - \frac{82gu_0h_0\delta}{2625\nu} - \frac{3264u_0^2h_0^2}{2625\delta^2}\right)$$

$$\frac{d\delta}{dx} - \frac{4g\delta}{5} = -\frac{12\nu u_0 h_0}{5\delta^2} \qquad (14)$$

When made nondimensional, equation (14) ultimately reduces to

$$\frac{d\bar{\delta}}{d\zeta} = \frac{350\alpha^2(\bar{\delta}^3 - \alpha)}{15\bar{\delta}^6 - 82\alpha\bar{\delta}^3 - 1088\alpha^2} \qquad (15)$$

where $\zeta = \eta^2$. This equation can also be solved numerically with the initial value $\bar{\delta}]_{\zeta=(\eta^*)^2} = \bar{\delta}^*$.

Numerical Results

Equation (9) is solved by a fourth-order Runge-Kutta formula to find the values of $\bar{\delta}$ for increasing values of η. The corresponding value of $\bar{h}$ is calculated from the expression (10) at each time using the values of η and $\bar{\delta}$ for a point on the wall. The process is continued until the values of $\bar{\delta}$ and $\bar{h}$ coincide for four decimal places for a given value of η. These values of η and $\bar{\delta}$, denoted as η^* and $\bar{\delta}^*$, respectively, satisfy expression (11). Now using $(\eta^*)^2$ and $\bar{\delta}^*$ as the starting values of ζ and $\bar{\delta}$, equation (15) is solved using the same Runge-Kutta method for increasing values of η. This process is again continued until two successive values of $\bar{\delta}$ become equal for four decimal places. For comparison, the values of $\bar{\delta}$ and $\bar{h}$ for the entrance region and $\bar{\delta}$ for the fully developed flow region are also calculated from Haugen's boundary layer equations, [2], using the same Runge-Kutta method. It may be verified that the numerical solution of Haugen's equations and their corresponding analytical solution are almost the same, where the respective results coincide for three decimal places.

Concluding Remarks

As shown in Figs. 1 and 2, and Table 1 the results of the present work using a cubic velocity profile differ substantially from those of Haugen [2], following a parabolic velocity profile. But, since the reduced boundary layer equations for both the profiles have been solved using a fourth-order Runge-Kutta formula, the numerical error introduced in either of the results is of the same order. It is hence inferred that the difference between these two results is due to the selection of different velocity profiles. Thus the results, presented in this investigation, are more reliable, since the cubic velocity profile, used here, satisfies the additional no-slip condition (3) as well as all other boundary conditions.

References

1 Hassan, N. A., ASME Journal of Applied Mechanics, Vol. 34, 1967, pp. 535–537.

2 Haugen, R., ASME Journal of Applied Mechanics, Vol. 35, 1968, pp. 631–633.

3 Yang, T. M. T., and Yarbrough, D. W., ASME Journal of Applied Mechanics, Vol. 40, 1973, pp. 290–292.

4 Cerro, R. L., and Whitaker, S., *Chemical Engineering Science*, Vol. 26, 1971, pp. 785–798.

Downloaded 02 May 2010 to 171.66.16.25. Redistribution subject to ASME license or copyright; see http://www.asme.org/terms/Terms_Use.cfm

Optimum Openings in Circular Cylindrical Shells Under Uniaxial Tension and Torsion by Conformal Transformation

K. Rajaiah and R. R. Kumar[1]

Introduction

Determination of optimum hole shapes that yield minimum stress concentration is important in engineering structures requiring maximum strength to weight ratio. The possibility of establishing such optimum hole shapes in circular cylindrical shells under tension and torsion has been shown recently by the use of photoelastic method [1, 2]. In this Note is brought out that the well-known conformal transformation technique due to Savin [3] can also be successfully used for the same purpose.

Analysis

Consider a smooth quasi-square hole of contour Γ on the surface of a shell (Fig. 1*a*) having a shape such that, for $\epsilon \ll 1$, the function $z = \omega(\zeta) = \zeta + \epsilon f(\zeta)$

$$(z = x + iy = re^{i\theta}, \zeta = \rho e^{i\gamma} \text{ and } f(\zeta) = \zeta^{-3}) \quad (1)$$

conformally transforms its projected contour in the z plane into a circular hole of unit radius in the ζ-plane.

It is seen that equation (1) can be utilized to generate a class of quasi-square holes by varying the parameter ϵ, with $\epsilon = \pm 1/9$ yielding a square hole with rounded corners with its orientation depending on the sign of ϵ. A study of the experimentally developed optimized hole shapes in a circular cylindrical shell under uniaxial tension and torsion [1, 2] shows that one of the quasi-square holes, corresponding to a negative (positive) value of ϵ (Fig. 1), very closely resembles the optimized shape for tension (torsion). In this Note, following Savin's analysis [3], the problem of a quasi-square hole in a circular cylindrical shell under uniaxial tension and torsion (Fig. 1) is analyzed for various values of curvature parameter β. The hole shapes that yield the minimum stress concentrations are examined more closely and the stress distributions around these holes are determined. Comparison is made with the corresponding experimental results wherever feasible.

Starting from a basic stress state $(\sigma_\rho^0, \sigma_\gamma^0, \ldots)$ corresponding to the shell without a hole, the problem of determining the additional stress state arising due to the presence of the hole requires the integration of the differential equation

$$\nabla^2 \nabla^2 \Phi + 8i\beta^2 (\partial^2 \phi / \partial x^2) = 0 \quad (2)$$

where

$\Phi = W + i\bar{n}\hat{\phi}$; $\bar{n} = \sqrt{12(1-\nu^2)}/Et^2$

$W, \hat{\phi}$ = Deflection and force functions, respectively,

$E, \bar{\nu}$ = Young's Modulus and Poisson's ratio respectively.

The solution to equation (2) must satisfy the conditions on the shell ends located at infinitely large distances away from the hole, as well as the corresponding boundary conditions on the contour Γ of the hole given by

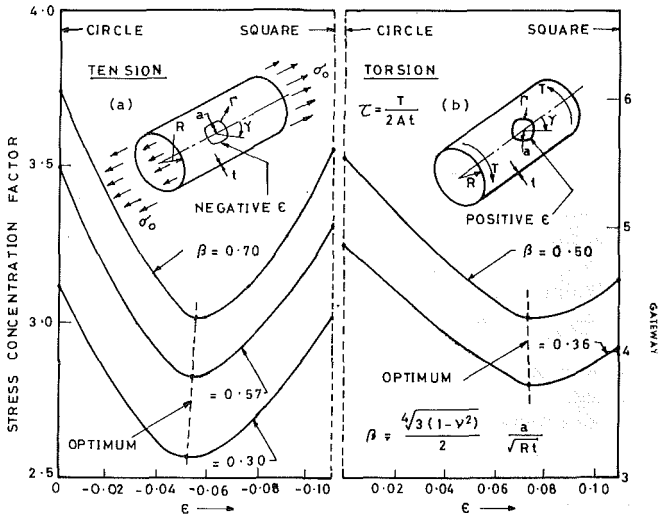


Fig. 1 Optimum values of ϵ for minimum s.c.f. for tension and torsion loading

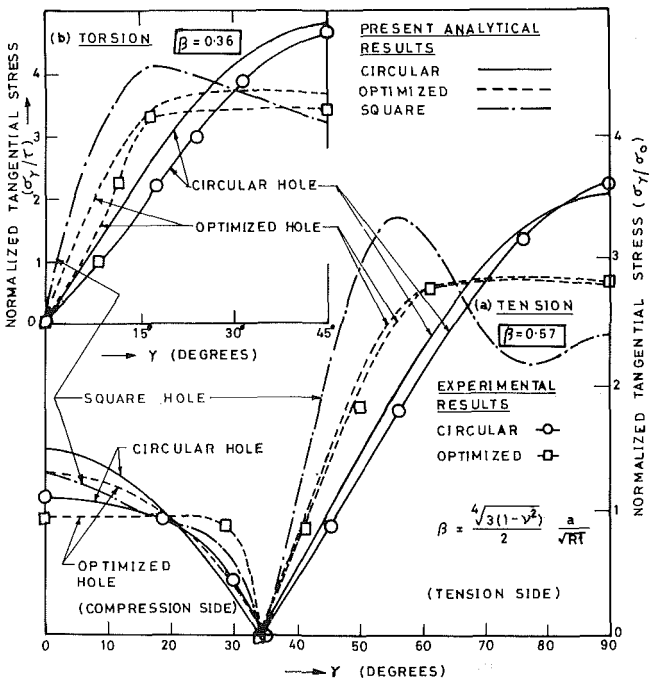


Fig. 2 Stress distribution around circular, square and optimized holes in circular cylindrical shell under tension and torsion

$$\sigma_\rho|_\Gamma = -\sigma_\rho^0, \quad \tau_{\rho\gamma}|_\Gamma = -\tau_{\rho\gamma}^0, \quad M_\rho|_\Gamma = 0, \quad Q_\rho|_\Gamma = 0 \quad (3)$$

where, M_ρ and Q_ρ refer to the moment and shear force.

Following the two-parameter (ϵ, β) perturbation method along with solution in polar trigonometric series form, one can arrive at the normalized tangential stress around the hole as a sum of the basic stress and the additional stress (*a*) for uniaxial tension[2] as

$$\begin{aligned}\sigma_\gamma/\sigma_0 = {} & 1 - 2\cos 2\gamma - \epsilon(2\cos 2\gamma - 6\cos 4\gamma + 6\cos 6\gamma) \\ & - \epsilon^2(2\cos 2\gamma + 6\cos 6\gamma - 18\cos 8\gamma + 18\cos 10\gamma) \\ & - \frac{\bar{\pi}\beta^2}{2}\{(\cos 2\gamma + \epsilon(1 + 3\cos 2\gamma + 3\cos 6\gamma) \\ & - \epsilon^2(2 - 2\cos 2\gamma - 6\cos 4\gamma - 9\cos 6\gamma \\ & - 9\cos 10\gamma)\} \end{aligned} \quad (4)$$

and (*b*) for torsion [2] as

$$\sigma_\gamma^{\times}/\tau = -4[\sin 2\gamma - \epsilon(\sin 2\gamma - 3\sin 6\gamma)$$

[1] Professor, and Research Scholar, respectively, Department of Aeronautical Engineering, Indian Institute of Technology, Bombay, India.

[2] Reference [3] contains several printing errors in the terms of equations (4) and (5) which have been corrected here.

Manuscript received by ASME Applied Mechanics Division, August, 1983; final revision, February, 1984.

Copyright © 1984 by ASME
Downloaded 02 May 2010 to 171.66.16.25. Redistribution subject to ASME license or copyright; see http://www.asme.org/terms/Terms_Use.cfm

$$+\epsilon^2(\sin 2\gamma - 3\sin 6\gamma + 9\sin 10\gamma)$$
$$+\frac{\pi\beta^2}{2}\{\sin 2\gamma - \epsilon(2\sin 2\gamma - 3\sin 6\gamma)$$
$$+\epsilon^2(3\sin 2\gamma - 6\sin 6\gamma + 9\sin 10\gamma)\}] \quad (5)$$

Numerical Results and Discussion

Numerical results have been generated for circular cylindrical shell for β values up to 0.7 for uniaxial tensile loading and for β values up to 0.5 for torsional case. Due to the limitation in the analysis, only small values of β are considered. For simplicity, only membrane stresses are determined. The hole shape parameter ϵ is varied and its effect on the hole shape and the stress concentration factor (s.c.f.) is studied.

Figure shows that, by changing the hole shape parameter ϵ and studying the peak stresses, one can determine the optimum value of ϵ that yields the minimum s.c.f. In the range of β values considered, the variation of ϵ_{opt} with β is very small. With this ϵ_{opt}, a quasi-square hole of double-barrel shape is obtained as the optimum shape, with its diagonal (*a*) at 45 deg to the axis of the shell for tension and (*b*) along the axis of the shell for torsion. Normalized tangential stress distributions around circular, square, and optimized holes for $\beta = 0.57$ are shown in Fig. 2(*a*) for tension and for $\beta = 0.36$ in Fig. 2(*b*) for torsion. It is seen that the optimized holes have nearly uniform distribution of stress along the boundary unlike the circular and square holes. Comparison with the earlier experimental results [2] yields a good correlation for both tension and torsion. For tensile loading, the optimized holes have resulted in a reduction in s.c.f. of 18–20 percent as β varies from 0 to 0.7 when compared to the circular hole values, while, for torsional loading, the reduction in s.c.f. is from 22–24 percent as β varies from 0 to 0.5.

References

1 Rajaiah, K., and Durelli, A. J., "Optimization of Hole Shapes in Circular Cylindrical Shells Under Axial Tension," *EXP. Mech.*, Vol. 21, 1981, pp. 201–204.

2 Rajaiah, K., and Kumar, R. R., "Optimum Hole Shapes in Circular Cylindrical Shells Under Tension and Torsion," *Mech. Res. Commun.*, Vol. 9, No. 2, 1982, pp. 85–93.

3 Savin, G. N., "Stress Distribution Around Holes," NASA TT F-607, 1970.

Disaster of the I-95 Mianus River Bridge. Where Could Lateral Vibration Come From?

A. M. Gorlov[1]

On June 28, 1983 a 30-meter-long section of the modern highway bridge over the Mianus River on Route I-95, Greenwich Connecticut, suddenly collapse into the river killing several drivers. Engineers and scientists alike are intrigued by the failure although they have a long way to go before various aspects of this catastrophe are cleared up and the cause of what happened is established. Nevertheless, there is evidence that it could have happended as a result of a lossening of one of the supporting hangers and slipping of the support pin out of its nest. This inevitably would trigger a chain failure of three other support hinges. If this was the case it could happen only under an action of a permanent lateral vibration.

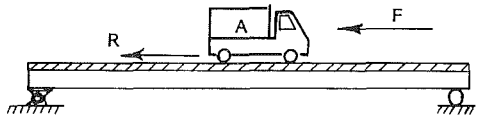


Fig. 1

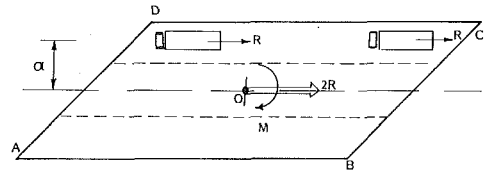


Fig. 2

Therefore, the key question is this: Where do the lateral vibrations come from? In Malcolm W. Browne's excellent article [1] the same point was formulated by an expert civil engineer in the following way: "What was the lateral force that drove the pin out of the hole? Obviously, no one imagined that this could happen."

As shown in the following, such a lateral vibration force does exist and it is conceivable that this was the prime factor that contributed to the hanger's failure.

To clarify the phenomenon of the lateral vibration let us consider the horizontal dynamical effect of a vehicle crossing the bridge (Fig. 1).

The vehicle A has to overcome an external resistance force F in order to maintain its velocity. It means that the load $R = F$ (we may call it the "repulsive" force) is applied by the vehicle's wheels to the road surface of a bridge span.

How big can the force R be? A number of factors contribute to it: air resistance, vehicle mass during its acceleration, front and side winds, road and vehicle tire conditions, road slopes, etc. We will evaluate R by three different approaches (air drag, fuel consumption, and road-load horsepower) and take into account the most conservative analysis. In the following calculations an average heavy truck is considered of total weight $W = 267$ kN (60 kips) and the frontal projected area of resistance $A = 10\text{m}^2$.

Air drag force is defined

$$F_{a.d.} = \tfrac{1}{2} C_p \rho A V^2 \quad (1)$$

where $C_p = 1.17$ is the drag coefficient for a vertical rectangular plate (equivalent to the frontal area of the truck, [2])

ρ = 1 kg/m^3 is the air density,

A = 10m^2 is the frontal resistant area,

V = 88.5$^{\text{km}}$/h (55 mi/h) is the truck speed.

After substituting, $F_{a.d.} = 3.60$ kN.

The drag force usually accounts for about 70 percent of the total force resistance at constant speed over a smooth road with no wind. The rest of the portion accounts for a rolling (primarily tire friction) resistance. Thus R can evaluated (this gives a lower value of R):

$$R = F_{a.d.}/0.7 = 5.15 \text{ kN} \quad (2)$$

We can also obtain the average magnitude of the force R from the concept of conservation of energy. Indeed, an automobile uses a portion of the consumed fuel to overcome external resistance to its motion. This overall resistance, as noted in the foregoing, is essentially our unknown force R. Thus, knowing the average rate of fuel consumption, namely W

[1]Professor, Department of Mechanical Engineering, Northeastern University, Boston, Mass. 02115.

Manuscript received by ASME Applied Mechanics Division, January, 1984; final revision, March 1984.

Downloaded 02 May 2010 to 171.66.16.25. Redistribution subject to ASME license or copyright; see http://www.asme.org/terms/Terms_Use.cfm

$$+\epsilon^2(\sin 2\gamma - 3\sin 6\gamma + 9\sin 10\gamma)$$
$$+\frac{\pi\beta^2}{2}\{\sin 2\gamma - \epsilon(2\sin 2\gamma - 3\sin 6\gamma)$$
$$+\epsilon^2(3\sin 2\gamma - 6\sin 6\gamma + 9\sin 10\gamma)\}] \quad (5)$$

Numerical Results and Discussion

Numerical results have been generated for circular cylindrical shell for β values up to 0.7 for uniaxial tensile loading and for β values up to 0.5 for torsional case. Due to the limitation in the analysis, only small values of β are considered. For simplicity, only membrane stresses are determined. The hole shape parameter ϵ is varied and its effect on the hole shape and the stress concentration factor (s.c.f.) is studied.

Figure shows that, by changing the hole shape parameter ϵ and studying the peak stresses, one can determine the optimum value of ϵ that yields the minimum s.c.f. In the range of β values considered, the variation of ϵ_{opt} with β is very small. With this ϵ_{opt}, a quasi-square hole of double-barrel shape is obtained as the optimum shape, with its diagonal (*a*) at 45 deg to the axis of the shell for tension and (*b*) along the axis of the shell for torsion. Normalized tangential stress distributions around circular, square, and optimized holes for $\beta = 0.57$ are shown in Fig. 2(*a*) for tension and for $\beta = 0.36$ in Fig. 2(*b*) for torsion. It is seen that the optimized holes have nearly uniform distribution of stress along the boundary unlike the circular and square holes. Comparison with the earlier experimental results [2] yields a good correlation for both tension and torsion. For tensile loading, the optimized holes have resulted in a reduction in s.c.f. of 18–20 percent as β varies from 0 to 0.7 when compared to the circular hole values, while, for torsional loading, the reduction in s.c.f. is from 22–24 percent as β varies from 0 to 0.5.

References

1 Rajaiah, K., and Durelli, A. J., "Optimization of Hole Shapes in Circular Cylindrical Shells Under Axial Tension," *EXP. Mech.*, Vol. 21, 1981, pp. 201–204.

2 Rajaiah, K., and Kumar, R. R., "Optimum Hole Shapes in Circular Cylindrical Shells Under Tension and Torsion," *Mech. Res. Commun.*, Vol. 9, No. 2, 1982, pp. 85–93.

3 Savin, G. N., "Stress Distribution Around Holes," NASA TT F-607, 1970.

Disaster of the I-95 Mianus River Bridge. Where Could Lateral Vibration Come From?

A. M. Gorlov[1]

On June 28, 1983 a 30-meter-long section of the modern highway bridge over the Mianus River on Route I-95, Greenwich Connecticut, suddenly collapse into the river killing several drivers. Engineers and scientists alike are intrigued by the failure although they have a long way to go before various aspects of this catastrophe are cleared up and the cause of what happened is established. Nevertheless, there is evidence that it could have happended as a result of a lossening of one of the supporting hangers and slipping of the support pin out of its nest. This inevitably would trigger a chain failure of three other support hinges. If this was the case it could happen only under an action of a permanent lateral vibration.

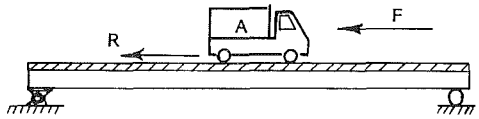


Fig. 1

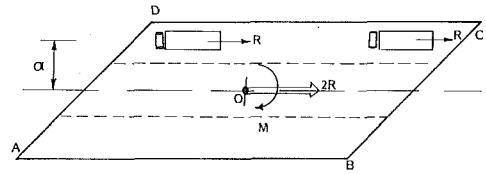


Fig. 2

Therefore, the key question is this: Where do the lateral vibrations come from? In Malcolm W. Browne's excellent article [1] the same point was formulated by an expert civil engineer in the following way: "What was the lateral force that drove the pin out of the hole? Obviously, no one imagined that this could happen."

As shown in the following, such a lateral vibration force does exist and it is conceivable that this was the prime factor that contributed to the hanger's failure.

To clarify the phenomenon of the lateral vibration let us consider the horizontal dynamical effect of a vehicle crossing the bridge (Fig. 1).

The vehicle A has to overcome an external resistance force F in order to maintain its velocity. It means that the load $R = F$ (we may call it the "repulsive" force) is applied by the vehicle's wheels to the road surface of a bridge span.

How big can the force R be? A number of factors contribute to it: air resistance, vehicle mass during its acceleration, front and side winds, road and vehicle tire conditions, road slopes, etc. We will evaluate R by three different approaches (air drag, fuel consumption, and road-load horsepower) and take into account the most conservative analysis. In the following calculations an average heavy truck is considered of total weight $W = 267$ kN (60 kips) and the frontal projected area of resistance $A = 10\text{m}^2$.

Air drag force is defined

$$F_{a.d.} = \tfrac{1}{2} C_p \rho A V^2 \quad (1)$$

where $C_p = 1.17$ is the drag coefficient for a vertical rectangular plate (equivalent to the frontal area of the truck, [2])

ρ = 1 kg/m^3 is the air density,

A = 10m^2 is the frontal resistant area,

V = 88.5$^{\text{km}}$/h (55 mi/h) is the truck speed.

After substituting, $F_{a.d.} = 3.60$ kN.

The drag force usually accounts for about 70 percent of the total force resistance at constant speed over a smooth road with no wind. The rest of the portion accounts for a rolling (primarily tire friction) resistance. Thus R can evaluated (this gives a lower value of R):

$$R = F_{a.d.}/0.7 = 5.15 \text{ kN} \quad (2)$$

We can also obtain the average magnitude of the force R from the concept of conservation of energy. Indeed, an automobile uses a portion of the consumed fuel to overcome external resistance to its motion. This overall resistance, as noted in the foregoing, is essentially our unknown force R. Thus, knowing the average rate of fuel consumption, namely W

[1]Professor, Department of Mechanical Engineering, Northeastern University, Boston, Mass. 02115.

Manuscript received by ASME Applied Mechanics Division, January, 1984; final revision, March 1984.

Copyright © 1984 by ASME
Downloaded 02 May 2010 to 171.66.16.25. Redistribution subject to ASME license or copyright; see http://www.asme.org/terms/Terms_Use.cfm

gallons per L miles, the overall vehicle efficiency n (engine-transmission-tires) and a higher fuel heating value c kcal/1, we can express the useful work U, produced by the motor fuel, in terms of the unknown force R:

$$U = RL = Wcn$$

or

$$R = \frac{Wcn}{L} = \frac{cn}{k} \tag{2}$$

where $k = L/W$ is the fuel consumption rate in liter per kilometer. The efficiency of an average vehicle can be taken as $n = 20$ percent, the higher heating value of motor gasoline as $c_1 = 8280$ kcal/1 (124,300 Btu/gal) and of truck diesel fuel as $c_2 = 9120$ kcal/1 = (137,000 Btu/gal), respectively. The fuel consumption rate L is considered in this analysis to be $k_1 = 7.5$ km/1 for an average midsized car and $k_2 = 1.3$ km/1 for a heavy truck. After substitution in (3) we will obtain magnitudes of the repulsive force produced:

$$\text{by a car} \quad R = 1.0 \text{ kN} \tag{4}$$

$$\text{by a truck} \quad R = 6.0 \text{ kN} \tag{5}$$

Finally, the force R can be found from an experimental data on the road horsepower required to propel a vehicle at constant speed over a smooth horizontal road. Automotive and tire manufacturers suggest various equations that express the power H in terms of the vehicle weight W speed V and fontal projected area A. We will use the following one (see, [3], p. 56):

$$H = \frac{V}{375}[(0.0001395\ V + 0.01676)W + 0.001128AV^2]. \tag{6}$$

After substitution $V = 88.5$ km/h (55 mph), $W = 267$ kN (60 kips), and $A = 10\text{m}^2$

$$H = 198kW(265 \text{ hp}) \tag{7}$$

Since $H = RV$ the resistance force becomes

$$R = 8 \text{ kN } (1.8 \text{ kips}) \tag{8}$$

The last figure for R is the most conservative of three and we will consider it in the further analysis.

Traffic on Route I-95 through the Mianus River Bridge is arranged in three lanes. Consequently, the repulsive forces obtained in the foregoing can be added in various combinations. One of the worst of such combinations occurs when two trucks cross a span simultaneously along the same side traffic lane (Fig. 2). As one can see, (see Fig. 3), the bridge spans are designed as diamond-shaped sections with the skewed angles of neighboring spans 53 deg. Those angles are dictated by the angle at which the bridge crosses the river and by the supporting concrete piers which had to be positioned along the water flow. Each span is supported by two roller bearings on one skewed side and two hangers along another (opposed) side. Such a supporting system transforms a span into a horizontal plane mechanism with a virtual rotational degree of freedom about the vertical axis through the centroid O.

Two vehicles crossing the span at a side traffic lane result in the total repulsive force $2R$ along with a twisting moment $M = 2Ra$ about the axis through the span's centroid. The moment M, in turn, exerts reactions in all four supports perpendicular to both diagonals of the span as is shown on Fig. 4.

These reactions can be evaluated by the following well-known approach:

$$F_A = F_C = \frac{Mr_1}{2(r_1^2 + r_2^2)} = \frac{R\,a\,r_1}{r_1^2 + r_2^2} \tag{9}$$

$$F_B = F_D = \frac{Mr_2}{2(r_1^2 + r_2^2)} = \frac{R\,a\,r_2}{r_1^2 + r_2^2} \tag{10}$$

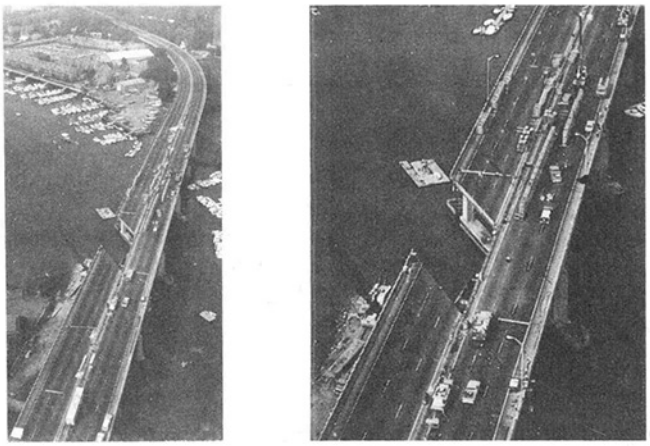


Fig. 3 An aerial view of I-95 after the catastrophe (photograph by John Madere)

Each of these forces F, in turn, causes a noncompensated lateral component F_{lat} which we are looking for.

One can notice from (9) and (10) that the forces F are directly proportional to the corresponding diagonals' lengths or

$$F_A = F_B \frac{r_1}{r_2} \tag{11}$$

Considering, for example, the greater force F_A we can now find the maximum lateral component $F_{A_{\text{lat}}} = F_A \cos\theta$ applied to the hanger A.

Taking into account $R = 8$ kN, approximate lengths of diagonals of the failed span as $d_{\max} = 49.2$ m and $d_{\min} = 18.6$ m, distance between traffic lanes $a = 3.8$ m, we will obtain from (9) and (10)

$$F_A = F_C = 1.08 \text{ kN}$$

$$F_B = F_D = 0.41 \text{ kN}$$

and the largest lateral force

$$F_{A_{\text{lat}}} = F_A \cos\theta = 1.05 \text{ kN}$$

In essence, F_{lat} is a high-frequency pulsation force because the moment M is a result of an impact interaction between a span and a vehicle crossing the bridge.

The duration of lateral force action on a bridge span depends on the vehicle speed and the span length. For a traffic speed of 88.5 km/h and a span length of 30 m the duration of a single lateral force action is about $T = 1.24$ sec. Such a short interval of a load application means that the bridge is actually subjected to an impact-forced vibration in the lateral direction. During this interval the force will be added to analogous forces produced by other vehicles of the same lane on the span.

The highest frequency of the lateral pulsation depends on the traffic intensity. Designating the distance between two vehicles in the same traffic lane by l we obtain a pulsation frequency of the moment M on a span as

$$f = \frac{v}{l} \tag{12}$$

where V is the vehicle velocity. For $V = 88.5$ km/h and $l = 13$ m during day rush hours

$$f_{\max} = 2 \text{ impacts/sec} \tag{13}$$

Thus, during the day rush hours the most remote hanger can be subjected to a lateral pulsating force up to 1.05 kN with vibration frequency up to 120 impacts/min. Such a dynamic force can represent a substantial lateral loading on the bridge's hangers. It is a well-known fact that a lateral dynamic load along with a high frequency of vibration, is one

Downloaded 02 May 2010 to 171.66.16.25. Redistribution subject to ASME license or copyright; see http://www.asme.org/terms/Terms_Use.cfm

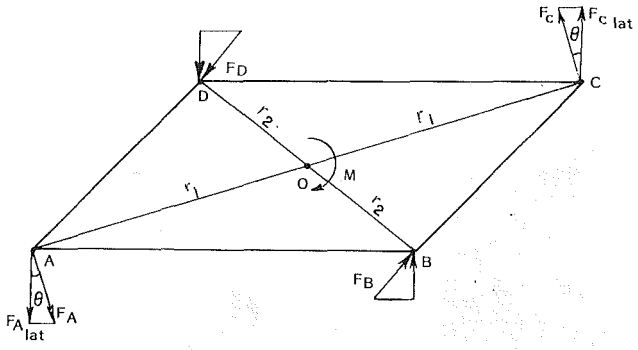


Fig. 4

of the most undesirable factors in bridge expolitation. Indeed, spans of bridges similar to the Mianus bridge are often rested on four-hinge supports designed primarily for longitudinal loading. Any substantial lateral load will inevitably cause dangerous horizontal shearing and bending reactions in support mechanisms. Besides, a pulsating force can result in accumulation of fatigue damage in the mechanical support elements.

We did not take into account the following factors which may protect the support mechanisms or deteriorate their work.

First, we considered in our analysis the worst position of the external loads, namely, an existance of two heavy trucks on the same side lane on a span. It is obvious that an existence of other vehicles at the same time on the opposite side lane will cause a moment of opposite direction and reduce the obtained above lateral forces.

Another positive factor which we neglected is a structural damping effect. Because of friction in the supports and the big mass of a span, a certain portion of the vibration energy would be absorbed by the span structure, protecting the support hinges.

At the same time, the repulsive force considered can be much greater in reality. Indeed, we obtained the force R from (2), (3), and (8) considering uniform motion of vehicles over a smooth horizontal road. But if a truck starts to accelerate or decelerate in heavy traffic crossing the bridge, this increases the repulsive force R many times. For example, the truck of weight $W = 267$ kN (considered in the foregoing) braking with the deceleration $a = 2.5$ m/sec^2 would develop the repulsive force $R = 70$ kN instead of 8 kN obtained from (8)! Note, that the deceleration $a = 2.5$ m/sec^2 means that the truck has to stop completely from the speed $V = 25$ km/h over the distance $s = 10$ m. This is quite a usual traffic situation.

As one can see, there are various positive and negative factors that are left out of scope of this paper. Nevertheless, those factors cannot change the prime nature of the lateral load pulsation considered in the foregoing.

In conclusion, it may be possible to point out a further factor that could have contributed to the bridge failure. This is the diamond shape of the bridge spans. As can be seen from Fig. 4 such a shape causes unequal reactions in the supports. As follows from (9) and (10), the lateral reactions in supports are functions of diagonal lengths of a bridge deck, such that the greater reactions will be developed in the most remote supports A and C. It means that the lateral reactions $F_{A_{lat}} = F_{C_{lat}}$ in a diamond shaped bridge would be greater than in a rectangular bridge of the same side length. This difference increases with stretching of a paralellogram. Note that the lateral reactions exist both in diamond and rectangular spans. Nevertheless, these reactions would be greater in the supports of a diamond shaped deck.

Skewed angles of the span sides are, as we mentioned, dictated by the angle at which the bridge crosses the river (Fig. 3). In the case of a rectangular span the lateral reactions in all supports would be $F_{lat} = F \cos 45 \text{ deg} = 0.707\ F$. Those reactions are smaller than the maximum F_{lat} of the same length skewed span because of two factors: shorter diagonal in the rectangle and smaller magnitude of the $\cos\theta$.

Thus, it may be said that if the bridge on Route I-95 was positioned perpendicular to the river, the lateral vibration would almost certainly be smaller because rectangular spans would have been used. This unwittingly reminds us of an old engineering joke: The very first problem that a bridge designer must solve is whether to position his bridge across or along the river . . . .

What should be done to deal with lateral vibration of the bridge over the Mianus River or other analogous bridges? First, the support hinges have to be redesigned to withstand the steady oscillating lateral forces. As a temporary measure for existing bridges it can be recommended to exclude heavy trucks from the outside traffic lanes. These vehicles allowed to move on the central lane would not cause the pulsating moment M about the centroidal axis.

References

1 Malcolm, W. Brown, "Disaster on I-95," *Discover*, September, 1983.
2 *Marks' Standard Handbook for Mechanical Engineer*, McGraw-Hill, pp. 11-68.
3 Obert, Edward E., *Internal Combustion Engines*, Harper & Row, 1983.

A Note on the Flow of a Viscous Liquid Over an Inclined Permeable Bed Under a Surface Traction

H. Guha[1] and T. K. Chaudhury[2]

Introduction

Flow over a permeable bed is of potential interest in several disciplines. Here, flow in the free fluid region is governed by Navier-Stokes equations and that in the porous matrix of the bed is usually governed by Darcy Law. However in clayey and other fine-grained soils, the departure from Darcy law, in as much as that there exists an initial gradient, has been observed. Again, at the surface of a saturated permeable bed instead of the usual no-slip condition, a slip condition suggested by Beavers and Joseph [1] and later confirmed by Taylor [2] and Richardson [3] should be used.

In the present paper we investigate the flow of a viscous liquid over an inclined permeable (saturated) bed within which there exists an initial gradient and at the surface of which Beavers and Joseph condition is satisfied. A uniform tangential stress S is assumed to act on the upper surface of the liquid for a finite interval of time. Among various other mechanisms, sometimes wind stress may also provide such a surface traction. It is of interest to find the slip velocity at the permeable boundary and the effect of permeability on the shear stress at the boundary.

Formulation and Solution to the Problem

The x-axis is taken along the bed in the direction of motion

[1]Research Scholar and Professor, respectively, Burdwan University, Burdwan, West Bengal, India.

Downloaded 02 May 2010 to 171.66.16.25. Redistribution subject to ASME license or copyright; see http://www.asme.org/terms/Terms_Use.cfm

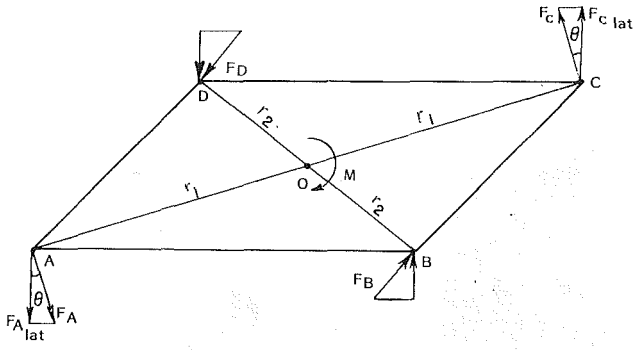


Fig. 4

of the most undesirable factors in bridge expolitation. Indeed, spans of bridges similar to the Mianus bridge are often rested on four-hinge supports designed primarily for longitudinal loading. Any substantial lateral load will inevitably cause dangerous horizontal shearing and bending reactions in support mechanisms. Besides, a pulsating force can result in accumulation of fatigue damage in the mechanical support elements.

We did not take into account the following factors which may protect the support mechanisms or deteriorate their work.

First, we considered in our analysis the worst position of the external loads, namely, an existance of two heavy trucks on the same side lane on a span. It is obvious that an existence of other vehicles at the same time on the opposite side lane will cause a moment of opposite direction and reduce the obtained above lateral forces.

Another positive factor which we neglected is a structural damping effect. Because of friction in the supports and the big mass of a span, a certain portion of the vibration energy would be absorbed by the span structure, protecting the support hinges.

At the same time, the repulsive force considered can be much greater in reality. Indeed, we obtained the force R from (2), (3), and (8) considering uniform motion of vehicles over a smooth horizontal road. But if a truck starts to accelerate or decelerate in heavy traffic crossing the bridge, this increases the repulsive force R many times. For example, the truck of weight $W = 267$ kN (considered in the foregoing) braking with the deceleration $a = 2.5$ m/sec^2 would develop the repulsive force $R = 70$ kN instead of 8 kN obtained from (8)! Note, that the deceleration $a = 2.5$ m/sec^2 means that the truck has to stop completely from the speed $V = 25$ km/h over the distance $s = 10$ m. This is quite a usual traffic situation.

As one can see, there are various positive and negative factors that are left out of scope of this paper. Nevertheless, those factors cannot change the prime nature of the lateral load pulsation considered in the foregoing.

In conclusion, it may be possible to point out a further factor that could have contributed to the bridge failure. This is the diamond shape of the bridge spans. As can be seen from Fig. 4 such a shape causes unequal reactions in the supports. As follows from (9) and (10), the lateral reactions in supports are functions of diagonal lengths of a bridge deck, such that the greater reactions will be developed in the most remote supports A and C. It means that the lateral reactions $F_{A_{lat}} = F_{C_{lat}}$ in a diamond shaped bridge would be greater than in a rectangular bridge of the same side length. This difference increases with stretching of a paralellogram. Note that the lateral reactions exist both in diamond and rectangular spans. Nevertheless, these reactions would be greater in the supports of a diamond shaped deck.

Skewed angles of the span sides are, as we mentioned, dictated by the angle at which the bridge crosses the river (Fig. 3). In the case of a rectangular span the lateral reactions in all supports would be $F_{lat} = F \cos 45 \text{ deg} = 0.707\ F$. Those reactions are smaller than the maximum F_{lat} of the same length skewed span because of two factors: shorter diagonal in the rectangle and smaller magnitude of the $\cos\theta$.

Thus, it may be said that if the bridge on Route I-95 was positioned perpendicular to the river, the lateral vibration would almost certainly be smaller because rectangular spans would have been used. This unwittingly reminds us of an old engineering joke: The very first problem that a bridge designer must solve is whether to position his bridge across or along the river . . . .

What should be done to deal with lateral vibration of the bridge over the Mianus River or other analogous bridges? First, the support hinges have to be redesigned to withstand the steady oscillating lateral forces. As a temporary measure for existing bridges it can be recommended to exclude heavy trucks from the outside traffic lanes. These vehicles allowed to move on the central lane would not cause the pulsating moment M about the centroidal axis.

References

1 Malcolm, W. Brown, "Disaster on I-95," *Discover*, September, 1983.
2 *Marks' Standard Handbook for Mechanical Engineer*, McGraw-Hill, pp. 11-68.
3 Obert, Edward E., *Internal Combustion Engines*, Harper & Row, 1983.

A Note on the Flow of a Viscous Liquid Over an Inclined Permeable Bed Under a Surface Traction

H. Guha[1] and T. K. Chaudhury[2]

Introduction

Flow over a permeable bed is of potential interest in several disciplines. Here, flow in the free fluid region is governed by Navier-Stokes equations and that in the porous matrix of the bed is usually governed by Darcy Law. However in clayey and other fine-grained soils, the departure from Darcy law, in as much as that there exists an initial gradient, has been observed. Again, at the surface of a saturated permeable bed instead of the usual no-slip condition, a slip condition suggested by Beavers and Joseph [1] and later confirmed by Taylor [2] and Richardson [3] should be used.

In the present paper we investigate the flow of a viscous liquid over an inclined permeable (saturated) bed within which there exists an initial gradient and at the surface of which Beavers and Joseph condition is satisfied. A uniform tangential stress S is assumed to act on the upper surface of the liquid for a finite interval of time. Among various other mechanisms, sometimes wind stress may also provide such a surface traction. It is of interest to find the slip velocity at the permeable boundary and the effect of permeability on the shear stress at the boundary.

Formulation and Solution to the Problem

The x-axis is taken along the bed in the direction of motion

[1]Research Scholar and Professor, respectively, Burdwan University, Burdwan, West Bengal, India.

Copyright © 1984 by ASME
Downloaded 02 May 2010 to 171.66.16.25. Redistribution subject to ASME license or copyright; see http://www.asme.org/terms/Terms_Use.cfm

and the y-axis is drawn into the fluid perpendicular to the bed. Assuming the velocity field in the free fluid region in the form $(u(y,t),0,0)$ the equations of motion give

$$\frac{\partial u}{\partial t} = g\sin\theta - \frac{1}{\rho}\frac{\partial p}{\partial x} + \nu\frac{\partial^2 u}{\partial y^2} \tag{1}$$

$$0 = g\cos\theta + \frac{1}{\rho}\frac{\partial p}{\partial y}, \tag{2}$$

where $\nu(=\mu/\rho)$ is the kinematic coefficient of viscosity and $\theta(0\le\theta\le\pi/2)$ is the inclination of the permeable bed with the horizontal.

The filter velocity Q in the porous matrix of the bed is

$$Q = \frac{K}{\mu}\left[-\frac{\partial p}{\partial x} + \rho g\sin\theta - I_0\right], \tag{3}$$

where K is the permeability of the medium and I_0 is the initial gradient.

The boundary conditions are

$$\frac{\partial u}{\partial y}\bigg|_{y=0} = \frac{\alpha}{\sqrt{K}}(U_1 - Q), \quad \text{[Beavers-Joseph condition]} \tag{4}$$

where $u|_{y=0} = U_1$ (slip velocity) and α is a dimensionless quantity depending on the material parameters that characterize the structure of the permeable material within the boundary region; and

$$\mu\frac{\partial u}{\partial y}\bigg|_{y=h} = S[H(t) - H(t-T)], \tag{5}$$

where h is the height of the upper surface of the fluid above the bed and $H(t)$ is the Heaviside function defined by

$$H(t) = 0 \quad \text{for} \quad t\le 0$$
$$= 1 \quad \text{for} \quad t>0$$

The initial condition is

$$u = 0 \quad \text{at} \quad t = 0 \tag{6}$$

We introduce the nondimensional quantities

$$u' = \frac{u}{U}, x' = \frac{x}{h}, y' = \frac{y}{h}, Q' = \frac{Q}{U}, K' = \frac{K}{h^2}, U_1' = \frac{U_1}{U}$$

$$p' = \frac{p}{\rho U^2}, t' = \frac{\nu}{h^2}t, T' = \frac{\nu}{h^2}T, I_0' = \frac{I_0 h}{\rho U^2}, S' = \frac{Sh}{\mu U}, \tag{7}$$

where U is a characteristic velocity (e.g., mean velocity over a cross section of unit breadth in the steady state, i.e., when $t\to\infty$), then drop the primes for convenience and get the nondimensional equations boundary and initial conditions.

Then applying the Laplace transform with respect to t (with parameter p) and denoting the transformed quantities by overbar we have for the free fluid velocity the following equation and the boundary conditions:

$$\frac{d^2\bar{u}}{dy^2} - p\bar{u} = -\frac{A}{p} \tag{8}$$

$$\frac{\partial\bar{u}}{\partial y}\bigg|_{y=0} = \frac{\alpha}{\sqrt{K}}\left[\bar{U}_1 - \frac{K(A - RI_0)}{p}\right] \tag{9}$$

$$\bar{u}|_{y=0} = \bar{U}_1 \tag{10}$$

$$\frac{\partial\bar{u}}{\partial y}\bigg|_{y=1} = \frac{S}{p}(1 - e^{-pT}), \tag{11}$$

where $R(-\partial p/\partial x + 1/F\ \mathrm{Sin}\theta) = A(A>0)$, $R = Uh/\nu$ is the Reynolds number, $F = U^2/gh$ is the Froude number and

$$K(A - RI_0) = Q \tag{12}$$

is the nondimensional filter velocity.

Solving equation (8) together with the boundary conditions (10) and (11), and eliminating $\bar{U}_1$ (which appears in the solution) with the help of (9) we get

$$\bar{u} = \frac{A}{p^2}\left[\frac{\alpha(Kp-1)\mathrm{Cosh}\sqrt{p}(1-y)}{\sqrt{Kp}\mathrm{Sinh}\sqrt{p} + \alpha\mathrm{Cosh}\sqrt{p}} + 1\right]$$

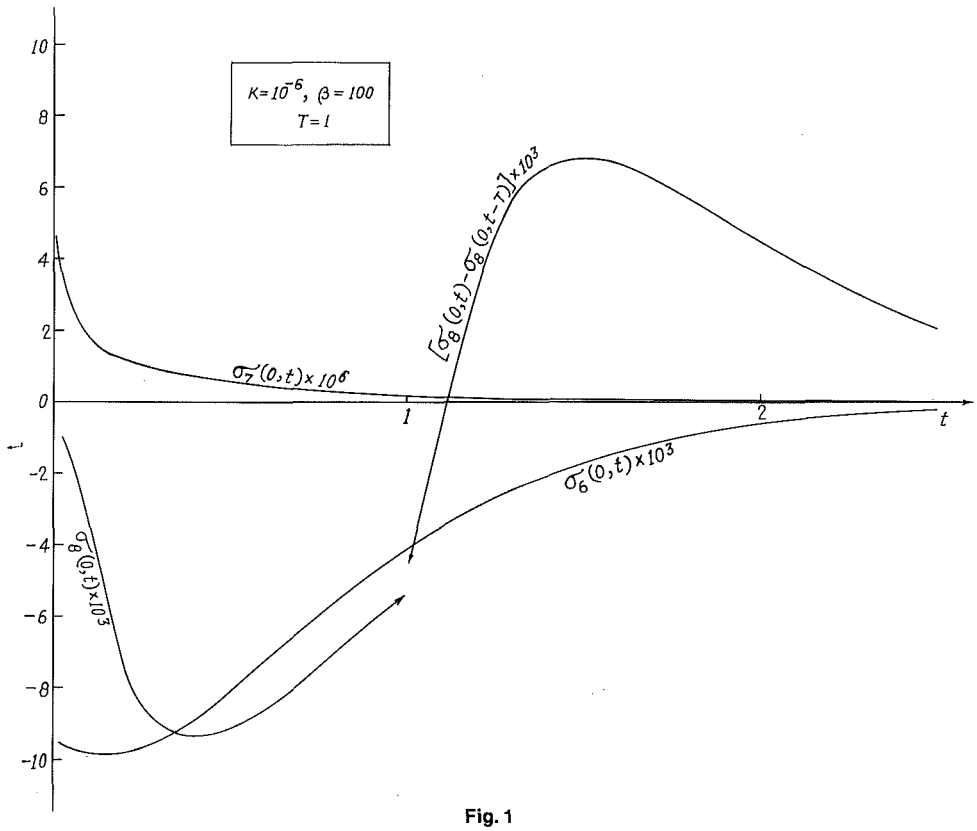


Fig. 1

Downloaded 02 May 2010 to 171.66.16.25. Redistribution subject to ASME license or copyright; see http://www.asme.org/terms/Terms_Use.cfm

$$-\frac{\alpha KRI_0\mathrm{Cosh}\sqrt{p}(1-y)}{p(\sqrt{Kp}\mathrm{Sinh}\sqrt{p}+\alpha\mathrm{Cosh}\sqrt{p})}$$

$$+\frac{S\sqrt{k}(1-\bar{e}^{pT})\mathrm{Cosh}\sqrt{p}(1-y)}{p\mathrm{Cosh}\sqrt{p}(\sqrt{Kp}\mathrm{Sinh}\sqrt{p}+\alpha\mathrm{Cosh}\sqrt{p})}+\frac{S(1-\bar{e}^{pT})\mathrm{Sinh}\sqrt{p}y}{p^{3/2}\mathrm{Cosh}\sqrt{p}}$$

Now by inversion of Laplace transform we have

$$u=\frac{A}{2\pi i}\int_{\gamma-i\infty}^{\gamma+i\infty}\left[\frac{\alpha(K\lambda-1)\mathrm{Cosh}\sqrt{\lambda}(1-y)}{\sqrt{K\lambda}\mathrm{Sinh}\sqrt{\lambda}+\alpha\mathrm{Cosh}\sqrt{\lambda}}+1\right]\frac{e^{\lambda t}}{\lambda^2}\,d\lambda$$

$$-\frac{\alpha KRI_0}{2\pi i}\int_{\gamma-i\infty}^{\gamma+i\infty}\frac{\mathrm{Cosh}\sqrt{\lambda}(1-y)}{\sqrt{K\lambda}\mathrm{Sinh}\sqrt{\lambda}+\alpha\mathrm{Cosh}\sqrt{\lambda}}\cdot\frac{e^{\lambda t}}{\lambda}\,d\lambda$$

$$+\frac{S\sqrt{K}}{2\pi i}\int_{\gamma-i\infty}^{\gamma+i\infty}\phi\cdot\frac{\mathrm{Cosh}\sqrt{\lambda}(1-y)}{\mathrm{Cosh}\sqrt{\lambda}[\sqrt{K\lambda}\mathrm{Sinh}\sqrt{\lambda}+\alpha\mathrm{Cosh}\sqrt{\lambda}]}\,\frac{e^{\lambda t}}{\lambda}\,d\lambda$$

$$+\frac{S}{2\pi i}\int_{\gamma-i\infty}^{\gamma+i\infty}\phi\cdot\frac{\mathrm{Sinh}\sqrt{\lambda}y}{\mathrm{Cosh}\sqrt{\lambda}}\cdot\frac{e^{\lambda t}}{\lambda^{3/2}}\,d\lambda,$$

where $\phi=1$ for $0<t<T$ and $\phi=1-\bar{e}^{\lambda T}$ for $t>T$ and where γ is a constant greater than the real part of all the singularities of the integrands.

The roots of $\sqrt{K\lambda}\mathrm{Sinh}\sqrt{\lambda}+\alpha\mathrm{Cosh}\sqrt{\lambda}=0$ are given by $-\xi_1^2$, $-\xi_2^2$, . . . where ξ_1, ξ_2, . . . are the roots of the equation

$$\xi\tan\xi=\frac{\alpha}{\sqrt{K}} \tag{13}$$

(cf. Carslaw and Jaeger [4]). Then evaluating the foregoing integrals by the standard method, we finally obtain

$$u=A\left[K+\frac{1}{\beta}+\frac{y(2-y)}{2}-\sigma_1(y,t)\right]+RI_0[\sigma_2(y,t)-K]$$

$$+S\left[y+\frac{1}{\beta}+\sigma_3(y,t)\right]\qquad\text{for}\qquad 0<t<T \tag{14a}$$

and

$$u=A\left[K+\frac{1}{\beta}+\frac{y(2-y)}{2}-\sigma_1(y,t)\right]+RI_0[\sigma_2(y,t)-K]$$

$$+S[\sigma_3(y,t)-\sigma_3(y,t-T)]\qquad\text{for}\qquad t>T, \tag{14b}$$

where

$$\sigma_1(y,t)=2\beta\sum_{n=0}^{\infty}\frac{\mathrm{Cos}\{\xi_n(1-y)\}\cdot(K+1/\xi_n^2)\cdot\bar{e}^{\xi nt}}{(\beta+\beta^2+\xi_n^2)\mathrm{Cos}\xi_n}$$

$$\sigma_2(y,t)=2\beta K\sum_{n=0}^{\infty}\frac{\mathrm{Cos}\{\xi_n(1-y)\}\cdot\bar{e}^{\xi_n^2t}}{(\beta+\beta^2+\xi_n^2)\cdot\mathrm{Cos}\xi_n}$$

$$\sigma_3(y,t)=-2\sum_{n=0}^{\infty}\frac{\mathrm{Cos}\{\xi_n(1-y)\}\cdot\bar{e}^{\xi_n^2t}}{(\beta+\beta^2+\xi_n^2)\cdot\mathrm{Cos}^2\xi_n}$$

$$\beta=\frac{\alpha}{\sqrt{K}}\cdot$$

The nondimensional slip velocity U_1 $(=u|_{y=0})$ is given by

$$U_1=A\left[K+\frac{1}{\beta}-\sigma_1(0,t)\right]$$

$$+RI_0[\sigma_2(0,t)-K]+S\left[\frac{1}{\beta}+\sigma_3(0,t)\right]$$

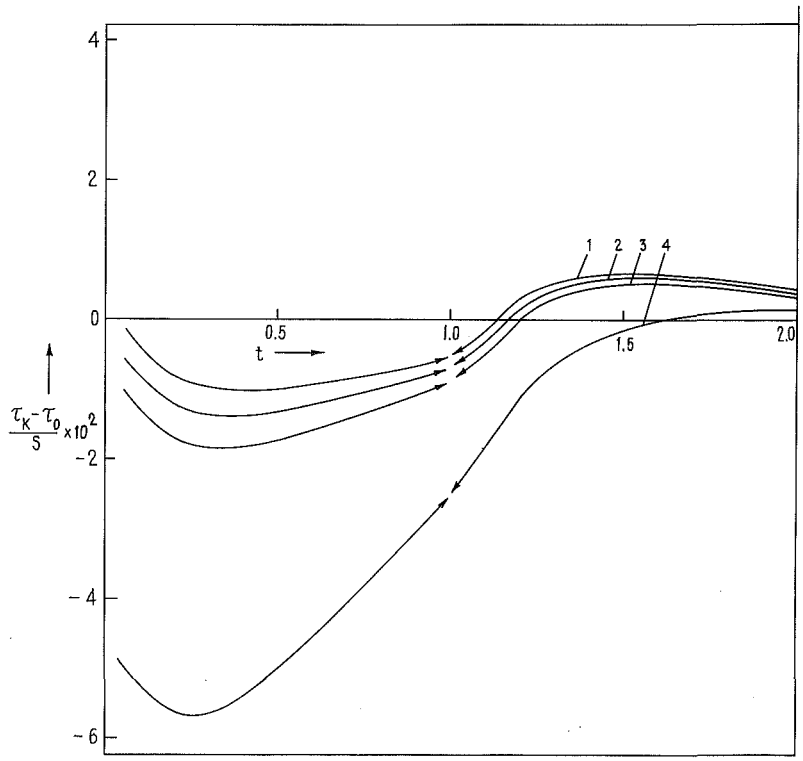
$$\text{for}\qquad 0<t<T \tag{15a}$$

and

$$U_1=A\left[K+\frac{1}{\beta}-\sigma_1(0,t)\right]+RI_0[\sigma_2(0,t-K)]$$

$$+S[\sigma_3(0,t)-\sigma_3(0,t-T)]\text{for}\qquad t>T \tag{15b}$$

Making $K\to 0$ in (14a) and (14b) and noting that as $K\to 0$



1: $\frac{A}{S}=0.1$, $\frac{RI^0}{S}=0.1$ 2: $\frac{A}{S}=0.5$, $\frac{RI^0}{S}=0.1$ 3: $\frac{A}{S}=1.0$, $\frac{RI^0}{S}=0.1$ 4: $\frac{A}{S}=5.0$, $\frac{RI^0}{S}=0.1$

Fig. 2

Downloaded 02 May 2010 to 171.66.16.25. Redistribution subject to ASME license or copyright; see http://www.asme.org/terms/Terms_Use.cfm

$\xi_n \to (n+\frac{1}{2})\pi$ and using (13), we get in the case of impervious bed

$$u = A\left[\frac{y(2-y)}{2} - \sigma_4(y,t)\right] + S[y - \sigma_5(y,t)]$$

$$\text{for} \quad 0 < t < T \tag{16a}$$

and

$$u = A\left[\frac{y(2-y)}{2} - \sigma_4(y,t)\right] - S[\sigma_5(y,t) - \sigma_5(y,t-T)]$$

$$\text{for} \quad t > T, \tag{16b}$$

where

$$\sigma_4(y,t) = 2\sum_{n=0}^{\infty} \frac{(-1)^n \cos\{(n+\frac{1}{2})\pi(1-y)\} \cdot \bar{e}^{(n+\frac{1}{2})^2\pi^2 t}}{(n+\frac{1}{2})^3\pi^3}$$

$$\sigma_5(y,t) = 2\sum_{n=0}^{\infty} \frac{(-1)^n \sin\{(n+\frac{1}{2})\pi y\} \cdot \bar{e}^{(n+\frac{1}{2})^2\pi^2 t}}{(n+\frac{1}{2})^2\pi^2}$$

In this case clearly $U_1 \to 0$. Denoting the wall skin friction $\partial u/\partial y|_{y=0}$ by τ_k for the permeable bed and by τ_0 for the impervious bed we find

$$\tau_K - \tau_0 = A\sigma_6(0,t) + RI_0\sigma_7(0,t) + S\sigma_8(0,t) \quad \text{for} \quad 0 < t < T \tag{17a}$$

and

$$\tau_K - \tau_0 = A\sigma_6(0,t) + RI_0\sigma_7(0,t) + S[\sigma_8(0,t) - \sigma_8(0,t-T)] \quad \text{for} \quad t > T, \tag{17b}$$

where

$$\sigma_6(0,t) = 2\sum_{n=0}^{\infty} \frac{\bar{e}^{(n+\frac{1}{2})^2\pi^2 t}}{(n+\frac{1}{2})^2\pi^2} - \beta\sigma_1(0,t)$$

$$\sigma_7(0,t) = \beta\sigma_2(0,t)$$

$$\sigma_8(0,t) = \beta\sigma_3(0,t) - 2\sum_{n=0}^{\infty} \frac{(-1)^n \bar{e}^{(n+\frac{1}{2})^2\pi^2 t}}{(n+\frac{1}{2})\pi}$$

Discussion

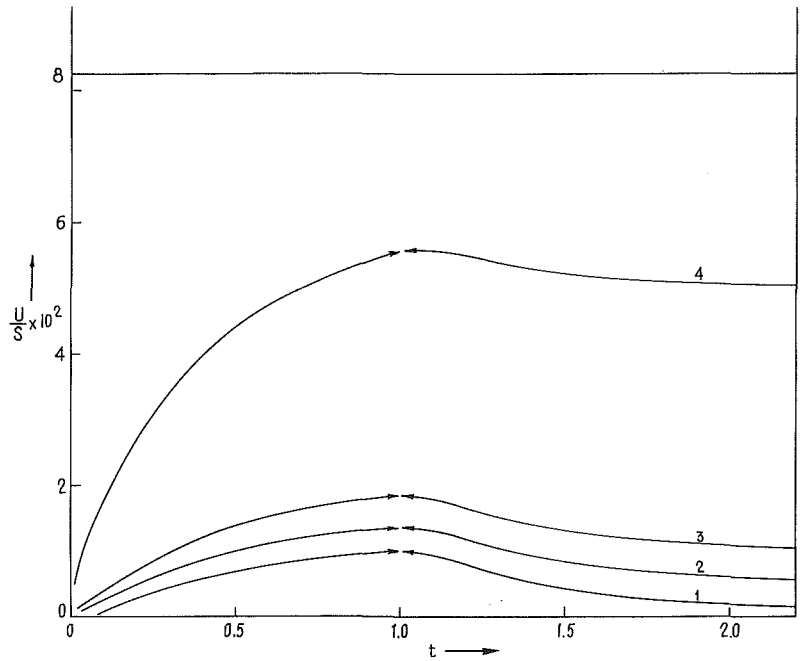
To have an idea about the nature of the effect of permeability we carry out some numerical computations with $K = 10^{-6}$ and $\beta = 100$ which are fairly representative values of the parameters (cf., Table 1 [17]), and give several graphs in Figs. 1-3. We find from these computations that in this case only first three terms in the summation suffice. We now make some observations from the graphs which are therefore valid for at least the set of values of the parameters K and β as given in the foregoing.

Graphs in Fig. 1 show that the value of $\sigma_6(0,t)$ is of the same order as that of $\sigma_8(0,t)$ whereas the value of $\sigma_7(0,t)$ is of much smaller order.

Thus we see that although the initial gradient always tends to increase the shear stress at the bed, $\sigma_7(0,t)$ being positive throughout, its effect is negligibly small as RI_0 cannot be greater than A for positive filter velocity Q [cf., [12]]. Thus it is interesting to note that the surface traction acting for a finite time on the fluid brings in its wake a higher shear stress on the permeable bed as compared to that on an imprevious bed.

Figure 2 shows that the shear stress at a permeable bed remains smaller than that at an impervious bed ($\tau_K < \tau_0$) during the period of application of the surface stress and also for a certain time after its withdrawal. After that the shear stress at the permeable bed becomes greater ($\tau_K > \tau_0$), the difference reaches a maximum, and then asymptotically falls to the steady state value for an impervious bed. The time during which τ_K remains less than τ_0 depends on A/S and increases with it (for a fixed RI_0/S).

Figure 3 shows that the nondimensional slip velocity U_1 increases with time during the application of the surface stress. After the withdrawal of the surface stress U_1 begins to



1: $\frac{A}{S}=0.1, \frac{RI^0}{S}=0.1$ 2: $\frac{A}{S}=0.5, \frac{RI^0}{S}=0.1$ 3: $\frac{A}{S}=1.0, \frac{RI^0}{S}=0.1$ 4: $\frac{A}{S}=5.0, \frac{RI^0}{S}=0.1$

Fig. 3

Downloaded 02 May 2010 to 171.66.16.25. Redistribution subject to ASME license or copyright; see http://www.asme.org/terms/Terms_Use.cfm

decrease with time and asymptotically falls to a constant value. This constant value depends on Δ/S and is larger for larger A/S (for a fixed RI_0). Here the initial gradient tends to decrease the slip velocity but its effect is negligibly small.

Acknowledgment

The authors are grateful to one of the reviewers for his valuable comments and suggestions. The first author (H.S.G.) is also thankful to the Council of Scientific and Industrial Research, India, for awarding him a Junior Research Fellowship.

References

1 Beavers, G. S., and Joseph, D. D., "Boundary Conditions at a Naturally Permeable Wall," *Journal of Fluid Mechanics*, Vol. 30, No. 1, 1967, pp. 197–207.

2 Taylor, G. I., "A Model for the Boundary Condition of a Porous Material, Part I," *Journal of Fluid Mechanics*, Vol. 49, No. 2, 1971, pp. 319–326.

3 Richardson, S., "A Model for the Boundary Condition of a Porous Material, Part II," *Journal of Fluid Mechanics*, Vol. 49, No. 2, 1971, pp. 327–336.

4 Carslaw, H. S., and Jaeger, J. C., *Operational Methods in Applied Mathematics*, Dover, 1963, p. 130.

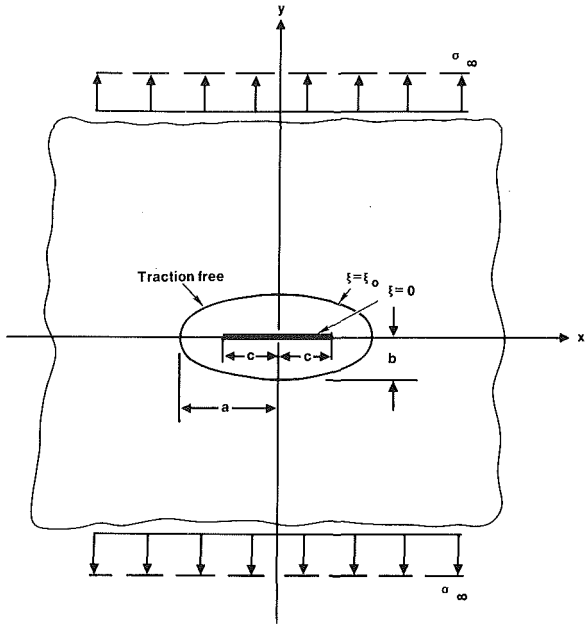


Fig. 1 A line crack in an infinite sheet, subjected to uniaxial tension perpendicular to the major axis. Here $x = c(\cosh\xi\cos\eta)$, $y = c(\sinh\xi\sin\eta)$.

An Elastic-Plastic Solution Around a Tensile Crack in Strain-Hardening Materials

C. Hatleberg[1]

Introduction

One of the more difficult problems in fracture mechanics has been determining an elastic-plastic solution for thin cracked sheets subject to uniaxial tension. Planar elastic solutions have long been available. The best known is by Ingles [1] for a single crack in an infinite sheet. These elastic results were used by Griffith [2] to establish a theory of brittle fracture. Irwin [3] modified Griffith's theory to include small-scale yielding, where the plastic zone is small compared to the crack dimensions. Small scale yielding has been assumed in the crack tip region for a tensile crack in a finite sheet of strain-hardening materials under plane stress conditions by Hutchinson [4]. Hilton and Sih [5] used this solution to solve for the plastic strain intensity factors for a tensile crack in an infinite sheet of strain-hardening materials. The solution presented here is based on the deformation theory of plasticity in conjunction with strain-hardening stress-strain relations, and is found by using the minimum of a modified complementary energy principle coupled with a modified Ritz method.

Analysis

Consider a tensile crack in an infinite sheet of strain-hardening materials under plane stress conditions. The problem is posed in elliptical coordinates (ξ,η), for which a line crack is shown in Fig. 1 as the limiting case of a collapsed ellipse subjected to uniaxial tension perpendicular to the major axis [6].

Based on the deformation theory of plasticity, the total stress components $\sigma_{\xi\xi}, \sigma_{\eta\eta}$ and $\tau_{\xi\eta}$ are related to the corresponding total strains $\epsilon_{\xi\xi}, \epsilon_{\eta\eta}, \gamma_{\xi\eta}$, as follows:

$$\epsilon_{\xi\xi} = \left[\frac{1}{E}\left(\sigma_{\xi\xi} - \upsilon\sigma_{\eta\eta}\right)\right] + \left[\left(\frac{1}{E_s} - \frac{1}{E}\right)\left(\sigma_{\xi\xi} - \frac{1}{2}\sigma_{\eta\eta}\right)\right],$$

$$\epsilon_{\eta\eta} = \left[\frac{1}{E}\left(\sigma_{\eta\eta} - \upsilon\sigma_{\xi\xi}\right)\right] + \left[\left(\frac{1}{E_s} - \frac{1}{E}\right)\left(\sigma_{\eta\eta} - \frac{1}{2}\sigma_{\xi\xi}\right)\right],$$

$$\gamma_{\xi\eta} = \left[\frac{1}{G}\tau_{\xi\eta}\right] + \left[3\left(\frac{1}{E_s} - \frac{1}{E}\right)\tau_{\xi\eta}\right]. \quad (1)$$

The first and second terms on the right-hand side of (1) define the elastic and plastic parts of the strains, and E_s denotes the secant modulus of the uniaxial stress-strain curve at an effective stress, σ_e, given by

$$\sigma_e = \left(\sigma_{\xi\xi}^2 + \sigma_{\eta\eta}^2 - \sigma_{\xi\xi}\sigma_{\eta\eta} + 3\tau_{\xi\eta}^2\right)^{1/2}. \quad (2)$$

In deformation theory, (1) and (2) are valid only if σ_e is continuously increasing at every point in the region; thus, the final solution must be examined to determine if unloading has taken place.

A Ramberg-Osgood stress-strain relations [7] is one way of approximating a uniaxial stress-strain relation for strain-hardening materials.

Another more popular way to approximate a uniaxial stress-strain relation for strain-hardening materials is to use a modified Ramberg-Osgood relation where,[2]

$$E\bar{\epsilon} = \bar{\sigma} \quad \text{for} \quad \bar{\sigma} \le 1.0,$$

$$E\bar{\epsilon} = (\bar{\sigma})^n \quad \text{for} \quad \bar{\sigma} > 1.0. \quad (3)$$

The secant modulus, E_s, is written as

$$E_s = E \quad \text{for} \quad \bar{\sigma} \le 1.0,$$

$$E_s = \frac{E}{(\bar{\sigma})^{n-1}} \quad \text{for} \quad \bar{\sigma} > 1.0. \quad (4)$$

Again, (3) is restricted to monotonically increasing stress or no unloading.

[1] Naval Ocean Systems Center, San Diego, Calif. 92152. Mem. ASME.

Manuscript received by ASME Applied Mechanics Division, November, 1983; final revision, February, 1984.

[2] Barred quantities have been nondimensional with respect to the yield stress, σ_y.

Downloaded 02 May 2010 to 171.66.16.25. Redistribution subject to ASME license or copyright; see http://www.asme.org/terms/Terms_Use.cfm

decrease with time and asymptotically falls to a constant value. This constant value depends on Δ/S and is larger for larger A/S (for a fixed RI_0). Here the initial gradient tends to decrease the slip velocity but its effect is negligibly small.

Acknowledgment

The authors are grateful to one of the reviewers for his valuable comments and suggestions. The first author (H.S.G.) is also thankful to the Council of Scientific and Industrial Research, India, for awarding him a Junior Research Fellowship.

References

1 Beavers, G. S., and Joseph, D. D., "Boundary Conditions at a Naturally Permeable Wall," *Journal of Fluid Mechanics*, Vol. 30, No. 1, 1967, pp. 197–207.

2 Taylor, G. I., "A Model for the Boundary Condition of a Porous Material, Part I," *Journal of Fluid Mechanics*, Vol. 49, No. 2, 1971, pp. 319–326.

3 Richardson, S., "A Model for the Boundary Condition of a Porous Material, Part II," *Journal of Fluid Mechanics*, Vol. 49, No. 2, 1971, pp. 327–336.

4 Carslaw, H. S., and Jaeger, J. C., *Operational Methods in Applied Mathematics*, Dover, 1963, p. 130.

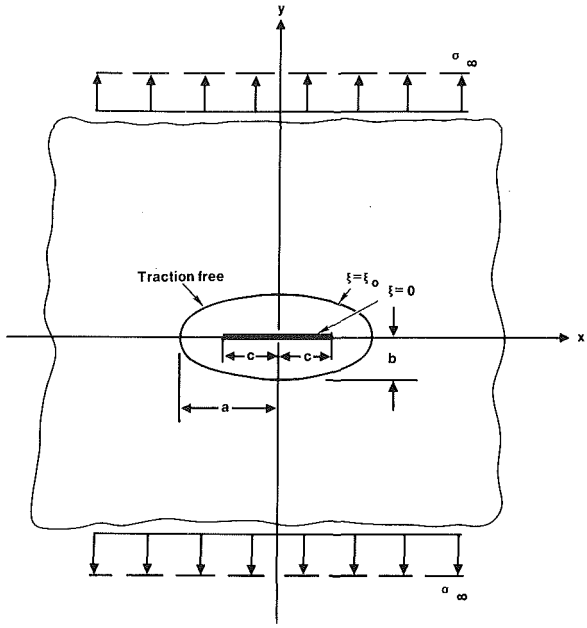


Fig. 1 A line crack in an infinite sheet, subjected to uniaxial tension perpendicular to the major axis. Here $x = c(\cosh\xi\cos\eta)$, $y = c(\sinh\xi\sin\eta)$.

An Elastic-Plastic Solution Around a Tensile Crack in Strain-Hardening Materials

C. Hatleberg[1]

Introduction

One of the more difficult problems in fracture mechanics has been determining an elastic-plastic solution for thin cracked sheets subject to uniaxial tension. Planar elastic solutions have long been available. The best known is by Ingles [1] for a single crack in an infinite sheet. These elastic results were used by Griffith [2] to establish a theory of brittle fracture. Irwin [3] modified Griffith's theory to include small-scale yielding, where the plastic zone is small compared to the crack dimensions. Small scale yielding has been assumed in the crack tip region for a tensile crack in a finite sheet of strain-hardening materials under plane stress conditions by Hutchinson [4]. Hilton and Sih [5] used this solution to solve for the plastic strain intensity factors for a tensile crack in an infinite sheet of strain-hardening materials. The solution presented here is based on the deformation theory of plasticity in conjunction with strain-hardening stress-strain relations, and is found by using the minimum of a modified complementary energy principle coupled with a modified Ritz method.

Analysis

Consider a tensile crack in an infinite sheet of strain-hardening materials under plane stress conditions. The problem is posed in elliptical coordinates (ξ,η), for which a line crack is shown in Fig. 1 as the limiting case of a collapsed ellipse subjected to uniaxial tension perpendicular to the major axis [6].

Based on the deformation theory of plasticity, the total stress components $\sigma_{\xi\xi}, \sigma_{\eta\eta}$ and $\tau_{\xi\eta}$ are related to the corresponding total strains $\epsilon_{\xi\xi}, \epsilon_{\eta\eta}, \gamma_{\xi\eta}$, as follows:

$$\epsilon_{\xi\xi} = \left[\frac{1}{E}\left(\sigma_{\xi\xi} - \upsilon\sigma_{\eta\eta}\right)\right] + \left[\left(\frac{1}{E_s} - \frac{1}{E}\right)\left(\sigma_{\xi\xi} - \frac{1}{2}\sigma_{\eta\eta}\right)\right],$$

$$\epsilon_{\eta\eta} = \left[\frac{1}{E}\left(\sigma_{\eta\eta} - \upsilon\sigma_{\xi\xi}\right)\right] + \left[\left(\frac{1}{E_s} - \frac{1}{E}\right)\left(\sigma_{\eta\eta} - \frac{1}{2}\sigma_{\xi\xi}\right)\right],$$

$$\gamma_{\xi\eta} = \left[\frac{1}{G}\tau_{\xi\eta}\right] + \left[3\left(\frac{1}{E_s} - \frac{1}{E}\right)\tau_{\xi\eta}\right]. \quad (1)$$

The first and second terms on the right-hand side of (1) define the elastic and plastic parts of the strains, and E_s denotes the secant modulus of the uniaxial stress-strain curve at an effective stress, σ_e, given by

$$\sigma_e = \left(\sigma_{\xi\xi}^2 + \sigma_{\eta\eta}^2 - \sigma_{\xi\xi}\sigma_{\eta\eta} + 3\tau_{\xi\eta}^2\right)^{1/2}. \quad (2)$$

In deformation theory, (1) and (2) are valid only if σ_e is continuously increasing at every point in the region; thus, the final solution must be examined to determine if unloading has taken place.

A Ramberg-Osgood stress-strain relations [7] is one way of approximating a uniaxial stress-strain relation for strain-hardening materials.

Another more popular way to approximate a uniaxial stress-strain relation for strain-hardening materials is to use a modified Ramberg-Osgood relation where,[2]

$$E\bar{\epsilon} = \bar{\sigma} \quad \text{for} \quad \bar{\sigma} \le 1.0,$$

$$E\bar{\epsilon} = (\bar{\sigma})^n \quad \text{for} \quad \bar{\sigma} > 1.0. \quad (3)$$

The secant modulus, E_s, is written as

$$E_s = E \quad \text{for} \quad \bar{\sigma} \le 1.0,$$

$$E_s = \frac{E}{(\bar{\sigma})^{n-1}} \quad \text{for} \quad \bar{\sigma} > 1.0. \quad (4)$$

Again, (3) is restricted to monotonically increasing stress or no unloading.

[1] Naval Ocean Systems Center, San Diego, Calif. 92152. Mem. ASME.

Manuscript received by ASME Applied Mechanics Division, November, 1983; final revision, February, 1984.

[2] Barred quantities have been nondimensional with respect to the yield stress, σ_y.

Copyright © 1984 by ASME
Downloaded 02 May 2010 to 171.66.16.25. Redistribution subject to ASME license or copyright; see http://www.asme.org/terms/Terms_Use.cfm

The elastic stress distribution in the infinite sheet is given by Ingles [1] and expressed in terms of elliptical coordinates (ξ,η) as,

$$\bar{\sigma}^E_{\xi\xi} = \frac{\bar{\sigma}\infty}{2A^2} F[\zeta, \cos(2, 4\eta)] \quad (5)$$

$$\bar{\sigma}^E_{\eta\eta} = \frac{\bar{\sigma}\infty}{2A^2} F[\zeta, \cos(2, 4\eta)] \quad (6)$$

$$\bar{\tau}^E_{\xi\eta} = \frac{\bar{\sigma}\infty}{2A^2} F[\zeta, \sin(2, 4\eta)] \quad (7)$$

Here,

$$A = 1 - 2\zeta^2\cos 2\eta + \zeta^4. \quad (8)$$

The total stress distribution in the plastic range may be written in the form [8],

$$\begin{aligned} \sigma_{\xi\xi} &= \sigma^E_{\xi\xi} + \sigma^P_{\xi\xi}, \\ \sigma_{\eta\eta} &= \sigma^E_{\eta\eta} + \sigma^P_{\eta\eta}, \\ \tau_{\xi\eta} &= \tau^E_{\xi\eta} + \tau^P_{\xi\eta}. \end{aligned} \quad (9)$$

The correction stresses ($\sigma^P_{\xi\xi}$, $\sigma^P_{\eta\eta}$ and $\tau^P_{\xi\eta}$) must vanish at infinity and give stress-free conditions on the boundary of the crack. They are derived in terms of coefficients, a_{pq}, and expressed in elliptical coordinates as

$$\bar{\sigma}^P_{\xi\xi} = -4\frac{\zeta^2}{A^2}(1-\zeta)F[A,\zeta,a_{pq}, \cos(2,4,6\eta)] \quad (10)$$

and

$$\bar{\sigma}^P_{\eta\eta} = 4\frac{\zeta^2}{A^2} F[A,\zeta,a_{pq}, \cos(2,4,6\eta)] \quad (11)$$

and

$$\bar{\tau}^P_{\xi\eta} = \frac{-8\zeta^2(1-\zeta)}{A^2} F[A,\zeta,a_{pq}, \sin(2,4,6\eta)] \quad (12)$$

The correction stresses now depend only on the unknown coefficients, a_{pq}, which are determined by using a variational approach in conjunction with a modified Ritz method.

Budiansky and Vidensek [8] considered a modified variational principle to determine the total stresses in an infinite elastic-plastic sheet of strain-hardening materials bounded by internal holes. Under conditions of plane stress, the modified complementary energy, F_{mod}, can be simplified to

$$F_{\text{mod}} = \lim_{R\to\infty}\left\{\int_{A_R}\left[W^P(\sigma_{\alpha\beta}) - W^P(\sigma^E_{\alpha\beta}) + \frac{(\sigma^P_e)^2}{2E}\right]dA - \int_{C_R}(u^P_\alpha T^P_\alpha)ds\right\}. \quad (13)$$

Here, W^P is the plastic stress-energy density, u_α and T_α are the displacement and tractions on the boundary; and A_R is the area between a large circle, C_R, of large radius, R, and the internal boundaries. W, the stress-energy density, is defined as

$$W(\sigma_{\alpha\beta}) = \int_0^{\sigma_{\alpha\beta}} \epsilon_{\alpha\beta}\, d\sigma_{\alpha\beta}, \quad (14)$$

where $\epsilon_{\alpha\beta}$ is the strain component. The subtracted quantities in (13) are valid for any given value of R contribute nothing to the variation. Thus, as the region becomes infinite, the complementary energy remains finite.

The Ritz method was modified by Kachanov [9] to solve the elastic-plastic torsion problem for a rod with a square cross section. This method is used here to overcome the difficulty arising from the nonquadratic nature of the functional, F_{mod}, thus enabling the construction of the correction stresses to the required accuracy. A solution to F_{mod} = min is accomplished through successive approximations of the total stresses associated with the a_{pq}.

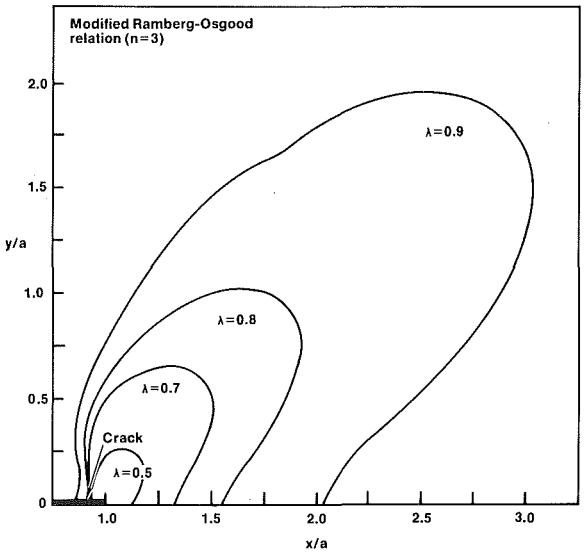


Fig. 2 Elastic-plastic boundaries based on modified Ramber-Osgood relation

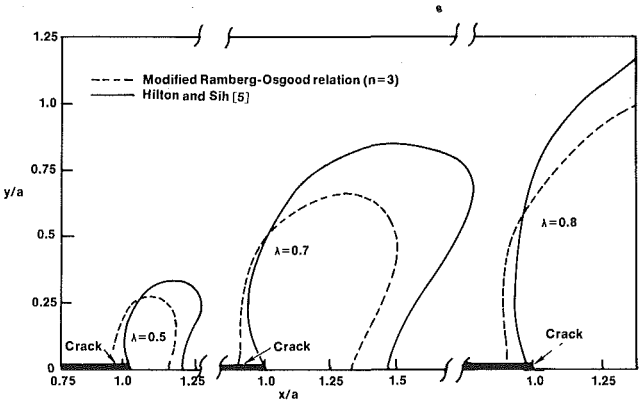


Fig. 3 Elastic-plastic boundaries compared with Hilton and Sih

Results

Using the two successive Simpson's rule approximations for the numerical integration of the associated integrals with the modified Ramberg-Osgood relation, (13) becomes

$$\frac{E}{2a^2\sigma_y{}^2}F_{\text{mod}} = \frac{\pi}{4}\left(\frac{E}{E_s}(r)-1\right)\left(a_{00}{}^{(r)} + 3a_{01}{}^{(r)}\right) + \frac{\pi\zeta_1}{24}\left(\frac{E}{E_s}(r)-1\right)\left(-2a_{00}{}^{(r)} + 2a_{10}{}^{(r)} - 6a_{01}{}^{(r)} + 3a_{11}{}^{(r)}\right) + \frac{\pi(1-\zeta_1)}{36n(2m-1)}\sum_{i=1}^{2m} S_i \sum_{j=1}^{2n} S_j$$

$$[I(i/2m, \pi j/2n)] = \min. \quad (15)$$

Here the superscript, r, refers to the rth approximation and ζ_1 is the first grid point. The terms in the first parentheses are the result of evaluating the line integral in (13) and the terms in the second parentheses are the limit of the area integral in (13) when $\zeta = 0$. In the third term, $2m$ and $2n$ are the number of grid points in the ζ and η direction and S_i and S_j are the Simpson weights associated with the two successive applications of Simpson's rule. For the modified Ramberg-Osgood relation, the term, I, becomes

$$I = \frac{A}{2\zeta^3}\left\{\left(\frac{E}{E_s^{(r)}} - 1\right)\left[\left(\bar{\sigma}_e^{(r)}\right)^2\right.\right.$$

Downloaded 02 May 2010 to 171.66.16.25. Redistribution subject to ASME license or copyright; see http://www.asme.org/terms/Terms_Use.cfm

$$- (\bar{\sigma}_e^E)^2 + (\bar{\sigma}_e^{P(r)})^2]\Big\}. \quad (16)$$

An examination of (5)–(7) and (10)–(12) indicates that a singularity in (9) from (8) develops in (16) as $\zeta \to 1$ and $\eta \to 0$ making the numerical calculation of (15) impossible. To overcome this difficulty, the limit of the term, I (included in (15) and stated in (16)), is computed at the crack tip and found to be zero. This value is then used in (16) at $\zeta = 1$ and $\eta = 0$.

The correction stress coefficients for five different materials, characterized by five different uniaxial stress-strain curves, approximated by a modified Ramberg-Osgood relation were found. Elastic-plastic boundaries are plotted in Fig. 2 where the boundary for the case $\lambda = 1.0$ is separated and not shown.

Budiansky's criterion [10] and unloading were checked and no violations were found over the range of the solution presented.

Comparison of Results

The solution can be examined with respect to the analytical dominant singular solution of Hutchinson [4] and the numerical solution of Hilton and Sih [5]. Qualitatively, the agreement with Hutchinson's solution (Fig. 8 in [4]) for similar Ramberg-Osgood parameters is good.

Figure 3 compares elastic-plastic boundaries from Hilton and Sih's numerical solution with the solution for the same loading factor, λ, and strain-hardening exponent, n.

Qualitatively, the agreement is good. The disparity in plastic zone size may be caused by the relationship of plastic behavior to the singular solution employed in [5] at the crack tip core region breaking down or due to the modified Ramberg-Osgood relation.

Acknowledgment

The author wishes to acknowledge the late Dr. Y.C. Hsu of the Department of Mechanical Engineering at the University of New Mexico who began this work in the early 1970s.

References

1 Ingles, C. E., "Stresses in a Plate Due to the Presence of Cracks and Sharp Corners," *Transactions of the Institute of Naval Architects*, London, Vol. 60, 1913, p. 219.

2 Griffith, A. A., "The Phenomena of Rupture and Flow in Solids," *Philosophical Transactions of the Royal Society*, London, Series *A*, Vol. 221, 1921, p. 163.

3 Irwin, G. R., "Fracture Dynamics," in: *Fracturing of Metals*, American Society for Metals, Cleveland, 1948, p. 147.

4 Hutchinson, J. W., "Plastic Stress and Strain Fields at a Crack Tip," *J. Mech. Phys. Solids*, Vol. 16, 1968, p. 337.

5 Hilton, P. D., and Sih, G. C., "Applications of the Finite Element Method to the Calculations of Stress Intensity Factors," in: *Mechanics of Fracture I*, Noordhoff, Leyden, 1973, p. 426.

6 Coker, E. G., and Filon, L. N. G., *A Treatise on Photo-Elasticity*, Cambridge University Press, London, 1957, pp. 159–161.

7 Ramberg, W., and Osgood, W. R., "Description of Stress-Strain Curves by Three Parameters," NACA TN902, 1943, p. 3

8 Budiansky, B., and Vidensek, R. J., "Analysis of Stresses in the Plastic Range Around a Circular Hole in a Plate Subjected to Uniaxial Tension," NACA TN3542, 1955, pp. 6–13.

9 Kachanov, L. M., *Foundations of the Theory of Plasticity*, American Elsevier, New York, 1971, pp. 370–375.

10 Budiansky, B., "A Reassessment of Deformation Theories of Plasticity," ASME JOURNAL OF APPLIED MECHANICS, Vol. 26, 1959, p. 259.

Downloaded 02 May 2010 to 171.66.16.25. Redistribution subject to ASME license or copyright; see http://www.asme.org/terms/Terms_Use.cfm

Journal of Applied Mechanics

Discussion

Buckling and Postbuckling of a Long-Hanging Elastic Column Due to a Bottom Load[1]

M. M. Bernitsas[2] and T. Kokkinis[2]. The results derived in the paper are valid in two cases:

(1) For columns for which one end can move freely laterally, i.e., an end that does not admit horizontal forces, and that have length greater than 10 bending lengths.

(2) For columns for which both ends are the same vertical line in the limit as their length approaches infinity.

However, in the second case the results are not applicable to columns of large finite length, which is the case of most practical applications. In this case the governing equation, corresponding to equation (4) in the paper, is inhomogeneous, because the column admits horizontal forces at both ends. Global equilibrium of the entire column in the deformed configuration proves this point. For this reason the convergence of the stability boundaries to those of a column of infinite length does not occur within 10 bending lengths. Actually it occurs within 1 percent for lengths greater than 10^{25} bending lengths.

Correct results for this case can be derived for all types of boundary conditions by quasi-asymphotic analysis of the solution to the inhomogeneous problem. The detailed mathematical derivation is in reference [1]. A summary is presented in reference [2].

References

1 Bernitsas, M. M., and Kokkinis, T., "Asymptotic Analysis of Riser Stability Boundaries," Department of Naval Architecture and Marine Engineering, The University of Michigan, Report #255, Nov. 1982.

2 Bernitsas, M. M., and Kokkinis, T., "Asymptotic Behavior of Column and Riser Stability Boundaries," submitted for publication to ASME JOURNAL OF APPLIED MECHANICS.

Author's Closure

My paper investigated the case where the bottom load is free to move horizontally. Drs. Bernitsas and Kokkinis correctly stated the validity of my results. I have not studied the interesting case where both ends are always vertically aligned.

[1] By C. Y. Wang, and published in the June 1983 issue of ASME JOURNAL OF APPLIED MECHANICS, Vol. 50, pp. 311-314.

[2] Department of Naval Architecture and Marine Engineering, North Campus, The University of Michigan, Ann Arbor, Mich. 48109.

An Analysis of Adhesive-Bonded Single-Lap Joints[1]

D. J. Allman[2]. I note that the paper by Chen and Cheng [1] develops an essentially indentical theory to my paper [2] published in the *Quarterly Journal of Mechanics and Applied Mathematics*, 1977. Although the latter paper is often referenced by British authors [3, 4], it seems to have not yet penetrated the American technical literature. The paper presents analytic solutions for a wide range of lap joints with very thin adhesive layers, rigid adherends, typical metal adherends, and typical composite adherends. It is also relevant to mention the finite element application of the theory to lap joints with dissimilar adherends which is described in reference [5].

References

1 Chen, D., and Cheng, S., "An Analysis of Adhesive-Bonded Single-Lap Joints," ASME JOURNAL OF APPLIED MECHANICS, Vol. 50, 1983, pp. 109-115.

2 Allman, D. J., "A Theory for Elastic Stresses in Adhesive Bonded Lap Joints," *Quarterly Journal of Mechanics and Applied Mathematic*, Vol. XXX, 1977, pp. 415-436.

3 Wake, W. C., *Adhesion and the Formulation of Adhesives*, Applied Science, 1982.

4 Allen, K. W., ed., *Adhesion 4*, Applied Science, 1980.

5 Brooker, M. J., "The Stress Distribution in Adhesively Bonded Lap Joints," MSC Thesis, Department of Aeronautics, Imperial College of Science and Technology, 1980.

Authors' Closure

The authors wish to thank Dr. Allman for bringing his paper to their attention and express their regret for having overlooked his work.

We wish to mention, however, that the method of approach of the two papers is quite different despite the fact that both are based on essentially similar assumptions and that the resulting governing differential equations are also different. We feel the method used in our paper, which deals directly with the components of stress which is the main object of the analysis, is more direct and simple. In this way, a closed-form solution that is adaptable for any possible adhesive layer flexibility and capable of satisfying all the boundary stress conditions of the joint is obtained. To illustrate the application of the present unified theory and to examine the

[1] By Du Chen and Shun Cheng, and published in the March 1983 issue of the ASME JOURNAL OF APPLIED MECHANICS, Vol. 50, pp. 109-115.

[2] Department of Materials and Structures, Royal Aircraft Establishment, Farnborough, Hants, England.

Copyright © 1984 by ASME
Downloaded 02 May 2010 to 171.66.16.25. Redistribution subject to ASME license or copyright; see http://www.asme.org/terms/Terms_Use.cfm

Journal of Applied Mechanics

Book Reviews

Finite Elements for Structural Analysis. By William Weaver Jr. and Paul R. Johnston. Prentice-Hall, Inc., Englewood Cliffs, N.J., 1984. 404 Pages. Price $38.95.

REVIEWED BY A. S. DOUGLAS[1]

The authors have provided another basic text on the use of the finite element method in structural mechanics. The reader is assumed to be familiar with the basic mathematics usually included in undergraduate engineering curricula (including matrix algebra) and is not required to have any previous exposure to elasticity. The principle of virtual work is used as the basis of the finite element procedure but while the potential energy basis is also given, no mention is made of variational calculus.

After a brief discussion on discretization of the solid continuum, the principle of virtual work is stated and used to develop the finite element method for the one-dimensional elastic beam element. This is followed by an introduction to generalized stresses and strains and to axis transformations. The first chapter is completed by brief comments on the potential energy basis for the finite element method and elementary criteria required for convergence.

Subsequent chapters develop the method for the basic structural systems beginning with plane stress and strain. All the details of the matrices are presented for linear strain elements. The calculation of the right-hand side vector is well presented. While the authors comment briefly on their choice of a mesh in an example, they do not give adequate attention to mesh characteristics, such as element aspect ratios and discontinuous changes in element size, which can adversely affect results.

Isoparametric elements for two-dimensional elements are clearly introduced and the authors explanation of their implementation is enhanced by macroflow charts. Only passing mention is made of super and subparametric elements. This development is extended to the general three-dimensional solid.

Attention is then given to those systems pertinent to the structural engineer. This begins with the details of axisymmetric solids which includes a useful discussion of nonaxisymmetric loads. (Uncharacteristically, the details of axisymmetric elements which have nodes on the axis of revolution are omitted.) Subsequent development includes plate and shell elements.

The authors now turn their attention to two important aspects of the behavior of the structural system, namely those of vibration analysis and stability analysis. While the presentation of the physical and mathematical basis for the existence of natural frequencies is terse, the construction of consistent and lumped mass matrices is well developed. For stability analysis, the authors return to the potential energy formulation, but their mathematical basis is again brief.

The text concludes with useful appendices covering integration formulas, Gaussian quadrature, and some computer methods for solving linear equations (including detailed flow charts). Each chapter is followed by examples, a macroflow chart (which clarifies the procedures developed), a number of problems, and a few important references. The problems are directed primarily at developing facility with the basic steps. Few of them are designed to entertain a critical analysis of the finite element method.

Overall, the authors have provided an excellent text for engineering students and practitioners who want to learn the basic procedures involved in the finite element method. The book contains much detail not found in other introductory texts, but, as the title implies, it is strictly limited to structual applications. This book has not attempted to foster a critical appraisal of the finite element method, nor does it address some important practical issues, such as the appropriate choice of elements and the rational prescription of meshes.

Numerical and Physical Aspects of Aerodynamic Flows II. Edited by Tuncer Cebeci. Springer-Verlag, New York, 1984. 416 Pages. Price $58.00.

REVIEWED BY S. WIDNALL[2]

This book contains a portion of the proceedings of a symposium by the same name held at California State University in January 1983. Exclusive of a keynote address by A. M. O. Smith, all of the papers are devoted to two-dimensional aerodynamic calcuations. The focus is on viscous-inviscid interactions in both subsonic and transonic flows. The papers deal with the development and evaluation of calculation methods for flows around airfoils, especially with regions of separated flow, and for downstream wakes. Subjects discussed include Navier–Stokes methods, interactive methods, and analytical methods. A review paper on the calculation of two-dimensional flow past airfoils by Cebeci, Stewartson, and Whitelaw opens the proceedings. The volume is dedicated to Keith Stewartson.

[1]Assistant Professor, Department of Mechanics, The Johns Hopkins University, Baltimore, MD 21218.

[2]Professor, Department of Aeronautics and Astronautics, Massachusetts Institute of Technology, Cambridge, Mass. 02139.

Copyright © 1984 by ASME
Downloaded 02 May 2010 to 171.66.16.25. Redistribution subject to ASME license or copyright; see http://www.asme.org/terms/Terms_Use.cfm

Nonlinear Deformation Waves. Edited by U. Nigul and J. Engelbrecht. Springer-Verlag, New York, 1983. 452 Pages. Price $42.50.

REVIEWED BY T. W. WRIGHT[3]

This volume contains the papers presented at an IUTAM Symposium held at Tallinn, Estonia, in August 1982. There are 45 papers in the volume, slightly more than half from Eastern European countries, principally Russia, the others from the rest of the world with 16 different countries represented in all. The book is divided into five parts: Part 1, Analytical Methods and Evolution Equations (13 papers); Part 2, Waves in Hereditary and Plastic Media (10 papers); Part 3, Inverse Problems (6 papers); Part 4, Nonlinear Acoustics (5 papers); and Part 5, Combined Fields and Applications (11 papers).

As might be expected in a symposium of this kind, the quality of the papers is rather uneven. Many of the best ones are surveys of the author's and related work, and as such they contain a number of references, which may serve as a useful, general guide to a somewhat specialized and often scattered literature. The papers by Taniuti, Crighton, Blackstock, and Grimshaw all fall in this category. Taniuti reviews the reductive perturbation method as applied to systems of equations with dispersion or dissipation for which the basic models are the Korteweg-de Vries or Burgers equations. Crighton summaries the ways in which a modified Burgers equation can be used to model the propagation of shock waves over large distances, including geometric and viscoelastic effects and the ways in which the shock structure can break down. Matched asymptotic expansions play a strong role here. Blackstock describes many interesting phenomena in the interaction of colinear sound beams, with application such as the parametric transmitting array, self-demodulation, and sound suppression. Grimshaw uses model equations to analyze the propagation of long waves in stratified shear flows, which has important applications in geophysical fluids. Solitary waves are especially emphasized. There are interesting research papers throughout the book which touch on topics as diverse as solitions in active media (Ostrovsky), gas or liquid filled tubes (Buggisch, and Mainardi and Buggisch), edge waves along a sloping beach (Akylas), localized deformation in metals and polymers (Barenblatt), nonlinear elastic surface waves (Parker and Talbot), and the propagation of domain walls in ferroelectric crystals (Maugin and Pouget), to single out just a few which appealed to this reviewer.

The many other papers cover a wide range of applications that arise in very disparate physical situations, but the preceding comments have already introduced most of the principal themes that recur throughout the book. These are model equations, solitary waves, and various asymptotic methods to describe evolutionary changes in systems where the nonlinearity is of relatively low order. The emphasis is decidedly analytical rather than experimental or computational although some work of the latter types is reported. It was disappointing to find only one example of similarity techniques and no example at all of the modifed simple wave analysis as developed by Varley and coworkers, since these two methods do find applications in problems with stronger nonlinearities.

Although the volume will appeal mostly to specialists, it serves a useful purpose in summarizing some of the principal methods in vogue today for analyzing problems of nonlinear wave propagation, and in showing the wide range of physical problems to which these methods may be applied.

[3]Ballistic Research Laboratory, Aberdeen Proving Ground, Md. 21005. Mem. ASME.

Finite Elasticity. Edited by D. E. Carlson and R. T. Shield. Martinus Nijhoff, The Netherlands, 1982. 460 Pages. Price $79.00.

REVIEWED BY M. M. CARROLL[4]

The IUTAM Symposium on Finite Elasticity was held at Lehigh University, Bethlehem, Pa., August 10–15, 1980. This Proceedings volume contains a Foreword by R. S. Rivlin, who chaired the international scientific committee, as well as the texts of the five general lectures and 24 invited papers. The committee is to be congratulated on constructing an excellent program, which embraces mathematical foundations, solution techniques, experimental investigations, and emphasizes new and exciting research directions in this important field.

The lectures and papers present excellent summaries of a wide variety of special topics, with useful references to earlier work. This volume should be required reading for workers in nonlinear elasticity. It is also very worthwhile reading for workers in other areas of nonlinear continuum mechanics. The complete list of topics and authors follow.

General Lectures

J. M. Ball, "Existence of Solutions in Finite Elasticity."

W. T. Koiter, "Elastic Stability, Buckling and Post-Buckling Behavior."

G. J. Lake and A. G. Thomas, "Mechanics of Fracture of Rubber-Like Materials."

P. M. Naghdi, "Finite Deformation of Elastic Rods and Shells."

R. S. Rivlin, "Some Thoughts on Material Stability."

Invited Papers

P. G. Ciarlet, "Two-Dimensional Approximations of Three-Dimensional Models in Nonlinear Plate Theory."

P. K. Currie and M. Hayes, "On Nonuniversal Finite Elastic Deformations."

G. Duvaut, "Nonlinear Boundary Value Problem in Thermoelasticity.

J. L. Ericksen, "Changes in Symmetry in Elastic Crystals."

G. Grioli, "A Variational Approach to Finite Elasticity."

M. E. Gurtin, "On Uniqueness in Finite Elasticity."

A. G. Herrmann, "On Physical and Material Conservation Laws."

J. M. Hill, "Finite Deformation of Thick-Walled Inner Tubes and Tyres Under Inflation and Rotation."

J. W. Hutchinson and K. W. Neale, "Finite Strain J_2 Deformation Theory."

F. John, "Instability of Finite Amplitude Elastic Waves."

J. K. Knowles, "Localized Shear Near the Tip of a Crack in Finite Elastostatics."

I. Müller, "Stress-Strain-Temperature Curves in Pseudoelastic Bodies."

J. T. Oden, "Penalty Methods for Constrained Problems in Nonlinear Elasticity."

R. W. Ogden and D. M. Haughton, "Deformation and Vibration of Rotating Elastic Cylinders."

[4]Professor, Department of Mechanical Engineering, University of California, Berkeley, California 94720. Mem. ASME.

Copyright © 1984 by ASME
Downloaded 02 May 2010 to 171.66.16.25. Redistribution subject to ASME license or copyright; see http://www.asme.org/terms/Terms_Use.cfm

A. C. Pipkin, "Boundary Integral Equations for Inextensible Materials."

K. N. Sawyers, "Stability of a Thick Neo-Hookean Plate."

R. T. Shield, "Finite Extension of Torsion of Thin Elastic Strips."

R. Skalak, "Growth as a Finite Displacement Field."

A. J. M. Spencer, "Stress Concentration Layers in Finite Deformation of Fiber-Reinforced Elastic Materials."

E. Stein, "Incremental Methods in Finite Elasticity, Especially for Rods."

T. Valent, "Local Theorems of Existence and Uniqueness in Finite Elastostatics."

T. W. Wright, "Nonlinear Waves in Rods."

L. J. Zapas, "The Strain-Energy Function for Rubber-Like Materials."

Handbook of Applied Mathematics: Selected Results and Methods, Second Edition. Edited by Carl E. Pearson. Van Nostrand Reinhold, New York, 1983. 1328 Pages. Price $67.50.

REVIEWED BY L. B. FREUND[5]

This volume contains 21 chapters on various topics in applied mathematics. The chapters have been written by 20 individuals, each of whom has been involved with the applications of mathematics, mostly in the physical sciences and engineering. The following topics are discussed in one or more chapters: basic analysis, vectors, tensors, complex variables, ordinary differential equations, partial differential equations, special functions, integral equations, transform methods, asymptotic methods, perturbation methods, linear algebra, functional approximation, numerical analysis, optimization techniques, probability, and statistics. Also included are chapters on several particular areas of application, namely, oscillations, wave propagation, and formulation of mathematical models.

The volume is not a handbook in the usual sense, that is, it is not a collection of tables and formulas. Instead, each chapter represents the author's summary description of the chapter topic, with emphasis on the ideas and techniques of potential value in problem solving. Motivation is provided from the applied sciences for most of the topics discussed and the presentation is generally descriptive, rather than formal. Based on a close look at several of the chapters in areas most familiar to me, the treatment is quite complete. The chapters have been prepared independently, without cross-referencing, so that some topics are covered more than once, usually from different points of view. The volume does include an extensive index of 32 pages, so that the place in which any particular topic is considered can easily be determined. For example, the Wiener-Hopf method can be found in the chapter on transform methods, variational methods are discussed mainly in the chapters on ordinary differential equations and on optimization, and the finite element method is briefly introduced in the chapter on partial differential equations of second and higher order.

The coverage appears to be quite complete within the branch of mathematics commonly termed analysis. The rationale for including two chapters on specific applications, namely, wave propagation and oscillations (nonlinear vibrations), is not clear. It would be difficult to argue that the treatment of any paticular topic in the Handbook would be preferable to that in one of those favorite text books most people have on their bookshelves. However, this volume has the advantage of providing a quick reference to a wide range of topics. The Handbook is a reference work of significant potential value to anyone concerned with application of analytical methods in applied mechanics.

[5] Professor, Division of Engineering, Brown University, Providence, R.I. 02912. Fellow, ASME.

Statistical Mechanics of Elasticity. By J. H. Weiner. Wiley, New York, 1983. 439 Pages. Price $49.50.

REVIEWED BY F. MILSTEIN[6]

Professor Weiner is to be congratulated for a timely, scholarly, and well-written book which makes a significant contribution to the pedagogic literature on atomic-based descriptions of the elastic behavior of both crystalline and polymeric solids. The content and style of the book reflect its origins; i.e., it is an outgrowth of a course, for graduate students in solid mechanics, "intended to provide an alternative to the usual course in statistical mechanics in which the major emphasis of application is to gases and liquids and to electronic and magnetic phenomena." Although the book is written mainly for the solid mechanics community (e.g., it employs advanced mathematics of continuum solid mechanics after but a brief chapter on the fundamentals of solid mechanics and classical thermodynamics), it also contains a wealth of material (including "standard" topics, recent research results, and an extensive list of references) that will be of immense value and interest to researchers and advanced graduate students in the fields of materials science and solid state physics (as well as solid mechanics).[7]

The book is divided into two parts; the first (which is about twice the length of the second), develops the principles of classical statistical mechanics and then presents a wide variety of applications of these principles in chapters on crystal elasticity, rubber elasticity, and rate theory in solids. The development of statistical mechanics follows "the approach that relates the quantities calculated by the methods of equilibrium statistical mechanics to time averages of observed properties." The author states that this treatment is heuristic; workers concerned with the foundations of statistical mechanics will no doubt find it so, although materials scientists and others who are mainly concerned with applications might find the development leaning toward rigor and formalism. The value of the book to researchers in mechanics and materials is enhanced by the authors choice of applications (which comprise over one-third of the book, and which, in many cases, are of current interest in the literature). The presentation on crystal elasticity contains discussions of the atomistic concept of stress, elastic constants and their temperature dependence, the Cauchy relations, and lattice dynamics. Two chapters on rubber elasticity include atomic structure, one and three-dimensional polymer models, the network theory of rubber elasticity, partition functions for rigid and flexible polymer models, stress and strain ensembles, and phantom networks. Impurity atom diffusion,

[6] Professor, Department of Mechanical and Environmental Engineering, University of California, Santa Barbara, Calif. 93106. Mem. ASME.

[7] Footnotes are effectively used throughout to provide important details, including selected references to original papers or to sources of additional information, and interesting historical notes; e.g., (p. 388) Einstein (1911) computed atomic frequencies from specific heats and from elastic properties and called "the agreement (~ 20 percent) between these two frequencies 'wahrhaft überraschend' [truly surprising]."

Copyright © 1984 by ASME
Downloaded 02 May 2010 to 171.66.16.25. Redistribution subject to ASME license or copyright; see http://www.asme.org/terms/Terms_Use.cfm

Brownian motion, and Kramer's rate formula are included in the rate theory chapter. One suggestion (for a possible second edition) would be the inclusion of more applications that are carried through to quantitative conclusions, such as specific atomic based-computations of elastic behavior of crystals, including finite, nonlinear deformation (some examples can be found in *Mechanics of Solids*, edited by H. G. Hopkins and M. J. Sewell, Pergamon Press, 1982).

The second part begins with a clear, concise, self-contained chapter on the basic concepts of quantum mechanics, intended for mathematically sophisticated readers without prior quantum mechanics background. In the subsequent chapters, quantum mechanical concepts are employed in discussions of interatomic interactions, and quantum statistical mechanics is formulated and applied to situations where quantum effects become important, including specific heat and elastic moduli at low temperature and quantum tunneling and its influence on rate processes. The variety of topics in the quantum mechanics sections is less extensive than in the sections on classical (i.e., nonquantum) phenomena, although a good selection of quantum-based applications is included (some of these, e.g., elastic moduli based on the Hellmann-Feynman theorem, evidently have not yet appeared in other texts). One omission that is notable (because of its usefulness in computing atomic bonding and elastic constants in a wide variety of crystals) in the pseudopotential method.

In summary, Professor Weiner has written a splendid book which should encourage workers and students in solid mechanics to focus their attention on the atomic bases of material deformation, as well as to provide materials scientists and solid state physicists with an appreciation for the value of combining solid mechanics and atomistic approaches in the study of mechanical properties.

Stress Analysis for Creep. By J. T. Boyle and J. Spence. Butterworths, Woburn, Mass., 1982. 283 Pages. Price $59.95.

REVIEWED BY Z. P. BAŽANT[8]

This book by well-known experts is a valuable addition to the literature on creep of metals at high temperatures. As the title suggests, the book is more concerned with engineering mechanics than with the problems of constitutive relation. The first two chapters explain the nature of creep, the consequences of this phenomenon for the behavior of structures, and the basic types of stress-strain relations for creep. The next two chapters present a set of typical simple examples of one-dimensional and three-dimensional structural response to steady, transient, and cyclic creep. Chapter five, dealing with steady-state creep analysis, concentrates on the use of energy principles but also explains iterative numerical methods where particular attention is paid to linearization by differentiation (quasilinearization). Chapter six discusses how the stress-strain law can be identified on the basis of reference data consisting only of uniaxial test results. In the next chapter, the authors focus on stress analysis for transient creep; first the mathematical statement of the problem is given and then numerical methods are discussed in detail, including both the explicit and implicit integrations in time, along with the questions of numerical stability of various schemes, error estimates and handling of stiff equations. This then leads to an exposition of approximate methods for transient creep problems in chapter eight, in which various bounding techniques and convergence questions are lucidly analyzed. Discussion of simplifications such as the exploitation of other known solutions based on comparison theorems are particularly useful. The subsequent two chapters examine two possible types of failure due to creep, i.e., creep rupture and creep buckling. The existing mathematical models to describe material damage are presented and a relatively new approach known as continuum damage mechanics is introduced. Creep buckling is illustrated by typical examples, and this discussion is then extended to creep in presence of large deformations. The final, eleventh chapter addresses the principal concern – the design for creep, including the current design methodologies and identification of the material parameters from the given creep data and their extrapolation.

The book represents an outstanding contribution to the literature on the subject, and only very few critical points can be raised. References in the text are in most chapters somewhat limited and selective bibliographies are substituted for reference lists. The discussion of continuous damage mechanics would have benefited by warning of possible material instability, such as strain-localization, and of the lack of the size effect in failure, which are inherent to this approach. The drawings of the inclined views of three-dimensional situations in Figs. 4.7 and 7.12 are self-contradictory; they ignore the principles of descriptive geometry, as abstract painters do, and are disturbing to the trained eye of an engineer. From the viewpoint of present practice the finite element approach could be treated in more detail, and more attention could be given to constitutive laws that often cause a greater error than the method of stress analysis. It is also curious that the step-by-step time integration is not treated systematically as a sequence of incremental elastic problems with initial strains, as is commonplace in the creep analysis of concrete structures. In fact, the book as a whole reflects the fact that the creep theories of metals and of concrete are evolving in isolation, although one of these could not doubt benefit from the other despite fundamental differences in the constitutive law (cf. Z. P. Bažant and F. H. Wittmann, editors, *Creep and Shrinkage in Concrete Structures*, Wiley, London, 1983).

These points are, however, minor in view of the many strong aspects, among which the up-to-date and perspicacious treatment of approximate methods and bounding technique may be emphasized. In contrast to previous books on the subject, the examples are not elementary but deal with real life situations in which the difficulties of stress analysis must be confronted. The authors work out their examples in considerable detail and make frequent use of the computer, in the spirit of their motto: "To appreciate creep analysis, the reader must compute. If he does not, his understanding of the subject will be poorer." On the whole, the book is highly recommended to students of the subject as well as researchers and practicing engineers.

Fundamental Concepts in the Numerical Solution of Differential Equations. By Joseph Botha and George Pinder. Wiley, New York, 1983. 202 Pages. Price $24.95.

REVIEWED BY A. T. PATERA[9]

This book presents the finite-difference, Galerkin-based finite-element, and collocation-based finite element techniques for numerical solution of elliptic, parabolic, and hyperbolic partial differential equations. The book contains seven chapters. The first chapter reviews notation and general

[8] Professor, Department of Civil Engineering, Northwestern University, Evanston, Ill. 60201. Mem. ASME.

[9] Assistant Professor, Massachusetts Institute of Technology, Cambridge, Mass. 02139.

Copyright © 1984 by ASME
Downloaded 02 May 2010 to 171.66.16.25. Redistribution subject to ASME license or copyright; see http://www.asme.org/terms/Terms_Use.cfm

ERRATA

Erratum on "An Extended Weight Function Method for Mixed-Mode Elastic Crack Analysis," by Y. Bortman and L. Banks-Sills, and published in the December 1983 issue of the ASME JOURNAL OF APPLIED MECHANICS, Vol. 50, pp. 907–909.

On page 909, equation (3.4) should read as follows:

$$K_I = \frac{1}{\sqrt{2\pi l}} \int_0^l \left\{ \frac{1-2\nu}{2(1-\nu)} \tilde{T}_x + \sqrt{\frac{x}{l-x}} \hat{T}_y \right\} dx$$

$$K_{II} = \frac{1}{\sqrt{2\pi l}} \int_0^l \left\{ \sqrt{\frac{x}{l-x}} \hat{T}_x - \frac{1-2\nu}{2(1-\nu)} \tilde{T}_y \right\} dx \quad (3.4)$$

where $\tilde{T}_i = T_i^{(+)} + T_i^{(-)}$, $\hat{T}_i = T_i^{(+)} - T_i^{(-)}$

Equation (3.6) should read as follows:

$$K_I = \frac{P}{2\sqrt{\pi a}} \sqrt{\frac{a+b}{a-b}} + \frac{Q}{4\sqrt{\pi a}} \frac{1-2\nu}{1-\nu}$$

$$K_{II} = \frac{Q}{2\sqrt{\pi a}} \sqrt{\frac{a+b}{a-b}} - \frac{P}{4\sqrt{\pi a}} \frac{1-2\nu}{1-\nu} \quad (3.6)$$

Copyright © 1984 by ASME
Downloaded 02 May 2010 to 171.66.16.25. Redistribution subject to ASME license or copyright; see http://www.asme.org/terms/Terms_Use.cfm